Development of Ground Damage and its Correlation with Underground Mining

Lead Guest Editor: Dezhong Kong
Guest Editors: Gaofeng Song, Hao Wu, Zhanbo Cheng, and Zhaohui Wang

Development of Ground Damage and its Correlation with Underground Mining

Development of Ground Damage and its Correlation with Underground Mining

Lead Guest Editor: Dezhong Kong
Guest Editors: Gaofeng Song, Hao Wu, Zhanbo Cheng, and Zhaohui Wang

Zhaofei Chu iD, China
Wonseok Chung iD, Republic of Korea
Donato Ciampa iD, Italy
Gian Paolo Cimellaro, Italy
Francesco Colangelo, Italy
Romulus Costache iD, Romania
Liviu-Adrian Cotfas iD, Romania
Antonio Maria D'Altri, Italy
Bruno Dal Lago iD, Italy
Amos Darko iD, Hong Kong
Arka Jyoti Das iD, India
Dario De Domenico iD, Italy
Gianmarco De Felice iD, Italy
Stefano De Miranda iD, Italy
Maria T. De Risi iD, Italy
Tayfun Dede, Turkey
Sadik O. Degertekin iD, Turkey
Camelia Delcea iD, Romania
Cristoforo Demartino, China
Giuseppe Di Filippo iD, Italy
Luigi Di Sarno, Italy
Fabio Di Trapani iD, Italy
Aboelkasim Diab iD, Egypt
Thi My Dung Do, Vietnam
Giulio Dondi iD, Italy
Jiangfeng Dong iD, China
Chao Dou iD, China
Mario D'Aniello iD, Italy
Jingtao Du iD, China
Ahmed Elghazouli, United Kingdom
Francesco Fabbrocino iD, Italy
Flora Faleschini iD, Italy
Dingqiang Fan, Hong Kong
Xueping Fan, China
Qian Fang iD, China
Salar Farahmand-Tabar iD, Iran
Ilenia Farina, Italy
Roberto Fedele, Italy
Guang-Liang Feng iD, China
Luigi Fenu iD, Italy
Tiago Ferreira iD, Portugal
Marco Filippo Ferrotto, Italy
Antonio Formisano iD, Italy
Guoyang Fu, Australia
Stefano Galassi iD, Italy

Junfeng Gao iD, China
Meng Gao iD, China
Giovanni Garcea iD, Italy
Enrique García-Macías, Spain
Emilio García-Taengua iD, United Kingdom
DongDong Ge iD, USA
Khaled Ghaedi, Malaysia
Khaled Ghaedi iD, Malaysia
Gian Felice Giaccu, Italy
Agathoklis Giaralis iD, United Kingdom
Ravindran Gobinath, India
Rodrigo Gonçalves, Portugal
Peilin Gong iD, China
Belén González-Fonteboa iD, Spain
Salvatore Grasso iD, Italy
Fan Gu, USA
Erhan Güneyisi iD, Turkey
Esra Mete Güneyisi, Turkey
Pingye Guo iD, China
Ankit Gupta iD, India
Federico Gusella iD, Italy
Kemal Hacıefendioğlu, Turkey
Jianyong Han iD, China
Song Han iD, China
Asad Hanif iD, Macau
Hadi Hasanzadehshooiili iD, Canada
Mostafa Fahmi Hassanein, Egypt
Amir Ahmad Hedayat iD, Iran
Khandaker Hossain iD, Canada
Zahid Hossain iD, USA
Chao Hou, China
Biao Hu, China
Jiang Hu iD, China
Xiaodong Hu, China
Lei Huang iD, China
Cun Hui iD, China
Bon-Gang Hwang, Singapore
Jijo James iD, India
Abbas Fadhil Jasim iD, Iraq
Ahad Javanmardi iD, China
Krishnan Prabhakan Jaya, India
Dong-Sheng Jeng iD, Australia
Han-Yong Jeon, Republic of Korea
Pengjiao Jia, China
Shaohua Jiang iD, China

Chayut Ngamkhanong (iD), Thailand
Trung Ngo, Australia
Tengfei Nian, China
Mehdi Nikoo (iD), Canada
Youjun Ning (iD), China
Olugbenga Timo Oladinrin (iD), United Kingdom
Oladimeji Benedict Olalusi, South Africa
Timothy O. Olawumi (iD), Hong Kong
Alejandro Orfila (iD), Spain
Maurizio Orlando (iD), Italy
Siti Aminah Osman, Malaysia
Walid Oueslati (iD), Tunisia
SUVASH PAUL (iD), Bangladesh
John-Paris Pantouvakis (iD), Greece
Fabrizio Paolacci (iD), Italy
Giuseppina Pappalardo (iD), Italy
Fulvio Parisi (iD), Italy
Dimitrios G. Pavlou (iD), Norway
Daniele Pellegrini (iD), Italy
Gatheeshgar Perampalam (iD), United Kingdom
Daniele Perrone (iD), Italy
Giuseppe Piccardo (iD), Italy
Vagelis Plevris (iD), Qatar
Andrea Pranno (iD), Italy
Adolfo Preciado (iD), Mexico
Chongchong Qi (iD), China
Yu Qian, USA
Ying Qin (iD), China
Giuseppe Quaranta (iD), Italy
Krishanu ROY (iD), New Zealand
Vlastimir Radonjanin, Serbia
Carlo Rainieri (iD), Italy
Rahul V. Ralegaonkar, India
Raizal Saifulnaz Muhammad Rashid, Malaysia
Alessandro Rasulo (iD), Italy
Chonghong Ren (iD), China
Qing-Xin Ren, China
Dimitris Rizos (iD), USA
Geoffrey W. Rodgers (iD), New Zealand
Pier Paolo Rossi, Italy
Nicola Ruggieri (iD), Italy
JUNLONG SHANG, Singapore

Nikhil Saboo, India
Anna Saetta, Italy
Juan Sagaseta (iD), United Kingdom
Timo Saksala, Finland
Mostafa Salari, Canada
Ginevra Salerno (iD), Italy
Evangelos J. Sapountzakis (iD), Greece
Vassilis Sarhosis (iD), United Kingdom
Navaratnarajah Sathiparan (iD), Sri Lanka
Fabrizio Scozzese (iD), Italy
Halil Sezen (iD), USA
Payam Shafigh (iD), Malaysia
M. Shahria Alam, Canada
Yi Shan, China
Hussein Sharaf, Iraq
Mostafa Sharifzadeh, Australia
Sanjay Kumar Shukla, Australia
Amir Si Larbi (iD), France
Okan Sirin (iD), Qatar
Piotr Smarzewski (iD), Poland
Francesca Sollecito (iD), Italy
Rui Song (iD), China
Tian-Yi Song, Australia
Flavio Stochino (iD), Italy
Mayank Sukhija (iD), USA
Piti Sukontasukkul (iD), Thailand
Jianping Sun, Singapore
Xiao Sun (iD), China
T. Tafsirojjaman (iD), Australia
Fujiao Tang (iD), China
Patrick W.C. Tang (iD), Australia
Zhi Cheng Tang (iD), China
Weerachart Tangchirapat (iD), Thailand
Xiaxin Tao, China
Piergiorgio Tataranni (iD), Italy
Elisabete Teixeira (iD), Portugal
Jorge Iván Tobón (iD), Colombia
Jing-Zhong Tong, China
Francesco Trentadue (iD), Italy
Antonello Troncone, Italy
Majbah Uddin (iD), USA
Tariq Umar (iD), United Kingdom
Muahmmad Usman, United Kingdom
Muhammad Usman (iD), Pakistan
Mucteba Uysal (iD), Turkey

Ilaria Venanzi (iD), Italy
Castorina S. Vieira (iD), Portugal
Valeria Vignali (iD), Italy
Claudia Vitone (iD), Italy
Liwei WEN (iD), China
Chunfeng Wan (iD), China
Hua-Ping Wan, China
Roman Wan-Wendner (iD), Austria
Chaohui Wang (iD), China
Hao Wang (iD), USA
Shiming Wang (iD), China
Wayne Yu Wang (iD), United Kingdom
Wen-Da Wang, China
Xing Wang (iD), China
Xiuling Wang (iD), China
Zhenjun Wang (iD), China
Xin-Jiang Wei (iD), China
Tao Wen (iD), China
Weiping Wen (iD), China
Lei Weng (iD), China
Chao Wu (iD), United Kingdom
Jiangyu Wu, China
Wangjie Wu (iD), China
Wenbing Wu (iD), China
Zhixing Xiao, China
Gang Xu, China
Jian Xu (iD), China
Panpan (iD), China
Rongchao Xu (iD), China
HE YONGLIANG, China
Michael Yam, Hong Kong
Hailu Yang (iD), China
Xu-Xu Yang (iD), China
Hui Yao (iD), China
Xinyu Ye (iD), China
Zhoujing Ye , China
Gürol Yildirim (iD), Turkey
Dawei Yin (iD), China
Doo-Yeol Yoo (iD), Republic of Korea
Zhanping You (iD), USA
Afshar A. Yousefi (iD), Iran
Xinbao Yu (iD), USA
Dongdong Yuan (iD), China
Geun Y. Yun (iD), Republic of Korea

Hyun-Do Yun (iD), Republic of Korea
Cemal YİĞİT (iD), Turkey
Paolo Zampieri, Italy
Giulio Zani (iD), Italy
Mariano Angelo Zanini (iD), Italy
Zhixiong Zeng (iD), Hong Kong
Mustafa Zeybek, Turkey
Henglong Zhang (iD), China
Jiupeng Zhang, China
Tingting Zhang (iD), China
Zengping Zhang, China
Zetian Zhang (iD), China
Zhigang Zhang (iD), China
Zhipeng Zhao (iD), Japan
Jun Zhao (iD), China
Annan Zhou (iD), Australia
Jia-wen Zhou (iD), China
Hai-Tao Zhu (iD), China
Peng Zhu (iD), China
QuanJie Zhu (iD), China
Wenjun Zhu (iD), China
Marco Zucca, Italy
Haoran Zuo, Australia
Junqing Zuo (iD), China
Robert Černý (iD), Czech Republic
Süleyman İpek (iD), Turkey

Contents

Research Article

Improvement of Gas Drainage Efficiency via Optimization of Sealing Depth of Cross-Measure Boreholes

Pu Li,[1,2] **Zhiheng Cheng** [ID],[3] **Liang Chen** [ID],[3] **Hongbing Wang,**[3] **and Jialin Cao**[3]

[1]*School of Energy Science and Engineering, Henan Polytechnic University, Jiaozuo, Henan 454000, China*
[2]*Zhengzhou Coal Industry (Group) Co. LTD, Zhengzhou, Henan 450042, China*
[3]*School of Safety Engineering, North China Institute of Science and Technology, Beijing 101601, China*

Correspondence should be addressed to Zhiheng Cheng; an958158@163.com and Liang Chen; 171753953@qq.com

The sealing depth of a gas-drainage borehole is critically important as it directly affects the efficiency of the whole drainage system. In order to determine the shortest reasonable sealing depth, in this paper, a theoretical drainage model using different sealing depths was proposed. Based on theoretical analysis presented, two parts of the fractures system surrounding the drainage borehole were proposed, i.e. the fractures induced by roadway excavation and the fractures induced by borehole drilling. A series of geological in-situ tests and simulations research were conducted to determine the stress and fracture distributions in the surrounding rock of the borehole. The depths of crushing zones, plastic zones and stress concentration zones were determined as 5 m, 2 m and 12 m, respectively. Meanwhile, stress simulation shows that the depth of the stress concentration zone was 12 m from the roadway wall and the stress peak was located at the depth of 8 m, which can be verified by the results of drilling penetration velocity analysis. To determine the optimum sealing depth, gas drainage holes with different sealing depths were drilled in the field. The field results revealed that the crushing zones were the main area for air leakage, and the stress concentration induced by roadway excavation assisted in the reduction of air leakage. Therefore, the optimized sealing depth should both cover the plastic zone and the stress concentration zone. The research achievements can provide a quantitative method for the determination of optimum sealing depth in cross-measure drainage boreholes.

1. Introduction

Coal mines in China have experienced the most serious coal and gas burst disasters in the world [1, 2]. With the increasing depth of mining, stress in strata and gas pressure in coal seams increases while the permeability of coal seams decreases, which makes coal and gas burst disaster more serious [3–6]. It has been proved that releasing the gas energy by CBM drainage is one of the most effective ways to eliminate this disaster [7–11]. Meanwhile, coal-bed methane (CBM) is a kind of clean energy (the heat of pure gas is more than 33 MJ/m^3). Also, there are more than 36.81×10^{12} m^3 of gas in coal seams up to the depth of 2000 m, which equals to 520×10^9 tons of standard coal by combustion heat [4, 12–14]. Furthermore, the greenhouse effect of methane is 25 times stronger than that of CO_2, which can cause severe

damage to the ozone layer [15, 16]. Therefore, extraction of CBM will not only be helpful to control the coal mine gas-induced disasters and to utilize this great source of clean energy but also to protect our environment [17–20].

The quantity of CBM drainage in China was 17 billion m^3 in 2014, including 13.3 billion m^3 extracted from underground, and this figure is increasing over time [21, 22]. CBM drainage in coal mines refers to a system which consists of boreholes pipes and pumps to extract the gas out from the coal seams, where the sealing of boreholes plays a critical important role to ensure its efficiency [23, 24]. The air leakage during drainage occurs when the integrity of the borehole is poor, i.e. air flows into the borehole through excavation-induced fractures [20, 25, 26]. Nearly two-third of mines undertaking gas drainage in China use a short sealing length, and most of them use different standards of

sealing depth, depending on their own experience [13, 27] or empirical formula calculation. Because of improper sealing techniques, the concentration of CBM drainage in 65% of actual working faces is less than 30% [22, 28, 29]; there are many factors that affect the sealing effect, such as sealing material which cannot lead to larger deformation under certain stress level, sealer which resist the unbalanced force inside and outside the borehole and sealing depth which can resist the negative pressure of gas drainage and leave fewer blank bands.

Scholars have carried out lots of research to enhance the sealing quality of borehole, and some methods were proposed to determine the sealing depth via in-situ tests [19, 30–34]. [20] analyzed the borehole drainage process by a compositional (CBM and air) model, and suggested that the air flow into the borehole through the excavation-induced fractures, which is the main cause for the air leakage of the borehole [19, 20, 35]. Suggested that the reasonable sealing depth should exceed the stress relief zone, which is the main area for the roadway excavation-induced fractures [36]. calculated the stress and physical state of the surrounding rock by FLAC^{3D} simulation and proposed that the sealing depth for the borehole should be beyond the stress concentration zone as there are some macro-fractures in this area [37]. suggested that rock with low permeability and high stress can prevent the air flowing into the borehole. He concluded that the sealing depth equals or exceed the depth of the maximum drilling sludge volume, due to the drilling sludge volume increase with the stress and permeability increase of the rock. In summary, the shortest reasonable sealing depth is closely related to the fracture and `stress distribution in the surrounding rock. This is vital to take those factors into consideration to find out more precious sealing depth. Besides, due to the geological complexity of different mining areas. It is clear that conclusions were applicable in specific coal mines, although most of them are different but good drainage results were achieved. Meanwhile, none of them did any research based on different sealing depths.

In the present study, an analytical model was to the sealing qualities with different sealing depths was proposed. Then, a numerical simulation was carried out to study the stress and deformation distribution characters and a new method was proposed to determine the sealing depth based on the rate of penetration of the drilling rig and in-situ crack zone test by ultrasonic detection. Furthermore, this method was tested through gas drainage experiment with different sealing depths.

2. Analysis of the Air Leakage with Different Sealing Depths

As shown in Figure 1, after being excavated, the surrounding rock of the roadway can be divided into 3 zones, the crushing zone, the plastic zone and the elastic zone, in succession [17]. The strength of the crushing zone is smaller as there are lots of cracks and fractures in it [38], which leads to soaring permeability in this area [15]. Moreover, the stress in

crushing zone is much smaller s due to its low strength. As a result, the overburden of the upper layer strata shifts into the plastic zone, which leads to high stress concentration in this area. There exist some macro-fractures in the plastic zone as the stress exceeds its strength. Therefore, the permeability is higher than it is in the original stress zone [22]. Meanwhile, the permeability decreases due to the closure of cleats and the shrinkage of porous structure under high effective stress in the rock mass. And the permeability of porous rock can be calculated as equation (1) [7].

$$k = k_0 e^{-\mu(\sigma - \sigma_0)}, \tag{1}$$

where σ_0 is initial effective stress, σ is effective stress, $-\mu$ is stress constant, k_0 is initial permeability of fractured rock mass, k is the permeability of rock mass under stress.

Likewise, there also exist similar stress and permeability distribution characters in the surrounding rock of the borehole, therefore the air can also get into the borehole through these fractures. Furthermore, the leakage of air from the roadway flowing into the borehole is inevitable during the drainage process. However, as the sealing part is to prevent the air leakage from the roadway wall to the borehole, the air leakage volume can be reduced by improving the sealing depth.

According to Darcy's fluid law, the flow volume through the porous medium can be calculated as equation (2).

$$Q = k\frac{\Delta p A}{\mu l}, \tag{2}$$

where Q is the gas flow volume per unit time, k is the permeability constant, Δp is the gas pressure drop, A is the cross section area of the seepage zone, μ is the dynamic viscosity of the gas flow, l is the seepage path length. Therefore, the air leakage volume with different sealing depths, as shown in Figure 1, can be calculated as equations (3)–(5).

(1) The sealing depth equals the crushing zone (stress relief zone), i.e., $l = l_0$

$$Q_1 = k_1 \frac{\Delta p A_1}{\mu l_0}. \tag{3}$$

(2) The sealing depth equals the plastic zone, i.e., $l_1 = l_0 + \Delta l_1$

$$Q_2 = k_2 \frac{\Delta p A_2}{\mu (l_0 + \Delta l_1)}. \tag{4}$$

(3) The sealing depth equals the stress concentration zone, i.e., $l_2 = l_0 + \Delta l_1 + \Delta l_2$

$$Q_3 = k_3 \frac{\Delta p A_3}{\mu (l_0 + \Delta l_1 + \Delta l_2)}. \tag{5}$$

According to the analysis above, it is clear that $A_1/A_2 > 1$, and $l_0 + \Delta l_1/l_0 > 1$, and $k_1/k_2 > 1$ combining equations (3) and (4), we obtain:
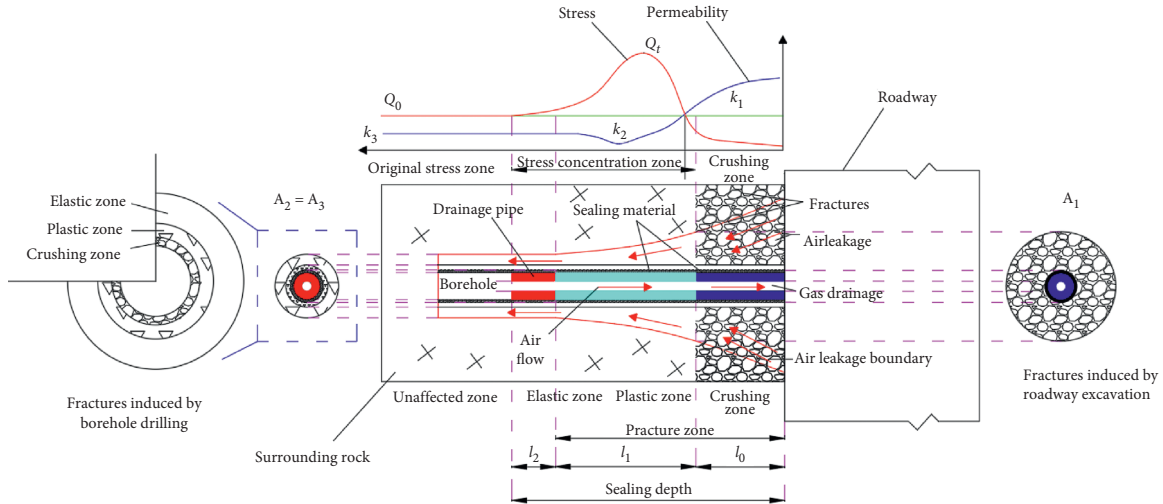
FIGURE 1: Distributions of stress and permeability in the surrounding rock of borehole.

$$\frac{Q_1}{Q_2} = \frac{k_1}{k_2} \times \frac{A_1}{A_2} \times \frac{l_0 + \Delta l_1}{l_0} > 1. \quad (6)$$

Therefore, the air leakage volume can be dramatically reduced if the sealing depth is improved from l_0 to l_1.

Similarly, it is clear that $A_2/A_3 = 1$, $l_1 + \Delta l_2 + \Delta l_3/l_0 + \Delta l_1 > 1$ and $k_2/k_3 = e^{(-\mu(\sigma - \sigma_0))}$, combining equations (4) and (5), we obtain:

$$\frac{Q_2}{Q_3} = \frac{k_2}{k_3} \times \frac{A_2}{A_3} \times \frac{l_1 + \Delta l_2 + \Delta l_3}{l_0 + \Delta l_1} = ne^{-\mu(\sigma - \sigma_0)}, \quad (7)$$

where $n = A_2/A_3 \times l_1 + \Delta l_2 + \Delta l_3/l_0 + \Delta l_1 > 1$, however, $e^{-\mu(\sigma - \sigma_0)} \in [0, 1]$, therefore it is unknown based on the equations if the sealing depth is improved from l_1 to l_2. Therefore, further research is needed to find out the shortest reasonable sealing depth.

3. Optimization of the Sealing Depth

3.1. Test Site.
ShaQu coal mine is located in the Liliu mining area in the central section of Hedong Coalfield in the western of Shanxi province, China. The coal mine is characterized by extremely close distances between coal seams, and with high gas content and gas burst proneness. The coal series strata in the coalfield are composed of the Taiyuan formation in the Upper Carboniferous system and the Shanxi Formation in the Lower Permian system. In total there are 3 production coal seams with an average gas content of $10.34 \, m^3/t$, as shown in Table 1. In order to eliminate the risk of gas burst disaster, the gas drainage roadway was excavated for gas drainage before the upper coal seam was mined, shown in Figure 2. The in-situ test research was held at the #97 gas drainage drilling field of No.1 bed plate gas drainage roadway. The overburden depth is approximately 645 m and the main floor is sandstone. The cross-measure drainage boreholes were drilled in the drilling fields which were located along both sides of the roadway. The distribution of the drilling field and size of the road way are shown in Figure 3.

From the analysis in last section, there are two parts of fracture zones in the fracture system of surrounding rock. The first part is the fractures induced by the borehole drilling and the second part is the fractures induced by the roadway excavation, shown in Figure 1. Meanwhile, both the crushing zone and plastic zone in each part can lead to air leakage during the drainage process due to the fractures and cracks surrounding the borehole. However, the scale and magnitude of the fracture system induced by the roadway excavation is much larger than that of the borehole. Therefore, the main purpose of sealing part is to control the air leakage through the fractures induced by the roadway excavation. In this paper, we mainly focus on the fracture and stress distributions in the surrounding rock of the drilling field, which is part of the roadway and the place where the boreholes are set.

3.2. Analysis of Fracture Zone.
Both the plastic zone and the crushing zone exists fractures, which is the path for air leakage in the drainage process. Therefore, these two parts are important to the determination of sealing depth. In this part, the plastic zone was calculated by FLAC^{3D} simulation and the crushing zone was in-situ tested by ultrasonic detection.

3.2.1. Simulation Analysis of Plastic Zone.
In order to replicate the same geological setting in Table 1 and Figure 3, a 3D model, where the size of the excavated roadway is 4 m (width) × 3 m (height) and the drilling field is 5 m (length) × 3 m (width) × 3 m (height), is created (shown in Figure 4). Mohr-Coulomb failure criterion was applied to represent plastic behavior of rock mass. The size of model is 30 m (width) × 30 m (length) × 20 m (height) which includes 165670 elements and 13468 nodes. The vertical stress applied for each element is 16 MPa due to simulate the weight coming from the overburden strata of 640 m in depth and horizontal stress of 20 MPa is also applied on the model based on the data of in-situ stress provided by Shaqu coal

TABLE 1: Basic parameters of the coal seams.

No.	Maximum original gas pressure (MPa)	Original gas content (m³/t)	Permeability (m²/MPa²•d)	Thickness (m)
#3	1.08	7–24.88	1.78–1.89	1.1
#4	1.30	7.3–17.82	3.52–3.785	2.2
#5	1.50	4.45–17.9	1.99–.23	3.77
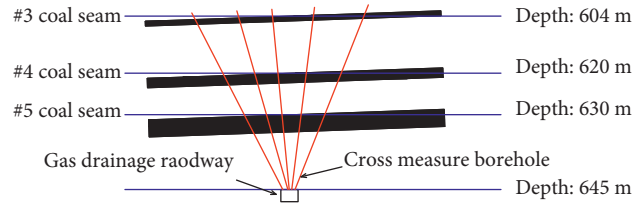
FIGURE 2: Illustration of the cross-measure boreholes in bed plate drainage roadway.
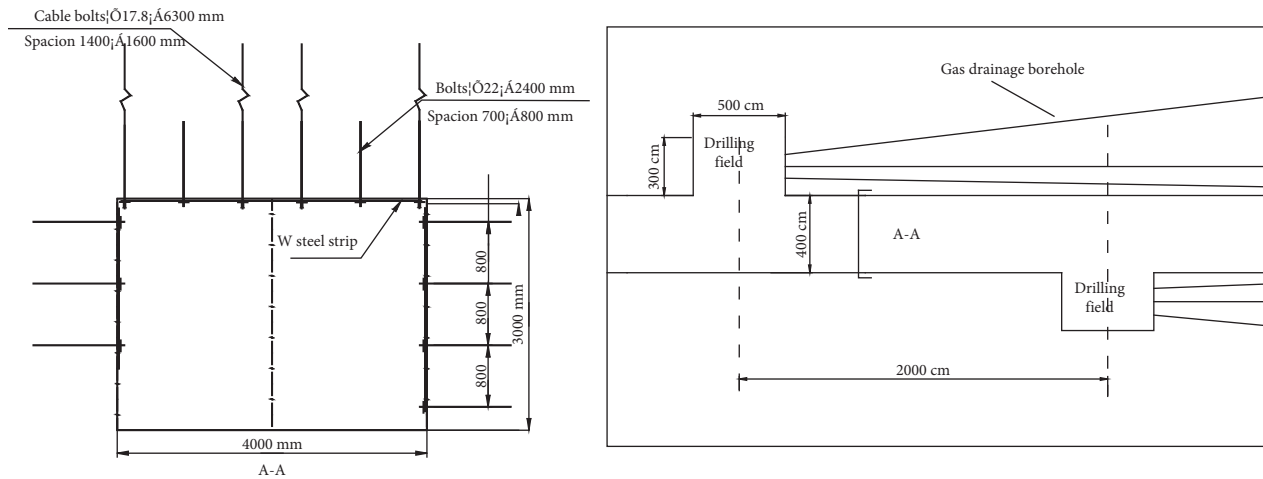
FIGURE 3: Distribution of drilling fields and drainage boreholes in the gas drainage roadway.

mine. The horizontal displacement of front, back, left, and right boundaries, as well as the vertical displacement of bottom are fixed. The mechanical parameters of the rock are shown in Table 2. Figure 4 shows the overburden strata and Figure 5 shows the mesh of the calculation model.

Figure 6 shows the distribution of plastic zone surround the drilling field and roadway. As the gas drainage boreholes mostly roll upward from the drilling field in z direction, the plastic zone in this area puts more influence on the decision for the sealing depth. As shown in the results, the thickness of the plastic zone surrounding the drilling field reached 5 m in 2 direction and 2 m in 2 direction. While, it comes to 3.7 m in x direction and also 5 m in z direction for thickness of plastic zone in the surrounding rock of roadway.

3.2.2. In-Situ Crushing Zone Test by Ultrasonic Detection. Ultrasonic detection has been adopted for detecting the crushing zone in the surrounding rock by researchers [11, 18, 22, 38]. The principles of the test are as follows: the velocity of the ultrasonic wave attenuates significantly due to the reflection and refraction effects between the interfaces

among the discontinuous fractures in the crushing zone and the duration time in certain distance increases rapidly with the number of fractures mounts. While the velocity of the ultrasonic wave attenuates slightly when the number of cracks decreases and the reflection and refraction effects drops. In other words, there exists a positive relationship between the duration of time of ultrasonic wave and the degree of deformation in the surrounding rock. Therefore, the distribution characters of the crack zone can be found by recording the duration time of the ultrasonic wave.

In this paper, the ultrasonic detection analyzer (BA-II, CCRI Co, Ltd) was adopted to test the duration time of ultrasonic wave in the rock of the drilling field. This analyzer consists of 3 parts which are the probe the host computer and the connecting wires as is shown in Figure 7. The transmitter and receiver are set in the probe with the length of 1 m. Therefore, the host computer will record the duration time and calculate the velocity of the ultrasonic wave based on the signals between the transmitter and receiver, shown in equation (8). The boreholes were tested 0.1 m by each step in depth. The arrangement of the two test boreholes are shown in Figure 8. Figure 9 shows the test results.

Strata	Lithology	Thickness (m)
	Coalseam#5	3.77
	Limestone	3.4
	Sandstone	2.8
	Mudstone	3.2
	Sandstone	0.8
	Coalseam#6	0.35
	Sandstone	5.7 m
	Drilling field	
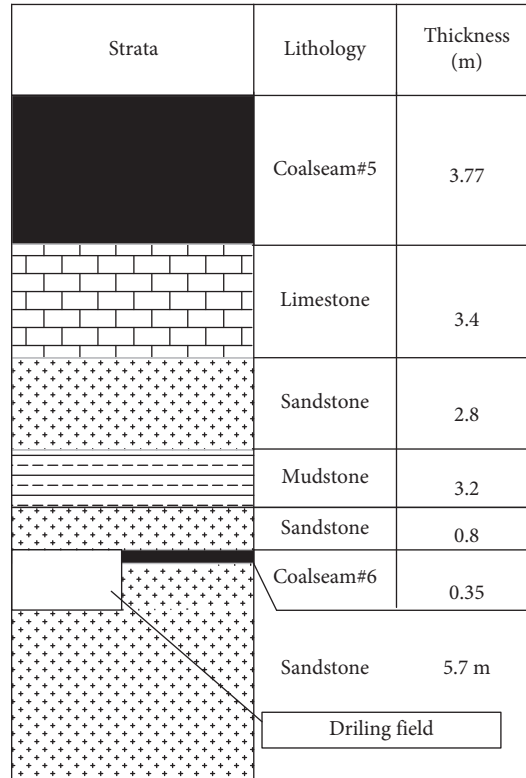
FIGURE 4: Stratigraphic column and position of the bed floor tunnel.

TABLE 2: Mechanical parameters of the surrounding rock of the drilling field.

No	Lithology	Elastic modulus (MPa)	Compression strength (MPa)	Density (10^{-5}N·mm^{-3})	Friction angle (°)	Cohesion (MPa)
1	Mudstone	20	25	2.4	25	10
2	Coal seam #5	10	15	1.4	20	1.8
3	Sandstone	64	76	2.6	27	20
4	Limestone	18	20	2.2	24	15
5	Coal seam #6	10	15	1.4	21	1.5
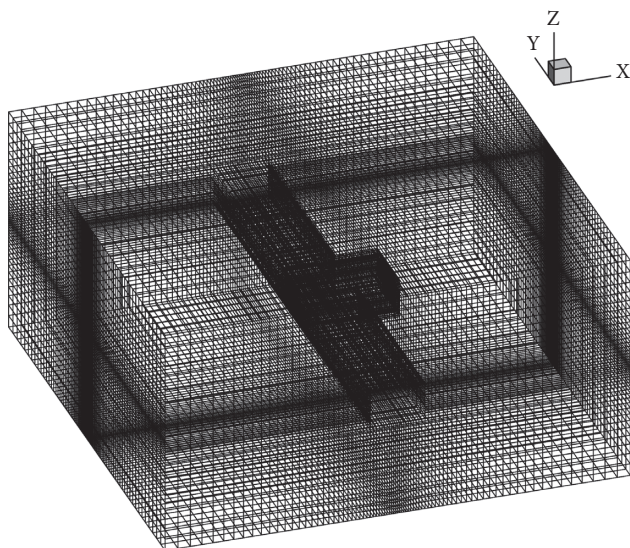
FIGURE 5: 3D mesh of the numerical model.

$$V = \frac{L}{t}, \tag{8}$$

where L is the distance of the transmitter and receiver and $L = 1$ m, t is the duration time the ultrasonic wave reaches the receiver coming from the transmitter, V is the velocity of the ultrasonic wave.

As the curves show in Figure 9, the duration time of the ultrasonic wave drops significantly at the depth of 0–2.0 m and it fluctuated at 45 ms/m slightly afterwards, which infers that the velocity increases in this area and the number of fractures and cracks induced by the excavation has decreased in this area. Therefore, the boundary of the crushing zone locates at the depth of 2.0 m.

3.3. Stress State of the Drilling Field. From the analysis above, the redistributed stress can significantly change the permeability of the rock mass. The permeability in the stress concentration zone decreases due to cleats closure and macro-pores shrinkage. While the permeability in the stress

(a)

(b)
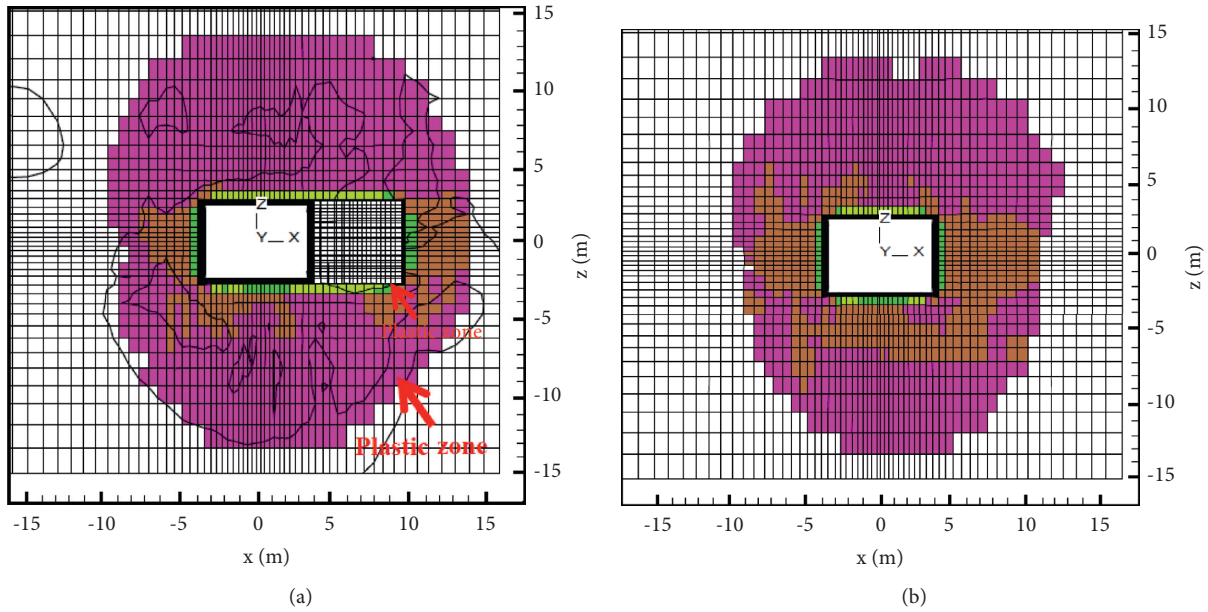
FIGURE 6: Vertical cross section distribution of the plastic zone in surrounding rock. (a) Drilling field. (b) Roadway.
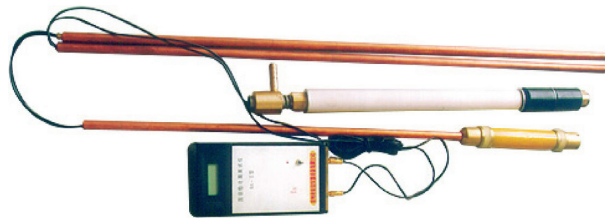
FIGURE 7: The ultrasonic detection analyzer unit.
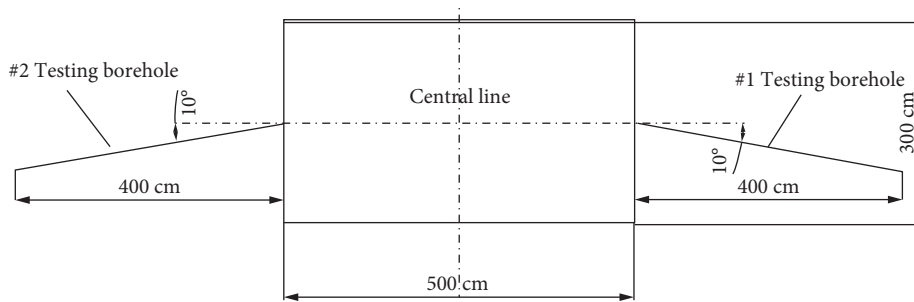
FIGURE 8: Arrangement of the boreholes for ultrasonic detection.

increases due to the swell of rock mass and cleats open. Therefore, the stress distribution is an important factor for the determination of sealing depth except for the fracture zone. In this paper, the stress distribution was calculated by FLAC^{3D} simulation and in-situ analyzed by the results of penetration velocity of drilling rod in the surrounding rock during the borehole drilling process.

3.3.1. FLAC^{3D} Simulation.
Based on the calculation model above, the vertical stress cloud contour on the horizontal cross section of the drilling field can be achieved, shown in

Figure 10. Two main characters can be drawn from this result: firstly, the vertical stress in the y direction of the surrounding rock shows high concentration. Secondly, the vertical stress decreases as the distance from the drilling field increases until it falls to the virgin field stress of 16 MPa at the distance around 12 m and the high vertical stress area (20–22 MPa) locates at the depth of 7-8 m. Taking the contour of 16 MPa as the boundary of the stress concentration zone, it is clear that the excavation-induced stress concentration zone reaches as far as 12 m. While, the vertical stress reaches its top (22 MPa) around the depth of 7-8 m.
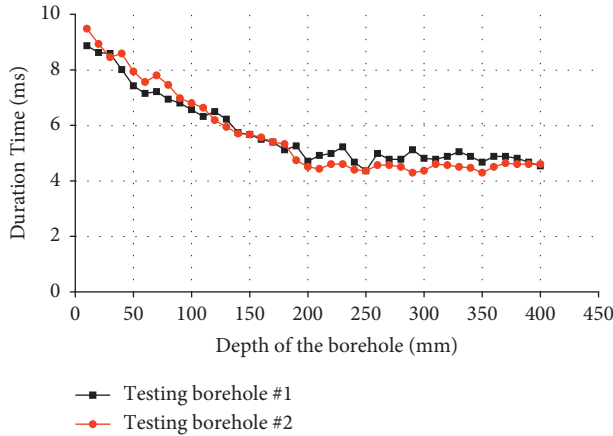
Figure 9: Ultrasonic testing results.

3.3.2. Stress Concentration Zone Analysis through Drilling Response. Drilling torque is the stress that the bit imposes on the rock during the drilling process. The value of the drilling torque depends on the size of the borehole, rate of penetration and drilling power, shown in equation (9) [24]. During the drilling process, the drilling torque may get unstable mainly caused by the change of the physical characters of the surrounding rock, such as the strength or the stress concentration characters. Given that the drilling constant and the drilling power W are fixed, the drilling torque T decreases as the surrounding rock gets less stress concentration or strength, the rate of penetration will increase. Likewise, when the drilling torque T increases as the surrounding rock gets more stress concentration or strength, the rate of penetration will decrease [39]. The curve of the rate of penetration against the drilling torque is shown in Figure 11.

$$T = c \frac{W}{v}, \tag{9}$$

where c is a drilling constant which is determined by the diameter of the borehole and the rotational speed of the drilling pipe, v is the rate of penetration and W is the drilling power.

The drilling duration time was recorded based on 4 testing boreholes. The basic parameters were shown in Figure 12 and Table 3. The in-situ drilling duration time and rate of penetration are tested 1 m by each step due to the length of the drill pipe is 1 m. As is shown in Figure 13, the testing curves have shown similar trends with the drilling depth goes up. Meanwhile, the rate of penetration has seen significant drop while the duration time soared up during the depth of 0-8 m. Moreover, the curves meet their turning point at the depth of 7-8 m. However, the rate of penetration gradually bounced back and the duration time decreases sharply after the drilling depth exceeds 8 m. The drop of the rate of penetration is mainly caused by the friction of drilling pipe due to the stress concentration in the surrounding rock. Therefore, it can be seen that the maximum stress concentration area locates at the depth of 7-8 m of the borehole, which verifies the simulation results.

4. Gas Drainage Test via Cross-Measure Boreholes

It can be concluded from Section 3 that the boundary of the crushing zone (B1), plastic zone (B2) and stress concentration zone (B3) is located at the depths of 2 m, 5 m and 12 m respectively. In order to determine the shortest sealing depth of the cross-measure gas drainage borehole, a contrast gas drainage experiment based on different sealing depths has been conducted. This experiment was to determine the relationship of the optimized sealing depth between the depths of B1, B2 and B3. Therefore, three contrasting experimental drainage groups were formed and each group has a unique sealing depth. The sealing depth for group 1 is 2 m which equals the depth of B1. The sealing depth for group 2 is 5 m which equals the depth of B2. And the sealing depth for group 3 is 12 m which equals the depth of B3. Table 4 shows the parameters of each borehole and Figure 14 shows the illustration for the sealing process. In order to minimize the influence from unstable drainage performance of single drainage borehole, each experiment group consists of 3 independent boreholes. Furthermore, the boreholes in each group are at interlaced arrangement to minimize the influence from the inhomogeneity of the coal-bed gas geology. Three monitoring lines group these boreholes to get the drainage performance data, shown in Figure 15.

The gas flow is the total mixed gas extracted out from the coal seam which consists of two parts, namely, the pure methane and air (other gas components). Therefore, the pure methane volume can be calculated by the product of methane concentration and gas flow volume. In this experiment, the monitoring was initiated immediately after the boreholes were sealed and connected to the drainage system. The gas concentration and the gas flow volume of each drainage borehole were monitored for every other day in the following 60 days during the drainage process. The drainage results of methane concentration of three monitoring lines were shown in Figure 16–18. Two main conclusions can be drawn from these curves. Firstly, the methane concentration in three monitoring lines stayed high in the early stage (day 0–10) of the drainage process. Then a negative exponential decline is observed due to the residual coal seam gas decreasing, which applies to all drainage boreholes. Secondly, the results of group 2 ($l = 10$ m) and 3 ($l = 15$ m) were comparable during the whole drainage process. While, the gas concentration of the group 1 ($l = 5$ m) were significantly lower than that of group 2 ($l = 5$ m) and group 3 ($l = 15$ m).

Tables 5 and 6 show the drainage performance of each borehole and each group respectively. Based on the results shown in Table 6, it is clear that the methane concentration of group 1 (15.1%) is lower than half that of group 2 (46.2%) and group 3 (51.6%), while the gas flow volume (18.9 L/min) is significantly higher than the rest two groups (13.9 L/min and 12.5 L/min, respectively). As a result, the pure gas volume of group 1 (2.8 L/min) is 50% less than that of group 2 (6.3 L/min) and group 3 (6.5 L/min). The direct cause for the low drainage efficiency of group 1 is, because of insufficient sealing depth, the air in the roadway flow into the

(a)

(b)
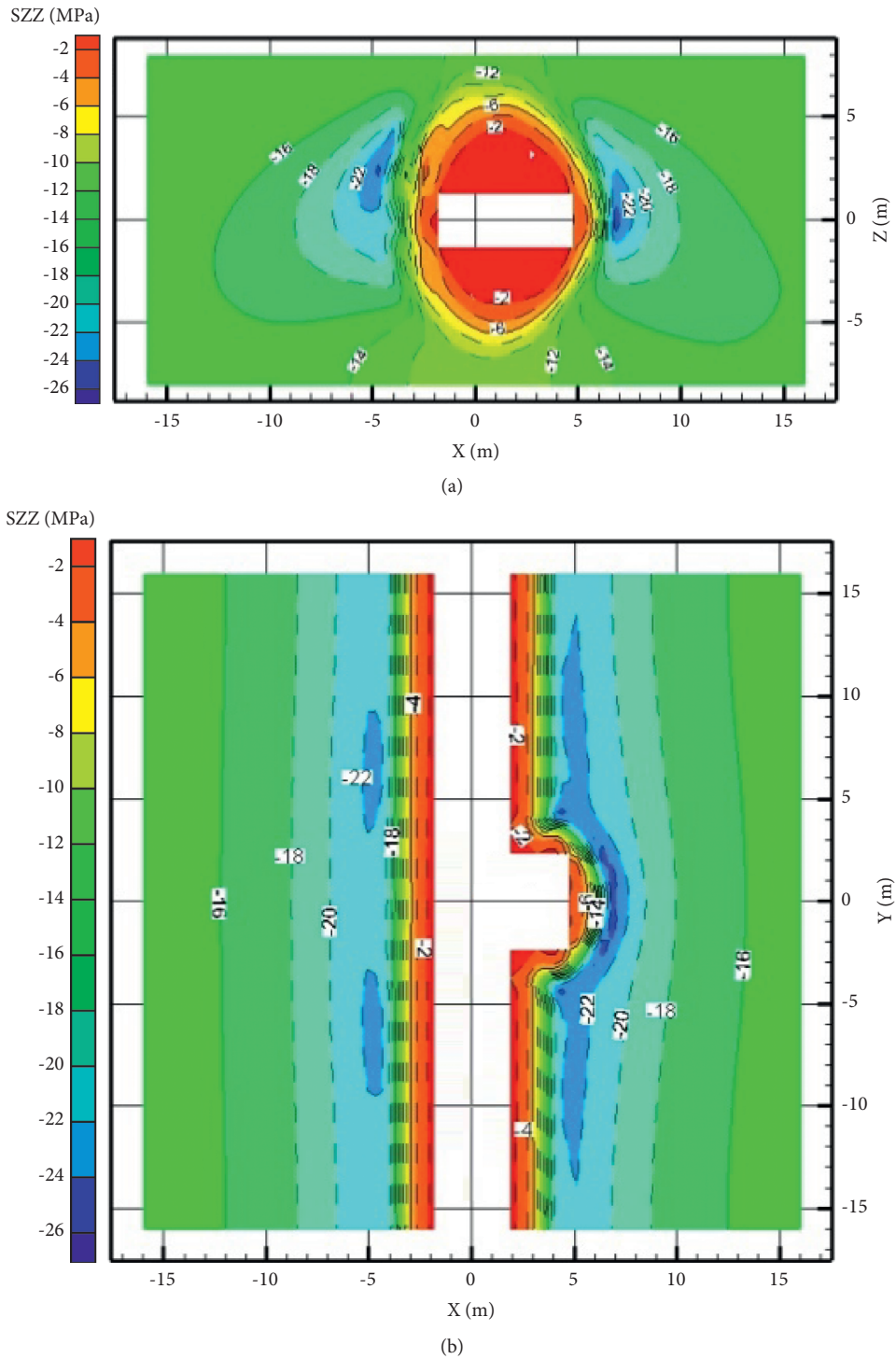
FIGURE 10: Vertical stress cloud contour in the surrounding rock. (a) Vertical cross section via the central of drilling field. (b) Horizontal cross section via the central of roadway.

borehole through the fracture system (both the fractures induced by the roadway excavation and borehole drilling) in the surrounding rock of the drilling field. Therefore, this result verifies that the air leakage volume can be dramatically reduced if the sealing depth is improved from the crushing zone (group 1) to the plastic zone (group 2), as shown in equation (6). Meanwhile, though both the sealing depths of group 2 and group 3 exceed the fracture zone induced by the roadway excavation, the methane concentration of group 2 (46.2%) is still 10.4% less than that of group 3 (51.6%), which indicates there still exist air leakage in group 2. A reasonable explanation is that, though the air leakage of drainage borehole is unavoidable due to the fracture system induced by the borehole drilling, the leakage volume still can be
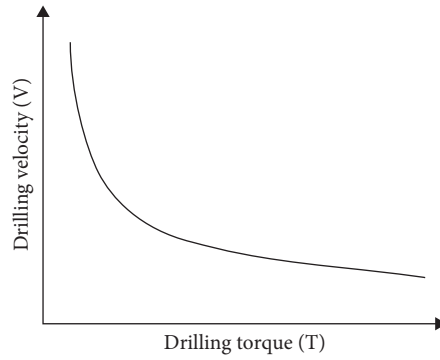
FIGURE 11: Curve of rate of penetration against drilling torque under fixed drilling power.
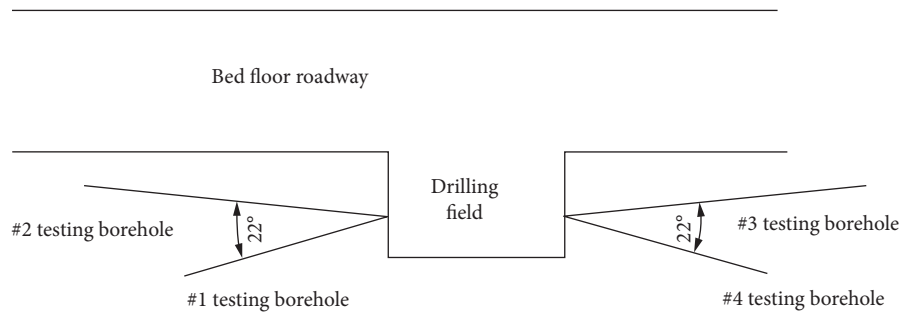
FIGURE 12: Arrangement of the testing boreholes.

TABLE 3: Parameters of the testing boreholes.

No.	Diameter (mm)	Dip angle (°)	Length (m)	Surrounding rock	Drilling power (KW)	Drilling rig
#1	94	15	12	Sandstone	45	ZDY-4000L
#2	94	15	12	Sandstone	45	ZDY-4000L
#3	94	15	12	Sandstone	45	ZDY-4000L
#4	94	15	12	Sandstone	45	ZDY-4000L
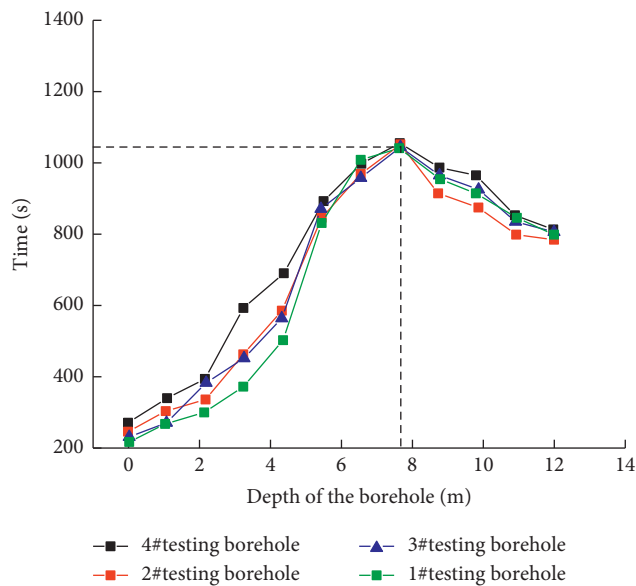
FIGURE 13: Curves of drilling time against rate of penetration.

TABLE 4: Basic parameters of the experiment boreholes.

Borehole no.	Diameter (mm)	Dip angle (°)	Length (m)	Sealing depth (m)	Group no.
#1–1	94	5	142	5	1
#1–2	94	9	80	5	1
#1–3	94	13	56	5	1
#2–1	94	5	142	10	2
#2–2	94	9	82	10	2
#2–3	94	13	54	10	2
#3–1	94	5	140	15	3
#3–2	94	9	82	15	3
#3–3	94	13	56	15	3
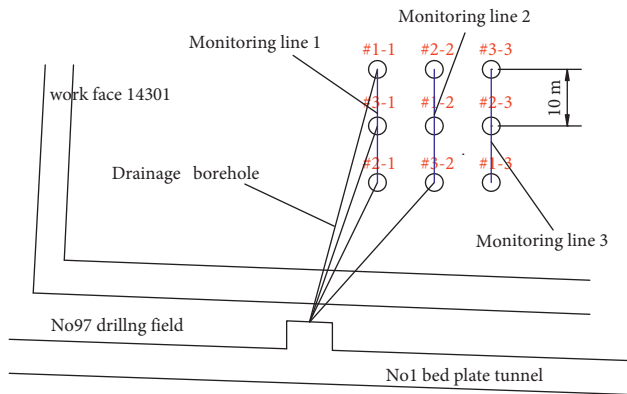
FIGURE 14: Simplified schematic of the borehole sealing in the drilling field.

FIGURE 15: Arrangement of the experiment boreholes.

FIGURE 16: Curves of gas concentration in boreholes at monitor line 1.

FIGURE 17: Curves of gas concentration in boreholes at monitor line 2.

reduced by improving the sealing depth. Meanwhile, as shown in equation (7), it can be concluded $Q_2/Q_3 = k_2/k_3 \times A_2/ A_3 \times l_1 + \Delta l_2 + \Delta l_3/l_0 + \Delta l_1 = ne^{-\mu(\sigma - \sigma_0)} > 1$.

In summary, the drainage result has verified the theoretical analysis of air leakage volume using different sealing depth. Meanwhile, three conclusions can be drawn based on the analysis above, firstly, the air leakage decreases with the increase of sealing depth, especially when the sealing depth is less than the crushing zone. Secondly, the fractures induced by roadway excavation are the main path for air leakage of the borehole. Thirdly, the permeability decrease caused by stress concentration is helpful to prevent the air flowing into the borehole through the fractures. Moreover, based on the

FIGURE 18: Curves of gas concentration in boreholes at monitor line 3.

TABLE 5: Drainage results of each test borehole.

Borehole no.	Methane concentration (%)	Gas flow volume (L/min)	Pure methane volume (L/min)	Drainage pressure (kPa)	Sealing depth (m)	Group no.
#1–1	13.5	20.3	2.74	−13	5	1
#1–2	15.1	18.8	2.83	−13	5	1
#1–3	16.9	17.5	2.95	−13	5	1
#2–1	46	13.8	6.34	−13	10	2
#2–2	42.4	14.8	6.27	−13	10	2
#2–3	50.3	13.0	6.43	−13	10	2
#3–1	50.1	12.8	6.41	−13	15	3
#3–2	50.6	12.7	6.42	−13	15	3
#3–3	54.1	12.1	6.54	−13	15	3

TABLE 6: Drainage results of each group.

Group no.	Methane concentration (%)	Gas flow volume (L/min)	Pure methane volume (L/min)	Sealing depth (m)
1	15.1	18.9	2.8	5
2	46.2	13.9	6.3	10
3	51.6	12.5	6.5	15

drainage performance of 3 groups, the optimized shortest sealing depth for the cross-measure borehole is 12 m, which should cover both the plastic zone and stress concentration zone.

5. Conclusions

To optimize the sealing depth of the cross-measure drainage borehole, a theoretical model was proposed to analyze the air leakage volume using different sealing depths. A series of in-situ tests were conducted for verification and further research. Based on the results of tests and analysis, the following conclusions can be drawn:

(1) Based on theoretical analysis presented, two parts of the fractures system surrounding the drainage borehole were proposed, i.e. the fractures induced by roadway excavation and the fractures induced by borehole drilling. Both parts can lead to air leakage of the drainage borehole. The first part consists of crushing zone and plastic zone. And the crushing zone is the main path for air leakage, which can be reduced by improving sealing depth. However, for the second part, the air leakage volume is affected by the stress concentration induced by roadway excavation.

(2) The stress and fracture distributions were analyzed by in-situ test and numerical simulation. The results show that the thickness of the plastic zone and the crushing zone was 5 m and 2 m, respectively. Meanwhile, stress simulation shows that the depth of the stress concentration zone was 12 m from the roadway wall and the stress peak was located at the

depth of 8 m, which can be verified by the results of drilling penetration velocity analysis.

(3) The drainage contrast experiment revealed that, though the air leakage volume decreased with the increase of sealing depth. However, different sealing depth stages have their unique causes. In the first stage, when the sealing depth was improved from crushing zone to plastic zone, the air leakage volume decreased due to the sealing material preventing the air flowing into the borehole through the fractures in the crushing zone. While in the second stage, when the sealing depth was improved from the plastic zone to the stress concentration zone, the air leakage volume decreased due to the permeability decrease caused by high stress imposing on the fractures induced by borehole drilling. The study case shows that the shortest optimized sealing depth is 12 m, which should both cover the plastic zone and the stress concentration zone [40].

Data Availability

The data used to support the findings of this study are currently under embargo while the research findings are commercialized. Requests for data, after publication of this article, will be considered by the corresponding authors.

Conflicts of Interest

The authors declare that they have no conflicts of interest.

Acknowledgments

References

[1] P. Wei, X. Li, S. Peng, and C. Huang, "Numerical simulation of boreholes for gas extraction and effective range of gas extraction in soft coal seams," *Energy Science & Engineering*, vol. 7, no. 5, pp. 1632–1648, 2019.

[2] Q. X. Yu and Y. P. Cheng, "Mine gas prevention and control," *China University of Mining and Technology Press*, vol. 12, no. 3, pp. 51–59, 2012.

[3] D. J. Black, "Review of coal and gas outburst in Australian underground coal mines," *International Journal of Mining Science and Technology*, vol. 29, no. 6, pp. 815–824, 2019.

[4] M. Cai, H. Peng, and H. Ji, "New development of hydraulic fracturing technique for in-situ stress measurement at great depth of mines," *Journal of University of Science and Technology Beijing*, vol. 15, no. 6, pp. 665–670, 2008.

[5] Q. Hu and X. Zhao, "Suggestions and countermeasures on the current situation of coal and gas outburst in China," *Ming safety & environmental protection*, vol. 39, no. 5, pp. 1–5, 2012.

[6] T. Liu, B. Lin, and X. Fu, "Mechanical criterion for coal and gas outburst: a perspective from multiphysics coupling," *International Journal of Coal Science & Technology (prepublish)*, 2021.

[7] D. Chen, P. Zhejun, Y. Zhihui, H. Bing, W. Di, and Y. Liang, "A unified permeability and effective stress relationship for porous and fractured reservoir rocks," *Journal of Natural Gas Science and Engineering*, vol. 29, pp. 401–412, 2016.

[8] Y. Cheng, J. Fu, and Q. Yu, "Development of gas extraction technology in coal mines of China," *Journal of Mining& Safety Engineering*, vol. 26, no. 2, pp. 127–139, 2009.

[9] H. Gao, Q. Wang, J. Bei, and P. Zhang, "Relationship between rock uniaxial compressive strength and digital core drilling parameters and its forecast method," *International Journal of Coal Science & Technology (prepublish) Technology*, vol. 8, no. 3, 2021.

[10] D. Rudakov and V. Sobolev, "A mathematical model of gas flow during coal outburst initiation," *International Journal of Mining Science and Technology*, vol. 29, no. 5, pp. 791–796, 2019.

[11] X. Wu, Y. Peng, J. Xu, Q. Yan, W. Nie, and T. Zhang, "Experimental study on evolution law for particle breakage during coal and gas outburst," *International Journal of Coal Science & Technology*, vol. 7, no. 1, pp. 97–106, 2020.

[12] P. F. Cui, Y. Banghua, L. Yong, W. Jianping, W. Zhihui, and L. Hui, "A new width measurement method of the stress relief zone on roadway surrounding rocks," *Geofluids*, vol. 2019, pp. 331–322, Article ID 9519353, 2019.

[13] C. Peng, "Present situation and problems of gas drainage and utilization in coal mines in China," *Safety In Coal Mines*, vol. 33, no. 2, pp. 62–65, 2007.

[14] Q. Zou, H. Liu, Z. Cheng, and T. Zhang, "Effect of slot inclination angle and borehole-slot ratio on mechanical property of pre-cracked coal: implications for ecbm recovery using hydraulic slotting," *Natural Resources Research*, vol. 29, pp. 1705–1729, 2019.

[15] S. Hu, Y. Liu, F. Zhou, and T. Xia, "Effective stress and permeability redistributions induced by successive roadway and borehole excavations," *Rock Mechanics and Rock Engineering*, vol. 48, no. 1, pp. 319–332, 2015.

[16] C. Karacan, R. Felicia, C. Michael, and P. Sally, "A review of capture and utilization practices with benefits to mining safety and to green-house gas reduction," *International Journal of Coal Geology*, vol. 86, pp. 121–156, 2011.

[17] Y. Huang and E. Wang, "Experimental study on coefficient of sensitiveness between percolation rate and effective pressure for low permeability rock," *Chinese Journal of Rock Mechanics and Engineering*, vol. 26, no. 2, pp. 410–414, 2007.

[18] X. Y. Jia and H. Song, "Test technology and discussion on loose zone of roadway surrounding rock," *West-China Exploration Engineering*, vol. 16, no. 10, pp. 148–150, 2004.

[19] F. Q. Wei, S. P. Lian, C. Zhang, and S. B. Liu, "Study on reasonable hole-sealing-depth down the seam of mengjin mine," *Henan university of technology (natural science edition*, vol. 32, no. 6, pp. 686–689, 2013.

[20] F. Q. Wei and S. B. Liu, "Determination and application of reasonable borehole sealing depth down seam for xinyi mine," *Coal Technology*, vol. 33, no. 5, pp. 46–49, 2014.

[21] B. Lin, "Theory and technology of gas prevention and control in mines," *Xu Zhou, China University of Mining and Technology Press*, vol. 14, no. 2, pp. 113–132, 2010.

[22] K. Zhang, K. Sun, B. Yu, and P. Ranjith, "Determination of sealing depth of in-seam boreholes for seam gas drainage based on drilling process of a drifter," *Engineering Geology*, vol. 210, pp. 115–123, 2016.

[23] C. J. Fan, S. Li, M. Luo, W. Du, and Z. Yang, "Coal and gas outburst dynamic system," *International Journal of Mining Science and Technology*, vol. 27, no. 1, pp. 49–55, 2017.

[24] Q. Liu, C. Yuanping, Y. Liang, F. Youxiang, S. Dezhou, and K. Shengli, "A new effective method and new materials for high sealing performance of cross-measure CMM drainage boreholes," *Journal of Natural Gas Science and Engineering*, vol. 21, pp. 805–813, 2014.

[25] D. Zhao and J. T. Pan, "Numerical simulation on reasonable hole-sealing depth of boreholes for gas extraction," *AIP Advances*, vol. 8, no. 4, pp. 146–153, 2018.

[26] Q. L. Zou, H. Liu, Z. Jiang, and X. Wu, "Gas flow laws in coal subjected to hydraulic slotting and a prediction model for its permeability-enhancing effect," *Energy Sources, Part A: Recovery, Utilization, and Environmental Effects*, 2021.

[27] Z. Wang and J. Liu, "Problems existing in methane drainage in coal mines of China and probing into the countermeasures," *Safety In Coal Mines*, vol. 36, pp. 29–32, 2005.

[28] C. Wang, S. Yang, C. Jiang et al., "A method of rapid determination of gas pressure in a coal seam based on the advantages of gas spherical flow field," *Journal of Natural Gas Science and Engineering*, vol. 45, pp. 502–510, 2017.

[29] Q. L. Zou, H. Liu, Y. Zhang, Q. Li, J. Fu, and Q. Hu, "Rationality evaluation of production deployment of outburst-prone coal mines: a case study of nantong coal mine in chongqing, China," *Safety Science*, vol. 122, pp. 201–221, 2020.

[30] J. B. Geng, J. Xu, W. Nie, S. Peng, C. Zhang, and X. Luo, "Regression analysis of major parameters affecting the intensity of coal and gas outbursts in laboratory," *International Journal of Mining Science and Technology*, vol. 27, no. 2, pp. 327–332, 2017.

[31] O. Jianchun, M. Liu, C. Zhang, Y. Liu, and J. Wei, "Determination of indices and critical values of gas parameters of the first gas outburst in a coal seam of the xieqiao mine," *International Journal of Mining Science and Technology*, vol. 22, no. 1, pp. 89–93, 2012.

[32] H. Jiang and Y. Luo, "Development of a roof bolter drilling control process to reduce the generation of respirable dust," *International Journal of Coal Science & Technology*, vol. 8, no. 2, pp. 199–204, 2021.

[33] K. Wang, Z. Lou, G. Wei, and W. Lu, "Reasonable minimum sealing length of in-seam boreholes for coal mine methane drainage: a case study," *Energy Sources, Part A: Recovery, Utilization, and Environmental Effects*, vol. 42, no. 18, pp. 2199–2213, 2019.

[34] K. Wang, Z. Lou, G. Wei, B. Qin, and L. Wang, "A novel anti-air-leakage method and an organic polymer material for improving methane drainage performance," *Process Safety and Environmental Protection*, vol. 129, pp. 152–162, 2019.

[35] H. Yu, S. Liu, Z. Liu, and H. Jia, "Macro and micro grouting process and the influence mechanism of cracks in soft coal seam," *International Journal of Coal Science & Technology (prepublish)*, 2021.

[36] J. He and K. Dong, "Research on rational sealing depth of gas drainage borehole in large section roadway," *China Coal*, vol. 4, no. 2, pp. 101–104, 2014.

[37] M. Bai, "Research and practice of reasonable hole sealing depth of the low permeability coal seam," *Coal and Chemical Industry*, vol. 36, no. 7, pp. 59–61, 2013.

[38] E. I. Shemyakin, G. L. Fisenko, M. V. Kurlenya et al., "Zonal disintegration of rocks around underground workings," *Part II: Rock fracture simulated in equivalent materials: Soviet Mining*, vol. 22, no. 3, pp. 223–232, 1986.

[39] H. Tian, G. P. Li, and A. R. Chen, "Degradation process assessment of prestressed concrete continuous bridges in life-cycle," *Journal of Central South University of Technology*, vol. 19, no. 5, pp. 1411–18, 2012.

[40] C. Zhai, B. Q. Lin, and L. Wang, "Status and problems of drainage and utilization of down hole coal bed methane in coal mines in China," *Natural Gas Industry*, vol. 28, no. 7, pp. 23–26, 2008.

Research Article

Research on Optimization of Mining Substitution in Wangzhuang Mine Based on System Dynamics

Shuheng Zhong [ID],[1] **Yuchen Guo** [ID],[1] **Yanjiao Li** [ID],[1] **and Ming Yang** [ID][2]

[1]*School of Energy and Mining, China University of Mining and Technology (Beijing), Beijing 10083, China*
[2]*School of Information Network Security, People's Public Security University of China, Beijing 10083, China*

Correspondence should be addressed to Yanjiao Li; 542805524@qq.com

The unbalanced mining replacement is a major problem restricting efficient mining. The optimization of mining replacement process can achieve perfect coordination of mining face and tunneling in time and ensure the efficient production of mine to the greatest extent. Based on this, this paper takes Wangzhuang Mine as the research background, applies system dynamics to mining replacement research, builds the Wangzhuang Mine mining-driving system simulation model, and uses this model to dynamically simulate the working face 9102 and its replaced heading face 7106. The research has found that there is an imbalance in the replacement between the two working faces, and the replacement process can be optimized by advancing the driving period or increasing the driving team to work in parallel at the appropriate time point, so as to meet the normal demand of mining replacement and provide guidance for the mining plan arrangement of other similar working faces.

1. Introduction

With the development of big data technology and mechanization and intelligence, the advancing speed of the working face has become faster and faster. Although the advancing speed of heading face has been improved, it still lags behind the working face, which causes the imbalance of mining replacement and affects the production efficiency of the mine. Therefore, in order to improve the coal output and to ensure the high efficiency of mine production, it is necessary to optimize the mining process [1–3]. Aiming at the problem that the excavation lags behind the mining, the main factors restricting the speed of roadway driving were summarized and the future development direction was proposed [4–6]. Some scholars have put forward prospects and suggestions for the improvement of driving speed from the aspects of tunneling technology and equipment [7–9]. Some scholars have established an intelligent decision system for mining replacement with the help of computers [10–12].

References [4–6] only put forward the problem of comprehensive roadway excavation in our country, indicate

the future development direction of tunneling, or just point out the overall process cycle optimization. References [7–9] explain the current situation of rapid tunneling technology, discuss key technical issues, or quickly optimize tunneling technology through theoretical calculation. References [10–12] abandon the traditional manual planning and gradually use the cross-platform and versatile software in the computer to prepare the mining succession planning system. The above research is committed to explore how to improve the speed of excavation to cooperate with mining face completing the excavation replacement both from the perspective of technology and intelligent decision and alleviate the imbalance problem of excavation replacement to a certain extent. However, it is rarely considered from the perspective of mining replacement optimization. The optimization of mining and driving replacement is to arrange the driving tasks reasonably in terms of time to meet the replacement demand and avoid the waste of resources, which is the prerequisite for the realization of intelligent mining. Based on this, this paper applies system dynamics to the study of optimization of mining and driving replacement to improve mine production efficiency better.

2. Model Building

System dynamics is a discipline which could study the dynamic development process of complex systems and uses computer simulation technology to simulate the dynamic development process of the system based on feedback control theory [13–15]. The modeling process mainly includes two aspects, model building (system boundary determination, causality analysis, and structural flow diagram drawing) and simulation (parameter setting, simulation analysis, countermeasures, and suggestions) [16, 17].

2.1. System Boundary Determination.

There are two mining levels of +630 and +540 in Wangzhuang Mine. The mining coal seam is No. 3 coal seam. Working plane which has been replaced recently includes 9102 mining face, 7106 ventilating roadway, and 7106 transportation roadway. The 9102 mining face is located in the 91 mining area. In the working face, there are 3 faults and 2 collapse columns (fault F304 $H = 5.0$ m $\angle 65°$, fault F317 $H = 8.5$ m $\angle 40°$, fault F318 $H = 1.4$ m $\angle 40°$, collapse column H51, and collapse column X14). The 7106 working face passes through five anomaly areas. They are the comprehensive response of coal seam thinning, crack development, concealed geological structure, or coal structure abnormality. From the perspective of current situation of the mine production, mining replacement is unbalanced. Through the analysis, the factors affecting the driving speed of heading face 7106 and the advancing speed of working face 9102 are summarized into the following six aspects, as shown in Table 1. In the table, "√" means that it will affect the system, and "×" means that it will not affect the system.

2.2. Causality Analysis.

Causality analysis can effectively analyze the relationship between various factors in the system [18, 19]. The causality diagram of the excavating system is based on the coal mining system and the driving system, illustrating the influence of various factors on the rapid driving of the roadway, the advancing speed of the mining face, and the interaction between the two systems. The factors that affect the excavating system mainly include geological structure, operating environment, mechanical equipment, regular circulation level, etc. The influence of each factor on the system is shown in Figure 1. The causal relationship between each factor is represented by a causal chain composed of causal arrows with positive (+) and negative (−) signs. Taking "Airflow Gas Concentration of Heading Face" as an example, the Airflow Gas Concentration of Driving Face ↑⟶ (−) Gas Level of Driving Face ↓⟶ (−) Operating Environment Level of Driving Face ↓⟶ (−) Tunneling footage ↓⟶ (−) Driving distance of Driving Face↓.

2.3. System Structure Flow Diagram.

Based on the analysis of the causality of the excavating system, the structure flow diagram of the excavating system is drawn with Vensim software, as shown in Figure 2. The structure flow diagram contains two rate variables: the driving speed and the advancing speed of the working face, and two state variables (cumulative quantities): the driving length and the advancing distance of the working face.

3. Simulation

The above established model is applied to the 9102 working face and 7106 heading face of Wangzhuang Mine. The 9102 working face has a total length of 3,500 meters, the actual mining distance is 2450 meters, and the mining time is 24 months. The total length of the 7106 ventilation roadway and transport roadway lane is 2500 meters, and the driving time is 27 months. Therefore, the system simulation time is set as 27 months and simulation step length is 1 month.

3.1. Parameter Setting

3.1.1. Weight Determination.

The weight values of each index are determined by the group AHP method except the two indexes of advanced roadway support level and the moving level of two sides of roadway, which were given by experts. The weight results are shown in Table 2.

3.1.2. Basic Parameter Setting.

The basic parameters mainly include the distance from the tunneling face to the geological structure zone, the failure rate of the tunneling face mechanical equipment, the gas concentration of the return air flow from the heading face, the distance from the mining face to the geological structure zone, the normal circulation rate of the mining face, etc.

3.1.3. Assignment of Auxiliary Variables.

The level of each influencing factor changes as the value of the factor changes. This paper uses table function to express the relationship between the level and the actual value of the influencing factors. The level of influencing factors was quantified with 40~100 scores. The influence degree is represented by the promotion or weakening effect on the numerical value of the affected factor, whose value may be greater than or less than 1. Considering the research results of many scholars, the paper defines the range of influence to be between 0.5 and 1.5 [20].

3.2. Simulation Analysis

3.2.1. Model Checking.

Vensim software has its own "check model" function, which can check the consistency of model units. The simulation model in this paper runs well, and the consistency of the model units is verified by the "check model" function. After running the model, it can be obtained that the simulated output value of driving length is 2,441.765 meters, and the error rate is −2.33% compared with the actual value of 2500 meters. Compared with the actual value of 2450 meters, the simulated output value of the advance distance of the coal mining face is 2526.87 meters, and the error rate is +3.14%. The absolute error value of both is less

TABLE 1: Key influencing factors of mining system.

The key factors	Detailed index	Driving system	Coal mining system
Geological structure level	Distance of geological structural zone (m)	√	√
Mine pressure level of underground roadway	Advance support distance of roadway (m)	×	√
	Two-sided displacement (mm)	×	√
Working environment level	Water inflow per unit time at mining face (m^3/h)	√	√
	Roof crushing degree	√	√
	Roof falling capacity (mm)	√	√
	Roof subsidence rate (mm/min)	√	√
	Return air flow gas concentration at the mining face (%)	√	√
Regular circulation level	Normal circulation rate (%)	√	√
Mechanical and electrical equipment failure level	Electromechanical equipment accident rate (%)	√	√
Power on level	Operating rate (%)	√	√
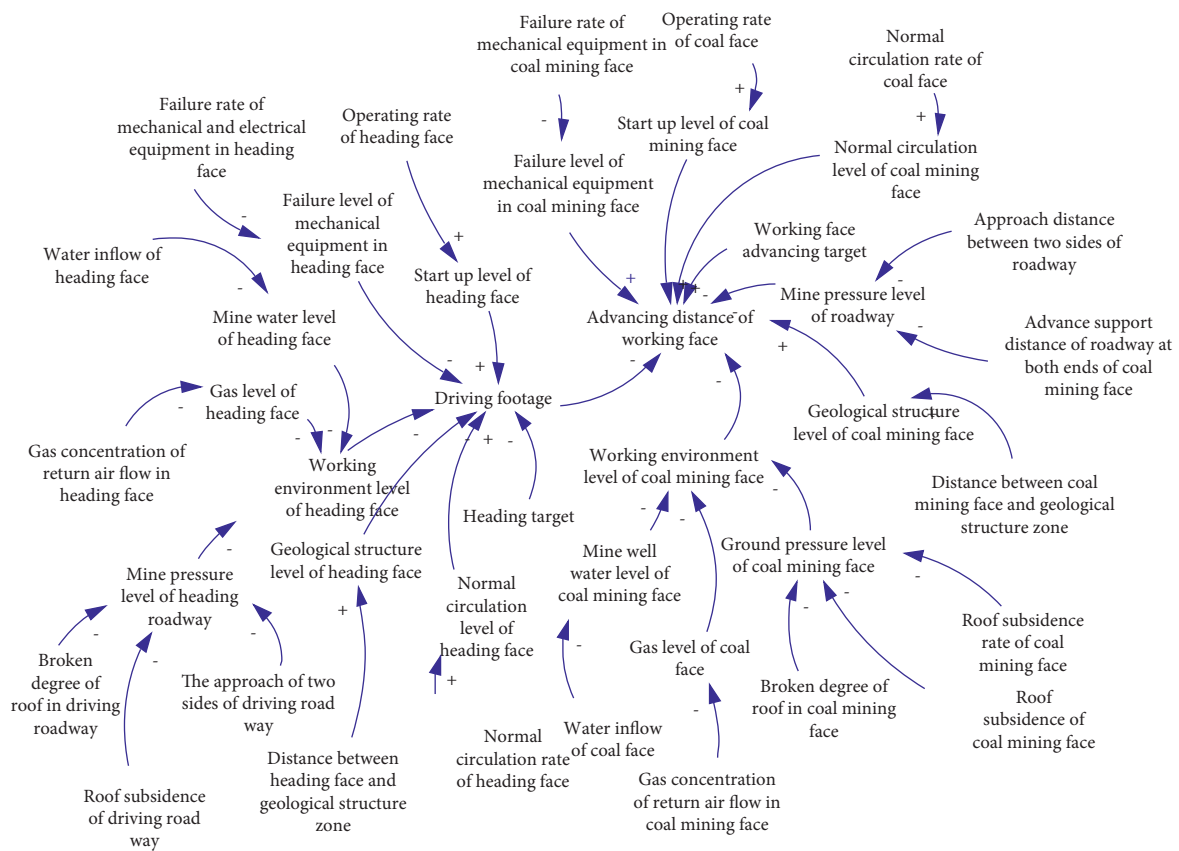
FIGURE 1: Causality diagram of mining-driving system.

than 5%, indicating that the model has a good effect and is qualified.

3.2.2. Analysis of Simulation Results

(1) The relationship between the level of each influencing factor and the driving speed is shown in Figures 3(a) and 3(b). It can be seen from the figure that all influencing factors have an impact on the driving speed. The level of geological structure reached its lowest point in the 5th and 19th months,

and the level of other influencing factors reached their lowest in the 6th and 20th months. Driving speed also reached its lowest point in the 6th and 20th months correspondingly. The curve trend of the driving speed was roughly the same as the horizontal curve trend of each influencing factor.

(2) The relationship between the level of each influencing factor and the advancing speed of the working face is shown in Figures 4(a) and 4(b). It can be seen from the figure that various factors have an impact on the advancing speed of the
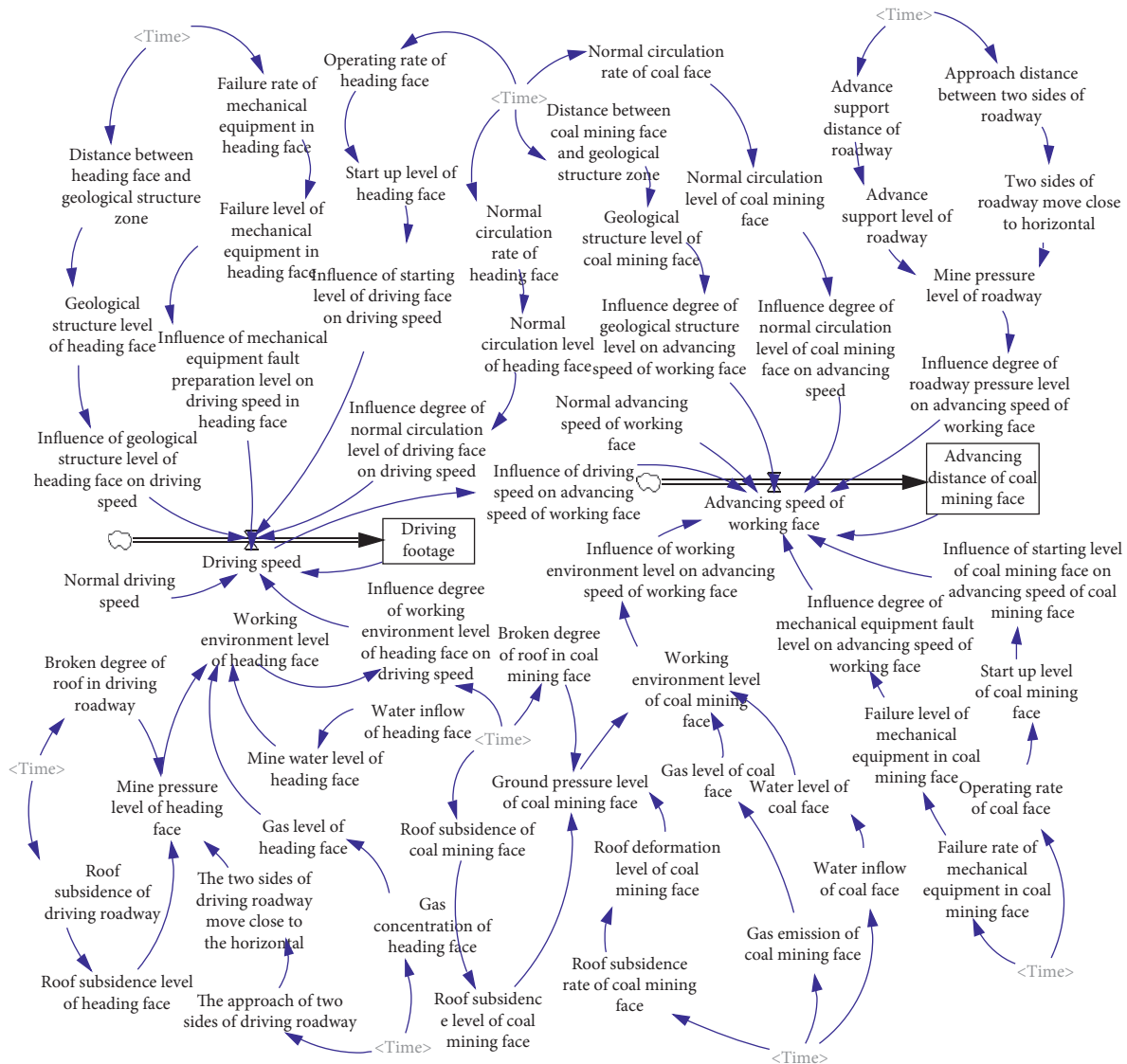
Figure 2: Structure flow diagram of mining-driving system.

working face. The level of geological structure remained at a relatively low level from 4th to 9th and 16th to 18th months, while other factors also fluctuated at a low level during this period. The driving speed reached its lowest point in the 6th and 17th months, and the trend of the tunneling speed curve of the working face was roughly consistent with that of the horizontal curve of the influencing factors.

(3) The simulation results of the mining-driving system are shown in Figures 5(a)–5(d). From Figure 5(a), it can be seen that the advancing speed of the 9102 working face has been significantly slower since April. Also, for nearly 5 months thereafter, its speed remained at a low level, rose in the 11th month, and then significantly decreased in the 17th month. But the duration is short. It returned to above the normal advancing speed in the 20th month. The main reason

is that the 9102 working face was getting closer and closer to the F304 fault in the fourth month, and the span of F304 is 490 meters. Therefore, under the influence of the fault, the driving speed remained at a low state for a long time. In the 17th month, the working face encountered collapse columns H51 and X14 one after another. The two collapse columns were adjacent and the span was relatively small. Therefore, the impact time on the speed was relatively short. Correspondingly, the working face advance distance curve slowed down as its speed decreased. It can be seen from Figure 5(b) that the driving speed of the heading face decreased significantly in the 4th month, reached the lowest point in the 6th month, then decreased significantly in the 16th month, and reached the lowest point in the 20th month. The lowest speed was lower than that in the 6th month. The main reason is that the heading face is getting closer to anomaly area 3 in 4 and 16

TABLE 2: Simulation model weight assignment.

Index	W_j	Weight value
Influence of geological structure level of heading face on heading speed	W_1	0.3176
Influence of working environment level of heading face on heading speed	W_2	0.3175
Influence of normal level of heading face on heading speed	W_3	0.123
Influence of starting level of heading face on heading speed	W_4	0.123
Influence of mechanical equipment fault level coal mining on heading face speed in heading face	W_5	0.1189
Mine pressure level of heading face	W_6	0.3008
Gas level of heading face	W_7	0.4901
Mine water level of heading face	W_8	0.2091
Roof breakage degree of heading roadway	W_9	0.4012
Roof subsidence level of heading face	W_{10}	0.2908
Approaching level of two sides of tunneling roadway	W_{11}	0.308
Influence of geological structure level on advancing speed of coal mining face	W_{12}	0.2986
Influence of working environment level of coal mining face on advancing speed of working face	W_{13}	0.1962
Influence of the normal level of the working face on the advancing speed of the working face	W_{14}	0.0616
Influence of mining face level on working face advancing speed	W_{15}	0.0792
Influence of mechanical equipment failure level of coal mining on working face advancing speed	W_{16}	0.0835
Influence of roadway end management level on working face advancing speed	W_{17}	0.099
Influence of driving speed on advancing speed of working face	W_{18}	0.1819
Mine pressure level of coal mining face	W_{19}	0.3325
Gas level in coal mining face	W_{20}	0.5278
Mine water level of coal mining face	W_{21}	0.1397
Roof breakage degree of coal mining face	W_{22}	0.3062
Roof subsidence level of coal mining face	W_{23}	0.3012
Roof deformation level of coal mining face	W_{24}	0.3926
Roadway advanced support level	W_{25}	0.35
The approaching level of two sides of roadway	W_{26}	0.65

(a)

(b)
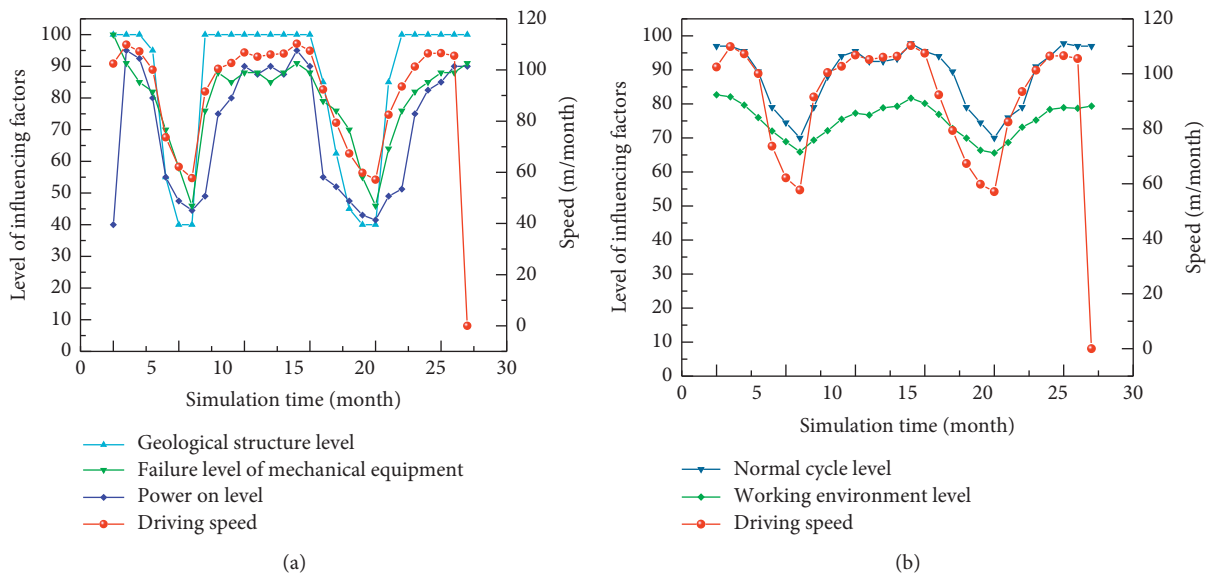
FIGURE 3: Relationship between driving speed and influencing factors.

months, and the return air roadway traverses the anomaly area, so it has a greater influence on it. As a result, the driving speed is lower and the duration is longer in the 20th month, thus affecting the normal replacement between roadway driving. The driving footage is the cumulative amount of the driving speed. According to the driving footage curve, it can also be seen that the trend of the driving footage curve becomes slow in the month with a lower driving speed. It can be seen from Figure 5(c) that under normal circumstances, the driving speed is lower than the advancing speed of the working face, and it has a certain impact on the advancing speed of the working face. The trends are not exactly the same because the advancing speed of working face is also affected by other factors. Figure 5(d) shows that the
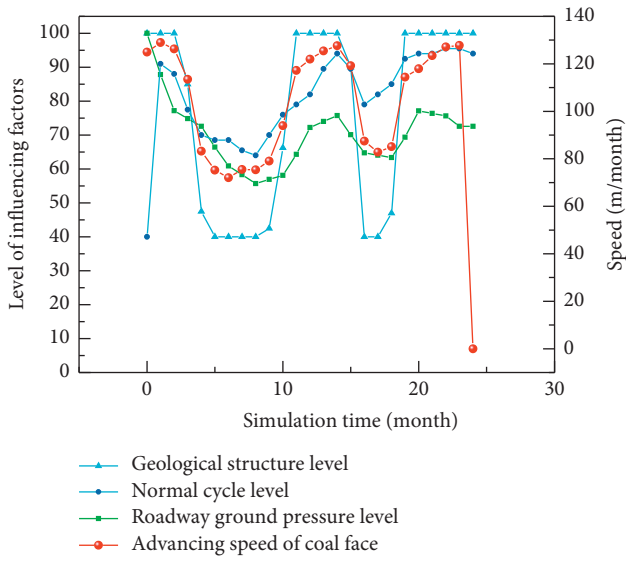
(a)
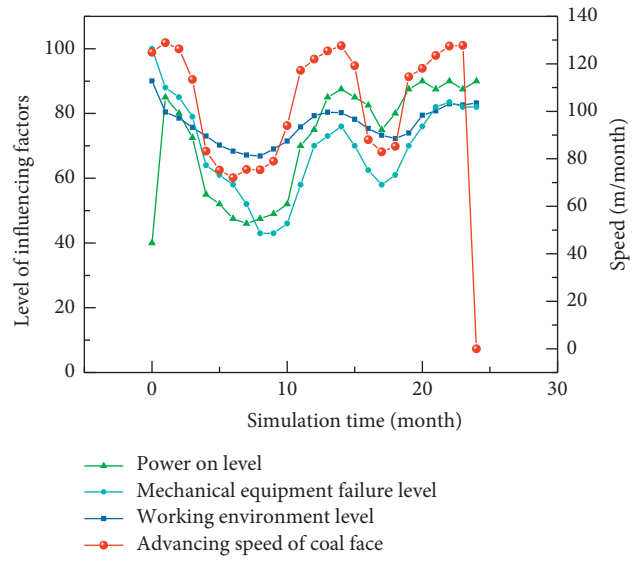
(b)

FIGURE 4: Relationship between the level of each influencing factor and the advancing speed of coal mining face.
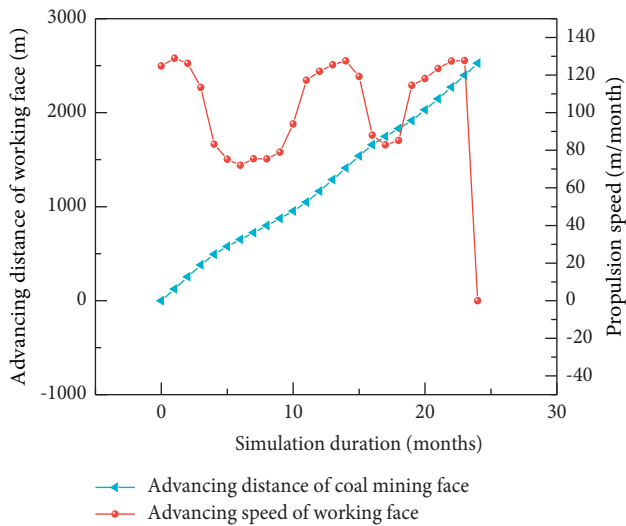
(a)
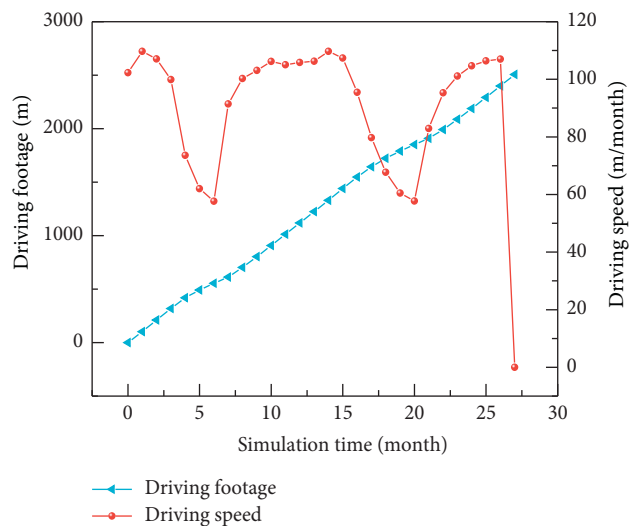
(b)

FIGURE 5: Continued.

(c)

(d)
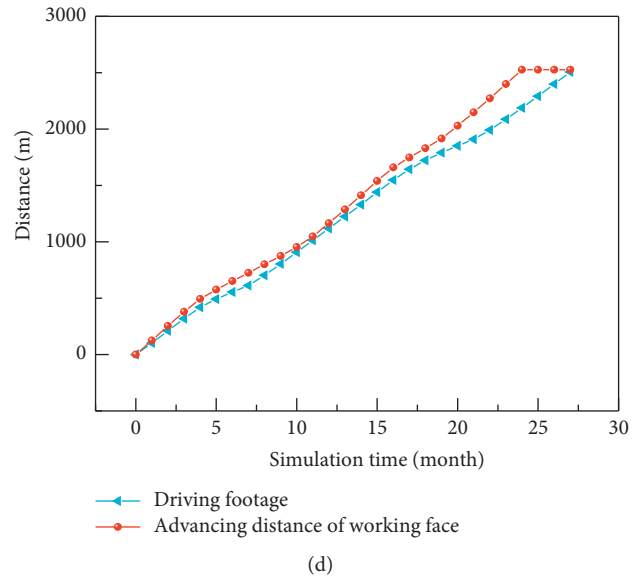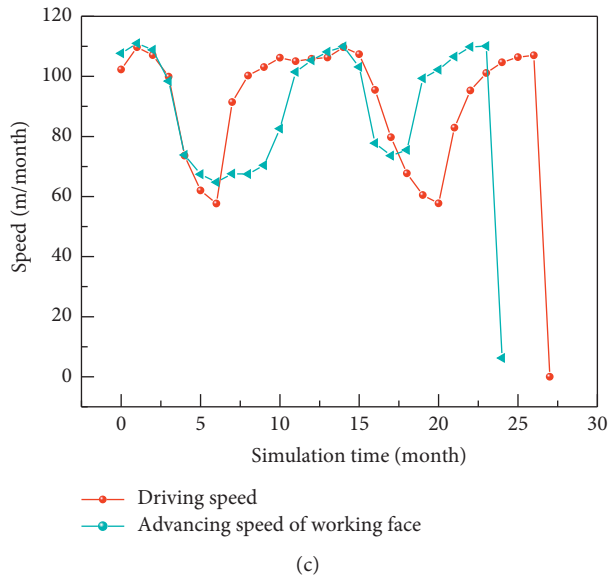
FIGURE 5: Simulation results of mining-driving system: (a) relationship between advancing speed and advancing distance of working face; (b) relationship between driving speed and driving footage; (c) relationship between driving footage and advancing distance of working face; (d) relationship between driving speed and advancing speed of working face.

(a)

(b)

FIGURE 6: Continued.

(c)
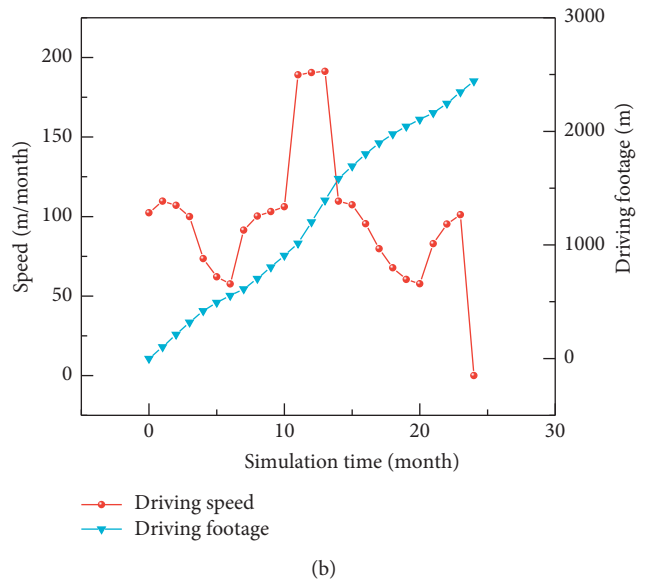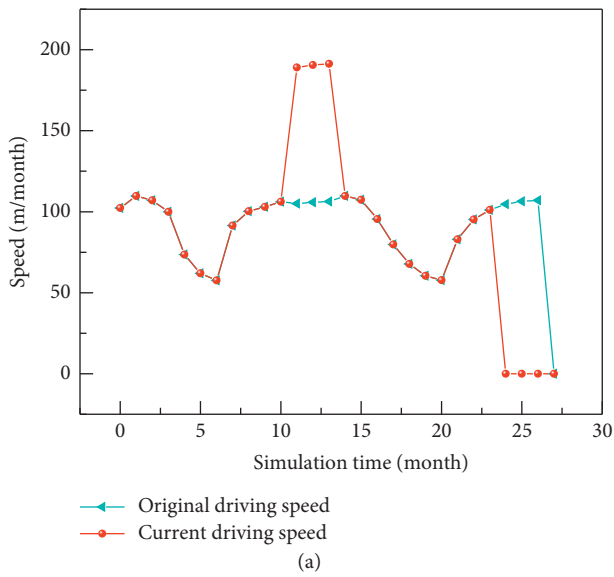
(d)
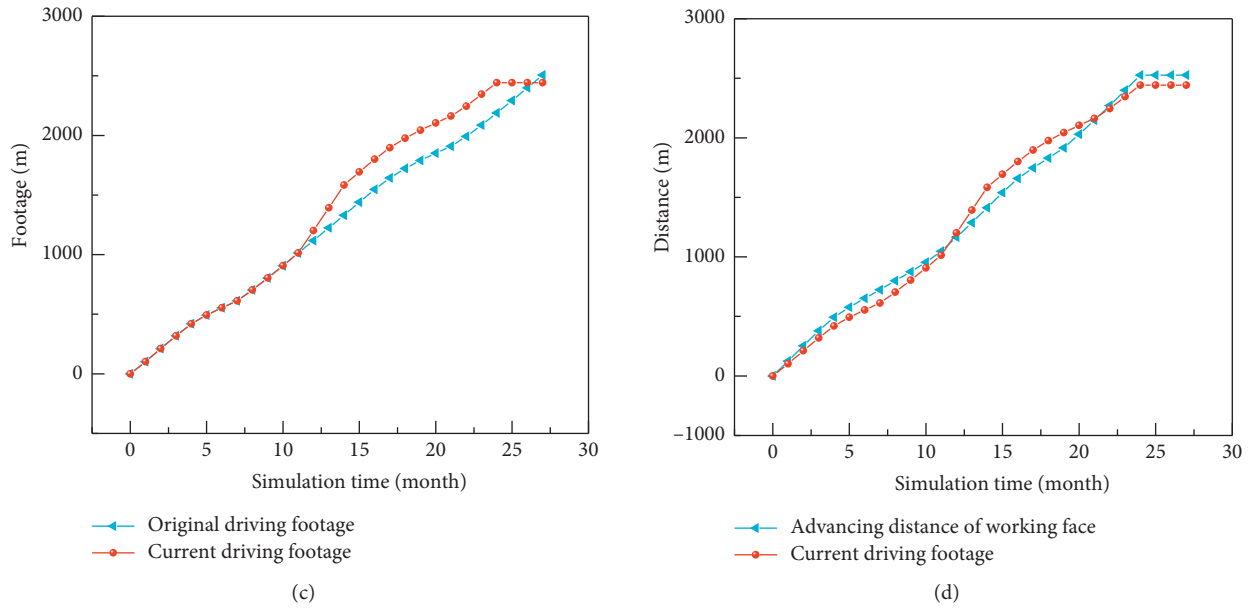
FIGURE 6: Simulation results of mining plan arrangement: (a) relationship between original driving speed and current driving speed; (b) relationship between current driving speed and driving footage; (c) relationship between original driving footage and current driving footage; (d) relationship between working face advancing distance and current driving footage.

fully mechanized mining team completed the entire construction period in the 24th month, while the tunneling team completed the entire construction period in the 27th month, which is 3 months later than the mining face, and there is an imbalance problem between mining and driving.

3.3. *The Optimization of Mining and Driving Replacement.* It can be seen from the simulation results that there is an imbalance problem in the replacement of mining and driving. Due to the relatively complicated process of the tunneling face itself, the normal driving speed is relatively slow. Secondly, the tunneling face encountered anomaly area 3 in the 4th and 16th months, which affected the normal driving speed. For the reason that most of the factors affecting the driving speed are the changes of geological conditions, resulting in the change of other factors, and most of them belong to the mine hydrogeological factors, it is difficult to improve the driving speed by changing these factors. In order to ensure the balance of mining replacement, the following two aspects can be considered.

(1) Advance tunneling period: from Figure 5(d), it can be seen that the coal mining team completes the construction period 3 months earlier than the tunneling team. If the tunneling team starts working three months earlier, the construction period will be completed at the same time as the mining team to ensure the normal replacement of mining.

(2) Arranging more tunneling teams at the right time: when the resources are sufficient, two driving teams can be reasonably arranged to work. The tunneling working face is composed of transport lane and

return air lane, and the two roadways do not affect each other when working, which can meet the requirements of two tunneling teams working at the same time. Through further simulation, the paper found that in the 11th month, a new driving team was added to start work in the transport lane, and the two teams worked in parallel from 11 to 13 months, and after the 13th month (return air lane driving task is completed), the remaining roadway driving tasks are completed independently by the second team. The specific simulation results are shown in Figure 6.

It can be seen from Figure 6(a) that in the 11th month, due to the simultaneous operation of the two teams, the driving speed has increased significantly. After the 13th month, since only one team is operating, the driving speed has dropped to the original level. It can be seen from Figure 6(b) that at the current driving speed, the driving team's driving footage reached 2,441.765 meters in the 24th month, which is still nearly 60 meters away from completing the task. However, after the completion of the construction period, the working face will take time to move. Therefore, it has basically completed the driving task. Figure 6(c) shows that the improved driving plan completes the task 3 months earlier than the original plan. Figure 6(d) shows that the replacement of mining and driving has basically worked properly.

4. Conclusions

Based on the system dynamics modeling, the dynamic simulation structure model of mining-driving system in Wangzhuang Mine was established with the help of Vensim software, and the dynamic simulation of 9102 mining face and 7106 heading face was carried out. The results show that

there exists the phenomenon of replacement imbalance between mining and driving. Advancing the driving schedule or adding a new driving team can meet the demand of normal replacement. It can provide guidance for making driving and mining planning in other similar working faces. Optimizing the driving process reasonably helps to realize the perfect coordination of mining face and roadway driving in time and avoid the emergence of mining face replacement tension and resource waste phenomenon, which ensures the mine efficiency and production safety to the utmost extent.

Data Availability

All data and models used to support the findings of this study are included within the article.

Conflicts of Interest

The authors declare that they have no conflicts of interest.

Acknowledgments

References

[1] G. F. Wang, F. Liu, X. J. Meng, J. D. Fan, and Q. Y. Wu, "Research and practice of coal mine intelligence (primary stage)," *Coal Science and Technology*, vol. 47, no. 8, pp. 1–36, 2019.

[2] D. Z. Kong, S. J. Pu, Z. H. Cheng, G. Wu, and Y. Liu, "Coordinated deformation mechanism of the top coal and filling body of gob-side entry retaining in a fully mechanized caving face," *International Journal of Geomechanics*, vol. 21, no. 4, 2021.

[3] S. H. Zhang, *Dynamic Simulation and Optimization of Mining Replacement and Ventilation System in Outburst Mine*, China University of Mining, Xuzhou, China, 2012.

[4] H. Wang, "Development of comprehensive mechanized tunneling technology in China 40a," *Journal of China Coal Society*, vol. 35, no. 11, pp. 1815–1820, 2010.

[5] S. Yang, X. Z. Hua, P. Yang, and X. Liu, *Determination and Engineering Practice of Unsupported Roof Distance for Rapid Excavation of Roadway with Thick and Hard Basic Roof*, (prepublish), Geotechnical and Geological Engineering, Netherlands, Europe, 2021.

[6] Y. Chen, Y. Zhang, J. Y. Geng, and F. T. Wang, "Process optimization and support technology of integrated rapid excavation of high-stress coal roadway with driving and anchoring," *Coal mine safety*, vol. 50, no. 7, pp. 120–123, 2019.

[7] Z. G. Zhang, "Development trend and key technology of coal roadway rapid excavation system," *Coal Science and Technology*, vol. 44, no. 01, pp. 55–60, 2016.

[8] A. Arabaninezhad and A. Fakher, "A practical method for rapid assessment of reliability in deep excavation projects," *Iranian Journal of Science and Technology, Transactions of Civil Engineering*, vol. 45, 2020.

[9] Y. D. Liu, J. Lin., J. W. Yang, and P. F. Jiang, "Rapid excavation and support technology of extra-thick top coal roadway based on the integration of driving and anchoring," *Coal Science and Technology*, vol. 45, no. 10, pp. 60–65, 2017.

[10] J. F. Lou, F. Q. Gao, J. H. Yang et al., "Characteristics of evolution of mining-induced stress field in the longwall panel: insights from physical modeling," *International Journal of Coal Science Technology*, vol. 20, no. 8, pp. 15–26, 2021.

[11] Y. F. Yan, *Research on Coal Mine Tunneling Replacement Network Model and Reasoning System*, Taiyuan University of Technology, Taiyuan, China, 2017.

[12] Z. M. Tian, *Research and Design of Intelligent Decision Support System for Mine Excavation Replacement*, Hebei University of Engineering, Handan, China, 2014.

[13] Y. J. Yuan, Y. Tian, and J. Sun., "System dynamics modeling and simulation of the stability of industry-university-research technology alliance," *Science of Science and Science and Technology Management*, vol. 34, no. 4, pp. 3–9, 2013.

[14] Y. W. Jia and L. M. Jia, "The construction of system dynamics model for sustainable development of high-tech enterprises in universities," *Research and Development Management*, vol. 26, no. 3, pp. 97–103, 2014.

[15] M. Wu, *Analysis of Land Use Carbon Emissions and System Dynamics Simulation in Wuhan City*, Huazhong Agricultural University, Wuhan, China, 2017.

[16] G. He, *System Analysis of Coal Mine Safety Influencing Factors and Research on System Dynamics Simulation*, Anhui University of Science and Technology, Huainan, China, 2009.

[17] B. Zhang, Z. H. Yu, Q. Sun, S. Li, M. X. Huang, and L. Q. Wang, "Environment and sustainable development," *Introduction to System Dynamics and Summary of Related Software*, vol. 35, no. 2, pp. 1–4, 2010.

[18] J. B. Chen, J. Z. Zhong, and B. S. Xie, "Research on system dynamics simulation of building materials supply chain," *Journal of Physics: Conference Series*, vol. 1864, no. 4, 2021.

[19] J. J. Wang, Q. Guo, F. Wang, K. B. Aviso, R. R. Tan, and X. Jia, "System dynamics simulation for park-wide environmental pollution liability insurance," *Resources, Conservation and Recycling*, vol. 170, 2021.

[20] L. Mai and Y. Song, "Research on traffic congestion based on system dynamics," *Car practical technology*, vol. 46, no. 4, pp. 29-30+65, 2021.

Research Article

Mechanical Parameters of Deep-Buried Coal Goaf Rock Mass Based on Optimized GSI Quantitative Analysis

Qingqiu Wang,[1,2] Mo Xu ,[1] Yunhui Zhang ,[3] Xinyu Cen,[1] and Xingwang Chang[1,2]

[1]*State Key Laboratory of Geohazard Prevention and Geoenvironment Protection, College of Environment and Civil Engineering, Chengdu University of Technology, Chengdu 610059, China*
[2]*China Railway Eryuan Engineering Group Co., Ltd., Chengdu 610031, China*
[3]*Faculty of Geosciences and Environmental Engineering, Southwest Jiaotong University, Chengdu 611756, China*

Correspondence should be addressed to Mo Xu; xm@cdut.edu.cn

In order to obtain the accurate mechanical parameters of deep-buried coal goaf rock mass, the limitation of geological strength index (GSI) in concealed rock mass is analyzed. Based on the test result and analysis of the current normative standards, the classification indexes of rock mass structural are optimized based on discontinuity distance d and rock mass integrity index K_v. The ratio of rock mass saturated strength to dry strength, η, is introduced, quantization formula of structural surface conditions is proposed, and the influence of groundwater and rock types is included in structural surface condition classification. The GSI system is improved to better suit all types of deep-buried and water-rich rock masses. Furthermore, the rock mass disturbance factor D's quantitative formula is listed according to the Hoek–Brown (HB) criterion. Taking the goaf roof under railway as an example, the parameters of deep-buried rock mass are obtained based on the improved quantitative GSI system and HB criterion. This research provides a scientific reference for achieving geological parameters and engineering designing in goaf areas.

1. Introduction

There are different types of discontinuities in rock mass with the complex geological process, and mechanical parameters of rock mass are important factors of qualitative evaluation for engineering analysis and design [1]. The foundation stability and cost of project are closely correlated with the mechanical parameters, and parameter estimation of rock mass in the recent research is one of the hot topics [2, 3]. Now, great achievements have been made in obtaining mechanical parameters of rock mass by scholars. The main methods are theory analysis based on in situ experiment and empirical formula based on test [4]. However, size effect on rock mass in situ test is an unavoidable problem, and large-scale in situ test cannot be completely carried out with current test equipment [5, 6]. It is more necessary and valuable to research the method of achieving deep-buried rock mass mechanical parameters based on field and laboratory tests.

Hoek and Brown proposed the Hoek–Brown (HB) failure criterion in 1980 to estimate intact rock mass strength, and they introduced geological strength index (GSI) and disturbance factor D and proposed the generalized HB criterion to estimate the jointed rock mass mechanical parameters in 2002 [7]. HB criterion is widely accepted and has been applied in a large number of projects. The GSI value mainly depends on rock mass structure and structural surface conditions. Rock mass structure is determined by classification of the rock mass integrity, structural surface conditions are determined by roughness, weathering, and infilling of the surface, and all factors are qualitatively and subjectively evaluated. Later, many scholars have researched the methods on achieving the GSI value, and rock mass structure can be quantified by the number of joints J_v [8]. J_v is an important index to evaluate the integrity of rock mass. However, it is difficult to obtain the volumetric joint number of deep-buried rock mass by field measurements; in addition, the influence of groundwater on the rock mass

mechanical parameters has not been included when the GSI value is estimated.

In order to solve the problem that the volumetric joint number J_v of concealed rock mass cannot be obtained by field measurement, Xia et al. [9] established a formula of geological strength index (GSI) by longitudinal wave velocity V_p of rock mass, where GSI $= 15V_p - 7.5$, but this method is proposed on the basis of intact rock mass tests. When growing rock mass fissures are in-filled with groundwater, the wave velocity is larger than that without groundwater, and the GSI value is also larger, which easily leads to the wrong conclusion that the rock mass is more complete than it really is.

The influence of groundwater on rock mass is mainly reflected in lubrication, softening, and chemical erosion of rock mass structural surface. Groundwater can easily soften and alter rock mass structural surface conditions. The crack water pressure can reduce the effective stress and mechanical parameters. However, groundwater has little effect on rock mass structure, which is determined by discontinuities. Therefore, the influence of groundwater on the rock mass GSI can only be considered in the rock mass structural surface conditions. In addition, it can also minimize the error caused by the large wave velocity of broken rock mass filled with groundwater.

2. Estimation of Rock Mass Mechanical Parameters Based on HB Criterion

Now, the nonlinear HB criterion for rock masses is widely accepted and has been applied in many projects around the world to estimate the strength and deformation characteristics of heavily jointed rock masses [10]. It also has been widely used in mining engineering [7, 11]. Rock mass cohesion C_m, friction angle ϕ_m, and compressive strength σ_{cm} can be estimated by the empirical formulas as follows.

$$C_m = \frac{\sigma_{ci}\left((1 + 2a)s + (1 - a)m_b\sigma_{3n}\right)\left(s + m_b\sigma_{3n}\right)^{a-1}}{(1 + a)(2 + a)\sqrt{1 + \left(6am_b\left(s + m_b\sigma_{3n}\right)^{a-1}\right)/(1 + a)(2 + a)}}, \quad (1)$$

$$\phi_m = \sin^{-1}\frac{6am_b\left(m_b\sigma_{3n} + s\right)^{a-1}}{2(1 + a)(2 + a) + 6am_b\left(m_b\sigma_{3n} + s\right)^{a-1}}, \quad (2)$$

$$\sigma_{3n} = \frac{0.47\sigma_{cm}^{0.06}(\gamma H)^{0.94}}{\sigma_{ci}}, \quad (3)$$

$$m_b = m_i\exp\frac{\text{GSI} - 100}{28 - 14 D}, \quad (4)$$

$$\sigma_{cm} = \sigma_{ci} \cdot \frac{\left(m_b + 4s - a\left(m_b - 8s\right)\right)\left(m_b/4 + s\right)^{a-1}}{2(1 + a)(2 + a)}, \quad (5)$$

$$\sigma_t < \sigma_3 < \frac{\sigma_{ci}}{4},$$

where σ_{ci} is the uniaxial compressive strength of the intact rock mass, γ is the unit weight of the rock mass, H is depth of rock mass below surface, σ_t is the tensile strength of intact

rock, m_i refers to material constants of intact rock, which can be determined by references [12, 13], and s refers to the rock mass material constants, given by

$$s = \exp\left(\frac{\text{GSI} - 100}{9 - 3 D}\right). \quad (6)$$

a is rock mass feature factor, given by

$$a = \frac{1}{2} + \frac{1}{6}\left(\exp\left(\frac{-\text{GSI}}{15}\right) - \exp\left(\frac{-20}{3}\right)\right). \quad (7)$$

Hoek and Diederichs corrected the deformation modulus of intact rock with modulus ratio and established the empirical formula [14], as follows:

$$E_m = E_i\left(0.02 + \frac{1 - D/2}{1 + \exp\left((60 + 15 D - \text{GSI})/11\right)}\right), \quad (8)$$

where E_m and E_i are the jointed and intact rock mass deformation moduli and D is the rock mass disturbance factor, which can be determined by reference [7].

The formulas above are all related to the geological strength index (GSI). How to correctly achieve GSI value is the key to the calculation.

3. Determination and Optimization of Geological Strength Index (GSI)

The geological strength index (GSI) value is related to rock mass structure and structural surface conditions and discussed separately below.

3.1. Quantification of Rock Mass Structure. In order to quantify the rock mass structure of the GSI system, Sonmez and Ulusay [15] classified rock mass structure by introducing rock mass volumetric joint number J_v. On the basis of assuming that rock mass is isotropic, J_v is given by

$$J_v = \frac{N_x}{L_x}\frac{N_x}{L_x}\frac{N_x}{L_x}, \quad (9)$$

where N_x, N_y, and N_z are the joint numbers along scan lines (L_x, L_y, and L_z) and L_x, L_y, and L_z are the lengths along perpendicular direction.

The goaf roof is affected by the stress redistribution after coal excavation, and many cracks develop along rock mass strike and dip. Affected by the force of gravity, the roof rock masses constantly produce bed separation or cracks. Joints and fissures distribute unevenly and irregularly in rock mass, and it is very difficult to measure the joint number of buried rock mass in engineering geological investigation. Fortunately, many scholars found that there is a good correspondence between the volumetric joint number J_v and integrity index K_v of rock mass based on the extensive field test [16], and the relationship between J_v and K_v is listed in Table 1.

According to the corresponding relations between J_v and K_v, the corresponding formula between them can be shown as

TABLE 1: Relationship between volumetric joint number J_v and integrity index K_v of rock mass [16].

Volumetric joint number J_v (per cubic metre)	<3	3–10	10–20	20–35	>35
Integrity index K_v	>0.75	0.75–0.55	0.55–0.35	0.35–0.15	<0.15

$$K_v = -0.043 + 0.9 \ \exp\left(\frac{-J_v}{23.5}\right). \tag{10}$$

The correlation coefficient of function fitting is 0.998, and they fit well.

Distance and number of discontinuities are important indexes for describing rock mass structure, and various structural characteristics of rock mass are described in detail and quantized in books, such as Standard for Engineering Classification of Rock Mass [16] and Geological Engineering Handbook [17]. Rock mass structure classification according to normative standards is shown in Table 2.

Coal measure strata belong to sedimentary strata; generally, lots of shallow cracks developed in the rock surface are caused by the stress release of denudation, when the ground stress is small and the rock mass structure is not developed. The cracks decrease gradually with increasing depth and thus deep rock mass is intact. Stable coal seam is generally excavated along strike and dip. When the stress of coal roof and floor is released, intact rock will be destroyed by strike and dip discontinuities. As a result, rock mass displacement and bed-separation fractures develop towards goaf. Therefore, the discontinuities of rock mass include dip fractures, strike fractures, bed-separation fractures along the rock mass surface, and primary fractures. Sonmez et al. [18] proposed the method to calculate rock mass volumetric joint number according to joint sets of rock mass surface.

$$J_v = D_n \frac{1}{s}, \tag{11}$$

where D_n is the rock mass joint set number and s is the average size of rock block or rock slice (in general, it is considered to be equal to the space between joints). Therefore, the rock mass structure can also be classified based on joint set number and the average size of rock block or rock slice. Assuming that the block is cut by the discontinuities and rock masses are made up of many cubes or polyhedrons, the size of rock mass is the distance between discontinuities. Substituting equation (11) into equation (10), the factor K_v can be expressed as

$$K_v = 0.9 \ \exp\left(\frac{-D_n}{23.5s}\right) - 0.043. \tag{12}$$

Now the classification in the standards of tunnel surrounding rock [16, 17] is different from the widely used GSI system [10], and it is necessary to refine the structure classification.

In Table 2, rock mass with discontinuity distance larger than 1.0 m belongs to intact structure, that with discontinuity distance between 1.0 m and 0.4 m belongs to blocky structure, and that with discontinuity distance between 0.4 m and 0.2 m belongs to very blocky-interlocked structure. Based on the rock mass classification of tunnel [19] and soil classification [20], the fragmented rock larger

than 0.06 m and the pebble larger than 0.02 m are distinguished from the fractured rock. Pebble with diameter 0.06 m to 0.02 m and brecciated rock mass influenced by tectonics and shear stress are also separately classified. So, rock mass with discontinuity distance between 0.2 m and 0.06 m belongs to fractured rock, rock mass with discontinuity distance between 0.06 m and 0.02 m belongs to extremely fractured rock, and rock mass with discontinuity distance less than 0.02 m belongs to conglomeratic rock. In European standards [21], the space of discontinuities is distinguished by 0.2 m, 0.06 m, and 0.02 m, and the size of rock mass is distinguished by 0.2 m and 0.06 m, which is basically consistent with the qualitative classification of the GSI system. Therefore, it is reasonable to distinguish discontinuities by 0.2 m, 0.06 m, and 0.02 m. The rock mass integrity index K_v can be calculated by equation (12). The new rock mass structure classification is shown in Table 3.

3.2. Quantification of Structural Surface Conditions. The rock mass structural surface conditions in the geological strength index (GSI) system involve roughness, weathering, and infilling of structural surface only. Palmstrom [22] quantified the structure surface conditions of rock mass by the three factors above and left out the effect of groundwater. Jiang et al. [23] suggested reducing the GSI value to reflect the influence of groundwater; in this method, the values of structural surface conditions and rock mass structure are reduced in the same proportion. In fact , rock mass structure is determined by the density of discontinuities; groundwater only has an effect on structural surface conditions, and it is inconsistent with the mechanism of groundwater action on rock mass, so this method needs further discussion.

The influence of groundwater on the rock mass mechanical parameters is more obvious, and all the parameters of the eroded rock are reduced to varying degrees [24]. Liu et al. [25] found based on experiment that the uniaxial compressive strength and deformation modulus of saturated argillaceous sandstone are 58.51% and 51.64% compared with dry rock mass. Wang et al. [26] experimented and analyzed saturated sandstone samples of different sizes, and the uniaxial compressive strength and deformation modulus are 56.5% and 45.6% compared with dry rock samples. Chen et al. [27] analyzed the effect of fissure water on rock mass effective stress based on triaxial test, and the results show that the effective stress decreases with the increasing pressure of crack water; the effective stresses of the specimens are about 59.02% and 45.17% of dry specimens with the confining pressures 15 MPa and 30 MPa. In this paper, the strength of dry and saturated goaf rock mass is tested and statistically analyzed, and the test results of compressive strength and deformation

TABLE 2: Rock mass classification of integrity according to normative standards [16, 17].

Rock mass integrity	Rock mass joint number J_v	Average distance between discontinuities (m)	Rock mass structure
Extremely intact rock	< 3	> 1.0	Intact structure
Relatively intact rock	3–10	1.0–0.4	Blocky structure
Relatively fractured rock	10–20	0.4–0.2	Very blocky-interlocked structure
Fractured rock	20–35	< 0.2	Blocky and disturbed structure
Extremely fractured rock	> 35	—	Disintegrated and laminated structure

TABLE 3: New rock mass structure classification by K_v and distance between discontinuities.

Rock mass integrity	Rock mass integrity index K_v	Average distance between discontinuities (m)	Number of structure sets	Structure of rock mass
Extremely intact rock	> 0.75	> 1.0	1–3	Intact or massive rock with few widely spaced discontinuities
Relatively intact rock	0.75 ~ 0.55	1.0–0.4	3-4	Blocky rock mass consisting of cubical blocks formed by 3-4 intersecting discontinuity sets
Relatively fractured rock	0.55 ~ 0.35	0.4–0.2	3-4	Very blocky-interlocked and partially disturbed mass with multifaceted angular blocks formed by 3-4 joint sets
Fractured rock	0.35 ~ 0.01	0.2–0.06	4	Block folded by 4 intersecting discontinuity sets
Extremely fractured rock	< 0.01	0.06–0.02	4 or more	Disintegrated, poorly interlocked, and heavily broken rock mass made up of mixture of angular and rounded rock pieces
Conglomeratic rock mass		< 0.02	4 or more	Laminated/sheared, with lack of blockiness due to close spacing of weak schistosity or shear planes

modulus of shale, sandstone, and limestone are shown in Table 4.

According to Table 4, the saturated compressive strength is 64.9% to 77.5% of dry compressive strength, and the saturated deformation modulus is 62.1% to 86.5% of dry deformation modulus. The influence of groundwater on rock mass mechanical parameters is not constant for different types of rock masses and geological environments.

The rock mass rating (RMR) system was modified over years and has stood the test of time, and it conformed with the international standards and procedures. So, this paper refers to the RMR system to quantify the influence on structural surface by groundwater. Roughness, weathering, infilling, and groundwater are the main factors which affect the rock mass structural surface conditions. According to Bieniawski's RMR system [28], the full value of roughness, weathering, and infilling is 6, respectively, and the total value is 18, a higher value indicating better rock mass conditions. The full effective value of groundwater on structural surface conditions is 15. Assuming that the groundwater influence coefficient on mechanical parameters of the different types and geological environments of rock masses is α, the quantitative formula of rock mass structural surface conditions is given by the following formula:

$$\text{SCR} = R_r + R_w + R_f + \alpha R_u, \qquad (13)$$

where R_r, R_w, and R_f are the roughness, weathering, and infilling of structural surface conditions and R_u is the influence of groundwater on structural surface. The values of structural surface conditions are shown in Tables 5 and 6 .

Groundwater and fissure water reduce effective stress of the rock mass and the friction coefficient of rock mass discontinuities, and the ability of rock mass to resist deformation and failure is reduced. The influence of groundwater on rock mass mainly includes two aspects: the weakening of rock mass structure surface conditions and the damage of rock mass caused by the microcracks in rock mass which are caused by groundwater. The micropores and microcracks in rock can cause the change of rock mass structure surface conditions, and the effect is macroscopically manifested as rock mass volume increasing and the mechanical properties decreasing. Experiments have shown that the compressive strength and deformation modulus decrease linearly with the change of rock mass volume caused by micropores and microcracks [29], and the deformation modulus is linearly related to the RMR value [28]. Therefore, it can be assumed that the compressive strength and deformation modulus of rock mass have a linear relationship with the value of the structural surface conditions, and the compressive strength can be given by

$$\sigma_{cm} = \sigma_{ci}\, k\big(R_r + R_w + R_f + \alpha R_u\big), \qquad (14)$$

where k refers to the coefficients related to discontinuities of rock mass.

If the rock mass is intact without groundwater, the groundwater has no effect on the rock mass, $R_u = 15$, and the compressive strength of dry intact rock is given by

Table 4: Compressive strength and deformation modulus of shale, sandstone, and limestone.

Compressive strength and deformation modulus based on test	Range value of dry rock	Average value of dry rock	Range value of saturated rock	Average value of saturated rock	The ratio of saturated average value to dry average value
Compressive strength of shale (MPa)	33.8–36.9	35.32	17.6–28.3	22.91	64.9%
Deformation modulus of shale (GPa)	26.2–35.2	33.0	11.8–39.9	20.5	62.1%
Compressive strength of sandstone (MPa)	42.2–58.1	47.76	24.9–39.0	31.91	66.8%
Deformation modulus of sandstone (GPa)	23.7–46.0	34.8	10.9–27.1	21.0	60.3%
Compressive strength of limestone (MPa)	51.9–101.6	80.4	53.8–85.1	62.3	77.5%
Deformation modulus of limestone (GPa)	70.0–95.9	84.9	61.1–87.3	73.4	86.5%

Table 5: Values of structural surface conditions R_r, R_w, and R_f.

Structural surface conditions	Description and value				
Roughness R_r	Very rough 6	Rough 5	Slightly rough 3	Smooth 1	Slickensided 0
Weathering R_w	Unweathered 6	Slightly weathered 4	Moderately weathered 3	Highly weathered 1	Decomposed 0
Infilling R_f	None 6	Hard filling <5 mm 4	Hard filling >5 mm 2	Soft filling <5 mm 2	Soft filling >5 mm 0

Table 6: Value of structural surface conditions R_u.

Structural surface conditions	Description and value				
Water inflow per 50 square metre (l/min)	No water	<10	10–25	25–125	>125
Ratio (joint water pressure/major principal stress)	0	<0.1	0.1-0.2	0.2-0.5	>0.5
General conditions	Dry	Damp	Wet	Dripping	Flowing
Value R_u	15	10	7	4	0

$$\sigma_{cm\,d} = \sigma_{ci} k (18 + 15\alpha). \tag{15}$$

If the rock mass is saturated, $R_u = 0$, and the compressive strength of saturated intact rock mass is given by

$$\sigma_{cms} = 18\sigma_{ci} k. \tag{16}$$

Assuming that $\eta_\sigma = (\sigma_{cms}/\sigma_{cm\,d})$, the influence of groundwater on the compressive strength and deformation modulus of rock mass is different, and comprehensive influence η can be replaced by the average value of them two.

$$\eta = \frac{\eta_\sigma + \eta_E}{2}, \tag{17}$$

$$\eta_E = \frac{E_{cms}}{E_{cm\,d}}, \tag{18}$$

where σ_{cms} and $\sigma_{cm\,d}$ are the compressive strengths of saturated and dry intact rock mass and E_{cms} and $E_{cm\,d}$ are the deformation moduli of saturated and dry intact rock mass.

Substitute equations (16) and (17) into equation (15):

$$\alpha = \frac{18(1-\eta)}{15\eta}. \tag{19}$$

Substitute equation (19) into equation (13):

$$SCR = R_r + R_w + R_f + \frac{18(1-\eta)}{15\eta} R_u. \tag{20}$$

If the rock mass is intact without groundwater,

$$SCR_{max} = \frac{18}{\eta}. \tag{21}$$

Assuming that the maximum quantized value of rock mass discontinuity conditions is 1.0, the quantized value K_{SCR} of different rock mass structural surface conditions can be given by

$$K_{SCR} = \frac{\eta}{18}\left(R_r + R_w + R_f\right) + \left(\frac{1-\eta}{15}\right)R_u. \tag{22}$$

The new quantitative value sheet of the GSI system is given based on optimized quantification of rock mass

structure and structural surface conditions. Buried rock mass structure is classified based on the average distance between discontinuities and integrity index K_v, and the influence of groundwater and different rock types is fully considered in discontinuity condition classifications. The modification can improve the utility of the GSI system. The quantitative value sheet of the improved GSI system is shown in Figure 1.

3.3. Determination of Rock Mass Disturbance Factor.

The disturbance factor D is also a very important factor in the HB criterion, which is mainly used to indicate the degree of rock mass disturbance in blasting or excavation. However, there are only six discontinuous qualitative evaluation values [7]. In addition, the rock mass disturbance factor proposed by Hoek refers to the disturbance of fresh rock mass that is not affected by blasting and excavation because human activities such as blasting and excavation or rock mass weathering only affect the integrity of rock mass surface. So, the rock mass disturbance factor is the damage degree of rock mass caused by the influence of discontinuities. It is necessary to revise the classification of rock mass structure determined by the surface structure affected by blasting, and the classification of rock mass discontinuity conditions determined by weathered discontinuities should also be revised [13]. Therefore, it is necessary to further discuss the value of disturbance factor D.

The original stress state of coal roof changes after coal excavation, rock mass is broken under the unbalance stress, and rock mass deformation modulus will decrease; the deformation modulus is closely correlated with rock mass integrity, and the effective area of section decreases with the development of joints and fissures, while it is difficult to measure the effective bearing area of rock mass. Lemaitre [30] proposed the concept of equivalent stress; assuming that the deformation of the damaged material can be represented by effective stress, the strain of the damaged material is given by

$$\varepsilon\prime = \frac{\sigma\prime}{E} = \frac{\sigma}{(1-D)E_m} = \frac{\sigma}{E_i}. \tag{23}$$

Disturbance factor D can be expressed by

$$D = 1 - \frac{E_m}{E_i}. \tag{24}$$

According to equation (24), rock mass disturbance factor D can be calculated by the deformation modulus of disturbance and intact rock mass. The deformation modulus of disturbed rock mass is difficult to get by laboratory test and small field tests; however, integrity index K_v is the important index widely accepted to evaluate rock mass integrity. Therefore, the deformation modulus of rock mass can be calculated based on the HB criterion and the improved GSI system, which is classified according to rock mass integrity index K_v. Substituting equation (24) into equation. (6), the formula can be changed as follows:

$$D = 0.98 - \frac{1 - D/2}{1 + \exp\left((60 + 15\ D - \mathrm{GSI})/11\right)}. \tag{25}$$

GSI can be obtained by the improved GSI system; according to the equation (25), the relationship between disturbance factor D and the geological strength index (GSI) is listed in Table 7.

When GSI in the table is 100 or 0, the factor D is not 0 or 1 because there are more microfissures in rock mass in nature, and there is no absolutely intact or completely disturbed rock mass. So, the corresponding relationship is reasonable. The relative curve between them is drawn in Figure 2.

According to Figure 2, the factor D of heavily disturbed rock mass changes slowly with the increase of GSI; in other words, in severely jointed rock mass, the disturbance factor D varies in a small range. When the GSI value is 40 to 90, the factor D is nearly linearly correlated with GSI. The problem of nonuniform quantitative standards is solved, and the rock mass integrity in engineering can be better evaluated.

4. Application of Improved GSI System

This paper takes the coal goaf under railway as an engineering case to obtain the rock mass mechanical parameters. The direction of railway is parallel to strike of the stratum. The stratum distribution in this area is relatively stable, mainly including soil layers, shale, sandstone, and limestone. The maximum depth of coal is 140 m, and the strata from top to bottom are described as follows.

Soil with average thickness of 10.0 m is made of clay and sand. 9 coal is the first coal mined with average thickness of 0.9 m, and the roof is shale with average thickness of 22.0 m. 11 coal top roof is shale with average thickness of 10.7 m, 11 coal lower roof is sandstone with average thickness of 24.1 m, and 11 coal is the second coal mined with average thickness of 1.8 m. 13 coal top roof is shale with average thickness of 12.8 m, the middle roof is sandstone with average thickness of 22.0 m, the lower roof is limestone with average thickness of 5.5 m, and 13 coal is the third coal mined with average thickness of 1.5 m. 15 coal roof is shale with average thickness of 16.0 m, and 15 coal is the fourth coal mined with average thickness of 1.3 m. Lots of joints and fissures developed in rock mass are affected by the coal mined, the length of typically drilled rock is shorter than 30 cm, the rock quality designation is between 28.6 and 51.0, and the coal roofs belong to fractured rock mass. Groundwater has been largely pumped from the mine. Hence, the structural suface is weakly eroded due to the absence of groundwater. The rock mass structural surface conditions are rough, weakly eroded, unfilled, and wet. Disturbance factor D can be calculated with equation (25). According to the improved GSI system, the rock mass quantitative GSI values of all goaf roofs are given in Table 8.

According to equations (1)–(8), based on the results of laboratory test and field test, rock mass mechanical parameters of goaf roofs can be calculated by the HB criterion, and the results are shown in Table 9.

Rock mass mechanical parameters of compressive strength, deformation modulus, and friction angle from field

Sketch map of rock mass structure	Structural characteristics of rock mass	Integrity index Kv	Average distance between structure plane d[m]	Structural surface characteristics of rock mass				
				Very good. Very rough, fresh, unweathered and dry surfaces	Good. Rough, maybe slightly weathered and damp iron stained surface	Fair, Smooth, moderately weathered, wet and altered surfaces	Poor. Slickensided, highly weathered surfaces, coatings with filling of angular fragments, very wet	Very poor. Slickenside, highly weathered, coating surfaces with soft lay or filling, flow
				K_{SCR} (include the influence of groundwater and rock types) $K_{SCR} = (\eta/18)(R_r + R_w + R_f) + ((1 - \eta)/15)R_u$				
				1.0 0.8	0.6	0.4	0.2	0
	Intact or massive rock with few widely spaced discontinuities	0.75	1.0	90 80			N/A	N/A
	Blocky rock mass consisting of cubical blocks formed by 3-4 intersecting discontinuity sets	0.55	0.4		70 60			
	Very blocky-interlocked, partially disturbed mass with multi-faceted angular blocks formed by 3-4jiont sets	0.35	0.2			50 40		
	Block folded by 4 intersecting discontinuity sets	0.01	0.06				30	
	Disintegrated, poorly interlocked, heavily broken rock mass with mixture of angular and rounded rock pieces	<0.01	0.02				20	
	Laminated/sheared, lack of blockingss due to close spacing of weak schistosity or shear planes		<0.02	N/A	N/A			10

FIGURE 1: The quantitative value sheet of the improved GSI system.

side pressure test are statistically calculated and listed in Table 10. The rock mass mechanical parameters obtained with the method of optimized new GSI system are similar to those from field test.

The excavation of coal has caused surface subsidence, building cracking, and ground collapse. In order to eliminate the main influence on the newly built railway, the goaf areas under railway were filled with cement slurry. Only 9 coal, 11 coal, and 13 coal goafs were filled. After grouting, wave velocity of rock mass was tested again, and the rock mass mechanical parameters required for three-dimensional

numerical model are estimated based on the test results, improved GSI system, and HB criterion.

The coal strate having the dip of 18 degree was excavated in the width of 100 m. The three-dimensional numerical analysis model takes railway as the center, the model is 250 m high, 400 m long along dip and 200 m along strike, peripheral and bottom boundaries of model are set as fixed constraints, and the surface is free. The model is divided into 52580 cells. The numerical model is shown in Figure 3.

According to the numerical simulation analysis based on the mechanical parameters in Table 11, the surface

TABLE 7: Relationship between disturbance factor D and geological strength index (GSI).

GSI	100	90	80	70	60	50	40	30	20	10	0
D	0.010	0.069	0.169	0.312	0.480	0.646	0.785	0.880	0.934	0.960	0.972
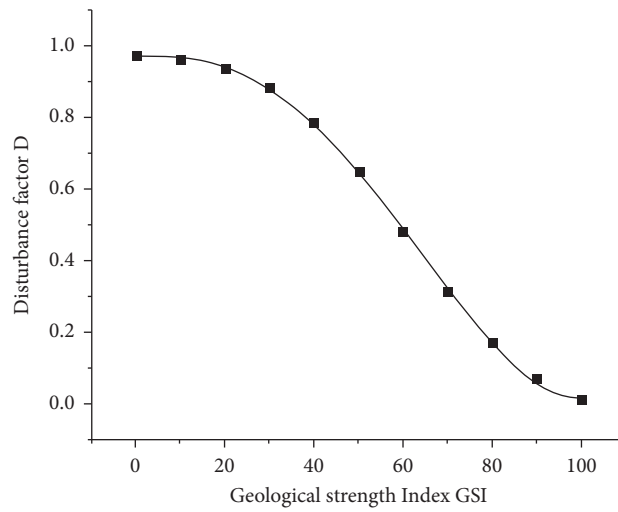
FIGURE 2: The relative curve between disturbance factor (D) and geological strength index (GSI).

TABLE 8: Quantitative GSI values of all goaf roofs.

Roof strata	K_v	d	K_{SCR}	GSI	D	Integrity of rock mass
9 coal roof sandstone and shale	0.23	11.7	0.70	44.3	0.72	Soft rock, broken rock
11 coal top roof shale	0.29	15.7	0.70	46.8	0.69	Soft rock, broken rock
11 coal lower roof sandstone	0.43	27.6	0.77	56.6	0.54	Harder rock, broken rock
13 coal top roof shale	0.59	51.9	0.82	68.0	0.36	Harder rock, broken rock
13 coal middle roof sandstone	0.63	62.8	0.77	70.0	0.32	Harder rock, broken rock
13 coal lower roof limestone	0.34	19.5	0.80	54.0	0.58	Harder rock, broken rock
15 coal roof shale	0.43	27.6	0.76	56.6	0.70	Soft rock, broken rock

TABLE 9: Rock mass mechanical parameters of goaf roof.

Roof strata	GSI	σ_{ci}	E_i	M_i	m_b	S	a	Compressive strength (MPa)	Deformation modulus (GPa)	Friction angle (°)
9 coal roof sandstone and shale	44.3	46.9	20.6	6	0.266	0.29×10^{-3}	0.508	3.12	1.49	38.5
11 coal top roof shale	46.8	48.5	28.4	6	0.330	0.46×10^{-3}	0.507	3.64	2.53	37.3
11 coal lower roof sandstone	56.6	75.2	21.3	9	1.074	2.8×10^{-3}	0.504	10.60	4.46	49.5
13 coal top roof shale	67.9	37.1	25.2	6	1.488	17.5×10^{-3}	0.502	6.97	12.06	42.7
13 coal middle roof sandstone	70.0	61.2	34.9	9	2.511	23.9×10^{-3}	0.501	14.56	18.73	50.3
13 coal lower roof limestone	54.0	87.1	76.9	12	1.181	1.8×10^{-3}	0.504	12.64	12.84	48.8
15 coal roof shale	56.6	45.4	34.3	6	0.553	1.9×10^{-3}	0.504	4.63	5.60	34.7

TABLE 10: Goaf roof mechanical parameters from field test.

Roof strata	Compressive strength (MPa)	Deformation modulus (GPa)	Friction angle (°)
9 coal roof sandstone and shale	3.53	1.52	40.5
11 coal top roof shale	3.91	2.85	39.7
11 coal lower roof sandstone	11.10	4.65	48.8
13 coal top roof shale	7.25	12.58	41.0
13 coal middle roof sandstone	14.82	19.02	51.8
13 coal lower roof limestone	12.97	12.43	47.1
15 coal roof shale	5.13	5.52	35.6
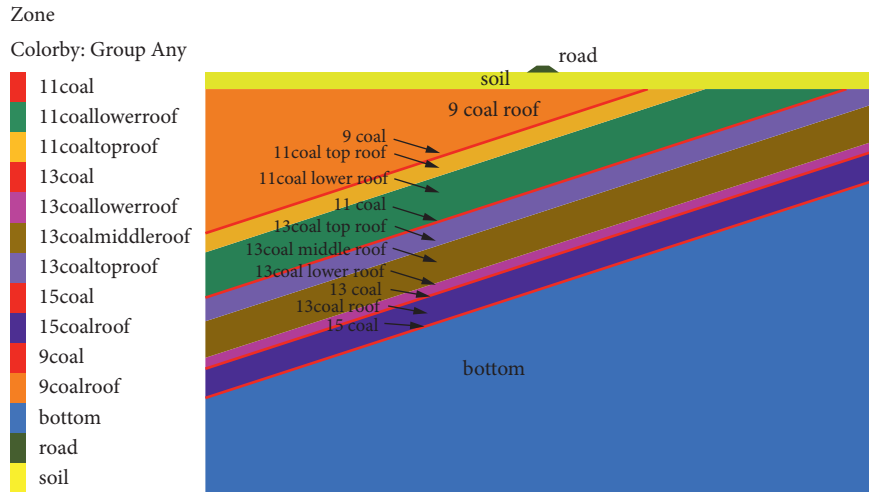
FIGURE 3: The three-dimensional numerical model of coal goaf under railway.

TABLE 11: Rock mass mechanical parameters of filled goafs for numerical model.

Roof strata	K_v	GSI	Deformation modulus (GPa)	Cohesion (MPa)	Friction angle (°)
9 coal roof sandstone and shale	0.46	55.0	1.49	0.22	38.5
11 coal top roof shale	0.54	59.2	2.53	0.31	37.3
11 coal lower roof sandstone	0.51	62.0	4.46	0.71	49.5
13 coal top roof shale	0.65	70.5	12.06	1.01	42.7
13 coal middle roof sandstone	0.69	73.0	18.73	1.58	50.3
13 coal lower roof limestone	0.53	64.0	12.84	0.80	48.8
15 coal roof shale	0.43	56.6	5.60	0.48	34.7
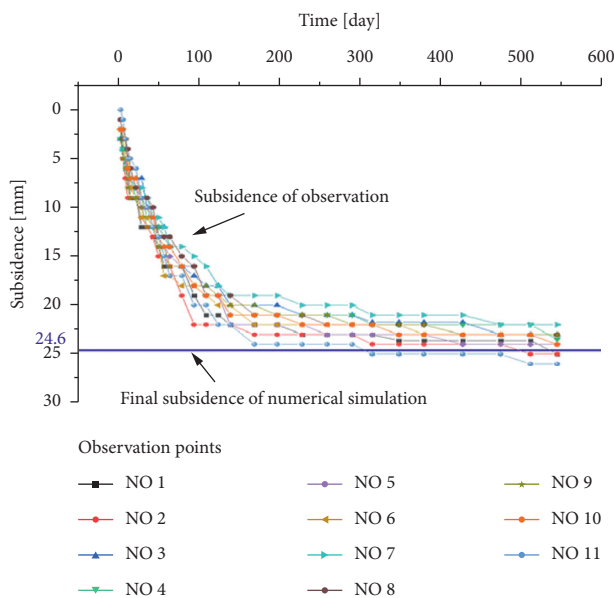
FIGURE 4: The curve of subsidence over time and the results of numerical simulation analysis.

subsidence can be effectively controlled after 9, 11, and 13 goafs are filled. The subsidence of the grouted area has been observed for a long time until it reached stability, and total observation time was 544 days. Observation points were set along the edge of the railway embankment with the

distance of 20 m. The observation points are numbered 1 to 11. The curve of subsidence over time and the results of numerical simulation analysis are shown in Figure 4.

At the beginning, the subsidence value increases quickly with time. With the continuous solidification of backfill, the mechanical parameters and strength of rock mass will increase. Hence, ground subsidence has been limited to 22 to 26 mm, which is effectively controlled. Notably, the average of measurement value is very close to the analyzed values.

5. Conclusion

The traditional classification of rock mass structure is based on the volumetric joint number of rock mass, while it is difficult to accurately get deep-buried rock mass volumetric joint number. Rock mass structure is quantitatively classified by the discontinuity distance or average size of rock block d and rock mass integrity index K_v which can be easily obtained in the field test. The traditional structural surface conditions (SCR) include only roughness, weathering, and infilling, and the influence of groundwater and rock types is left out. In order to solve the problem, the ratio η of rock mass saturated strength to dry strength is introduced, and the quantization formula of structural surface conditions is proposed. The improved geological strength index (GSI) system is adapted to all types of deeply buried rock masses. Disturbance factor D is listed based on the theory of damaged material and HB criterion, which can reduce the influence caused by discontinuous parameters. The research has been well applied in the goaf areas.

Data Availability

The data used to support the findings of this study are available from the corresponding author upon request.

Conflicts of Interest

The authors declare that they have no conflicts of interest.

References

[1] D. Kong, Z. Cheng, and S. Zheng, "Study on the failure mechanism and stability control measures in a large-cutting-height coal mining face with a deep-buried seam," *Bulletin of Engineering Geology and the Environment*, vol. 78, no. 8, pp. 6143–6157, 2019.

[2] Y. Zhou, L. Wang, J. F. Ding, and H. Wu, "Particle flow code analysis of multi-scale jointed rock mass based upon equivalent rock mass technique," *Rock and Soil Mechanics*, vol. 37, no. 7, pp. 2085–2095, 2016.

[3] D. Kong, Y. Lou, S. Zheng, and S. Pu, "The characteristics of roof breaking and the law of ground pressure behavior in fully mechanized top-coal caving face with large mining height," *Geotechnical & Geological Engineering*, vol. 39, no. 1, pp. 285–297, 2021.

[4] A. Palmetrom and R. Singh, "The deformation modulus of rock masses comparisons between in-situ test and indirect estimates," *Tunnelling and Underground Space Technology*, vol. 16, no. 3, pp. 115–131, 2001.

[5] He Wang, Ye Yuan, H. Cao, and Z. Wang, "Mechanical parameters selection of rock mass based on representative element volume," *China Mining Magazine*, vol. 28, no. 11, pp. 131–135, 2019.

[6] T. Zhou and J. Li, "Numerical simulation of prefabricated defects rock mass based on secondary development of FLAC3D," *Safety In Coal Mines*, vol. 50, no. 9, pp. 192–196, 2019.

[7] E. Hoek, C. Carranaz Torres, and B. Corkum, "Hoek-brown failure criterion-2002 edition," in *Proceedings of the Narms-Tac Conference*, pp. 267–273, University of Toronto, Toronto, Canada, January 2002.

[8] S. Hu, "Estimation of rock mass parameters based on quantitative GSI system and Hoek-Brown criterion," *Rock and Soil Mechanics*, vol. 32, no. 3, pp. 861–866, 2011.

[9] K. Xia, C. Chen, X. Liu, and Y. Zheng, "Estimation of rock mass mechanical parameters based on ultrasonic velocity of rock mass and hoek-brown criterion and its application to engineering," *Chinese Journal of Rock Mechanics and Engineering*, vol. 32, no. 7, pp. 1458–1466, 2013.

[10] E. Hoek and E. T. Brown, "The Hoek-Brown failure criterion and GSI - 2018 edition," *Journal of Rock Mechanics and Geotechnical Engineering*, vol. 11, no. 3, pp. 445–463, 2019.

[11] C. Yan and G. Xu, "Stability analysis of mined-out areas influenced by blasting vibration with Flac3D," *Chinese Journal of Rock Mechanics and Engineering*, vol. 24, no. 16, pp. 2894–2899, 2005.

[12] E. Hoek and E. T. Brown, *Underground Excavations in Rock*, Institution of Mining and Metallurgy, London, 1980.

[13] E. Hoek and E. T. Brown, "Practical estimates of rock mass strength," *International Journal of Rock Mechanics and Mining Sciences*, vol. 34, no. 8, pp. 1165–1186, 1997.

[14] E. Hoek and M. S. Diederichs, "Empirical estimation of rock mass modulus," *International Journal of Rock Mechanics and Mining Sciences*, vol. 43, no. 2, pp. 203–215, 2006.

[15] H. Sonmez and R. Ulusay, "Modifications to the geological strength index (GSI) and their applicability to stability of slopes," *International Journal of Rock Mechanics and Mining Sciences*, vol. 36, no. 6, pp. 743–760, 1999.

[16] Ministry of Water Resources of the PRC, *Standard for Engineering Classification of Rock Mass (GB/T 50218-2014)*, China Planning Press, Beijing, China, 2014.

[17] Engineering Geology Handbook Editorial Board, *Geological Engineering Handbook*, China Building Industry Press, Beijing, China, 2018.

[18] H. Sonmez, H. A. Nefeslioglu, and C. Gokceoglu, "Determination of wJd on rock exposures including wide spaced joints," *Rock Mechanics and Rock Engineering*, vol. 37, no. 5, pp. 403–413, 2004.

[19] First Survey and Design Institute of the Ministry of Railway, *Handbook of Railway Engineering Geology*, China Railway Publishing House, Beijing, China, 1999.

[20] Ministry of Water Resources of the People's Republic of China, *Standard for Engineering Classification of Soil*, China Planning Press, Beijing, China, 2008.

[21] Editee et Diffusee Par I Association Francaise, *Reconnaissance et seeais geotechniques denomination, description et classification des roches*, Partie 1: Denomination et description, 2003.

[22] A. Palmstrom, "Characterizing rock measses by the RMI for use in practical rock engineering, part 1：the development of the rock mass index (RMI)," *Tunnelling and Underground Space Technology*, vol. 11, no. 2, pp. 175–188, 1996.

[23] G. Jiang, N. Hu, G. Hong, G. Li, and G. Pang, "Determination of rock mass mechanical parameters based on quantification and correction method of GSI value," *Rock and Soil Mechanics*, vol. 39, no. 6, pp. 1001–1008, 2018.

[24] Y. Fu, Y. Wenhan, X. Liu, L. Miao, and W. Xie, "Deterioration rules of strength parameters of sandstone under cyclical wetting and drying in acid-based environment," *Rock and Soil Mechanics*, vol. 39, no. 9, pp. 3331–3339, 2018.

[25] X. Liu, D. Li, L. Zhang, and Z. Wang, "The research on the wet-dry cycl's influence on the mechanical properties and microstructure change law of shaly sandstone," *Chinese Journal of Geotechnical Engineering*, vol. 38, no. 7, pp. 1291–1300, 2016.

[26] C. Wang, C. Liu, and D. Liu, "Experimental study on volume effect of saturated fractured sandstone under uniaxial compression," *Chinese Journal of Underground Space and Engineering*, vol. 15, no. 5, pp. 1331–1340, 2019.

[27] Y. Chen, W. Liang, J. Yang, H. Lian, and N. Xiao, "Study on the effective stress characteristic of rough rock fractures with water pressure," *Chinese Journal of Rock Mechanics and Engineering*, vol. 37, pp. 3850–3860, 2018.

[28] Z. Bieniawski, *Engineering Rock Mass Classifications*, The Wiley-Interscience Publication, Hoboken, NJ, US, 1989.

[29] Y. Liu, *Damage Evolution and Rheological Behavior of Deeo Rock Mass under Water-Rock Interaction*, Central South University, Changsha, China, 2012.

[30] J. Lemaitre, "How to use damage mechanics," *Nuclear Engineering and Design*, vol. 80, no. 2, pp. 233–245, 1984.

Research Article

Study on the Influence of In Situ Stress Distribution on the Stability of Roadway Surrounding Rock

Tao Li [iD],[1,2] **Hao Gong,**[1] **and Guoliang Xu** [iD][1]

[1]*School of Energy and Mining Engineering, China University of Mining and Technology-Beijing, Beijing 100083, China*
[2]*Department of Resource Engineering, Heilongjiang University of Technology, Jixi 158100, China*

Correspondence should be addressed to Tao Li; litao5555@126.com

In order to understand the instability characteristics of surrounding rock in the process of deep roadway excavation, a three-dimensional numerical model was established by FLAC[3D] to systematically analyze the influence of roadway surrounding rock stability under different in situ stress distribution forms, and the environmental coefficient of mining-induced stress η was defined, the larger the environmental coefficient of mining-induced stress is, the larger the surrounding rock stress environment is, and the range where the η coefficient is greater than 0.2 is called with the destruction-danger zone. When the initial vertical stress is maximum principal stress and minimum principal stress, by comparing the roadway along the middle ground stress direction and minimum or maximum in-situ stress direction, the variation characteristics of displacement, failure zone and failure hazard zone of roadway surrounding rock are obtained, which provides theoretical basis for the treatment of disaster accidents such as roadway surrounding rock instability and rock burst caused by deep high in-situ stress.

1. Introduction

All underground engineering activities must be carried out in the earth's crust. Coal mining is to take the crustal rock mass and coal seam as the main research object, so it is extremely important to study the natural properties of underground rock mass and the in situ stress distribution [1, 2]. In 1912, the concept of geostress was first proposed by Heim, a Swiss geologist [3]. It is pointed out that the rock is in a state of approximate hydrostatic pressure due to the rheological action for a long time under the continuous action of large stress [4–6]. The stress is equal to the gravity of the overlying rock mass, i.e., $\sigma_x = \sigma_y = \sigma_z = \gamma H$. Under hydrostatic pressure, there is no shear stress, and any direction is the principal stress. In 1926, Soviet scholars proposed the following theory [7]: assuming that the rock mass is uniform and continuous elastic medium and according to the theory of elasticity, it is proposed that the vertical stress of the rock mass is equal to the pressure of the rock strata above it, i.e., $\sigma_v = \gamma H$. And the horizontal stress $\sigma_x = \lambda \gamma H$. For the gravitational field with the ground level,

the lateral pressure coefficient $\lambda = v/(1 - v)$, and $\lambda = 1$ when the hydrostatic pressure. However, the measured value may be greater than 1.0 or less than 1.0 depending on the area and position of the measured result of λ [8–10]. Literature [11, 12] showed that the anchor bolt not only provides supporting force on the roadway surface but essentially forms a load-bearing structure with certain strength through the coupling action of anchor bolt and surrounding rock. In literature [13–15], the stress evolution, displacement field, local deformation, overall distribution, and destroy characteristics of surrounding rock anchoring structures were studied with different bolt spacing through model tests. In literature [16, 17], the influence of bolt preloading force and bolt spacing on the supporting strength of surrounding rock anchoring structure through numerical simulation software was analyzed, the supporting scheme of excavation roadway was designed, and the effectiveness of the supporting scheme by adopting the roadway displacement measurement scheme was verified. Literature [18–20] showed that under the action of high stress, the two-side coal seam is soft, the stress is uneven, the range of loosening circle is large, and the

surface deformation shows the characteristics of "two-side displacement amount greater than roof subsidence amount greater than floor heave amount."

With the deepening of coal mining depth in recent years, the original rock stress of underground rock mass is also increasing, and the anisotropy is significant [21, 22]. As a result, the excavation roadway deformation speed is accelerated; roof caving, side deflection, and floor heave are increasingly serious; and the bursting liability is more intense. The number of roadway repair is also increasing correspondingly, and the repair rate of some soft rock roadway has reached more than 90% [23–25]. Redistribution of in situ stress caused by roadway excavation is closely related to the original rock stress distribution state. In order to accurately grasp the influence of in situ stress distribution on the stability of roadway surrounding rock [26–28], based on the discussion of the distribution form of in situ stress, this paper systematically analyzes the displacement curve of surrounding rock, the range of plastic zone, and the volume of destruction-danger zone to judge the influence on the stability of surrounding rock [29, 30].

2. The Engineering Background and Numerical Model

2.1. The Engineering Background. This paper takes 7703 bottom pumping roadway in Zouzhuang Mine, Huaibei, Anhui Province, as the engineering background. The construction horizon of the bottom pumping roadway is in sand and mudstone interbed and 16–30 m away from the coal seam. The lithology is mainly purple piebald mudstone and aluminum mudstone, followed by siltstone and fine sandstone. The occurrence of strata is relatively stable. The direct roof is mudstone, gray to dark gray, massive, with slippery surface, a large number of plant fossil fragments, flat fracture, brittle, fragile, thickness of 1.91~4.13 m, and average of 3.15 m. The old top is fine siltstone, light gray, fine grain, massive, with thin siltstone bands, a few cracks filled by calcite veins, medium sorting, calcareous cementation, parallel bedding, dense, thickness of 4.10~90.2 m, and average of 6.12 m. The direct bottom is mudstone, dark gray, argillaceous structure, local silty content is high, relatively dense, flat fracture, a large number of plant rhizome fossils, thickness of 1.02~3.95 m, and average of 2.39 m. The old bottom is fine silty sandstone, gray, silty structure, the local with high fine sand content, banded, flat and dense fracture, a large number of plant rhizome fossils in the lower part, longitudinal fractures, parallel bedding, thickness of 2.90~5.61 m, and average of 4.47 m. The comprehensive histogram of roof and floor within the area of working face 7703 is shown in Figure 1.

2.2. The Establishment of Numerical Model. Roadway surrounding rock stability of the numerical model is set up by using FLAC^{3D}, as shown in Figure 2; the model size is 80 m ∗ 60 m ∗ 80 m, and the actual depth of the coal seam is 720-800 m. The numerical model includes 9 layers from top to bottom. The sandstone is 11 meters, mudstone is 9 meters,

Rock stratum	Histogram	Thickness (m)	Rock character
Sandstone		11	Gray, massive, thick bedded, intercalated with thin mudstone, gentle wave bedding, dense.
Mudstone		9	Light gray, massive, uneven fracture, local silt, upper siderite oolite, brittle.
Siltstone		7	Gray, fine grain, good sorting, siliceous cementation, hard.
Glutenite		4	Gray, massive, flat fracture.
Mudstone		5	Dark gray, massive, flat fracture.
Siltstone		4	Gray, fine grain, good sorting.
Mudstone		23	Massive, thick bedded, locally intercalated with thin siltstone, gentle wave bedding, with a small amount of carbonaceous layer, relatively dense.
Sandstone		5	Gray, massive, gentle wave bedding, dense.
Mudstone		12	Dark gray, massive, flat fracture, see a large number of plant fossil fragments, the layer is carbonaceous, brittle.

Figure 1: Comprehensive histogram of borehole.

siltstone is 7 meters, conglomerate is 4 meters, mudstone is 5 meters, siltstone is 4 meters, mudstone is 23 meters, sandstone is 5 meters, mudstone is 12 meters, respectively, and the cumulative thickness is 80 meters. The dip angle of each rock stratum is 15°. Physical and mechanical parameters of rock strata are shown in Table 1.

Excavation roadway is located in the middle of the model 23 meters mudstone environment, occurrence depth of 760 m; roadway cross section adopts the design of arch section, the section size of 5 meters wide and 4 meters high, along the *Y* direction for excavation, excavation length of 60 m, model size greater than the roadway section size, thereby eliminating the boundary effect on the result of numerical calculation. The Mohr–Coulomb model is used to simulate the mechanical response characteristics of the surrounding rock mass in the process of excavation. A fixed displacement boundary condition is adopted at the bottom and around the model, and a vertical stress is applied at the top of the model to simulate other overburden strata that have not been built into the numerical model. The step-by-step characteristics of surrounding rock stress, displacement, plastic zone, and failure risk zone caused by roadway excavation are analyzed to evaluate the stability of surrounding rock under the influence of mining.

3. Influence of In Situ Stress Distribution on the Stability of Roadway Surrounding Rock

3.1. Influence of In Situ Stress Distribution on Roadway Surrounding Rock Displacement. In order to quantitatively analyze the influence of different forms of in situ stress distribution on the displacement of surrounding rock, a vertical survey line was arranged on the roof and floor of the roadway, respectively, and a horizontal survey line was arranged on the left and right sides of the roadway, respectively. According to the elastic mechanics knowledge, the excavation of the chamber in the undisturbed rock will inevitably cause the redistribution of the original rock stress, resulting in the production of plastic zone (and plastic zone). According to the analytical formula of the Gilch solution, the

(a) (b)
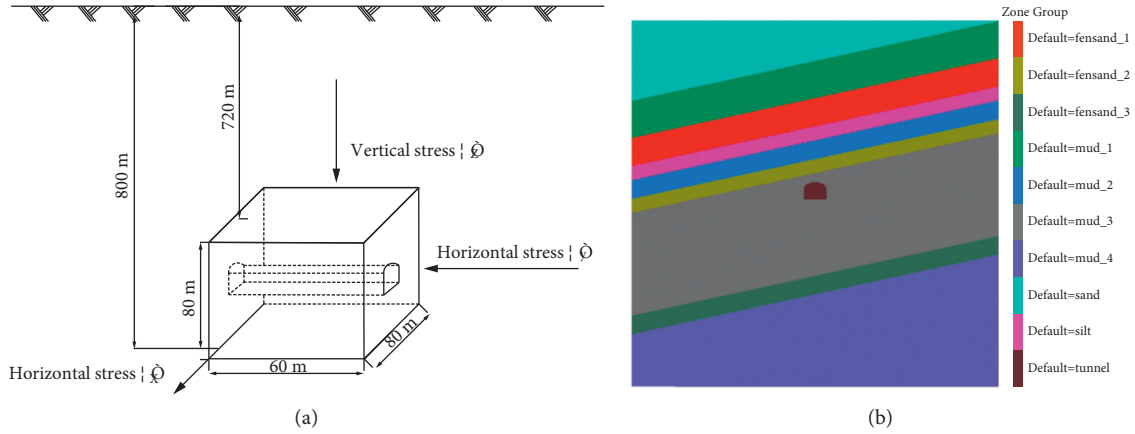
Figure 2: Numerical analysis model of surrounding rock stability of roadway: (a) force analysis diagram; (b) numerical model diagram.

Table 1: Physical and mechanical parameters of rock strata.

Rock parameter	Siltstone	Mudstone	Glutenite	Sandstone
Bulk modulus (GPa)	1.11	0.83	1.0	0.97
Shear modulus (GPa)	0.83	0.38	0.6	0.72
Cohesive forces (MPa)	6.0	3.0	4.0	5.0
Angle of internal friction (°)	38	32	34	38
Angle of dilatancy (°)	10	10	10	10
Tensile strength (MPa)	2.5	1.0	1.5	2.0

range of the plastic zone is generally 3–5 times of the length of the chamber rock mass. And the width of the section size in the numerical model is 5 m, so the range of the plastic zone caused by excavation is about 15–25 m. Therefore, the maximum length of 25 m is adopted here as the analysis area. The numerical model of the roadway surrounding rock cross survey line was established, as shown in Figure 3.

The vertical displacement of the survey line of the top and bottom was extracted and curves were drawn, as shown in Figure 4. When the initial vertical stress is the maximum in situ stress, the deformation degree of surrounding rock is higher when the roadway is tunneling along the middle in situ stress direction than when the roadway is tunneling along the minimum in situ stress direction. Under the condition of hydrostatic pressure, the surface deformation of surrounding rock of roadway is higher than the first two types of in situ stress distribution and deep roadway surrounding rock deformation is lower than the first two types of ground stress. For the above three kinds of in situ stress condition, vertical displacement shows slowly lowering trend from the roadway surface to the deep roadway direction, and surface reduced to 0 about 15 m away from the roadway. When the initial vertical stress is the minimum in situ stress, the degree of vertical displacement of surrounding rock on the roadway surface is higher than that in the direction of maximum in situ stress when the roadway is excavated along the middle in situ stress direction, and the
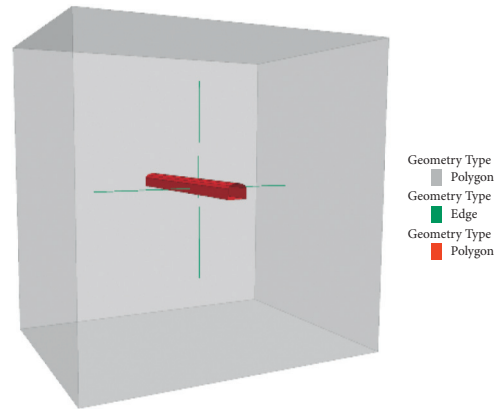
Figure 3: Numerical model of roadway surrounding rock cross survey line.

degree of vertical displacement of surrounding rock on the roadway surface is smaller than that in the case of tunneling along the maximum in situ stress direction when the initial vertical stress is the minimum in situ stress. Compared with the case where the initial vertical stress is the maximum in situ stress, when the initial vertical stress is the minimum in situ stress, the vertical stress decreases faster from the roadway surface to the depth of the surrounding rock.

The horizontal displacement of the left and right sides of the survey line was extracted and curves were drawn, as shown in Figure 5. When the initial vertical stress is the maximum in situ stress, the horizontal deformation decreases rapidly from the roadway surface to the deep surrounding rock. Surrounding rock of roadway is excavated along minimum in situ stress direction of horizontal deformation degree which is higher than the tunneling of the intermediate principal stress, and hydrostatic pressure is bigger than the horizontal deformation of roadway under the conditions of the first two types of in situ stress distribution. It is important to note that the roadway is excavated along the middle ground stress direction, horizontal smaller range of compression zone. When the initial vertical stress is the minimum in situ stress, the decrease rate of horizontal deformation from the roadway surface to the
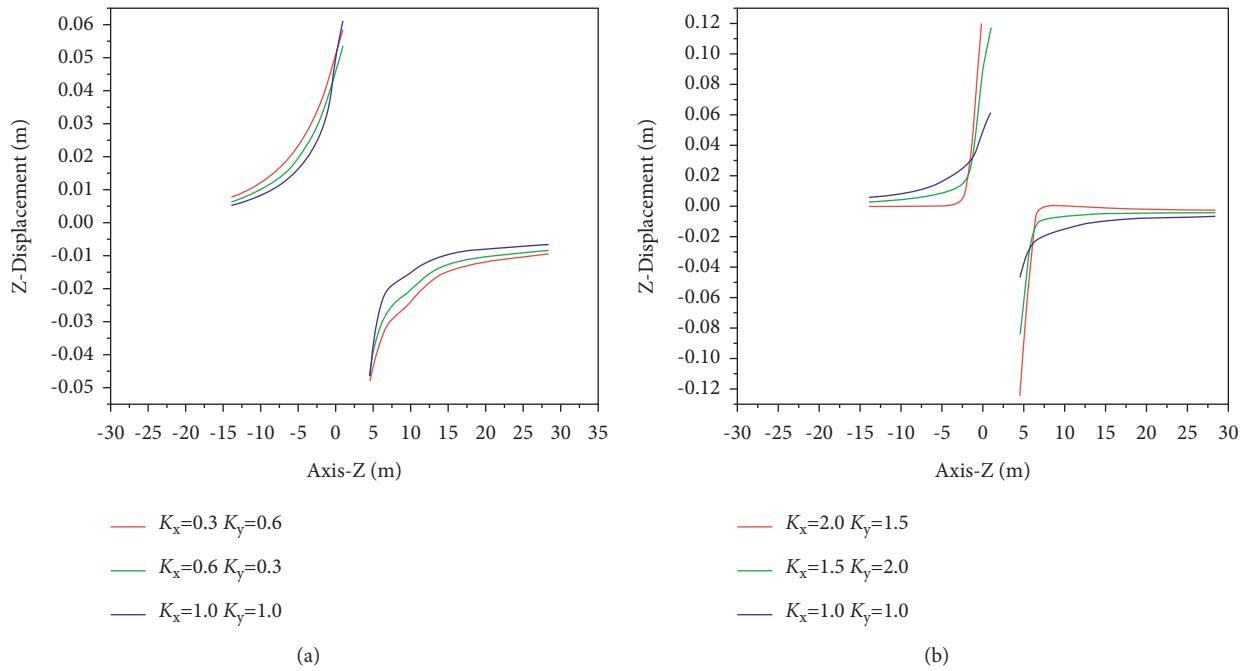
FIGURE 4: Influence of in situ stress on vertical displacement curve of roadway surrounding rock: (a) the vertical stress is the maximum principal stress; (b) the vertical stress is the minimum principal stress.
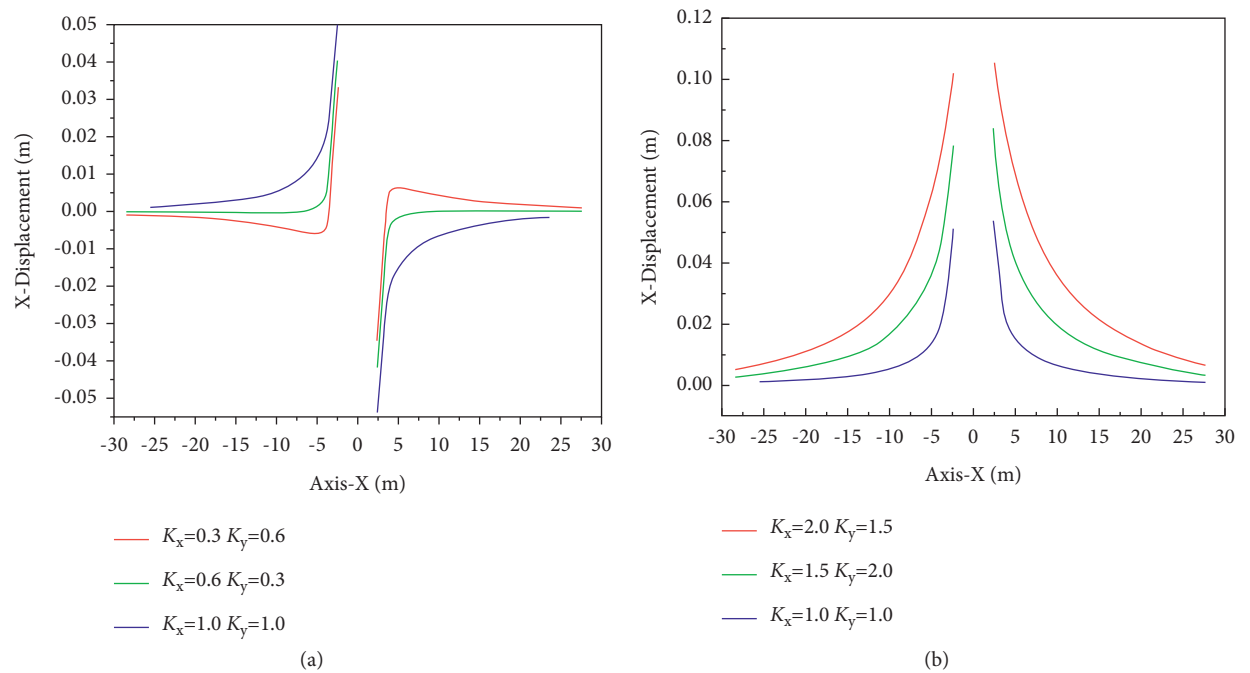
FIGURE 5: Influence of in situ stress on horizontal displacement curve of roadway surrounding rock: (a) the vertical stress is the maximum principal stress; (b) rhe vertical stress is the minimum principal stress.

deep surrounding rock is significantly less than that of the initial vertical stress which is the maximum in situ stress. The horizontal deformation of the tunnel is obviously higher than that of the tunnel with the maximum ground stress. According to the geological conditions, the rock strata have

an inclination angle of 15°, which leads to the different gravity of the overlying rock strata at the positions of the two sides of the roadway after excavation. Therefore, the stress redistribution process is not symmetrical. However, according to the influence curve of ground stress on the

(a)

(b)

(c)

(d)

Figure 6: Continued.

(e)

Figure 6: Influence of in situ stress on the morphology of plastic zone of roadway surrounding rock: (a) $K_x = 0.3$, $K_y = 0.6$; (b) $K_x = 0.6$, $K_y = 0.3$; (c) $K_x = 1$, $K_y = 1$; (d) $K_x = 1.5$, $K_y = 2.0$; (e) $K_x = 2.0$, $K_y = 1.5$.

horizontal displacement curve of surrounding rock in Figure 3, the difference between the left and right sides of the deformation displacement is small, so the support of the roadway can still adopt the symmetric support method for surrounding rock reinforcement.

3.2. Influence of In Situ Stress Distribution on Plastic Zone of Roadway Surrounding Rock.

The influence of different in situ stress distribution forms on the plastic zone of roadway surrounding rock is shown in Figure 6. Under the condition that the initial vertical stress is the maximum in-situ stress, when the roadway is extracted along the middle in-situ stress direction, the failure zone of the surrounding rock is mainly concentrated on the two sides of the roadway and expands to four shoulder angles at the same time. The failure of surrounding rock only occurs on the roadway surface of the roof and floor, and the failure range is obviously smaller than that of the two sides of the roadway. The failure zone of the two sides extends to the interface between mudstone and upper siltstone and stops expanding. When the roadway was tunneling along the direction of the minimum in situ stress, the plastic zone of the surrounding rock mainly developed on the two sides of the roadway and no longer expanded to the four shoulder angles of the roadway. The plastic zone of the surrounding rock of the roof and floor was similar to that of the roadway tunneling along the direction of the intermediate principal stress but only developed in the surface rock. Compared with the roadway tunneling along the intermediate principal stress direction, the failure range of surrounding rock of the roadway is obviously reduced, and the spatial distribution of the roadway is contracted to the two sides of the roadway. Under the condition of hydrostatic pressure, the plastic zone of surrounding rock around the roadway basically presents uniform distribution. Compared with the previous two types of in situ stress distribution, the range of plastic zone of surrounding rock on both sides of the roadway decreases, while the range of plastic zone of surrounding rock on the roof and floor increases.

When the initial vertical stress is the minimum in situ stress and the roadway is excavated along the direction of maximum in situ stress, the failure range of surrounding rock of the roadway roof and floor is slightly larger than that of the roadway sides, but the failure area of surrounding rock still presents uniform distribution characteristics. When the roadway is extracted along the middle stress direction, the failure phenomenon of the two sides of the roadway only appears in the shallow surrounding rock. The failure zone is mainly concentrated in the roof and floor surrounding rock of the roadway, and the roof failure zone stops developing at the boundary of mudstone and upper siltstone. Compared with the roadway extracting along the direction of maximum in-situ stress, the failure area of surrounding rock on both sides of the roadway is significantly contracted, and the failure area of surrounding rock on top and bottom is expanded. Compared with hydrostatic pressure conditions, the latter two types of in situ stress lead to lower damage degree of surrounding rock on both sides of roadway and higher damage degree of surrounding rock on roof and floor.

The in situ stress distribution not only has a significant influence on the spatial failure modes of surrounding rock but also leads to significant differences in the range of plastic zones. In order to quantitatively analyze the failure range of surrounding rock, the total volume of failure units was calculated by accumulating the failure units, and a histogram was drawn, as shown in Figure 7. It can be seen from the figure that when the initial vertical stress is the maximum in situ stress, the plastic zone of surrounding rock when the roadway was tunneled along the middle in situ stress is significantly larger than that when the roadway was tunneled along the minimum in situ stress. When the initial vertical stress is the minimum in situ stress, the range of surrounding rock plastic zone when the roadway is driven along the middle in situ stress direction is slightly higher than that along the maximum in situ stress direction.

3.3. Influence of In Situ Stress Distribution on Roadway Surrounding Destruction-Danger Zone.

The rock fracture
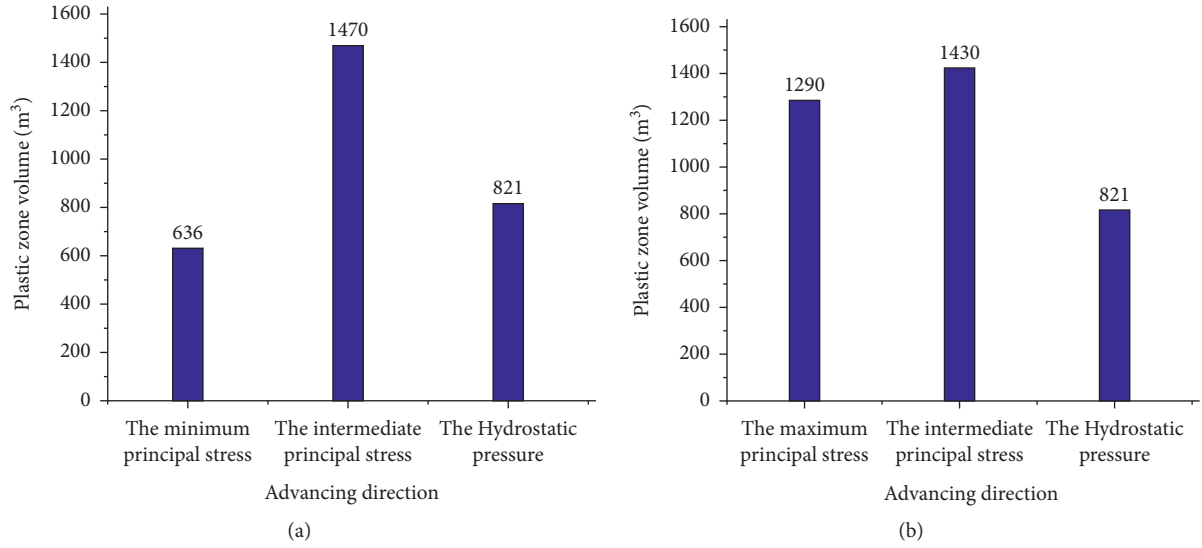
FIGURE 7: Influence of in situ stress on the range of plastic zone of roadway surrounding rock: (a) the vertical stress is the maximum principal stress; (b) the vertical stress is the minimum principal stress.

which is within the scope of the roadway destruction area grows highly, and destruction area is the key of support and reinforcement. The neighboring area is a part of the destruction rock though it is within range of the elastic state, but its mining stress environment is very bad, it is easily affected by external disturbances and enters a state of destruction, and it will become a damage zone of surrounding rock of the region. When the bolt or anchor cable support is carried out, it is necessary to pay attention to that the anchor end cannot be completely in the destruction-danger zone. Otherwise, once the destruction-danger zone enters the failure state under the external disturbance, the overall failure of the supporting structure will be caused and the reliability of roadway support will be reduced. In order to characterize the advantages and disadvantages of the stress environment in the surrounding rock of the roadway, the mining-induced stress environmental coefficient is defined as

$$\eta = \frac{\sqrt{J_2}}{I_1}, \tag{1}$$

where I_1 is the first invariant of the principal stress and J_2 is the second invariant of deviatoric stress, and those can be expressed as follows:

$$J_2 = \frac{1}{2}\left(s_1^2 + s_2^2 + s_3^2\right),$$
$$I_1 = \sigma_1 + \sigma_2 + \sigma_3, \tag{2}$$

where σ_1, σ_2, and σ_3 are the maximum, intermediate, and minimum principal stresses, respectively, and S_1, S_2, and S_3 are maximum, intermediate, and minimum deviatoric stresses, respectively, σ_0, S_i, and σ_i ($i = 1, 2, 3$) are hydrostatic stress, deviatoric stress, and principal stress, respectively, and and $S_i = \sigma_i - \sigma_0$, $\sigma_0 = I_1/3$.

Since the first invariant of principal stress I_1 represents the compression degree of the surrounding rock in three

directions, the larger its value is, the better the stress environment the surrounding rock is. The second invariant of deviatoric stress, J_2, represents the shear degree of surrounding rock. And the larger the value is, the worse the stress environment of surrounding rock is. And the mining stress environment factor is defined the ratio of the second invariant deviatoric stress to first principal stress invariants. Due to rock compressive shear, the greater the value of mining stress environment factor, the easier the rock mass is to be destroyed. And the rock shear strength is about 10%–40% of rock compressive strength, so the scope of mining stress environment factor greater than 0.2 is defined as a destruction-danger zone. The spatial distribution morphology of surrounding rock in the destruction-danger zone under different in situ stress conditions was extracted, as shown in Figure 8. When the initial vertical stress is the maximum in-ground stress, the destruction-danger zone around the roadway takes on a butterfly shape, and its range is obviously larger than that of the plastic zone. When the roadway is excavated along the direction of the middle in-ground stress, the destruction-danger zone has the largest range, and when the roadway is excavated along the direction of the middle in-ground stress, the destruction-danger zone presents a tendency of contraction. Under the condition of hydrostatic pressure, the destruction-danger zone around the roadway is basically uniformly distributed, and its range is slightly larger than that of the plastic zone. When the initial vertical stress is the minimum in situ stress and the roadway is excavated along the direction of the maximum in situ stress, the failure danger area is basically uniform in the two sides of the roadway and the surrounding rock of the floor, and the scope of the failure danger area in the floor increases obviously. When the roadway was excavated along the direction of the middle ground stress, the destruction-danger zone of the surrounding rock on both sides of the roadway contracted obviously, and the
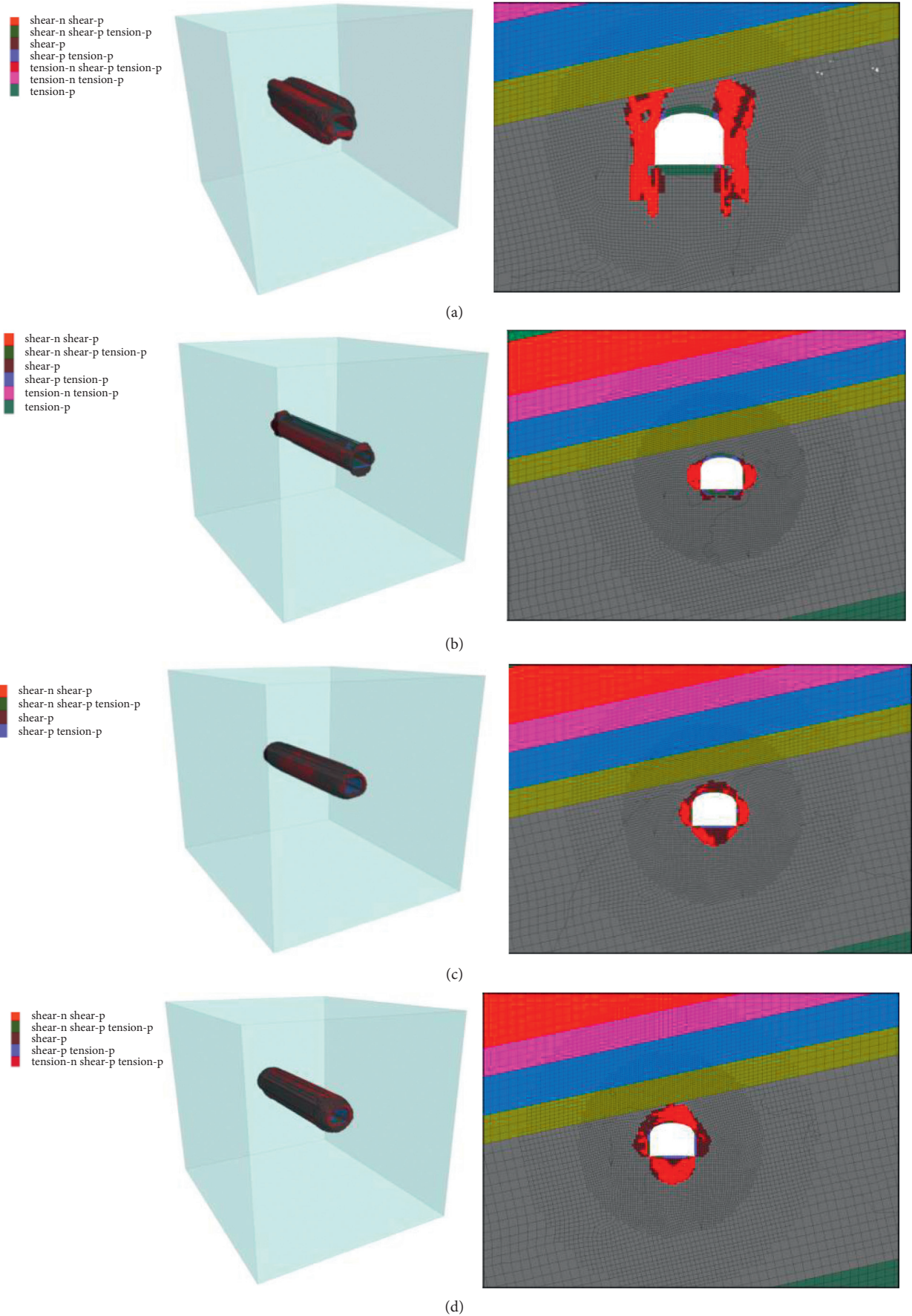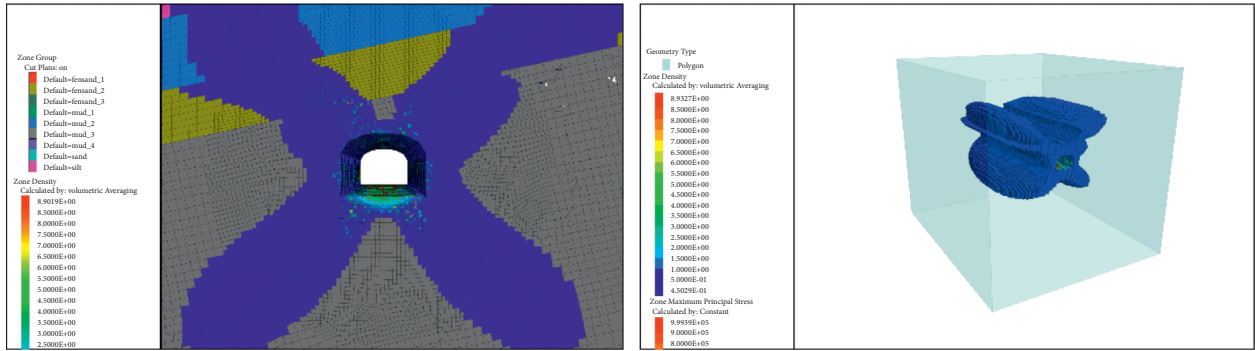
(a)
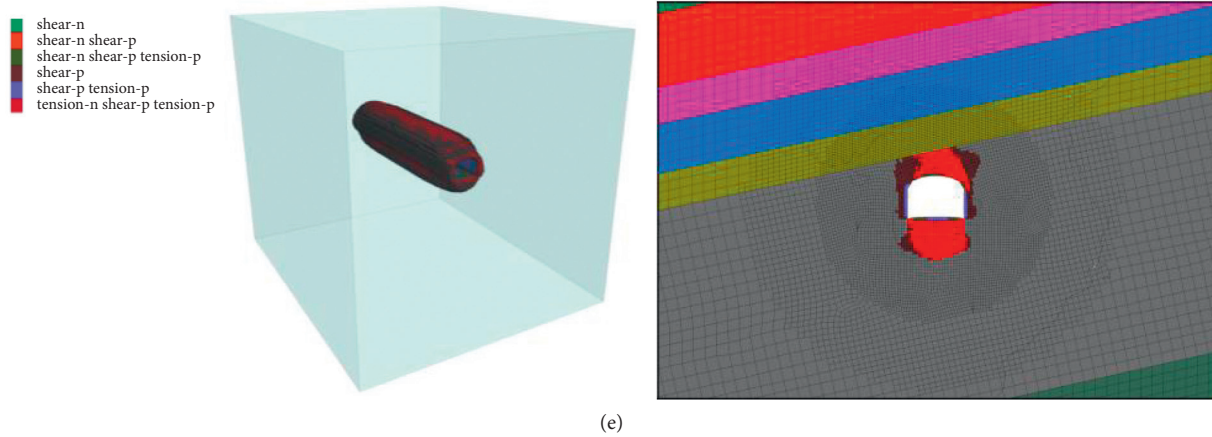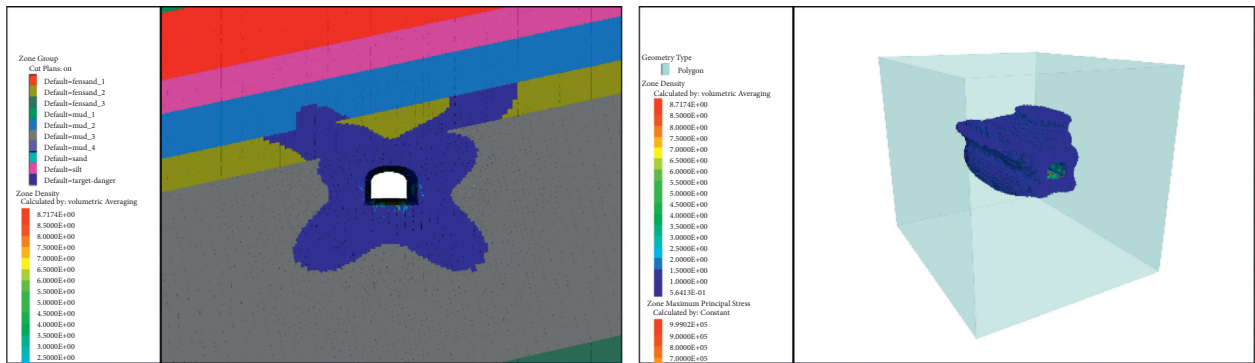
(b)
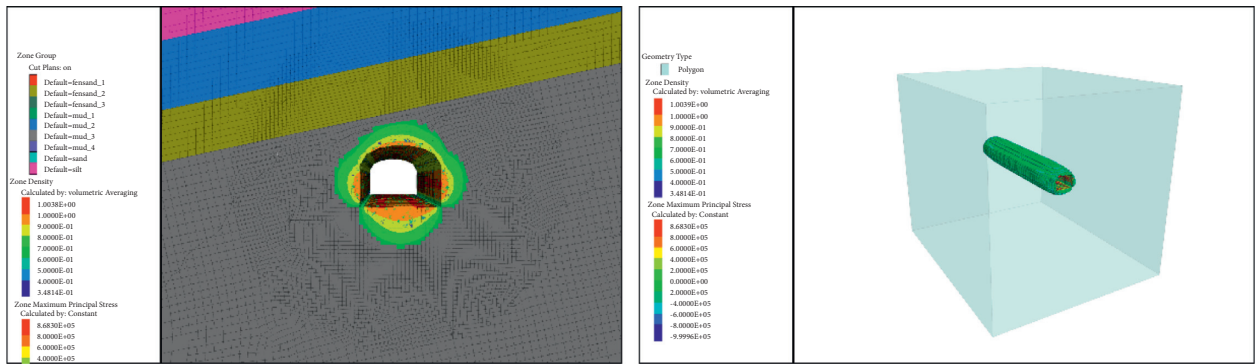
(c)
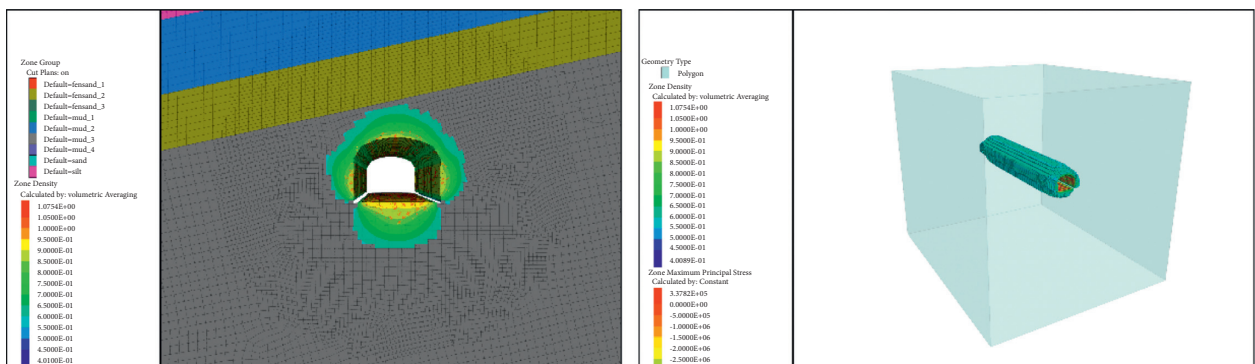
(d)

Figure 8: Continued.

(e)
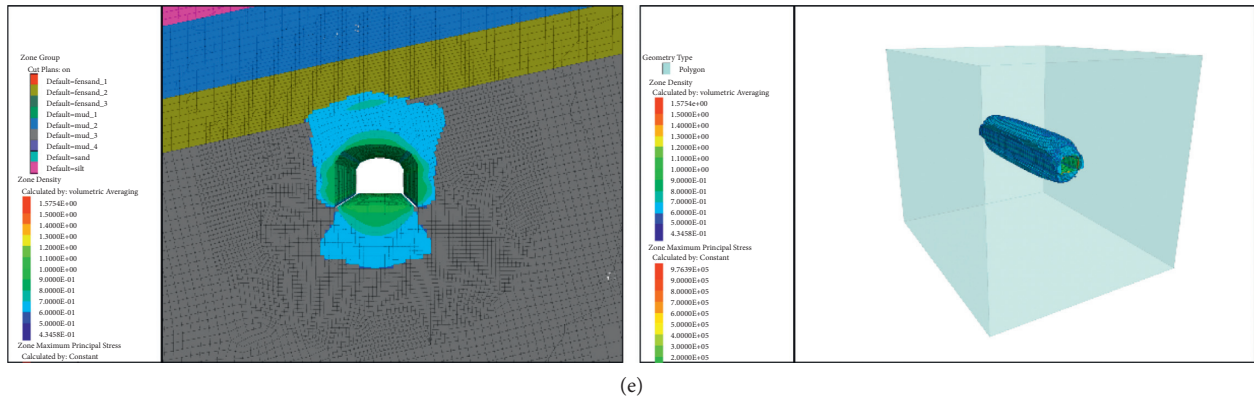
FIGURE 8: Influence of in situ stress on the morphology of destruction-danger zone of roadway surrounding rock: (a) $K_x = 0.3$, $K_y = 0.6$; (b) $K_x = 0.6$, $K_y = 0.3$; (c) $K_x = 1$, $K_y = 1$; (d) $K_x = 1.5$, $K_y = 2.0$; (e) $K_x = 2.0$, $K_y = 1.5$.
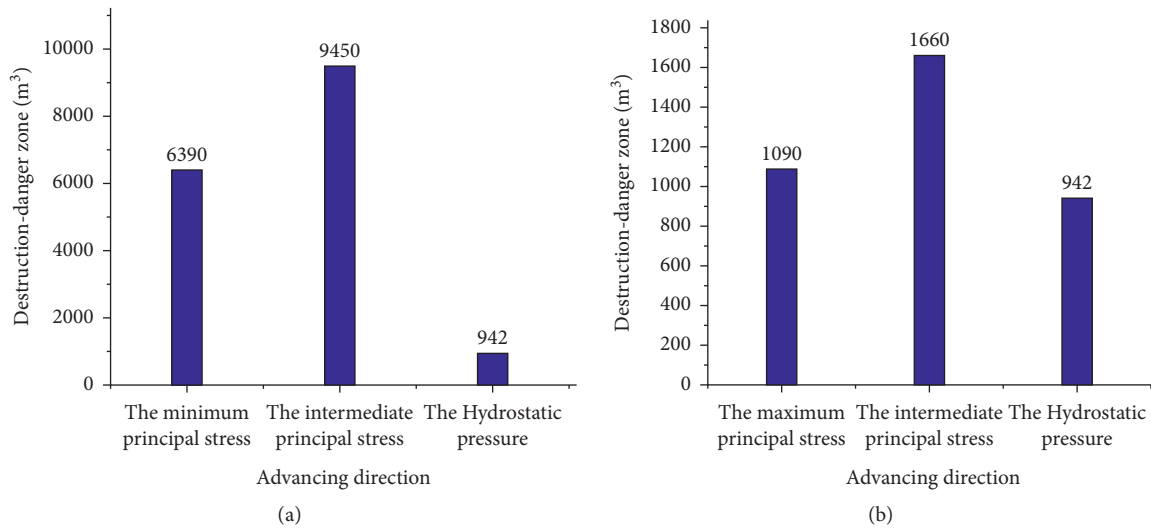
FIGURE 9: Influence of in situ stress on the failure hazard range of roadway surrounding rock: (a) the vertical stress is the maximum principal stress; (b) the vertical stress is the minimum principal stress.

destruction-danger zone of the surrounding rock on the roof and floor expanded obviously, and the spatial distribution of the destruction-danger zone was like a wine glass. Compared with the hydrostatic pressure condition, the latter two types of in situ stress lead to the increase in the uneven distribution of the failure risk zones around the roadway and the expansion of the development range.

The volume of all units within the scope of the destruction-danger zone was accumulated, and the column diagram of the destruction-danger zone range of the surrounding rock of the roadway under different in-ground stress distribution was obtained, as shown in Figure 9. Under the condition of hydrostatic pressure, the stress environment of surrounding rock is relatively good, and the range of failure danger of surrounding rock is obviously smaller than the other four types of in situ stress distribution. When the initial vertical stress is the maximum in situ stress, the range of destruction-danger zone is higher when the roadway is tunneling along the middle in situ stress direction than when the roadway is tunneling along the minimum principal stress

direction. When the initial vertical stress is the minimum in situ stress, the range of surrounding rock destruction-danger zone is higher when the roadway is tunneling along the middle in situ stress direction than when the roadway is tunneling along the maximum in situ stress direction.

4. Conclusion

(1) When the initial vertical stress is the maximum in situ stress, the roof subsidence and floor bulge of the roadway are significantly greater than those when the initial vertical stress is the minimum in situ stress, but the displacement of the two sides of the roadway is significantly higher than that when the initial vertical stress is the minimum in situ stress.

(2) When the initial vertical stress is the maximum in situ stress, the range of plastic zone of surrounding rock is significantly higher than that of the minimum principal stress when the roadway is excavated along the direction of intermediate principal stress. When

the initial vertical stress is the minimum in situ stress and the roadway advances along the direction of the maximum in situ stress, the scope of the plastic zone around the roadway is slightly smaller than that along the direction of the middle in situ stress.

(3) In order to characterize the advantages and disadvantages of the stress environment in the surrounding rock of the roadway, the environmental coefficient of mining-induced stress is defined. The larger the environmental coefficient of mining-induced stress is, the larger the surrounding rock stress environment is. The range of this coefficient greater than 0.2 is defined as the destruction-danger zone.

Data Availability

The data used to support the findings of this study are included within the article.

Conflicts of Interest

The authors declare that they have no conflicts of interest.

Acknowledgments

References

[1] M. C. He and Q. H. Qian, *Fundamentals of Deep Rock Mechanics*, Science Press, Beijing, China, 2010.

[2] J. C Wang, *Mining Theory and Technology of Thick Coal Seam*, Metallurgical Industry Press, Beijing, China, 2009.

[3] F. Gao, *Research on In-Situ Stress Distribution Law and its Effect on the Stability of Roadway Surrounding Rock*, China University of Mining and Technology, Xuzhou, China, 2009.

[4] J. C Wang and Q. Fu, "Theory and application of granular medium flow in top coal emission from fully mechanized coal caving in low position," *Journal of China Coal Society*, vol. 27, pp. 337–340, 2002.

[5] J. L. Lu, *Soft Rock Roadway Support Technology*, Jilin Science and Technology Press, Changchun, China, 1995.

[6] S. R. Ning, H. Su, and J. Gao, "Research on automatic section precision forming of boom-type roadheader," in *Proceedings of the International Conference on Intelligent Systems Research and Mechatronics Engineering*, pp. 1250–1256, Zhengzhou, China, April 2015.

[7] Y. P. Cheng and X. L. Zhang, "Environmental impact of coal mine methane emissions and responding strategies in China," *International Journal of Greenhous Gas Control*, vol. 5, no. 1, pp. 157–166, 2010.

[8] J. Yuan and I. Naruse, "Effects of air dilution on highly preheated air combustion in a regenerative furnace," *Energy & Fuels*, vol. 13, no. 1, pp. 99–104, 1999.

[9] Q. X. Huang and Y. W. Liu, "Limit self-stabilizing balanced arch theory of roadway surrounding rock support," *Journal of Mining and Safety Engineering*, vol. 31, pp. 354–358, 2014.

[10] N. J. Ma, Z. Q. Zhao, and J. C. Feng, "Supporting technology of tunnel butting long bolt under difficult condition," *Coal Science and Technology*, vol. 41, pp. 117–121, 2013.

[11] N. J. Ma, X. D. Zhao, and Z. Q. Zhao, "Stability analysis and control of roof in deep mining roadway," *Journal of China Coal Society*, vol. 40, pp. 2287–2295, 2015.

[12] M. C. He and Z. B. Guo, "Mechanical characteristics and engineering application of transversely resistant large deformation anchor bolt," *Chinese Journal of Rock Mechanics and Engineering*, vol. 33, pp. 1297–1308, 2014.

[13] J. C. Wang, L. Wang, and Y. Guo, "Determination of support resistance based on roof and coal wall control," *Journal of China Coal Society*, vol. 39, pp. 1619–1624, 2014.

[14] Y. Guglielmi, P. Cook, and F. Soom, "In situ continuous monitoring of borehole displacements induced by stimulated hydrofracture growth," *Geophysical Research Letters*, vol. 48, 2021.

[15] A. V. Azarov and A. V. Patutin, "Investigation of hydraulic fracture growth near a mine opening," *Conference Series: Earth and Environmental Science*, vol. 773, 2021.

[16] D. Pymonenko, "Influence of paleodislocation intensity and modern movements on the stressed state of massif," *Web of Conferences*, vol. 168, 2020.

[17] H. W. Jing, J. Y. Wu, Q. Yin, and K. Wang, "Deformation and failure characteristics of anchorage structure of surrounding rock in deep roadway," *International Journal of Mining Science and Technology*, vol. 30, pp. 593–604, 2020.

[18] G. Masoud, S. Korosh, S. Mostafa, and M. Reza, "A critical review on the developments of rock support systems in high stress ground conditions," *International Journal of Mining Science and Technology*, vol. 30, pp. 555–572, 2020.

[19] H. B. Wen and Y. Q. Li, "Study on stress distribution law and stress performance characteristics of multiple data mining for harbour portal crane detection," *IOP Conference Series: Earth and Environmental Science*, vol. 631, Article ID 012039, 2021.

[20] D. Priyan and J. Paul, "What is the body of knowledge for engineers involved with civil engineering systems? - a 2020 vision," *Civil Engineering and Environmental Systems*, vol. 37, Article ID 1858065, 2020.

[21] G. T. Masterton.Gordon and J. Paul, "Integrating the liberal arts into the body of knowledge for civil engineering systems engineers," *Civil Engineering and Environmental Systems*, vol. 37, Article ID 1832086, 2020.

[22] W. Jowitt Paul, "Systems and sustainability," *Civil Engineering and Environmental Systems*, vol. 37, Article ID 1839892, 2020.

[23] K. Daniel and P. Frederick, "Shealy.tripp et al,"recognizing differences in underrepresented civil engineering students' career satisfaction expectations and college experiences"," *Journal of Management in Engineering*, vol. 37, 2021.

[24] M. Dag, "Review of turbulence in coastal and civil engineering by B. Mutlu Sumer and David R. Fuhrman," *Journal of Waterway, Port, Coastal, and Ocean Engineering*, vol. 147, 2021.

[25] V. Sorin, M. Marin, and D. Ovidiu, "Vibration properties of a concrete structure with symmetries used in civil engineering," *Symmetry*, vol. 13, p. 656, 2021.

[26] D. Z Kong, S. J Pu, Z. H. Cheng, G. Y. Wu, and Y. Liu, "Co-ordinated deformation mechanism of the top coal and filling body of gob-side entry retaining in a fully mechanized caving face," *International Journal of Geomechanics*, vol. 21, 2021.

[27] D.-Z. Kong, Z.-B. Cheng, and S.-S. Zheng, "Study on the failure mechanism and stability control measures in a large-cutting-height coal mining face with a deep-buried seam," *Bulletin of Engineering Geology and the Environment*, vol. 78, no. 8, pp. 6143–6157, 2019.

[28] J. Lou, F. Gao, J. Yang et al., "Characteristics of evolution of mining-induced stress field in the longwall panel: insights from physical modeling," *International Journal of Coal Science & Technology*, 2021.

[29] W. Jiachen, W. Weijie, and Z. Jinwang, "Theoretical description of drawing body shape in an inclined seam with longwall top coal caving mining," *International Journal of Coal Science & Technology*, vol. 7, no. 1, pp. 182–195, 2020.

[30] J. Wang, S. Yang, W. Wei et al., "Drawing mechanisms for top coal in longwall top coal caving (LTCC): a review of two decades of literature," *International Journal of Coal Science & Technology*, 2021.

Research Article

Effect of Advancing Direction of Working Face on Mining Stress Distribution in Deep Coal Mine

Yuesong Tang [iD],[1,2] **Wenchao Sun** [iD],[1] **Xin Zhang** [iD],[1,2] **and Pengju Liu** [iD][1]

[1]*School of Energy and Mining Engineering, China University of Mining Technology-Beijing, Beijing 100083, China*
[2]*Coal Industry Engineering Research Center of Top-Coal Caving Mining, Beijing 100083, China*

Correspondence should be addressed to Yuesong Tang; tang_yuesong@163.com

Deep mining has become the normal state of coal mining; compared with the mine with shallow buried depth, the consequent high level of in situ stress and complex distribution have brought severe threats to the stability of the stope and the surrounding rock of the roadway. In this research, taking the 121304 working face of Kouzidong Mine as the engineering background, the characteristics of mining-induced stress distribution under complex in situ stress environment in deep mining are analyzed by using on-site measurement of the original rock stress and mining stress, establishing a theoretical model centered on the middle section of the working face, and establishing large-scale numerical calculation models for different advancing directions. It was found that under deep mining conditions, the maximum stress of the original rock is 25.12 MPa, and the direction is vertical. The advanced influence range of mining stress is about 150 m, and the abutment pressure presents a three-peak distribution characteristic in front of the working face. The research results provide important theoretical guiding value for guiding the mining of coal mines with similar geological conditions.

1. Introduction

As the level of modern industry increases year by year, the eastern part of China needs more energy supplies [1–6]. The shallow resource was exhausted, and the deep ones begin to develop. As a result, the level of ground stress has risen and the distribution law has become more complicated [7–11]. The stability maintenance of surrounding rock during mining and roadway excavation is more complicated [12–16]. The critical factor which causes the fracture of the rock strata of the stope and roadway is in situ stress [17–20].

Radwan et al. [21] have determined the ground stress field, pore pressure, stress regime, and fracture gradient through on-site measurement of ground stress. It is discovered that the stress field rotates affected by geologic structure and the influence of the stress field rotation on the effect of resource extraction, thereby providing a reliable guarantee for the efficient exploitation of resources. Saeidi et al. [22] analyzed the in situ stress distribution characteristics of Niobec Mine, Quebec (Canada) and the influence

of in situ stress uncertainty on stability evaluation of open-pit slope. Whether a mining plan can be exploited successfully to a deeper mining level depends largely on whether the magnitude and direction of the in situ stress state can be fully considered. Many mines use in situ stress to evaluate the stability of structure of underground and, at the same time, the interpretation of various aspects of mine data and engineering judgments are generally based on mine depth functions and methods which are determined by the value of ground stress obtained from the results of stress measure. Guo et al. [23] statistically analyzed the distribution features and rules of ground stress in Chinese mines according to a massive data of measured results of ground stress and summarized the relationship between stress field type, stress magnitude, stress value, and buried depth. In order to study the splitting failure of high sidewall cavern under high in situ stress, Zhang et al. [24] carried out true three-dimensional (3D) geomechanical model test. In Zhang's paper, the main powerhouse of Pubudou Hydropower Station is taken as an example. By using self-developed 3D loading system and

analogue materials, Zhang reproduced the splitting failure of high sidewall cavern under high ground stress. The formation factor and collapse feature of the split failure of the high side rock cavern have been revealed in this model test. Furthermore, it summarized credible evidence for further researches on the formation mechanism of the split failure of the high sidewall cavern under the action of high ground stress. Yang et al. [25] put forward stress initialization methods. According to the results from simulations, the stress initialization results obtained by implicit-explicit sequence method and dynain file method had a close relationship to the material model of rock. Compared with other methods, the explicit DR method has an obvious advantage in solution time. According to the on-site measurement of a deep mine, Qin et al. [26] have found that the immediate cause of the roadway deformation is the ground stress. A kind of support form of high strength prestressed bolt and cable anchor is proposed, and the best prestress ratio of the bolt and cable anchor was proposed according to the corresponding geological conditions. Li et al. [27] proposed an intelligent monitoring and dynamic control method for coal gangue image recognition to provide the optimal illumination environment for coal gangue recognition.

In summary, the magnitude and direction of in situ stress play an important role in the control of surrounding rock. Especially in deep mines, in situ stress has a greater impact on mining work [28–33]. When the working face is in the condition of large buried depth, due to the influence of high ground stress, the mine pressure behavior will be more severe under the mining disturbance, and the creep deformation of the roadway will occur for a long time after the support [34–36]. The increase of working face length will lead to the increase of stress concentration factor at both ends of the working face, and the increase of the length will slow down the advancing speed, which makes it difficult to support the stope and roadway at the end of the working face and cause serious coal wall spalling. This paper analyzes the influence of the angle between the advancing direction and the initial minimum principal stress on the mining stress field. A better understanding of the influence of the angle on the mining stress field mentioned above can better strengthen the roadway in a targeted way and achieve safe and efficient production. The law of influence on the mining stress field is of great significance for guiding the study of the stability of the surrounding rock in deep mines.

2. Engineering Geological Background

The 121304 working face of Kouzidong Mine, AnHui, is taken as the engineering background. Due to the large buried depth of the working face, and the length of the working face is more than 350 m, it is a typical working face with complex ground stress and significant mine pressure. Rib spalling, roadway severe deformation, and floor heave are serious, as shown in Figure 1.

13-1 coal has been being mined at the working face, in which thickness is 5.2 m, and the comprehensive geological column chart is shown in Figure 2. The coal seam was mined by the process of mining all heights at one time. The on-site stress measurement of the working face found that the maximum principal stress is the vertical stress with a magnitude of 25.12 MPa. The intermediate principal stress is a horizontal stress with a magnitude of 21.84 MPa, and the direction is 35° west by north, and the minimum principal stress is the horizontal stress with a magnitude of 12.89 MPa, in which direction is perpendicular to the intermediate principal stress.

3. Distribution Characteristics of Coal Abutment Pressure

A simplified mechanical model of the working face section is established to analyze the distribution of abutment pressure in the coal seam area. As shown in Figure 3, the working face is regarded as a roadway with a circular cross section, surrounded by an equal-pressure homogeneous surrounding rock environment. According to the content and assumption of elastic mechanics, this is regarded as the stress distribution around the hole. In order to simplify the calculation, the weight of the surrounding rock within the range of $3–5r_0$ around the hole (working face) can be ignored in the calculation process. $4r_0$ is used in this paper.

Assuming the radius of the working face section is r_0, the polar coordinate system is established with the center of the section as the polar coordinate origin. The coordinates of any point outside the working face are (r, θ); by analysing the stress and strain of the point, the equilibrium differential equation of the point is listed as the following equation:

$$\left(\sigma_r + \frac{\partial \sigma_r}{\partial r} dr\right)(r + dr)d\theta - \sigma_r r d\theta - \left(\sigma_r + \frac{\partial \sigma_t}{\partial \theta} d\theta\right)dr \sin\frac{d\theta}{2} - \sigma_t dr \sin\frac{d\theta}{2}$$
$$+ \left(\tau_{\theta r} + \frac{\partial \tau_{\theta r}}{\partial \theta} d\theta\right)dr \cos\frac{d\theta}{2} - \tau_{\theta r} dr \cos\frac{d\theta}{2} + f_r r d\theta dr = 0, \tag{1}$$

where σ_r is the radial stress, σ_t is the tangential stress, and $\tau_{r\theta}$ represents the shear stress; in this model $\tau_{\theta r} = \tau_{r\theta} = 0$, f_r is the physical strength.

In order to simplify the calculation process, according to the characteristics of the engineering environment, equation (1) is simplified and further equation (2) is obtained,
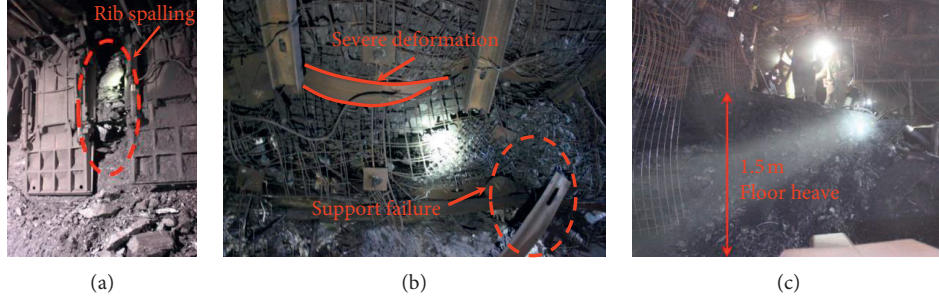
FIGURE 1: Damage to surrounding rock caused by high ground stress. (a) Rib spalling. (b) Roadway severe deformation. (c) Floor heave.

thickness (m)	Lithology
3.10	mudstone
4.10	Fine sandstone
5.40	Sandy mudstone
2.20	Fine sandstone
2.70	mudstone
3.25	Sandy mudstone
4.40	mudstone
5.18	13-1 coal
5.50	mudstone
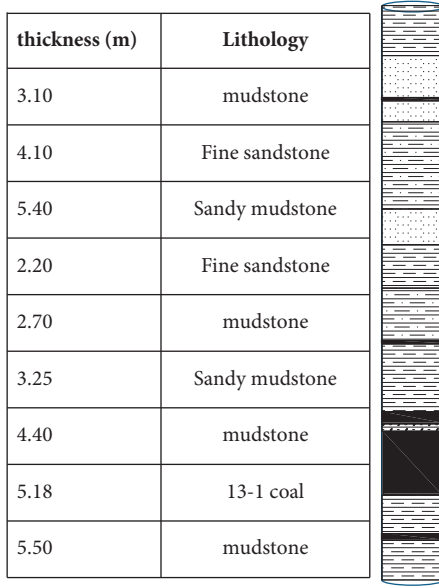
FIGURE 2: Coal seam comprehensive histogram.

$$(\sigma_r + d\sigma_r)(r + dr)d\theta - \sigma_r r d\theta - \sigma_r r d\theta - 2\sigma_t dr \sin\frac{d\theta}{2} = 0. \tag{2}$$

For the convenience of calculation, the equation is approximated,

$$\sigma_r - \sigma_t + r\frac{d\sigma_r}{dr} = 0. \tag{3}$$

Analyze the differential volume at this point and get the geometric equation, as shown in the following equation:

$$\varepsilon_r = \frac{(u + du) - u}{dr} = \frac{du}{dr},$$

$$\varepsilon_t = \frac{(r + u)d\theta - rd\theta}{rd\theta} = \frac{u}{r}, \tag{4}$$

where ε_r is the radial strain, ε_t is the tangential strain, and u is the radial deformation of differential volume.

According to the generalized Hooke's law, the strain expression of differential volume is obtained in the following equation,

$$\varepsilon_r = \frac{1}{E}\left[\sigma_r - \mu(\sigma_t + \sigma_z)\right],$$

$$\varepsilon_t = \frac{1}{E}\left[\sigma_t - \mu(\sigma_r + \sigma_z)\right], \tag{5}$$

where E is the elastic modulus, μ is Poisson's ratio, and σ_z is the axial stress of circular hole.

Taking the derivative of equation (4), one has

$$\frac{d\varepsilon_t}{dr} = \frac{1}{r}(\varepsilon_r - \varepsilon_t). \tag{6}$$

Substituting equation (5) into equation (6) leads to

$$\frac{d\varepsilon_t}{dr} = \frac{1}{rE}\left[\sigma_r - \sigma_t - \mu(\sigma_t + \sigma_z) + \mu(\sigma_r + \sigma_z)\right] = \frac{1 + \mu}{rE}(\sigma_r - \sigma_t). \tag{7}$$

From equation (6),

$$\frac{d\varepsilon_r}{dr} = \frac{1}{E}\left(\frac{d\sigma_t}{dr} - \mu\frac{\sigma_r}{dr}\right). \tag{8}$$

Combining equations (7) and (8),

$$\frac{1 + \mu}{r}(\sigma_r - \sigma_t) = \frac{d\sigma_t}{dr} - \mu\frac{\sigma_r}{dr}. \tag{9}$$

Coordinate transformation in the rectangular coordinate system σ_r, σ_t means, as shown in the following equation,

$$\sigma_r = \sigma_x\cos^2\theta + \sigma_y\sin^2\theta,$$

$$\sigma_t = \sigma_x\sin^2\theta + \sigma_y\cos^2\theta. \tag{10}$$

According to Lame's solution, let the internal pressure $q_1 = 0$ and $q_2 = \gamma H$ in the thick wall cylinder model.

$$\sigma_r = \gamma H\left(1 - \frac{r_1^2}{r^2}\right),$$

$$\sigma_t = \gamma H\left(1 + \frac{r_1^2}{r^2}\right). \tag{11}$$

By calculating the limit equilibrium area around the working face, the static equation is obtained as equation (3), according to the limit equilibrium condition.
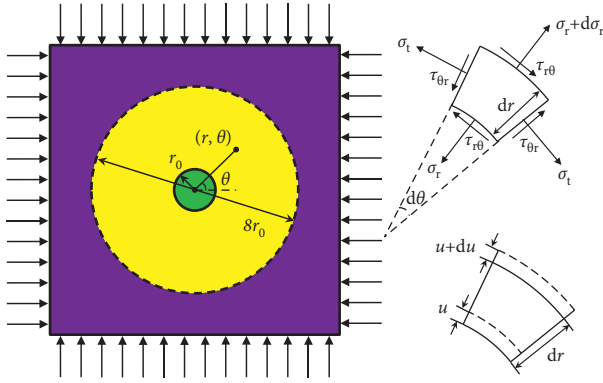
FIGURE 3: Simplified model of stress distribution around working face.

$$\sigma_t = \frac{1 + \sin \varphi}{1 - \sin \varphi} \sigma_r + \frac{2C \cos \varphi}{1 - \sin \varphi}, \tag{12}$$

where C is the cohesion and φ is the internal friction angle.

Combining equations (3) and (12) and integral,

$$\ln (\sigma_r + C \cot \varphi) = \frac{2 \sin \varphi}{1 - \sin \varphi} \ln r + \ln A, \tag{13}$$

where A is the integral constant.

Substituting the boundary conditions $r = r_1$ and $\sigma_r = 0$,

$$\sigma_r = C \cot \varphi \left[\left(\frac{r}{r_1} \right)^{(2 \sin \varphi / (1 - \sin \varphi))} - 1 \right],$$

$$\sigma_t = C \cot \varphi \left[\frac{1 + \sin \varphi}{1 - \sin \varphi} \left(\frac{r}{r_1} \right)^{(2 \sin \varphi / (1 - \sin \varphi))} - 1 \right], \tag{14}$$

when the roof caving behind the working face fills the goaf, the abutment pressure value in this area gradually recovers from 0 to the original rock stress,

$$\sigma_t = K \gamma H, \tag{15}$$

where K is the stress recovery factor.

According to the comprehensive analysis for the abutment pressure at the coal seam position, from the front of the working face to the rear, it can be divided into elastic zone (a), limit equilibrium zone (b), complete pressure relief zone (c), and stress recovery zone (d), as shown in Figure 4.

4. Numerical Analysis of Characteristics of Coal Mining Stress Distribution

4.1. Model Establishment and Parameter Determination. Large numerical calculation models are established based on the engineering geological background of Kouzidong Mine, as shown in Figure 5. In order to study the impact of the advancing direction on the distribution of mining stress, six groups of models with the angle between the advancing direction and the minimum principal stress direction of 0°, 15°, 35°, 45°, 60°, and 90° were established, respectively. According to the results of on-site stress measurement, X axis is determined as the minimum principal stress

direction, Y axis is the middle main stress direction, Z axis is the maximum main stress direction, and the top of the model is the stress boundary condition, where the vertical stress load is applied to simulate the weight of overburden which is not established, and the surrounding and bottom are fixed displacement boundary conditions. The length of each model working face is 350 m and the width of roadway is 6 m. In order to facilitate modeling and improve the accuracy of solution, the length, width, and height of each unit in the coal seam, roof, and floor located in the excavation range of the working face are 1 m, and the thickness of the coal seam is 6 m. After the working face is excavated, the excavated unit body is filled to simulate the goaf. Step by step excavation mode is adopted for the model with the same advancing direction as the actual site, which is calculated once for each excavation of 5 m to simulate the daily advance distance, and the goaf is filled with 20 m behind the coal wall.

In the process of simulation, the self-developed constitutive model is used to control the mechanical characteristics of coal and rock mass. In order to determine the model parameters, coal and rock samples are collected at 121304 working face to determine the rock mechanical parameters. According to the measured distribution characteristics of coal and rock fractures, combined with Hoek Brown criterion, the rock parameters of different layers are modified, and the rock mass parameters are obtained, as shown in Table 1. After excavation, the double yield model is used to simulate the compaction bearing characteristics of gangue in goaf. The model parameters are shown in Table 2. The parameters of the double yield model are determined by trial and error method: the model parameters are changed constantly to make the simulated stress-strain curve of gangue in goaf consistent with the prediction result of Salamon model.

4.2. Numerical Model Validation. In order to determine the reliability of the model, four borehole stress gauges were installed 200 m away from the front working face of the return airway, which will measure the distribution characteristics of air side leading abutment pressure of 121304 working face. The monitoring results are shown in Figure 6(a). When it is 150 m away from the working face, abutment pressure begins to be affected by mining, showing an upward trend, reaching a peak 10–12 m before the working face, and the coal body reached the limit equilibrium state; after that, the coal body entered the mining damage zone, the bearing capacity decreased, and the abutment pressure began to decrease. The coal wall near the working face is reduced to the minimum value, which is about the residual strength of the coal body. The abovementioned abutment pressure distribution characteristics indicate that the leading mining influence range of 121304 working face reaches 150 m, and the width of the coal body damage zone in front of working face reaches 10–12 m.

The on-site measurement and numerical calculation results are shown in Figure 6. Comparing the two results, it can be found that the trends of the two results are consistent on one side of the working face. In the length direction of the
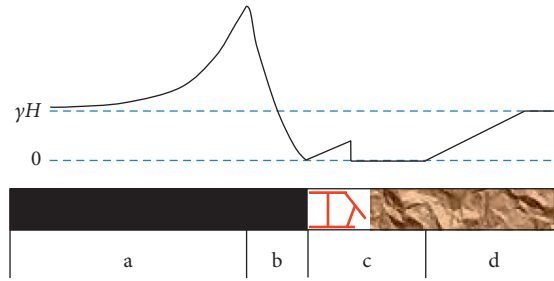
FIGURE 4: Abutment pressure distribution in advancing direction of working face.
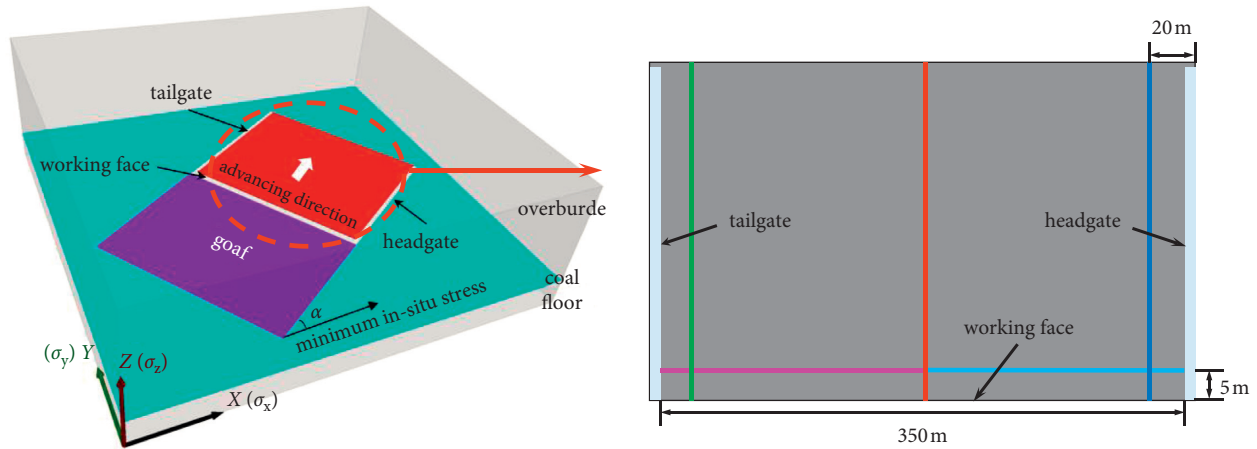
FIGURE 5: Numerical calculation model and the location of measuring line.

working face, there is a trend of first rising and then falling back from the end to the middle. Peaks appear on two sides of the working face. The measured results show that the peak value is close to 50 MPa. The numerical calculation results show that the peak position is 7 m away from the roadway. The abutment pressure reaches 57.8 MPa. Along the advancing direction, the change trend of the abutment pressure showed a first increase and then a decrease and finally approached the original rock stress. The peak points of numerical simulation and measured results are located 10–12 m in front of the working face, and the influence range was about 150 m. It can be seen that the numerical calculation model is basically consistent with the on-site measured results, and the calculation parameters are reliable.

4.3. Analysis of Numerical Results. In order to observe the variation characteristics of mining stress under different advancing directions, two measuring lines and a plane are arranged in the coal seam 5 m above the coal seam floor. The measuring plane is parallel to the horizontal plane. The position of measuring line is showed in Figure 5. As shown by the red line, one measuring line is arranged in the middle of the working face along the advancing direction, and the other measuring line is arranged at 5 m in front of the working face along the length direction, as shown by the pink line and the light blue line.

The influence of the advancing direction on the distribution characteristics of the maximum principal stress

is shown in Figure 7. Under the influence of coal seam mining, the maximum principal stress of the working face is obviously concentrated in advance of the working face, and the maximum principal stress concentration area is mainly distributed in front of the working face, and at both ends, the leading maximum principal stress presents a three-peak shape on the middle of the working face and both sides.

In the length direction of working face, the three peaks at different included angles change significantly, as shown in Figure 8(a). When the angle between the advancing direction and the minimum principal stress is 0°, the maximum principal stress peaks on both sides of the working face are greater than the peak in the middle of the working face, and the peaks on the left and right sides are 51 MPa. As the angle between the advancing direction of the working face and the minimum principal stress increases, the leading maximum principal stress of the working face first decreases and then increases. When the angle is equal to 45°, the maximum principal stress is the smallest. At this time, the peak at the middle position is 49 MPa and the peak at both sides is 47 MPa. When the included angle increases to 90°, the peak at the middle position is 53 MPa, and the peak at both sides is 51 MPa. In the distribution form of the maximum principal stress of the tendency, with the increase of the included angle, the measuring line in the direction of the tendency gradually began to show an asymmetric distribution, and the peak value of the maximum principal stress in the middle part was gradually greater than the peaks at both sides.

TABLE 1: Rock parameters.

Lithology	Elastic modulus (GPa)	Poisson's ratio	Cohesion (MPa)	Internal friction angle (°)	Tensile strength (MPa)	Softening parameter		
						m	n	k
Fine sandstone	21.22	0.16	10.0	38	1.29	0.001	0.70	750
Sandy mudstone	17.50	0.25	4.9	33	2.01	0.0015	0.65	400
Mudstone	14.69	0.25	2.4	32	0.58	0.002	0.56	320
Coal	2.83	0.20	1.25	30	0.15	0.0035	0.40	270

TABLE 2: Mechanical parameters of falling gangue in goaf.

Parameter name	Density (kg/m³)	Bulk modulus (GPa)	Shear modulus (GPa)	Cohesion (MPa)	Internal friction angle (°)	Tensile strength (MPa)	Blocking parameters		
							a (MPa)	b —	c (MPa)
Value	2000	1.2	0.6	0	30	0	60	15	20

In the advancing direction of working face, under different included angles, the maximum principal stress distribution of the working face is shown in Figure 8(b). The angle between the advancing direction and the minimum principal stress has a less impact to the maximum principal stress of the working face, and the leading influence range is about 40 m. When the included angle is 0°, the maximum principal stress peak position of the working face is 6 m in front of the working face, and the peak point is 51.9 MPa. As the included angle increases, the peak point position moves slightly to the front of the coal wall, and the maximum principal stress peak increases slightly. When the included angle increases to 90°, the maximum principal stress peak position of the working face is 4 m before the working face, and the peak point is 52.5 MPa. In general, the angle between the advancing direction and the minimum principal stress has little effect on the distribution of the maximum principal stress.

Figure 9 shows the maximum principal stress concentration factor of the working face under different angles between the advancing direction and the minimum principal stress. The stress concentration factor is expressed in η, where B is the peak stress of working face and A is the in situ stress without mining disturbance. As shown in Figure 9, the maximum stress concentration factor of principal stress appears to decrease first and then increase. The minimum value of the maximum principal stress concentration factor is at the angle of 15° with a value of 2.16. As the included angle continues to increase, the stress concentration factor gradually increases. When the included angle increases to 45°, the increase began to slow down. When the included angle increases to 90°, the stress concentration factor reaches the maximum value of 2.25.

In summary, the angle between the minimum principal stress and the advancing direction of the working face has a greater influence on the mining stress distribution in working face. In terms of stress, with the increase of the

angle, the mining stress as a whole shows a trend of decreasing first and then increasing. In terms of morphological distribution, the spatial division characteristics of mining stress are also affected by the included angle. With the increase of the included angle, the peak values of the double peaks on both sides are gradually smaller than the peaks in the middle.

Under the condition of different included angles between the direction of the initial minimum ground stress (X-axis) and the advancing direction of the working face, the evolution characteristics of the maximum principal stress rotation trajectory are shown in Figure 10. The red, green, and blue measuring lines are arranged along the advancing direction of the working face. The red measuring line is arranged in the middle of the working face, and the green and blue measuring lines are arranged 20 m away from the roadway at both ends. The pink and light blue measuring lines are arranged from both ends of the tailgate and headgate to the middle of working face along the length direction of the working face, 5 m ahead of the working face. The maximum principal stress rotation trajectory on the advancing direction measuring line always deflects in the direction of the goaf in the vertical plane parallel to the advancing direction of the working surface. Therefore, the angle between the 90–270 axis direction and the maximum principal stress rotation trajectory on the strike measuring line gradually increases. It always maintains the angle between the advancing direction of the working face and the initial minimum ground stress direction. The maximum principal stress rotation trajectory on the length direction measuring line always maintains the arc of the symmetry axis with the advancing measuring line, roughly toward the roadway on both sides of the working face direction. In summary, the size of the rotation angle of the maximum principal stress is less affected by the direction of propulsion, but the direction of rotation is obviously affected by the advancing direction.

(a)

(b)
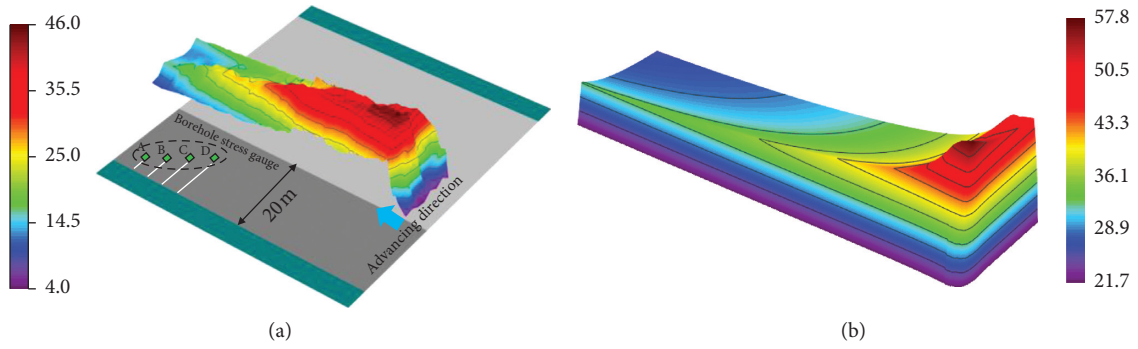
FIGURE 6: Comparison of on-site measurement results and numerical calculation results. (a) On-site measurement. (b) Numeral calculations.

(a)

(b)

(c)

(d)

FIGURE 7: Continued.

(e)

(f)
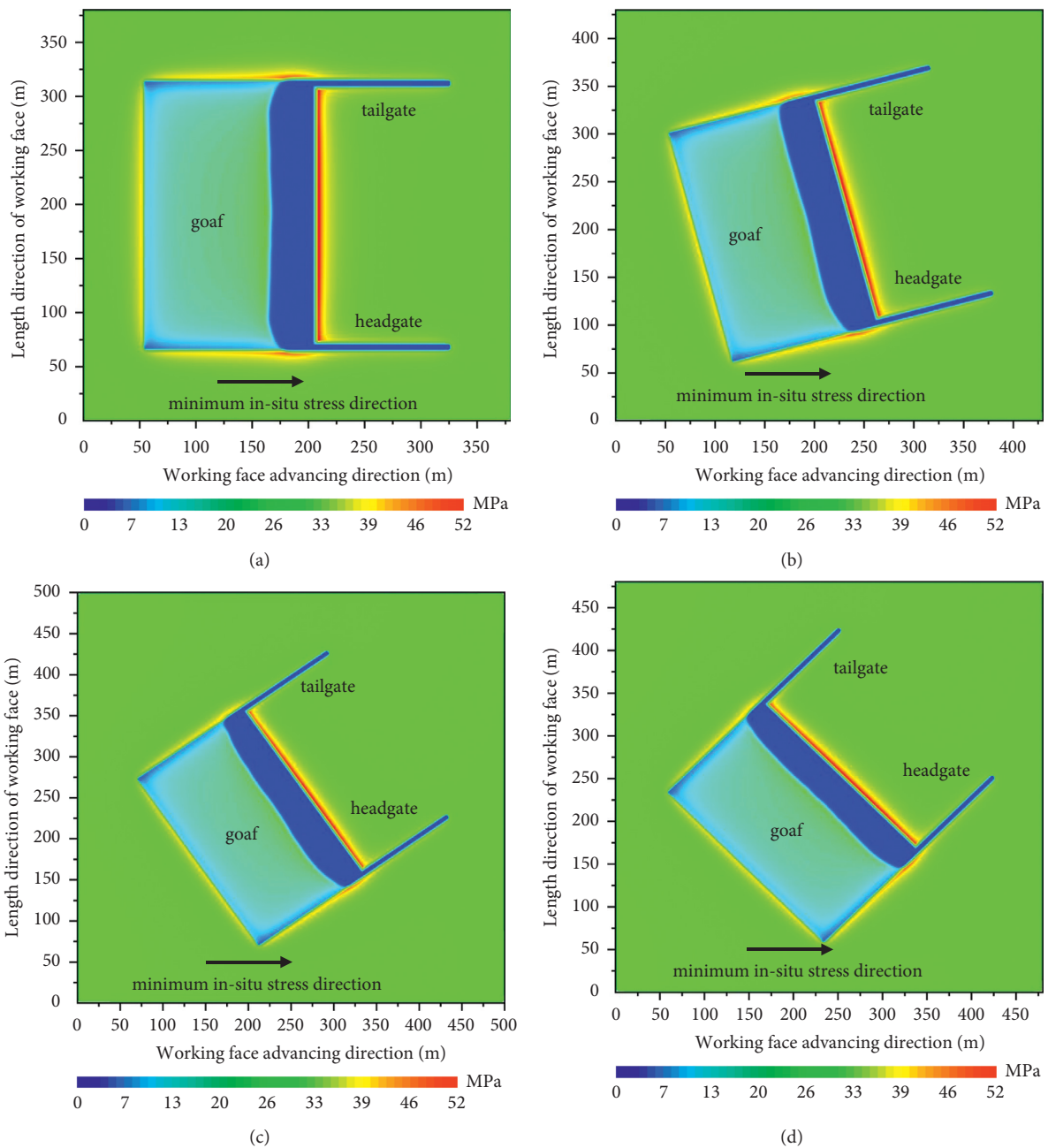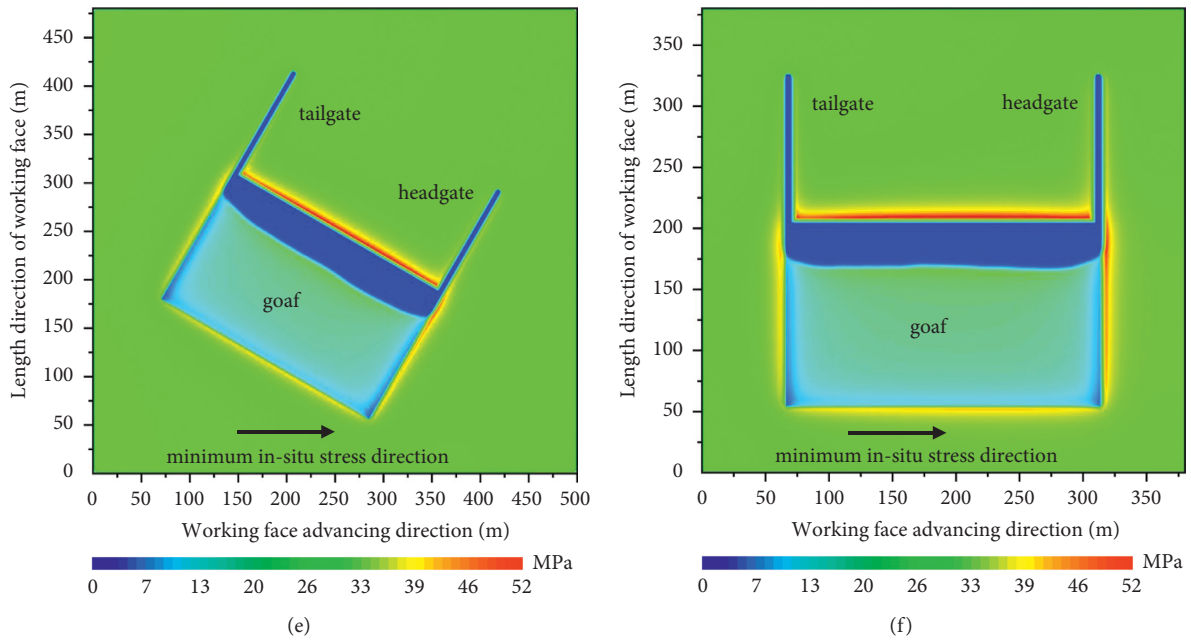
FIGURE 7: Influence of advancing direction on maximum principal stress distribution of working face. (a) 0˚. (b) 15˚. (c) 30˚. (d) 45˚. (e) 60˚. (f) 90˚.

(a)

(b)
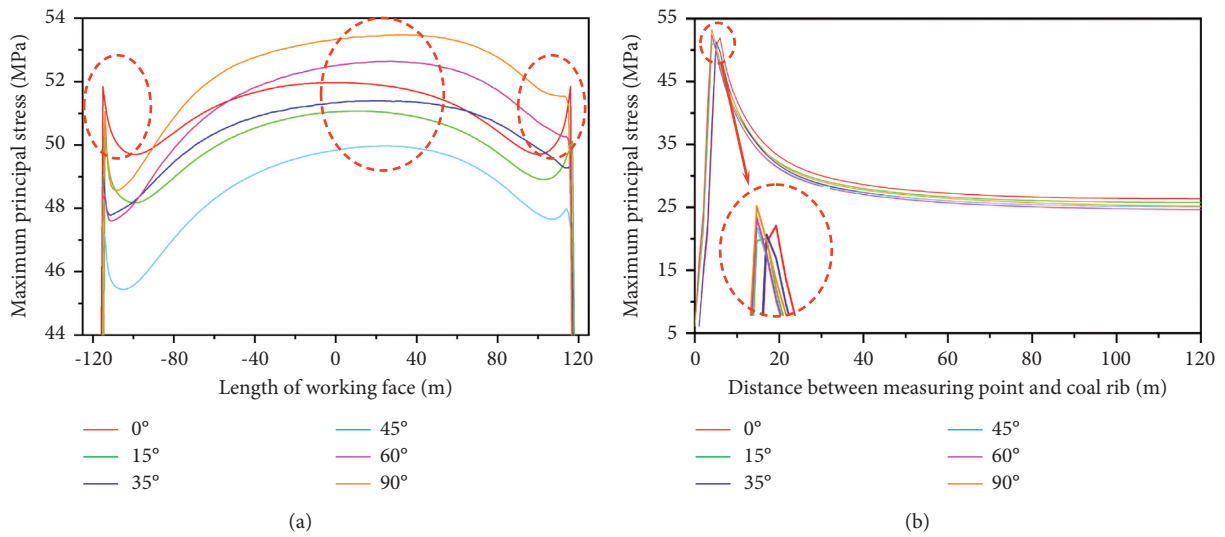
FIGURE 8: Maximum principal stress distribution of working face under different advancing direction and minimum principal stress angle. (a) The direction of length. (b) The direction of advancing.
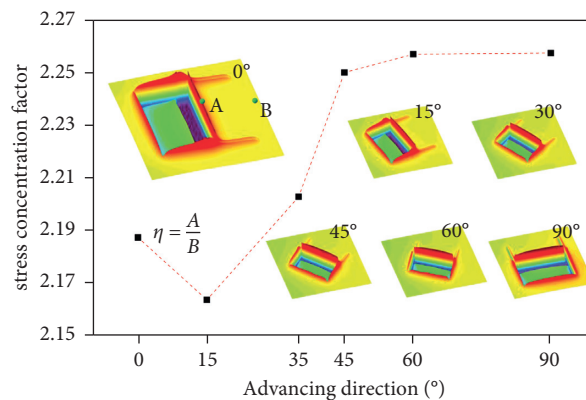
FIGURE 9: Maximum principal stress concentration factor of working face in different advancing directions.
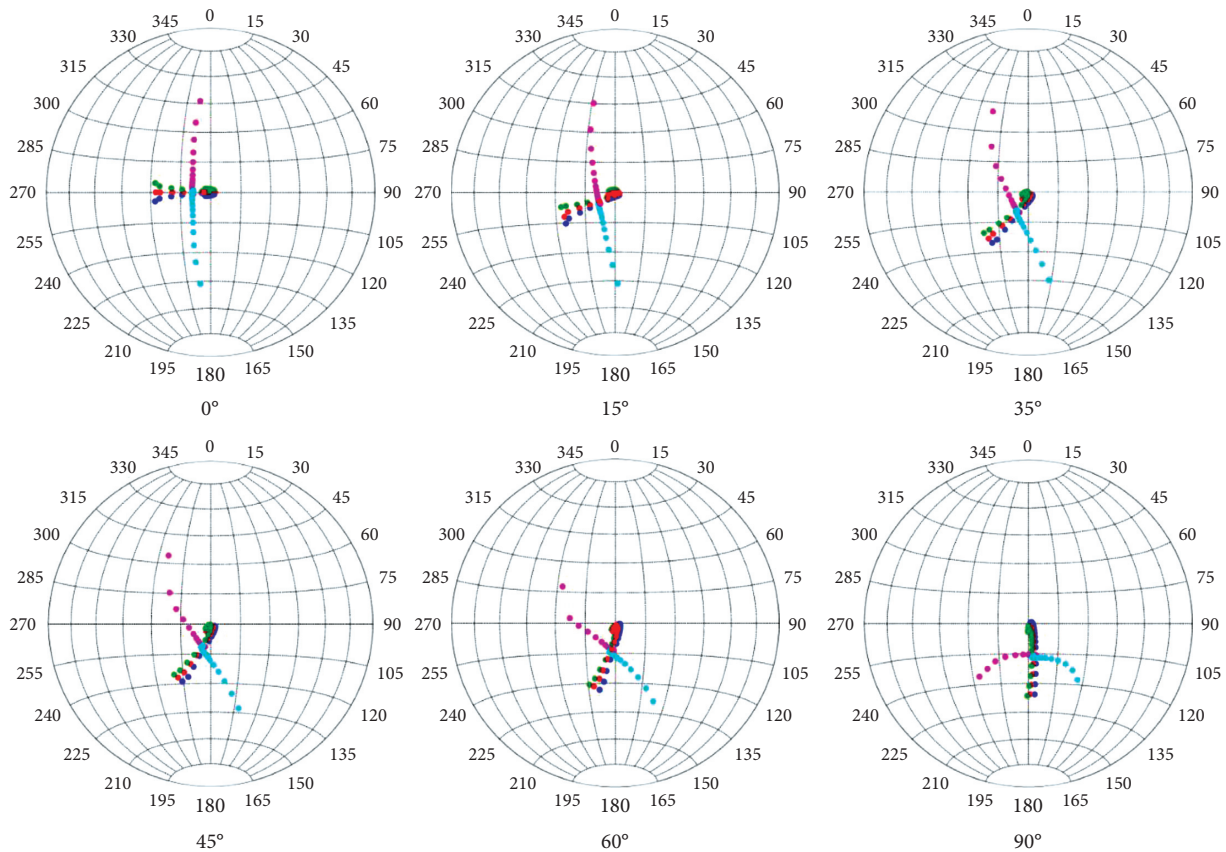
FIGURE 10: Rotation trajectory characteristics of maximum principal stress under different advancing directions.

5. Conclusions

(1) The on-site measurement has obtained the in situ stress distribution of the deep part of the Kouzidong Mine. The maximum principal stress direction is the vertical direction with a magnitude of 25.12 MPa. The direction of the minimum principal stress is east by north 55° of the horizontal direction, and the magnitude is 12.89 MPa. The deep mine of Kouzidong Mine has an advanced mining influence range of 150 m, and the maximum stress concentration position is about 10 m in front of the coal wall. The results of numerical simulation agree well with this feature.

(2) Under the influence of coal seam mining, the maximum principal stress of the working face is obviously concentrated in advance of the working face, and the maximum principal stress concentration area is mainly distributed in front of the working face, and at both ends, the leading maximum principal stress presents a three-peak shape on both sides of the working face and the middle of the working face.

(3) Through the establishment of numerical models of different advancing directions, it is found that the stress concentration is located at 7–10 m in front of the working face, and in the length direction of the working face, the distribution characteristics of three-peak stress are all presented. With the increase of the angle between the advancing direction and the minimum principal stress, the mining stress concentration first decreases and then increases and tends to be stable. Therefore, in the safe and efficient production of super-long working face in deep mine, it is necessary to consider the influence between the advancing direction and the minimum principal stress angle, so as to minimize the stress concentration of the working face and strengthen the support at the end and the middle of the working face to prevent the occurrence of rib spalling and other accidents.

Data Availability

The data used to support the findings of this study are included within the article.

Conflicts of Interest

The authors declare that they have no conflicts of interest.

Acknowledgments

References

[1] H. P. Xie, "Research review of the state key research development program of China: deep rock mechanics and mining theory," *Journal of China Coal Society*, vol. 44, no. 5, pp. 1283–1305, 2019.

[2] J. C. Wang, "Sustainable coal mining based on mining ground control," *Journal of Mining and Strata Control Engineering*, vol. 1, no. 2, pp. 40–47, 2019.

[3] Q. Wang, B. Jiang, R. Pan et al., "Failure mechanism of surrounding rock with high stress and confined concrete support system," *International Journal of Rock Mechanics and Mining Sciences*, vol. 102, pp. 89–100, 2018.

[4] J. Xie, J. Xu, and F. Wang, "Mining-induced stress distribution of the working face in a kilometer-deep coal mine-a case study in Tangshan coal mine," *Journal of Geophysics and Engineering*, vol. 15, no. 5, pp. 2060–2070, 2018.

[5] W. Pytel, J. Świtoń, and A. Wójcik, "The effect of mining face's direction on the observed seismic activity," *International Journal of Coal Science & Technology*, vol. 3, no. 3, pp. 322–329, 2016.

[6] K. Yang, X. He, L. Dou, W. Liu, L. Sun, and H. Ye, "Experimental investigation into stress-relief characteristics with upward large height and upward mining under hard thick roof," *International Journal of Coal Science & Technology*, vol. 2, no. 1, pp. 91–96, 2015.

[7] D. Z. Kong, S. J. Pu, Z. H. Cheng et al., "Coordinated deformation mechanism of the top coal and filling body of gobside entry retaining in a fully mechanized caving face," *International Journal of Geomechanics*, vol. 21, no. 4, 2021.

[8] D.-Z. Kong, Z.-B. Cheng, and S.-S. Zheng, "Study on the failure mechanism and stability control measures in a large-cutting-height coal mining face with a deep-buried seam," *Bulletin of Engineering Geology and the Environment*, vol. 78, no. 8, pp. 6143–6157, 2019.

[9] S. Li, M. Gao, X. Yang et al., "Numerical simulation of spatial distributions of mining-induced stress and fracture fields for three coal mining layouts," *Journal of Rock Mechanics and Geotechnical Engineering*, vol. 10, no. 5, pp. 907–913, 2018.

[10] J. M. Zhang, Q. S. Li, Y. Zhang et al., "Definition of deep coal mining and analysis of mining response," *Journal of China Coal Society*, vol. 44, no. 5, pp. 1314–1325, 2019.

[11] H. P. Xie, Z. T. Zhang, F. Gao et al., "Stress-fracture-seepage field behavior of coal under different mining lay-outs," *Journal of China Coal Society*, vol. 41, no. 10, pp. 2405–2417, 2016.

[12] J. C. Wang, Z. H. Wang, J. Yang et al., "Mining-induced stress rotation and its application in longwall face with large length in kilometer deep coal mine," *Journal of China Coal Society*, vol. 45, no. 3, pp. 876–888, 2020.

[13] H. P. Xie, H. W. Zhou, D. J. Xue et al., "Research and thinking on deep coal mining and extreme mining depth," *Journal of China Coal Society*, vol. 37, no. 4, pp. 535–542, 2012.

[14] M. C. He, H. P. Xie, S. P. Peng et al., "Research on rock mechanics in deep mining," *Chinese Journal of Rock Mechanics and Engineering*, vol. 24, no. 16, pp. 2803–2813, 2005.

[15] Y. F. Han, Z. H. Wang, and Y. S. Tang, "Principal stress rotation in longwall top-coal caving face adjacent to the gob," *Journal of China Coal Society*, vol. 45, no. S1, pp. 12–22, 2020.

[16] J. C. Wang and Z. H. Wang, "Propagating mechanism of top-coal fracture in longwall top-coal caving mining," *Journal of China Coal Society*, vol. 43, no. 9, pp. 2376–2388, 2018.

[17] J. Wang, W. Wei, and J. Zhang, "Theoretical description of drawing body shape in an inclined seam with longwall top coal caving mining," *International Journal of Coal Science & Technology*, vol. 7, no. 1, pp. 182–195, 2020.

[18] H. P. Kang, G. F. Wang, P. F. Jiang et al., "Conception for strata control and intelligent mining technology in deep coal mines with depth more than 1 000 m," *Journal of China Coal Society*, vol. 43, no. 7, pp. 1789–1800, 2018.

[19] J. C. Wang, S. L. Yang, W. J. Wei et al., "Drawing mechanisms for top coal in longwall top coal caving (LTCC): a review of two decades of literature," *International Journal of Coal Science & Technology*, 2021.

[20] J. F Lou, F. Q. Gao, J. H. Yang et al., "Characteristics of evolution of mining-induced stress field in the longwall panel: insights from physical modeling," *Int. J. Coal Sci. Technol.*, 2021.

[21] A. E. Radwan, W. K. Abdelghany, and M. A. Elkhawaga, "Present-day in-situ stresses in Southern Gulf of Suez, Egypt: insights for stress rotation in an extensional rift basin," *Journal of Structural Geology*, vol. 147, Article ID 104334, 2021.

[22] A. Saeidi, S. heidarzadeh, S. Lalancette et al., "The effects of in situ stress uncertainties on the assessment of open stope stability: case study at the Niobec Mine, Quebec (Canada)," *Geomechanics for Energy and the Environment*, vol. 25, Article ID 100194, 2021.

[23] H. J. Guo, M. Ji, and W. S. Zhao, "Analysis of the distribution characteristics and laws of in situ stress in China's coal mines," *Arabian Journal of Geosciences*, vol. 13, 2020.

[24] Q. Y. Zhang, F. Li, D. Kang et al., "Experimental investigation on splitting failure of high sidewall cavern under three-dimensional high in-situ stress," *Tunnelling and Underground Space Technology*, vol. 108, 2021.

[25] J.-c. Yang, K.-w. Liu, X.-d. Li, and Z.-x. Liu, "Stress initialization methods for dynamic numerical simulation of rock mass with high in-situ stress," *Journal of Central South University*, vol. 27, no. 10, pp. 3149–3162, 2020.

[26] Z. C. Qin, B. Cao, Y. L. Liu et al., "Study on in Situ Stress Measurement and Surrounding Rock Control Technology in Deep Mine," *Geofluids*, vol. 2020, Article ID 8839333, 12 pages, 2020.

[27] L. H. Li, J. C. Wang, S. L. Yang et al., "Smart control methodology for light sources based on halogen lamp - a solution for eco- and user- friendly lighting in underground mining," *Optik*, vol. 242, Article ID 167085, 2021.

[28] J. G. Wang, B. Hu, H. Liu, Y. Han, and J. Liu, "Effects of "soft-hard" compaction and multiscale flow on the shale gas production from a multistage hydraulic fractured horizontal well," *Journal of Petroleum Science and Engineering*, vol. 170, pp. 873–887, 2018.

[29] D. Li, Z. Sun, T. Xie, X. Li, and P. G. Ranjith, "Energy evolution characteristics of hard rock during triaxial failure with different loading and unloading paths," *Engineering Geology*, vol. 228, pp. 270–281, 2017.

[30] X. M. Song, T. F. Gu, and Z. H. Yan, "Research on the influence of the increase in the length of the large mining face in shallow buried seams on the appearance of ground pressure," *Chinese Journal of Rock Mechanics and Engineering*, vol. 26, 2007.

[31] X. B. Li, F. Q. Gong, S. F. Wang et al., "Dynamic and static combined loading mechanism and dynamic criterion of rockburst in deep hard rock mines," *Journal of Rock Mechanics and Engineering*, vol. 38, 2019.

[32] G. Z. Yin, X. Li, J. Lu et al., "Research on the disaster mechanism of composite dynamic disasters under dynamic

and static loads in deep mining," *Journal of China Coal Society*, vol. 42, 2017.

[33] W. Yang, B.-q. Lin, and J.-t. Xu, "Gas outburst affected by original rock stress direction," *Natural Hazards*, vol. 72, no. 2, pp. 1063–1074, 2014.

[34] V. I. Karev, D. M. Klimov, Y. F. Kovalenko, and K. B. Ustinov, "Fracture model of anisotropic rocks under complex loading," *Physical Mesomechanics*, vol. 21, no. 3, pp. 216–222, 2018.

[35] S. V. Kuznetsov and V. A. Trofimov, "Original stress state of coal seams," *Journal of Mining Science*, vol. 39, no. 2, pp. 107–111, 2003.

[36] A. H. Deliormanli and N. H. Maerz, "Stress related fracturing in dimension stone quarries," *IOP Conference Series: Earth and Environmental Science*, vol. 44, no. 5, 2016.

Research Article

The Drainage Horizon Determination of High Directional Long Borehole and Gas Control Effect Analysis

Yuqi Shang ⓘ **, Guiyi Wu** ⓘ **, Qinzhi Liu** ⓘ **, Dezhong Kong** ⓘ **, and Qiang Li** ⓘ

College of Mining, Guizhou University, Guizhou, Guiyang 550025, China

Correspondence should be addressed to Qinzhi Liu; 39850741@qq.com and Dezhong Kong; dzkong@gzu.edu.cn

In order to effectively solve the problem of gas concentration overrun in the upper corner of goaf and tailentry during the mining of panel 9303 in Anshun Coal Mine, based on the advantages of controllable trajectory and wide coverage area of directional drilling technology, high directional long boreholes are arranged in tailentry 9303 to extract pressure relief gas. Firstly, the principle of high directional long borehole drainage technology is introduced, and the fracture evolution of overlying strata is obtained through using numerical simulation, theoretical calculation, and field practice, and the fracture evolution range is determined to be 6–12.69 m, and rationality of fracture height obtained by theoretical analysis and numerical simulation is verified by the method of field borehole peep observation. Through the analysis, it is concluded that the best location of the final hole is within the range of 6–12.69 m of the roof of coal seam 9#. The field practice has proved that the final hole position of the high directional long borehole is arranged at 12 m from the roof of coal seam 9#, and the average gas extraction concentration can reach 40%–50% after the borehole enters the stable extraction stage, the purity of gas extraction is up to $8.5\,\text{m}^3/\text{min}$, and the gas concentration in the upper corner of panel 9303 is stable below 0.5% during mining, which achieves good gas drainage and control effect and provides a new way for gas control under similar geological conditions.

1. Introduction

The coal resource in Guizhou Province is very abundant, known as "Jiangnan Coal Sea." The coal industry is one of the pillar industries in Guizhou Province, but coal seam gas content is generally high in Guizhou Province; coal and gas outburst disasters are serious. In particular, the number of coal layers is large, and the coal seam spacing is close, when the coal seam is mined, the pressure relief gas in the adjacent coal seam is easy to flow into the goaf of the working face through the delamination fracture and broken fracture. With the improvement and popularization of directional drilling technology and equipment in China, the use of high directional long boreholes technology to control coal mine gas problems is widely used in major coal mines.

Coal seam mining causes the redistribution of stress field of overlying strata [1, 2], resulting in deformation and failure of overlying strata, thus forming mining-induced fractures. Therefore, study on fracture evolution law of overlying strata

on working face is very important to improve gas control ability of high-level directional long borehole technology. To determine the drainage horizon of efficient extraction of high directional long borehole, many studies have analyzed the fracture evolution law of overlying strata in goaf during coal mining. Wang and Mang [3] proposed the gas control mode of goaf by roof directional long borehole instead of high drainage roadway, and it is concluded that compared with the high drainage roadway, the roof directional long drilling can not only achieve the same treatment effect, but also greatly reduce the capital investment and shorten the construction period. Finally, the best drainage position is determined by $FLAC^{3D}$ numerical simulation. Xu et al. [4] on the basis of predecessors, according to the actual working face roof overlying strata characteristics and mining conditions, the establishment of coal mining numerical simulation model, not only according to the results of numerical simulation and theoretical analysis to determine the high directional long drilling layout horizon, but also optimize

the drilling structure, effectively reduces the gas concentration of the working face. Using the different-source prediction method, Cai et al. [5] analyzed gas emission source of working face, and the height range of caving zone and fracture zone in goaf is calculated theoretically, after the reasonable high drilling parameters are determined according to the specific situation of the mine. It was found that using roof strike high borehole gas drainage technology can effectively ensure the safe mining of working face. With the deepening of research on the overlying strata of working face, Cheng et al. [6] according to the simulation results of crack field, stress field, and strain field distribution, the range of fracture strengthening zone and compaction zone of goaf roof along the advancing direction of working face are divided. In their study, the borehole part in the fracture strengthening zone is the effective extraction area of boreholes; the length of the effective extraction section of boreholes and the development degree of fractures in the effective extraction section of boreholes jointly determine the extraction efficiency of long boreholes with high strike, revealing the mechanism of gas extraction by long boreholes with high strike in goaf roof. Li and Jin [7] simulate the mining process of panel 3304 in Zaozhuang Coal Mine by UDEC numerical simulation software, and combined with the theoretical analysis of rock fracture, according to the failure characteristics of coal seam roof and the change rule of displacement field in the simulation results, the maximum height position of roof rock caving zone and water flowing fault zone caused by mining is determined. The results show that the results obtained by field test are close to the numerical simulation results.

The above research, whether numerical simulation or model test, has carried on the beneficial exploration and the research to the goaf overburden law according to the different actual working condition and the geological condition [8] and has obtained the massive research results. Therefore, on the basis of previous studies, this paper adopts the method of combining numerical simulation, field test, and theoretical analysis to calculate and analyze the distribution range of caving zone and fracture zone, so as to determine the location of holes. Finally, the effect of gas drainage is investigated through field practice to verify the distribution range of fracture zone, and the directional drilling technology is used to accurately control the drilling trajectory, so that the drilling trajectory is always in the fracture zone, so as to intercept and extract the pressure relief gas in the adjacent layer and control the gas in the upper corner of the goaf to achieve the purpose of safe production.

2. Engineering Background

The panel 9303 of the Anshun Coal Mine has a buried depth of 398 m and belongs to a high gas mine. The dip angle of the coal seam is near horizontal, which are 8#, 9#, and 10# coal seams (as shown in Figure 1), respectively. The coal seam 8# and coal seam 10# are thin and therefore not mined. The mining coal seam 9# is 12.44–12.94 m below the 10# coal seam and 14–16.55 m above the coal seam 8#. The coal seam spacing is relatively close, so it is easy to cause disturbance to

the adjacent coal seam due to the excavation of the working face, making the pressure relief gas flows to the working face through the cracks. The panel 9303 adopts the U-type ventilation mode. The goaf is easy to accumulate gas, and there is a risk of exceeding the gas volume fraction in the upper corner.

The panel 9303 is located in coal seam 9# of 3rd panel, the panel length is 726 m, and the setup entry length is 173 m. The thickness of coal seam 9# is 1.52 m, and the recoverable reserves of panel 9303 are 290.3 million tons. Coal seam 9# roof is no false roof and direct top of silty mudstone, thickness 5.96 m. The basic roof is limestone with a thickness of 4.79 m. The direct bottom is fine sandstone with a thickness of 3.78 m. The old base is siltstone with a thickness of 8.12 m. The distance between coal seam 9# and coal seam 8# is about 15 m. The coal thickness of coal seam 8# is 0.2–0.58 m, and the average coal thickness is 0.43 m. The maximum gas content of coal seam 8# is 20.83 m^3/t.

3. Drainage Position Determination

3.1. Principle of Gas Drainage Technology with High Directional Long Borehole. Directional drilling technology and equipment reflect the most advanced level of underground drilling in coal mines at this stage [9, 10]. Directional drilling is a kind of drilling method which uses natural bending law of drilling hole or artificial deflecting tool to extend drilling hole to predetermined target according to design requirement [11, 12].

The principle of gas drainage by high directional drilling is based on the "three zones" distribution theory and "O" circle theory of overlying strata. When overlying strata move and destroy on the working face, "falling zone, fracture zone, and bending subsidence zone" are formed in the vertical direction, namely, "vertical three zones." "Coal wall support influence zone, separation zone, and recompaction zone" are formed in the horizontal direction, namely, "transverse three zones" [13, 14]. The separation zone is the mining fracture "O" circle. The "O" circle and the middle and lower parts of the fault zone are the main channels of gas migration and the main places for gas accumulation [15].

The horizon determination of high directional long borehole is crucial, which is directly related to the gas drainage effect, based on the distribution of the fracture zone of the overlying strata and "O" circle theory. On the one hand, the high directional long borehole cannot be arranged in the falling zone; otherwise, the rock crushing and caving will directly destroy the borehole, resulting in difficult drainage and even unable to extract. On the other hand, it cannot be arranged in the bending subsidence zone, because of the fracture development is poor in this zone, there is no effective gas flow channel between cracks, and the effect of gas extraction is poor. The best high directional long borehole arrangement horizon is the range of fracture zone in "three zones," because of the development of fractures in this zone, fractures are connected to each other to form an effective channel for gas flow, and will not cause serious damage to boreholes, which is conducive to gas extraction [16]. However, due to the different geological
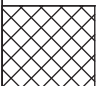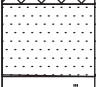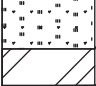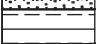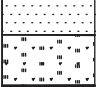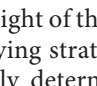
Column	Name of rock	Thickness (m)	Lithologic character
	Sandstone	12.50	Pale grayish white, containing carbonated plant debris, in obvious contact with sublayers
	Fine sandstone	7.99	Pale gray white, mainly composed of quartz.
	Siltstone	16.88	Light gray to gray, with horizontal stratification, slightly oblique stratification.
	Mudstone	14.73	Light gray, with horizontal bedding, loose and fragile, good water absorption
	8# Coal seam	0.43	Black powder, good coal quality, containing plant fossils
	Siltstone	4.26	Dark gray, silty structure, dense and brittle.
	limestone	4.79	Gray limestone containing chert nodules.
	Silty mudstone	5.96	Page-like or lamellar bedding, easy to crack into fragments when hit with hard objects, poor water permeability.
	9# Coal seam	1.5	Dark gray ~ gray, clumpy, patchy, containing fossil plant roots, strong water absorption, easy to weathering.
	Fine sandstone	4.56	Pale gray white, mainly composed of quartz, containing plant carbonized debris, and the underlying layer obviously contact.
	Siltstone	8.62	Dark gray, silty structure, dense and brittle.
	10# Coal seam	0.49	Black powder, good coal, contains plant fossils
	Medium sandstone	19.84	Dark gray ~ gray, clumpy, patchy, containing fossil plant roots, strong water absorption, easy to weathering.

FIGURE 1: Coal and rock strata histogram.

and mining conditions of working faces in different mining areas, the height of the "three zones" formed by the collapse of the overlying strata is also different. Therefore, in order to reasonably determine the high directional long boreholes arrangement horizon, it is necessary to determine the caving characteristics of overlying strata, the evolution of fractures, and the height of "three zones" of overlying strata.

3.2. Theoretical Calculation of "Three Zones" Height of Overlying Strata. The height of overlying strata falling zone and fracture zone is determined by the mining height of working face, coal seam dip angle, roof management method, roof lithology, and other factors. Considering the actual situation of working face, since the roof of coal seam 9# is silty mudstone, it belongs to soft rock. So, the following empirical formula is selected to calculate the height of falling zone and fracture zone [17, 18]:

$$H_1 = \frac{100M}{6.2M + 10.0} \pm 2.5, \qquad (1)$$

$$H_2 = \frac{100M}{3.1M + 6.0} \pm 6.5. \qquad (2)$$

In the formula, H_1 is the falling zone height. H_2 is the fracture zone height. M is the thickness of coal seam mining; take the average thickness of 1.5 m into formulas (1) and (2), the height of falling zone H_1 is 5.27–10.27 m, and the height of fracture zone H_2 is 7.58–20.58 m.

3.3. Numerical Simulation of Roof Crack Evolution in Goaf during Mining. In order to further accurately determine the fracture development characteristics of pamel 9303 under different advancing distances, based on the coal and rock strata histogram, physical and mechanical properties of coal strata, and panel 9303 mining conditions, the UDEC numerical simulation method is used to establish the evolution model of overlying strata fracture in the process of coal seam mining, so as to study the evolution characteristics of overlying strata fracture under different advancing distances and finally determine the most efficient hole arrangement horizon.

3.3.1. Establishment of Numerical Simulation Model. By cutting the blocks, UDEC separates the deformed materials into discrete block sets to represent the discontinuous medium. The block in the model uses the Mohr–Coulomb criterion to describe the deformation and failure process of rock materials [19], as shown in the following formula:

$$R = c \cdot \cos \varphi + \frac{1}{2} \left(\sigma_1 + \sigma_3 \right) \cdot \sin \varphi. \qquad (3)$$

In the formula, φ is the angle of internal friction of rock, c is rock cohesion, σ_1 is the maximum principal stress, σ_3 is the minimum principal stress, and R is the radius of stress circle, $R = (\sigma_1 - \sigma_3)/2$. And according to the geological prospecting report of Anshun Coal Mine, the mechanical parameters of the roof-floor of coal seam 9# are obtained, as shown in Table 1.

TABLE 1: The mechanical parameters of major rock mass for roof and floor.

Name of rock	Density (kg·m^{-3})	Bulk modulus (GPa)	Shear modulus (GPa)	Cohesion (MPa)	Angle of internal friction (°)	Tensile strength (MPa)
Sandstone	2600	5.27	11	2.3	39	4.35
Fine sandstone	2645	4.62	18	8.36	34	2.35
Siltstone	2700	5.6	7	5.3	35	2.86
Mudstone	2550	4.16	4.69	1.41	37	3.2
Coal seam 8#	1350	3.95	2.2	2	30	1.04
Siltstone	2700	5.6	3.8	5.3	35	2.86
Limestone	2540	6.85	1.47	1.26	10	1.2
Silty mudstone	2132	6	8.13	8.87	42	4.56
Limestone	2540	6.85	1.47	1.26	10	1.2
Silty mudstone	2132	6	8.13	8.87	42	4.56
Coal seam 9#	1300	4.33	5.1	2	38	1.04
Fine sandstone	2245	24.62	12	6.36	34	2.35
Siltstone	2100	5.6	7	5.3	35	2.86
Coal seam 10#	1350	3.95	2.2	2	30	1.04
Medium sandstone	2132	26	8.13	11.87	42	4.56

Based on this, establish a simplified two-dimensional model by UDEC. The model is 200 m in length and 120 m in height. Displacement constraints are applied to the vertical direction and lower boundary of the model, and equivalent stress loads are applied to the upper boundary. According to the calculation, the equivalent load is 7.11 MPa. The advance length of the model is 120 m for excavation, and the development law of rock strata caving cracks is simulated. 40 m is left at both ends to offset the boundary effect (as shown in Figure 2).

3.3.2. Analysis of Roof Fracture Development. In the process of working face advancing, due to the influence of excavation work, the stress field is redistributed, resulting in the continuous evolution of mining cracks with excavation work [20–23]. Due to the supporting effect of coal wall at both ends of working face and the different lithology of rock strata, the collapse and subsidence degree of each rock strata are different, so the separation of rock strata will occur first; thus, the separation cracks will appear first. In general, the gas flow and concentration in borehole extraction will be significantly higher than before after the emergence of separation cracks. With the further excavation of the working face, after the large-scale collapse of the overlying strata, the fracture cracks are formed at both ends of the open cut hole and the working face. With the further increase of the excavation distance, the cracks in the upper central area of the goaf are gradually compacted, and the separation cracks begin to evolve upward. These fractures are interconnected and gradually form fracture channels, resulting in the continuous inflow of free gas from the adjacent layer and surrounding rock into the goaf through this channel, resulting in the gas concentration overrun in the working face.

In order to analyze and study the overlying strata fracture evolution law, the fracture evolution diagram of working face advancing to 30 m, 50 m, 80 m, and 110 m is selected for analysis.

FIGURE 2: Numerical calculation model.

(1) When the working face advances 30 m, it can be seen from Figure 3 that the immediate roof reaches the bearing limit and begins to collapse due to the excavation work. When the working face is pressed for the first time, the stress of the rock strata is released, and under the action of the dead weight, bending and sinking occur, and the main roof cracks begin to develop. A small amount of delamination fracture appears in the overlying strata and the disturbed coal seam 8#. Broken fissures are formed at both ends of the working face and the open-off cut, and the delamination fracture in the overlying strata shows a parallel distribution. However, the evolution of the fissures has just begun, and the penetrating fissures have not yet occurred.

(2) When the working face advances 50 m, it can be seen from Figure 4 that the collapse range of the immediate roof and the main roof increases obviously, and the immediate roof has collapsed, the main roof is fractured, and the working face is under periodic weighting. The upper coal seam 8# is deformed, and the delamination fracture continues to expand upward. The key layer fracture is increasing. The rock strata near the open-off cut side and the working face side are supported by the coal wall to form a shear
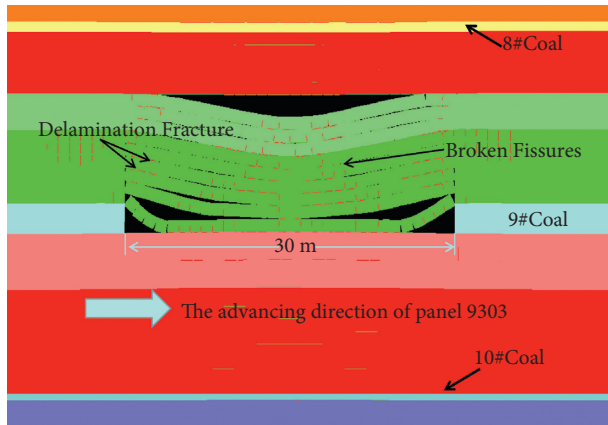
FIGURE 3: Evolution diagram of overlying strata fracture when working face advances to 30 m.
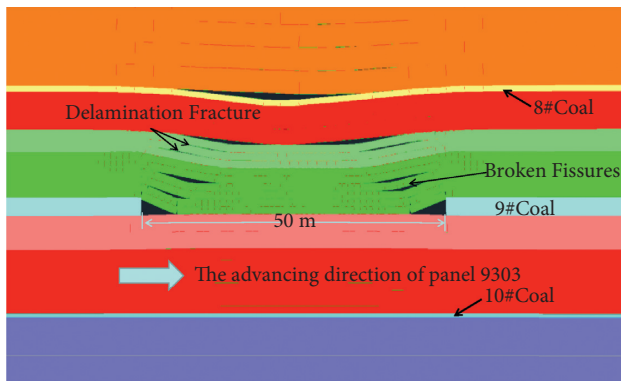
FIGURE 4: Evolution diagram of overlying strata fracture when working face advances to 50 m.

effect on the upper part, forming a shear failure and then forming a broken fissure.

(3) When the working face advances 80 m, it can be seen from Figure 5 that the roof fracture further expands to the overlying strata, and the overlying rock fracture area gradually expands. The delamination fracture and broken fissures continue to penetrate, and the key layer fracture develops well. The compaction area gradually forms in the middle of the overlying strata.

(4) When the working face advances 110 m, it can be seen from Figure 6 that the delamination fracture begins to develop laterally, and the fracture in the middle of the goaf gradually disappears. The delamination fracture at the top of the fracture field is gradually replaced by the broken fracture at the bottom. With the continuous advancement of the working face, after 110 m mining in the working face, the fracture distribution form and scope of the overlying strata are gradually stable in the vertical direction. In the horizontal direction, the development of overlying rock fractures moves forward synchronously with the mining of working face, but

does not continue to extend upward in the advancing direction. At this time, the fracture of overlying strata develops completely.

In summary, combined with the distribution of the fracture strengthening area and the compaction area of the overlying strata, the fracture strengthening area of the roof of the goaf is the main accumulation area of the pressure relief gas in the upper coal seam 8#. The gas content is high and the concentration is large, which is the best choice for the hole arrangement layer of the drainage borehole. Through the simulation results when the working face is excavated to 110 m, it can be obtained that the best fracture development of the overlying strata is with the height of 12.69 m.

The above empirical formula calculation and numerical simulation results show that when the working face advances to 110 m, the working face reaches full mining, the height of the "three zone" of the overlying strata is basically stable, and the maximum fracture zone is 12.69 m. Therefore, the high directional long borehole should be arranged in the position of about 12 m of the coal seam roof.

3.3.3. Mining Fracture Height by Field Test. The borehole peeping method has the advantages of intuitive and convenient, which is widely used in coal mines to detect the geological structure of surrounding rock and the development of fractures [24, 25]. This borehole peeping adopts the intrinsically safe borehole peeper for mining. The minimum diameter of the peeping borehole is 25 mm, and the length of the observable borehole is 30 m. The working principle is to use the probe to convert light into electronic signals, and the signal is transmitted to the image receiver through the cable, so as to observe, record, and store the rock mass structure image in the borehole [26, 27].

This study mainly wants to obtain the fracture evolution height of roof strata affected by mining in panel 9303 during mining, so as to verify the rationality of numerical simulation and empirical formula calculation [28]. When arranging the peep boreholes test points, considering that a large amount of dust will be generated during the drilling construction, the test points are selected in the return airway. Combined with the actual position and advancing speed of the working face, two boreholes are constructed at 50 m, 100 m, and 150 m away from the open-off cut as the test points of peep boreholes. The layout of the observation borehole is shown in Figure 7, two boreholes are in one group, and the plane surface of each group is shown in Figure 8. The borehole design of each group is the same. According to the actual situation of Anshun Mine, the vertical height of the final borehole position is determined to be 18 m.

In order to analyze the development of fracture at different heights, so as to determine the fracture zone of the overlying strata on the roof, the borehole images of the same borehole with the advance of the working face in different periods and depths are intercepted, as shown in Figures 9 and 10.
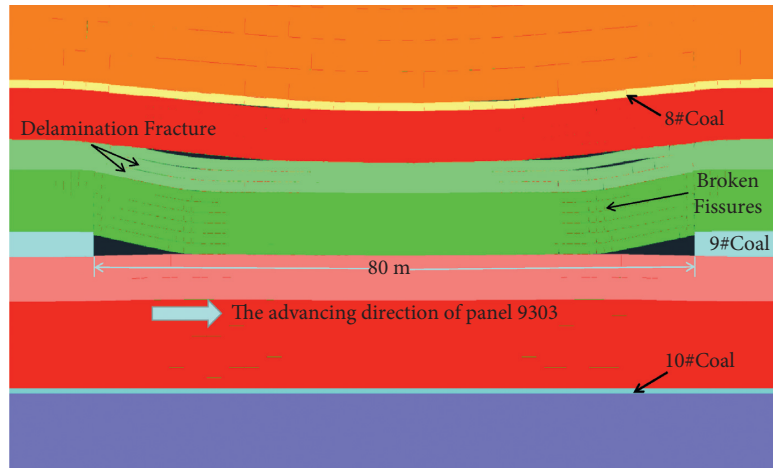
FIGURE 5: Evolution diagram of overlying strata fracture when working face advances to 80 m.
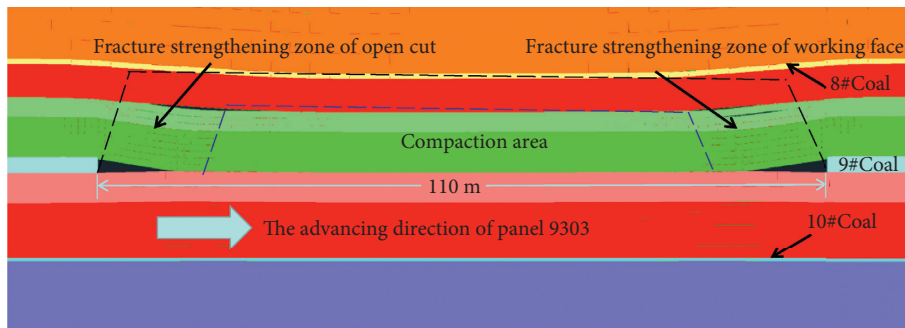
FIGURE 6: Distribution of fracture strengthening zone and compaction zone in overlying strata after stable fracture development.
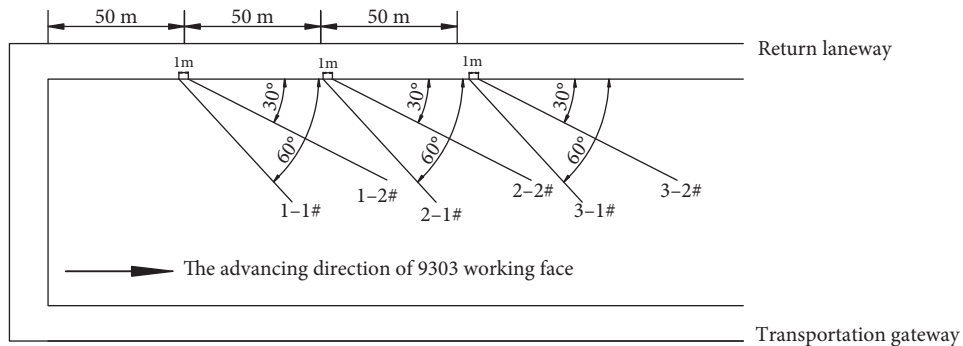
FIGURE 7: Peeping borehole layout schematic diagram.
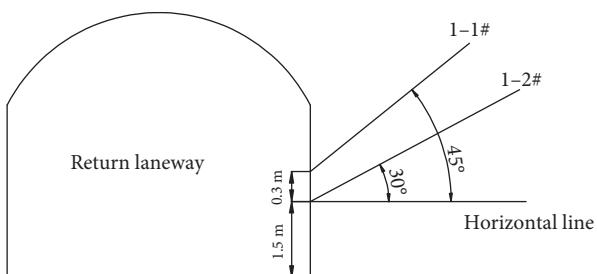
FIGURE 8: Peeping hole layout plane diagram.

From Figures 9 and 10, it can be seen that, from the opening up into the fracture zone, the fracture is more developed, the hole wall is broken until 10 m, and then to the upper rock layer is more complete, but at the end hole height of 15 m, there is a more broken section, which may be broken again after mining stress compression shear failure. The upper hole wall is basically intact, only a few places have slight damage. Therefore, the borehole observation results show that the height of water flowing fractured zone is not more than 15 m.
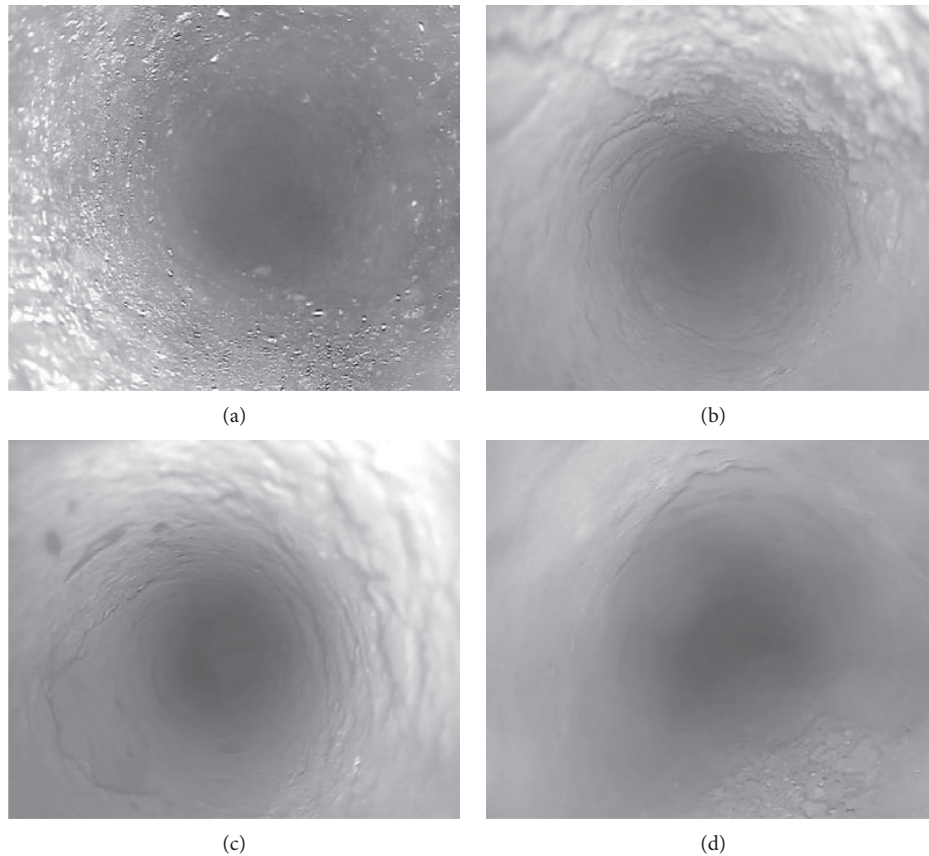
FIGURE 9: Drilling peep at different depths of 1-2# observation hole when working face advances to 50 m. (a) Final hole height 2 m. (b) Final hole height 6 m. (c) Final hole height 10 m. (d) Final hole height 15 m.

In summary, according to the same drilling hole in different hole depth peep, the analysis found that the fractures are mainly produced in the range of 6 m to 15 m above the roof, and the range changes with the advance of the working face. Through the analysis of images with different advancing distances and different borehole depths, it is found that when the working face advances to 100 m, according to the peep images of 3-1# and 3-2# two boreholes, the fracture development situation shown by the images of 2-2# boreholes is similar. It can be concluded that the fracture development height gradually tends to be stable. Fracture zone range is within 6–15 m.

4. Parameter Design of Long Height Directional Drilling

Comprehensively considering the results of empirical formula calculation and numerical simulation, and according to the field measurement verification, it can be seen that the hole arrangement layer of gas directional drilling in goaf of panel 9303 is selected at 12 m above coal seam 9#. Due to the first use of directional drilling rig in this mine, in order to simplify the construction technology, the directional high drilling design adopts single-hole parallel arrangement and does not open branch holes.

In order to verify the above theoretical research results, the directional drilling rig drilling site is constructed in the lower side of tailentry 9303 (the drilling site position is shown in Figure 11). The drilling site specification is wide × deep × high = 10 × 5 × 3 m. The opening position is located at 0.5–1 m of the coal seam roof and the opening spacing is 0.5–0.8 m. The design inclination of the opening section is 10–14°. After drilling the sandstone on the roof of coal seam 9#, the drilling direction is adjusted until the drilling reaches the predetermined position: 12 m above coal seam 9# (as shown in Figure 12), and the final hole spacing is 7 m. The parameters for five specific boreholes are as follows:

(1) Design parameters of 1-1 borehole: opening angle is 14°, opening azimuth is 331.9°, opening height is 0.3 m above coal seam roof, final hole height is 12 m above coal seam, and final design hole depth is 325 m. The final hole is 8 m away from the roadway side.

(2) Design parameters of 1-2 borehole: opening angle is 14°, opening azimuth is 328.9°, opening height is 0.3 m above coal seam roof, final hole height is 12 m above coal seam, and final design hole depth is 335 m. The final hole is 15 m away from the roadway side.

(3) Design parameters of 1–3 borehole: opening angle is 14°, opening azimuth is 325.9°, opening height is 0.3 m above coal seam roof, final hole height is 12 m

(a)

(b)

(c)

(d)
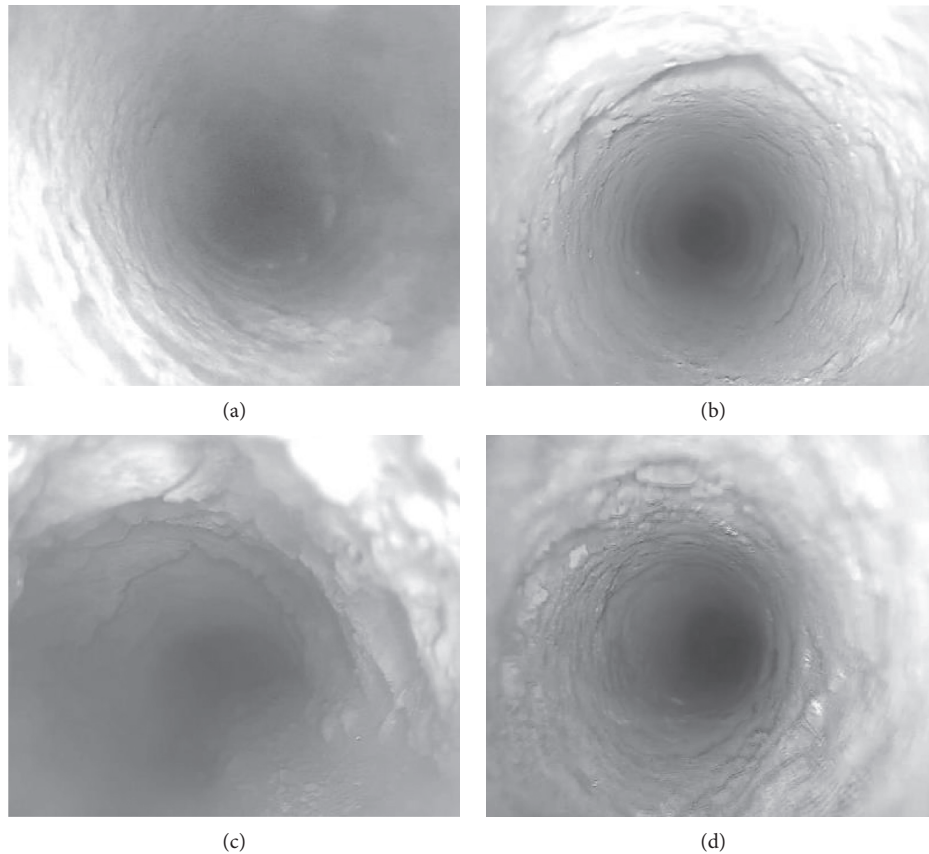
FIGURE 10: Drilling peep at different depths of 2-2# observation hole when working face advances to 100 m. (a) Final hole height 2 m. (b) Final hole height 6 m. (c) Final hole height 10 m. (d) Final hole height 15 m.

above coal seam, and final design hole depth is 335 m. The final hole is 22 m away from the roadway side.

(4) Design parameters of 1–4 borehole: opening angle is 14°, opening azimuth is 322.9°, opening height is 0.3 m above coal seam roof, final hole height is 12 m above coal seam, and final design hole depth is 335 m. The final hole is 29 m away from the roadway side.

(5) Design parameters of 1–5 borehole: opening angle is 14°, opening azimuth is 319.9°, opening height is 0.3 m above coal seam roof, final hole height is 12 m above coal seam, and final design hole depth is 335 m. The final hole is 39 m away from the roadway side.

5. Extraction Effect Analysis

During the mining of panel 9303, the drainage effect of five high directional boreholes constructed by directional drilling field is significant. Gas drainage is shown in Figure 10. The extraction flow and gas concentration of five boreholes at different advancing distances were counted (as shown in Figure 13). When the mining face is 0~30 m, the gas concentration of borehole extraction increases significantly, and the pure gas flow rate shows a rising trend to 5.5 m^3/min. At

this stage, panel 9303 overlying strata has begun to form cracks due to the mining influence, and with the continuous development of cracks, drainage concentration and drainage gas flow are also rising. Subsequently, when the working face advances from 30 m to 110 m, the concentration of gas drainage and the pure flow of gas drainage gradually increase. Since the overlying strata activities of the stope are continuously intensified, this causes disturbance to the upper coal seam 8# and makes the gas in the coal seam 8# continue to flow downward through the intertwined separated fractures and broken fractures. When the working face advances to 30 m, the first weighting of the working face, the expansion deformation of the coal seam 8#, and the gas pressure relief occur. When the working face advances to 50 m, periodic weighting occurs. Before the periodic weighting, the borehole drainage flow and drainage concentration have a significant downward trend. After the periodic weighting, the borehole drainage concentration and drainage flow have a significant upward trend and then tend to be stable until the next periodic weighting. Subsequently, when the working face advances to 110 m, the overall drainage effect of the borehole tends to be stable, entering the stage of efficient and lasting stable drainage. The drainage concentration reaches about 43%, and the maximum pure gas flow rate reaches 8.5 m^3/min.
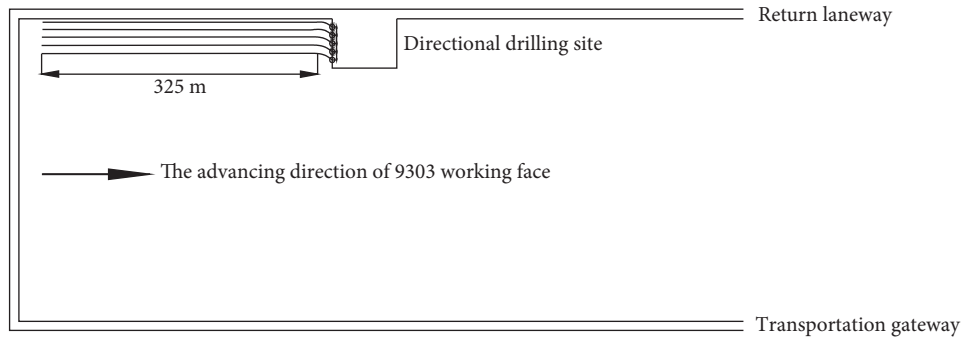
FIGURE 11: Indication diagram of directional long drilling field layout.
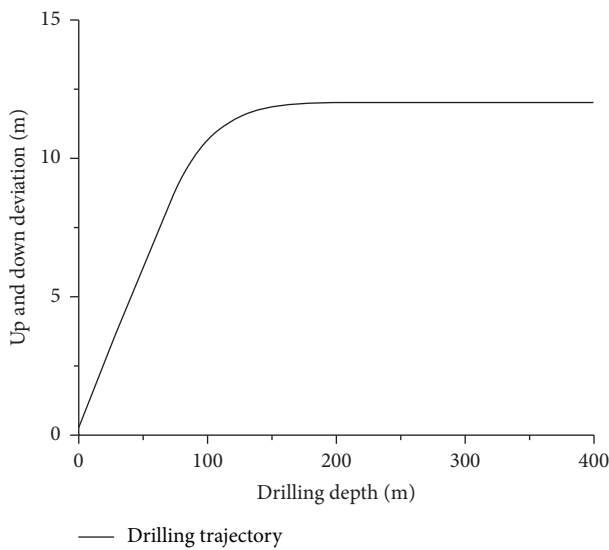
FIGURE 12: Design plane surface of directional drilling in return airway.
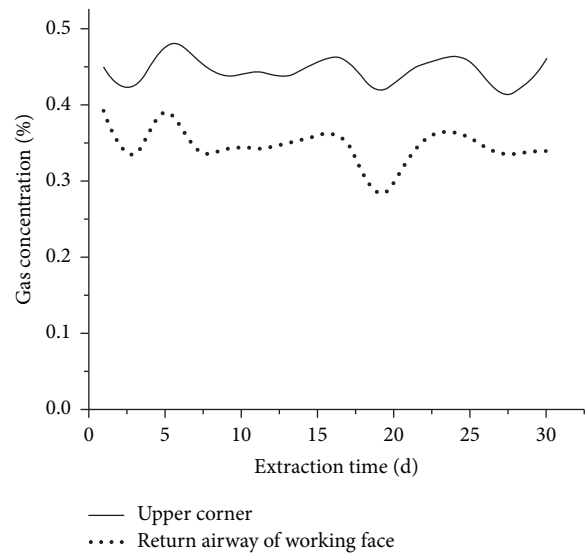
FIGURE 14: Gas condition of return airway and upper corner in working face.
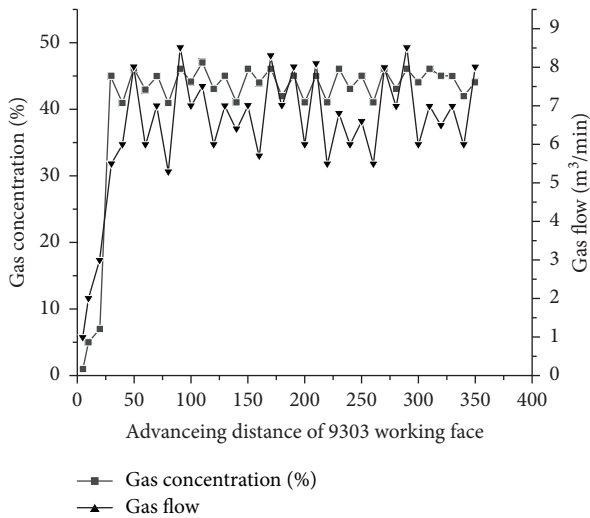
FIGURE 13: Gas extraction by directional long borehole.

During the mining period, the gas concentration in the return airway of the working face was 0.25%–0.4%, and the gas concentration in the upper corner was also lower than 0.5%, as shown in Figure 14. The high directional long borehole can effectively prevent the pressure relief gas of coal from 8# entering the return air flow through the fracture into the goaf, which leads to the problem of gas concentration overrun in the working face. At the same time, compared with the traditional high pumping roadway, the preparation time of the working face is shortened, the production cost is reduced, and the safe and efficient mining of the working face is ensured.

6. Conclusions

(1) Through theoretical analysis and numerical simulation under the real geological parameters condition, it is obtained that during the mining period of panel 9303 in Anshun Coal Mine, when the working face advances to 110 m position, the working face reaches fully mining, and the height range of "three zones" of overlying strata is basically stable. At this time, the development range of fracture zone is 6–12.69 m, and this area is the best high drainage borehole final hole layer. The rationality of the development height of fracture zone obtained by theoretical analysis and numerical simulation is

verified by the method of borehole peeping observation.

(2) By analyzing the field drainage effect of high directional long drilling, after the high directional long drilling in panel 9303 enters the stable and efficient extraction stage, the gas extraction rate is between 40% and 45%, and the pure gas extraction amount is up to $8.5\,\mathrm{m}^3$/min. The results show that the high directional long drilling has the advantages of gas concentration, large extraction amount, and stable flow, and the drilling drainage interception and extraction of adjacent layer gas is effective. It can provide reference for the arrangement of gas drainage boreholes in adjacent working faces and similar geological conditions.

Data Availability

The data used to support the findings of this study are included within the article.

Conflicts of Interest

The authors declare that they have no conflicts of interest regarding the publication of this study.

Acknowledgments

References

[1] D.-Z. Kong, Z.-B. Cheng, and S.-S. Zheng, "Study on the failure mechanism and stability control measures in a large-cutting-height coal mining face with a deep-buried seam," *Bulletin of Engineering Geology and the Environment*, vol. 78, no. 8, pp. 6143–6157, 2019.

[2] D. Z. Kong, S. J. Pu, Z. H. Cheng, G. Wu, and Y. Liu, "Coordinated deformation mechanism of the top coal and filling body of gob-side entry retaining in a fully mechanized caving face," *International Journal of Geomechanics*, vol. 21, no. 4, 2021.

[3] Y. Wang and J. K. Mang, "Study on gas drainage technology of roof directional long borehole replacing roadway with borehole," *Mining Safety & Environmental Protection*, vol. 46, no. 5, pp. 95–98, 2019.

[4] C. Xu, F. Liu, and J. Fang, "Analysis on gas drainage technology and effect of long height directional drilling," *Coal Engineering*, vol. 49, no. 6, pp. 78–81, 2017.

[5] W. P. Cai, J. Liu, D. S. Sun et al., "Research and application of high level borehole gas drainage technology in roof strike," *Journal of Safety Science and Technology*, vol. 9, no. 12, pp. 35–38, 2013.

[6] Z. H. Cheng, Y. Lu, S. L. Su et al., "Study on high efficiency gas drainage mechanism of long height direction drilling in goaf roof," *Coal Science and Technology*, vol. 48, no. 2, pp. 136–142, 2020.

[7] Z. F. Li and X. M. Jin, "Numerical simulation of roof 'three zones' range division by UDEC," *Mining Safety & Environmental Protection*, vol. 42, no. 4, pp. 21–24, 2015.

[8] D. Z. Kong, Y. Xiong, Z. B. Cheng, N. Wang, G. Wu, and Y. Liu, "Stability analysis of coal face based on coal face-support-roof system in steeply inclined coal seam," *Geomechanics and Engineering*, vol. 25, no. 3, pp. 233–243, 2021.

[9] Z. J. Shi, Q. X. Li, and K. Yao, "Development path and key technology analysis of intelligent directional drilling in coal mine," *Journal of China Coal Society*, vol. 45, no. 6, pp. 2217–2224, 2020.

[10] B. Y. Yan, "Study on drilling technology of high directional long borehole," *Coal Science and Technology*, vol. 44, no. 4, pp. 55–58, 2016.

[11] N. P. Yao, J. Zhang, X. Jin, and H. Huang, "Status and development of directional drilling technology in coal mine," *Procedia Engineering*, vol. 73, pp. 289–298, 2014.

[12] Y. M. Li, "Study on gas control in upper corner based on long height directional drilling," *Coal Science and Technology*, vol. 46, no. 1, pp. 215–218, 2018.

[13] G. A. Zhu, B. W. Liu, L. M. Kou et al., "Simulation of working face mining process based on gob compaction effect," *Journal of China University of Mining & Technology*, vol. 48, no. 4, pp. 775–783, 2019.

[14] J. Zhang and J. P. Wang, "High similarity simulation and empirical study of mining overburden three zones," *Journal of Mining and Safety Engineering*, vol. 31, no. 2, pp. 249–254, 2014.

[15] J. G. Zhao, "Construction technology and development trend of high - level directional drilling in coal seam roof," *Coal Science and Technology*, vol. 45, no. 6, pp. 137–141, 2017.

[16] G. H. Chen, Z. Y. Wei, D. F. Liang et al., "Practice of gas drainage by high directional long borehole in close distance coal seam group," *Mining Safety & Environmental Protection*, vol. 46, no. 5, pp. 66–69, 2019.

[17] Q. Wu, S. Q. Zhao, S. N. Dong et al., *Coal Mine Water Prevention Manual*, China Coal Industry Publishing House, Beijing, China, 2013.

[18] F. H. Wang, "Determination method of height of gas caving zone and fracture zone in high borehole drainage," *Coal Technology*, no. 8, pp. 75-76, 2008.

[19] X. G. Zhu, H. C. Xia, and Z. C. Wang, "UDEC numerical simulation of overburden movement in coal seam mining," *Journal of Liaoning Technical University*, vol. 35, no. 12, pp. 1402–1410, 2016.

[20] J. C. Wang and Z. H. Wang, "Stress driving mechanism of crack propagation in top coal in fully mechanized caving mining," *Journal of China Coal Society*, vol. 43, no. 9, pp. 2376–2388, 2018.

[21] P. Yang, "Similar simulation study on mining fracture evolution law of overlying strata in mining field," *Coal Science and Technology*, vol. 42, no. 8, pp. 121–124, 2014.

[22] Y. Xue, J. Liu, P. G. Ranjith, X. Liang, and S. Wang, "Investigation of the influence of gas fracturing on fracturing characteristics of coal mass and gas extraction efficiency based on a multi-physical field model," *Journal of Petroleum Science and Engineering*, vol. 206, Article ID 109018, 2021.

[23] L. Zhu, F. Dang, Y. Xue, K. Jiao, and W. Ding, "Multivariate analysis of effects of microencapsulated phase change materials on mechanical behaviors in light-weight aggregate

concrete," *Journal of Building Engineering*, vol. 42, Article ID 102783, 2021.

[24] Y. W. Peng, Q. X. Qi, Y. G. Wang et al., "Field measurement and application of coal mining fracture," *Chinese Journal of Rock Mechanics and Engineering*, vol. 29, no. S2, pp. 4188–4193, 2010.

[25] B. S. Nie, H. Zhang, S. J. Cui et al., "Method and application of extracting borehole information from forward - looking borehole peeping video," *Journal of China Coal Society*, vol. 41, no. 5, pp. 1316–1322, 2016.

[26] W. J. Yu and K. Li, "Deformation mechanism and control technology of surrounding rock in the deep-buried large-span chamber," *Geofluids*, vol. 2020, Article ID 8881319, 22 pages, 2020.

[27] H. Sun, G. C. Li, Y. H. Wei et al., "Application of geophysical prospecting combined with borehole peeping in rock mass structure detection," *Safety In Coal Mines*, vol. 45, no. 4, pp. 141–144, 2014.

[28] W. J. Yu, K. Li, Z. Liu, B. An, P. Wang, and H. Wu, "Mechanical characteristics and deformation control of surrounding rock in weakly cemented siltstone," *Environmental Earth Sciences*, vol. 80, p. 337, 2021.

Research Article

Control of the Internal and External Staggered Distance of Coal Mining Face to the Water-Conducting Fissures in the Overlying Strata of the Near Coal

Zhiyuan Jin [1] **and Tao Peng** [1,2]

[1]*School of Mining Engineering, Guizhou Institute of Technology, Guiyang, Guizhou 550003, China*
[2]*School of Resources & Safety Engineering, Central South University, Changsha, Hunan 410083, China*

Correspondence should be addressed to Tao Peng; pxt198712@126.com

In Northwest China, rainfall is low, water resources are scarce, and the ecological environment is fragile. For shallow-buried and close-spaced coal seams with a thickness of upper coal bed >60~70 m, the water-conducting fissures of the overlying rock will not penetrate the water-isolating layer after the upper coal seam is mined; the internal and external gap angles of the water-conducting fissures are not generated from the water-isolating layer. We set out to explore the critical internal and external dislocations for the second significant development of water-conducting fissures in the overlying rock after coal mining under control. A calculation model for the critical internal and external staggered distances of coal mining face in shallow-buried and close-spaced coal seams is established, the calculation formula is given, and the calculation formula for the critical seam mining ratio under the condition of internal staggered mining mode is given. Numerical simulation performed by UDEC methods: taking the overburden strata in the shallow-buried and close-spaced coal seam mining area of Shigetai Coal Mine as a prototype, it was verified that the critical internal and external offsets of the coal mining face in shallow-buried and close-spaced coal seams have a significant effect on the overlying water flow cracks in the mining of the lower coal seam. For the feasibility of developmental control, according to the engineering geological conditions of Shigetai, through the calculation method of external staggered distance, it is concluded that the distance of the open cut of the lower coal face and the upper coal face is only 21~27 m, which is much smaller than the water barrier. It does not produce the critical distance of the water-conducting cracks. Therefore, in the process of mining the lower coal seam, the water-proof layer will produce water-conducting cracks, lose its water-proof performance, and cause water loss. This is also the cause of the water inrush accident in Shigetai Coal Mine.

1. Introduction

Taking the geological parameters that affect the development of water-conducting fissures in the overlying rock as the basic conditions, starting with the mining parameters, find the control methods. There is a soft rock water barrier in the shallow-buried and close-spaced Shendong coal mining area. Once the water barrier is stretched and damaged and eventually water-conducting cracks are formed, water resources will be lost. Looking for a control method for the development of water-conducting fissures in the overlying rock in the repeated disturbance zone is to find a control method that does not produce water-conducting fissures in the water barrier [1–6].

For the first type of shallow-buried and close-spaced coal seams in Northwest China (the thickness of the upper seam's bedrock <50–60 m), when the full-thickness long-wall mining method is adopted to mine the coal seam, the overburden water-conducting fissures will penetrate the ground surface, causing water resource loss. For such shallow-buried and close-spaced coal seams, even if the full-mining and full-filling coal mining method is adopted in the mining of the lower coal seam, the loss of water resources cannot be prevented, unless the overburden water-

conducting fissures are grouted and blocked. For the second type of shallow-buried and close-spaced coal seams (the thickness of the upper seam's bedrock >60~70 m), when the full-thickness long-wall mining method is adopted to mine the coal seam, after the upper coal seam is mined, due to the expansion of the water-resistant layer existence, the water-conducting cracks in the overlying rock will not penetrate the water-impermeable layer in the end. When mining the lower coal seam, whether the water-conducting cracks in the overlying rock will penetrate the water-resistant layer is mainly related to the control method adopted. Therefore, exploring the control methods for the development of water-transmitting fissures in the overlying rock in shallow-buried and close-spaced coal seams will be carried out for the second type of shallow-buried and close-spaced coal seams.

Starting from the mining layout (the inner and outer staggered layouts of the mining face of the upper and lower coal seams), the effective way to is find the second significant development of the overlying water-conducting fissures in the smallest area after the mining of the lower coal seam.

2. The Critical Inner and Outer Distances of the Water Barrier That Do Not Produce Water-Conducting Cracks

Coal mining will cause overlying strata to move. Under sufficient mining conditions, the surface above the mined-out area will sink to form a sinking basin. In the main section of the surface subsidence basin, the angle between the line from the edge point to the boundary point of the corresponding mined-out area and the horizontal line is called the strata movement boundary angle. The center of the sinking basin is a flat, no-deformation zone, and the angle between the line from the edge point to the boundary point of the corresponding mined-out area and the horizontal line is called the full-mining angle of rock formation. For shallow-buried and close-spaced coal seams, the boundary angles and full-mining angles of the upper and lower coal seams during mining can be used to determine the critical inner and outer displacements of the aquifer without water-conducting cracks.

2.1. Internal Staggered Layout.
When the upper and lower coal mining face adopts the internal staggered layout, if the development of the overlying water-conducting fissures near the upper coal seam's mining boundary can be maintained at the original stable state and no longer continue to develop after the lower coal seam is mined, then this type of internal error distance under the conditions is the critical internal error distance. After the coal seam is mined, the overlying rock layer is broken, forming a rock layer breaking line. The angle between the rock fracture line and the horizontal line is the rock fracture angle, generally 60–78°. The fracture angle of the rock formation is often greater than the full-mining angle of the rock formation movement [7].

When adopting the internal staggered layout, if the moving edge point of the water barrier (the intersection of the boundary line of the rock formation and the top surface

of the water barrier) during the mining of the lower coal seam is located in the no-deformation zone of the sinking basin of the water barrier after the mining of the upper coal seam, then, during the mining process of the lower coal seam, the secondary development of water-conducting fissures in the overlying rock on the side of the cut-off cut in the upper coal seam will not occur. When mining shallow-buried and close-spaced coal seams, the critical internal staggered layout of the upper and lower coal mining faces is shown in Figure 1.

According to the calculation model of the critical internal offset of the coal mining face in shallow-buried and close-spaced coal seams (as shown in Figure 2), the calculation formula of the critical internal offset $L_{\ln c}$ is

$$L_{\ln c} = \left(h_{xf} - w_{sg}\right)\cot \psi_s + \left(h_{xf} + h_{cj} - w_{sg}\right)\cot \delta_x, \quad (1)$$

where h_{xf} is the total thickness of the rock above the upper coal seam and below the aquifer, m; ψ_s is the full-mining angle after the upper coal seam is mined; δ_x is stratum movement boundary angle after mining of the lower coal seam; w_{sg} is the maximum subsidence value of the aquifer when the upper coal seam is mined, m; h_{cj} is the thickness of interbedded rock in shallow-buried and close-spaced coal seams, m.

2.2. External Staggered Distance L_{lwc}.
Figure 3 shows the overall external staggered layout of the coal face under the shallow-buried and close-spaced coal seam. When the shallow-buried and short-distance coal seam adopts the external staggered layout, if the boundary point of the no-deformation zone of the sinking basin of the lower coal seam is located at the boundary point of the water-resisting layer movement during the mining of the upper coal seam (the boundary line of the rock layer movement and the water barrier except for the intersection point of the top surface of the seam), the mining of the lower coal seam will not cause the secondary development of water-conducting fissures in the upper coal seam on the side of the cut.

The calculation model of the critical distance for shallow-buried and close-spaced coal seams is shown in Figure 4. The calculation formula for the critical distance is as follows:

$$L_{lwc} = \left(h_{cj} + M_s + h_{xf}\right)\cot \psi_x + h_{xf} \cot \delta_s, \quad (2)$$

where h_{cj} is the thickness of interlayer rock, m; M_s is the upper seam's thickness, m; ψ_x is the full-mining angle when mining the lower coal seam; and δ_s is stratum movement boundary angle during upper coal mining.

The seam mining ratio is proposed for the mining of close-spaced coal seams, and its meaning is the ratio of the thickness of the interlayer rock layer to the mining height of the lower coal seam, η; that is, $\eta = h_{cj}/M_x$.

When the external staggered layout is adopted, the development of water-transmitting fissures in the overlying rock during the mining process of the shallow-buried and close-spaced coal seam can be regarded as a single coal seam (lower coal seam) mining for research. In some cases, due to the restriction of the production geological conditions, the
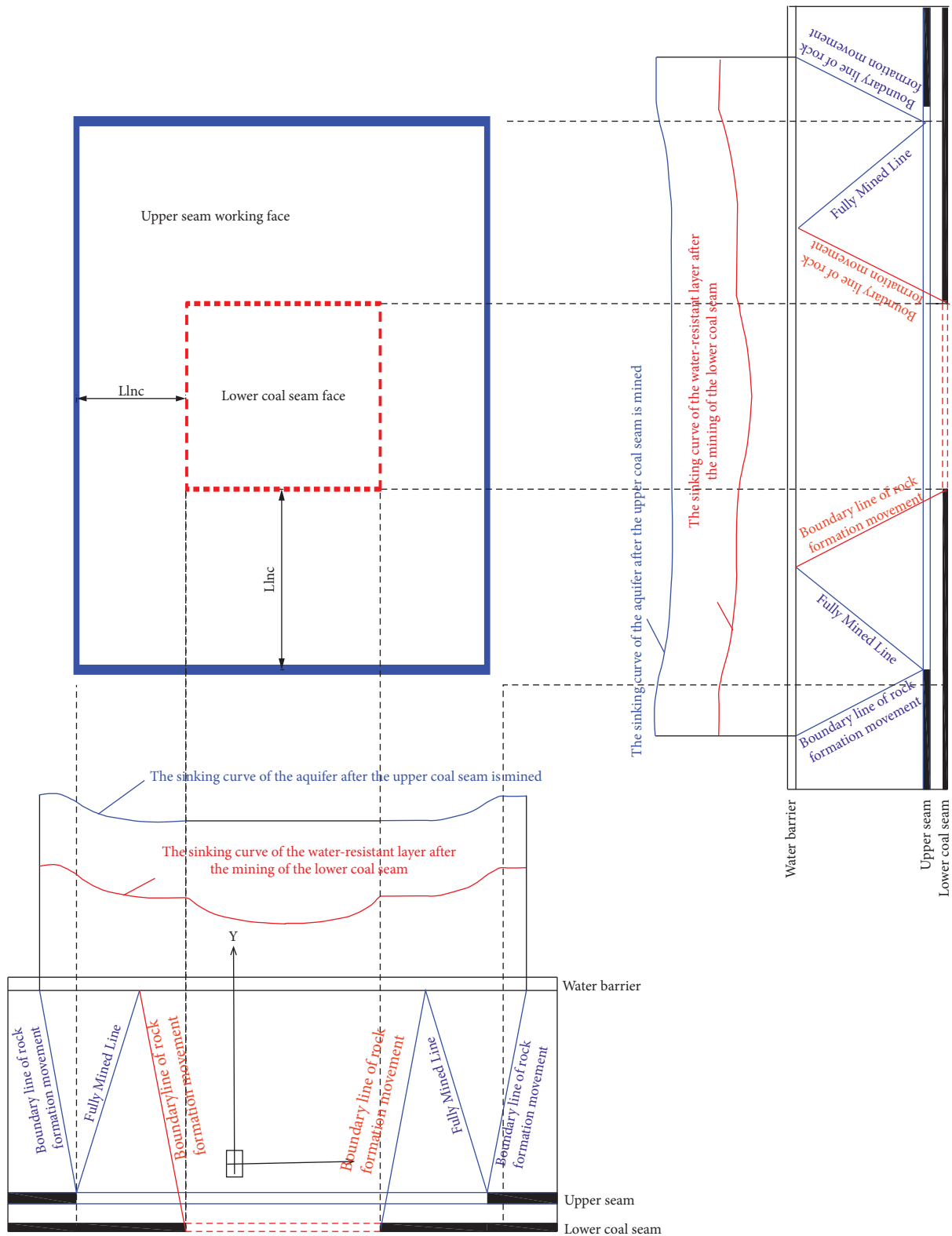
FIGURE 1: Internal displacement of the whole working face in the lower coal seam of shallow-buried short-distance coal seams.

internal staggered layout is required. Then, it is necessary to study the critical stratum mining ratio that does not produce water-conducting cracks in the water barrier.

2.2.1. The Minimum Value of the Maximum Subsidence Value When the Water Barrier Does Not Produce Water-Conducting Cracks. According to existing research results,
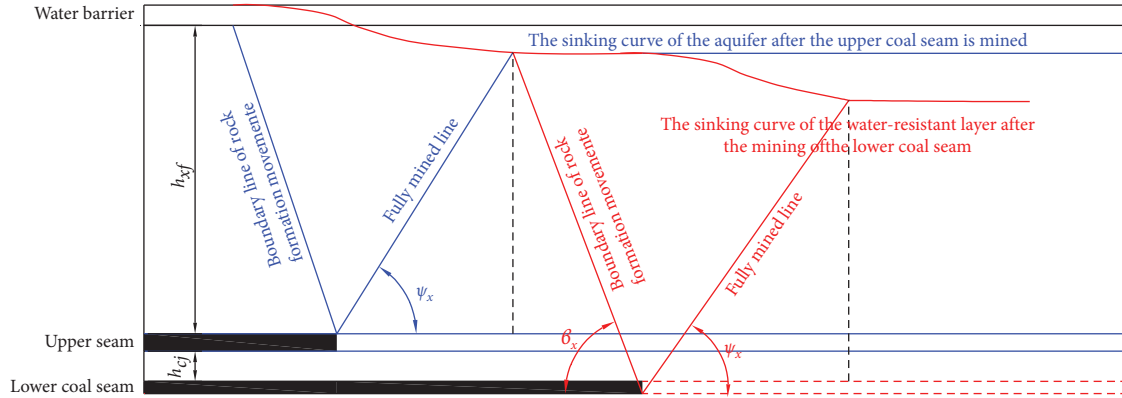
FIGURE 2: Calculating model of internal dislocation of the whole working face in the lower coal seam of shallow-buried short-distance coal seams.

the relationship between the crack width of the aquifer and its maximum subsidence value is

$$d = 0.9273 \ln w + 0.7463, \tag{3}$$

where d is the water barrier crack width; w is the maximum subsidence value when the water barrier does not produce water-conducting cracks.

The nonhydrophilic water barrier material measured by the lateral restraint expansion experiment is $L_{pz} = 0.605$ mm. To ensure that water resources are not lost, $d_{dx} \geq 0$; that is, $d > 2 \ L_{pz} = 1.210$ mm. Substituting formula (3), we have $w_{lj} \leq 1.649$ m.

Therefore, $w_{lj} = 1.649$ m is the minimum maximum subsidence value when the water barrier does not produce water-conducting cracks. When it is $w_{lj} > 1.649$ m, water-conducting fissures will occur in the water barrier.

2.2.2. Critical Layer Mining Ratio Where the Water Barrier Does Not Produce Water-Conducting Cracks η_{lj}. Shallow-buried and close-spaced coal seams adopt internal staggered arrangement. When the internal staggered distance is greater than the critical inner staggered distance, the area where the overlying strata moved and the cracks developed due to the mining of the lower coal seam is located in the no-deformation zone of the sinking basin after the upper coal seam is mined; that is to say, before the mining of the lower coal seam, the rock layers in the repeated disturbance zone were in a horizontal state. The hard rock layers were broken into blocks and squeezed and closed horizontally, while the soft rock water barrier did not undergo horizontal tensile deformation and did not produce water-conducting cracks.

Whether there are water-conducting cracks in the water barrier is mainly related to the height of the effective sinking space below, in addition to its physical and mechanical properties and hydraulic properties. The factors that determine the height of the effective sinking space are the thickness of the underlying rock layer and its residual swelling coefficient. According to existing research results, for close-spaced coal seams, after the lower coal seam is mined, the residual breaking expansion coefficient of the rock strata in the upper coal seam mining caving zone will

become smaller, but the magnitude is not large, and the rock strata in the upper coal seam mining fracture zone will enter the caving zone, and the residual breaking expansion coefficient will increase, but the amplitude is not very large. On the whole, after the lower coal seam is mined, the residual breaking expansion coefficient of the overlying rock of the upper coal seam can be regarded as unchanged, and the shallow-buried and close-spaced coal seams also conform to this law. Therefore, for shallow-buried and close-spaced coal seams, when the internal fault distance is greater than the critical internal fault distance, the lower coal seam can be regarded as a single coal seam mining, and the thickness of the overlying rock layer is the layer spacing. Under the condition of the internal staggered arrangement, the critical condition for the water barrier not to produce water-conducting cracks is

$$w_{lj} \geq M_x - h_{cj} \cdot \left(\overline{k_{cc}} - 1 \right) = M_x \left(1 - \eta_{lj} \cdot \left(\overline{k_{cc}} - 1 \right) \right), \tag{4}$$

where $\overline{k_{cc}}$ is the average residual breaking expansion coefficient of the interlayer rock formation.

It is concluded that the critical layer mining ratio for the water barrier without water-conducting cracks is

$$\eta_{lj} = \frac{M_x - w_{lj}}{M_x \cdot \left(\overline{k_{cc}} - 1 \right)}. \tag{5}$$

At the same time, according to formulas (5) and (6), it can also be determined that the reasonable mining height of the lower coal seam when the water-resistant layer does not produce water-conducting cracks is

$$M_{hx} \leq w_{lj} + h_{cj} \cdot \left(\overline{k_{cc}} - 1 \right). \tag{6}$$

3. Numerical Simulation Analysis

Taking the overburden strata in the shallow-buried and close-spaced coal mining area of Shigetai Coal Mine as a prototype, the overburden parameters are shown in Table 1 [8–11].

Using UDEC's stress-seepage coupling system, simulation calculation, and analysis of the development law and seepage characteristics of the internal and external
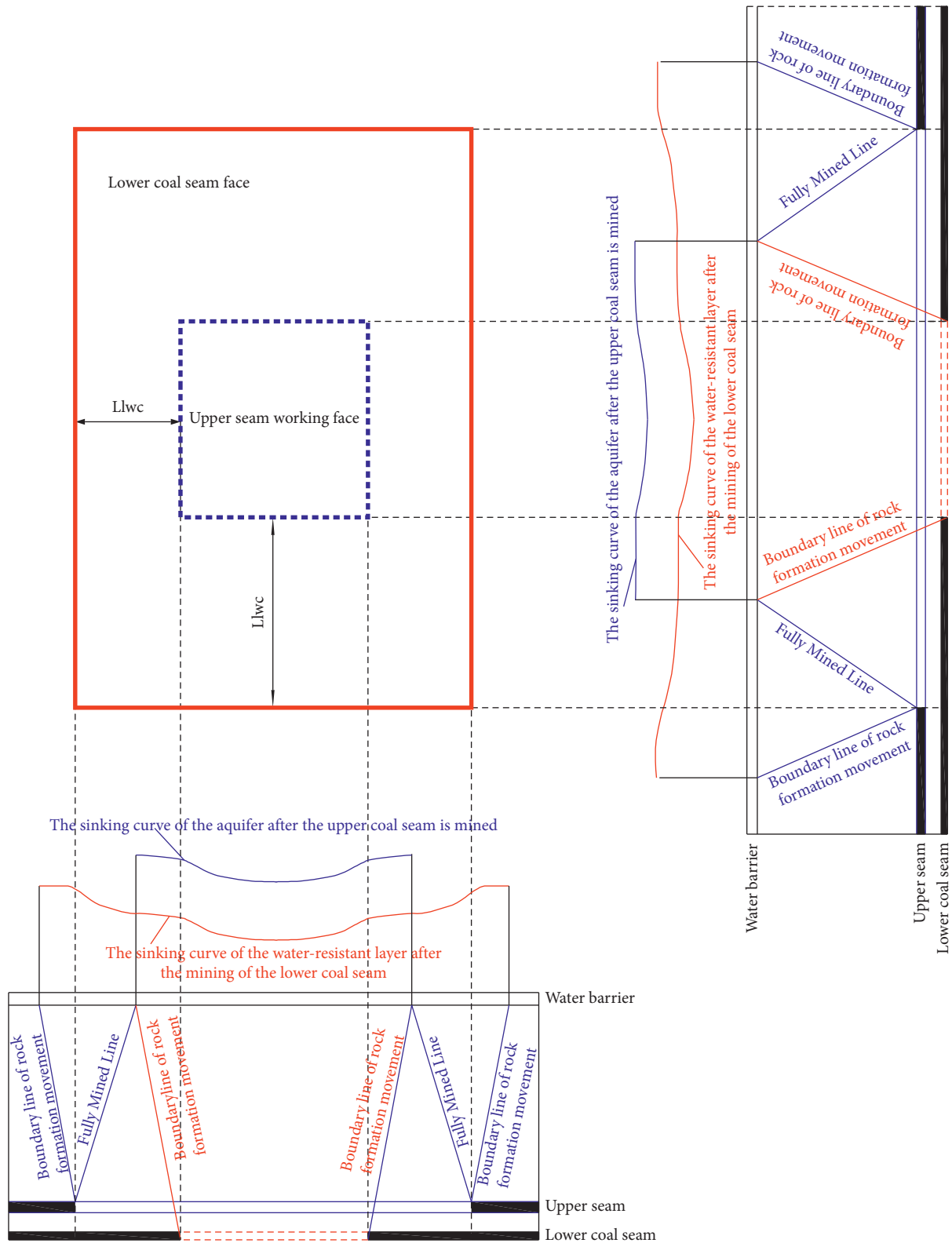
FIGURE 3: Outward displacement of the whole working face in the lower coal seam of shallow-buried short-distance coal seams.

offsets to the overburden seepage fissures during the mining of shallow-buried and close-spaced coal seams, according to the measured physical and mechanical parameters of the overburden, the model parameters are assigned. The rock mechanical parameters are shown in Table 2, and the rock joint parameters are shown in Table 3. The boundary conditions are as follows: the left and right sides and the lower part of the model are
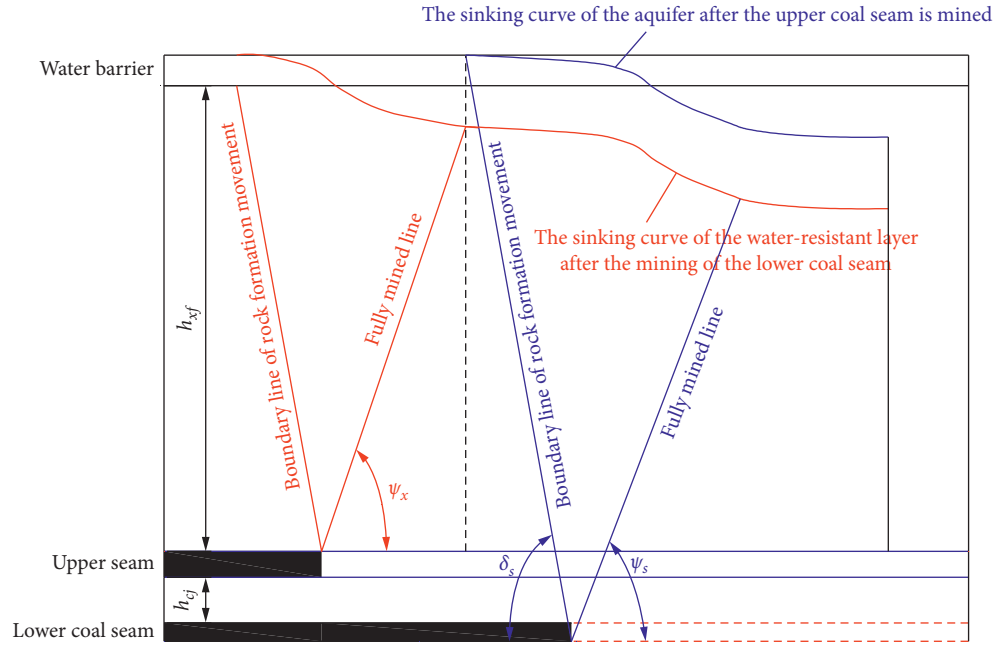
FIGURE 4: The calculation model of outward dislocation of the whole working face in the lower coal seam of shallow-buried short-distance coal seams.

TABLE 1: The overburden parameters.

Serial number	Lithology	Thickness	Remarks
1	Loose layer	5	
2	Loess	6	Water barrier
3	Sandy mudstone	6	
4	Silt sandstone	7	
5	Medium-grained sandstone	3	
6	Fine-grained sandstone	16	Thick hard rock
7	Sandy mudstone	6	
8	Medium-grained sandstone	9	
9	Silt sandstone	7	
10	Coarse-grained sandstone	3	
11	Medium-grained sandstone	10	Basic top
12	Sandy mudstone	5	
13	Upper seam	2.5	
14	Silt sandstone	7	
15	Medium-grained sandstone	14	
16	Coarse-grained sandstone	10	
17	Lower coal seam	3	
18	Fine-grained sandstone	5	

displacement boundaries and nonseepage boundaries. The simulated solid-liquid coupling adopts SET steady flow, and the joint characteristics adopt the default setting (the second type). The initial pore pressure is set as pp = 0.125 MPa.

3.1. The Influence of Internal Staggered Distance on the Water-Conducting Fissures.
Numerical models of different internal error distances are established, and the simulation results are shown in Figure 5.

From the analysis of Figure 5, it can be seen that, with the increase of the internal staggered distance, the secondary development degree of the water-conducting fissures on the side of the cut-off cut in the upper coal seam gradually decreases. When the internal staggered distance is less than 80 m, the mining of the lower coal seam will cause the water-conducting fissures on the side of the open cut to develop twice; when the internal staggered distance is 80 m, the water-conducting fissures on the side of the open cut will not be affected by the mining of the lower coal seam. Without secondary development, it can maintain the original stable

TABLE 2: The mechanical parameters of rock.

Rock formation	Density d (kg·m^{-3})	Bulk modulus k (GPa)	Shear modulus g (MPa)	Cohesion c (MPa)	Internal friction angle f (°)	Tensile strength σ_t (MPa)
Coal seam	1400	2.3	2	1.25	27	0.6
Silt sandstone	2420	30.3	13	9.6	33	6
Coarse-grained sandstone	2480	19	12.1	4.3	32	6
Medium-grained sandstone	2500	37.5	19.5	4.3	33	3.2
Fine-grained sandstone	2510	40.8	20.2	4.3	33	3.2
Sandy mudstone	2410	6.3	6.9	6.7	31.5	2
Loess	1720	20	14.2	3	15	4.3
Loose layer	2200	14	11.5	10	32	2

TABLE 3: The mechanical parameters of the rock joints.

Rock formation	Normal stiffness (MPa)	Tangential stiffness (MPa)	Cohesion (MPa)	Joint penetration factor (Pa^{-1}·s^{-1})	Initial gap (mm)	Residual gap (mm)
Coal seam	1600	1100	0.313	166.7	0.5	0.1
Silt sandstone	7600	5200	0.800	166.7	0.5	0.1
Coarse-grained sandstone	7900	5600	0.688	166.7	0.5	0.1
Medium-grained sandstone	7500	5500	0.712	166.7	0.5	0.1
Fine-grained sandstone	8800	6600	0.690	166.7	0.5	0.1
Sandy mudstone	6400	4500	0.375	101.5	0.5	0.1
Loess	9000	7900	0.311	15	0.1	0.1
Loose layer	2200	1300	0.100	300	3.0	0.1
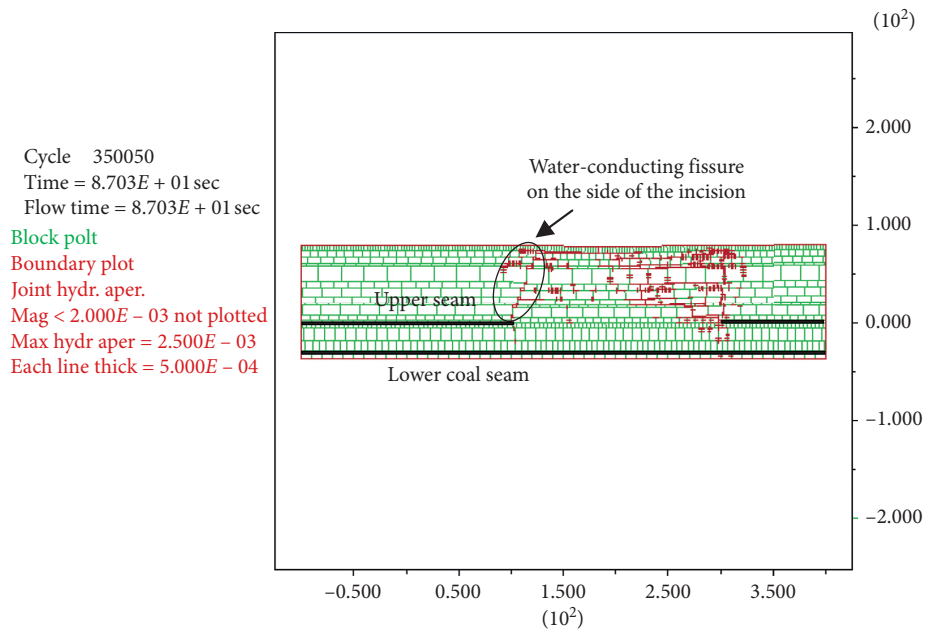
(a)

FIGURE 5: Continued.

(b)

(c)
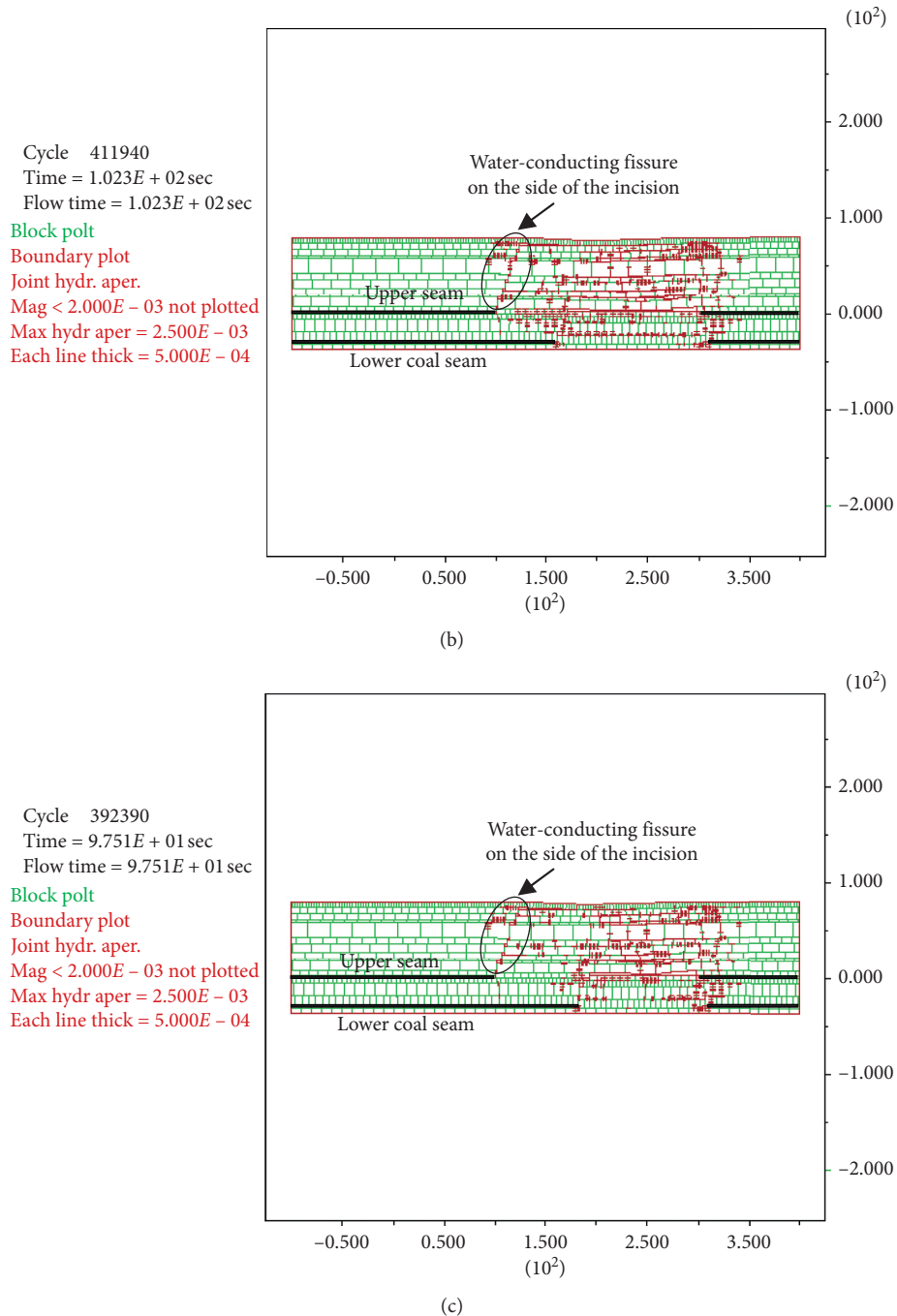
FIGURE 5: Water flowing fractures development characteristics of overburden rock with the different internal dislocation of shallow-buried short-distance coal seams. (a) After the upper seam is mined. (b) Internal staggered distance of 60 m. (c) Internal staggered distance of 80 m.

state after the upper coal seam is mined (before the lower coal seam is mined).

3.2. The Influence of External Staggered Distance on the Water-Conducting Fissures of the Overlying Rock.
Numerical models of different external error distances are established, and the simulation results are shown in Figure 6.

It can be seen from the analysis of Figure 6 that, with the increase of the external staggered distance, the development degree of the overlying rock water-conducting fissures on the side of the cut-off cut in the upper coal seam gradually decreases. When the offset distance is less than 80 m, the mining of the lower coal seam will cause the secondary development of the water-conducting fissures on the open cut side of the upper coal seam; and when the external staggered distance is greater than 90 m, the water-conducting fissures on the open cut side of the upper coal seam will not develop. Affected by the mining of the lower coal seam, new water-conducting fissures are generated in the

(a)

(b)

Figure 6: Continued.

Cycle   433900
Time = 1.077E + 02 sec
Flow time = 1.077E + 02 sec
Block polt
Boundary plot
Joint hydr. aper.
Mag < 2.000E − 03 not plotted
Max hydr aper = 2.500E − 03
Each line thick = 5.000E − 04

Water-conducting fissure on
the side of the incision

Upper seam

Lower coal seam

(c)

Cycle   438601
Time = 1.089E + 02 sec
Flow time = 1.089E + 02 sec
Block polt
Boundary plot
Joint hydr. aper.
Mag < 2.000E − 03 not plotted
Max hydr aper = 2.500E − 03
Each line thick = 5.000E − 04

Water-conducting fissure
on the side of the incision

Upper seam

Lower coal seam
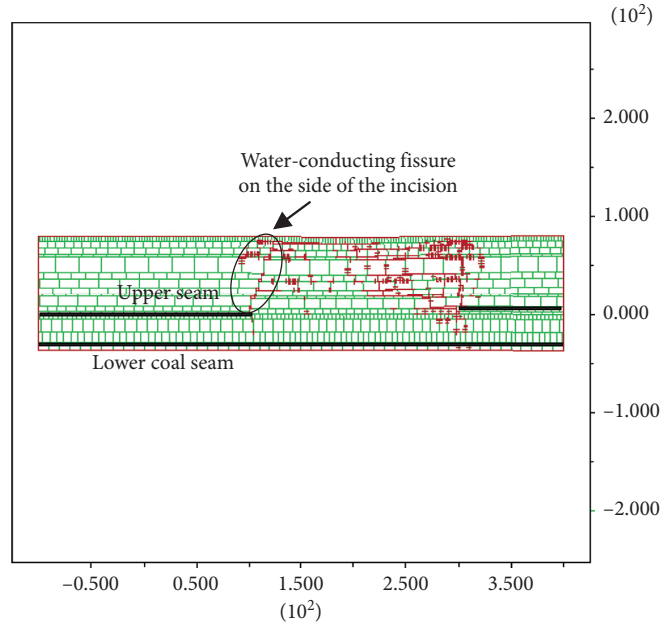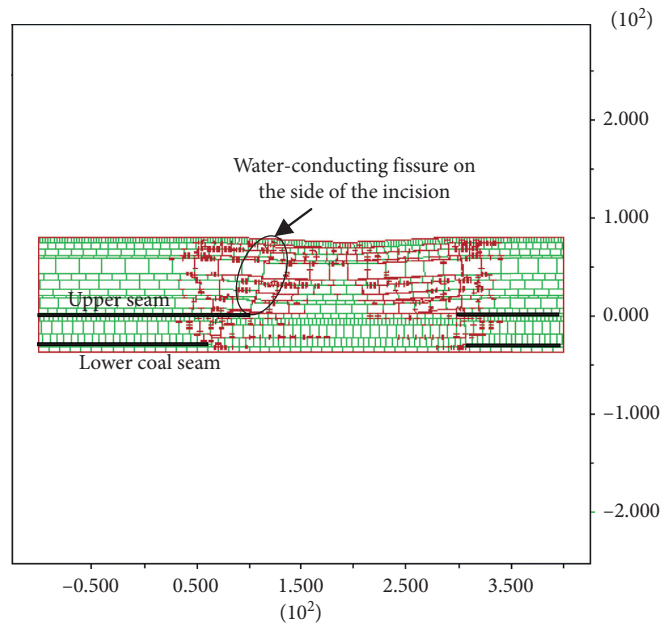
(d)
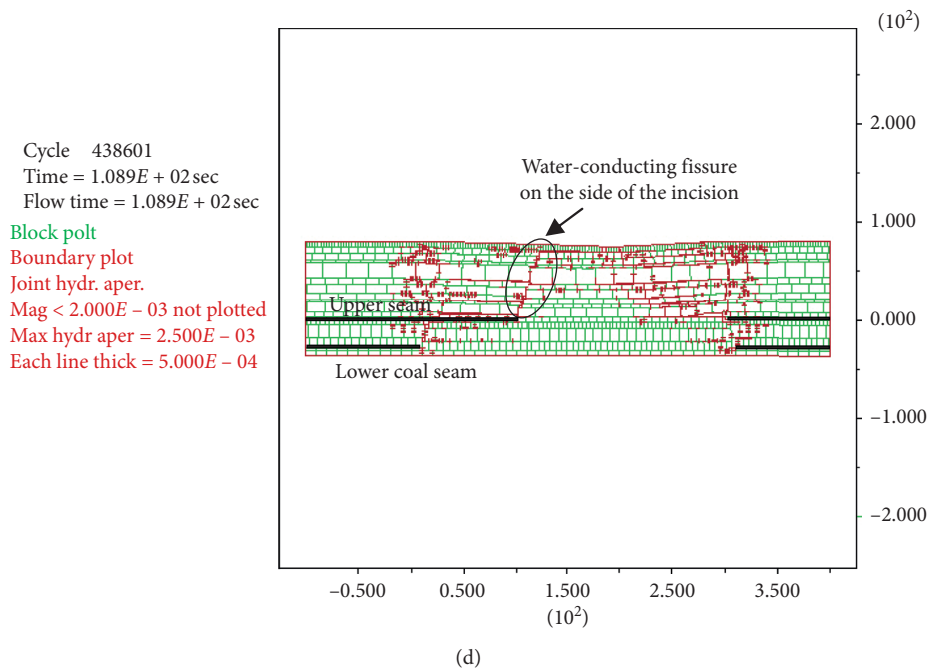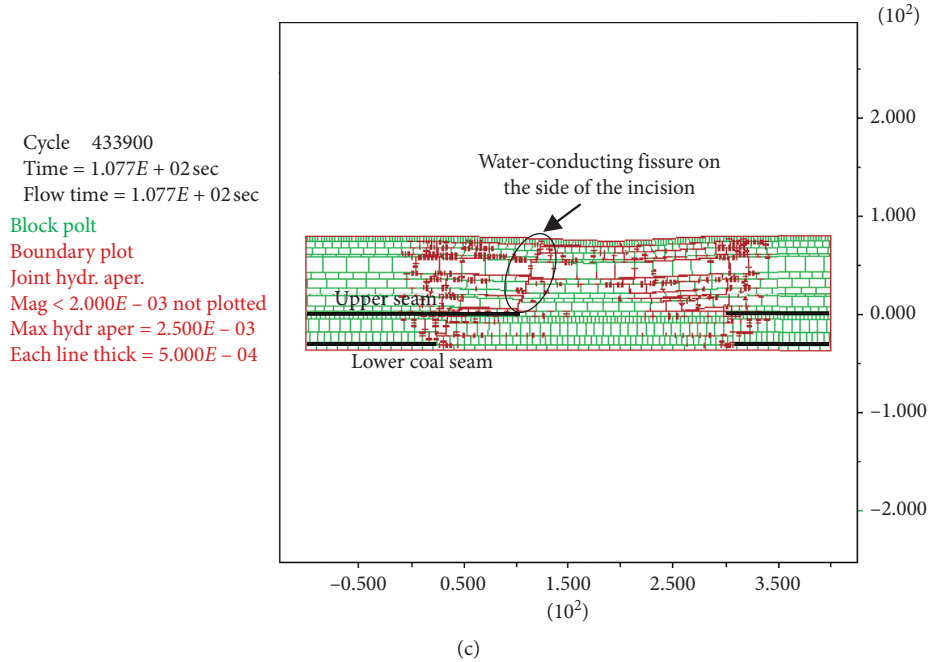
FIGURE 6: Water flowing fractures development characteristics of overburden rock with the different outward dislocation of shallow-buried short-distance coal seams. (a) After the upper seam is mined. (b) External staggered distance of 40 m. (c) External staggered distance of 80 m. (d) External staggered distance of 90 m.

overlying rock near the mining boundary of the lower coal seam.

4. Reverse Verification of Project Examples

At 5:50 in the morning on August 2, 2010, the head of the lower coal seam was advanced by 17.5 m and the tail was advanced by 21.5 m. A roof water gushing accident occurred. The total amount of water gushing was about 47,000 m^3,

causing the equipment in the fully mechanized mining face to be flooded. The location of the water gushing is shown in Figure 7, and the actual photo of the scene is shown in Figure 8 [12].

According to the geological conditions of the water gushing site in Shigetai Coal Mine, the distance between the upper coal seam and the lower coal seam is 2.6 m, and the bedrock thickness of the upper coal seam is 76.37 m. According to the calculation method of the critical external
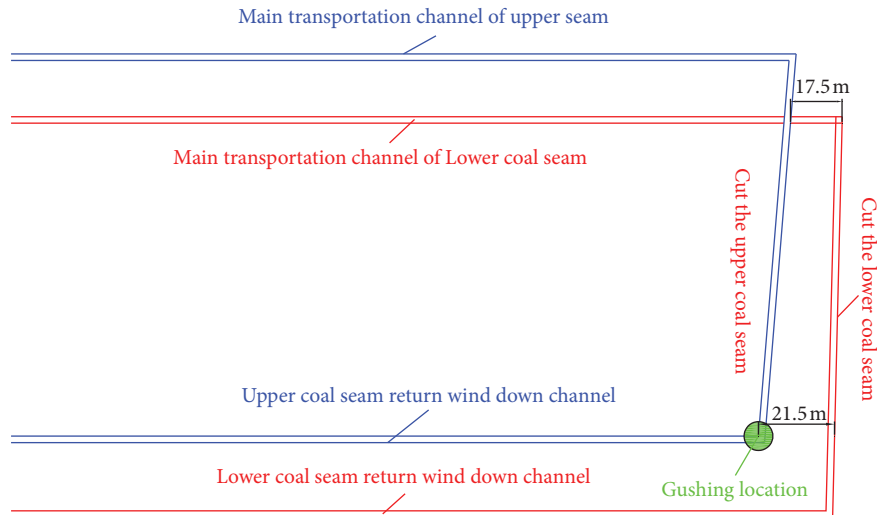
Figure 7: Water gushing position on upper coal seam face.

Figure 8: The actual photo of the scene.

offset, $\psi_s = 60°$, $\delta_x = 73°$, $h_{cj} = 2.6$ m, $h_{xf} = 76.37$ m, and $w_{sg} = 0.86$ m, substituted into equations (1)–(6), and the calculation is $L_{\ln c} = 68.12$ m. At the site of the roof water gushing accident, the distance between the lower seam face and the upper seam face is only 21~27 m, which is far smaller than the critical outer staggered distance where the water barrier does not produce water-conducting cracks. Therefore, in the process of mining the lower coal seam, the water-proof layer will produce water-conducting cracks, lose the water-proof performance, and cause water loss.

5. Conclusion

(1) For the second type of shallow-buried and close-spaced coal seams (the thickness of the base rock of the upper coal seam >60~70 m), under the conditions of repeated disturbance and multiple mining, the lower water-conducting cracks of the overburden water-proof layer are given. The calculation formula for the critical inner and outer staggered distances of the coal seam determines the calculation method for the critical stratum mining ratio that does not produce water-conducting cracks in the overburden water-resistant layer under the condition of inner staggered layout.

(2) The roof water gushing accident at the fully mechanized coal mining face of Shigetai Coal Mine's coal seam 12 caused the equipment in the working face to be flooded. The main reason was that the distance between the open cut of the lower coal face and the upper coal face was only 21~27 m, which is smaller than the critical distance of the water barrier that does not produce water-conducting cracks.

Data Availability

The data used to support the findings of this study are included within the article.

Conflicts of Interest

The authors declare that they have no known conflicts of interest that could influence the work reported in this paper.

Acknowledgments

References

[1] Q. X. Huang, *Research on Roof Structure and Strata Control of Longwall Mining in Shallow Coal Seam*, China University of Mining and Technology Press, Xuzhou, China, 2000.

[2] Q. X. Huang, "Roof structure theory and support resistance determination longwall face in shallow seam," *Journal of Coal Science and Engineering*, vol. 29, pp. 21–24, 2003.

[3] S.S. Peng, *Coal Mine Ground Control*, Wiley-Inter Science Publication, New York, NY, USA, 1978.

[4] D. S. Zhang, G. W. Fan, L. Q. Ma, and X. F. Wang, "Aquifer protection during longwall mining of shallow coal seams: a case study in the Shendong coalfield of China," *International Journal of Coal Geology*, vol. 86, no. 2-3, pp. 190–196, 2011.

[5] D. Zhang, G. Fan, Y. Liu, and L. Ma, "Field trials of aquifer protection in longwall mining of shallow coal seams in China," *International Journal of Rock Mechanics and Mining Sciences*, vol. 47, no. 6, pp. 908–914, 2010.

[6] L. Q. Ma and D. S. Zhang, *Research on the Mechanism and Application of Water-Retaining Mining in Longwall Working Face in Shallow Coal Seam*, China University of Mining and Technology Press, Xuzhou, China, 2012.

[7] G. Q. He, L. Yang, G. D. Ling et al., *Mining Subsidence Science*, China University of Mining and Technology Press, Xuzhou, China, 1991.

[8] Z. Y. Jin, *The Development and Control of Water-Transmitting Fissures in the Overlying Rock in the Repetitively Disturbed Area of Shallow and Close Coal Seams*, China University of Mining and Technology, Xuzhou, China, 2015.

[9] D. Z. Kong, S. J. Pu, Z. H. Cheng, G. Y. Wu, and Y. Liu, "Coordinated deformation mechanism of the top coal and filling body of gob-side entry retaining in a fully mechanized caving face," *International Journal of Geomechanics*, vol. 21, no. 4, 2021.

[10] D.-Z. Kong, Z.-B. Cheng, and S.-S. Zheng, "Study on the failure mechanism and stability control measures in a large-cutting-height coal mining face with a deep-buried seam," *Bulletin of Engineering Geology and the Environment*, vol. 78, no. 8, pp. 6143–6157, 2019.

[11] J. F. Lou, F. Q. Gao, J. H. Yang et al., "Characteristics of evolution of mining-induced stress field in the longwall panel: insights from physical modeling," *International Journal of Coal Science & Technology*, 2021.

[12] "Report on water inrush accident at 12105 working face of Shigetai Coal Mine," 2010, http://wenku.baidu.com/view/94b01ec6d5bbfd0a7956737e.html.

Research Article

Case Study on the Mechanism of Influence of Stoppage on Ground Pressure under Different Rates of Advance

Xiaoxu Gao,[1,2] Xinyu Shi [1,3] and Weibin Guo[1,2]

[1]*Xi'an University of Science and Technology, Xi'an 710054, China*
[2]*Key Laboratory of the Ministry of Education on Mining and Disaster Prevention in Western China, Xi'an 710054, China*
[3]*Shaanxi Coal Group Huangling Mining Co., Ltd., Yan'an 727307, China*

Correspondence should be addressed to Xinyu Shi; 390359325@qq.com

Because of daily maintenance, equipment damage, gas overrun, and other force majeure factors, the continuous stopping of the working face causes the roof pressure to accumulate, which leads to causing accidents such as coal wall spalling and roof falling. To address the roof safety problem caused by continuous stoppages, the 620 working face in the Huangling mining area is taken as the research object. Through field measurement, theoretical analysis, numerical simulation, and other research methods, the influence and mechanism of stopping pressure under different rates of advance are studied. The results show that the velocity factor of roof load transfer is positively correlated with the advancing velocity of the working face; the reasonable length of the suspended roof is mainly affected by the number of caving holes and the effect of pressure relief; and comparing the two stages of advance speed of 4.8 m/d and 12.8 m/d, the periodic weighting step distance of the latter increases by 24.4% compared with the former, and the rate of increase of support load caused by stopping mining increases by 42.1% compared with the former. The roof pressure accumulation caused by stopping mining is increased. Taking appropriate measures for local forced caving of the working face can release the roof pressure and reduce the risk of local caving of the working face. The study can provide a theoretical basis for roof control of continuous stopping under similar engineering conditions.

1. Introduction

Due to force majeure factors such as daily maintenance of working face, equipment damage, special geological structures, and gas overrun, the continuous stoppage of mining in the normal advancing process of working face is inevitable, and the characteristics of ground pressure show obvious differences under different rates of advance [1]. In this regard, Xie [2–4] analysed the failure field and stress field of the fully mechanised top coal caving face under different rates of advance through numerical simulation and similar simulation methods. The results show that when the unit mining depth increases, the extent of failure zones in the rock around the working face decreases, but a large amount of energy accumulates inside the rock mass, and the possibility of local rock burst increases; according to Yang and Liu [5, 6], the integrity of surrounding rock and the volume

of broken rock block are positively correlated with the rate of advance of working face in shallow coal seams; S. Yang and J. Yang [7–13] believed that, in high-intensity mining, the rate of occurrence of coal and rock disasters is affected by the rate of advance and the working face length. The greater the coal rock disaster rate, the greater the first weighting step of the working face roof; Zhu and Xu [14, 15] analysed the damage to a coal and rock mass under different geological conditions by combining numerical simulation and field measurement methods. The analysis results show that the faster the working face advances, the greater the stress concentration on both sides of the working face, and the extent of the plastic zone is reduced. These research results used weighting characteristics of working face and coal and rock catastrophes under different rates of advance but fail to reveal the ground pressure on the working face when the mining is stopped. Due to special reasons, if the advance

distance has not reached the collapse step distance, a large amount of energy accumulated in the roof cannot be released, the risk of a roof fall in the working face is greatly increased, and, at the same time, the hydraulic support movable column shrinks and the hydraulic pipe bursts. In view of this kind of engineering problem, the author, by means of numerical simulation and field measurement, took the 620 working face of a mine in the Huangling mining area as the research background and investigated the ground pressure behaviour upon continuous stoppage at the working face in the process of high-speed advance thereof.

At present, the 620 working face of No. 2 Coal Seam in Huangling coal mine is being mined. The average thickness of the coal seam is 2.4 m, the dip angle is 0° to 6°, the average burial depth of the working face is 380 m, the width is 235 m, the advancing length is 2267 m, the current daily rate of advance is 12.8 m/d, the working face relies on the ZY6800/11.5/24d hydraulic support to automatically support the roof, the rated support resistance is 6800 kN, and the support is equipped with a PM32 electrohydraulic control system, which can record the live column load in real time. The roof and floor of the coal seam are thus as follows: the main roof is siltstone and fine sandstone and the thickness is 11.8 m; the direct roof is fine sandstone and the thickness is 8.7 m; and the direct bottom is mudstone and the thickness is 2.8 m. Due to force majeure factors such as daily maintenance, equipment damage, and gas overrun, the phenomenon of continuous stoppage affects mine safety. For face 620, the phenomenon of support pressing and hydraulic pipe bursting occurs regularly during the stoppage of the 620 working face (Figure 1). The table of rock mechanics parameters is shown in Table 1.

2. The Influence of Working Face Ground Pressure under Different Rates of Advance

To analyse the influences of ground pressure and the performance characteristics of stoppage pressure under different rates of advance, two different advancing sections of the 620 working face are selected for *in situ* testing (Table 2 and Figure 2). The stoppage points marked in Figure 2 are caused by local gas overrun of the working face. According to an investigation of the mining area, when the rate of advance is 4.8 m/d and 12.8 m/d, the basis for the judgment of periodic weighting is as follows: the end resistance of circulation reaches 35 MPa and 25 MPa, respectively, the high-level gas drainage concentration increases instantaneously, and the coal wall spalling is severe. When the working face stops mining, the bearing degree of the support increases, but it has not reached the average load for periodic weighting. After stopping mining, the roof pressure will be released with the continuous advance of the working face.

Combined with the load conditions of support in Figures 2(a) and 2(b), the measured weighting characteristics are listed in Table 3. The measured results show that when the rate of advance is 4.8 m/d and 12.8 m/d, the periodic weighting step distance of the latter is 24.4% higher than that of the former, and the support load rise rate caused by stoppage of the latter is 42.1% higher than that of the

former, and the risk of roof fall of working face is greatly increased. Therefore, avoiding the fluctuation of the mining speed of the working face can decelerate the accumulation of dangerous roof pressure on the working face and play a positive role in the control of the rock strata; by comparing the rise of the support load when stopping mining under the two rates of advance, it is found that when the rate of advance is large, the accumulated pressure on the roof is also high, and the risk of a local roof fall in the working face is relatively low. Appropriate measures should be taken to release the roof pressure to ensure safe production at the working face.

3. Theoretical Analysis

3.1. Speed Factor of Load Transfer. Some research results show that, with the increase of the rate of advance, the peak load increases and moves forward [16–18]; and when the rate of advance is rapid, the mining failure caused by the direct roof is incomplete, the roof load increase caused by mining cannot fully act on the support, and the support load remains low [19, 20]. On the other hand, when the main roof collapses, the main load is provided by the load layer on the top of the main roof. The load transfer process and the rate of advance have a time effect. That is, when the working face is advancing normally, the load transfer characteristics of the main roof are such that it unloads first, then arches, and after that unloads, until the original state of stress in the rock is restored. However, when the rate of advance is decelerated due to special reasons, secondary unloading will occur. For this reason, some scholars have proposed a time transfer factor KT [21–25], as given by the following:

$$K_t = \frac{P_z}{K_r h_1 l \rho g},\tag{1}$$

where P_Z is the load acting on the key block; K_r is the lithology factor; h_1 is the thickness of the loading layer; L is the length of the key block; and ρ represents the average bulk density of the key layer.

At the same time, the author thinks that the time factor K_t will change with time in the transformation process of the key blocks of the main roof. Therefore, the following formula can be obtained:

$$K_t = mt,\tag{2}$$

where m is the time factor.

Based on the above results, a velocity transfer factor K_V suitable for the main roof load in the Huangling mining area is proposed. The velocity transfer factor K_V will change with the speed, and the following formula can be obtained:

$$K_v = nv,\tag{3}$$

where n is the velocity factor.

During the periodic weighting of the main roof, when the rate of advance is kept constant, the periodic weighting step length is quasiconstant; therefore, it is considered that the periodic weighting step is a constant S_Z, and the load

(a)

(b)

Figure 1: A failed support and hydraulic pipe explosion.

Table 1: Rock mechanics parameters.

Serial number	Rock properties	Thickness (m)	Shear modulus (GPa)	Bulk modulus (GPa)	Density (g/cm^3)	Cohesion (MPa)	Internal friction angle (°)	Tensile strength (MPa)
1	Medium sandstone	28	6.23	5.07	2450	6.25	39	1.20
2	Siltstone	11.8	7.13	5.13	2350	4.24	37	1.12
3	Fine sandstone	8.7	5.78	4.70	2320	4.05	35	1.10
4	Coal	2.1	2.81	1.68	1347	0.64	32	0.32
5	Mudstone	2.8	4.87	3.06	2100	1.32	34	0.66

Table 2: Comparison of rate of advance of working face in different periods

Advance time (2019)	Advance duration (d)	Advance speed (m/d)	Advance distance (m)
6.1~6.18	18	4.8	86.4
7.23~7.29	7	12.8	89.6

speed transfer factor K_v at this time is deduced, as shown in the following formula:

$$K_v = \frac{mnS_zK_rh_1l\rho g}{P_z}. \tag{4}$$

When the rate of advance changes, the periodic weighting step distance of the main roof also changes. The greater the rate of advance, the larger the periodic weighting step distance; therefore, the correction coefficient m is introduced. According to the measured results of periodic weighting step distance of working face in the Huangling mining area, the value of correction coefficient m is set (it is positively correlated with the rate of advance of the working face). Taking the advance speed of the 620 working face as an example, $m = 1.2$, therefore, the load transfer speed factor K_{v1} applicable to the 620 working face is shown in the following formula:

$$K_{v1} = \frac{mn1.2 \cdot S_zK_rh_1l\rho g}{P_z}. \tag{5}$$

Taking the load of the key block of the main roof, the extreme value of the speed factor K_{v0} for load transmission can be deduced as follows:

$$K_{v0} = 1.2S_zK_rmn. \tag{6}$$

It can be seen from formula (6) that K_{v0} is jointly affected by periodic weighting step S_Z and lithologic factor K_r as determined by the thickness of load layer, lateral pressure coefficient, and internal friction angle, that is, given K_r, m, and n being constant, it can be considered that K_{v0} is positively correlated with periodic weighting step S_Z. At the same time, periodic weighting step S_Z is positively correlated with the rate of advance of the working face and load transfer factor K_{v0} is positively correlated with the rate of advance.

3.2. Reasonable Suspended Roof Length for Roof Pressure Relief.

After the first fracture of the roof, with the continuous advance of the working face, one end of the roof rock beam is fixed on solid coal, and the other is suspended, showing a cantilever beam structure, and with the continuous advance of the working face, the roof periodically collapses [1, 26, 27]. If the roof load is evenly distributed, roof pressure will accumulate when stoppage occurs. Based on previous research results [28–30], the design relies on the drilling of several caving holes in the direct roof of the

(a)

(b)
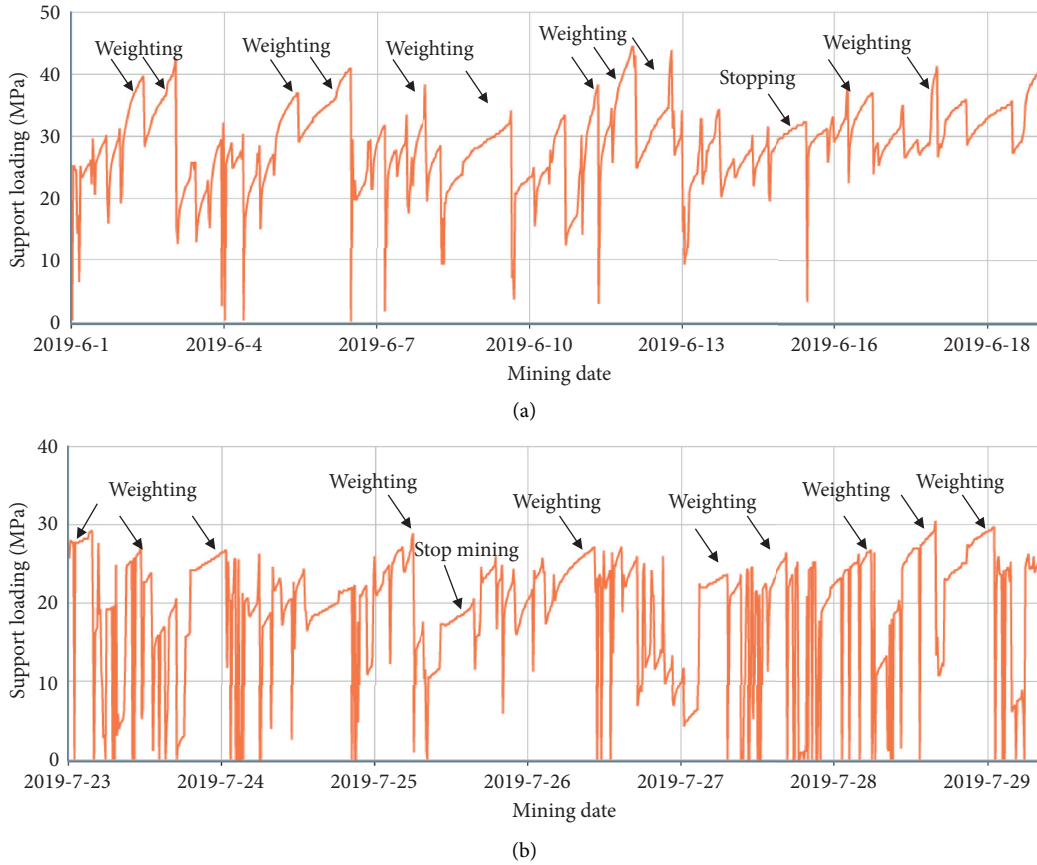
FIGURE 2: Load distribution on the support at different rates of advance. (a) Load distribution on the working face support when the rate of advance is 4.8 m/d. (b) Load distribution on the working face support when the rate of advance is 12.8 m/d.

TABLE 3: Measured pressure characteristics.

Advance speed (m/d)	Times of periodic weighting (frequency)	Average periodic weighting step (m)	Stoppage time (h)	Load rise (MPa)	Load rise rate (MPa/h)
4.8	11	7.2	6	5.7	0.95
12.8	9	8.96	3	8.4	2.8

gateway to release the roof pressure and assist the roof caving. Two sections are made along the gateway and the working face, and the mechanical model of roof pressure relief fracture is drawn, as shown in Figure 3 [31–33].

It can be seen from Figure 3 that the load layer above the main roof exerts a uniform load Q on the main roof. If there are I caving holes under construction and the load released by each caving hole is Q, the support resistance provided by the support to the working face is the allowable support resistance $[P]$. According to the fact that the support can bear all the loads within the roof control area, then

$$\frac{1}{2}[P]a^2 = \frac{1}{2}(Q - iq)L^2,$$

$$[P] = \frac{(Q - iq)(a + b)^2}{a^2},$$

(7)

where a is the distance of support control, L is the distance of hanging roof, and $L = a + b$.

Forced caving is used to ensure that the working resistance P provided by the support is not greater than the allowable support resistance $[P]$ in case of periodic roof fracture. Then,

$$P \leq [P] = \frac{(Q - iq)(a + b)^2}{a^2},$$

$$b \geq a\left(\sqrt{\frac{[P]}{Q - ip}} - 1\right).$$

(8)

The reasonable length of the suspended roof based on the pressure relief of the caving hole and the allowable support resistance $[P]$ of the support can be calculated:

$$L \leq a\sqrt{\frac{[P]}{Q - ip}}.$$

(9)

According to formula (9), after the working face is determined, the roof control distance of the support and the
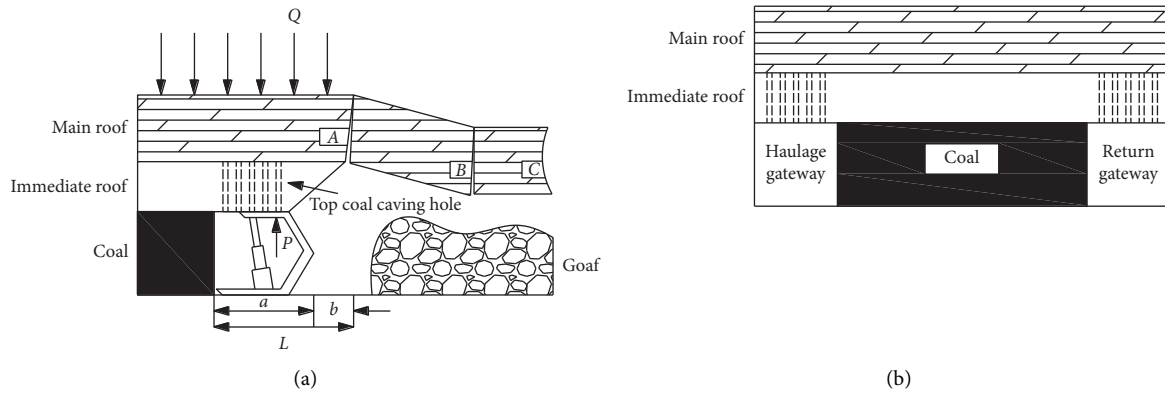
FIGURE 3: Mechanical model of roof pressure relief.

allowable support resistance of the support are determined, and the main roof load is also determined. Therefore, the reasonable hanging roof length is mainly affected by the number of caving holes and the pressure relief effect.

4. Numerical Simulation Study

4.1. Establishment of Model. FLAC^{3D} finite difference simulation software is used here: the Mohr–Coulomb constitutive relationship is set for rock stratum and a strain-softening constitutive relationship is applied to model the coal seam. The mechanical parameters of rock mass are provided by the mine. To simplify the stratum, the strike direction is 345 m, the advancing direction length is 300 m, the vertical thickness is 81 m, and the thickness of the coal seam is 3 m. A total of 354,960 elements and 371,124 nodes are established. We limit the displacement around the model, fix the bottom, apply a 5 MPa uniform load to the top of the model, and assume a lateral pressure coefficient of 1.2. The numerical simulation model is shown in Figure 4. The numerical simulation mainly analyses the distribution of advance abutment pressure after the working face reaches a stable rate of advance. After the working face is advanced by 100 m, three measuring lines are established to monitor the abutment pressure distribution characteristics within 50 m ahead of the working face. The three monitoring lines are located on both sides of goaf and the middle of goaf, respectively. When simulating the advancing process of working face, the unit mining depth of the working face is replaced by time steps, and the difference of rate of advance is characterised by the difference in total operation steps [2, 7, 8]. Among them, the same excavation step distance and different excavation steps are used to replace the propulsion speed. The specific advancing scheme is summarised in Table 4 .

4.2. Analysis of Simulation Results

(1) Analysis of advance abutment pressure distribution under different rates of advance:

Figure 5 shows the distribution diagram of abutment pressure on the advancing (by 100 m) mining face under different rates of advance. Combined with the data in Figure 4, the characteristics of roof pressure at different rates of advance are plotted, using data in Table 5. The analysis shows that, with the continuous increase of the rate of advance, the bearing pressure first decreases and then decelerates. When the rate of advance of the working face reaches 15 m/d, the weakening trend of the advanced abutment pressure will diminish. Compared with the rate of advance of 20 m/d, the stress concentration in each case is similar. Compared with the slow rate of advance, the stress concentration is smaller when the rate of advance reaches 15 m/d; at the same time, it is concluded that, in a certain range of rate of advance, increasing the rate of advance reduces the working face pressure, but when the rate of advance reaches a certain value, the change in the rate of advance has little influence on the weighting of the working face.

(2) Analysis of advance abutment pressure distribution in different times of stopping mining under different rates of advance:

Taking survey line 1 as an example, the difference in abutment pressure at different stopping times under different rates of advance is analysed. Figure 6 shows the distribution of advanced abutment pressure at different stopping times at different rates of advance of line 1, and Table 6 shows the concentrated characteristics of stopping production pressure at different rates of advance of line 1. Accordingly, the peak position of advanced abutment pressure appears at about 12 m from the coal wall, and the abutment pressure first increases and then decreases with the distance of the leading coal wall; at the same time, the degree of concentration of abutment pressure also increases with the extension of the stoppage time. According to the data in Table 6, the range of pressure change is not large when the mining is stopped for 2 days or 3 days, so it is speculated that the roof pressure concentration had stabilised.

(3) Analysis of maximum eigenvalue variation of abutment pressure at different rates of advance:
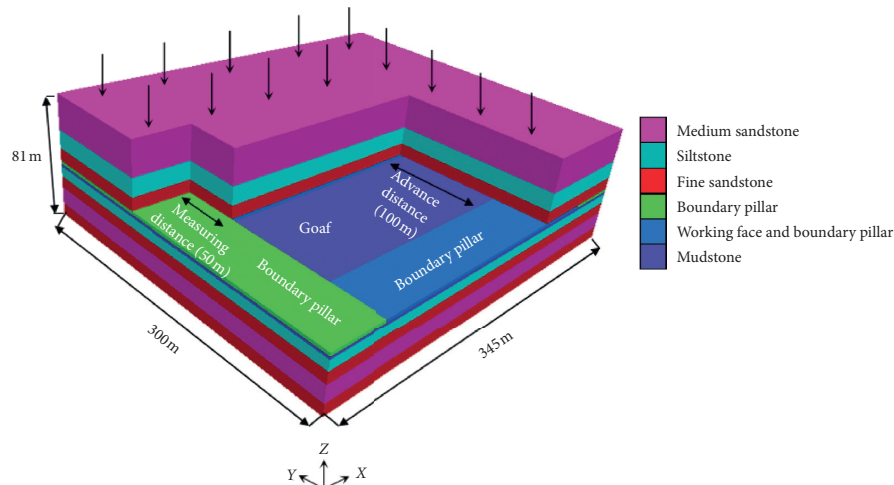
Figure 4: Numerical simulation model.

Table 4: Design of different face-advance schemes.

Serial number	Programme	Unit mining depth (m)	Advance speed (m/d)	Advance time steps of primary mining	Total steps
1	Advancing 100 m	5	5	2000	40000
2	Advancing 100 m and stopping for 1 day	5	5	4000	42000
3	Advancing 100 m and stopping for 2 days	5	5	6000	44000
4	Advancing 100 m and stopping for 3 days	5	5	8000	46000
5	Advancing 100 m	10	10	2000	20000
6	Advancing 100 m and stopping for 1 day	10	10	4000	22000
7	Advancing 100 m and stopping for 2 days	10	10	6000	24000
8	Advancing 100 m and stopping for 3 days	10	10	8000	26000
9	Advancing 100 m	15	15	2000	14000
10	Advancing 100 m and stopping for 1 day	15	15	4000	16000
11	Advancing 100 m and stopping for 2 days	15	15	6000	18000
12	Advancing 100 m and stopping for 3 days	15	15	8000	20000
13	Advancing 100 m	20	20	2000	10000
14	Advancing 100 m and stopping for 1 day	20	20	4000	12000
15	Advancing 100 m and stopping for 2 days	20	20	6000	14000
16	Advancing 100 m and stopping for 3 days	20	20	8000	16000

Figure 7 shows the variation in the maximum eigenvalue of different rates of advance. It can be seen from Figure 6 that the maximum eigenvalue gradually decreases with the increase of the rate of advance, and the increment of the stress peak value changes to a significant extent in the process of the gradual acceleration of the rate of advance. When the rate of advance reaches 15 m/d, the peak stress increase presents a downward trend. Compared with the four curves in Figure 7, it can be seen that, with the continuous increase of the rate of advance of the working face, the increase of the maximum eigenvalue is significant: the rate of change of abutment pressure increment at different stoppage times is also accelerated. When the working face stops mining for 1 day, the increment of abutment pressure changes most, then, with the increase of stoppage time, the increment of abutment pressure gradually decreases and finally diminishes; therefore, it can be concluded that the faster the rate of advance of working face, the greater the roof pressure caused by stopping mining. When the rate of advance reaches a certain value, the roof pressure will increase and the increment of abutment pressure then will decrease.

5. Engineering Application

Combining with the characteristics of support load distribution in the 620 working face with different rates of advance in the past, it is necessary to take some pressure relief measures according to the pressure accumulation phenomenon when stopping mining at different rates of advance in the 620 working face, so as to release the roof pressure and maintain the safety and stability of the working face. Taking the stoppage of 620 working face on 8 August 2019 as an example, the current daily rate of advance is 12.8 m/d, and the method of constructing a caving hole is adopted to release roof pressure locally to assist goaf caving. The MQT-120T pneumatic drill pipe machine is used for construction. The first row is 3 m from the coal wall of the
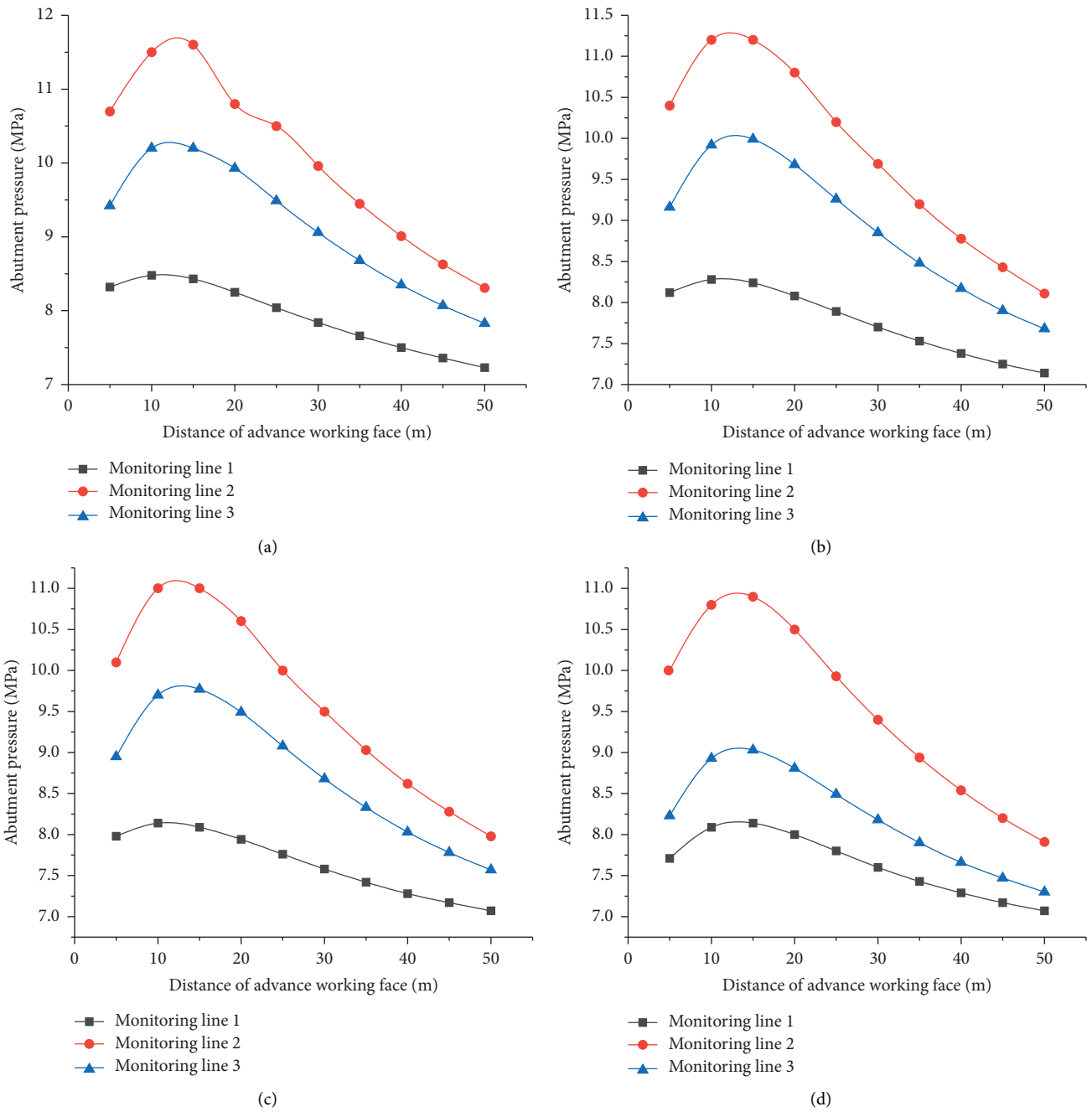
FIGURE 5: Distribution of advance bearing pressure of the working face under different rates of advance. Advance speed of (a) 5 m/d, (b) 10 m/d, (c) 15 m/d, and (d) 20 m/d.

TABLE 5: Roof pressure characteristics at different rates of advances.

Advance speed (m/d)	Abutment pressure peak value (MPa)			Peak stress concentration factor		
	Survey line 1	Survey line 2	Survey line 3	Survey line 1	Survey line 2	Survey line 3
5	8.48	11.6	10.2	1.37	1.87	1.65
10	8.28	11.2	9.99	1.34	1.81	1.61
15	8.14	11.0	9.77	1.31	1.77	1.58
20	8.14	10.9	9.03	1.31	1.76	1.45

(a)

(b)

(c)

(d)
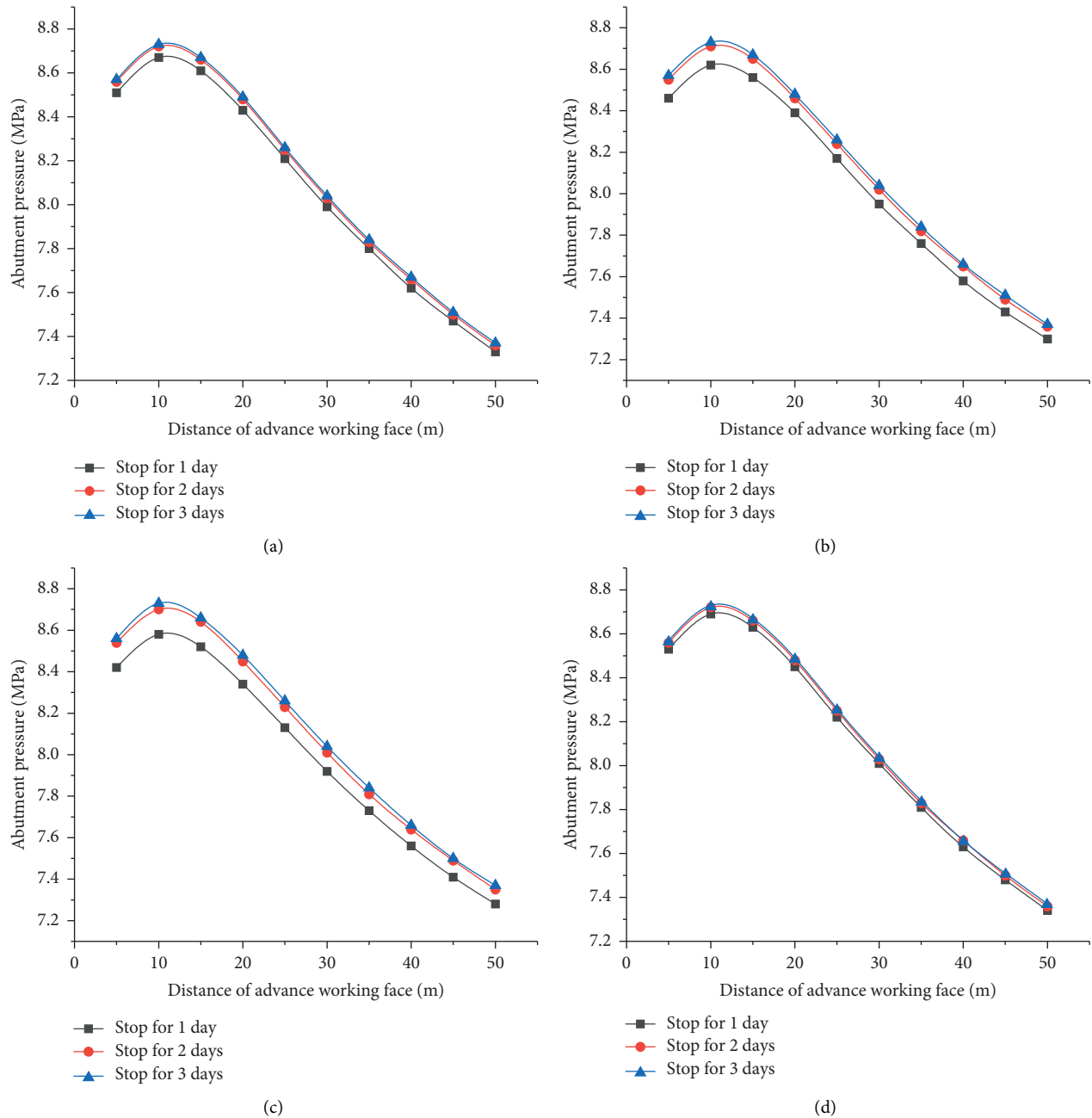
FIGURE 6: Distribution of advance support pressures at different stoppage times at different rates of advance. Advance speed of (a) 5 m/d, (b) 10 m/d, (c) 15 m/d, and (d) 20 m/d.

goaf, with 13–15 rows in each row. The spacing between rows is 300×4000 mm, the hole depth is 8 m, and the hole diameter is 28 mm. At the same time, a discharge top hole is constructed at a spacing of 300 mm from the side slope of the solid coal (Figure 8).

As shown in Figure 9, the two instances of the sudden drop of support load to zero are due to the decline of working face support and the separation of support top beam and roof, resulting in no load above the support. Periodic weighting occurs at the working face at about 06 : 00, and the peak load on the support is 36.2 MPa. The roof then collapses and the support load decreases. The time from

peak weighting to stoppage is about 6 h. During this period of time, at about 11 : 00, the top beam of the support dropped and separated from the roof, resulting in a sudden drop of the support load to zero, and at 15 : 07, the working face suffers from tile failure. At this time, the support load increases slowly, the peak load is 23.8 MPa, the load increase is 6.3 MPa, and the duration of pressurisation is 1.8 h. At the same time, forced caving measures are taken to release the roof pressure. At this time, the support load drops sharply, the final load decreases to 11.7 MPa, and the cumulative load decreases by 12.1 MPa. Compared with the support load before and after pressure relief, the load rise rate caused by

TABLE 6: Concentration characteristics of stoppage pressure at different rates of advance: line 1.

Advance speed (m/d)	Abutment pressure peak value (MPa)			Amount of abutment pressure increase (MPa)			Rate of increase (%)		
	Stop mining for 1 day	Stop mining for 2 days	Stop mining for 3 days	Stop mining for 1 day	Stop mining for 2 days	Stop mining for 3 days	Stop mining for 1 day	Stop mining for 2 days	Stop mining for 3 days
5	8.67	8.72	8.73	0.19	0.24	0.25	2.24	2.83	2.95
10	8.62	8.71	8.73	0.34	0.43	0.45	4.11	5.19	5.43
15	8.58	8.70	8.73	0.44	0.56	0.59	5.41	6.87	7.25
20	8.69	8.72	8.73	0.55	0.58	0.59	6.76	7.12	7.25
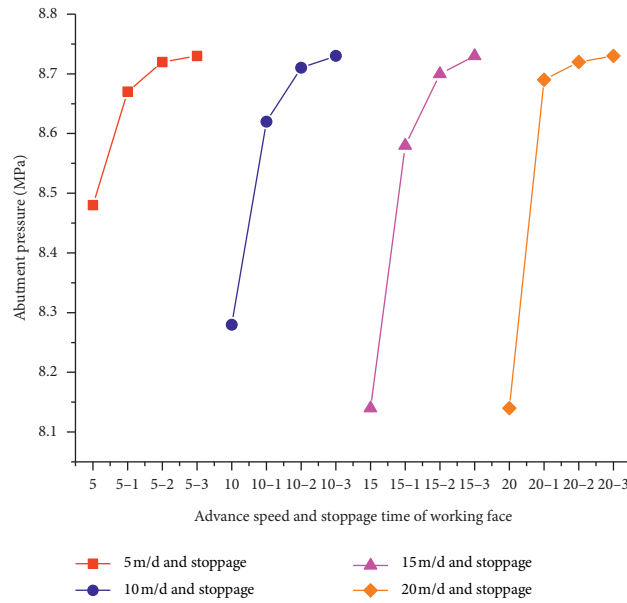
FIGURE 7: Maximum characteristic value changes for different rates of advance.
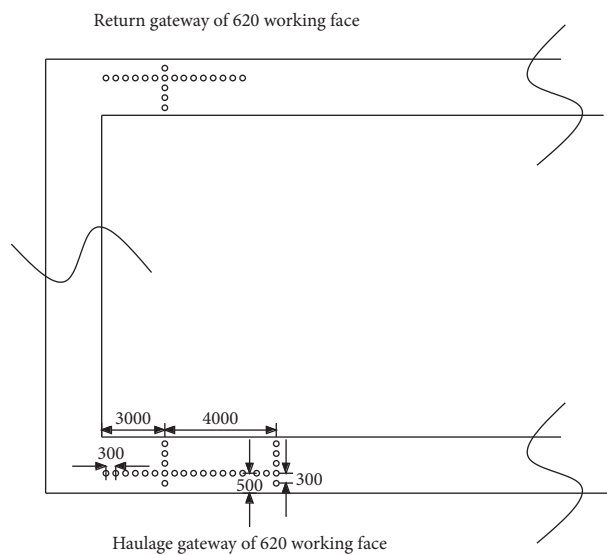
FIGURE 8: Caving hole layout parameters.
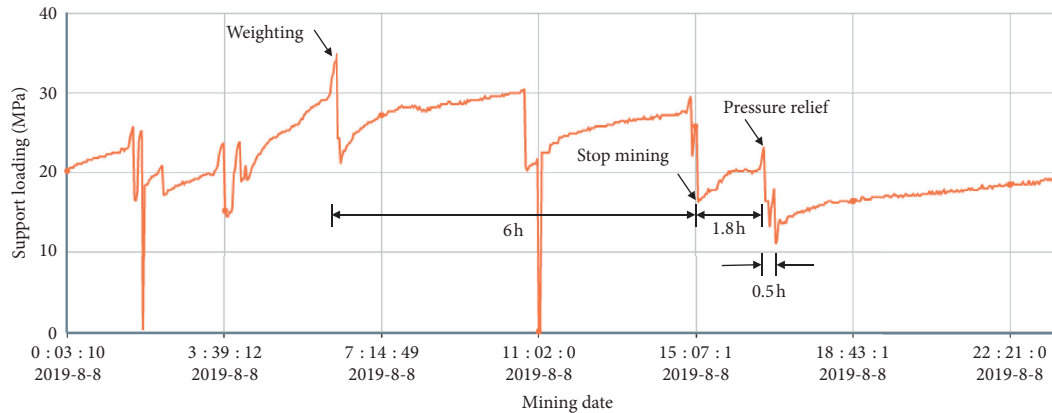
FIGURE 9: Load distribution on the support on 8 August 2019.

stopping mining is 3.5 MPa/h, that caused by forced caving is 23.4 MPa/h, the load drop rate is 6.68 times the previous rate of rise, and the forced caving pressure relief effect is obvious.

6. Conclusion

(1) The load transfer velocity factor K_v of a working face is affected by lithology factor K_r and the periodic weighting step. After the working face is calculated, K_v is determined accordingly; that is, the load transfer speed factor applicable to the working face is positively correlated with the rate of advance of the working face.

(2) The reasonable hanging roof length based on the allowable support resistance of the support is mainly affected by the number of caving holes and the pressure relief effect.

(3) With the continuous increase of the rate of advance of working face, the advance abutment pressure first decreases and then tends to be stable. At different stoppage times, the incremental trend of roof abutment pressure varies: with the continuous extension of stoppage time, the increment of roof abutment pressure decreases, but when the rate of advance increases to within a certain range, the trend of abutment pressure increment decreases.

(4) The roof has accumulated part of energy after the working face has been excavated continuously after normal cycle weighting. If a stoppage then occurs, the roof pressure accumulation is significant, so it is necessary to take forced roof caving measures to control the roof pressure.

Data Availability

The data used to support the findings of this study are available from the corresponding author upon request.

Conflicts of Interest

The authors declare that they have no conflicts of interest.

References

[1] M. G. Qian, P. W. Shi, and J. L. Xu, *Mine Pressure and Strata Control*, China University of mining and Technology Press, Xu Zhou, China, 2010.

[2] G. X. Xie, J. C. Chang, and X. Z. Hua, "Influence of mining velocity on mechanical characteristics of surrounding rock in fully mechanized top-coal caving face," *Chinese Journal of Geotechnical Engineering*, vol. 29, no. 7, pp. 963–967, 2007.

[3] G. Xie, Z. Yin, L. Wang, Z. Hu, and C. Zhu, "Effects of gas pressure on the failure characteristics of coal," *Rock Mechanics and Rock Engineering*, vol. 50, no. 7, pp. 1711–1723, 2017.

[4] Q. Li, G. X. Xie, and P. Zou, "Energy source and energy dissipation mechanism of coal and gas outburst based on microscope," *Acta Microscopica*, vol. 29, no. 4, pp. 1900–1910, 2020.

[5] D. F. Yang, *Study on Roof Cutting Mechanism of High Intensity Mining in Western Shallow Seam*, China University of mining and Technology, Beijing, China, 2016.

[6] Q. M. Liu, "Analysis on the effect of advancing speed on the ground pressure appearance in shallow fully mechanized mining face," *Coal Science and Technology*, vol. 38, no. 7, pp. 24–26, 2010.

[7] S. L. Yang, Z. H. Wang, Z. H. Wang, and J. H. Yang, "Analysis on the effect of advancing speed of coal rock disaster in high strength mining face," *Journal of Coal Science*, vol. 41, no. 3, pp. 586–594, 2016.

[8] S. L. Yang, G. F. Song, and J. H. Yang, "An analytical solution for the geometric broken characteristics of the overlying strata and its physical modeling study in longwall coal mining," *Arabian Journal Of Geosciences*, vol. 13, no. 3, 2020.

[9] Z. B. Cheng, S. L. Yang, L. H. Li, and L. F. Zhang, "Support working resistance determined on top-coal caving face based on coal-rock combined body," *Geomechanics & Engineering*, vol. 19, no. 3, pp. 155–168, 2020.

[10] S. L. Yang, G. F. Song, and D. Z. Kong, "An evaluation of longwall face stability in thick coal seams through a basic understanding of shield-strata interaction," *Journal of Geophysics and Engineering*, vol. 16, no. 1, pp. 125–135, 2019.

[11] D. Z. Kong, Y. Liu and S. S. Zheng, "Sensitivity analysis of influencing factors and control technology for coalface failure," *Arabian Journal Of Geosciences*, vol. 12, no. 17, 2019.

[12] G. F. Song, K. Ding, and D. Z. Kong, "Assessing longwall shield-strata interaction using a physical model," *The Quarterly Journal of Engineering Geology and Hydrogeology*, vol. 52, no. 4, 2019.

[13] J. H. Yang, S. L. Sun and D. Z. Kong, "The effect of face length and advance speed on the occurrence of pressure in high strength mining face," *Rock and Soil Mechanics*, vol. 36, no. S2, pp. 333–339, 2015.

[14] Z. J. Zhu, H. W. Zhang, and Y. Chen, Y. P. Li and W. D. Wu, "The influence of the advancing speed of the working face on the mine pressure appearance in the extra thick coal seam," *Journal of Safety and Environment*, vol. 16, no. 3, pp. 126–129, 2016.

[15] Y. F. Xu, S. K. An, C. Xu, Y. C. Chen, and H. Yi, "Influence of advancing speed on strata beh-aviors in fully-mechanized face with hard roof," *Journal of Safety Science and Tech-nology*, vol. 15, no. 10, pp. 88–94, 2019.

[16] L. F. Feng, L. M. Dou, X. D. Wang, D. W. Ji, and W. Cai, "Mechanism of mining speed on energy release from hard roof movement," *Journal of Coal Science*, vol. 44, no. 11, pp. 3329–3339, 2019.

[17] C. Y. Wang, "Effect of mining speed on bump manifestation of fully-mechanized mining face in deep and thick coal seam," *Coal Science and Technology*, vol. 47, no. 8, pp. 96–101, 2019.

[18] F. F. Zheng, Z. G. Sun, and S. G. Li, "Yield mining theory and roof control technology at end mining stage of fully mech-anized face," *Mining safety & Environmental protection*, vol. 42, no. 2, pp. 64–67, 2015.

[19] X. Z. Wang, J. L. Xu, W. B. Zhu, and J. F. Ju, "Influence of high mining velocity on periodice weighting during fully-mech-anized mining in a shallow seam," *Journal of China University of Science & Technology*, vol. 41, no. 3, pp. 349–354, 2012.

[20] X. Z. Wang, J. F. Ju, and J. L. Xu, "Theory and applicable of yield mining at ending stage of fully-mechanized face in shallow seam at shendong mine area," *Journal of Mining & Safety Engineering*, vol. 29, no. 2, pp. 151–156, 2012.

[21] Q. X. Huang, "Studies on load-transmitting factor of thick sandy soil layer on key roof stratum in shallow seam mining," *Chinese Journal of Geotechnical Engineering*, vol. 27, no. 6, pp. 672–676, 2005.

[22] Q. X. Huang, J. L. Zhou, and J. Cao, "Key stratum structure and support working resistance of longwall face with large mining height in the shallow coal seams, China," *Advances in Civil Engineering*, vol. 2020, Article ID 8834403, 14 pages, 2020.

[23] Q. X. Huang and J. Cao, "Research on coal pillar malposition distance based on coupling control of three-field in shallow buried closely spaced multi-seam mining," *Energies*, vol. 12, no. 3, 2019.

[24] Q. X. Huang, Y. P. He, and F. Li, "Research on the roof advanced breaking position and influences of large mining height working face in shallow coal seam," *Energies*, vol. 13, no. 7, 2020.

[25] P. Zhang, *Study on Roof Dynamic Structure of Shallow Seam Longwall Mining*, Xi'an University of science and technology, Xian, China, 2012.

[26] J. F. Ju, J. L. Xu, and Q. X. Wang, "Cantilever structure moving type of key strata and its influence on ground pressure in large mining height workface," *Journal of Coal Science*, vol. 36, no. 12, pp. 2115–2120, 2011.

[27] S. H. Yan, X. W. Yin, G. J. Hu, G. Xu, and L. Yu, "Roof structure of short cantilever-articulated rock beam and cal-culation of support resistance in full-mechanized face with large mining height," *Journal of Coal Science*, vol. 36, no. 11, pp. 1816–1820, 2011.

[28] Z. H. Chen, J. J. Feng, C. C. Xiao, and R. H. Li, "Fracture mechanical model of key roof for fully-mechanized top-coal caving in shallow thick coalseam," *Journal of Coal Science*, vol. 5, pp. 449–452, 2007.

[29] K. Wang, T. H. Kang, H. T. Li, and W. M. Han, "Study of control caving methods and reasonable hanging roof length on hard roof," *Chinese Journal of Rock Mechanics and En-gineering*, vol. 28, no. 11, pp. 2320–2327, 2009.

[30] J. Li, H. Duan, D. Yue, P. J. Chen and Z. H. Li, "Study on the fracture mechanics model of forced caving of hard roof," *Coal Geology & Exploration*, vol. 46, no. 6, pp. 128–132, 2018.

[31] D. Z. Kong, Z. B. Cheng, and S. S. Zheng, "Study on the failure mechanism and stability control measures in a large-cutting-height coal mining face with a deep-buried seam," *Bulletin of Engineering Geology and the Environment*, vol. 78, no. 8, pp. 6143–6157, 2019.

[32] Z. B. Cheng, L. H. Li, and Y. N. Zhang, "Laboratory inves-tigation of the mechanical properties of coal-rock combined body," *Bulletin of Engineering Geology and the Environment*, vol. 79, no. 4, pp. 1947–1958, 2020.

[33] J. F. Lou, F. Q. Gao, and J. H. Yang, "Characteristics of evolution of mining-induced stress field in the longwall panel: insights from physical modeling," *International Journal of Coal Science & Technology*, 2021.

Research Article

Influencing Factors' Analysis of Disturbance Degree of Key Stratum Based on the Response Surface Method

Yang Li, Nan Wang, Yuqi Ren ⬡, Xiangji Ou, Yikun Liu, Junbo Luo, and Canqi Mei

School of Energy and Mining Engineering, China University of Mining and Technology-Beijing, Beijing 100083, China

Correspondence should be addressed to Yuqi Ren; ryq2019cumtb@126.com

The key stratum controls the activities of the overlying strata or the whole strata up to the surface, which is one of the important research objects in the coal seam mining. Based on the analysis of several geological factors affecting on the key stratum, the definition of "disturbance degree of key stratum" (KSDD) was proposed. And, the KSDD is quantified by the value among 0 to 10. Through the response surface method, experiments of three factors (mining height, buried depth, and interlayer spacing) with three different lithology types (soft, medium, and hard) between key stratum and coal seam are signed. And, the KSDD of each scheme is calculated by the developed calculation system. The response surface regression models of KSDD with three lithology types are established. And, the single influence and interactive influences of the three factors on the KSDD with different lithology types are studied. The results show that the following. (1) Mining height and buried depth are positively correlated with the value of KSDD, and the interlayer spacing is negatively correlated with KSDD. However, when the value of interlayer spacing exceeds 30 m, the change of the KSDD tends to be gentle. (2) The value of KSDD is not only affected by a single factor but also affected by the interaction of various factors. With the increase of burial depth, the decrease of interlayer spacing and the impact of mining height on key stratum are more severe. (3) The influence order of each factor on KSDD is as follows: the interlayer spacing > mining height > buried depth. (4) Although the three factors interact with each other, the three factors decrease with the increase of the lithology proportional coefficient. According to the above research results, based on the calculation results of KSDD on five mines, the variation laws of KSDD with actual situation are analysed. And, the calculation results further verify the above experimental rules, which provide a certain reference and theoretical basis for the design of backfilling parameters and the management of the roof.

1. Introduction

Rock strata with different thickness and strength were formed above the coal seam because of different diagenetic time periods. According to the key stratum theory, the stratum which controls the whole or part of rock mass activity are called key stratum [1, 2]. A large number of engineering practice show that the key stratum was hard. So, a new structure still can be formed to support the overlying strata when key stratum was broken [3–5]. Therefore, the studies of key stratum, such as the breaking position, structural stability, and integrity of key stratum, are of great significance to the safety and production of coal seam mining [6–10].

A large number of scholars have enriched and expanded the theory of key stratum in order to control strata movement. Based on the medium-thick plate theory, the influences of the thickness on the fracture mode of the key layer have been studied. The criterion of fracture mode of key stratum with different thickness has been obtained [11, 12]. Based on the theory of double key strata, the roof structure models of double key strata have been established, and the mining methods of graded water conservation have been obtained [13, 14]. Based on the model of the key stratum structure after sliding and instability, the restability condition of the key stratum has been obtained [15]. The degree of subsidence deflection has been proposed through the establishment of the surface deflection subsidence model. Based on the key stratum theory, the influences of the thickness of loose strata and the bulking factor on the surface deflection subsidence have been analysed [16]. The stability

and periodic pressure mechanism of single and double key strata in overlying strata with large mining height have been revealed. The calculation formula of support resistance has been obtained [17]. Based on numerical simulation, the influences of different distances of double seams' mining on overlying water resisting key stratum have been studied [18]. The above studies have analysed various failure laws of key stratum under different geological conditions. A series of relatively complete theoretical and surrounding rock control methods are established. However, the current research studies mainly focus on the influences of key stratum on the working face. And, there are few studies on the influences of mining geological conditions on the disturbance of key stratum. In addition, there is no corresponding evaluation method and theoretical basis.

Therefore, in order to explore the influences of different geological conditions on key stratum, this paper focuses on the following three research objectives. (1) Several geological factors affecting the key stratum and the proposal of the "disturbance degree of key stratum" are analysed (hereinafter referred to as KSDD). (2) The Design-Expert software will be used to design the response surface [19–21] experimental scheme of three factors (mining height, buried depth, and interlayer spacing) with three different lithology types (soft, medium, and hard) between key stratum and coal seam. The response surface regression model of KSDD will be established. (3) The single influence and interactive influences of the three factors on the KSDD with different lithology types will be explored. These studies will provide a certain reference and theoretical basis for the stability identification of key water resisting stratum, the design of backfilling parameters, and the control of surface subsidence.

2. Definition and Influencing Factors of the KSDD

2.1. The Definition of KSDD.
Underground coal mining breaks the original stress state of surrounding rock [22–24]. Due to the coal seam mining, the degrees of disturbance on the stratum above the coal seam are different. Therefore, in order to explore the change laws of disturbance degree on key stratum with different mining geological conditions. The degree of disturbance caused by coal seam mining on key stratum is defined as the "Disturbance Degree of Key Stratum" (KSDD), which is expressed by the symbol φ.

According to the definition of the KSDD, which means the key stratum is greatly affected by the disturbance with coal seam mining with large value of KSDD, the key stratum under the same conditions is more likely to be destroyed at this time. Conversely, the key stratum is relatively affected by the disturbance with coal seam mining with a small value of KSDD. And, the key stratum under the same conditions is easier to keep intact at this time.

2.2. The Calculation Formula of KSDD.
The related factors are considered comprehensively, including quantitative discrimination method of the feasibility of upward mining in close multiple coal seams [25], mining height, buried depth

[26], distance between key stratum and coal seam (hereinafter referred to as interlayer spacing), tensile strength, and rock hulking coefficient. Then, according to the definition of KSDD, the disturbance intensity of the key stratum caused by coal mining is quantified by the value from 0 to 10. Formula (1) [25] is obtained:

$$\varphi = 10 - \left[\lambda \sum_{i=1}^{n} \left(K_{p_i} \cdot \frac{H_i}{H} \cdot R_{t_i} \right) \cdot \frac{H^2}{D \cdot M} + C \right], \qquad (1)$$

where φ is the disturbance degree of key stratum (KSDD), M is the mining height, m, H is the interlayer spacing, m, D is the buried depth of the coal seam, m, H_1, $H_2 \ldots H_i$ are the thicknesses of the ith ($i = 1, \ldots, n$) rock above the mining coal seam, m, R_{t1}, $R_{t2} \ldots R_{ti}$ are the tensile strength of the ith($i = 1, \ldots, n$) rock above the mining coal seam, MPa, K_{P1}, $K_{P2} \ldots K_{Pi}$ are the rock bulking factors of the ith ($i = 1, \ldots, n$) rock above the mining coal seam, n is the number of all rock strata between the Kay stratum and coal seam, λ is the influence factor of the disturbance degree of the key stratum, and C is the geological constant.

The value of KSDD is closer to 10, and the disturbance effect of coal mining on the key stratum is greater. In contrast, the value of KSDD is closer to 0, and the disturbance effect of coal mining on the key stratum is smaller.

2.3. The Influencing Factors of KSDD.
The location distribution of the various factors included in formula (1) are shown in Figure 1:

In order to simplify formula (1), according to the location relationship of various factors, the ratio of the interlayer spacing and the mining height (H/M) in formula (1) is defined as "disturbance influence coefficient." The ratio of the interlayer spacing and the buried depth (H/D) is defined as "interburden-to-overburden," And, the $K_{p_i} \cdot (H_i/H) \cdot R_{t_i}$ in formula (1) is defined as "lithology proportion coefficient," which is expressed by the symbol ξ.

In order to simplify the experimental research and analysis, based on formula (1), the lithology proportion coefficient (ξ) is expressed as follows:

$$K_{p_i} \cdot \frac{H_i}{H} \cdot R_{t_i} = K_{p_i} \cdot R_{t_i} \cdot \frac{H_i}{H}$$
$$= \alpha \cdot \beta = \xi, \qquad (2)$$

where ξ is the lithology proportional coefficient, α is the lithology strength coefficient, and β is the lithology ratio:

$$\alpha = K_{p_i} \cdot R_{t_i},$$
$$\beta = \frac{H_i}{H}. \qquad (3)$$

Figure 2 shows the relationship between the defined above and the factors in formula (1) with the KSDD.

2.4. Calculation System of KSDD.
As the geological conditions of coal seam are complex and various, the calculation process of KSDD is cumbersome. Therefore, based on
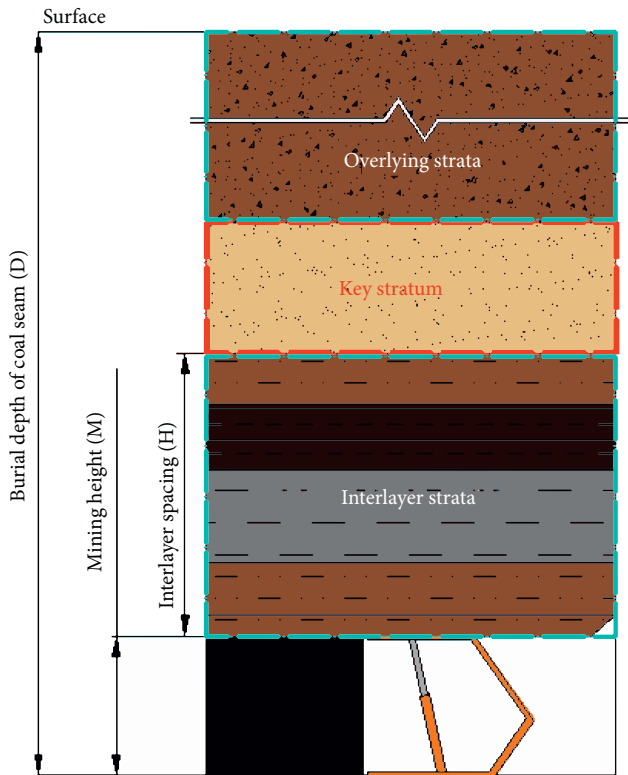
Figure 1: The location relationship of various factors.
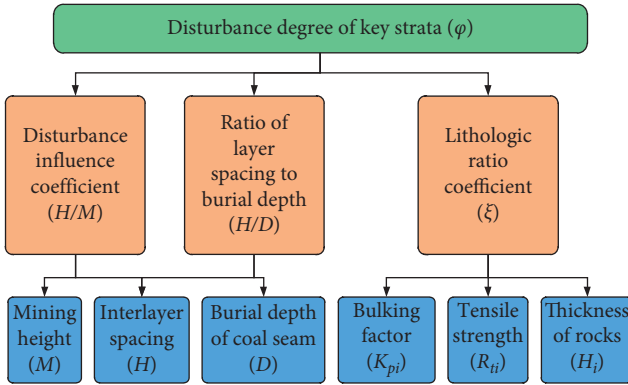
Figure 2: The relationship between influencing factors and KSDD [25].

Figure 3: Calculation system of KSDD.
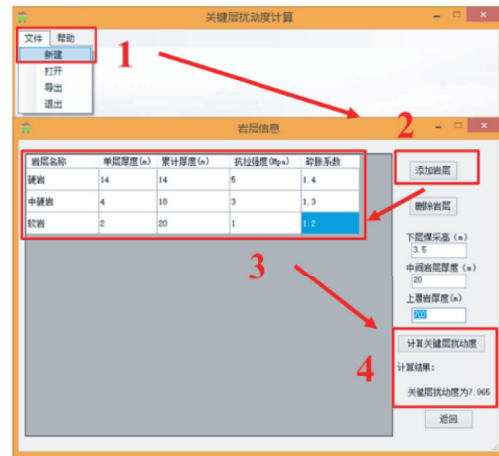
Figure 4: Calculation process of KSDD.

Figure 5: Operation flow of batch calculation for KSDD.

formula (1), the calculation system of KSDD is developed with C# language on ". NET" platform. The home page of the system is shown in Figure 3.

According to Figure 4, the calculation of KSDD can be divided into the following four steps. (1) Click "File"-"New" to enter the calculation interface. (2) Click "Add Rock Stratum" to enter the rock information input interface. (3) Input parameters including the rock strata, the thickness of the single stratum, the cumulated thickness of the rock strata, the tensile strength, the bulking factor, the mining height, the interlayer spacing, and the buried depth. (4) Finally, click to "Calculate the KSDD" to get calculation results.

In addition, batch calculation can be performed according to Figure 5, and the calculation steps are as follows. (1) Save relevant data as ".csv" file in fixed "Excel" format. (2) Click "File"-"Import" and select the ".csv" data file to be imported. (3) After the data are imported, the

KSDD can be calculated. (4) Wait until the data calculation is completed, click "File"-"Export" to get a lot of data.

3. Experimental Design

In order to simplify the subsequent data analysis, the lithology between key stratum and coal seam is set as soft, medium, and hard, respectively. According to the actual geological conditions, the tensile strength of three lithology is set as 1 MPa, 3 MPa, and 5 MPa, respectively. Similarly, the bulking factor is set as 1.2, 1.3, and 1.4, respectively, as shown in Table 1.

In order to obtain the lithology proportion coefficient and show the superimposed influences between strata, three experimental schemes are set up. As shown in Table 2, the soft rock in Scheme 1 reaches 80%, which means the overall lithology between the key stratum and the coal seam is relatively soft. However, the hard rock in Scheme 3 reaches 80%, which means the overall lithology between the key stratum and the coal seam is relatively hard.

According to Table 2, the influences of various factors on KSDD are studied in three schemes. Each scheme selected mining height (M), buried depth (D), and interlayer spacing (H) as the research object. Then, three levels are obtained. The final three factors and three levels' experimental scheme is shown in Table 3.

4. Results and Analysis

4.1. The Experimental Results. The Box–Behnken in Design-Export [27] is used to obtain the experimental design table. The KSDD of each scheme is calculated by the calculation system, and the results are shown in Table 4. In addition, the response surface functions of KSDD with the three kinds of lithology matching schemes are obtained as follows.

(1) Soft:

$$Y_1 = 0.213X_1 + 0.128X_2 - 0.3525X_3 + 0.0502X_1X_2$$
$$- 0.2543X_1X_3 - 0.1518X_2X_3 + 0.0081X_1^2$$
$$- 0.0049X_2^2 + 0.02531X_3^2 + 7.25(R^2 = 0.96).$$
(4)

(2) Medium:

$$Y_1 = 0.1316X_1 + 0.0791X_2 - 0.218X_3 + 0.0312X_1X_2$$
$$- 0.157X_1X_3 - 0.094X_2X_3 + 0.0051X_1^2$$
$$- 0.0029X_2^2 + 0.1569X_3^2 + 4.48(R^2 = 0.96).$$
(5)

(3) Hard:

$$Y_1 = 0.0184X_1 + 0.0184X_2 - 0.0406X_3 + 0.0045X_1X_2$$
$$- 0.0227X_1X_3 - 0.0272X_2X_3 + 0.0003X_1^2$$
$$- 0.0009X_2^2 + 0.0456X_3^2 + 1.28(R^2 = 0.96).$$
(6)

TABLE 1: Value of lithological strength coefficient.

Lithology	Tensile strength R_{ti} (MPa)	Bulking factor K_{Pi}	Lithological strength coefficient α
Soft	1	1.2	1.2
Medium	3	1.3	3.9
Hard	5	1.4	7.0

TABLE 2: Value of lithology proportion coefficient.

Scheme number	Lithology ratio			Lithology proportion coefficient
	Soft (%)	Medium (%)	Hard (%)	
1 (soft)	80	10	10	2.05
2 (medium)	10	80	10	3.94
3 (hard)	10	10	80	6.11

TABLE 3: Three factors and three levels' design.

Factors	Levels		
	−1	0	1
Mining height (M) (m)	1	3	5
Buried depth (D) (m)	300	500	700
Interlayer spacing (H) (m)	20	40	60

The goodness-of-fit (R^2) of three schemes are close to 1, so the three regression models are significant.

4.2. The Analysis of Variance. The results of response surface variance are shown in Table 5.

In response surface experiment, the significance of each factor in the regression model is related to P valued. If $P < 0.05$, it means that the factor is significant, otherwise, it is not significant. In addition, if the F valued is larger, it means that the factor has a greater impact on the dependent variable [28, 29].

As shown in Table 5, it can be seen that the three factors are significant because P valued of three factors are more than 0.05. However, when the lithology proportional coefficient increases, the significance of the model decreases. Moreover, by comparing the F valued with three schemes, the influence order of each factor on KSDD can be obtained as follows: interlayer spacing > mining height > buried depth.

4.3. The Analysis of Single Factor. In order to more intuitively analyse the influence of each factor on KSDD, the relationships between each factor and the value of KSDD are obtained as shown in Figures 6–8.

4.3.1. Influences of Mining Height. As shown in Figure 6, the values of KSDD are linearly positively correlated with the mining height. That is to say, the increase of mining height increases the disturbance effect on the key stratum. In addition, the range of KSDD between 1 m and 5 m is 0.238 in (a), the range 1 m and 5 m is 0.147 in (b), and the range between 1 m and 5 m is 0.043 in (c). It can be inferred that, as the lithology proportion coefficient increases, the impacts' range of mining height changes on the key stratum decreases.

TABLE 4: Response surface calculation results.

Scheme number	Input			Output		
	Mining height (M)	Buried depth (D)	Interlayer spacing (H)	KSDD (φ) (soft)	KSDD (φ) (medium)	KSDD (φ) (hard)
1	1	700	40	7.152	4.421	1.286
2	3	700	20	8.175	5.054	1.470
3	1	300	40	7.106	4.393	1.278
4	3	300	60	7.117	4.400	1.280
5	3	500	40	7.246	4.479	1.303
6	5	500	60	7.200	4.451	1.295
7	3	500	40	7.246	4.479	1.303
8	1	500	20	7.306	4.517	1.314
9	3	700	60	7.179	4.438	1.291
10	3	500	40	7.246	4.479	1.303
11	1	500	60	7.097	4.387	1.276
12	5	500	20	8.426	5.209	1.515
13	5	700	40	7.493	4.632	1.347
14	3	500	40	7.246	4.479	1.303
15	5	300	40	7.246	4.479	1.303
16	3	500	40	7.246	4.479	1.303
17	3	300	20	7.506	4.640	1.350

TABLE 5: Variance results of the regression model.

Scheme number	Origins	Sum of squares	Freedom	Mean square	F valued	P valued
	Model	2.12	9	0.2357	17.72	0.0005
	Mining height	0.363	1	0.363	27.29	0.0012
1 (soft)	Buried depth	0.1311	1	0.1311	9.85	0.0164
	Interlayer spacing	0.9941	1	0.9941	74.73	0.0001
	Residual error	0.0931	7	0.0133		
	Summation	2.21	16			
	Model	0.8113	9	0.0901	17.7	0.0005
	Mining height	0.1386	1	0.1386	27.22	0.0012
2 (medium)	Buried depth	0.0501	1	0.0501	9.84	0.0165
	Interlayer spacing	0.3802	1	0.3802	74.67	0.0001
	Residual error	0.0356	7	0.0051		
	Summation	0.8469	16			
	Model	0.0684	9	0.0076	17.54	0.0005
	Mining height	0.0038	1	0.0038	8.65	0.0217
3 (hard)	Buried depth	0.0019	1	0.0018	4.15	0.0809
	Interlayer spacing	0.0088	1	0.0088	20.3	0.0028
	Residual error	0.003	7	0.0004		
	Summation	0.0715	16			

4.3.2. Influences of Buried Depth. As shown in Figure 7, the buried depth of coal seam has a positive linear correlation with KSDD. To be specific, the increase of buried depth increases the disturbance effect on the key stratum. In addition, the range of KSDD between 300 m and 700 m is 0.143 in (a), the range 300 m and 700 m is 0.088 in (b), and the range between 300 m and 700 m is 0.026 in (c). It can be inferred that, as the lithology proportion coefficient increases, the impacts of buried depth changes on the key stratum decrease.

4.3.3. Influences of the Interlayer Spacing. As shown in Figure 8, the values of KSDD are negatively correlated with the interlayer spacing. That is to say, the increase of interlayer spacing decreases the disturbance effect on the key

stratum. Then, when the value of interlayer spacing is less than 30 m, the influence is more severe. However, when the value of interlayer spacing is more than 50 m, the disturbance effects on the key stratum tend to be gentle. In addition, as the lithology proportion coefficient increases, the impacts of interlayer spacing changes on the key stratum decrease.

4.3.4. Influences of Disturbance Influence Coefficient. As shown in Figure 9, with the increase of the disturbance influence coefficient, the impact on the key stratum decreases. However, when the disturbance influence coefficient increases to a certain value, the decrease of KSDD tends to be gentle. And, when the disturbance influence coefficient is less than 10, the impact on the key stratum is more serious,
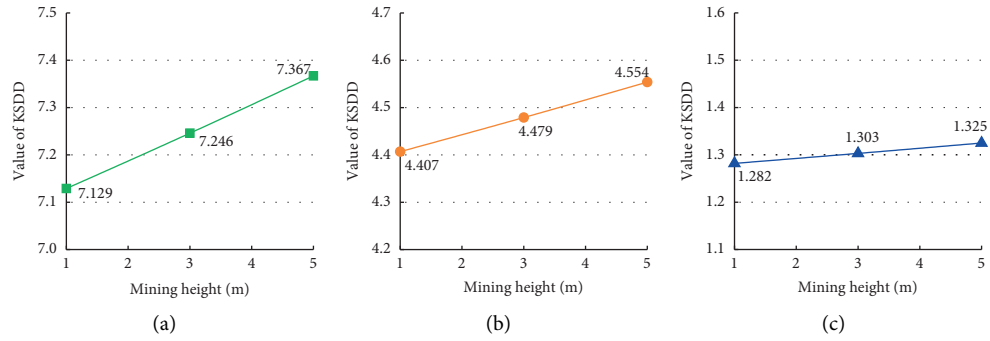
FIGURE 6: Impacts of mining height with different lithology proportion coefficients on the key stratum. (a) Soft. (b) Medium. (c) Hard.
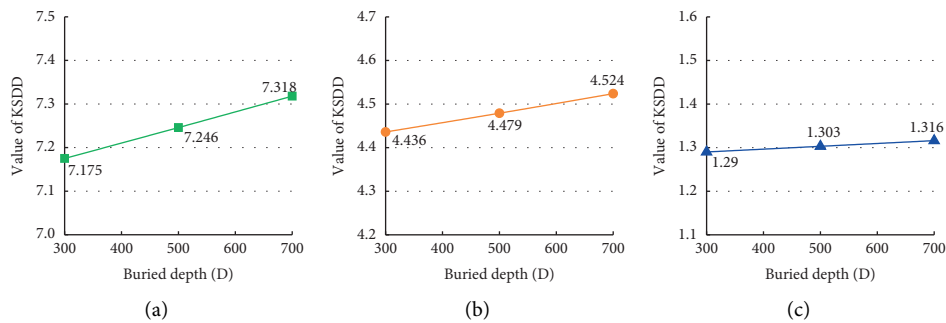
FIGURE 7: Impacts of buried depth with different lithology proportion coefficients on the key stratum. (a) Soft. (b) Medium. (c) Hard.
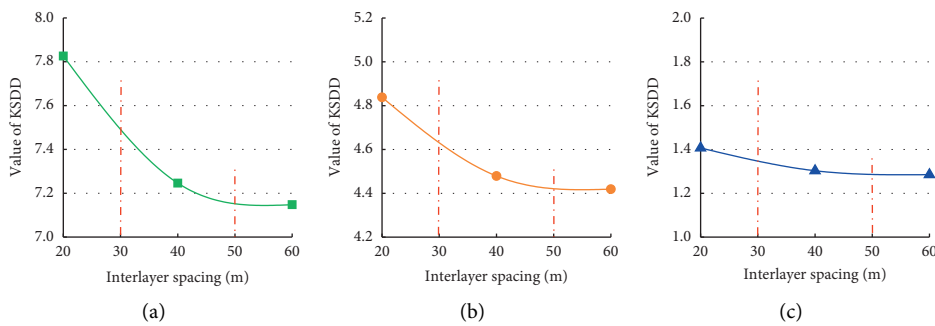
FIGURE 8: Impacts of interlayer spacing with different lithology proportion coefficients on the key stratum. (a) Soft. (b) Medium. (c) Hard.

but when the disturbance influence coefficient is more than 10, the impact is gentle. In addition, as the lithology proportion coefficient increases, the curve gradually becomes gentle. That is to say, the increase of lithology proportion coefficient reduces the influence range of the disturbance influence coefficient.

4.3.5. Influences of Interburden-to-Overburden. Similarly, with the increasing values of interburden-to-overburden, the impacts on the key stratum decrease, as shown in Figure 10. However, when the value of interburden-to-overburden increases to a certain value, the decrease of KSDD tends to be gentle. And, when the value of interburden-to-overburden is less than 0.06, the impact on the key stratum is more serious, but when the disturbance influence coefficient is more than 0.06, the impact is gentle. In addition, as the lithology

proportion coefficient increases, the curve gradually becomes gentle. That is to say, the increase of lithology proportion coefficient reduces the influence range of interburden-to-overburden.

In general, the impacts of disturbance influence coefficient and interburden-to-overburden on KSDD are roughly similar. However, compared with the disturbance influence coefficient, the impact of interburden-to-overburden on the key stratum is relatively small. It further shows that the impact of buried depth on the key stratum is less than mining height.

4.4. The Analysis of Multifactors. The KSDD is affected not only by the single factor (mining height, buried depth, interlayer spacing, and lithology proportional coefficient) but also by the interaction of factors. Therefore, in order to
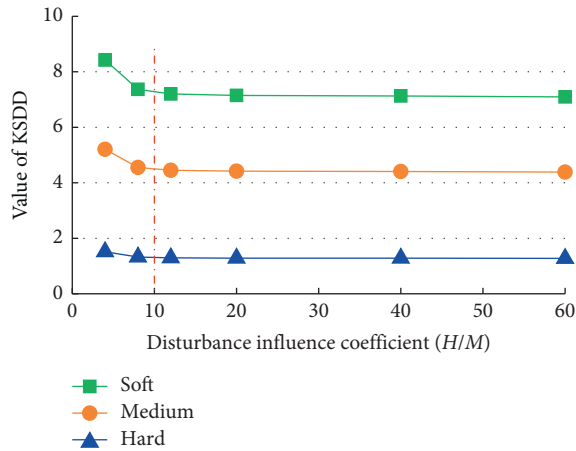
FIGURE 9: Impacts of disturbance influence coefficient on the key stratum.
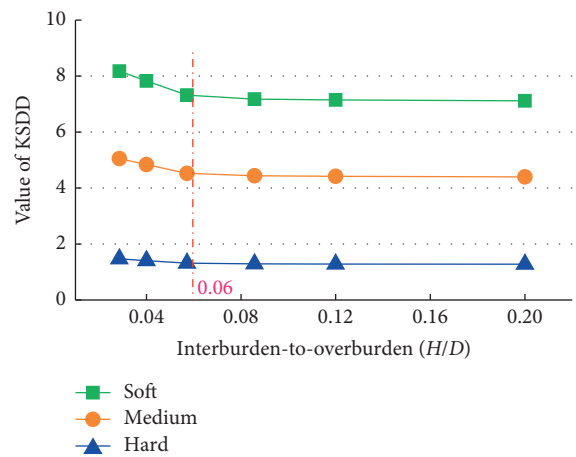
FIGURE 10: Influence of interburden-to-overburden on disturbance degree of the key stratum.

explore the impacts of the interaction between factors on the key stratum, based on the calculation results of KSDD, the 3D response surfaces of each factor interaction are obtained (Figures 11–13).

4.4.1. Interaction between Mining Height and Buried Depth on Key Stratum. As shown in Figure 11, with the increase of mining height and burial depth, the response surface becomes steeper, which indicates that the impacts on the key stratum increase. However, with the increase of the lithology proportion coefficient, the response surface gradually tends to be gentle. That is to say, the increase of lithology proportion coefficient decreases the range of impacts by mining height and buried depth on the key stratum. In addition, according to the distribution trend of contour, with the increase of buried depth, the disturbance effect of mining height on the key stratum is strengthened.

4.4.2. Interaction between Mining Height and Interlayer Spacing on Key Stratum. As shown in Figure 12, with the increase of interlayer spacing and the decrease of mining

height, the response surface gradually becomes gentle, which indicates that the impacts on the key stratum decrease. However, with the increase of the lithology proportion coefficient, the response surface gradually tends to be gentle. That is to say, the increase of the lithology proportion coefficient decreases the range of impacts by interlayer spacing and mining height on the key stratum. In addition, according to the distribution trend of contour, the impacts on the key stratum is the most severe when the interlayer spacing is within 30 m. Therefore, when the key stratum is close to the coal seam, the mining height can be appropriately reduced to slow down the disturbance effect of coal mining on the key stratum.

4.4.3. Interaction between Buried Depth and Interlayer Spacing on Key Stratum. As shown in Figure 13, with the increase of interlayer spacing and the decrease of coal seam buried depth, the response surface gradually becomes gentle, which indicates that the impacts on the key stratum decrease. However, with the increase of lithology proportion coefficient, the response surface gradually tends to become gentle. That is to say, the increase of lithology proportion coefficient decreases the range of impacts by interlayer spacing and buried depth on the key stratum. In addition, according to the distribution trend of contour, it can be seen that, with the increase of buried depth, the range of impacts by interlayer spacing on the key stratum increases. Therefore, when coal seam is in the deep area or the coal seam is close to the key stratum, the key stratum is more seriously affected by coal seam mining. And the method of backfilling can be used to reduce the disturbance effect of coal seam mining on the key stratum.

5. Engineering Verification

Based on the geological data of Longde Coal Mine [30], Yuhua Coal Mine [31], Da'anshan Coal Mine [32], Qianjiaying Coal Mine [25], and Fangezhuang Coal Mine [33], the values of KSDD in each mining area is calculated by the calculation system of KSDD. The results are shown in Table 6.

As shown in Table 6, when the buried depth and interlayer spacing are basically the same, the values of KSDD are affected by mining height and lithology proportion coefficient. Therefore, roof management should be strengthened in areas with large mining height to prevent roof fall and other disasters caused by mining height increase. When the mining height and interlayer spacing are basically the same, the values of KSDD are mainly affected by the buried depth and the lithology proportion coefficient. Therefore, when mining in Yuhua Coal Mine and other areas with large buried depth, the key stratum is more likely to be destroyed, which makes the overlying strata more difficult to control and easily bring disasters such as rock burst. When the lithology proportion coefficient decreases, the values of KSDD are greatly affected by the changes of mining height, buried depth, and interlayer spacing. That is to say, when there is
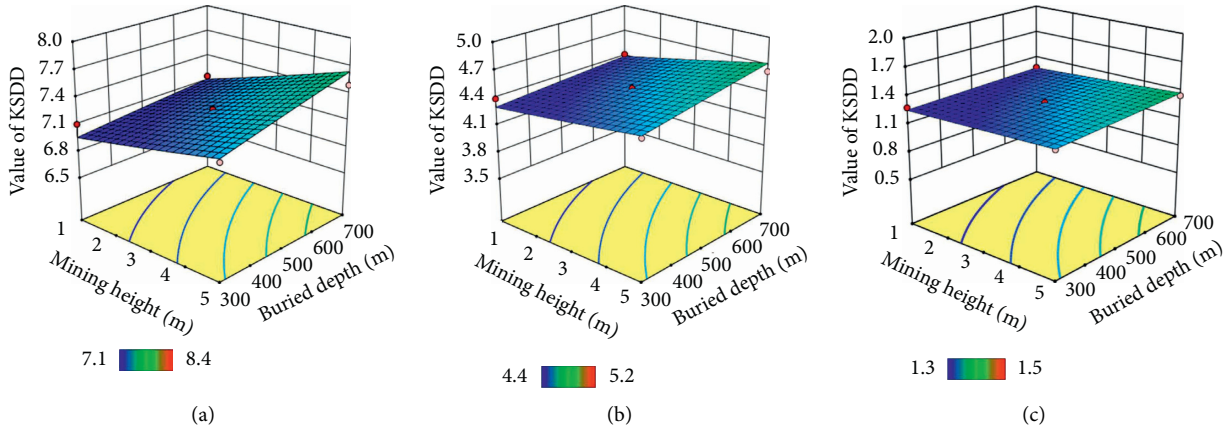
FIGURE 11: 3D response surface of interaction between mining height and buried depth. (a) Soft. (b) Medium. (c) Hard.
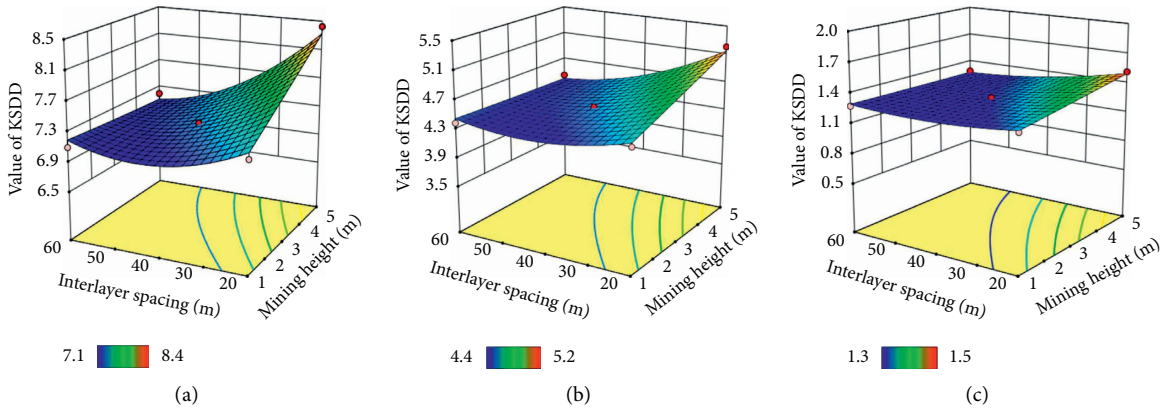
FIGURE 12: 3D response surface of interaction between mining height and interlayer spacing. (a) Soft. (b) Medium. (c) Hard.
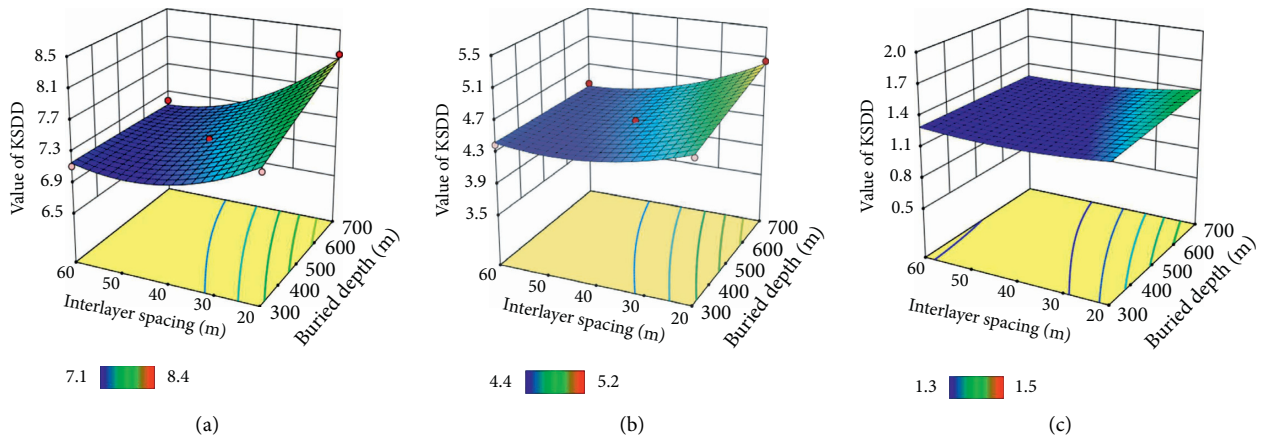
FIGURE 13: 3D response surface of interaction between buried depth and interlayer spacing. (a) Soft. (b) Medium. (c) Hard.

less intermediate hard rock, the changes of mining height, buried depth, and interlayer spacing need to be paid attention to, which will lead to more damage to the key stratum. In general, the above rules are basically consistent with the actual situation, which further verifies the above experimental results.

TABLE 6: Statistics of KSDD in each mine.

| Number | Name of mine | Mining height M (m) | Buried depth D (m) | Interlayer spacing H (m) | Intermediate stratum | | Disturbance degree of key stratum |
					Lithology	Percentage (%)	
1	Longde	3.96	120	80	Sandstone	65.97	2.823
					Mudstone	34.03	
2	Yuhua	6.87	600	20	Siltstone	33.00	2.566
					Mudstone	2.50	
					Fine sandstone	67.50	
3	Da'anshan	2.23	500	10	Siltstone	65.00	6.64
					Mudstone	35.00	
4	Fangezhuang	3.16	500	15	Siltstone	35.00	4.512
					Fine sandstone	65.00	
5	Qianjiaying	2.3	500	14	Carbonaceous mudstone	19.70	3.138
					Siltstone	80.30	

6. Conclusion

Synthesizing the experiment designed of response surface, calculation results of KSDD, and analyses of single factor and multifactors, the following main conclusions are drawn:

(1) Though the analysis of the key stratum affected by several geological factors, the definition of "disturbance degree of key stratum" (KSDD) was proposed. To be specific, KSDD is the degree of disturbance caused by coal seam mining on the key stratum. Based on the calculation formula of KSDD, the calculation system is developed. And, the value of KSDD is quantified by the value among 0 to 10. In addition, the response plane method is used to design the experiment of three kinds of lithology proportional coefficient with a different mining height, buried depth and interlayer spacing. The response surface regression models of three lithology proportional coefficients are established.

(2) By analysing the disturbance effect of a single factor on the key stratum and its significance, the following are found. ① The order of influence intensity of each factor on the KSDD is as follows: interlayer spacing > mining height > buried depth. ② Mining height and buried depth are positively correlated with the value of KSDD. ③ The interlayer spacing is negatively correlated with KSDD, but when the interlayer spacing increases to a certain value, the influence range of KSDD tends to be small.

(3) The KSDD is affected not only by a single factor but also by the interaction of various factors. That is to say, with the increase of buried depth, the impacts of mining height on the key stratum increase. And, with the decrease of interlayer spacing, the disturbance effects of mining height on the key stratum are more severe. In addition, with the increase of buried depth, the change of interlayer spacing increases the influence range of KSDD. However, with the increase of lithology proportional coefficient, the influence range of KSDD decreases with the three factors.

(4) The actual geological data of five mines are selected to calculate the value of KSDD. And, the variation law of KSDD in each mine is analysed. The calculation rules of KSDD of five mines further verified the above experimental results, which provide some reference and theoretical basis for the management of the roof and the design of backfilling parameters.

Data Availability

The data used to support the findings of this study are included within the article.

Conflicts of Interest

The authors declare that there are no conflicts of interest regarding the publication of this paper.

Acknowledgments

References

[1] M.-G. Qian and P.-W. Shi, *Mine Pressure and Strata Control*, China University of mining and Technology Press, Xuzhou, China, 2003.

[2] M.-G. Qian, X.-X. Miao, and F.-L. He, "Key block analysis of "masonry beam" structure in stope," *Journal of China Coal Society*, vol. 6, pp. 557–563l, 1994.

[3] M.-G. Qian and J.-L. Xu, "Behaviors of strata movement in coal mining," *Journal of China Coal Society*, vol. 44, no. 4, pp. 973–984, 2019.

[4] J.-L. Xu, "Strata control and scientific coal mining—a celebration of the academic thoughts and achievements of academician minggao qian," *Journal of Mining & Safety Engineering*, vol. 36, no. 1, pp. 1–6, 2019.

[5] S.-L. Yang, H. Yue, G.-F. Song, J. Wang, Y. Ma, and F. Liu, "3D physical modelling study of shield-strata interaction

under roof dynamic loading condition," *Shock and Vibration*, vol. 2021, Article ID 6618954, 7 pages, 2021.

[6] D.-Z. Kong, S.-J. Pu, Z.-H. Cheng, and G. Wu, "Coordinated deformation mechanism of the top coal and filling body of gob-side entry retaining in a fully mechanized caving face," *International Journal of Geomechanics*, vol. 21, no. 4, 2021.

[7] M.-G. Qian, J.-L. Xu, and J.-C. Wang, "Further on the sustainable mining of coal," *Journal of China Coal Society*, vol. 43, no. 1, pp. 1–13, 2018.

[8] J.-C. Wang, "Sustainable coal mining based on mining ground control," *Journal of Mining and Strata Control Engineering*, vol. 1, no. 2, pp. 40–47, 2019.

[9] D.-Z. Kong, Z.-B. Cheng, and S.-S. Zheng, "Study on the failure mechanism and stability control measures in a large-cutting-height coal mining face with a deep-buried seam," *Bulletin of Engineering Geology and the Environment*, vol. 78, no. 8, pp. 6143–6157, 2019.

[10] Y.-F. Ren, "Analysis of dynamic stress characteristics and surrounding rock structure in shallow-buried longwall mining face," *Coal Science and Technology*, vol. 48, no. 8, pp. 50–56, 2020.

[11] S.-L. Yang, J.-C. Wang, and L.-H. Li, "Deformation and fracture characteristics of key strata based on the medium thick plate theory," *Journal of China Coal Society*, vol. 45, no. 8, pp. 2718–2727, 2020.

[12] S.-L. Yang, Z.-H. Wang, and H.-Y. Lv, "Analysis of structure stability of main roof and dynamic loading effect during periodic weighting in a large mining height stope," *Journal of Mining & Safety Engineering*, vol. 36, no. 2, pp. 315–322, 2019.

[13] Q.-H. Huang, J. L. Zou, L.-T. Ma, and P. Tang, "Double key strata structure analysis of large mining height longwall face in nearly shallow coal seam," *Journal of China Coal Society*, vol. 42, no. 10, pp. 2504–2510, 2017.

[14] Q.-H. Huang, "Research on roof control of water conservation mining in shallow seam," *Journal of China Coal Society*, vol. 42, no. 1, pp. 50–55, 2017.

[15] H.-K. Han, X.-L. Wang, J.-L. Xu, Y. Wu, and Y. Ji, "Study on the movement characteristics and "re-stabilization" conditions of overlying key stratum structure after losing stability," *Journal of Mining & Safety Engineering*, vol. 35, no. 4, pp. 734–741, 2018.

[16] Q.-G. Yu, H.-X. Zhang, W.-N. Deng et al., "Analysis of influencing factors of surface skewed subsidence based on key strata theory," *Journal of China Coal Society*, vol. 43, no. 5, pp. 1322–1327, 2018.

[17] J.-L. Zhou and Q.-H. Huang, "Stability analysis of key stratum structures of large mining height longwall face in shallow coal seam," *Chinese Journal of Rock Mechanics and Engineering*, vol. 38, no. 7, pp. 1396–1407, 2019.

[18] X.-Y. Shun, M.-J. Lu, C. Li, and M. Miao, "Optimal selection of staggered distance mining in double seams and its influence on water-resisting key strata," *Journal of Mining & Safety Engineering*, vol. 38, no. 1, pp. 51–57+67, 2021.

[19] C. Zang, X.-L. Wang, S.-G. Li, C. Liu, J. Xue, and H. Liu, "Optimization of the ratio of modified alkaline solution for hydrogen sulfide treatment in coal mine based on response surface method," *Journal of China Coal Society*, vol. 45, no. 8, pp. 2926–2932, 2020.

[20] H. Yang, W. Zhou, G. Ma, S. Li, and X. L. Chang, "Inversion of instantaneous and rheological parameters of high rockfill dams based on response surface method," *Rock and Soil Mechanics*, vol. 37, no. 6, pp. 1697–1705, 2016.

[21] G.-R. Feng, X.-Q. Jia, Y.-X. Guo et al., "Study on mixture ratio of gangue-waste concrete cemented paste backfill," *Journal of Mining & Safety Engineering*, vol. 33, no. 6, pp. 1072–1079, 2016.

[22] J.-F. Lou, F.-Q. Gao, and J.-H. Yang, "Characteristics of evolution of mining-induced stress field in the longwall panel: insights from physical modeling," *International Journal Coal Science and Technology*, vol. 6, 2021.

[23] Z.-B. Cheng, L.-H. Li, and Y.-N. Zhang, "Laboratory investigation of the mechanical properties of coal-rock combined body," *Bulletin of Engineering Geology and the Environment*, vol. 79, no. 4, pp. 1947–1958, 2020.

[24] J.-F. Lou, "Research and application of hydraulic support simulation system for large-scale working face physical modeling experiment," *Coal Science and Technology*, vol. 46, no. 5, pp. 67–73+80, 2018.

[25] Y. Li, M.-X. Lei, Q.-X. Zheng, D. Liushu, N. Lui, and L. H. Liu, "Quantitative criterion on coordinated ascending mining in close multiple "thin-medium-thick" coal seams," *Journal of China Coal Society*, vol. 44, no. S2, pp. 410–418, 2019.

[26] Y. Li, J.-P. Wang, Y.-D. Chen et al., "Study on effect of interburden on movement of overburden in multiple coal seams," *Coal Science and Technology*, vol. 48, no. 4, pp. 246–255, 2020.

[27] Design-Export, 12.0.3.0, 2019, Stat-Ease, 1300 Godward Street Northeast, Suite 6400, Minneapolis, MN 55413, file:///J:/Program%20Files/Design-Expert%2012/help/designs/rsm.html#randomized, 10/09/2019.

[28] D. Li, G.-R. Feng, Y.-X. Guo et al., "Analysis on the strength increase law of filling material based on response surface method," *Journal of China Coal Society*, vol. 41, no. 2, pp. 392–398, 2016.

[29] J.-K. Jiao, W.-J. Ju, and Y.-L. Feng, "Multi-factors analysis of the stability of roadway under coal pillar based on response surface method," *Journal of Mining & Safety Engineering*, vol. 34, no. 5, pp. 933–939, 2017.

[30] L.-Y. Li, "Study on field measuring of overburden failure height in fully-mechanized coal mining with large mining height in thick coal seam with shallow buried depth and thin bedrock," *China Energy and Environmental Protection*, vol. 39, no. 5, pp. 206–209, 2017.

[31] S.-C. Gu, X.-M. Wang, J. Xue et al., "Analysis of the relationship between floor heave deformation and abutment pressure in mining roadway of deep well," *Mining Safety & Environmental Protection*, vol. 1-6, 2021.

[32] B. Liang, L.-H. Shan, G. Li, and J. Jin, "Feasibility study of upward mining of close distance and inclined coal seam group in daanshan mining area," *Science and Technology Review*, vol. 30, no. 33, pp. 45–49, 2012.

[33] X.-H. Wang, "Mine pressure behavior law and feasibility study of upward mining for short distance coal seams in Fan'gezhuang coal mine," *China Mining*, vol. 30, no. 2, pp. 189–196, 2021.

Research Article

Research on the Influence of Weak Interlayer in Open-Pit Slope on Stability

Zhong Shuheng and Miao Yinjun [ID]

School of Energy and Mining Engineering, China University of Mining & Technology (Beijing), Beijing 100083, China

Correspondence should be addressed to Miao Yinjun; miaoyinjun@yeah.net

Received 3 June 2021; Accepted 30 June 2021; Published 8 July 2021

Academic Editor: Dezhong Kong

The weak interlayer in the slope meets with water threatening the overall stability of the slope. Sequestration location of the weak layer has an impact on the stability of the slope. Based on this, taking the south-side slope of Fushun West Open-Pit Mine as the background, the limit equilibrium method was used to study the influence of different depths and dip angles of weak interlayers on the factor-of-safety and sliding mode of the slope. After analyzing the effect, a bottom friction experiment was conducted to verify the theoretical results. The research results show that, as the buried depth of the weak layer becomes larger and the dip angle becomes smaller, the safety factor of the slope increases. Dip angle and depth both affect the sliding mode of the slope. This can provide a reference for study of the influence mechanism of weak interlayer on slope stability in multi-weak-layer slopes.

1. Introduction

Slope landslide is one of the three natural disasters. There are about 35,000 instability accidents due to weak interlayers in slopes ever year in China. These accidents pose a serious threat to the national property and people's lives [1].

In reality, the geological structure of the slope is complex, usually containing more than one weak interlayer. Studying which weak interlayer has the greatest impact on slope stability and the reasons are of great significance to the prevention and control of landslides.

Sloan [2] analyzed the slope with weak interlayer and verified that the weak interlayer is the main factor controlling the slope landslide. Li et al. [3] conducted a large-scale geomechanical model experiment to study the influence of rainfall infiltration on the slope characters. Liu et al. [4] studied the influence of the hydrological characteristics of the fracture zone composed of clay minerals on the slope stability. Li [5] studied the potential slip surface of the representative section of the southern slope of Fushun West Open-Pit Mine and determined that the potential slip surface is the weak interlayer in the slope. Sun and Li [6] studied open-pit mine slope stability based on improved TOPSIS method. In summary, as for research on the weak interlayers in slope, domestic scholars have focused on the changes in the mechanical properties of weak interlayers after being softened by water. However, there are few studies on the influence of the location of the softened weak layer on the overall stability and sliding mode of the slope. In this paper, the influence of the buried depth and dip angle of the weak layer on the slope stability and sliding mode is analyzed based on the background of the south slope of Fushun West Open-pit Mine. Then, a similar model experiments is conducted to validate the analysis results.

2. Influence of Weak Interlayer on Slope Stability and Sliding Mode

2.1. Mechanism of Weak Interlayer Softening. The weak interlayer is rich in clay minerals and has strong expansibility when exposed to water, which greatly reduces the shear strength of the weak interlayer [7–9]. According to the unsaturated soil strength theory [10,11], there is the following relationship between soil shear strength and matrix suction:

$$\tau_f = c' + (\sigma - u_\alpha)\tan \phi' + (u_\alpha - u_w)\tan \phi^b, \quad (1)$$

where τ_f is the shear strength, c' is the effective cohesion, σ is the normal stress, u_α is the atmosphere pressure, u_w is the

pore water pressure, $u_\alpha - u_w$ is the matrix suction, ϕ' is the friction angle in saturated state, and ϕ^b is the friction angle that varies with suction.

It can be seen from formula (1) that there is a linear function relationship between the shear strength of the weak interlayer and the suction force of the matrix. When the water content of the weak layer increases, the pore water pressure will increase, the matrix suction will decrease, and the shear strength will decrease.

2.2. Limit Equilibrium Analysis of Weak Layer Affecting Slope Stability. The model used in this paper comes from the E1200 section of the south slope of the Fushun West Open-Pit Mine. The stratigraphic composition is mainly Archean granite-gneiss, strongly weathered basalt, and weakly weathered basalt. There are 3 weak interlayers that can be proven. The simplified slope profile is shown in Figure 1. In Figure 1, the weak interlayers are marked as weak layer 1, weak layer 2, and weak layer 3 from top to bottom. Strongly weathered basalt is located above weak layer 1, and weakly weathered basalt is located between weak layer 1 and granite-gneiss.

By collecting, summarizing, and analyzing the rock and soil test results of previous projects, the rock mechanics parameters required for this calculation are shown in Table 1.

The factor-of-safety and factor-of-safety reduction ratio of the slope after softening of different weak interlayers are calculated based on the limit equilibrium method. The results are shown in Tables 2 and 3, respectively.

After comparing the safety factor reduction ratio of the three softened weak layers, obviously the softening of weak layer 1 has the greatest impact on the overall stability of the slope, followed by weak layer 2 and weak layer 3, the smallest in the model studied in this paper.

Judging from the sequestration location of the three weak layers in the slope, the buried depths and dip angles of the three weak layers are different, resulting in different degrees of influence on the slope of the three weak interlayers. The following uses the limit equilibrium method to calculate the safety factor of the slope to explore how the buried depth and dip angle of the weak interlayer affect the stability of the slope. Due to the dip angle, the buried depth of the weak layer has no definite value. In this paper, the vertical distance between the weak layer and the slope toe is defined as the buried depth of the weak interlayer. According to the above research model, the in situ burial depth of weak interlayer 1 is 40 m, and the base rock below the weak layer does not slide. The weathered basalt lies above the weak layer. The burial depth of the weak interlayer is increased by 20 m, and the safety factor of the slope and changing trend of slip surface is calculated by the limit equilibrium method. The results are shown in Table 4.

As shown in Table 4, when the buried depth of the weak interlayer increases while other factors remain unchanged, the safety factor of the slope gradually increases. The buried depth increases from the original 40 m to 80 m, and the sliding mode of the slope is sliding along the weak layer.

When the buried depth is greater than 99 m, the safety factor is still increasing, but its sliding mode becomes shallow sliding along the slope surface. Therefore, when the dip angle is 23°, the buried depth of 99 m is the critical value for the change of the slope sliding mode.

According to the research model, the dip angle of weak interlayer 1 in the original position is 23°. Set the part below the weak layer as a non-slip bedrock, and the part above it as a strongly weathered basalt. Inclination angle increment is 3°. The results of the safety factor of the slope and changing trend of slip surface calculated by the limit equilibrium method are shown in Table 5.

It can be seen from Table 5 that when the dip angle of the weak interlayer decreases while other factors remain unchanged, the safety factor of the slope gradually increases. When the dip angle of the weak interlayer decreases from the original 23° to 9°, the sliding mode of the slope is sliding along the weak layer. When the dip angle of the weak interlayer is less than 8°, the safety factor is still increasing, but the sliding mode changes, and the sliding mode at this time becomes a shallow sliding along the slope.

Selecting the buried depth as 10 m, 70 m, and 140 m, when the slope is in the critical state of sliding along the shallow layer of the slope, the trend of the dip angle is shown in Table 6.

Taking the buried depth as the horizontal axis and the dip angle as the vertical axis, linear fitting is performed from the results obtained in Table 6. The law of the sliding mode of the slope is shown in Figure 2.

It can be seen from Figure 2 that the relationship between the buried depth and the dip angle is linear. The fitted straight line divides the first coordinate system into two parts. Take the value of the buried depth and dip angle at the upper left of the line; the slope will slide along the weak interlayer, and take the value of the buried depth and dip angle at the lower right of the line; the slope will slide shallowly, and the dividing line is the straight line obtained by linear fitting.

3. Bottom Friction Experiment

3.1. Design of the Experiment. When the three weak interlayers in the model are softened, it is the interlayer 1 that affects the stability of the slope most. Therefore, this section studies the influence of different dip angles and buried depths of weak layer 1 on slope stability and sliding mode to verify the calculation result of the limit equilibrium method.

Generalize the geological prototype. The generalized prototype is 1000 m long and 450 m high. Combined with the actual situation of the bottom friction test bench size: length × width × thickness = 1.0 m × 1.0 m × 0.05 m, the geometric similarity ratio of the simulation test is determined as $C1 = 1000:1$. The test model is shown in Figure 3.

Similar model experiment requires that the model is not only similar in geometry to the prototype, but also requires the physical quantities included in the test process to be similar to the prototype. This experiment uses a mixed material of sand, lime, and gypsum in different proportions to simulate the bedrock and basalt above it [12]. After
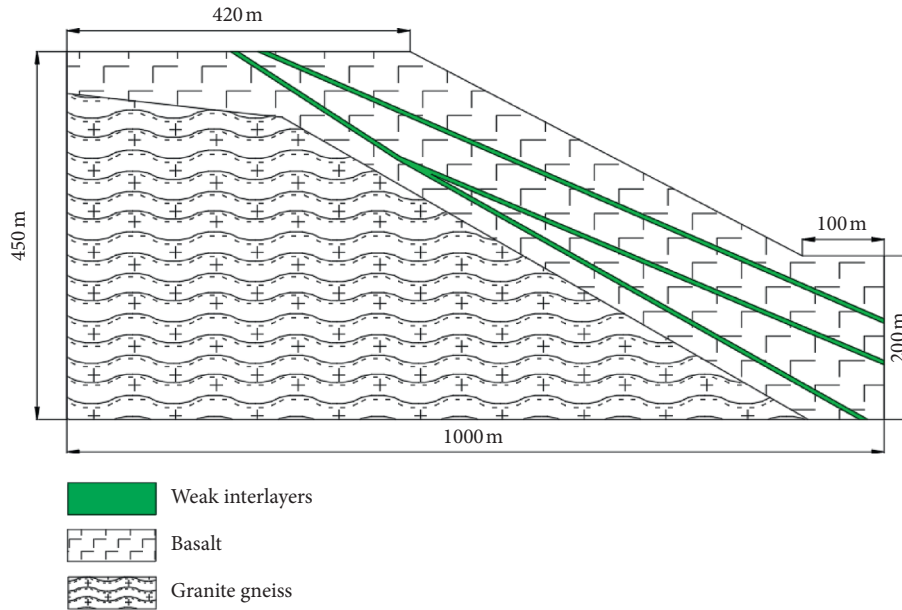
FIGURE 1: Simplified map of E1200 geological section.

TABLE 1: Rock mechanical parameters of each rock formation.

	Elastic modulus, E (MPa)	Cohesion, C (kPa)	Friction, Φ (°)	Poisson's ratio, v	Volumetric weight, ρ (g·cm^{-3})
Granite gneiss	50000	30000	50	0.23	2.8
Weakly weathered basalt	11892	1810	37.2	0.26	2.6
Strongly weathered basalt	7824	1690	36.7	0.28	2.43
Weak interlayer 1	1076	220	21.6	0.32	2.4
Weak interlayer 2	1506	330	25.1	0.3	2.35
Weak interlayer 3	2500	450	30	0.3	2.0

TABLE 2: Factor-of-safety of the slope after softening of different weak layers.

	Factor-of-safety			
	Ordinary	Bishop	Janbu	Janbu generalized
Dry slope	1.068	1.100	1.068	1.109
Weak layer 1 softening	0.689	0.613	0.607	0.713
Weak layer 2 softening	0.950	0.971	0.912	1.048
Weak layer 3 softening	1.068	1.100	1.068	1.109

TABLE 3: Factor-of-safety reduction ratio of the slope after softening of different weak layers.

	Factor-of-safety reduction ratio			
	Ordinary (%)	Bishop (%)	Janbu (%)	Janbu generalized (%)
Weak layer 1 softening	35.48	44.27	43.16	35.71
Weak layer 2 softening	11.05	11.73	14.61	5.5
Weak layer 3 softening	0	0	0	0

Table 4: The relationship between buried depth of weak interlayer and slope stability.

Buried depth (m)	Safety factor	Sliding mode
40	1.069	Sliding along the weak layer
60	1.185	Sliding along the weak layer
80	1.314	Sliding along the weak layer
99	1.460	Shallow sliding on slope
120	1.461	Shallow sliding on slope

Table 5: The relationship between dip angle of weak interlayer and slope stability.

Dip angle (°)	Safety factor	Sliding mode
23	1.069	Sliding along the weak layer
20	1.158	Sliding along the weak layer
17	1.232	Sliding along the weak layer
14	1.307	Sliding along the weak layer
11	1.394	Sliding along the weak layer
8	1.460	Shallow sliding on slope

repeated tests, the percentage of each material is determined as shown in Table 7.

In order to verify the influence of the dip angle and buried depth of the weak interlayer on the stability and sliding mode of the rock slope, a total of four sets of experiments were designed: experiment 1—the weak layer is in the original position (23°, 44 mm); experiment 2—the dip angle decreases (8°, 44 mm); experiment 3—the buried depth increases (23°, 120 mm); and experiment 4— the dip angle and the buried depth both increase (29°, 100 mm).

3.2. Experiment Results and Analysis

3.2.1. Experiment 1: The Weak Layer Is in the Original Position (23°, 44 mm). When the slope is in the original state, the break process of the slope is shown in Figure 4.

Start the bottom friction machine; after running for 21 seconds (Figure 4(b)), the first crack L1 appeared at the foot of the basalt layer slope, the crack width was about 1 mm, and it penetrated the weak interlayer of the lower layer; after 23 seconds (Figure 4(c)), a new crack L2 appeared at the foot of the basalt slope, and a crack L3 appeared at the slope surface, which also penetrated the weak interlayer; after 26 seconds (Figure 4(d)), cracks L4, L5, and L6 appeared on the slope. At this time, the foot of the basalt in the upper part of the slope was completely destroyed; after 33 seconds (Figure 4(e)), the basalt part lost the support of the slope toe, and the entire basalt part was destroyed, sliding along the weak interlayer and cracks everywhere. At the end of the experiment (Figure 4(f)), the basalt layer sank 5 cm from the bedrock, and the overall displacement in the horizontal direction was 10 cm. The slope eventually broke. From the perspective of the break process of the slope, the toe of the slope was damaged first. The reason is that the toe of the slope is a stress concentration area. The toe of the slope was squeezed by the upper rock layer to cause shear failure. Secondly, cracks appeared on the surface of the slope, and

the cracks gradually propagated upward from the middle and lower parts of the slope, and finally the slope appeared as a whole landslide. After the toe of the slope was damaged, the rock layer at the slope lost the support at the toe of the slope. The basalt layer in the middle and lower parts of the slope broke the connection with the rock layer in the middle and upper part under the action of gravity, resulting in damage. In short, after losing the support of the slope toe, the upper rock layer of the slope will be broken and destroyed step by step under the action of gravity. The slope eventually loses stability along the weak interlayer, and its sliding mode is in good agreement with the results of the limit equilibrium method.

3.2.2. Experiment 2: The Dip Angle Decreases (8°, 44 mm). When the dip angle of the weak interlayer is changed from the original 23° to 8°, and the other parameters remain unchanged, the photos of the slope at different moments are shown in Figure 5.

Start the bottom friction machine; after 15 seconds (Figure 5(b)), the shallow area on the top of the slope began to damage; after 23 seconds (Figure 5(c)), the scope of the slope top damage became larger, and the damage in the shallow area develops toward the middle part. At the same time, two cracks appeared on the slope surface. Crack L1 was arc-shaped, the entrance was at the top of the slope, and the exit was at the middle and upper part of the slope. Crack L2 is about 7 cm long and sloped upward along the slope. After 27 seconds (Figure 5(d)), a new crack L3 appeared on the sliding body; the crack was a vertical crack, about 5 cm long. In the end (Figure 5(e)), the shallow layer damage at the top of the slope has progressed to the middle layer, and the scope of damage has become larger. At the same time, a new crack L4 appeared on the upper sliding body, which is connected with L1 and L4 and divides the sliding body into four.

From the perspective of the break process, the break of the slope first occurred at the top of the slope. The slope top was damaged under the action of its own weight stress. With the rotation of the belt, the damage gradually develops to the slope surface. The cracks on the slope gradually increased, but the cracks did not extend to the interior of the slope. The slope was only partially damaged, and the whole slope remained stable. When the belt stopped rotating, the damage range at the top of the slope became larger than it was at the beginning, and the cracks on the slope increased. Generally speaking, the damage is shallow and local, and the slope does not slide along the weak interlayer. The slope remains stable as a whole.

3.2.3. Experiment 3: The Buried Depth Increases (23°, 120 mm). When the buried depth of the weak interlayer is changed from the original 40 m to 120 mm, and the other parameters remain unchanged, the photos of the slope at different moments are shown in Figure 6.

Start the bottom friction machine. After 20 seconds (Figure 6(b)), the model began to break. The first crack L1 appeared in the middle and upper parts of the slope. After 26 seconds (Figure 6(c)), two cracks L2 and L3 appeared on the

TABLE 6: The general law of sequestration location of the weak layer affecting the slope slip mode.

Buried depth (m)	10	40	70	99	140
Dip angle (°)	0	8	16	23	32
Sliding mode	Along the weak layer	Along the weak layer	Along the weak layer	Along the weak layer	Along the weak layer
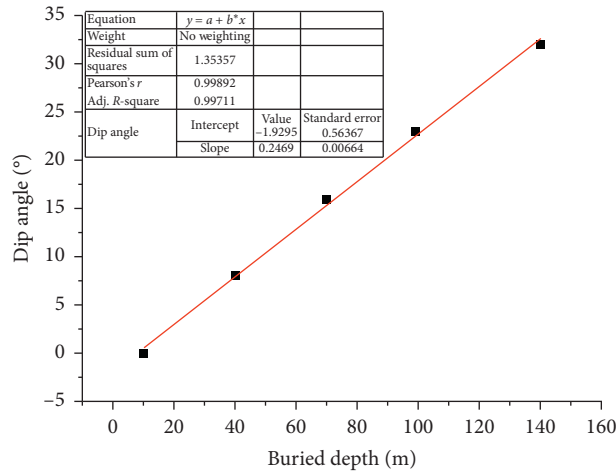
FIGURE 2: The general law of sequestration location of the weak layer affecting the slope slip mode.
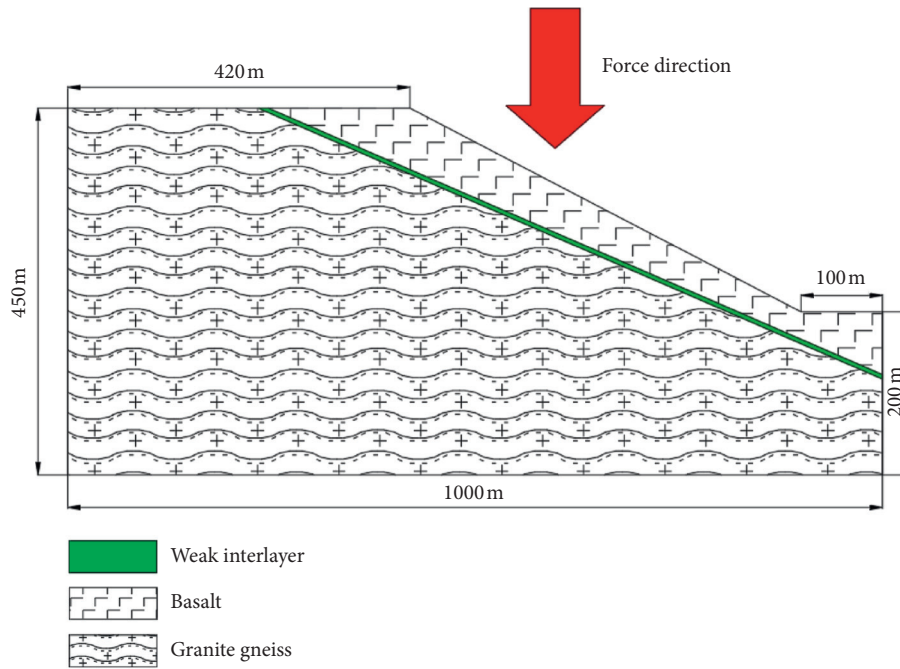
FIGURE 3: Generalized model section.

TABLE 7: Mass percentage of each material.

Rock formation	Sand	Lime	Plaster
Granite gneiss	80	12	8
Weak interlayer	—	—	—
Basalt	80	16	4

(a)

(b)

(c)

(d)

(e)

(f)
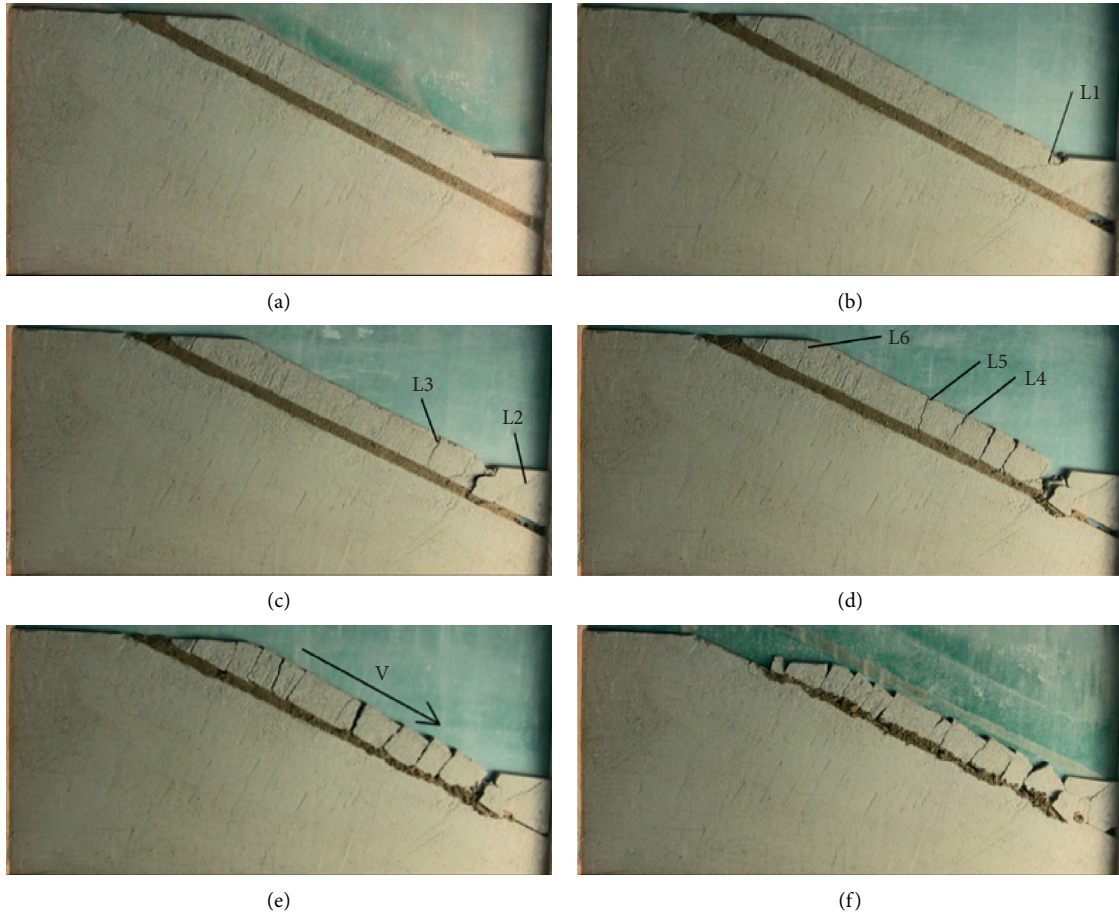
FIGURE 4: Model break process of experiment 1. (a) Initial state. (b) After 21 s. (c) After 23 s. (d) After 26 s. (e) After 33 s. (f) End of run.

(a)

(b)

(c)

(d)
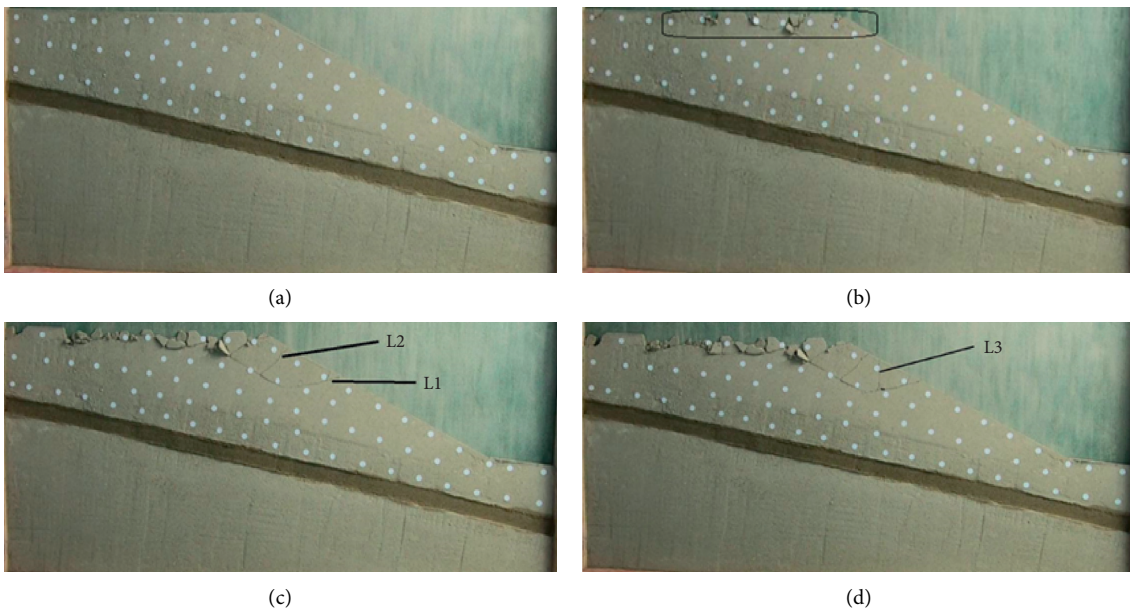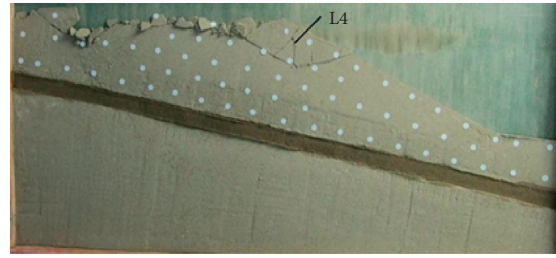
FIGURE 5: Continued.

(e)

FIGURE 5: Model break process of experiment 2. (a) In the beginning. (b) After 15 s. (c) After 23 s. (d) After 27 s. (e) End of run.
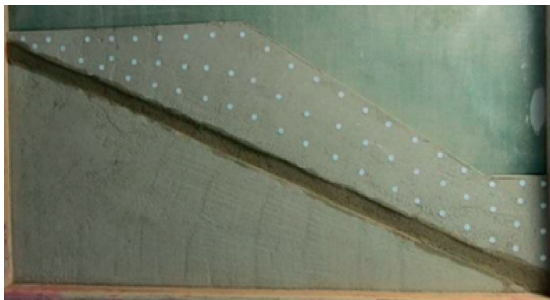
(a)
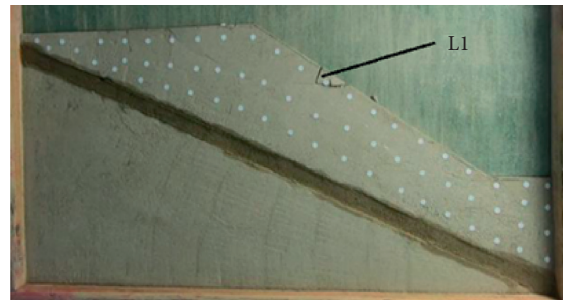
(b)
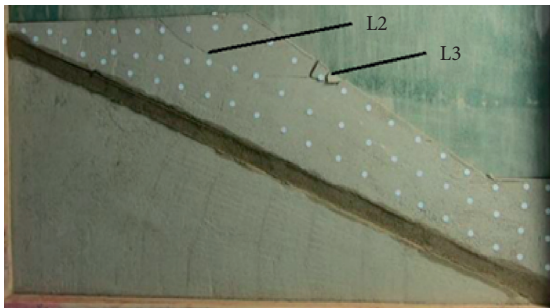
(c)
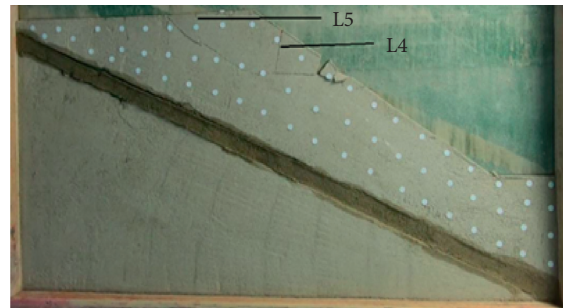
(d)

FIGURE 6: Model break process of experiment 3. (a) In the beginning. (b) After 20 s. (c) After 26 s. (d) End of run.
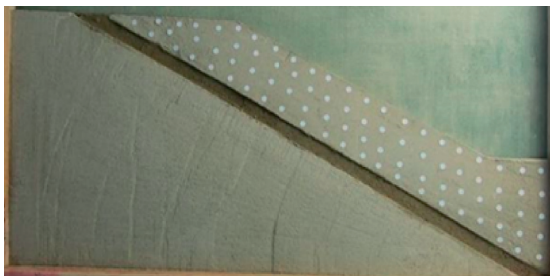
(a)

(b)

FIGURE 7: Continued.

(c)

(d)

(e)
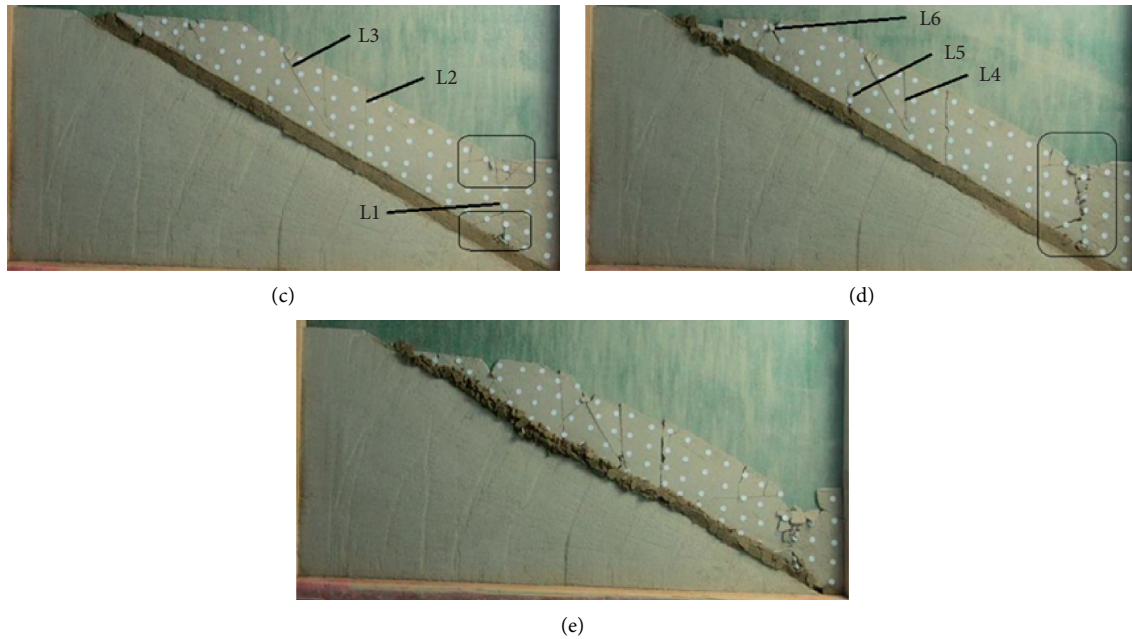
Figure 7: Model break process of experiment 4. (a) In the beginning. (b) After 25 s. (c) After 32 s. (d) After 37 s. (e) End of run.

slope. Crack L2 was arc-shaped and connected to crack L1. The entrance of crack L2 was in the center of the top of the slope, and the exit was in the center of the surface of the slope. L2 cut the slope into an arc-shaped slip surface. Crack L3 appeared in the middle of the small area cut by L1, dividing the small area into two. In the end (Figure 6(d)), new cracks L4 and L5 appeared in the middle of the sliding surface. Both cracks were vertical. The length of L4 was about 8 cm and the length of L5 was about 4 cm. The sliding body was divided into several blocks.

Observing the break process of the model, the break of the slope first started at the slope surface. Small cracks firstly appeared on the slope surface. When the small break area generated, the supporting force of the area at the slope surface is weakened. An arc-shaped failure surface appeared at the slope surface. The bottom friction machine continued to run until the end, and the supporting force on the right side of the arc-shaped failure surface area was weakened. Under the action of gravity, the sliding body lost the support on the right side, and two new cracks appeared, dividing the sliding body into four pieces. From the perspective of the failure process, the failure of the slope is a local small-scale failure, the sliding body on the slope surface has not slipped as a whole, and the slope has no large-scale damage.

3.2.4. Experiment 4: The Dip Angle and the Buried Depth Both Increase (29°, 100 mm).

When the buried depth of the weak interlayer increases to 100 mm, the dip angle increases to 29°. The photos of the slope selected at different moments are shown in Figure 7.

Start the bottom friction machine and begin the test. After 25 seconds (Figure 7(b)), the first small-scale damage occurred in the toe of the slope. After 32 seconds

(Figure 7(c)), the damage range of the shallow layer at the toe of the slope became larger, and 3 penetration cracks appeared at the toe of the slope and the slope at the same time. Crack L1 appeared at the toe of the slope, which was vertical, about 17 cm long, connected to the first damaged area, and extended to the weak interlayer. There was also a small area of damage in the toe of the slope where the weak interlayer connects with the upper strata. Crack L2 appeared in the center of the slope and was vertical, about 15 cm long. The crack completely penetrated the upper rock layer until it connected with the weak interlayer of the lower layer. Crack L3 appeared in the middle and upper part of the slope and extended to the upper left and was about 22 cm long. The crack also completely penetrated the upper rock layer and was connected to the weak interlayer. After 37 seconds (Figure 7(d)), the cracks at the toe of the slope have completely penetrated the upper and lower areas of the failure of the toe, and the damage range has become larger. Three new through cracks appeared in the upper rock layer. Crack L4 appeared in the middle of the slope and was vertical. It was connected to crack L3, which completely penetrates the upper rock layer and connects to the weak interlayer. Crack L5 appeared at the upper left of crack L3 and was vertical. It completely penetrated the upper rock layer and connected to the weak interlayer. Crack L6 appeared at the top of the slope and is curved upward; it was connected with the weak interlayer. At this time, the upper rock layer of the slope had a tendency to squeeze the weak interlayer, and the upper rock layer had a displacement of about 3 cm in the vertical direction. In the end (Figure 7(e)), the toe of the slope was completely broken, the slope was densely cracked, and the slope as a whole slid along the weak interlayer to the toe, and the slope was eventually destroyed.

Judging from the break process of the slope, the first place where the slope was damaged was at the toe of the slope. Large-scale damage occurred at the toe of the slope first, and then cracks occurred at the slope. The uneven settlement of the weak interlayer resulted in vertical cracks at the toe of the slope. Then, under the action of gravity, the rock strata at the slope surface was pulled apart and slid down along the weak interlayer under the action of gravity. When the slope fails, it slides downward as a whole, and its failure mode is in good agreement with the calculation results of the limit equilibrium method.

4. Conclusions

In this paper, the limit equilibrium method is used to study the relationship between the safety factor and sliding mode of the slope and the sequestration of the weak interlayer in the slope. When the dip angle decreases and the buried depth increases, the safety factor will increase. The sliding mode of the slope follows the rule illustrated in Figure 2. If the point of dip angle and buried depth are at the top left of the line, the slope will break along the weak layer. Otherwise, the slope will break in the shallow part.

The bottom friction experiment verifies the results of limit equilibrium method. In experiments 1 and 4, the slope breaks along the weak interlayer. In these two experiments, the point decided by the sequestration location of the weak interlayer is at the top left of the line in Figure 2. According to the result of limit equilibrium method, the slope will break along the weak interlayer, the same as the experiment. Experiments 2 and 3 also show the same results as the limit equilibrium method, as expected.

Data Availability

The data used to support the findings of this study are available from the corresponding author upon request.

Conflicts of Interest

The authors declare that they have no conflicts of interest regarding the publication of this paper.

Acknowledgments

References

[1] K. Sang, "Statistics and analysis of landslide disaster data in China in the past 60 years," *Technology Communication*, vol. 10, pp. 154–159, 2013.

[2] S. W. Sloan, "Geotechnical stability analysis," *Géotechnique*, vol. 63, no. 7, pp. 531–571, 2013.

[3] L. Q. Li, S. X. Luo, W. K. Wei et al., "Model test study on the influence of rainfall infiltration on the behavior of bedding rock slopes with weak interlayers," *Chinese Journal of Rock Mechanics and Engineering*, vol. 32, no. 9, pp. 1772–1778, 2013.

[4] Z. Z. Liu, L. T. Fa, N. Ma et al., "Influence of hydraulic characteristics of broken zone on slope stability of dagushan iron mine," *Metal Mine*, vol. 7, pp. 56–58, 2012.

[5] Z. C. Li, *Research on the Sliding Mechanism and Landslide Failure Time Prediction and Prediction of the South Side Landslide in Fushun West Open-Pit Mine*, Jilin University, Changchun, China, 2017.

[6] Z. Q. Sun and J. T. Li, "Study on open-pit mine slope stability based on improved TOPSIS method," *IOP Conference Series: Earth and Environmental Science*, vol. 781, no. 2, 2021.

[7] X. L. Liu and D. P. Zhou, "Stability evaluation of rock slope with weak interlayer," *Journal of Southwest Jiaotong University*, vol. 4, pp. 382–386, 2002.

[8] B. T. Xu, C. H. Yan, H. Y. Chen et al., "Experimental study on the mechanical characteristics of weak intercalation of slope rock mass," *Rock and Soil Mechanics*, vol. 11, pp. 3077–3081, 2008.

[9] D. Z. Kong, S. J. Pu, Z. H. Cheng et al., "Coordinated deformation mechanism of the top coal and filling body of gob-side entry retaining in a fully mechanized caving face," *International Journal of Geomechanics*, vol. 21, no. 4, Article ID 04021030, 2021.

[10] W. X. Chen and W. Y. Yu, "The influence of weak interlayer on the stability of open-pit mine slope," *Inner Mongolia Coal Economy*, vol. 2, pp. 30–51, 2016.

[11] G. Behzad, "Unsaturated hydraulic conductivity in dual-porosity soils: percolation theory," *Soil and Tillage Research*, vol. 212, 2021.

[12] C. Chen and J. Zhang, "Experimental study on bottom surface friction model of slope deformation and failure of dumping site with inclined basement," *Metal Mine*, vol. 10, pp. 150–154, 2016.

Research Article

Roof Control Technology of Mining Roadway under the Influence of Advanced Supporting Pressure

Zhiyuan Jin [ID],[1] **Youlin Xu,**[1] **Tao Peng** [ID],[1,2] **and Linsheng Gao**[3]

[1]School of Mining Engineering, Guizhou Institute of Technology, Guiyang, Guizhou 550003, China
[2]School of Resources & Safety Engineering, Central South University, Changsha, Hunan 410083, China
[3]School of Safety Engineering, North China Institute of Science and Technology, Langfang, Hebei 065201, China

Correspondence should be addressed to Tao Peng; pengxitong2018@163.com

In order to solve the problem of controlling the roof of the stoping roadway in 1204 fully mechanized face under the influence of advanced support pressure, according to the characteristics of the stoping roadway section, the single hydraulic prop and π-shaped steel beam were selected to verify the shrinkage of the single hydraulic support and establish mechanics. The model calculates that at least 3 single hydraulic props and at least 2 material lanes are required for the transportation lane; through the numerical simulation method, a reasonable roof control plan for the stoping roadway in the advance support section is determined, that is, 0~ in front of the material lane. The one-beam three-column method is adopted within 30 m, and the row spacing is 0.8 m; the one-beam four-pillar method is adopted within 0–20 m of the working front of the transportation lane; and the one-beam three-pillar method is adopted within 20–30 m, and the row spacing is 0.8 m. On-site industrial test practice proved that the proposed roof control scheme is reasonable, and the roadway section can meet the actual production requirements.

1. Introduction

Under the action of the advanced supporting pressure, the mining roadway will experience roof subsidence, bottom heave, and two-side shrinkage deformation so that the section of the mining roadway cannot meet the actual production requirements and affects the normal mining of the coal mining face. There are many technologies for the roof control of mining roadways. For example, Sun Jiuzheng published the book "Control Technology and Engineering Practice of Thin Composite Roof of Mining Roadways," which discussed the mechanical characteristics, changing laws, and influencing factors of thin composite roofs of mining roadways. The deformation and failure mechanism of the thin composite roof of the roadway and the deformation and failure laws of the thin composite roof of the mining roadway are summarized. Qiu Wenhua et al. proposed roof control technology for semicoal and rock

roadways under complex conditions. Due to the different production geological conditions of each mining area, the roof control technology of the fully mechanized mining face is different under the influence of the advanced support pressure. According to the specific production conditions of the 1204 working face, relevant research is carried out to put forward a reasonable technical plan for the roof control of the mining roadway in the fully mechanized mining face.

2. Engineering Geological Conditions

The 1204 working face is arranged in the 2# coal seam, the ground elevation is +948~+1103 m, the underground elevation is +495~+541 m, the strike length is 1980 m, and the dip length is 167 m. The thickness of the coal seam is 2.5 to 3.95 m, with an average of 3.2 m; the inclination angle of the coal seam is 3° to 8°, with an average of 6°. The occurrence of roof and floor is shown in Table 1.

TABLE 1: The lithology of the roof and floor.

Roof and floor name	Rock name	Thickness (m)	Lithology
Basic top	Sandy shale argillaceous shale	6.5	Dense and hard, not easy to fall
Direct top	Partially sandy shale	1.6	Broken, cracks developed, easy to straddle
Pseudotop	Mudstone	0.2	Fall with the mining
Direct bottom	Sandy shale	2.4	Siltstone lenticular horizontal bedding with fissures
Old bottom	Fine-grained sandstone	2.42	Horizontal bedding fissures are developed and hard, $f = 6$ or so

3. Determination of the Key Parameters of the Roof Control of the Mining Roadway

According to the production geological conditions of 1204, the roof control mode of the advanced support section of the super 1204 fully mechanized face is determined to be "single hydraulic prop + π beam".

3.1. Single Hydraulic Prop and π-Shaped Steel Beam Selection.
According to the cross section characteristics of the two lanes in the 1204 working face, the single hydraulic prop of the transportation lane uses the DZ-35 type, and the π-shaped steel beam uses the DFB4000-300 type. The single hydraulic prop of the material lane is DZ-28, and the π-shaped steel beam is DFB3600-300. The main technical characteristics of the single hydraulic prop and the π-shaped steel beam are shown in Tables 2 and 3, respectively.

3.2. Verification of the Shrinkage of Single Hydraulic Support.
After the roadway is excavated, the basic support is performed, and the initial deformation of the old roof is given [1]. The allowable shrinkage amount should satisfy the movement and development of the old roof and reach the final stable state, that is, the basic support of the roadway. The allowable roof shrinkage of the protective structure should at least meet the expected deformation of the surrounding rock [2, 3].

$$\Delta h + \Delta h_j > \Delta h_0, \tag{1}$$

where Δh is the required shrinkage of the basic support in the lane, Δh_j is the amount of compression of the auxiliary supporting structure, and Δh_0 is the moving amount of the roof and floor of the roadway under a given deformation state of the old roof, generally 200~300 mm.

The roof control method of the roadway in 1204 fully mechanized coal mining face adopts "single hydraulic prop + π beam," the compression of the auxiliary support structure is 0, and the estimated roadway roof and floor moving in the given deformation state of the old roof is 300 mm. The required shrinkage of the basic stent should be greater than 300 mm. The selected single hydraulic prop has a stroke of 800 mm, which can meet the requirements.

3.3. Supporting Density of Single Hydraulic Prop.
According to the supporting force of the single hydraulic prop under the given deformation of the old roof and the given load of the roof, the bearing capacity of the π-shaped beam is considered, and the supporting density is determined by comprehensive analysis.

3.3.1. Under a Given Deformation State.
Under the given deformation working condition required by the old roof, the supporting structure in the roadway should control the direct roof and make it close to the old roof. Therefore, the supporting force should be at least sufficient to balance the rock weight of the direct roof.

$$N = 10\lambda\gamma hBd, \tag{2}$$

where N is the supporting force, kN; λ is the dynamic pressure coefficient, 2; γ is the bulk density of the direct roof, 2.5 t/m³; h is the thickness of the direct roof, 1.6 m; d is row spacing, 0.8 m; and B is the width of the lane, the transportation lane is 5 m, and the material lane is 4 m.

It is calculated that the required supporting force $N = 320$ kN for the transportation lane and the required supporting force $N = 256$ kN for the material lane. Therefore, in this case, the transport lane needs at least 2 single hydraulic props and at least 2 material lanes.

3.3.2. Under a Given Load State.
Since the roof falling shape is arched, it is analyzed according to Platts' pressure-free arch theory [4], as shown in Figure 1.

The damage range of the roadway gang is given by [5]

$$C = \left(\frac{k_c rHv}{1000\sigma_m} - 1\right)h\tan\left(45° - \frac{\phi}{2}\right). \tag{3}$$

In the above formula, the squeezing stress concentration coefficient around the roadway is generally taken as 3; r is the average gravity density of the rock formation, which is 25 kN/m³; v is the mining influence coefficient, 2; H is the buried depth and the maximum value is 487 m; σ_m is the uniaxial compressive strength of the top plate, 20 MPa; ϕ is the internal friction angle of the top plate, 20°; and h is the height of the roadway, the transportation lane is 3.1 m, and the material lane is 2.5 m.

By using formula (3), the damage range of the transportation lane ledge is calculated as 2.99 m and the damage range of the material lane ledge is calculated as 2.41 m.

The maximum loosening range of the top plate is given by [6]

$$b = \frac{L/2 + C}{f_m}, \tag{4}$$

TABLE 2: The main technical characteristics of single hydraulic prop.

Model	Rated work resistance (kN)	Rated work hydraulic (MPa)	Setting force (kN)	Pump station hydraulic (kN)	Maximum height (mm)	Minimum height (mm)	Stroke (mm)	Stroke base area (cm²)
DZ-35	200	25.5	118~157	15~20	3500	2700	800	113
DZ-28	250	31.8	118~157	15~20	2800	2000	800	113

TABLE 3: The main technical characteristics of π type steel beam.

Model	Material	Width (mm)	Length (mm)	Height (mm)	Thickness (mm)	Bearing capacity (kN)
DFB4000-300	27simn	100	4000	90	8	300~400, that is, when the beam span is
DFB3600-300			3600			700 mm, concentrated load at beam center
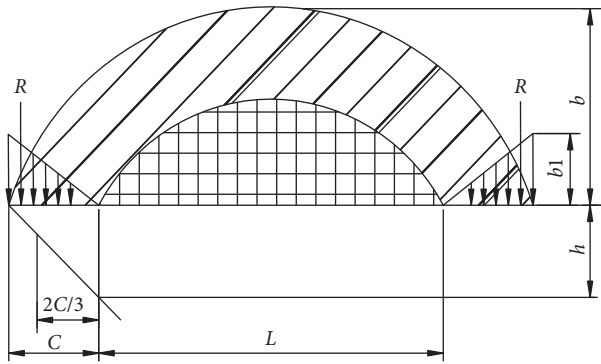
FIGURE 1: The map of roof caving arch.

where f_m is roof rigidity coefficient, taking 2, and L is the width of the lane. The transportation lane is 5 m, and the material lane is 4 m.

By using formula (4), the loosening range of the roof of the transportation lane is calculated as 2.74 m and the loosening range of the roof of the material lane is calculated as 2.21 m.

Considering the most dangerous situation, the weight of the rock mass within the loose roof range is borne by the single hydraulic prop. The required single hydraulic prop supporting force is given by

$$N = br\,(2C + L)d. \tag{5}$$

By using formula (5), the supporting force of the single hydraulic prop required by the transportation lane is calculated as 603 kN and the supporting force of the single hydraulic prop required by the material lane is calculated as 389 kN. Therefore, in this case, at least 3 single hydraulic props are required for the transportation lane and at least 2 for the material lane.

3.3.3. Considering the Bearing Capacity of π-Shaped Steel Beams. Since the length of the π-shaped beam is much larger than that of the hinged top beam, its overall supporting effect is good, which avoids the phenomenon of large top pressure and wedge pressing on the hinged top beam [7–12]. When the roof control mode is one beam and two columns, it is simplified as a simply supported beam for calculation, as shown in Figure 2(a); when the roof control mode is one beam and three columns, it is simplified as a statically indeterminate beam for calculation as shown in Figure 2(b).

When the roof control mode is one beam and two columns, it satisfies

$$[\sigma] = \frac{M_{max}}{W_z} = \frac{1/8 \cdot q \cdot L^2}{W_z} = \frac{1/8 \cdot F \cdot L}{W_z}. \tag{6}$$

When the roof control mode is one beam and three columns,

$$[\sigma] = \frac{M_{max}}{W_z} = \frac{9/512 \cdot q \cdot L^2}{W_z} = \frac{9/512 \cdot F \cdot L}{W_z}, \tag{7}$$

where $[\sigma]$ is the allowable stress, MPa; M_{max} is the maximum bending moment, kN*m; W_Z is the bending section modulus, m3; q is the uniform load, kN/m; L is beam span, m; and F is the equivalent concentrated force, kN.

It can be seen from Table 2 that when the beam span is 700 mm, the central load of the beam is 300–400 kN. Since the π-shaped steel beam $[\sigma]$ and W_Z are constants, the bearing capacity of the π-shaped steel beam at different individual hydraulic prop spacings is obtained (see Table 4).

The calculation results in Table 4 show that when the roof control mode is one beam and two columns, the bearing capacity of the π-shaped steel beam is less than the required supporting force N under the given deformation of the old roof and the given load state of the roof; when the roof control mode is one beam and three columns, the bearing capacity of the π-shaped steel beam in the material lane can meet the requirements, and the bearing capacity of the π-shaped steel beam in the area affected by the weak forward supporting pressure of the transportation lane can also meet the design requirements, but the loading capacity of the π-shaped steel beam in the severely affected area
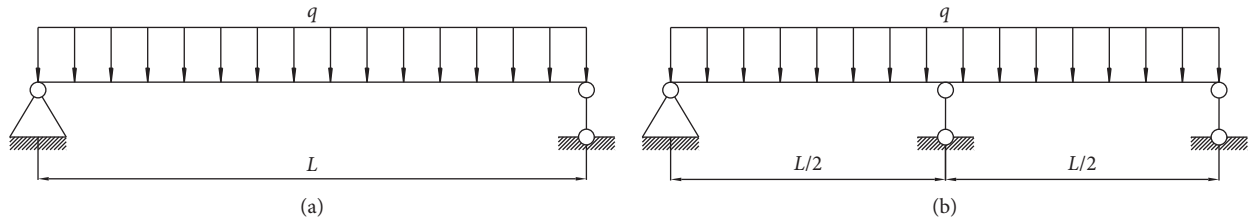
FIGURE 2: The advanced support simplified mechanical model. (a) One beam and two columns. (b) One beam and three columns.

TABLE 4: The carrying capacity of π type steel beam in different spans.

Mode	Beam span (mm)		
	4000 (kN)	3600 (kN)	700 (kN)
One beam and two columns	52.5	58.3	400
One beam and three pillars	373	415	

of the transportation lane cannot satisfy the design requirements.

4. Research and Demonstration of Roof Control Scheme

4.1. Feasible Plan. In order to further determine the roof control plan of the stoping roadway in 1204 fully mechanized mining face, the influence range of the advanced support is considered as 30 m. Due to the different section sizes of the transportation lane and the material lane, four feasible plans are proposed, respectively. Under the normal mining situation of the simulation study, different methods are adopted. When the advance support plan is used, the surrounding rock deformation law and plastic zone distribution characteristics of the two lanes are used to optimize and determine the reasonable roof control plan of the mining roadway. The specific plan is as follows.

4.1.1. Material Lane

Option 1: the roof control of the mining roadway adopts one beam and three pillars, and the row spacing is 1.6 m

Option 2: the roof control of the mining roadway adopts the one-beam three-pillar method, and the row spacing is 0.8 m

Option 3: the roof control of the mining roadway adopts one beam and three pillars, and the row spacing is 0.4 m

Option 4: the roof control of the mining roadway adopts the one-beam four-pillar method, and the row spacing is 0.8 m

4.1.2. Transportation Lane

Option 1: the roof control of the mining roadway adopts one beam and three pillars, and the row spacing is 1.6 m

Option 2: the roof control of the mining roadway adopts the one-beam three-pillar method, and the row spacing is 0.8 m

Option 3: the roof control of the mining roadway adopts one beam and four pillars, and the row spacing is 0.8 m

Option 4: the roof control of the mining roadway adopts the one-beam four-pillar method within 0–20 m from the working face, and one-beam three-pillar method within 20–30 m, and the row spacing is 0.8 m

4.2. Plan Demonstration and Determination. With the help of FLAC^{3D} software, the above feasibility schemes are researched and demonstrated. Establish a horizontal model, excavate 80 m, and arrange surface displacement measurement points in two lanes 50 m ahead of the work face, as shown in Figure 3. By comparing and analyzing the deformation law of the surrounding rock of the mining roadway and the distribution characteristics of the plastic zone in different schemes, the reasonable advance support technical scheme is optimized and determined [13, 14].

4.2.1. Material Lane. The plastic zone distribution of surrounding rock under different schemes is shown in Figure 3, and the surface displacement characteristics of the transportation lane under different schemes are shown in Table 5.

From the analysis in Figure 3, it can be seen that when option 1 is adopted, the distribution range of the plastic zone of the surrounding rock of the material lane is obviously larger than that of options 2, 3, and 4, while when the option 2, 3, and 4 are adopted, the distribution range of the plastic zone of the surrounding rock of the material lane is similar. It means that the roof of the roadway in the advanced support section of the working face has been effectively controlled when the second, third, and fourth options are adopted, but the first-time control effect of the program is poor.

From the analysis of Figure 3 and Table 5, it can be seen that when the first scheme is adopted, the roof control mode of the mining roadway is one beam and three columns, the row spacing is 1.6 m, and the cumulative displacement of the roof and floor and the cumulative displacement of the two sides have reached 460 mm and 501 mm, respectively. When the second scheme is adopted, the roof control method of the mining roadway remains unchanged, and the row spacing becomes 0.8 m. Compared with the first scheme, the cumulative displacement of the roof and floor and the
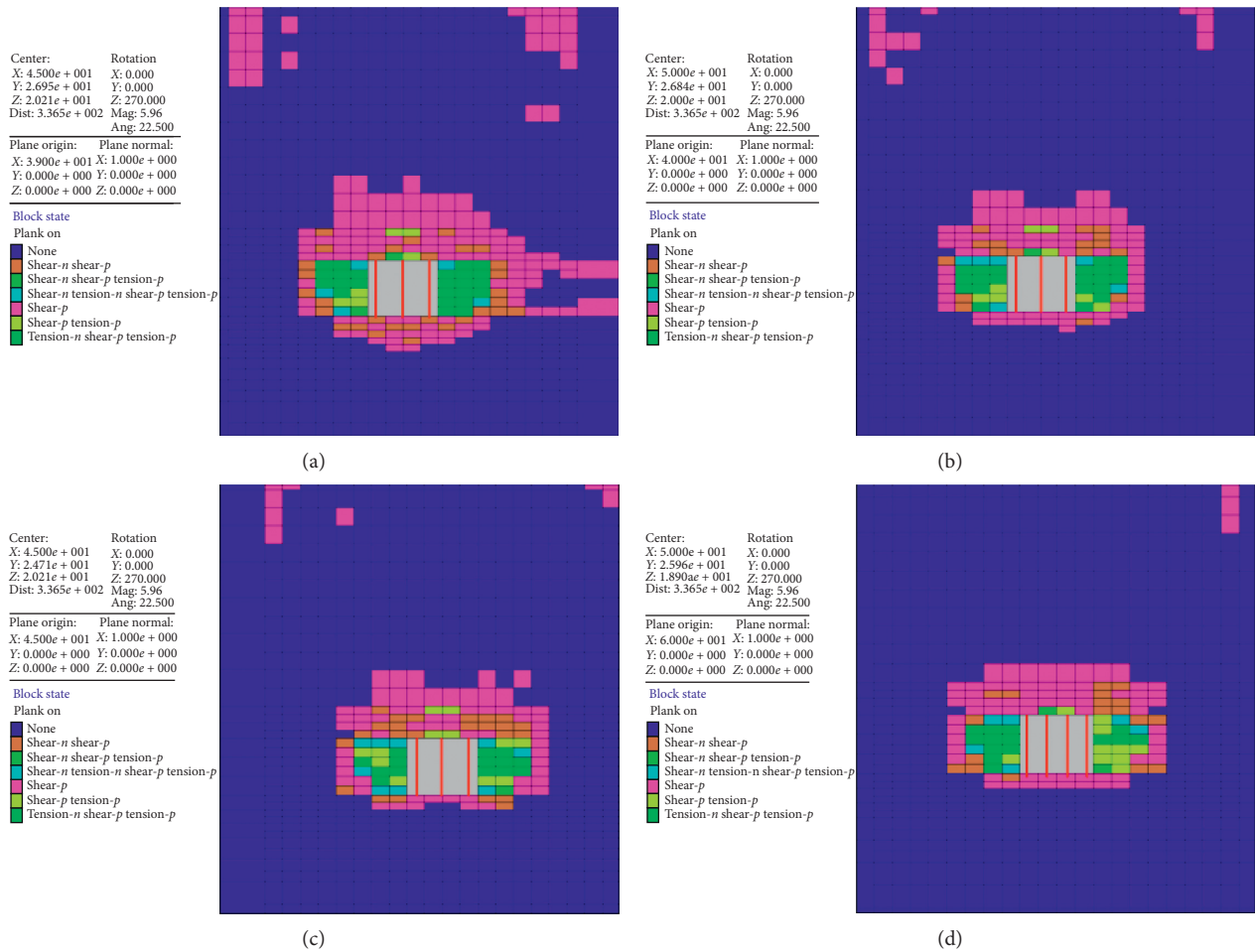
FIGURE 3: Plastic zone distribution of the material roadway's surrounding rock. (a) Option 1. (b) Option 2. (c) Option 3. (d) Option 4.

TABLE 5: The displacement curve about the material roadway's surface in different advanced support schemes.

Option	Cumulative displacement (mm)	
	Top and bottom	Two gangs
1	460	501
2	299	331
3	273	303
4	281	311

cumulative displacement of the two sides are reduced by 179 mm and 170 m respectively; when the scheme is adopted at 3 o'clock, the roof control method of the mining roadway remains unchanged, and the row spacing becomes 0.4 m. However, compared with the second plan, the cumulative displacement of the roof and floor and the cumulative displacement of the two sides are only reduced by 26 mm and 28 mm, respectively. In the fourth plan, the roof control mode of the mining roadway becomes one beam and four columns with a row spacing of 0.8 m. Compared with the second plan, the cumulative displacement of the roof and floor and the cumulative displacement of the two sides are only reduced by 18 mm and 20 mm, respectively, which shows reducing the spacing between rows can improve the roof control effect of the advanced support section. However, the simulation study shows that the material lane roof is effectively controlled when the second, third, and fourth options are adopted, but the effect is not much different. The ratio control effect is very obvious; therefore, the second option is determined as the optimal one.

4.2.2. Transportation Lane. The plastic zone distribution of surrounding rock under different schemes is shown in Figure 4, and the surface displacement characteristics of the transportation lane under different schemes are shown in Table 6.

From the analysis in Figure 4, it can be seen that when the transportation lane adopts Option 1, the plastic zone of the surrounding rock is the largest, followed by Option 2, the smallest in Option 3 and Option 4, and when Option 3 and Option 4 are adopted, the distribution range of the plastic zone of the surrounding rock of the material roadway is not much different. The distribution range is not much different, indicating that when schemes 3 and 4 are adopted, the roadway roof control effect in the advanced support section of the working face is better.

From the analysis of Figure 4 and Table 6, it can be seen that when the first scheme is adopted, the roof control mode of the mining roadway is one beam and three columns, the

(a)

(b)

(c)

(d)
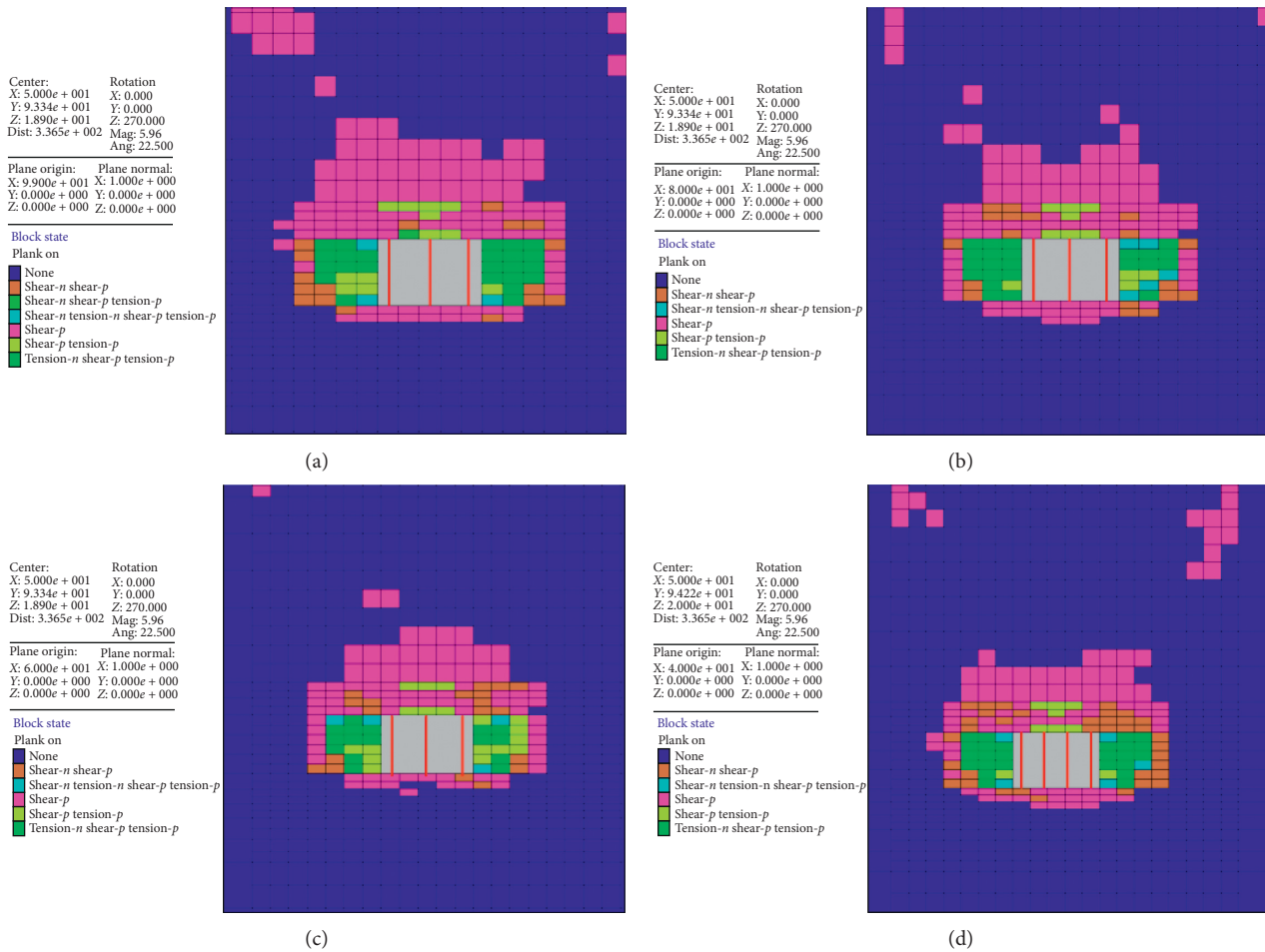
FIGURE 4: Plastic zone distribution of the surrounding rock. (a) Option 1. (b) Option 2. (c) Option 3. (d) Option 4.

TABLE 6: The displacement curve about transportation roadway surface in different advanced support schemes.

Serial number	Cumulative displacement (mm)	
	Top and bottom	Two gangs
Option 1	511	589
Option 2	403	451
Option 3	337	389
Option 4	321	377

row spacing is 1.6 m, and the cumulative displacement of the roof and floor and the cumulative displacement of the two sides reach 511 mm and 589 mm, respectively. When the second plan is adopted, the advance support method remains unchanged, and the row spacing becomes 0.8 m. Compared with the first plan, the cumulative displacement of the top and bottom plates and the cumulative displacement of the two sides are reduced by 108 mm and 148 mm, respectively; when the third is adopted at the same time, the advance support method remains unchanged, and the row spacing is changed to 0.4 m. However, compared with the case of using the second scheme, the cumulative displacement of the top and bottom plates and the cumulative displacement of the two sides are only reduced by 66 mm and 62 mm, respectively; when the fourth scheme is adopted and when the working front is 0–20 m, one beam and four columns are used, and one beam and three columns are used within 20–30 m, and the row spacing is 0.8 m. Compared with scheme 3, the cumulative displacement of the top and bottom plates and the cumulative displacement of the two sides are only reduced. The values of 16 mm and 12 mm indicate that the control effect of the surrounding rock in the advanced support section of the working face of scheme 3 and scheme 4 is better, but the difference in the control effect between the two is very small. Considering comprehensively, the fourth option is determined as the best option.

Therefore, the optimal design plan for the roof control of the mining roadway in 1204 fully mechanized mining face is determined as follows: ① material lane: one beam and three columns are used within 0–30 m in front of the work face, with a row spacing of 0.8 m; ② transportation lane: when the working front is 0–20 m, one beam and four columns are used inside, and one beam and three columns are used within 20–30 m, and the row spacing is 0.8 m.

5. On-Site Industrial Test

5.1. Station Layout. In order to verify the roof control effect of the mining roadway, the roadway surface displacement
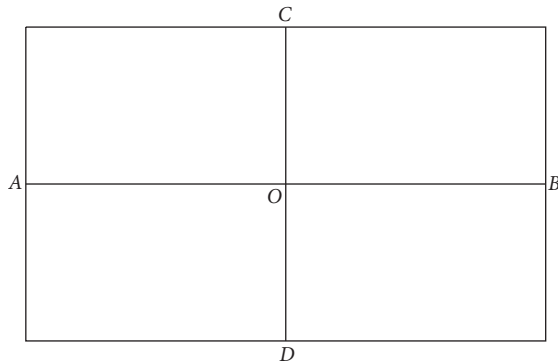
Figure 5: Sketch map of the displacement of tunnel surface.

observation stations were arranged in the transportation lane and the material lane, respectively, and the "cross measurement method" was used for observation. The measurement points are set up as shown in Figure 5. A drill hole with a depth of 400∼500 mm is constructed on the top and bottom and the two sides, and a round steel or steel rod with a diameter of 16∼18 mm is buried in the hole and fixed with a resin coil. The roadway shows that the displacement monitoring mainly includes roof subsidence OC, floor heave OD, left side approach OA, and right side approach OB.

5.2. Analysis of Observation Results. Field measurements show that the cumulative approach of the two sides of the material lane is 477 mm, the cumulative approach of the roof and floor is 411 mm, the cumulative approach of the two sides of the transportation lane is 354 mm, and the cumulative approach of the top and floor is 301 mm. The roof of the mining roadway in 1204 fully mechanized mining face has been effectively controlled, and the roadway section can meet the actual production requirements.

6. Conclusion

(1) The roof control support equipment suitable for the mining roadway of 1204 fully mechanized mining face is determined, namely, the single hydraulic prop of the transportation lane is DZ-35, the π-shaped steel beam is DFB4000-300, the single hydraulic prop of the material lane is DZ-28 type, and π-shaped steel beam is DFB3600-300 type.

(2) According to the supporting force of the single hydraulic prop required under the given deformation of the old roof and the given load of the roof, and considering the bearing capacity of the π-shaped beam, comprehensive analysis is used to determine the supporting density, combined with FLAC^{3D} numerical simulation method. Research and demonstration of the roof control scheme of the mining roadway were carried out, and the optimal scheme was determined, that is, the severely affected area within the advanced support range of the transportation lane adopts the one-beam four-pillar method, and the weakly affected area within the advanced support range of the material lane adopts the one-beam three-column method.

(3) Field engineering tests show that it is reasonable to propose the roof control plan of the stoping roadway in 1204 fully mechanized mining face. The cumulative approach of the two sides of the material roadway is 477 mm, the cumulative approach of the roof and floor is 411 mm, and the cumulative approach of the two sides of the transportation lane is 354 mm. The cumulative moving distance of the roof and floor is 301 mm, and the roof of the mining roadway is effectively controlled.

Data Availability

The data used to support the findings of this study are included within the article.

Conflicts of Interest

The authors declare that they have no known conflicts of interest that could influence the work reported in this study.

Acknowledgments

References

[1] Z. Q. Song, *Practical Mine Pressure Control*, China University of Mining and Technology Press, Xuzhou, China, 1988.

[2] Z. Q. Song, J. Q. Jiang, and Y. X. Liu, "The appearance of underground pressure across mining roadways and uphill and the reasonable layout of roadways," *Coal Science and Technology*, vol. 5, pp. 60-61, 1987.

[3] Z. Q. Song, J. Q. Jiang, and Y. Song, "About mine pressure control design of stope roadway," *Journal of Shandong Institute of Mining And Technology*, vol. 3, pp. 1–11, 1985.

[4] L. W. Liu, *Research On the Surface Subsidence Law of Shield Tunnel Construction of Subway in Composite Stratum*, China University of Mining and Technology, Xuzhou, China, 2009.

[5] Y. X. Yu, *Deformation and Failure Mechanism of Surrounding Rock of Rectangular Roadway and its Application in Wangcun Coal Mine*, Xi'an University of Science and Technology, Xi'an, China, 2013.

[6] Y. X. Yu and S. C. Gu, "Research on measurement and control technology of loosening range of surrounding rock in rectangular roadway," *Journal of Mining and Safety Engineering*, vol. 6, pp. 828–835, 2013.

[7] L. S. Cao, "The application of π-shaped beam in the support of general mining face," *Jiangxi Coal Science and Technology*, vol. 3, pp. 34-35, 2010.

[8] F. Fan, "Application of π-shaped beam under broken roof," *Jiangxi Coal Science and Technology*, vol. 2, pp. 11-12, 2003.

[9] C. Q. Wang, Y. H. Liu, and S. W. Lu, "Application of π-shaped beams in complex working faces," *Modern Mining*, vol. 3, pp. 101-102+127, 2012.

[10] D. Z. Kong, S. J. Pu, Z. H. Cheng, G. Y. Wu, and Y. Liu, "Coordinated deformation mechanism of the top coal and filling body of gob-side entry retaining in a fully mechanized caving face," *International Journal of Geomechanics*, vol. 21, no. 4, Article ID 04021030, 2021.

[11] S. Yang, H. Yue, G. Song, J. Wang, Y. Ma, and F. Liu, "3D physical modelling study of shield-strata interaction under roof dynamic loading condition," *Shock and Vibration*, vol. 2021, Article ID 6618954, 7 pages, 2021.

[12] J. F. Lou, F. Q. Gao, J. H. Yang et al., "Characteristics of evolution of mining-induced stress field in the longwall panel: insights from physical modeling," *International Journal of Coal Science & Technology*, vol. 8, pp. 1–18, 2021.

[13] J. Z. Sun, Q. S. Wan, and Q. D. Liu, *Thin Composite Roof Control Technology and Engineering Practice of Mining Roadway*, Coal Industry Press, Beijing, China, 2008.

[14] W. H. Qiu, L. H. Kong, Y. Ou, H. H, and H. H. Wan, "Research on roof control technology of semi-coal and rock roadway under complex conditions," *Coal Engineering*, vol. 49, no. 11, pp. 45–49, 2017.

Research Article

Study on Development Law of Mining-Induced Slope Fracture in Gully Mining Area

Tao Yang,[1,2] **Yiran Yang** ORCID**,**[1,2,3] **Jie Zhang,**[1,2] **Shoushi Gao,**[1,2] **and Tong Li**[1,2]

[1]*Xi'an University of Science and Technology, Xi'an 710054, Shaanxi, China*
[2]*Key Laboratory of Western Mine Exploitation and Hazard Prevention with Ministry of Education,*
 Xi'an University of Science and Technology, Xi'an 710054, China
[3]*Shaanxi Key Laboratory of Safety and Durability of Concrete Structures, School of Civil Engineering, Xijing University,*
 Xi'an 710054, Shaanxi, China

Correspondence should be addressed to Yiran Yang; 1306373793@qq.com

The development law of mining cracks in shallow coal seams under gully topography was used as the research base to analyze the development characteristics of mining cracks in the 5-2 coal mining face of Anshan Coal Mine, and the weak strength was established. The basic top force model under the action of the overburden is the "nonuniformly distributed load beam" structure model. Through similar simulation research and theoretical calculation analysis, the fracture development law of the working face passing through the valley is studied. Based on the mechanical analysis of the beam structure with nonuniform load, the discriminant conditions of the stability of the bearing structure of the bedrock are derived, the calculation formulas of the parameters such as the pressure, shear force, and the ultimate span of the basic roof at both ends are determined, the influence law of the thickness and slope change of the weak strength overburden on the mining crack spacing is revealed, and the influence of the slope of the weak strength overburden on the weighting step distance on the beam with nonuniform load is obtained. The phenomenon is that the burial depth has a great influence on the step distance of weighting. The practice shows that the distance between the mining-induced fractures determined by the nonuniformly distributed load beam model and the periodic weighting step, the height of fracture development, and the buried depth are approximately the same; the mining-induced fractures in the overburden develop and evolve periodically with the failure and instability of the bedrock. The research results will clarify the development mechanism of surface cracks in the gully mining area, which is of great significance to reduce terrain disasters.

1. Introduction

The area where the working face of Shenfu coalfield is located has complex and craggy terrain. In most areas, the coal seam is buried shallowly, only dozens of meters away from the surface, and thin bedrock outcropping is common. The bedrock is covered by thick Quaternary loess and Neogene laterite. Compared with other coal mines, the characteristics of overlying strata fracture, the form of instability movement, and the evolution law of mining-induced fracture are significantly different.

Since the 1990s, with the expansion of the mining of shallow-buried coal seams, in-depth studies have been conducted on the instability characteristics of overlying strata failure and the development law of fracture. Until now, many achievements have been obtained. Through the study on the stability of roof structure, the mechanism of roof failure and instability is well revealed, and the collapse pattern of overlying strata is vividly described [1–3]. Based on the study of strata behaviors when the working face is mining in gully in Shendong mining area, the reason of roof cutting and caving occurs easily when the working face is in the uphill stage is pointed out, which provides important theoretical guidance for the determination of the location of the overlying strata failure and instability during the mining [4]. Based on the roof failure characteristics and the development height of two zones in the shallow-buried working face with large mining height, the measured law

which is closer to the traditional calculation formula of caving zone height is obtained [5, 6], providing an important guarantee for safe mining. On the basis of fractal geometry theory and numerical simulation, the fracture development characteristics of mining-induced rock mass are well characterized from the perspective of fractal dimension, providing references for the study of fracture development under different damage degrees [7, 8]. In view of overlying strata structure fracture, the factors and mechanism that affect the distribution of surface fractures in goaf are given, which can provide some ideas for the prevention and control of surface disasters under similar conditions [9, 10]. Based on the study of fracture development characteristics under different mining intensities in the Yushenfu mining area, the zoning of ground fissures distribution is revealed [11, 12]. Taking Shendong mining area as the study target, the dynamic development law of ground fissures is revealed using continuous field monitoring, and the corresponding function relationship is established [13, 14]. Based on the method of overlying strata composite structure and rock strata tensile deformation, the correlation between the development law of water-conducting fracture zone and strata structure was studied, and a reasonable formula for calculating tensile ratio was deduced [15].

In summary, the existing study results have made significant achievements in rock structure failure and instability, caving morphology of overlying strata, and fracture development law [16, 17]. However, the mechanism and law of dynamic evolution of mining-induced fractures caused by the bedrock failure and instability in the mining of shallow-buried coal seam with thin bedrock in gully remain to be studied [18–20]. Anshan coal mine belongs to the Loess Hilly and gully area, with deep gully, steep slope, and thick soil layer load on the surface. When the working face passes through the gully bottom, the coal wall spalling is serious, and the support working resistance increases. This is inconsistent with the mine pressure behavior law of the working face passing through the gully bottom under general conditions, and whether there will be dynamic load and other contents need to be further studied, which is also the key to the prevention of mine pressure in Anshan coal mine. Therefore, in combination with the mining conditions of 5-2 working face in Anshan coal mine, the mechanism and law of dynamic evolution of mining-induced fractures caused by bedrock failure and instability in the mining of shallow-buried coal seam with thin bedrock in gully were studied in this paper.

2. Engineering Overview

Anshan minefield is in a typical loess ridge landform. The lowest elevation is 1075.9 m, and the highest elevation is 1364.5 m, with a large drop. In this region, there are many gullies with the buried depth of coal seam about 20~70 m. The topography of the minefield is shown in Figure 1.

Currently, the main coal seam of the mine is 5-2. The average coal thickness of 125203 working face is 2.3 m, the inclination angle is 0~1°, the strike length of working face is 3152 m, the dip length is 270.5 m, the horizontal elevation of
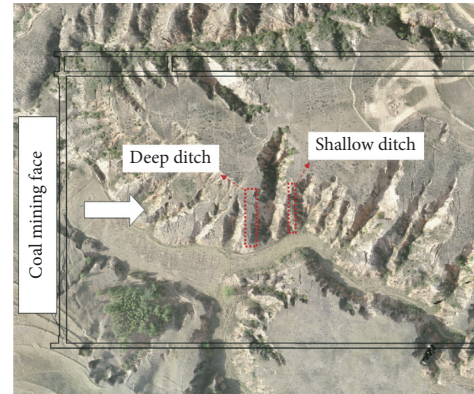
Figure 1: Landform map of Anshan mine field.

the coal seam is +1165 m, and the ground elevation is +1191~+1304 m. It is located in the north side of Shasongliang and the northwest side of Caigou. The working face adopts a full-height and long-wall comprehensive mechanized coal mining method, and the roof is treated by the full caving. According to the drilling data and outcrop information, the lithology of the roof is generally stable. The average thickness of the pseudo-roof is 0.2 m, and it is carbonaceous shale. The direct roof is fine-grained sandstone with an average thickness of 1.12 m. The basic roof is a silty, fine-grained sandstone with an average thickness of 12 m, and the bedrock is covered by a sandy soil layer.

3. Similar Simulation Experiment Analysis

3.1. Experiment Design. During working face stoping, it is difficult to obtain the dynamic development law of mining-induced fractures induced by bedrock failure and instability through on-site detection. This paper aims to study intuitively the dynamic evolution of mining fractures induced by bedrock failure and instability when different surface forms (deep gully and shallow gully) are in the downslope, gully bottom, and upslope stages. Therefore, based on the actual occurrence of 125203 working face in Anshan coal mine, this paper builds a plane simulation test platform as shown in Figure 2 according to the similarity theory. The size of the similar model was $3000 \times 1000 \times 200$ mm, and the geometric similarity ratio was $1:100$. When the material is prepared, river sand is used as aggregate, and gypsum and calcium carbonate are used as cement. In the laying process of the model, mica sheets were laid to reduce the size effect caused by the whole layer laying. The thickness and ratio of the model are shown in Table 1. The stratum selection is based on the geological data provided by the mine. The reason for selecting these six strata is that these strata can represent the coal seam occurrence conditions of the mine. The material ratio is based on the authors' previous research results.

The soil layer (the overburden) is mainly distributed in the Xinmin district and exposed on the surface, which is a very poor water area. Laterite is mainly distributed in Yushen mining area, which is located between the aquifer of Salawusu formation and the overlying bedrock of the coal seam. In the ancient gully section, due to erosion, the
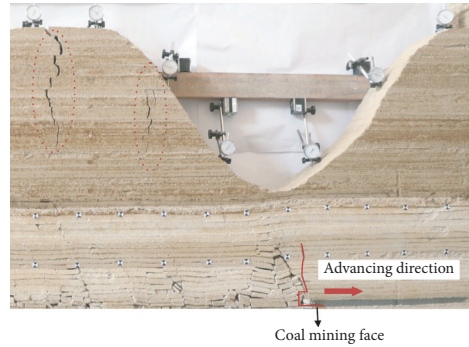
FIGURE 2: Deep ditch downhill stage.

TABLE 1: Material ratio of selected typical strata.

Number	Strata	Height (cm)	Mean thickness (cm)	Material ratio					
				Ratio number	Sand	Gypsum	White powder	Coal ash	Loess
1	Soil	100.0	83.0	Sand : soil (20 : 1)	9.14	—	—	—	0.45
2	Siltstone	17.0	3.0	837	8.53	0.32	0.75	—	—
3	Fine-sandstone	14.0	6.0	846	8.53	0.43	0.64	—	—
4	Siltstone	8.0	3.0	746	8.40	0.48	0.72	—	—
5	5-2 coal	5.0	2.5	20 : 1 : 5 : 20	4.17	0.21	1.04	4.17	—
6	Fine-sandstone	2.5	2.5	746	8.40	0.48	0.72	—	—

weathered rock remains thin. After long-term weathering, the physical and chemical properties of the bedrock have changed significantly, and the hydrogeological characteristics have also changed. The pumping data show that the unit water inflow is less than 0.01 l/s·m, and the permeability coefficient is between 0.006 and 0.04 m/d. It can be seen that the water yield and conductivity of the weathering zone are very weak, and it has good water resistance, but it also reduces the strength of the rock mass.

As mentioned above, in the mountain gully of the shallow-thin bedrock coal seam, the overlying strata are prone to full-thickness cutting off, and the mine pressure is obvious. Therefore, the plane simulation model is divided into left and right gully depth terrains for comparative study. A steel ruler and protractor were used to measure the bedrock breaking step, mining-induced fracture characteristic parameters (fracture development angle, fracture opening and height, etc.), and the evolution law during working face advancement. All data are recorded in real time [21, 22].

3.2. Analysis of Dynamic Evolution Law of Mining-Induced Fracture. When the initial pressure of the working face occurs in the advancing process of the deep gully downhill section (as illustrated in Figure 2), the basic roof is ruptured behind the coal wall, causing slipping instability. However, the full-thickness cutting off of the overlying strata does not occur along with the basic roof failure, but the whole cutting off occurs first at the lower part of the overlying strata. Although there are vertical cracks developed in the upper part of the overlying strata, the friction force on the upper part of the overlying strata is greater than its gravity due to horizontal stress, and the overlying strata do not slide. As the

working face continues to advance, the overlying strata will collapse as the bedrock cuts down along the coal wall. The vertical cracks are developed through the surface, and the surface forms step-subsidence.

When the working face passes through the bottom of the gully, the bedrock is subjected to nonuniform loads. Because the load above the coal wall is relatively small, and the load behind the coal wall is relatively large, the rotation of the rock pillar near the bottom of the gully causes the cracks that penetrate the ground surface, and the development angle is approximately vertical. However, the fractures in the gully are gradually closed by horizontal compression caused by two different turning directions of the upward and downward slope. Surface uplift appeared, water-air leakage of overlying strata was reduced, and the air leakage in the gully was not the maximum. Therefore, the fracture development of overlying strata is different from that of other areas.

During the advancing of working face in the upslope of deep gully (Figure 3), because the load above the coal wall is relatively large, the load behind the coal wall is relatively small, and the overlying strata at the back of the working face are airborne in the horizontal direction; the bedrock gradually transforms from cantilever beam structure to hinged structure under nonuniformly distributed loads. The overlying strata above the working face are stretched to form "inverted trapezoidal" open fractures with wide upper and narrow lower. As the working face continues to advance, with the increase of bedrock rotation angle, the hinge of bedrock will eventually be crushed, and the hinged rock block will slip and become unstable. The fractures penetrated the ground surface. There was obvious step-subsidence, and the rear fractures gradually closed under the turning of the overlying strata.
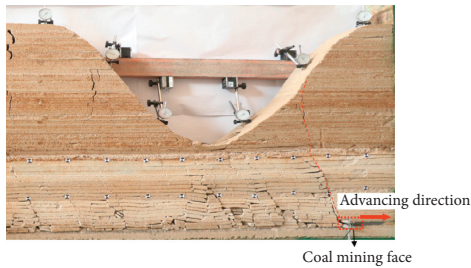
Figure 3: Deep ditch uphill stage.

Figure 4: Shallow ditch downhill stage.

Figure 5: Shallow ditch uphill stage.

During the advancing of working face in the downslope of the shallow gully (Figure 4), the lower part of the overlying strata slipped and destabilized as the bedrock broke, while the upper part deflected backward under nonuniformly distributed loads, forming new tensile fractures. Fractures show obvious asynchrony in spatiotemporal development. When the working face is advancing in a shallow gully, because the gully bottom is relatively flat, the stress on bedrock is more uniform, and the opening and misalignment of surface fracture are small after the bedrock is cut integrally.

During the advancing of the working face in the upslope of the shallow gully (Figure 5), affected by the friction of the overlying strata above the working face, the bedrock breaks into a hinged structure with the adjacent rocks behind. New tensile ground fissures are formed in the upper part of the overlying strata as the bedrock rotates, while rear ground fissures close as the bedrock rotates. After the working face continues to advance for a certain distance, the hinged block slips and becomes unstable. In other words, the whole bedrock is cut off behind the coal wall. However, compared with the previous stages, the transmission speed of bedrock fracture becomes faster and the weighting interval becomes smaller.

The change law of the two groups of overburden movement measuring points after coal seam mining is shown in Figure 6. The data of displacement measurement points analyzed and arranged show that no matter in the downhill mining and uphill mining area of the valley, or in the general terrain mining area, the bedrock of the goaf has obvious cutting subsidence, and the subsidence near the coal wall is small, which indicates that the goaf is basically compacted due to the large breaking angle. The subsidence of bedrock under goaf in downhill mining and uphill mining area is the largest, the maximum value of deep valley is 1450 mm, and the maximum value of shallow valley is 1320 mm, which indicates that the whole overburden cutting phenomenon is obvious, while the subsidence of bedrock in general terrain mining area is relatively small, the maximum value is only 790 mm, and the formation of a certain hinge structure in the goaf slows down part of the surface cutting subsidence.

In conclusion, during the mining of shallow-buried coal seam in the gully, mining-induced fractures in the weak overlying strata show the characteristics of periodic dynamic development with the failure and instability of bedrock. The overlying strata slide with the bedrock instability, and
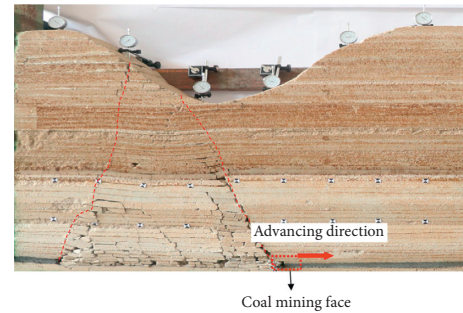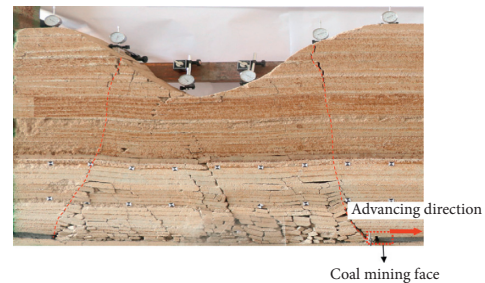
fracture morphology develops and changes rapidly. The surface macroscopic cutting is obvious, and collapsed and stepped mining fractures are relatively developed, forming periodically distributed water-air leakage channels. Under the influence of time effect and horizontal stress, the horizontal opening and vertical misalignment of surface fractures constantly change with the periodic pressure of the working face, and the opening of temporary open fractures gradually becomes small. Since the back of the overlying strata above the working face in the uphill stage is empty, the fracture opening in the uphill stage is larger than that in the downhill stage. The fractures in the deep gully are gradually closed by horizontal compression caused by two different turning directions of upward and downward slope. Surface uplift appeared, water-air leakage of overlying strata was reduced, and the air leakage in the gully was not the maximum.

4. Theoretical Model Analysis

4.1. Model Mechanics Analysis. According to the above analysis, the mining-induced fracture is controlled by the limit span. The failure and instability of bedrock directly cause the overall movement of overlying strata, resulting in penetrating mining-induced fractures. As a result, further study on the fracture mechanism and its influencing factors of shallow-thin bedrock in gully can lay an important foundation for the analysis of the development law of penetrating mining fractures in shallow coal seam mining.

The overlying strata above the bedrock are semi-consolidated with low strength. Therefore, when the self-
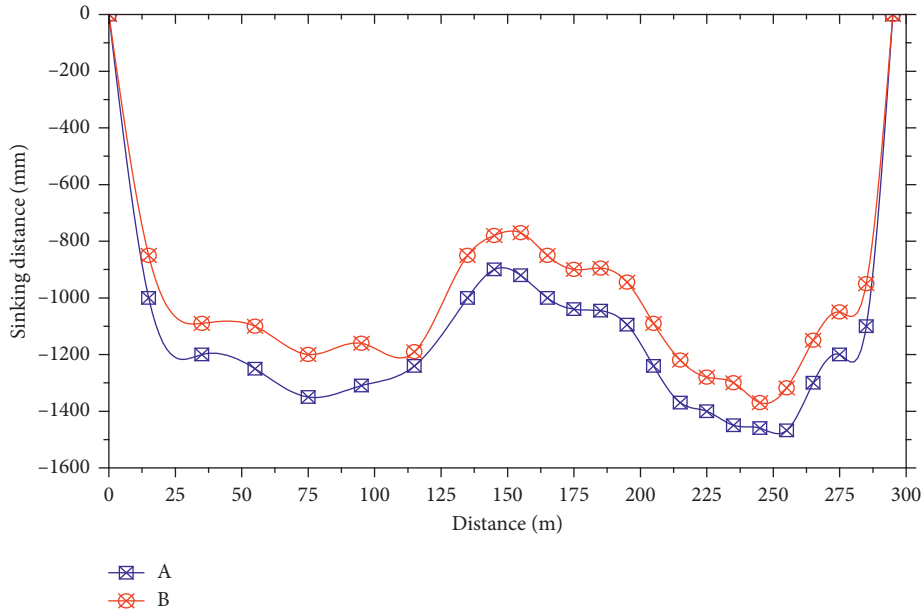
FIGURE 6: Surface subsidence data.

weight stress of the overlying strata is greater than the friction force, the overlying strata will undergo bar-type full-thickness cutting off as the basic roof break after working face stopping. The actual pressure of the bedrock bearing structure is the difference between the weight and the friction force on both sides of the overlying strata. If the weighting interval of the basic roof is taken as the limit span of the bearing structure, when the working face is mined in the gully, the mechanical model of surrounding rock is formed under the action of overlying strata, as shown in Figure 7.

In this study, in order to facilitate the calculation of load bearing structure, the following assumptions are made: ① it is assumed that the development angle of mining-induced fractures is a right-angle and ② the self-weight of bedrock is negligible.

Taking $ABCD$ as the sliding overlying strata, it can be known from the static balance equation of the beam that

$$
\begin{cases}
F_{RA}L + F_{AC}L - \gamma L \dfrac{a+b}{2} \cdot \left[L - \dfrac{2a+b}{3(a+b)} L \right] = 0, \\[2mm]
\gamma L \dfrac{a+b}{2} \cdot \dfrac{2a+b}{3(a+b)} L - F_{RB}L - F_{BD}L = 0, \\[2mm]
F_{AC} = \dfrac{1}{2} \gamma b^2 \tan\ \phi, \\[2mm]
F_{BD} = \dfrac{1}{2} \gamma a^2 \tan\ \phi.
\end{cases}
\tag{1}
$$

Then, the magnitude of the bearing reaction at both ends of the nonuniformly distributed load beam is
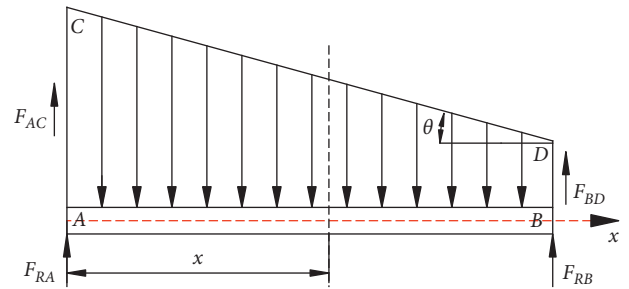
FIGURE 7: Mechanical model of the beam with nonuniform load.

$$
\begin{cases}
F_{RA} = \dfrac{a+2b}{6} \gamma L - \dfrac{1}{2} \gamma b^2 \tan\ \phi, \\[2mm]
F_{RB} = \dfrac{2a+b}{6} \gamma L - \dfrac{1}{2} \gamma a^2 \tan\ \phi,
\end{cases}
\tag{2}
$$

in which F_{RA}, F_{RB} are the bearing reaction at both ends of the nonuniformly distributed load beam, kN; a and b are the buried depth of the shallow and deep ends of the overlying strata above the nonuniform load beam, respectively, m; γ is the average volume force of the overlying strata, kN/m^3; L is the ultimate span of the bearing structure, m; $\tan\varphi$ is the friction coefficient of the slipping surface of the overlying strata, which is generally 0.3 [3].

According to equation (2), the difference of the bearing reaction at both ends of the nonuniformly distributed load beam is

$$
F_{R(A-B)} = \frac{1}{2} \gamma (b-a) \left[\frac{1}{3} L - (a+b) \tan\ \phi \right].
\tag{3}
$$

Therefore, when the limit span $L < 0.9(a+b)$, the difference between the two ends of the nonuniformly

distributed load beam is less than zero. In other words, the nonuniformly distributed load beam is subjected to greater pressure at the shallow-buried end, where it is more likely to cause the fracture development of the surrounding rock. When $a = b$, the bearing reaction at both ends of the load beam are equal, and the fracture development is basically synchronous.

In the AB section of the nonuniformly distributed load beam, for any section with a distance of x from the origin, the shear force is

$$\begin{cases} F_S(x) = F_{RA} + F_{AC} - \dfrac{2b - x \tan \theta}{2} \gamma x, \\ \\ \tan \theta = \dfrac{b - a}{L}, \end{cases} \tag{4}$$

where $F_S(x)$ is the shear force on the section at x from the origin, kN, and $\tan\theta$ is the surface slope of the overlying strata.

The shear force on the bedrock plane on this section is

$$F_S(x) = \frac{b - a}{2L} \gamma x^2 - b\gamma x + \frac{a + 2b}{6} \gamma L. \tag{5}$$

According to equation (5), the shear force on each section of the nonuniformly distributed load beam changes with x. In order to see how it works, take the derivative of x and make it equal to zero. Thus, it can be known that the nonuniformly distributed load beam simply decreases in the interval $(0, L)$, and the extreme value of the shear force is

$$\begin{cases} F_S(0) = \dfrac{a + 2b}{6} \gamma L, \\ \\ F_S(L) = -\dfrac{2a + b}{6} \gamma L, \\ \\ F_S\left(b\gamma - \dfrac{L\sqrt{a^2 + ab + b^2}}{\sqrt{3}\,(b - a)} \right) = 0. \end{cases} \tag{6}$$

4.2. Theoretical Analysis Results

(1) If the working face advances in the uphill direction, the maximum shear stress of the nonuniformly distributed load beam is located at the coal wall of the working face. When the shear stress of the basic roof is greater than its shear strength, the shear failure will occur along the coal wall, which will result in full-thickness cutting off in the overlying strata and cause the surface step-subsidence. If the working face advances along the downhill direction, the nonuniformly distributed load beam will break under the maximum shear stress behind the working face, resulting in the tensile shear failure near the coal wall of the basic roof.

(2) The ratio of the shear stress on the deep and shallow ends of the nonuniformly distributed load beam is $F_S(0)/F_S(L) = -(a + 2b/2a + b)$. Its value is only related to the buried depth of the loose overlying strata at the left and right ends of the nonuniformly distributed load beam, which has nothing with other parameters and the direction of the shear force on both ends is opposite.

(3) When $x = b\gamma - (\sqrt{a^2 + ab + b^2}/\sqrt{3} \tan \theta)$, the shear stress of the nonuniformly distributed load beam is zero. The determination of this position provides an important theoretical basis for the determination of the coal pillar in the working face of shallow-buried and thin bedrock coal seam, the filling mining of goaf, and the retracting position of the working face. Meanwhile, it shows that the greater the slope of the overlying strata, the closer the position, where the shear stress is zero, to the deeper buried end, and the smaller the fracture spacing.

Based on the mechanical properties of the basic roof and the stress environment, the study on the stability of the working face during mining is the basis of mechanical research to predict the weighting interval of shallow-buried thin bedrock in the gully. Under the maximum shear force, when the nonuniformly distributed load beam breaks, its maximum shear stress is

$$\tau_{\max} = \frac{a + 2b}{4h} \gamma L, \tag{7}$$

where $\tau_{\max}$ is the maximum shear stress of the nonuniformly distributed load beam, MPa, and h is the thickness of the nonuniformly distributed load beam, m.

As a result, when the maximum shear stress of the nonuniformly distributed load beam reaches its shear strength, its ultimate span is

$$L_S = \frac{4h[\tau]}{(a + 2b)\gamma}, \tag{8}$$

in which $[\tau]$ is the ultimate shear strength of the nonuniformly distributed load beam, MPa.

The above relationship shows the following:

(1) The limit span of nonuniformly distributed load beam is $L_S \in [4h[\tau]/3b\gamma, 4h[\tau]/3a\gamma]$. It is obviously different from the limit span of the basic roof calculated according to the uniformly distributed load beam. The larger the difference between a and b, that is, the larger the slope, the larger the error of the limit span of basic roof calculated according to the uniformly distributed load beam. When calculated by the average of the sum of the buried depth at both ends, the error may reach 25%.

(2) Under the limit span of the nonuniformly distributed load beam, the magnitude of the bearing reaction on both ends is shown in equation (9). It lays

an important theoretical foundation for the selection of support resistance in working face:

$$\begin{cases} F_{RA}(L_S) = \dfrac{2h[\tau]}{3} - \dfrac{1}{2}\gamma b^2 \tan \phi, \\[3mm] F_{RB}(L_S) = \dfrac{2h[\tau](2a + b)}{3(a + 2b)} - \dfrac{1}{2}\gamma a^2 \tan \phi. \end{cases} \tag{9}$$

5. Field Investigation and Management Discussion

5.1. Field Investigation. This study investigated the development characteristics of surface mining-induced fractures in the shallow-buried coal mining face of Anshan Coal Mine. According to the development morphology and scale characteristics of mining-induced fractures, it can be known that two types of typical mining-induced fractures are easily formed in the upper and lower mining stages of the working face, namely, collapsed and stepped mining fractures. The horizontal opening or vertical misalignment of stepped fractures is large, but the opening of the two wings of the collapsed fractures is small. In gentle areas, parallel fractures with small misalignment and small opening are easy to form, as shown in Figure 8. However, fractures develop periodically with the advance of the working face. That is, the bedrock fracture causes the overlying strata to slip, thus resulting in the surface fractures, and with the advance of the working face and the rear surface fractures gradually closed.

5.2. Management Discussion. The development of surface fractures above the working face will form a good water-air leakage channel, which seriously threatens safe mining. Therefore, the treatment of mining-induced fractures should fully consider the landform and occurrence conditions, optimize the layout of the working face, and formulate scientific prevention measures according to local conditions. In engineering application, the following measures are suggested for the treatment of mining-induced fractures:

(1) Technical control measures: ① for the working face with a direct water source or confined aquifer, reasonable filling materials and techniques should be selected according to the stress distribution characteristics of the working face. The purpose is to prevent the mining from directly connecting the mine water source and causing air leakage at the working face. ② For the working face without the above-mentioned water source conditions, scientific treatment measures should be formulated according to the topographic conditions. For example, filling mining is not necessary in gentle areas. After the overall subsidence, the ground fissure sealing technology can be used for landfill

and repair and ecological management. For the gully, according to the amount of surface water, it should be decided whether to adopt backfilling mining to prevent it.

(2) Management and prevention measures: specialized personnel shall be arranged to carry out fine exploration in the mining area, and gullies and the places where obvious subsidence or fractures have been formed shall be recorded one by one. The basic data is supplemented and improved timely, and the areas with the threat of water-air leakage are circled. Targeted prevention and control measures should be formulated, and forces are efficiently organized for timely governance.

Because the "nonuniform load beam" seriously impacts the support when the working face passes through the valley, the ordinary working face can not effectively prevent the occurrence of dynamic load mine pressure. When the working face passes through the valley, the advancing direction of the working face and the direction of the valley can be adopted to advance at a 15° angle, that is, the advancing speed of the upper and lower ends of the working face can be adjusted, so as to avoid the roof accident caused by the large-area hanging roof in the goaf.

At the same time, in order to accurately predict the pressure law of the working face and the pressure position of the working face, an online KJ513 mine pressure monitoring system is used to monitor the mine pressure of the working face in real time when the working face passes through the valley. Three measuring lines are arranged at the upper, middle, and lower parts of the working face, respectively. The monitoring range is 50 m before and after the trench bottom; that is, the working face is 45 m away from the open cut, and the observation is 100 m. Until the working face advances to the position 145 m away from the open cut, the working resistance curve of the upper, middle, and lower supports of the working face with the advancing of the working face is shown in Figure 9. In this process, there are 6 times of periodic weighting, and the maximum weighting is at the bottom of the ditch. At this time, the working resistance of the upper, middle, and lower supports of the working face is 41 MPa, 40 MPa, and 42 MPa, respectively, with an average of 41 MPa. The dynamic load coefficient is 1.37, 1.33, and 1.4, respectively, with an average of 1.37. The weighting strength is not very large. The rated working resistance of ZY8000/14/28 shield type hydraulic support selected in 20304 working face is 8000 kN, which can meet the requirements and realize the safe mining of working face. At the same time, the moving frame with pressure in the process of advancing can speed up the advancing speed of the working face, so as to reduce the movement range of the overlying strata and reduce the mine pressure behavior strength.

FIGURE 8: Morphological development of surface fissures in shallow seam mining.
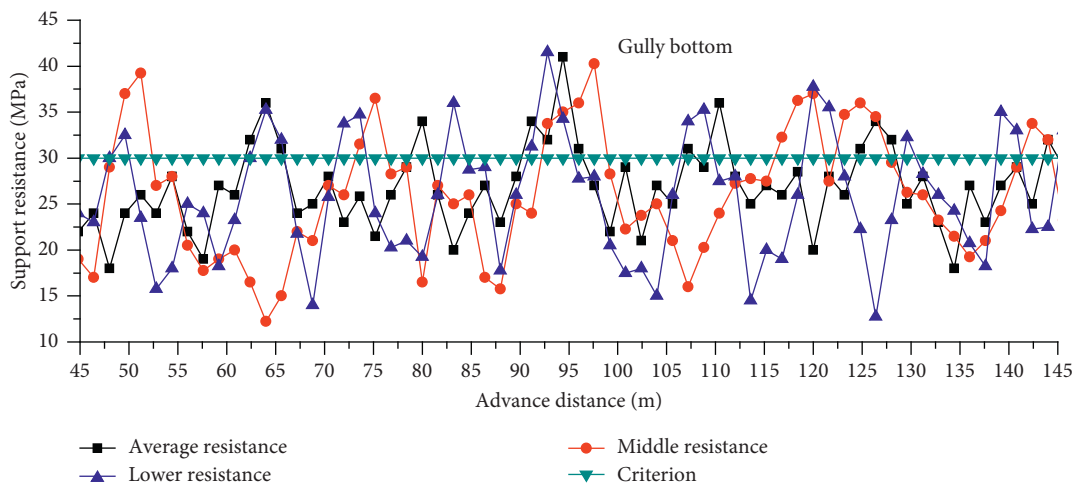
FIGURE 9: Support working resistance curves as the working face advances.

6. Conclusion

(1) During the mining in the gully, mining-induced fractures in the weak overlying strata show the characteristics of periodic dynamic development with the failure and instability of bedrock. The overlying strata slide with the bedrock instability, and collapsed and stepped mining fractures are relatively developed. In the uphill stage, the fracture opening is larger than that in the downhill stage. The fractures in the deep gully are gradually closed under the action of rotation, and the surface is uplifted.

(2) Based on the structural characteristics of surrounding rock in shallow-buried thin bedrock gully terrain, a structural mechanics model of surrounding rock with nonuniformly distributed load beam is established. The discriminant conditions for the stability of the surrounding rock structure are derived, and the calculation of the parameters such as the pressure at both ends of the basic roof, the shear force, and the ultimate span is determined.

(3) The slope of overlying strata above the nonuniformly distributed load beam has little effect on the weighting interval, while the buried depth has a great effect on the weighting interval. When the sum of buried depth at both ends is equal, the smaller the surface slope is, the larger the interval between the mining fractures will be. Surface fractures are basically equidistant and parallel development under gentle terrain conditions.

Data Availability

All data generated or analyzed during this study are included within this article.

Conflicts of Interest

The authors declare no conflicts of interest.

Authors' Contributions

T. Y. and J. Z. conceived and designed the experiments; Y. Y. and T. L. conducted data analysis; and T. Y. and S. G. wrote the paper.

Acknowledgments

References

[1] T. Yang and J. Zhang, "Experimental research on simulation material for water-resisting soil layer in mining physical simulation," *Advances in Materials Science and Engineering*, vol. 2020, Article ID 3456913, 8 pages, 2020.

[2] M. Qian, X. Miao, and J. Xu, "Theoretical study of key stratum in ground control," *Journal of China Coal Society*, vol. 21, no. 3, pp. 2–7, 1996.

[3] Z. Hou, "Analysis of combinatorial key strata stability in shallow coal seam with thick loose bed," *Journal of China Coal Society*, vol. 25, no. 2, pp. 127–131, 2000.

[4] J. Xu, W. Zhu, X. Wang et al., "Influencing mechanism of gully terrain on ground pressure behaviors in shallow seam longwall mining," *Journal of China Coal Society*, vol. 37, no. 2, pp. 179–185, 2012.

[5] Y. Fu, X. Song, P. Xing et al., "Study on simulation of caving and evolution law of roof strata of large mining height workface in shallow thick coal seam," *Journal of China Coal Society*, vol. 37, no. 3, pp. 366–371, 2012.

[6] Y. Fu, X. Song, and P. Xing, "Study of the mining height of caving zone in large mining height and super-long face of shallow seam," *Journal of Mining & Safety Engineering*, vol. 27, no. 2, pp. 190–194, 2010.

[7] Z. Li, X. Ding, and Z. Cheng, "Research on fractal characteristics of overlying strata crack evolution in coal seam with thin bedrock," *Journal of Mining & Safety Engineering*, vol. 27, no. 4, pp. 576–580, 2010.

[8] G. Wang, G. Yu, Y. Yu et al., "Study on cracks fractal evolution laws of mining rock mass," *Journal of Mining & Safety Engineering*, vol. 29, no. 6, pp. 859–863, 2012.

[9] X. Yu and Y. Qiu, "Analysis of subsidence status formation mechanisms in shallow mining seam of ravine cutting area," *Journal of Xi'an University of Science and Technology*, vol. 32, no. 3, pp. 269–274, 2012.

[10] P. Wang, X. Yu, and J. Liu, "Study on cracking failure mechanism of surface ground above underground high cutting ccal mining face in shallow mining depth seam," *Coal Engineering*, vol. 46, no. 5, pp. 84–86, 2014.

[11] L. Fan, X. Zhang, M. Xiang et al., "Characteristics of ground fissure development in high intensity mining area of shallow seam in Yushenfu coal field," *Journal of China Coal Society*, vol. 40, no. 6, pp. 1442–1447, 2015.

[12] L. Fan, "On coal mining intensity and geo-hazard in Yulin-Shen-mu-Fugu mine area," *China Coal*, vol. 40, no. 5, pp. 52–55, 2014.

[13] H. Liu, K. Deng, S. Lei et al., "Dynamic developing law and governance standard of ground fissures caused by underground mining," *Journal of Mining & Safety Engineering*, vol. 34, no. 5, pp. 884–890, 2017.

[14] Z. Hu, X. Wang, and A. He, "Distribution characteristic and development rules of ground fissures due to coal mining in windy and sandy region," *Journal of China Coal Society*, vol. 39, no. 1, pp. 11–18, 2014.

[15] W. Huang, Y. Gao, B. Wang et al., "Evolution rule and development height of permeable fractured zone under combined-strata structure," *Journal of Mining & Safety Engineering*, vol. 34, no. 2, pp. 330–335, 2017.

[16] J. Lou, F. Gao, J. Yang et al., "Characteristics of evolution of mining-induced stress field in the longwall panel: insights from physical modeling," *International Journal of Coal Science & Technology*, vol. 8, no. 1, 2021.

[17] H. Wu, B. Dai, L. Cheng et al., "Experimental study of dynamic mechanical response and energy dissipation of rock having a circular opening under impact loading," *Mining, Metallurgy & Exploration*, vol. 38, no. 2, pp. 1111–1124, 2021.

[18] Z. B. Cheng, L. H. Li, and Y. N. Zhang, "Laboratory investigation of the mechanical properties of coal-rock combined body," *Bulletin of Engineering Geology and the Environment*, vol. 79, no. 5, pp. 1947–1958, 2019.

[19] D. Z. Kong, Z. B. Cheng, and S. S. Zheng, "Study on the failure mechanism and stability control measures in a large-cutting-height coal mining face with a deep-buried seam," *Bulletin of Engineering Geology and the Environment*, vol. 78, no. 2, pp. 6143–6157, 2019.

[20] H. Wu, G. Zhao, and W. Liang, "Mechanical properties and fracture characteristics of pre-holed rocks subjected to uniaxial loading: a comparative analysis of five hole shapes," *Theoretical and Applied Fracture Mechanics*, vol. 105, Article ID 102433, 2020.

[21] X. Kong, S. Li, E. Wang et al., "Dynamics behaviour of gas-bearing coal subjected to SHPB tests," *Composite Structures*, vol. 256, Article ID 113088, 2021.

[22] X. Kong, S. Li, E. Wang et al., "Experimental and numerical investigations on dynamic mechanical responses and failure process of gas-bearing coal under impact load," *Soil Dynamics and Earthquake Engineering*, vol. 142, Article ID 106579, 2021.

Research Article

A New Dynamic Prediction Model for Underground Mining Subsidence Based on Inverse Function of Unstable Creep

Hua Cheng,[1,2] **Liangliang Zhang** [1] **Longhui Guo,**[1] **Xiaojian Wang,**[1] **and Shilong Peng**[3]

[1]*School of Civil Engineering and Architecture, Anhui University of Science and Technology, Huainan 232001, China*
[2]*School of Resources and Environmental Engineering, Anhui University, Hefei 230022, China*
[3]*School of Civil Engineering, Anhui Jianzhu University, Hefei, 230601, China*

Correspondence should be addressed to Liangliang Zhang; zllaust@163.com

In this study, an improved Knothe time function model is established via analogical reasoning from a phenomenological perspective, based on an inverse "Hohai creep model" function, in accordance with the antisymmetric relationship between the unstable creep curve and surface dynamic subsidence curve. An empirical method and fitting method are proposed to determine the parameters of the improved model based on the availability of measured field data. The accuracies of the two models are compared with monitored data from eight monitoring points in the main strike profile of the Guotun coal mine subsidence basin. The results show that the improved model can more accurately reflect the dynamic process of surface subsidence. The average relative standard deviation of the improved model is only 4.9%, which is far lower than the 23.1% associated with the Knothe model. This verifies the improved model's accuracy and reliability. The model parameters for different monitoring stations obtained using the fitting method are similar, which shows that the model parameters are regular and can be easily applied.

1. Introduction

The surface subsidence caused by coal mining is a dynamic process [1, 2]. A series of problems associated with surface subsidence, including environmental deterioration, land desertification, groundwater level decline, and the formation of ground-based building and infrastructure cracks, have been a concern within academic and engineering field [3]. The accurate prediction and effective control of surface subsidence in order to recommend reasonable excavation schemes and ground building protection measures has thus been identified as a difficult problem requiring solution [4]. Surface subsidence is not only related to the hydrogeological conditions of coal seams but is also closely related to mining methods and processes. With the increase of the scope of goaf, the mining-related range of surface-level disturbance expands, and a stable subsidence basin gradually forms on the surface after mining is halted for a period of time. The scale of the subsidence basin is far larger than that of the mined-out area. A specific point on the surface will experience the whole process of initial subsidence, rapid subsidence, and slow subsidence before finally reaching a stable state [5, 6]. Therefore, surface subsidence is a continuous function of time, and the key to accurate prediction of surface subsidence is the determination of the time function model and the model parameters.

At present, Knothe time function model is widely used in mining engineering. However, with more in-depth research, the shortcomings of the Knothe time function model are becoming increasingly apparent [7, 8]. Therefore, many experts use the methods of parameter modification, piecewise modeling, and theoretical analysis to establish more accurate and applicable prediction models. Hu et al. [9, 10] proposed the probability integral method to solve the parameters of the Knothe time function model according to the general characteristics of surface movement and deformation caused by mining subsidence and the critical size of the goaf when fully mined out. Cui et al. [11] proposed Knothe time function model parameters in line with real-world situations by comprehensively considering the driving speed

of the working face and the critical size of the goaf during full mining. Liu and Zhuang [12, 13] added a power index with constant K as a parameter in the Knothe time function and put forward an improved Knothe model in line with the actual surface subsidence characteristics. Li [14] proposed the concept of overburden lithologic parameters and established the relationship between these parameters and the time function model parameters, thus improving the Knothe time function model. Taherynia et al. [15] used a circular network to determine the compaction effect of the entire reservoir on the field surface, based on the Knothe and Geertsma influence functions.

These research results have been well applied to the prediction of surface subsidence in coal mining. However, there are many defects in the model, such as the large number of parameters and the difficulty involved in their determination. In this study, an inverse "Hohai creep model" function is solved according to the antisymmetric relationship between the unstable creep curve and the surface dynamic subsidence curve. From a phenomenological perspective, an improved Knothe time function model based on an inverse "Hohai creep model" function is established by analogical reasoning. Additionally, the rationality and applicability of the improved model are verified by using monitored data from the main profile of the surface strike of the 1301 working face in the Guotun mine.

2. Knothe Time Function Model

The Knothe time function model was proposed by the Polish scholar Knothe in 1952 [16]. At present, it is widely used to predict the dynamic subsidence of a specific point on the surface caused by mining. The expression of Knothe time function model is as follows [17, 18]:

$$\begin{cases} W(t) & = W_0\left(1 - e^{-ct}\right), \\ V(t) & = cW_0 e^{-ct}, \\ a(t) & = -c^2 W_0 e^{-ct}, \end{cases} \tag{1}$$

where c is a time influence parameter; $W(t)$ is the surface subsidence; $V(t)$ is the subsidence velocity; $a(t)$ is the surface subsidence acceleration.

According to equation (1), the Knothe time function curve is obtained, as shown in Figure 1.

According to equation (1) and Figure 1, it can be seen that the surface subsidence increases gradually, $V(t)$ decreases gradually, and $a(t)$ is always less than 0 throughout the subsidence process, which is clearly inconsistent with the actual surface subsidence characteristics.

Lots of field monitoring data show that the process of surface subsidence can generally be divided into initial subsidence, rapid subsidence, and slow subsidence to a stable state. The surface subsidence curve approximates an "S" type curve, while the surface subsidence velocity curve approximates a normal distribution curve [19, 20]. However, $W(t)$, $V(t)$, and $a(t)$ represented by Knothe model are monotonic

functions of time, so the model is not suitable for describing the dynamic surface subsidence process.

3. Improved Knothe Model

According to the rock creep theory, rock will undergo unstable creep under high stress levels as shown in the blue curve in Figure 2 (the curve does not include the instantaneous strain generated during stress loading). It can be seen that the shape of the unstable creep curve is similar to a reverse "S" curve, which is the inverse of the surface subsidence curve. In view of this and taking $\varepsilon(t) = t$ as the axis of symmetry, it is proposed that the inverse image of the unstable creep curve can be obtained as shown by the red "S" curve in Figure 2, and this can be used to describe dynamic surface subsidence. According to basic mathematics, the functions represented by the red curve and the blue curve are inverse functions of each other. Therefore, as long as the unstable creep function is determined and its inverse function is calculated, the time function describing the dynamic surface subsidence can be established.

The establishment of the unstable creep function is always a difficulty in the study of rock creep mechanics. Because the parameters of the classical Kelvin creep model, the Burgers creep model, and the Nishihara creep model do not change with time, it is difficult to use these models to describe the unstable creep that occurs when the stress exceeds the long-term strength of rock [21]. In order to effectively solve this problem, experts have proposed the use of nonlinear elements as replacements for the linear elements present in the classical models to establish a nonlinear creep model that can describe unstable rock creep. This has led to the establishment of the "Hohai creep model" [22]. In this model, the ideal viscous body is replaced by a nonlinear viscous body and paralleled with a plastic body. The "Hohai creep model" can be used to describe unstable rock creep. The "Hohai creep" mechanical model is shown in Figure 3.

According to the nonlinear creep theory, the differential constitutive relation of the "Hohai creep model" can be obtained as follows:

$$\sigma - \sigma_S = \frac{\eta}{nt^{n-1}} \frac{d\varepsilon(t)}{dt}, \tag{2}$$

where σ is stress; σ_S is long-term strength; η is the viscosity coefficient of the "Hohai creep model"; n is model order; ε is strain; and t is time.

$(d\varepsilon(t)/dt)$ in equation (2) is regarded as the independent variable x and $\sigma - \sigma_S$ as the dependent variable y. The functional relationship between x and y can then be obtained as follows:

$$y = \frac{\eta}{nt^{(n-1)}} x. \tag{3}$$

The inverse function of equation (3) can be solved to obtain the new relationship between the independent and dependent variables. At this time, the independent variable
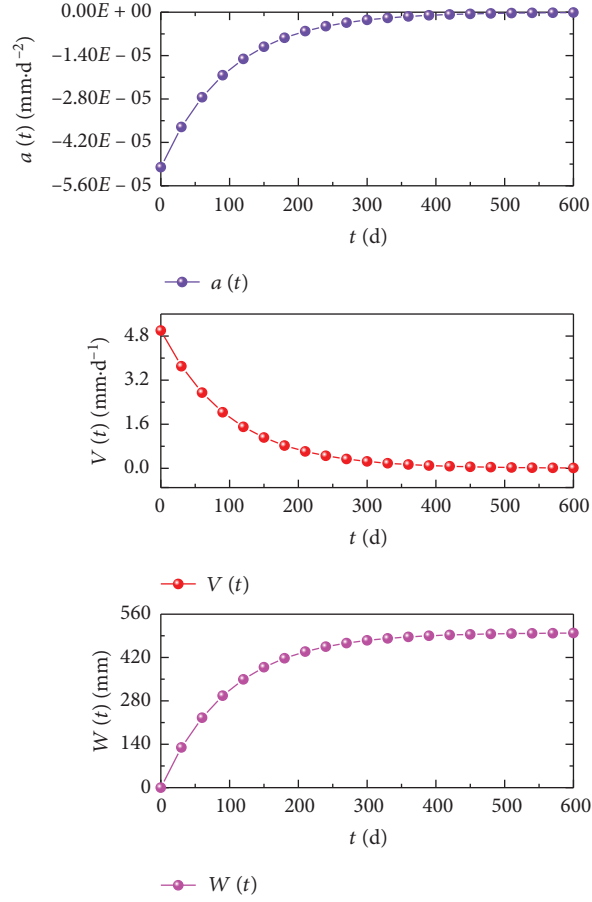
FIGURE 1: The Knothe time function curve.

is $\sigma - \sigma_S$ and the dependent variable is $(d\varepsilon(t)/dt)$. Therefore, the inverse function of equation (3) can be expressed as follows:

$$\frac{d\varepsilon(t)}{dt} = \frac{nt^{n-1}}{\eta}(\sigma - \sigma_S). \tag{4}$$

From the perspective of phenomenology, we can use analogical reasoning to equate $(d\varepsilon(t)/dt)$ to $(dW(t)/dt)$, $(1/\eta)$ to C, σ to W_0, and σ_S to $W(t)$. This allows the proposal of an improved Knothe model expression as follows:

$$\frac{dW(t)}{dt} = Cnt^{n-1}[W_0 - W(t)], \tag{5}$$

where C is a time influence parameter of the improved model.

Solving equation (5) and considering the initial condition $W(t)|_{t=0} = 0$, equation (5) can then be simplified as follows:

$$W(t) = W_0[1 - \exp(-Ct^n)]. \tag{6}$$

The dynamic surface subsidence velocity and acceleration can then be derived from equation (6) as follows:

$$\begin{cases} V(t) = W_0 Cnt^{n-1}\exp(-Ct^n), \\ a(t) = W_0 Cn\exp(-Ct^n)[(n-1)t^{n-2} - Cnt^{2n-2}]. \end{cases} \tag{7}$$

When $n = 1$, equations (6)~(7) can be simplified into equation (1), which shows that the Knothe model is a special case of the improved model established in this study.

The surface subsidence curve, subsidence velocity curve, and subsidence acceleration curve of the improved model are shown in Figure 4. It can be seen that the surface subsidence curve is approximately S-shaped, and the surface subsidence velocity curve approximates a normal distribution curve. The surface subsidence characteristics that are reflected are consistent with the real-world process and can thus be used to describe the dynamic process of surface subsidence.

4. Determination of Model Parameters

According to equation (6), there are only two parameters in the improved model: C and n. Therefore, compared with the Knothe model, the improved model is not only more
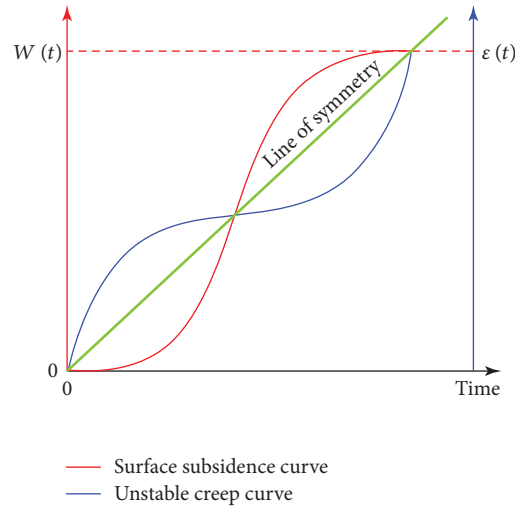
FIGURE 2: Unstable creep and surface subsidence curves.

accurate but is also easily applied in the field due to the reduced number of required parameters. Additionally, its practical operability is superior to other complex improved models.

4.1. Empirical Method.

By analyzing a large amount of surface subsidence monitoring data, we can get the following empirical equation [23]:

$$W(t)|_{V(t)=V_{max}} = 0.98W_0. \tag{8}$$

Taking equation (9) into equation (7), we get $n = 3.26$.

According to empirical analysis and research, when the length of goaf reaches the full mining value, W_{max} will be approximately $0.98 W_0$ [24]. According to equation (6), the parameter C can be calculated as follows:

$$0.98W_0 = W_0\left[1 - \exp\left(-C\left(\frac{2H}{v\tan\varphi}\right)^{3.26}\right)\right], \tag{9}$$

where $(2H/\tan\varphi)$ is the critical gob dimension [25], v is the mining velocity, H is the seam depth, and φ is the full subsidence angle.

Equation (9) is simplified and the parameter C is obtained as follows:

$$C = -\left(\frac{v\tan\varphi}{2H}\right)^{3.26}\ln 0.02. \tag{10}$$

4.2. Fitting Method.

The empirical method mentioned in Section 4.1 has the following limitations:

(1) When determining the parameters C and n, it is necessary to determine the time when the surface subsidence reaches its maximum velocity along with the critical gob dimension L_f. However, these two parameters are not easy to determine accurately for actual coal seam mining.

(2) Due to the application of different mining methods and differing geological conditions, not all surface point subsidence values are half of the final subsidence value when the subsidence velocity reaches its maximum value. In addition, neither is the maximum surface subsidence equal to $0.98 W_0$ when the scale of the coal seam mining reaches the critical value of full mining.

Therefore, C and n determined by applying empirical methods are associated with a certain error that is independent of the error caused by measurement. When there is a large amount of surface subsidence monitored data, the fitting method [26] can be used to determine the improved Knothe time function model parameters according to the field monitoring data. This method can ensure minimization of the error between the fitting value and the monitored value. In addition, it is easy to use and is thus widely favored by researchers.

5. Model Validation

Monitored data and results predicted by the model were compared and analyzed in order to verify the rationality of the improved model. The surface subsidence monitored data from the 1301 working face in Guotun coal mine, Shandong Province, China, were used in the investigation. The 1301 working face is located to the southwest of the Juye mining area. The coal seam thickness varies from 1 to 3.6 m, and the dip angle is 12°. Mining began on the working face in the first ten days of November 2010 and ended in the middle of December 2012. The first observation was performed on October 18, 2010, and the maximum detected surface subsidence was 16 mm.

The length of the strike observation line of the 1301 working face is 4200 m. It contains 126 monitoring points, numbered Z1–Z126. The length of the inclination observation line is 2300 m, and it contains 60 monitoring points, numbered H1–H60. The distance between two adjacent monitoring points is 30 m. To satisfy the requirements of this
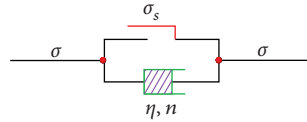
FIGURE 3: "Hohai creep model."
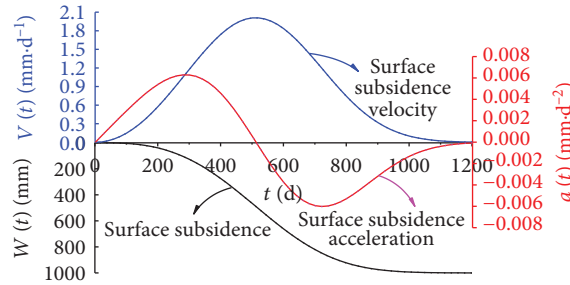
FIGURE 4: Subsidence, subsidence velocity, and subsidence acceleration curve of improved Knothe model.

research, the layout of some monitoring points was selected as shown in Figure 5. Due to the extended observation duration and the large amount of monitored data, monitored data from points Z29, Z37, Z41, Z44, Z45, Z47, Z50, and Z53 were randomly selected to analyze the accuracy of the Knothe time function model and the improved Knothe time function model in terms of surface subsidence prediction.

Table 1 shows the measured subsidence values from 8 monitoring points taken at different dates. It can be seen from the table that the final stable subsidence values of Z29 and Z37 are smaller than those of the other monitoring points. However, the subsidence trend at all monitoring points shows a clear "S" shape, allowing the phenomenon to be described by the improved model.

Combined with the monitored data, the Knothe model and the improved model were used to predict the surface subsidence. The results obtained using the two models can be compared with the measured data from the eight monitoring points, as shown in Figure 6.

The parameters of the improved model and Knothe model were determined according to the fitting method as shown in Table 2. It can be seen from a comparison of the results shown in Figure 5 that there is a big difference between the fitted values of the Knothe time function model and the monitored data. Additionally, the model curve flows a gradual slope with respect to time, which does not reflect the "S" type curve of surface point subsidence with respect to time. The improved model curve is highly consistent with

the monitored data, which accurately reflects the dynamic characteristics of surface point subsidence with respect to time. In addition, the model parameters C and n obtained by fitting the monitored data of monitoring points Z41, Z44, Z45, Z47, Z50, and Z53 are similar, showing little difference. This indicates that the model is relatively stable and that the model parameters are regular and easily applied.

6. Discussion

As shown in equation (11), the standard deviation m and relative standard deviation f can be used to verify the accuracy of the improved model. The calculation results are shown in Table 3. From Table 3, we can see that the improved model's average relative standard deviation was only 4.9%, which is far lower than the 23.1% of the Knothe model. Although the accuracy of the improved Knothe time function model is higher than that of the Knothe model, the improved model is only suitable for describing the law of surface subsidence after full mining and can not accurately reflect the characteristics of surface subsidence in the process of insufficient mining.

$$\begin{cases} m = \pm \sqrt{\dfrac{\sum_{i=1}^{N}\left(W_j - W_l\right)^2}{N-1}}, \\ f = \left|\dfrac{m}{W_0}\right|, \end{cases} \tag{11}$$
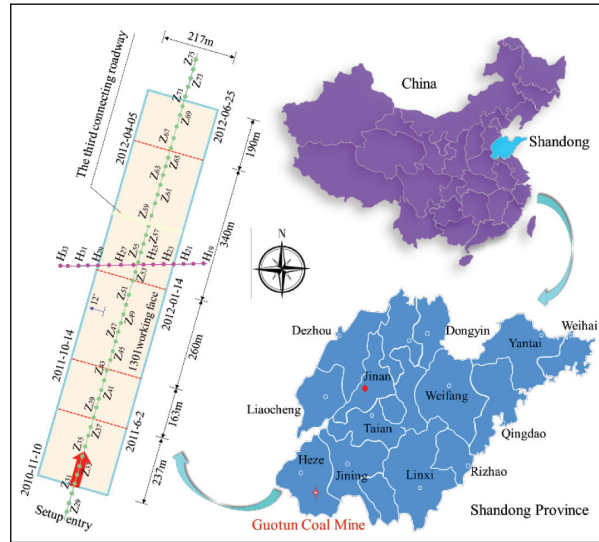
FIGURE 5: The location of 1301 working face.

TABLE 1: Surface subsidence monitored data from Z29, Z3, Z41, Z44, Z45, Z47, Z50, and Z53.

Observation times	Observation date	Relative observation (time/d)	Subsidence (value/mm)							
			Z29	Z37	Z41	Z44	Z45	Z47	Z50	Z53
1	2010/10/18	0	0	0	0	0	0	0	0	0
2	2010/12/27	69	0.006	0.006	0.006	0.005	0.005	0.006	0.003	0.004
3	2011/1/23	95	0.012	0.008	0.007	0.006	0.004	0.007	0.006	0.003
4	2011/3/2	134	0.020	0.018	0.017	0.014	0.010	0.011	0.009	0.010
5	2011/3/27	159	0.027	0.024	0.020	0.015	0.009	0.009	0.006	0.005
6	2011/4/27	189	0.066	0.074	0.055	0.039	0.030	0.026	0.013	0.008
7	2011/5/14	206	0.080	0.097	0.066	0.046	0.036	0.028	0.014	0.008
8	2011/6/2	224	0.104	0.126	0.100	0.071	0.058	0.047	0.026	0.014
9	2011/6/29	251	0.138	0.185	0.151	0.109	0.092	0.074	0.041	0.023
10	2011/7/27	279	0.153	0.227	0.189	0.137	0.119	0.092	0.043	0.024
11	2011/9/17	329	0.168	0.249	0.208	0.151	0.131	0.102	0.045	0.025
12	2011/10/14	356	0.241	0.394	0.371	0.296	0.265	0.211	0.133	0.080
13	2011/11/3	375	0.283	0.498	0.630	0.569	0.440	0.370	0.241	0.142
14	2012/1/14	446	0.305	0.619	0.717	0.713	0.687	0.630	0.489	0.333
15	2012/3/4	496	0.342	0.700	0.859	0.916	0.917	0.898	0.829	0.691
16	2012/4/5	527	0.364	0.735	0.919	1.003	1.015	1.018	1.005	0.926
17	2012/5/15	567	0.373	0.750	0.940	1.033	1.050	1.060	1.070	1.022
18	2012/6/25	607	0.383	0.765	0.960	1.063	1.085	1.103	1.136	1.119
19	2012/7/24	636	0.390	0.773	0.969	1.072	1.094	1.112	1.147	1.130
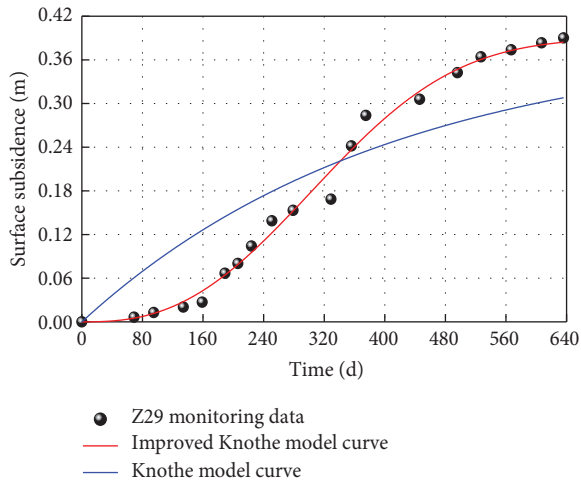
(a)
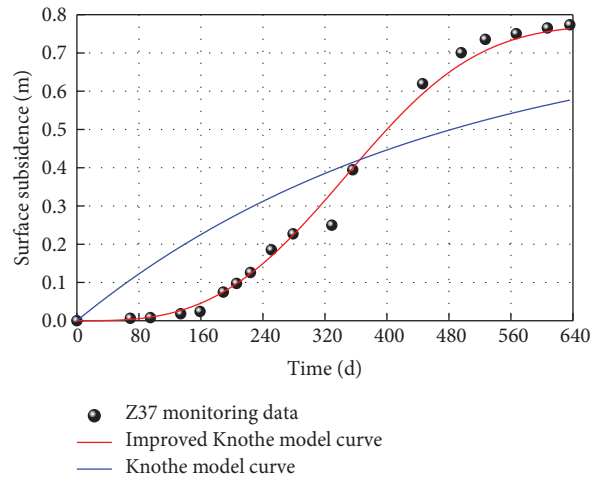
(b)
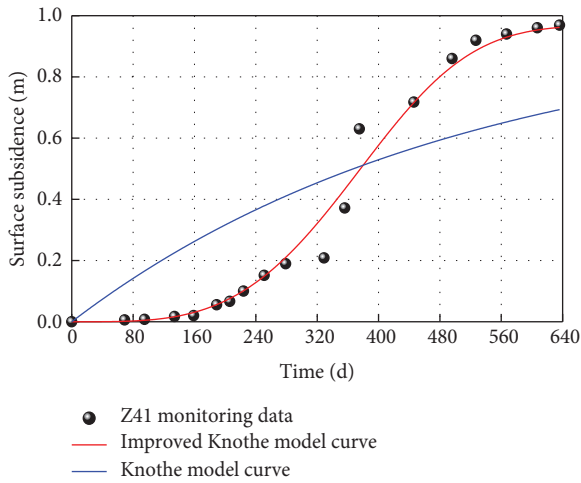
(c)
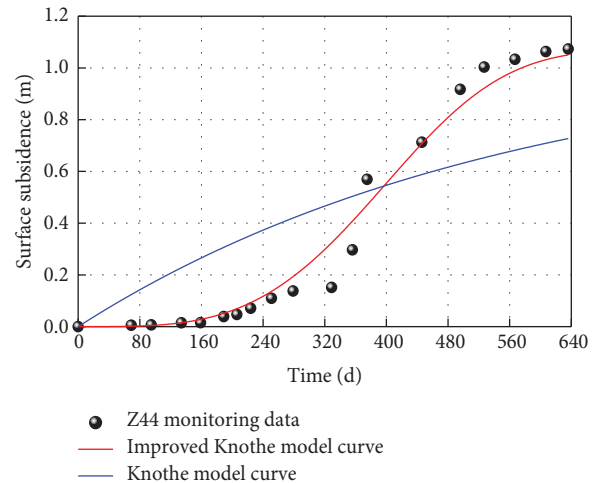
(d)
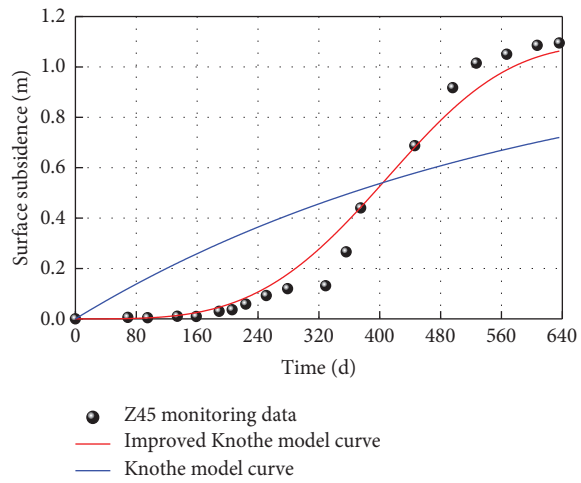
(e)
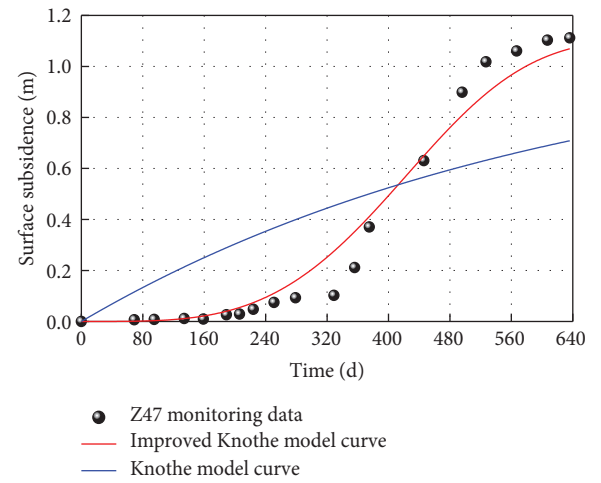
(f)

Figure 6: Continued.

(g)

(h)
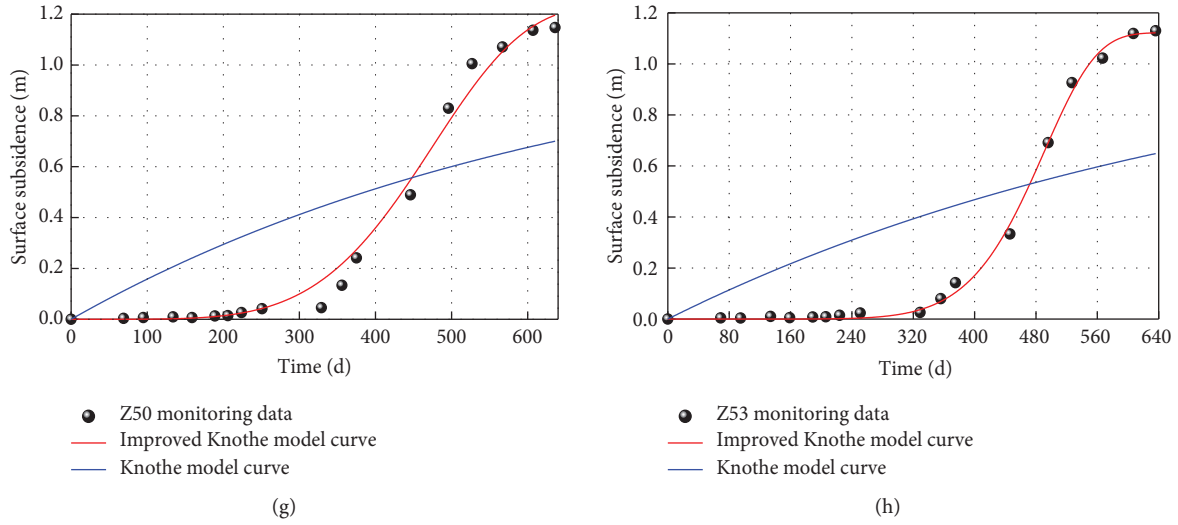
FIGURE 6: Comparison of two time function models. (a) Z29; (b) Z37; (c) Z41; (d) Z44; (e) Z45; (f) Z47; (g) Z50; and (h) Z53.

TABLE 2: Time influence parameters of different monitoring points.

Monitoring points	Improved Knothe model			Knothe model	
	$C/(d^{-n})$	n	R^2	$c/(10^{-3}·d^{-1})$	R^2
Z29	2.24×10^{-7}	2.59	0.992	2.45	0.787
Z37	9.54×10^{-9}	3.09	0.993	2.15	0.715
Z41	3.30×10^{-10}	3.63	0.984	1.97	0.663
Z44	3.17×10^{-10}	3.60	0.979	1.78	0.625
Z45	2.33×10^{-10}	3.63	0.979	1.69	0.607
Z47	1.42×10^{-10}	3.69	0.973	1.59	0.586
Z50	0.87×10^{-10}	3.75	0.985	1.48	0.562
Z53	0.89×10^{-10}	3.79	0.986	1.31	0.529

TABLE 3: Error of monitored and predicted values.

Monitoring points	Improved model		Knothe model	
	m (mm)	f (%)	m (mm)	f (%)
Z29	13	3.3	66	16.8
Z37	24	3.1	158	20.4
Z41	48	4.9	222	22.9
Z44	76	6.3	259	24.1
Z45	62	5.6	270	24.6
Z47	72	6.4	280	25.2
Z50	63	5.5	289	25.2
Z53	64	4.8	288	25.5
Average value	53	4.9	229	23.1

where W_j and W_l are monitoring value and theoretical value, respectively; N is the total number of monitoring points.

7. Conclusions

(1) Theoretical analysis shows that Knothe model is not suitable for describing the process of surface dynamic subsidence. An improved Knothe time function model based on an inverse "Hohai creep model" function is established from a phenomenological perspective using analogical reasoning according to the antisymmetric relationship between the unstable creep curve and the surface dynamic subsidence curve.

(2) The improved model can describe the actual process of surface subsidence and only contains two model parameters, which is convenient for practical engineering application.

(3) The result of error analysis shows that the average relative standard deviation of the improved model was only 4.9%, which is far lower than the 23.1% of the Knothe model, thus verifying that the accuracy

and reliability of the improved Knothe model are superior to those of the Knothe model.

Data Availability

The monitoring data used to support the findings of this study are included within the article.

Conflicts of Interest

The authors declare that there are no conflicts of interest regarding the publication of this paper.

Acknowledgments

References

[1] M. S. Alam, D. Kumar, R. S. Chatterjee, and V. Upreti, "Assessment of land surface subsidence due to underground metal mining using integrated spaceborne repeat-pass differential interferometric synthetic aperture radar (DInSAR) technique and ground based observations," *Journal of the Indian Society of Remote Sensing*, vol. 46, no. 10, pp. 1569–1580, 2018.

[2] L. Zhang, H. Cheng, Z. Yao, and X. Wang, "Application of the improved Knothe time function model in the prediction of ground mining subsidence: a case study from Heze City, Shandong Province, China," *Applied Sciences*, vol. 10, no. 9, Article ID 3147, 2020.

[3] R. Luo, G.-Y. Li, L. Chen, Q.-Y. Yang, C.-W. Zang, and W.-Z. Cao, "Ground subsidence induced by pillar deterioration in abandoned mine districts," *Journal of Central South University*, vol. 27, no. 7, pp. 2160–2172, 2020.

[4] Y. Cai, X. Li, W. Xiao, and W. Zhang, "Simulation of mining-induced ground damage using orthogonal experiments to determine key parameters of super-large coalface: a case study in Shendong coalfield in China," *Applied Sciences*, vol. 10, no. 7, Article ID 2258, 2020.

[5] Q. F. Hu, X. M. Cui, G. Wang et al., "Key technology of predicting dynamic surface subsidence based on Knothe time function," *Journal of Software*, vol. 6, no. 7, pp. 1273–1280, 2011.

[6] B. L. Wang, J. L. Xu, and D. Y. Xuan, "Time function model of dynamic surface subsidence assessment of grout-injected overburden of a coal mine," *International Journal of Rock Mechanics and Mining Sciences*, vol. 104, no. 1–8, 2018.

[7] A. M. Suchowerska Ianec, J. P. Carter, and J. P. Hambleton, "Geomechanics of subsidence above single and multi-seam coal mining," *Journal of Rock Mechanics and Geotechnical Engineering*, vol. 8, no. 3, pp. 304–313, 2016.

[8] A. Kowalski, "Surface subsidence and rate of its increaments based on measurements and theory," *Archives Mining Sciences*, vol. 46, pp. 391–406, 2001.

[9] Q. F. Hu, X. M. Cui, L. Kang et al., "Impact of parameter on Knothe time function and its calculation model," *Journal of Mining & Safety Engineering*, vol. 31, no. 1, pp. 122–126, 2014.

[10] Q. Hu, X. Deng, R. Feng, C. Li, X. Wang, and T. Jiang, "Model for calculating the parameter of the Knothe time function based on angle of full subsidence," *International Journal of Rock Mechanics and Mining Sciences*, vol. 78, pp. 19–26, 2015.

[11] X. Cui, J. Wang, and Y. Liu, "Prediction of progressive surface subsidence above longwall coal mining using a time function," *International Journal of Rock Mechanics and Mining Sciences*, vol. 38, no. 7, pp. 1057–1063, 2001.

[12] Y. C. Liu and Y. H. Zhuang, "Model for dynamic process of ground surface subsidence due to underground mining," *Rock and Soil Mechanics*, vol. 30, no. 11, pp. 3406–3410, 2009.

[13] Y. C. Liu, "Dynamic surface subsidence curve model based on Weibull time function," *Rock and Soil Mechanics*, vol. 34, no. 8, pp. 2409–2413, 2013.

[14] D. Li, "Influence of cover rock characteristics on time influencing parameters in process of surface movement," *Chinese Journal of Rock Mechanics and Engineering*, vol. 23, no. 22, pp. 3780–3784, 2004.

[15] M. H. Taherynia, S. M. Fatemi Aghda, A. Ghazifard, and E. Moradi, "Prediction of subsidence over oil and gas fields with use of influence functions (case study: south pars gas field, Iran)," *Iranian Journal of Science and Technology, Transactions A: Science*, vol. 41, no. 2, pp. 375–381, 2017.

[16] S. Konthe, "Effect of time on formation of basin subsidence," *Archives of Mining Steel Industry*, vol. 1, no. 1–7, 1953.

[17] L. Li, K. Wu, and D.-W. Zhou, "AutoCAD-based prediction of 3D dynamic ground movement for underground coal mining," *International Journal of Rock Mechanics and Mining Sciences*, vol. 71, pp. 194–203, 2014.

[18] C. Gonzalez-Nicieza, M. I. Alvarez-Fernandez, A. Menendez-Diaz, and A. E. Alvarez-Vigil, "The influence of time on subsidence in the Central Asturian coalfield," *Bulletin of Engineering Geology and the Environment*, vol. 66, no. 3, pp. 319–329, 2007.

[19] Z. F. Yang, J. J. Zhu, Z. W. Li et al., "Analysis of law of kinematic mining subsidence by integrating InSAR and leveling measurements," *Journal of Central South University (Science and Technology)*, vol. 46, no. 10, pp. 3743–3751, 2020.

[20] L. Nie, H. Wang, and Y. Xu, "Application of the arctangent function model in the prediction of ground mining subsidence deformation: a case study from Fushun City, Liaoning Province, China," *Bulletin of Engineering Geology and the Environment*, vol. 76, no. 4, pp. 1383–1398, 2016.

[21] L. L. Zhang and X. J. Wang, "Viscoelastic-plastic damage creep model for rock," *Chinese Journal of Geotechnical Engineering*, vol. 42, no. 6, pp. 1085–1092, 2020.

[22] W. Y. Xu, S. Q. Yang, and W. J. Chu, "Nonlinear viscoelasto-plastic rheological model (Hohai model) of rock and its engineering application," *Chinese Journal of Rock Mechanics and Engineering*, vol. 25, no. 3, pp. 433–447, 2006.

[23] Z. Q. Chang and J. Z. Wang, "Study on time function of surface subsidence—the improved Knothe time function," *Chinese Journal of Rock Mechanics and Engineering*, vol. 22, pp. 1496–1499, 2003.

[24] X. J. Zhu, G. L. Guo, J. F. Zha et al., "Surface dynamic subsidence prediction model of solid backfill mining," *Environmental Earth Sciences*, vol. 75, no. 12, Article ID 1007, 2016.

[25] J. Z. Wang, Z. Q. Chang, and Y. Chen, "Study on mining degree and patterns of ground subsidence in condition of mining under thick unconsolidated layers," *Journal of China Coal Society*, vol. 28, no. 3, pp. 230–234, 2003.

[26] H. Li, J. Zha, and G. Guo, "A new dynamic prediction method for surface subsidence based on numerical model parameter sensitivity," *Journal of Cleaner Production*, vol. 233, pp. 1418–1424, 2019.

Research Article

Risk Assessment and Prevention of Surface Subsidence under Buildings by Cemented Paste Filling and Strip Mining Methods: A Case Study

Sun Qiang [1,2] **Zhou Nan,** [1] **Song Weijian,** [1] **and Zhao Xu** [3]

[1]State Key Laboratory of Coal Resources and Safe Mining, School of Mines, China University of Mining & Technology, Xuzhou 221116, China
[2]State Key Laboratory for Geomechanics and Deep Underground Engineering, China University of Mining & Technology, Xuzhou 221116, China
[3]School of Civil, Environmental, and Mining Engineering, The University of Western Australia, Perth 6009, Australia

Correspondence should be addressed to Sun Qiang; kkysun@126.com

Intensive and continuous mining of coal resources in China implies their gradual exhaustion, especially in the eastern regions. While some mines face closure, others have to extract residual coal resources under buildings, water bodies, and industrial sites. Thus, safe and efficient mining of the residual coal resources requires innovative techniques, which would account for the particular site's geological conditions. In this study, two schemes of roadway mining with cemented paste backfilling (RMCPB) and strip mining are put forward. After analyzing the type, construction, and protection standard of the buildings, the probability integration method and the prediction model are used to assess the surface subsidence and deformation. The research results show that both schemes can control the surface deformation to a certain extent, but RMCPB combines the advantages of a high coal recovery rate and disposal of gangue waste. According to the surface subsidence predicted and measured data, the RMCPB method can effectively control the surface subsidence, deformation, and buildings' safety. It also yields significant economic and environmental benefits.

1. Introduction

About half of the world's coal is produced in China, mainly (90%) by underground mining. Intensive and continuous extraction of coal resources leads to their gradual exhaustion in east-central densely populated areas of China [1–3]. Furthermore, environmental problems in coal mining, including surface subsidence and solid waste accumulation affected by multiple mining, become very topical [4–6]. Statistics indicate that the subsiding areas induced by caving coal mining annually amount to about 40,000 hm^2, resulting in the annual financial losses of about 300 million USD. At present, the total area of coal mining-induced surface subsidence in China has reached 700,000 hm^2 [7]. On the other hand, waste gangue is produced and accumulated on the ground, occupying significant land resources and polluting the environment [8, 9]. An effective technique for controlling surface subsidence with simultaneous disposing of the resulting solid waste in coal mining is urgently required to mitigate these problems.

Several studies have been conducted to substantiate and develop such techniques. Yu et al. [10] examined the rationality of the strip mining scheme with a large mining depth under dense buildings and analyzed the reasonable range of strip mining and reserved widths. The Wilson theory and FLAC numerical simulation were used to predict the surface movement and deformation under different mining conditions. The reasonable strip mining width was assessed at 120 m, ensuring the safe and economic mining under the surface village buildings. Zhang et al. [11] analyzed

the risk assessment and prevention of surface subsidence in deep multiple coal seam mining under dense above-ground buildings using numerical simulation and surface subsidence prediction methods in solid backfill mining. Teng et al. [12] studied the surface subsidence characteristics of grout injection into overburden on the side of a stopping line (SSL) of a long wall via in situ monitoring, whereas areas with grouting were compared with those without it. Based on the key strata theory and numerical simulation experiment, Liu et al. [13] studied the space-time relationship between the breaking of key strata and surface subsidence in high water filling, analyzed the main factors affecting the surface subsidence, and evaluated the control effect of surface subsidence in high water filling. The above research studies promoted the green and efficient mining of coal resources. However, because of the difference between the backfill materials and filling costs, a rapid and economic backfill coal mining method suitable for residual coal resources in small- and medium-sized coal mines has not been proposed and widely implemented yet.

Alternatively, the cemented paste backfilling (CPB) technology, which offered both economic and environmental benefits, has been used extensively in China's underground mines [14, 15]. Besides, CPB provides ground and wall support, which also facilitates mine waste disposal. Thus, it limits the likelihood of caving and prevents subsidence. Moreover, CPB technology significantly improves underground mine operations' safety and increases productivity. Therefore, it is now considered a standard practice in mining operations worldwide. In this study, the mining geological conditions, type, construction, and buildings' protection standards are analyzed. Then, two schemes of RMCPB and strip mining methods are discussed in detail. The prediction model of the probability integration method is proposed to study the surface subsidence and deformation during the mining. The surface subsidence predictions and field measurements are compared, and conclusions on the most lucrative mining scheme are drawn.

2. Description of the Area under Study

2.1. Mining Geological Conditions.
The coal mine studied in this study belongs to the Xinwen Mining Group Co., Ltd., and is located in Shandong Province of China. The construction of the mine began in November 1971 and was put into operation in July 1982. The mine's design capacity is 0.45 million tons per year, and the approved production capacity was 0.9 million tons per year in 2006. The mine design adopts vertical and inclined shaft, multilevel, main crosscut, horizontal main roadway, and mixed development of up and downhills. There are three mining areas in the mine design: the first mining area, the fourth mining area, and the sixth mining area. The mining method adopts the strike longwall retreating mining method, both caving and filling methods to manage the roof. Besides, the strip mining method is adopted for special blocks, such as coal resources under buildings. No. 4 coal seam is the main mining coal seam, which has been mined out except the coal resources under the industrial square and buildings. The coal resources of the safety coal

pillar at a depth of 300 m below the industry square amount to 1.29 million tons, including the main and auxiliary shaft coal pillars resourced of 0.65 million tons. Coal resources under buildings in the Western area are about 0.50 million tons.

According to the geological report on the mine, No. 4 coal seam is the main mineable coal seam with black-colored, brittle coal developed in endogenous fractures. The average thickness of the coal seam is 2.0 m. The fracture surface has usually a ladder-and-shell pattern. The coal petrography is mainly composed of bright coal and vitrinite, and the coal rock type belongs to the semibright type. Its bulk density is 1.37, hardness is 2.5~3.0, and medium ash is low sulfur, while the ash melting point is quite high. The main roof is grayish-white medium sandstone with a thickness of about 15 m. The composition is mainly quartz, followed by feldspar. The intermittent oblique bedding is developed and hard. The upper part is intercalated with a thin layer of siltstone, interbedded with developed fractures, and partially filled with calcite. The immediate floor is light gray siltstone with a thickness of about 8 m. The roof is rich in plant fossils, and the middle part is intercalated with a thin layer of carbonaceous shale or gray clay shale. The main floor is light gray, fine-grained sandstone with a thickness of 3 m. The composition is mainly quartz, followed by feldspar and calcareous (relatively hard) cementation. The distribution of surface buildings and generalized stratigraphic column in the study area are shown in Figure 1.

2.2. Antideformation Capacity and Reinforcement Criteria.
The investigated mining area is located south of the industry square; the mining area is about 0.21 square kilometers. The investigation results of surface buildings showed that they varied in dimensions, layout, and structure. The buildings mainly included a village, a hospital, a coal washery, and a workshop with brick and timber structures of a certain antideformation ability, as shown in Figure 2. The protection requirements of surface buildings in this area were not high, so strip mining was adopted in the original design. According to the four-level classification of damage to surface brick-concrete structures of the Chinese State Bureau of Coal Industry (2000) given in Table 1, the area's building damage was controlled within level I (negligible damage, no repair required), and the maximum subsidence was controlled within 300 mm.

3. Mining Scheme and Surface Subsidence Prediction

3.1. Mining Scheme Design.
According to the distribution characteristics of surface buildings and antideformation capacity in the studied mining area, the strip mining and backfilling mining methods were designed. In the first scheme, the studied mining area was subdivided into four strip mining faces: 1402, 1404, 1406, and 1408, in which the caving mining method is adopted. The width of mining faces and safety coal pillars was about 40 m. In the second scheme, the studied mining area was subdivided into eight backfill mining faces, 1401~1408, in which the roadway

No.	Columnar	Lithology	Thickness (m)	Description
1		Topsoil	9.20	The upper part is yellowish brown clay and the lower part is water bearing sand gravel layer
2		Clayey sandstone	35.03	It is mainly purplish red clayey siltstone with no bedding and thin conglomerate
3		Sandstone	75.91	It is composed of red fine medium sandstone, quartz feldspar, and argillaceous cementation
4		Siltstone	24.55	It is mainly composed of light gray siltstone and grayish green medium sandstone, and locally, it is gravelly coarse sandstone with argillaceous cementation. The original water level elevation of this layer is +185.79m, and the average unit water inflow (q) is 0.0596 L/s·m.
5		Medium sandstone	2.70	
6		Mudstone	10.25	
7		Coarse sandstone	15.38	It is composed of 5–6 layers of medium coarse-grained sandstone with clay and calcium
8		Medium sandstone	20.00	It is light gray with gray black composition, mainly quartz, followed by feldspar
9		Fine sandstone	4.00	It is gray black, dense, brittle, containing plant fossils and carbonized plants
10		Mudstone	1.02	Light gray, mainly composed of quartz, containing plant rhizome fossils
11		Siltstone	6.00	Dark gray, hard in texture, developed in cross-bedding, and contains plant fossils
12		Siltstone	5.00	Light gray, mainly composed of quartz, hard, containing plant rhizome fossils, locally broken
13		Medium sandstone	15.00	Gray white, mainly composed of quartz, feldspar, calcareous cementation, hard
14		Coal seam	2.00	It is black, streaked brown, brittle, massive and granular, bright, carbonaceous mudstone
15		Siltstone	8.00	It is light gray, with plant fossils, and a thin layer of carbonaceous shale or gray clay shale

Figure 1: Distribution of surface buildings and generalized stratigraphic column in the study area.

(a)

(b)

(c)

(d)

Figure 2: Photos of above-ground buildings: (a) hospital, (b) village, (c) coal washery, and (d) workshop.

mining with the cemented paste backfilling (RMCPB) method was adopted. For the first mining method, it is relatively mature with low investment cost, but less coal production. The second method needs to increase the backfilling equipment, the investment cost is relatively high, but the coal production is large, and the solid waste products of the mine can be treated at the same time. The width of RMCPB faces was about 40 m. The roadway layouts of the mining face for both methods are shown in Figure 3.

TABLE 1: Classification of damage to surface brick-concrete structures [16].

Damage level	Surface deformations Horizontal deformation (mm/m)	Curvatures (mm/m²)	Inclinations (mm/m)	Classification	Structural processing
I	≤2.0	≤0.2	≤3.0	Negligible damage Very slight damage	No repair Light repair
II	≤4.0	≤0.4	≤6.0	Slight damage	Minor repair
III	≤6.0	≤0.6	≤10.0	Medium damage	Medium repair
IV	>6.0	>0.6	>10.0	Severe damage Very severe damage	Heavy repair Demolition and construction
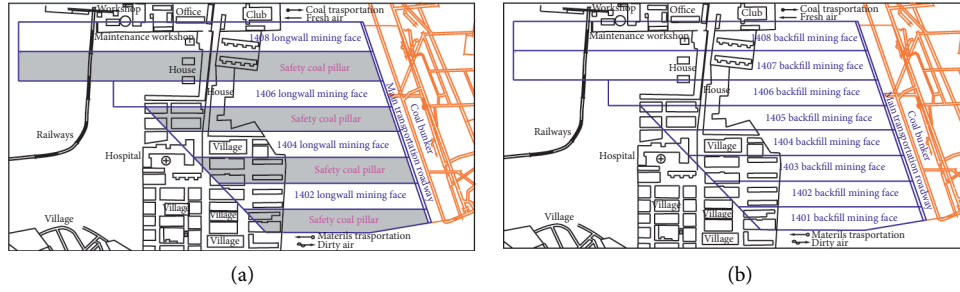
FIGURE 3: Roadway layouts of mining face for two mining methods: (a) strip mining; (b) RMCPB.

Based on the conventional coal mining method's production system, RMCPB is a backfill mining method with circulation operation of "driving roadway for mining and filling one by one" [17–19]. The principle is to excavate the crossheading between two roadways of a fully mechanized road header's working face. The gangue and fly ash are used as the main filling materials. Under the action of cementitious materials, high-concentration slurry without dehydration treatment is prepared according to a certain mix proportion, and the filling material is transported underground via a filling pump and a pipeline. The related equipment is mainly composed of coal mining, filling, and transportation subsystems. The first one includes a fully mechanized road header and a local ventilator. Filling equipment contains a filling pump, a crusher, a vibrating screen, a mixer, a batching machine, and a filling pipeline. The transportation equipment mainly includes a scraper conveyor and a belt conveyor. The preparation process of RMCPB material includes four steps: dry material preparation, filling materials mixing, mix and stir with water, and pumping of filling material. In this study, gangue accounts for 80%, cement and fly ash 20%, and the compressive strength of the material can reach 2.0 MPa in 7 days and 5.0 MPa in 28 days. Hbmg 110/14–500 backfilling industrial pump was selected according to the backfilling distance. The technical principle and filling process of RMCPB are shown in Figure 4.

3.2. Surface Subsidence Prediction. The probability integral method was adopted in this study to predict surface movement and deformation with the two coal mining methods according to the principles of surface subsidence control based on the equivalent mining height (EMH)

theory [20–23]. In this model, the surface movement and deformation were calculated by the following equations:

$$W(x) = \frac{Mq \cos a (1-\varphi)}{2} \left[erf\left(\frac{\sqrt{\pi}}{r} x\right) + 1 \right],$$

$$U(x) = bMq \cos a (1-\varphi) e^{-(\pi x^2/r^2)},$$

$$i(x) = \frac{Mq \cos a (1-\varphi)}{r} e^{-(\pi x^2/r^2)}, \tag{1}$$

$$\varepsilon(x) = -2\pi b \frac{Mq \cos a (1-\varphi)}{r^2} x e^{-(\pi x^2/r^2)},$$

$$k(x) = -2\pi \frac{Mq \cos a (1-\varphi)}{r^3} x e^{-(\pi x^2/r^2)},$$

where $W(x)$ is the subsidence, $U(x)$ is the horizontal movement, $i(x)$ is the inclination, $\varepsilon(x)$ is the horizontal deformation, $k(x)$ is the curvature deformation, M is the mining height, q is the surface subsidence coefficient, b is the horizontal movement coefficient, a is the angle of inclination of the coal seam, and φ is the backfill materials' compression ratio. The above formulas also feature $r = H/\tan\beta$, where r is the radius of influence, H is the mining depth, and $\tan\beta$ is the tangent of the main angle of influence. In actual engineering, the surface subsidence coefficient q is set as 0.85, $b = 0.31$, $\tan\beta = 2.0$, $a = 0$, and $\varphi = 90\%$.

The Surfer of Golden Software and CAD commercial packages were used to process the surface deformation data. The horizontal surface deformation, inclination, curvature, horizontal movement, and subsidence along the north-south and east-west lines in RMCPB are shown in Figures 5∼9. The
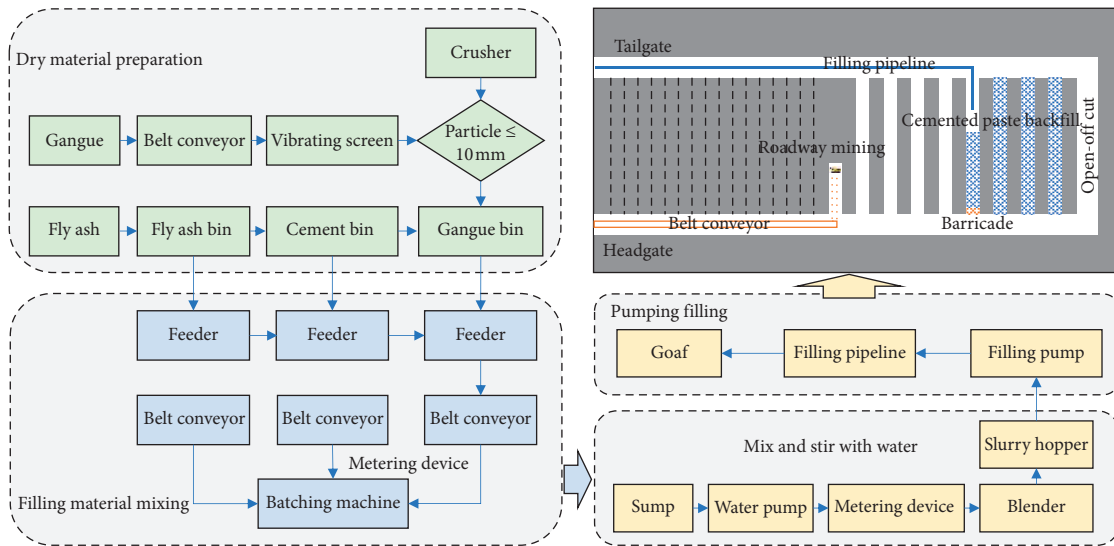
FIGURE 4: Technical principle and the filling process of RMCPB.

(a)

(b)
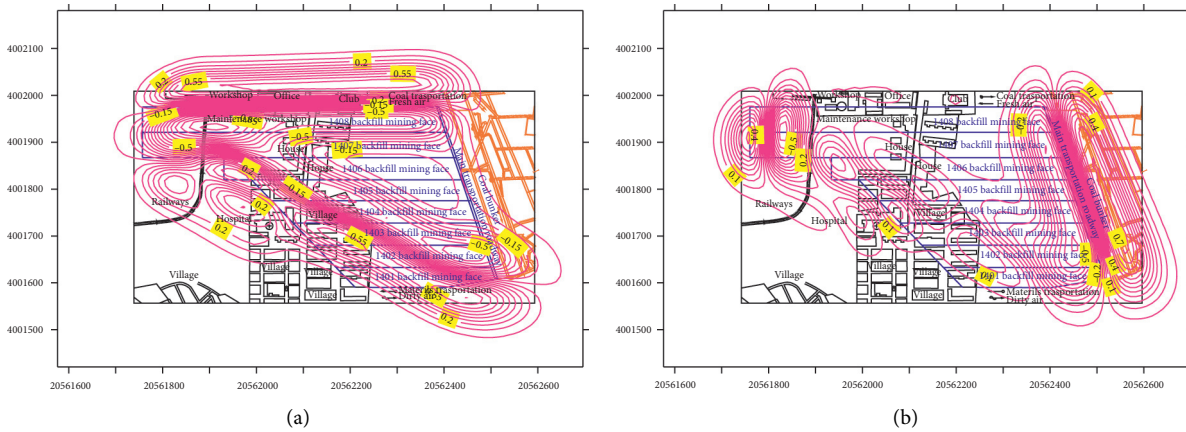
FIGURE 5: Contour map of horizontal surface deformation in RMCPB.

(a)

(b)
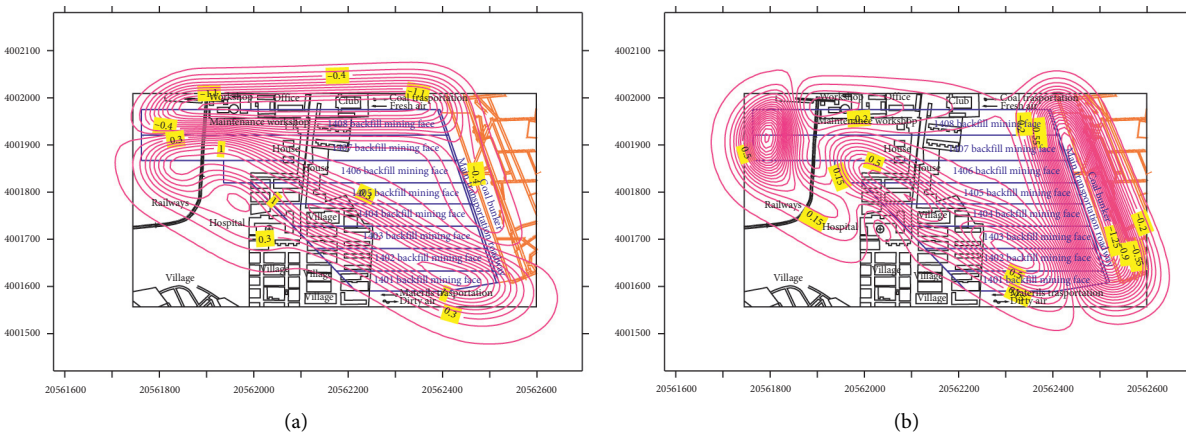
FIGURE 6: Contour map of surface inclination in RMCPB.

surface movement and deformation extremum is given in Table 2.

Similarly, the horizontal surface deformation, inclination, curvature, horizontal movement, and subsidence, along the north-south and east-west lines in strip mining were derived and are shown in Figures 10~14. The surface movement and deformation extrema are listed in Table 3.

(a)

(b)
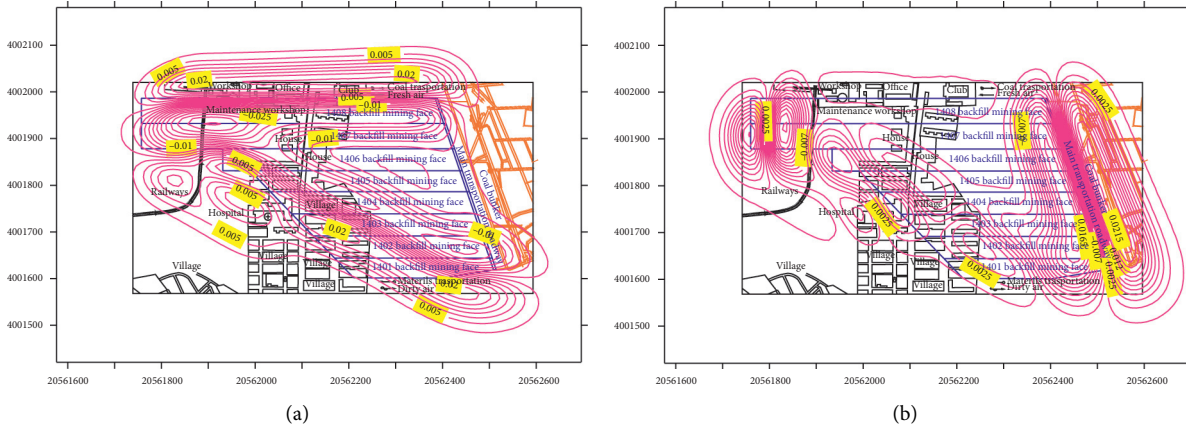
Figure 7: Contour map of surface curvature in RMCPB.

(a)

(b)
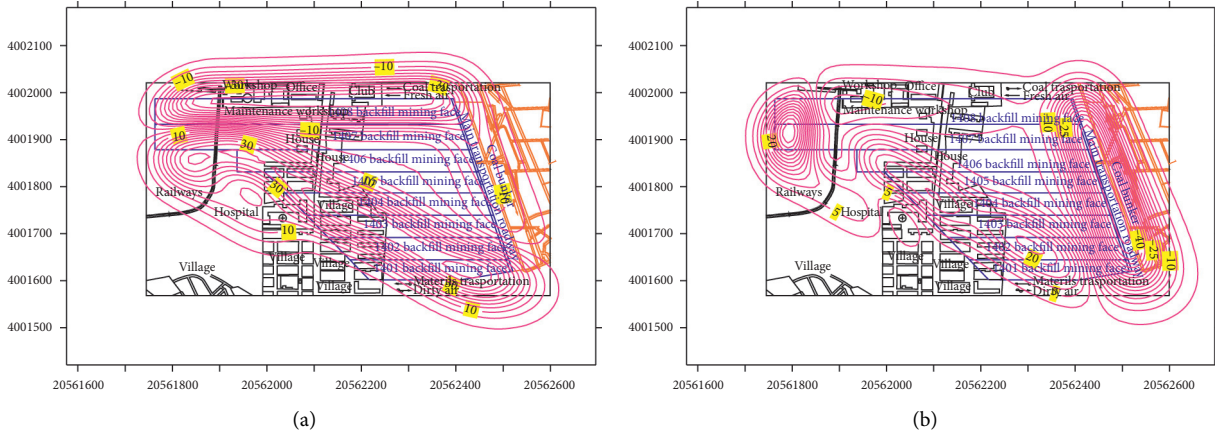
Figure 8: Contour map of horizontal surface movement in RMCPB.
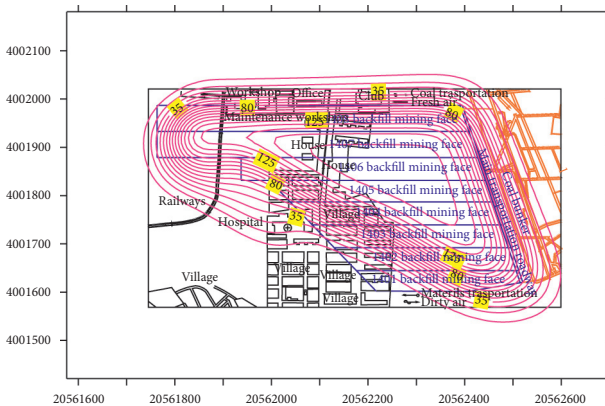
Figure 9: Contour map of surface subsidence in RMCPB.

It can be seen from Figures 5–9 and Table 3 that the maximum subsidence of the surface above the studied mining area with RMCPB was 170 mm; the maximum horizontal movement of the ground surface along the south-north line was 55 mm and that along the east-west one was 50 mm. The maximum horizontal deformation of the surface in the south-north line was 0.8 mm/m and that in the east-west one was 1.2 mm/m. The maximum inclination along the south-north and east-west lines was 1.6 and 1.8 mm/m, respectively. The maximum curvature along the south-north and east-west lines was 0.03 and 0.04 mm/m^2, respectively.

Figures 10–14 and Table 4 show that the maximum subsidence of the surface above the studied mining area with strip mining was 230 mm; the maximum horizontal movement of the ground surface along the south-north line was 100 mm and that along the east-west one was 110 mm. The maximum horizontal deformations of the surface along the south-north and east-west lines were 0.38 and 0.40 mm/m, respectively. The maximum inclinations along the south-north and east-west lines were identical and equal to 0.35 mm/m. The maximum curvatures along the south-north and east-west lines were 0.03 and 0.04 mm/m^2, respectively.

From the above analysis, the extreme values of surface deformation under both mining schemes fell within the level I of damage to surface buildings. Still, the overall disturbance degree and mining influence area of RMCPB was weak, being mainly reflected in the subsidence and horizontal movement. In strip mining, the subsidence and horizontal

TABLE 2: Surface movement and deformation extrema in RMCPB.

Subsidence (mm)	Horizontal movement (mm)		Horizontal deformation (mm/m)		Inclination deformation (mm/m)		Curvature (mm/m^2)	
	South-north	East-west	South-north	East-west	South-north	East-west	South-north	East-west
170	55	50	0.8	1.2	1.6	1.8	0.03	0.04

(a)

(b)
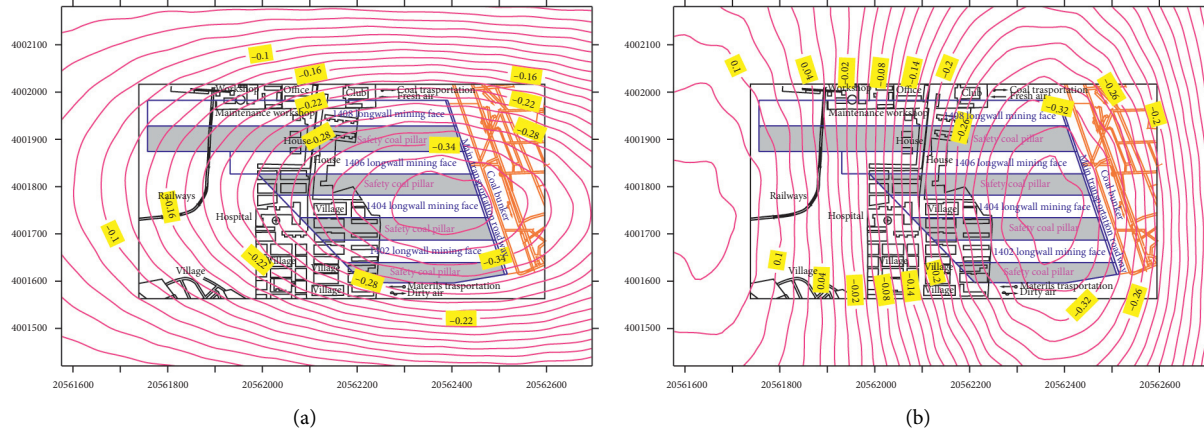
FIGURE 10: Contour map of horizontal surface deformation in strip mining.

(a)

(b)
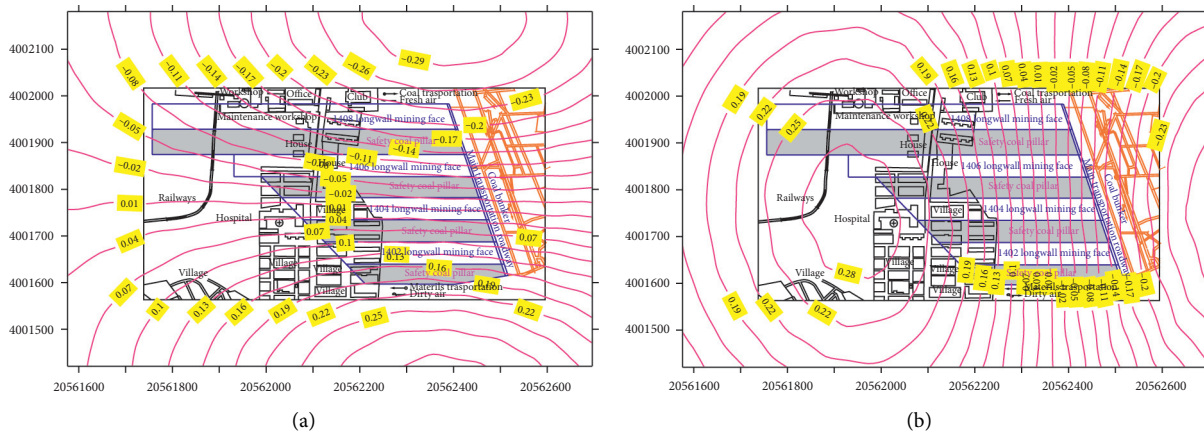
FIGURE 11: Contour map of surface inclination in strip mining.

(a)

(b)
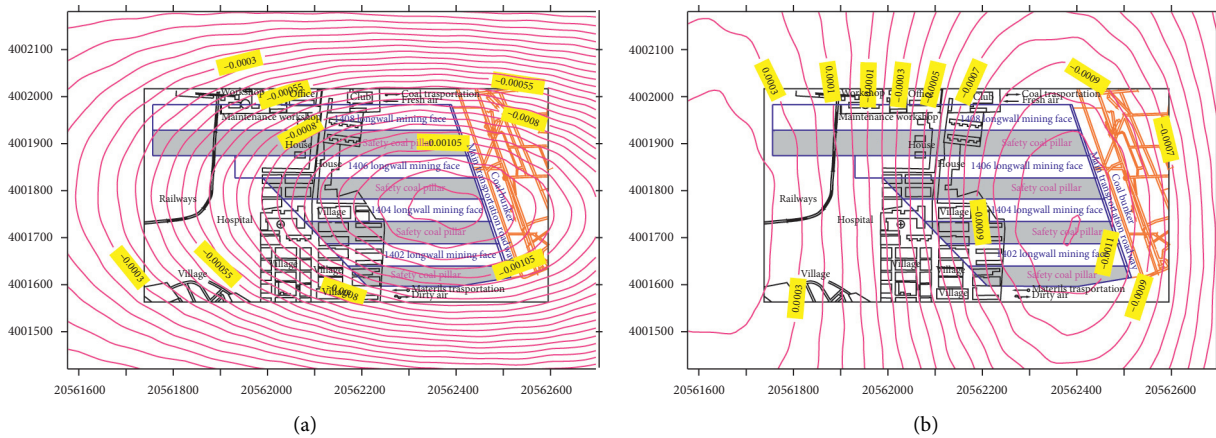
FIGURE 12: Contour map of surface curvature in strip mining.

(a)   (b)
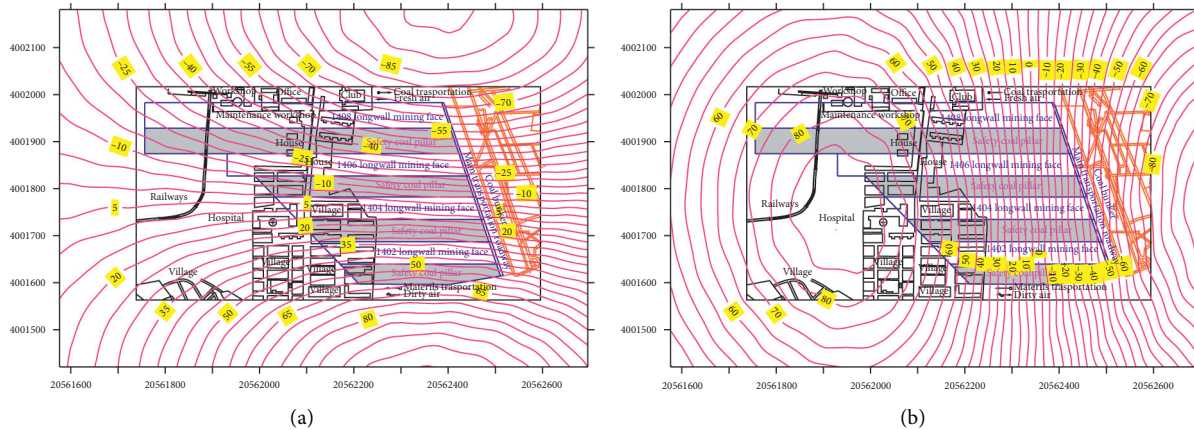
FIGURE 13: Contour map of horizontal surface movement in strip mining.
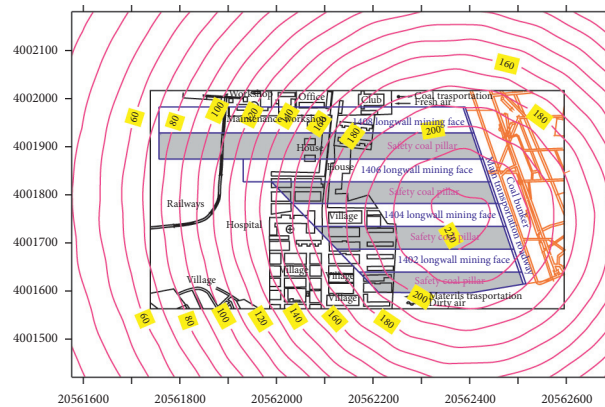
FIGURE 14: Contour map of surface subsidence in strip mining.

TABLE 3: Surface movement and deformation extremum in strip mining.

Subsidence (mm)	Horizontal movement (mm)		Horizontal deformation (mm/m)		Inclination deformation (mm/m)		Curvature (mm/m²)	
	South-north	East-west	South-north	East-west	South-north	East-west	South-north	East-west
230	100	110	0.38	0.40	0.35	0.35	0.03	0.04

movement extreme values were relatively high, and the mining influence area was large. Still, the horizontal surface and inclined deformations were relatively small due to the protection of coal pillars. After coal mining in this area, the buildings and structures within the influence range of surface deformation were not affected. The main workshop, office building, clothing factory, and other buildings located south to the industrial square and at the edge of the mining area had different degrees of movement and deformation. Still, the extreme values of inclined and horizontal deformations were within the damage level I, which met the requirements of building antideformation capacity and reinforcement criteria.

4. Discussion

The field measurements under strip mining in the eastern mining area show that for the longwall mining face width of

40 m, and protective coal pillars' width of 40 m, the maximum subsidence was 440 mm, the maximum surface horizontal deformation was −1.85 mm/m, and the maximum inclination was −3.5 mm/m. Meanwhile, the maximum subsidence of the residential building was 75 mm, the maximum surface horizontal deformation was 0.85 mm/m, and the maximum inclination was −1.7 mm/m. As for the water pipe station, its maximum values of subsidence, surface horizontal deformation, and inclination were 110 mm, 1.1 mm/m, and 2.0, respectively. The major part of the village was within level I of damage, the remaining part reaching level II. Considering the protection level of surface structures and the control requirements of reinforcement standards, the strip mining method greatly affected the safety of surface buildings and structures. To ensure the stability of surface residential buildings, signal towers, and high-voltage line towers, scheme I of RMCPB is recommended to achieve safe mining under the buildings. In this

TABLE 4: Integrated benefit analysis.

| Method | Economical benefits | | | | Environmental benefits |
	Mined coal reserves (mln ton)	Cost (USD/ton)	Profit (USD/ton)	Total profit (mln USD)	Gangue treatment (mln ton)
RMCPB	0.46	64.50	10.50	4.83	0.66
Strip mining	0.24	52.50	22.50	5.40	0.00

scheme, coal resources under buildings can be maximally utilized, and a large volume of abandoned waste gangue can be backfilled into the goaf to control surface subsidence. This scheme allows one to achieve economical, ecological, and environmental benefits listed in Table 4, in comparison to strip mining.

It can be seen in Table 4 that, after the RMCPB of the mining area under study, the output of coal resources was 0.46 million tons and exceeds that of strip mining by 0.22 million tons. After considering the backfilling system, equipment, and personnel costs, the total profit in RMCPB was 4.83 mln USD, being only by 10.5% less than that in strip mining (5.4 mln USD). The main advantage of the former method over the latter one was that it made possible the underground treatment of 0.66 million tons of waste gangue. The integrated analysis of mined coal resources, mine service life, and environmental protection, revealed that the RMCPB application to the case study mining area comprehensively combined economic and environmental benefits.

5. Conclusions

In this study, the mining geological conditions of the case study coal mine, its type, construction, and buildings' protection standards were analyzed. The RMCPB and strip mining methods were applied to extract residual coal resources under buildings. The prediction model of the probability integration method was elaborated to study the surface subsidence and deformation via both mining methods. The research results show that the maximum subsidence of the surface above the mining area with RMCPB was 170 mm. The maximum horizontal movement of the ground surface was 55 mm, and the maximum horizontal deformation was 1.2 mm/m. The maximum inclination and curvature was 1.8 mm/m and 0.04 mm/m^2, respectively. In case of strip mining, the maximum subsidence of the surface above the mining area was 230 mm. The maximum values of horizontal movement, horizontal deformation, inclination, and curvature were 110 mm, 0.40 mm/m, 0.35 mm/m, and 0.04 mm/m^2. To ensure the stability of surface buildings, RMCPB via scheme I is recommended to achieve safe mining under the buildings. In this scheme, coal resources under buildings can be maximally utilized, and a large volume of abandoned waste gangue can be backfilled into the goaf to control surface subsidence. The proposed method combines economic and environmental benefits, which make it lucrative for wide implementation in similar mining areas below industrial sites with surface buildings.

Data Availability

The data used to support the findings of this study are available from the corresponding author upon request.

Conflicts of Interest

The authors declare that they have no conflicts of interest.

Acknowledgments

References

[1] M. Li, J. Zhang, and R. Gao, "Compression characteristics of solid wastes as backfill materials," *Advances in Materials Science and Engineering*, vol. 2016, Article ID 2496194, 7 pages, 2016.

[2] D. Z. Kong, S. J. Pu, Z. H. Cheng, G. Y. Wu, and Y. Liu, "Coordinated deformation mechanism of the top coal and filling body of gob-side entry retaining in a fully mechanized caving face," *International Journal of Geomechanics*, vol. 21, no. 4, p. 04021030, 2021.

[3] J. Lou, F. Gao, J. Yang et al., "Characteristics of evolution of mining-induced stress field in the longwall panel: insights from physical modeling," *International Journal of Coal Science & Technology*, 2021.

[4] T. Jirina and S. Jan, "Reduction of surface subsidence risk by fly ash exploitation as filling material in deep mining areas," *Natural Hazards*, vol. 53, no. 2, pp. 251–258, 2010.

[5] G. Fan, D. Zhang, and X. Wang, "Reduction and utilization of coal mine waste rock in China: a case study in Tiefa coalfield," *Resources, Conservation and Recycling*, vol. 83, pp. 24–33, 2014.

[6] J. Zhang, H. Jiang, X. Deng, and F. Ju, "Prediction of the height of the water-conducting zone above the mined panel in solid backfill mining, mine water and the environment," *Mine Water Environment*, vol. 33, no. 4, pp. 317–326, 2014.

[7] M. Li, J. X. Zhang, Y. L. Huang, and N. Zhou, "Effects of particle size of crushed gangue backfill materials on surface subsidence and its application under buildings," *Environment Earth Science*, vol. 76, no. 17, p. 603, 2017.

[8] S. S. Brake, H. K. Dannelly, and K. A. Connors, "Controls on the nature and distribution of an alga in coal mine-waste environments and its potential impact on water quality," *Environmental Geology*, vol. 40, no. 4-5, pp. 458–469, 2001.

[9] E. K. Skierszkan, K. U. Mayer, D. Weis, and R. D. Beckie, "Molybdenum and zinc stable isotope variation in mining waste rock drainage and waste rock at the Antamina mine, Peru," *Science of the Total Environment*, vol. 550, pp. 103–113, 2016.

[10] X. Y. Yu, X. W. Mao, N. Lu, and Q. Guo, "Research on strip mining with large mining depth under dense buildings," *Coal Mining Technology*, vol. 23, no. 6, pp. 71–76, 2018.

[11] J. X. Zhang, Q. Sun, A. Fourie, F. Ju, and X. J. Dong, "Risk assessment and prevention of surface subsidence in deep multiple coal seam mining under dense above-ground buildings: case study," *Human Ecological Risk Assessment*, vol. 25, no. 4, pp. 1–15, 2018.

[12] H. Teng, J. L. Xu, D. Y. Xuan, and B. L. Wang, "Surface subsidence characteristics of grout injection into overburden: case study of Yuandian No. 2 coalmine, China," *Environment Earth Science*, vol. 75, no. 6, pp. 1–11, 2016.

[13] H. Liu, K. Z. Deng, C. G. He, C. D. Sun, Z. L. Dong, and A. B. Zhang, "Surface subsidence law of filling with super-high-water material and skip mining," *Journal of China Coal Society*, vol. 38, no. z2, pp. 272–276, 2013.

[14] H. Liu, J. Zhang, B. Li et al., "Environmental behavior of construction and demolition waste as recycled aggregates for backfilling in mines: leaching toxicity and surface subsidence studies," *Journal of Hazardous Materials*, vol. 389, p. 121870, 2020.

[15] H. Jiang, M. Fall, E. Yilmaz, Y. Li, and L. Yang, "Effect of mineral admixtures on flow properties of fresh cemented paste backfill: assessment of time dependency and thixotropy," *Powder Technology*, vol. 372, no. 15, pp. 258–266, 2020.

[16] State Bureau of Coal Industry, *Regulations of Coal Pillar Design and Extraction for Buildings, Water Bodies, Railways, Main Shafts and Roadways*, Coal Industry Press, Beijing, China, 2000.

[17] X. J. Deng, *Ground Control Mechanism of Mining Extra-Thickcoal Seam Using Upward Slicing Longwall-Roadway Cemented Backfilling Technology*, Ph.D. thesis, China University of Mining and Technology, Xuzhou, China, 2017.

[18] X. J. Deng, B. Klein, J. X. Zhang, D. Hallbom, and B. De Wit, "Time-dependent rheological behaviour of cemented backfill mixture," *International Journal of Mining, Reclamation and Environment*, vol. 32, no. 3, pp. 145–162, 2018.

[19] H. Liu, J. Zhang, W. Zhang, F. Gao, H. Yan, and T. An, "Experimental investigation of perceptual characteristics of functional cemented backfilling materials in coal mines," *Minerals*, vol. 9, no. 1, pp. 55–70, 2019.

[20] J. Li, J. Zhang, Y. Huang, Q. Zhang, and J. Xu, "An investigation of surface deformation after fully mechanized, solid back fill mining," *International Journal of Mining Science and Technology*, vol. 22, no. 4, pp. 453–457, 2012.

[21] G.-L. Guo, X.-J. Zhu, J.-F. Zha, and Q. Wang, "Subsidence prediction method based on equivalent mining height theory for solid backfilling mining," *Transactions of Nonferrous Metals Society of China*, vol. 24, no. 10, pp. 3302–3308, 2014.

[22] J. X. Zhang, *Study on Strata Movement Controlling by Raw Waste Backfilling with Fully-Mechanized Coal Mining Technology and Its Engineering Applications*, Ph.D. thesis, China University of Mining and Technology, Xuzhou, China, 2008.

[23] J. F. Lou and C. M. Branch, "Research and application of hydraulic support simulation system for large-scale working face physical modeling experiment," *Coal Science and Technology*, vol. 46, no. 5, pp. 67–73+80, 2018.

Research Article

Identifying Delay Time of Detonator for a Millisecond Blasting

Song Zhifei [iD],[1] **Ke Man** [iD],[1] **and Liu Xiaoli**[2]

[1]*College of Civil Engineering, North China University of Technology, Beijing 100144, China*
[2]*State Key Laboratory of Hydroscience and Hydraulic Engineering, Tsinghua University, Beijing 100084, China*

Correspondence should be addressed to Ke Man; man_ke@sina.cn

Based on wavelet transform, the blasting vibration signals are analyzed here. For millisecond blasting, the blasting effect is mostly affected by the actual delay time. Local characteristics of the analyzed signals could be highlighted by the wavelet transform. The simultaneous initiation of large explosive quantity could be avoided by the use of multistage detonators, while the vibration resistance effect could be better. For the same level of detonator segment, the larger the arranged time interval, the less the possibility of initiation at the same time, which is not conducive to the vibration resistance. Therefore, it is suggested to use high-level detonators with detonating cord or high-precision digital electronic detonators to minimize the initiation error. Furthermore, by identifying the delay time using wavelet transform, the interval delay time of different detonator segments could be obtained. Moreover, the nominal delay time, actual delay time, and interval delay time are further compared and analyzed. It is suggested that the millisecond delay series of detonators should be selected in the whole section blasting, and the segment should be jumped as much as possible, so as to increase the secondary breakage time. Detonators with longer interval delay time should be avoided to the full.

1. Introduction

Millisecond blasting is a kind of blasting technology, which is initiated in a certain sequence at millisecond intervals. This technology has been widely used in reducing seismic effect, rationally utilizing explosive energy, reducing explosive unit consumption, and improving blasting fragmentation [1–3]. To determine the reasonable delay time is the key to the successful implementation of millisecond blasting. And the delay initiation of different charges is mainly realized by ordinary delay detonators in engineering. It is well known that a vital problem of accuracy initiation has existed for the common detonators; that is, the delay of each detonator has a positive or negative error. Even if the high-precision detonator, it also has reached the error of ±10 ms. The intuitive phenomenon is that sometimes the front section detonator will initiate later than the latter section detonator; that is, the jumping of detonator section has appeared [4–9].

Particularly, reliable electronic detonator has reached the level of practicality, and the delay control error of electronic detonator could be up to microsecond or even zero error. However, the cost of electronic detonator is always 10 times higher than that of ordinary detonator, which makes it still have a long time to be applied in engineering [10, 11]. Therefore, even if the reasonable millisecond time of a certain blasting can be calculated accurately, the actual millisecond time cannot be controlled exactly because of the error of detonator itself.

Therefore, it is very important to select an appropriate detonator and identify the accurate delay time. Furthermore, the appropriate detonator section and delay time should be selected based on the cross section of the tunnel, the layout of blasting boreholes and geological conditions, and so on [12–20]. Most importantly, it plays a vital role in the improvement of blasting footage and the control of vibration. The principle and feasibility of the wavelet analysis method in the identification of delay time have been demonstrated here. Moreover, combining with the specific blasting vibration signal, the initiation time and delay interval time of each detonator are identified separately. The following is a description of the mentioned method.

2. Principle of Time and Energy Density Analysis Based on Wavelet Transform

2.1. Wavelet Transform. Let $\psi(t) \in L^2(R)$, in which $L^2(R)$ is a signal space with limited energy, and its Fourier transform could be expressed as $\hat{\psi}(w)$. When $\hat{\psi}(w)$ is satisfied, one has the following condition [21, 22]:

$$C_\psi = \int_R \frac{\left|\hat{\psi}(w)\right|^2}{|w|}\, \mathrm{d}w < \infty, \tag{1}$$

where $\psi(t)$ could be called the basic wavelet. Through scaling and shifting of the basic wavelet, the wavelet sequence is obtained here:

$$\psi_{a,b}(t) = |a|^{-\frac{1}{2}}\psi\left(\frac{t-b}{a}\right), \tag{2}$$

where a and b are scaling factor and shifting factor, respectively.

For any function $f(t)$ with limited energy, the definition of continuous wavelet transform concerning $\psi(t)$ is as follows:

$$W_f(a,b) = \langle f, \psi_{a,b}\rangle = |a|^{-\frac{1}{2}}\int_R f(t)\overline{\psi\left(\frac{t-b}{a}\right)}\mathrm{d}t. \tag{3}$$

2.2. Time and Energy Density Analysis. According to the inner product theorem, that is, Moyal theory [23], the following formula could be

$$\frac{1}{C_\psi}\int_R \frac{\mathrm{d}a}{a^2}\int_R \left|W_f(a,b)\right|^2 \mathrm{d}b = \int_R |f(t)|^2\mathrm{d}t. \tag{4}$$

Formula (4) shows that the integral of the square of the wavelet amplitude is proportional to the signal energy to be analyzed. It is well known that, in the study of nonstationary random signal, due to the limitation of the Heisenberg uncertainty principle, the instantaneous energy density of a point in time-frequency space cannot be determined; that is, the energy at a certain frequency at a certain time is conceptually nonexistent. However, in equation (4), $1/a^2 C_\psi |W_f(a,b)|^2$ can be regarded as the energy density function on the (a, b) plane. Therefore, $1/a^2 C_\psi |W_f(a,b)|^2\Delta a\Delta b$ can be considered as the energy centered on scale a and time b, with scale interval Δa as well as time interval Δb. According to the concept of energy density, formula (4) can be expressed as follows:

$$\int_R |f(t)|^2\mathrm{d}t = \int_R E(b)\mathrm{d}b. \tag{5}$$

Here,

$$E(b) = \frac{1}{C_\psi}\int_R \frac{1}{a^2}\left|W_f(a,b)\right|^2 \mathrm{d}a. \tag{6}$$

For the wavelet transform, the so-called scale a corresponds to frequency w in a sense, so the energy distribution of all frequency bands of signal with time b has been given in formula (6), which could be termed time energy density function. In practical application, the upper and lower bounds of integration can be changed so that the integration interval falls within a certain frequency range of the signal to be analyzed. Therefore, the distribution characteristics of energy density of the signal in the frequency band with time could be obtained.

2.3. Actual Delay Time of Millisecond Blasting Judged by Time and Energy Density Method. If a certain blasting could be considered as a system, the initiation of each detonator is the process of input energy to the system. In the meantime, a sudden change in the energy density of the system would be inevitably caused by each initiation [24]. Therefore, the energy density of blasting vibration in the main frequency band can be calculated according to formula (6) by choosing the appropriate upper and lower bounds of integration, and the time and energy density map could be drawn. Based on the peak position in the map, the actual initiation time of each detonator could be obtained, and the actual millisecond delay time in blasting would be further determined.

3. Wavelet Transform in Delay Recognition of Blasting

3.1. Blasting Vibration Signal. Figure 1 shows the blasting holes' layout in this section. In Figure 1, six holes are evenly distributed around the empty hole, that is, No. 1. The full-face blasting excavation method is adopted here. Meanwhile, the millisecond detonators are used, that is, MS1, MS3, MS5, MS7, MS8, MS9, MS10, MS11, MS13, MS15, and MS19, respectively. The emulsion explosive is used and the weight of each roll is 300 g. The charge quantity and other blasting parameters are shown in Table 1. Meanwhile, the blasting footage is 2 m.

Blasting vibration waveform can be analyzed intuitively by blasting vibration instrument system. Therefore, the vibration amplitude, main frequency, and duration could be obtained. The intuitive analysis method of blasting vibration signal is to directly analyze the measured waveform and determine the characteristic quantity of blasting vibration from the waveform diagram itself.

A typical blasting vibration signal is selected here to analyze the representative characteristics, as shown in Figure 2. Furthermore, the initiation time and delay time of this blasting are identified and recognized separately.

3.2. Wavelet Transform Using for Delay Time Identification. From the definition of wavelet transform, the time-frequency window of wavelet transform has its uniqueness. It means that only the window position on the time axis of the phase plane is affected by the shifting factor b, while not only the window position on the frequency axis but also the window shape is influenced by the scaling factor a. Therefore, the sampling step of wavelet transform in time domain
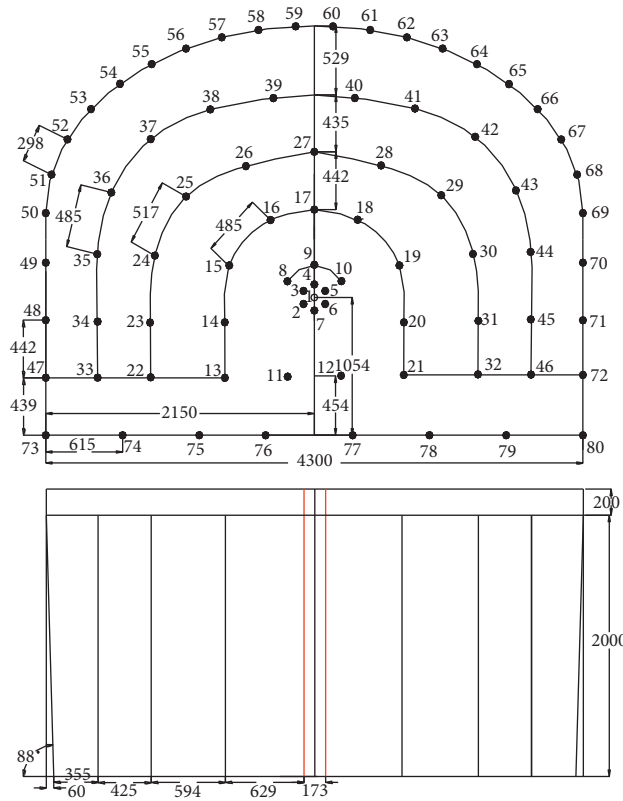
FIGURE 1: Layout of blasting holes (mm).

TABLE 1: Blasting parameters.

Hole name	Hole no.	Number of holes	Charge quantity		Detonator order
			Each hole	Total weight (kg)	
Empty hole	1	1	0	0.0	
Cutting hole	2–7	6	5	9.0	1
Auxiliary hole	8–10	3	5	4.5	3
Auxiliary hole	11–12	2	5	3.0	5
Auxiliary hole	13–18	6	4.5	8.1	7
Auxiliary hole	19–21	3	4	3.6	8
Auxiliary hole	22–27	6	3	5.4	9
Auxiliary hole	28–32	5	3	4.5	10
Auxiliary hole	33–38	6	2.5	4.5	11
Auxiliary hole	39–46	8	2.5	6	13
Peripheral hole	47–54	8	2	4.8	15
Peripheral hole	55–72	18	1.5	8.1	19
Bottom hole	74–79	6	3	5.4	15
Bottom hole	73–80	2	3	1.8	19
Total	—	80	—	68.7	

is adjustable for different frequencies, that is, the time resolution is poor at low frequencies, while the frequency resolution is high, and the time resolution is high at high frequencies, while the frequency resolution is low. Considering the filter point, the wavelet transform makes the signal pass through a series of band-pass filters, respectively. The center frequency and bandwidth of the band-pass filter are proportional to the scaling factor a. That is to say, the ability of wavelet transform to highlight the local characteristics of the signal is different under different value.

Millisecond blasting is often applied in engineering blasting, and the number of millisecond detonator sections depends on the specific blasting conditions and purposes. If a certain blasting is considered as a system, the initiation of each detonator is the process of input energy to the system, and the initiation of each detonator will inevitably cause a sudden change of energy in the system. Therefore, the monitored blasting vibration signal could be transformed using the wavelet transform method, and the time of signal mutation can be
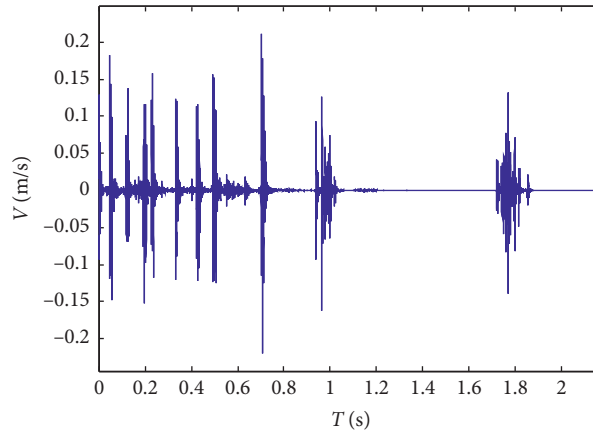
FIGURE 2: Blasting vibration waveform.

effectively identified by the modulus maxima of the wavelet transform. That is to say, the initiation time of each detonator in millisecond blasting can be precisely determined by the means mentioned above, and the actual millisecond delay time in blasting could be further confirmed.

For the signal processed by wavelet analysis, how to select an optimal wavelet base is much more important, because results could be various even for the same problem by different wavelet bases. Furthermore, the function with fast attenuation and good similarity between the waveform and the analyzed signal should be chosen as the wavelet basis function. Therefore, the selection of the wavelet basis is closely related to the properties and characteristics of the analyzed signal. Four common waveforms of wavelet basis functions are listed in the following, as shown in Figure 3.

When choosing a wavelet basis, besides the requirement of compact support, that is, the speed at which the function converges from a finite value to zero, and regularity, which has a great influence on the smoothing effect of signal reconstruction, the curve shape of the wavelet basis is also required to be similar to that of the analyzed signal.

The waveforms of the four main wavelet bases are similar to those of the analyzed signals. However, there is much more information contained in the sym7 and db8 waveforms and the waveforms of the analyzed signals could be matched better with them. That is, the information of the analyzed waveforms reflected by the two waveforms is more accurate.

Furthermore, the waveform of db8 is more consistent with the analyzed signal than that of sym7, and the fluctuation trend of db8 is more similar to that of the analyzed signal. Among these common series of wavelet functions, Daubechies wavelet series have good compactness, smoothness, and approximate symmetry and have been successfully applied to the analysis of nonstationary signal problems, such as blasting.

Therefore, db8 is chosen as the basis function of wavelet analysis for the blasting vibration signal. The original signal is modeled by continuous wavelet transform on scaling factor $a = 16$. The singularity of energy contained in blasting

vibration is identified by the modulus maximum point. The transformed modulus diagram is shown in Figure 4.

Through continuous wavelet transform using db8 wavelet method (scaling factor $a = 16$), several local singularities appear obviously in Figure 4. Time of local singularities is 0.00075, 0.04462, 0.1276, 0.2021, 0.233, 0.3347, 0.4249, 0.4984, 0.7084, 0.9645, and 1.771, respectively. It is clear that the millisecond blasting vibration signal shown in Figure 4 is formed by the superposition of 11 blasting vibration waveforms.

The delay time interval of millisecond blasting can be defined as the time interval between the initiation time of two adjacent detonators. Here, for the identified convenience, the time position of the first local singularity point is determined as the initiation time of the lowest detonator segment (MS1). The actual initiation delay interval of each detonator obtained by this method is 43.87 ms, 82.98 ms, 74.5 ms, 30.9 ms, 101.7 ms, 90.2 ms, 73.5 ms, 210 ms, 256.1 ms, and 806.5 ms, respectively, as shown in Table 2. It should be noticed that the data in Table 2 is obtained from the blasting test through wavelet analysis, while the blasting parameters are from Table 1.

4. Discussion

Wavelet packet analysis can provide a more precise method for signal analysis. Wavelet packet analysis divides the time-frequency plane more carefully, and its resolution to the high-frequency part of the signal is higher than other wavelets. Moreover, it introduces the concept of optimal basis selection on the basis of wavelet analysis theory. According to the characteristics of the signal to be analyzed, dividing the frequency band into several levels, the best basis function is adaptively selected to match the signal, to improve the signal analysis ability.

Referring to the calibrated error intervals of different detonators provided by detonator manufacturers, the above analyzed time points correspond to the detonator segments 1, 3, 5, 7, 8, 9, 10, 11, 13, 15, and 19, respectively. The allowable errors of delay time of each detonator are ±10, ±15, ±20, ±25, ±30, ±35, ±40, ±50, ±60, and ±130, respectively. At
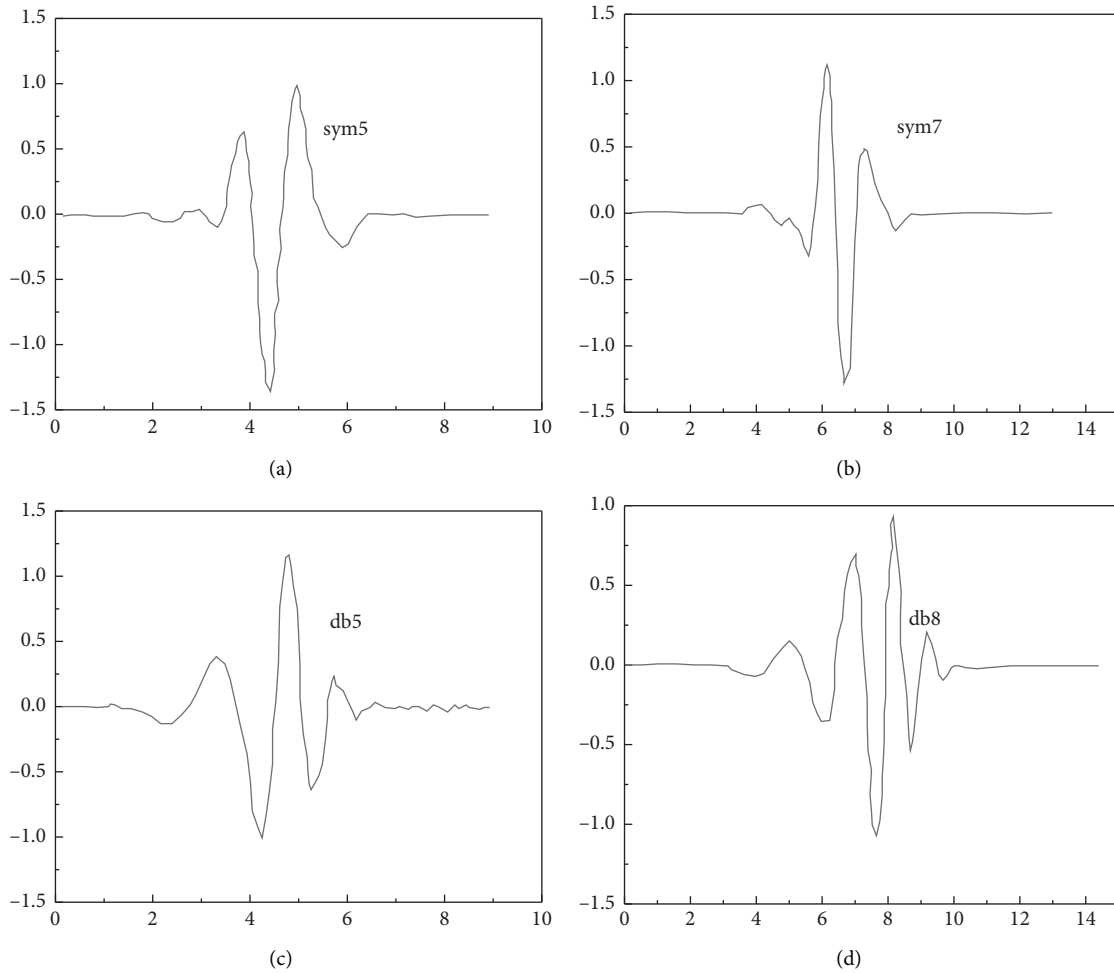
FIGURE 3: Several common series of wavelet functions.
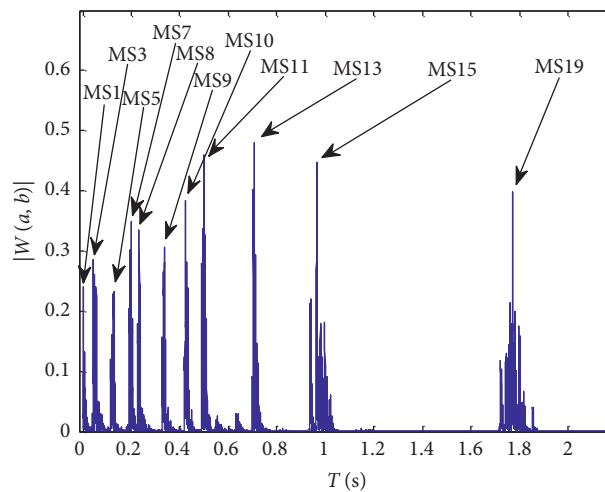
FIGURE 4: Modulus value map by db8 continuous wavelet transform ($a = 16$).

the same time, the higher the detonator segment is, the worse the precision is.

Through longitudinal comparison, simultaneous initiation with a large amount of explosive can be avoided using different detonators with multisegments, which reduced the vibration effect better. However, as for a same one detonator segment, the larger the allowable error range of the detonator, the less possibility of simultaneous detonation would

TABLE 2: Initiation time and time interval of each detonator.

Detonator segment	Initiation time (s)	Detonator interval	Delay time interval (ms)
MS1	0.00075	—	—
MS3	0.04462	MS1~MS3	43.87
MS5	0.1276	MS3~MS5	82.98
MS7	0.2021	MS5~MS7	74.5
MS8	0.233	MS7~MS8	30.9
MS9	0.3347	MS8~MS9	101.7
MS10	0.4249	MS9~MS10	90.2
MS11	0.4984	MS10~MS11	73.5
MS13	0.7084	MS11~MS13	210
MS15	0.9645	MS13~MS15	256.1
MS19	1.771	MS15~MS19	806.5

TABLE 3: Detonator deferment stages, deferral times, and actual differential intervals.

Detonator segment	Initial time	Modulus maximum	Notional delay time (ms)	Error ratio of notional delay time	Arranged time interval (ms)	Monitored time interval (ms)	Whether early explosion or refusal
MS1	0.00075	0.2411	<13	—	0~13	0	No
MS3	0.04462	0.285	50 ± 10	0.2	0~50	43.87	No
MS5	0.1276	0.2324	110 ± 15	0.1364	35~85	82.98	No
MS7	0.2021	0.349	200 ± 20	0.1	55~125	74.5	No
MS8	0.233	0.335	250 ± 25	0.1	5~95	30.9	No
MS9	0.3347	0.3057	310 ± 30	0.0968	5~115	101.7	No
MS10	0.4249	0.3836	380 ± 35	0.0921	5~135	90.2	No
MS11	0.4984	0.4587	460 ± 40	0.0869	5~155	73.5	No
MS13	0.7084	0.4793	650 ± 50	0.0769	100~280	210	No
MS15	0.9645	0.4467	880 ± 60	0.0682	120~340	256.1	No
MS19	1.771	0.3984	1700 ± 130	0.0765	630~1010	806.5	No

naturally occur. That is to say, with the increase of detonator segment, the detonators in the same segment but high section are liable to produce interference and fail to achieve a good vibration reduction effect.

The detonator segment, delay time, and actual time interval of detonators in this test are shown in Table 3.

The relationship between nominal delay time and error ratio of the nominal delay time of detonators is shown in Figure 5. It can be seen that the error ratio of nominal delay time decreases gradually with the increase of detonator segments.

The relationship between the actual initiation time and the actual interval delay time of detonators is shown in Figure 6. It can be seen that although the error ratio of nominal delay time decreases gradually, the absolute error of delay time of high-level detonators increases. Particularly, the error of delay time of MS19 detonator reaches 130 ms, which is not conducive to blasting and shock absorption effect.

Therefore, it is suggested to adopt a high-level detonator with detonating cord or a high-precision digital electronic detonator in peripheral holes to minimize the initiation error, in other words, to ensure the same detonator initiation at the same time, especially the high-level detonator segments.

Time intervals of kinds of detonator segments are shown in Figure 7, which illustrates the relationship between the monitored time interval and the arranged time interval. It can be seen that interval delay times of each detonator are within the arranged interval delay times, which shows that the detonators of this blasting have given full play to their respective performances and the blasting is controlled accurately.

Furthermore, it can be seen from Table 3 that the jumping segment use of low-level detonators, for example, MS1~MS5, reduces the error of delay time to a certain extent, which is beneficial for blasting vibration reduction. Contrarily, using adjacent detonator segments will lead to the overlapping of specified errors and increase the scale range of errors in time. For example, MS8~MS11 detonator segments have been continuously used the lower limit of error range is 5 ms, and the upper limit is increased from 95 ms to 155 ms with an equal interval of 20 ms. Rock could not be broken sufficiently as the interval time is too short. Moreover, the explosion pile is not conducive to be discharged and transported. At the same time, it will increase the accident probability of early explosion and antiexplosion.

The interval time between MS15 and MS19 detonators is 806.5 ms, and the interval time is too long, which leads to a long vibration duration. While the vibration energy accumulation is easy to be produced, it should be avoided to reduce the blasting negative effect.

Therefore, it is suggested that the millisecond delay series of detonators should be selected in the whole section

(a)

(b)
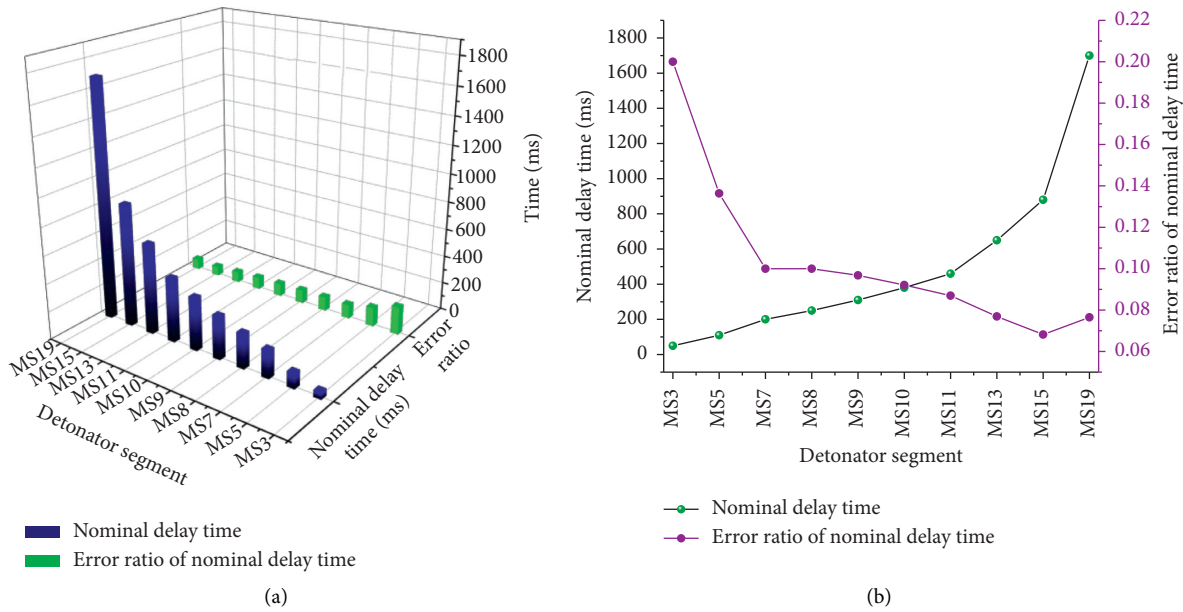
Figure 5: Nominal delay time and its error ratio.
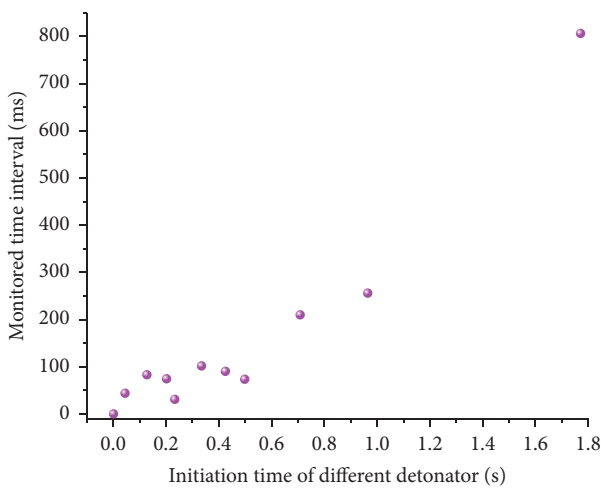
Figure 6: Initiation time and monitored time interval of detonators.

⊦ Interval delay time and the arranged interval ranges
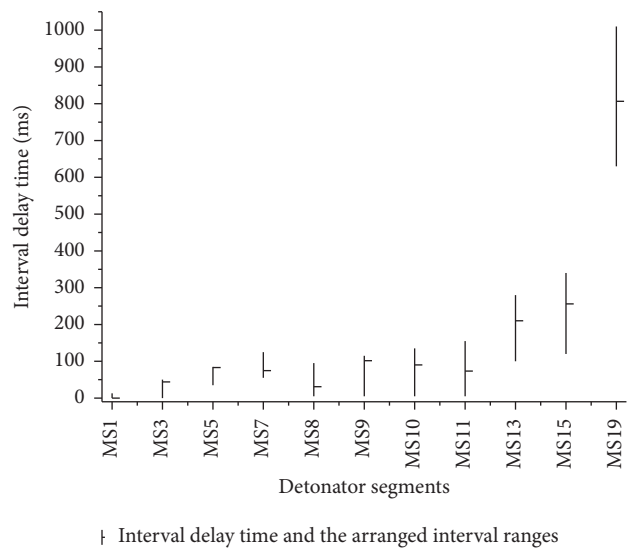
Figure 7: Interval delay time under kinds of detonator segments.

blasting, and the segment should be jumped as much as possible, so as to increase the secondary breakage time. Detonators with longer interval delay time should be avoided to the full.

5. Conclusions

For millisecond blasting, the blasting effect is mostly affected by the actual delay time. The blasting vibration signals are analyzed using the wavelet transform method to identify the actual delay time, and the following conclusions are obtained here:

(1) Using the ability of wavelet transform to highlight the local characteristics of the analyzed signals, the initiation time of detonators can be effectively identified by wavelet transform, and then the actual delay time could be determined.

(2) Furthermore, the allowable error of different detonator segments is analyzed. It is considered that the simultaneous initiation of large explosive quantity can be avoided by the use of multistage detonators, and the vibration resistance effect could be better. However, for the same level of detonator segment, the larger the arranged time interval, the less the possibility of initiation at the same time, which is not conducive to the vibration resistance. Therefore, it is suggested to use high-level detonators with detonating cord or high-precision digital electronic detonators to minimize the

initiation error, that is, to ensure that the same detonator segment initiates at the same time.

(3) By identifying the delay time, the interval delay time of different detonator segments is obtained. The nominal delay time, actual delay time, and interval delay time are further compared and analyzed. It is suggested that the millisecond delay series of detonators should be selected in the whole section blasting, and the segment should be jumped as much as possible, so as to increase the secondary breakage time. And detonators with longer interval delay time should be avoided fully.

Data Availability

The data used to support the findings of this study are available from the corresponding author upon reasonable request.

Conflicts of Interest

The authors wish to confirm that there are no known conflicts of interest associated with this publication and there has been no significant financial support for this work that could have influenced its outcome.

Acknowledgments

References

[1] D. Xiong and Y. Gu, *New Advances in Rock Blasting Theory and Technology*, Metallurgical Industry Press, Beijing, China, 2002.

[2] L. B. Jayasinghe, H. Y. Zhou, A. T. C. Goh, Z. Y. Zhao, and Y. L. Gui, "Pile response subjected to rock blasting induced ground vibration near soil-rock interface," *Computers and Geotechnics*, vol. 82, no. 2, pp. 1–15, 2017.

[3] E. Sáez, G. S. Pardo, and C. Ledezma, "Seismic response of a pile-supported excavation on Santiago gravel," *Soil Dynamics and Earthquake Engineering*, vol. 76, no. 9, pp. 2–12, 2015.

[4] D.-C. Lin, H. Shi, C. Bai, and Q. Zhang, "Time-frequency characteristic analysis of blasting vibration based on wavelet transform," *Chinese Journal of Rock Mechanics and Engineering*, vol. 23, no. 1, pp. 101–106, 2004.

[5] T. H. Ling and X. Li, "The features of energy distribution for blast vibration signals in underground engineering by wavelet packet analysis," *Explosion and Shock Waves*, vol. 24, no. 1, pp. 63–68, 2004.

[6] Z. Mingjie, Y. Xiaoming, and D. Wu, "The wavelet-Fourier analysis of blasting seismic signal," *Journal of Chongqing Jiaotong University*, vol. 18, no. 3, pp. 35–41, 1999.

[7] H. Wen-Hua, X. Quan-Jun, S. Wei et al., "Application of wavelet transform in evaluation of blasting vibration damage," *Engineering Blasting*, vol. 7, no. 1, pp. 24–27, 2001.

[8] Y. Junwei, L. Yuan, F. Xiang et al., "Time-frequency characteristics extracting and analysis of blasting seismic wave based on wavelet packet transformation," *Journal of Vibration and Shock*, vol. 26, no. 4, pp. 25–29, 2007.

[9] D.-W. Liu, S. Chuang, and Y.-G. Gong, "New method for blasting hazards evaluation based on wavelet analysis for blasting vibration signals," *Journal of Central South University (Science and Technology)*, vol. 41, no. 4, pp. 1574–1577, 2010.

[10] Y. Changbin, W. Guijun, S. Shouliang et al., "Analysis of acoustic wave frequency spectrum characters of rock mass under blasting damage based on wavelet (packet) transformation," *Chinese Journal of Rock Mechanics and Engineering*, vol. 29, no. 7, pp. 1496–1502, 2010.

[11] H. Jun, Y. Ya-Lun, and L. Wen-Ji, "Wavelet analysis for blasting seismic signals," *Chinese Journal of Geotechnical Engineering*, vol. 20, no. 1, pp. 47–50, 1998.

[12] X. Liu, G. Han, E. Wang, S. Wang, and K. Nawnit, "Multiscale hierarchical analysis of rock mass and prediction of its mechanical and hydraulic properties," *Journal of Rock Mechanics and Geotechnical Engineering*, vol. 10, no. 4, pp. 694–702, 2018.

[13] C. Liu, X. Liu, X. Peng, E. Wang, and S. Wang, "Application of 3D-DDA integrated with unmanned aerial vehicle-laser scanner (UAV-LS) photogrammetry for stability analysis of a blocky rock mass slope," *Landslides*, vol. 16, no. 9, pp. 1645–1661, 2019.

[14] X. L. Liu and S. Y. Wang, "Mine water in rush forecasting during the mining under waters," *Disaster Advances*, vol. 5, no. 4, pp. 877–882, 2012.

[15] X. Liu, S. Wang, S. Wang, and E. Wang, "Fluid-driven fractures in granular materials," *Bulletin of Engineering Geology and the Environment*, vol. 74, no. 2, pp. 621–636, 2015.

[16] C. Xu, X. Liu, E. Wang, Y. Zheng, and S. Wang, "Rockburst prediction and classification based on the ideal-point method of information theory," *Tunnelling and Underground Space Technology*, vol. 81, pp. 382–390, 2018.

[17] Q. H. Du, X. L. Liu, E. Z. Wang, and S. J. Wang, "Strength reduction of coal pillar after CO_2 sequestration in abandoned coal mines," *Minerals*, vol. 7, no. 2, p. 26, 2017.

[18] H. Sun, X. L. Liu, S. G. Zhang, and K. Nawnit, "Experimental investigation of acoustic emission and infrared radiation thermography of dynamic fracturing process of hard-rock pillar in extremely steep and thick coal seams," *Engineering Fracture Mechanics*, vol. 226, p. 106845, 2020.

[19] B. Hu, H. B. Zhao, S. J. Wang et al., "Pull-out model test for tunnel anchorage and numerical analysis," *Rock and Soil Mechanics*, vol. 30, no. 6, pp. 1575–1582, 2009.

[20] P. Lin, X. L. Liu, Y. Hu, W. Xu, and Q. B. Li, "Deformation stability analysis of Xiluodu arch dam under stress-seepage coupling condition," *Chinese Journal of Rock Mechanics and Engineering*, vol. 32, no. 6, pp. 1145–1156, 2013.

[21] J. Cui, *Introduction to Wavelet Analysis*, Xi'an Jiaotong University Press, Xi'an, China, 1998.

[22] C. Hu, J. Zhang, J. Xia et al., . *System Analysis and Design Based on MATLAB - Wavelet Analysis*, Xi'an University of Electronic Science and Technology, Xi'an, China, 2000.

[23] H. R. Ma, H. M. Qian, J. W. Lou et al., "Use of time frequency distributions for processing the signals of blasting vibration," *Engineering Blasting*, vol. 10, no. 2, pp. 8–12, 2004.

[24] T. Ling and X. Li, "The actual delay time of millisecond blasting is determined based on the time-energy distribution of wavelet transform," *Journal of Rock Mechanics and Engineering*, vol. 23, no. 13, pp. 2266–2270, 2004.

Research Article

Movement Laws of Overlying Strata above a Fully Mechanized Coal Mining Face Backfilled with Gangue: A Case Study in Jiulishan Coal Mine in Henan Province, China

Zhengkai Yang,[1,2] **Zhiheng Cheng** [ID],[3,4] **Zhenhua Li** [ID],[5] **Chunyuan Li,**[6] **Lei Wang,**[7] **Shuaifeng Yin,**[3] **and Jinhu Zhang**[8]

[1]*School of Energy and Mining Engineering, China University of Mining Technology-Beijing, Beijing 100083, China*
[2]*China Coal Research Institute, Beijing 100013, China*
[3]*North China Institute of Science & Technology, Beijing 100013, China*
[4]*NCIST Zhongan Technology (Beijing) Co., Ltd., Beijing 101601, China*
[5]*School of Energy Science and Engineering, Henan Polytechnic University, Jiaozuo, Henan 454000, China*
[6]*Deep Mining and Rock Burst Research Institute, China Academy of Coal Science, Beijing 100013, China*
[7]*China Coal Society, Beijing 101601, China*
[8]*CCTEG Coal Mining Research Institute, Coal Mining Branch, China Coal Research Institute, Beijing 100013, China*

Correspondence should be addressed to Zhiheng Cheng; an958158@163.com and Zhenhua Li; jzlizhenh@163.com

The aim of this study is to obtain movement laws of overlying strata above a fully mechanized coal mining face backfilled with gangue and solve the problem of surface subsidence during coal mining. This study was carried out based on gangue backfilling mining of Jiulishan Coal Mine (Jiaozuo City, Henan Province, China) from the perspectives of deformation of backfilled gangue under compaction, surrounding rock of a stope, and activities of key strata. The method combining with rock mechanics, viscoelastic mechanics, control theory of rock mass under mining, and numerical simulation was used based on physical and mechanical characteristics of backfilled gangue. On this basis, the research analyzed the temporal-spatial relationships of activities of surrounding rock of the stope, compressive deformation of backfilling body, failure depth of the floor, deformation characteristics of the main roof with laws of surface subsidence. The movement characteristics of overlying strata above the fully mechanized coal mining face backfilled with gangue and the traditional fully mechanized mining face were compared. It is found that, under the same conditions of overlying strata, movement laws of overlying strata are mainly determined by the mining height of coal seams and the heights of a caving zone and a fracture zone are nearly linearly correlated with the mining height. Through analysis based on thin-plate theory and key stratum theory, the location of the main roof of the fully mechanized coal mining face backfilled with gangue in coal seams first bending and sinking due to load of overlying strata was ascertained. Then, it was determined that there are two key strata and the main roof belongs to the inferior key stratum. By using the established mechanical model for the main roof of the fully mechanized coal mining face backfilled with gangue and the calculation formula for the maximum deflection of the main roof, this research presented the conditions for breaking of the main roof. In addition, based on the theoretical analysis, it is concluded that the main roof of the fully mechanized coal mining face backfilled with gangue does not break, but bends. The numerical simulation results demonstrate that, with the continuous increase of strength of backfilled gangue, the stress concentration degree of surrounding rock reduces constantly, so does its decrease amplitude. Moreover, the compressive deformation of backfilling, failure depth of the floor, and bending and subsidence of the main roof continuously decrease and tend to be stable. The mechanical properties of backfilling materials determine effects of gangue backfilling in controlling surface subsidence. Gangue backfilling can effectively control movement of overlying strata and surface subsidence tends to be stable with the increase of elastic modulus of gangue.

1. Introduction

Coalbed methane development, groundwater exploitation, and mineral exploitation are main factors leading to surface subsidence; particularly, surface subsidence is more obvious in the case of full-seam mining or mining with a large mining height (Figure 1). The main influences of coal seam mining on the surface are characterized by surface subsidence and large cracks on the surface. This leads to surface subsidence, landslide, and damage to farmland, houses, and roads. In particular, surface subsidence caused by coal mining usually occurs in the form of surface collapse. Surface collapse refers to a phenomenon of sudden surface subsidence to form small or large sinkholes or pits, which poses a particularly great threat to landscape and human life, because there is no premonitory phenomenon before it occurs. It can cause many harms, such as surface change, landslide of steep cliffs, and damage to farmland, houses, and roads [1–14].

At present, a lot of research has been conducted on the prediction, characteristics, mechanisms, and control methods of surface subsidence, and a variety of methods have been developed [15–20]. However, their performances in backfilling and subsidence control are quite different [21–26]. So far, a large number of attempts have been made in the world to fully understand the surface subsidence process. These attempts mainly focus on the characteristics, prediction methods, mechanisms, and control measures of surface subsidence [27–44] and most of the studies are based on the continuity assumption. In the meanwhile, the overlying strata in the western China are relatively thin and buried between 221 m and 375 m underground. Without stopping and backfilling, the surface subsidence and damage will be more obvious. Based on the requirements of environmental protection and sustainable development of mines, the backfilling mining technology develops rapidly [4]. According to incomplete statistics, the amount of coal mining under buildings, railways, and water-bodies of production mines is up to $1.43 \times 10^{10} t$ [1] and the cumulative amount of gangue piled up over the years in China is about $4.5 \times 10^9 t$. Moreover, there are more than 1,600 gangue dumps on the surface of coal mines in China, occupying a land area of $1.5 \times 10^4 \, hm^2$ [1, 4, 6], so gangue has become the main hazard source of environmental pollution in mines [2, 3, 7, 45]. Therefore, scholars in China put forward the scientific mining concept of developing green mining technologies [5], including the coal mining technology for coal mining under buildings, railways, and water-bodies by directly backfilling solid wastes (gangue, fly ash, loess, yellow sand, etc.) in mining areas [4, 16]. Miao [4, 15, 16] systematically introduced the research progress of fully mechanized solid backfilling mining technology and mainly discussed the control theory of strata movement during backfilling mining with dense backfilling body. The theoretical breakthrough is the premise of developing new technologies, mainly including the equivalent mining height theory for controlling strata movement during backfilling

mining, the continuous medium mechanics model and the calculation formula for strata movement during backfilling mining, and analysis on mine pressure in a stope and support stress during solid backfilling. Therefore, the compactness of backfilling materials is the key factor controlling strata movement in the backfilling mining face. By experimentally studying different filling media, Liu and Qingbiao [46] basically mastered the reasonable mixing ratio of filling materials and mechanical properties, such as compactness, rheology, and weathering characteristics of various filling materials. Based on the analysis of the moving characteristics of the roof during fully mechanized backfilling mining, Zhang et al. [23] established the mechanical model of key blocks in the main roof during fully mechanized mining backfilling. According to the deformation law under compaction of waste fillings and cracked immediate roof, they deduced the relational expression of mechanics of support strength in the backfilled fully mechanized coal mining face. The study proves the feasibility of gangue backfilling mining and concludes the law of strata behaviors in fully mechanized coal mining face backfilled with gangue through field application. In the meanwhile, based on the characteristics of strata movement of solid backfilling mining technology, Guo et al. [47] proposed the surface subsidence prediction method based on the equivalent mining height theory and described the parameter selection guideline of this method. While comparing the parameters of caving mining with equivalent height, the subsidence efficiency can be calculated according to the mining height and bulk factors of sagging zone and fracture zone. By conducting a field experiment in a Chinese coal mine located under thick unconsolidated layers, Wang et al. [48] proposed a backfilling strip mining method via determination of the appropriate longwall face length and mining height, to protect the bearing structure from being damaged, thus avoiding surface collapse. They found that no surface collapse occurred in the mining process. The research results indicate that the method can prevent surface collapse during longwall mining under thick unconsolidated layers. Zhao et al. built physical and numerical models for controlling backfill in steeply dipping coal seams to determine an optimum backfilling approach to control surface collapse. The physical modeling results show that, for mining without backfill, the thickness of the largest roof collapse is approximately twice that of the mined seams, the movement of roof strata tends to be asymmetrical, and there is a relatively large empty zone in the upper gob area. Numerical simulation results demonstrate that floor strata mainly undergo nearly horizontal displacement, while roof strata mainly experience vertical subsidence, either with or without backfilling. The integrity of roof strata is improved as the extent of backfilling increases and the range of displacement increases. The conclusions are proved by results from a field experiment. The similar simulation and field measurement are performed on movement laws of overlying strata above the working face backfilled with gangue, which provides a reliable theoretical basis for backfilling mining [21, 22]. By

(a) (b) (c) (d)

(e)
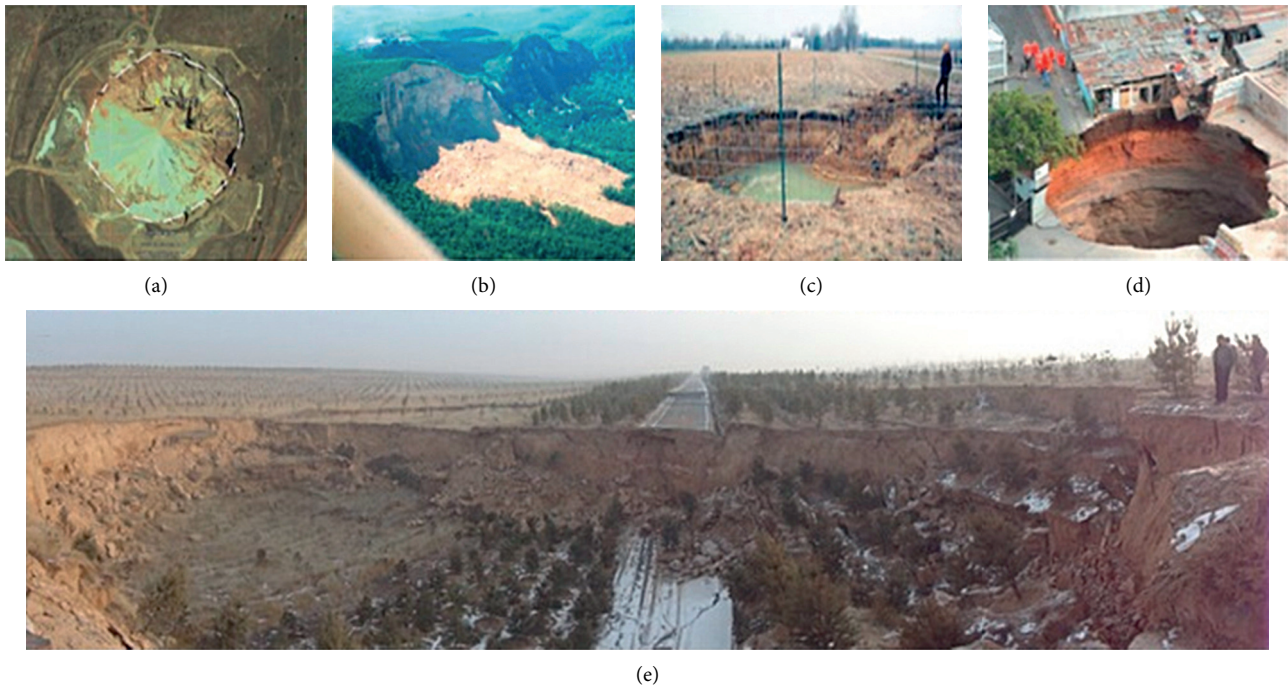
Figure 1: Problems caused by surface subsidence and surface cracks. (a) Surface subsidence in Australia; (b) landslide in Australia; (c) damage to farmland in India; (d) damage to roads in China.

using two test plans, the deformation and seepage test and the seepage test, Li et al. [49] compared and studied the permeable behaviors of gangue during the time related deformation process and obtained the permeability of gangue when the seepage is stable under each stress level. During gangue backfilling, physical and mechanical properties of gangue have important influences on displacement of overlying strata and surface subsidence and the effects of different types of gangue are not clear. Moreover, selecting appropriate gangue plays an important role in controlling surface subsidence.

In the process of gangue backfilling mining, the compaction and bearing of backfilling materials are particularly important, and the compressive deformation of backfilling materials directly affects the movement and deformation of the surface. However, little attention had been paid to stress distribution of overlying strata under gangue backfilling conditions, the influences of hierarchical optimization of particle size and elastic moduli of backfilled gangue. On this basis, this study firstly determined the stress distribution characteristics in a stope of a gangue backfilling face based on the thin-plate theory and then carried out a theoretical analysis to determine stress distribution characteristics in overlying strata. Secondly, key strata of the working face backfilled with gangue were determined and the deformation characteristics of the roof under mining were defined. Finally, this study analyzed gangue with different elastic moduli, clarified influences of mechanical parameters of gangue on surface subsidence, and determined reasonable physical and mechanical parameters of gangue.

2. Overview of the Study Area

At present, many development roadways in Jiulishan Coal Mine in Jiaozuo City, Henan Province, China, are being expanded and repaired. When taking measures for regional gas control, many rock roadways (at present, there are nearly 20 heading faces of rock roadways in the whole mine) need to be excavated, and the daily discharge of gangue reaches 1,400 t, which leads to the busy auxiliary haulage systems in the mine. Jiulishan Coal Mine has accumulated nearly $9.4 \times 10^5 \, m^3$ of gangue on the ground and at present, there is a serious shortage of gangue disposal sites. Mining with gangue backfilling technology not only makes lifting of existing gangue to the ground unnecessary and reduces the cost of gangue discharge, but also can consume the existing gangue on the ground and reduce costs for discharge, transportation and lifting of gangue and construction and maintenance of gangue discharge sites. This fundamentally solves the problem of land occupation and management of gangue dumps and greatly reduces environmental pollution in the coal mine. Based on this, taking Jiulishan Coal Mine as the research object, gangue excavated from the coal mine was used in the test. The physical and mechanical characteristics of gangue are shown in Table 1.

In the mining test with gangue backfilling, the 12031 working face, located in the north wing of No. 12 mining area of Jiulishan Coal Mine, was mined. No. 12 mining area was mined with backfilling in Jiulishan Coal Mine, with a mining area of 430,400 m^2, geological reserve of 3.443×10^6 t, and the ground elevation of +93 m. The coal pillars were retained for protecting villages and industrial squares in this

TABLE 1: Mechanical parameters of rock samples.

Strata	Compressive strength (MPa)	Elastic modulus (GPa)	Poisson's ratio	Cohesion (MPa)	Angle of internal friction (°)	Protodyakonov coefficient	Deformation modulus (GPa)
Sandstone	5.90	69.80	0.16	39.48	35.30	9.30	9.20
Mudstone	3.25	38.90	0.21	47.09	29.20	5.58	7.40

area. The layout of roadways in the fully mechanized coal mining face backfilled with gangue is displayed in Figure 2.

3. Movement Characteristics of Overlying Strata above the Fully Mechanized Mining Face

3.1. Movement Characteristics of Overlying Strata above the Traditional Fully Mechanized Mining Face. After the coal mining, the original stress equilibrium state around the goaf is damaged, inducing stress redistribution. As a result, this causes deformation, damage and movement of rock strata, which develops upwards to the surface to induce surface movement. Such a process and phenomenon is known as strata movement [3]. A large number of observations [2, 3] show that when the goaf is treated with the fully caving method, the goaf can be divided into three zones, namely, a caving zone, a fracture zone, and a bending zone, according to the degree of movement and damage of overlying strata therein. The schematic diagram of movement of overlying strata above the traditional fully mechanized mining face is demonstrated in Figure 3.

3.2. Movement Characteristics of Overlying Strata above the Fully Mechanized Coal Mining Face Backfilled with Gangue. The heights of the caving zone and fracture zone are related to lithology and the mining height of coal seams [2]. The harder the overlying strata of coal seams are, the smaller the heights of the caving zone and fracture zone are [46]. In accordance with the concept of equivalent mining height proposed by Professor Miao Xiexing, mining with gangue backfilling is equivalent to reducing the mining height. In other words, it is same as mining thin coal seams, which is equivalent to reducing the heights of the caving zone and fracture zone. For the fully mechanized working face mined by the technology of backfilling goaf with gangue, with the advance of the working face, the goaf is backfilled with gangue when the immediate roof does not cave. Because of bulking characteristics of gangue for backfilling and caved from the immediate roof, the goaf backfilled with gangue changes with time and the gangue backfilling body is compressed and deformed under load of overlying strata. The deformation of the gangue backfilling body is mainly elastic and plastic. The deformation of the gangue backfilling body leads to the caving of the main roof, which is in direct contact with the broken immediate roof. The soft strata borne by the main roof are gradually separated from the key strata after subsidence and the key strata bend and deform due to load of overlying strata. However, confined by the separation space, the key strata and their bearing body

directly act on the soft layers below. With the increase of deformation, the supporting force provided by the lower soft layers is strengthened, thus limiting the bending deformation of the key strata [46]. The strata movement characteristics during fully mechanized mining with gangue backfilling are illustrated in Figure 4.

The heights of the caving zone and fracture zone have a correlation with factors, such as the mining height, dip angle of coal seams, and mining methods as well as lithology and structure of overlying strata. Due to different mining heights from the traditional fully mechanized mining face, movement laws of overlying strata above the fully mechanized coal mining face backfilled with gangue are mainly determined by the mining height of coal seams under the same conditions of overlying strata. The heights of the caving zone and fracture zone are nearly linearly related to the mining height [7]. Gangue backfilling greatly reduces the heights of the caving zone and fracture zone, which well controls movement of overlying strata and effectively prevents water inrush accidents in the working face, thus providing favorable conditions for safe mining of the working face.

4. Stress Analysis on the Main Roof during Mining with Gangue Backfilling

4.1. Analysis of the Main Roof of the Fully Mechanized Coal Mining Face Backfilled with Gangue Based on Thin-Plate Theory

4.1.1. Establishment of the Mechanical Model. The 12031 working face of Jiulishan Coal Mine is mined by gangue backfilling. The upper part of the working face has been a goaf, while the lower part contains unmined coal mass. The initial support conditions of the main roof of the stope are set as follows: it is fixed on three sides and simply supported on one side. Therefore, by using the mechanical model with the fixed support on three sides and simple support on one side (Figure 5(a)), the stress distribution and breaking laws of the roof of the working face backfilled with gangue were analyzed [2].

4.1.2. Stress Distribution Laws in the Roof of the Stope of the Working Face Backfilled with Gangue. Based on the mechanical model of the main roof of the stope of the 12031 working face in Jiulishan Coal Mine, stress analysis was conducted on the roof of the stope (Figure 5(b)). In accordance with the boundary conditions of the mechanical model of the roof with the fixed support on three sides and simple support on one side, the calculation formula for stress distribution in the main roof during gangue backfilling mining is shown as follows:
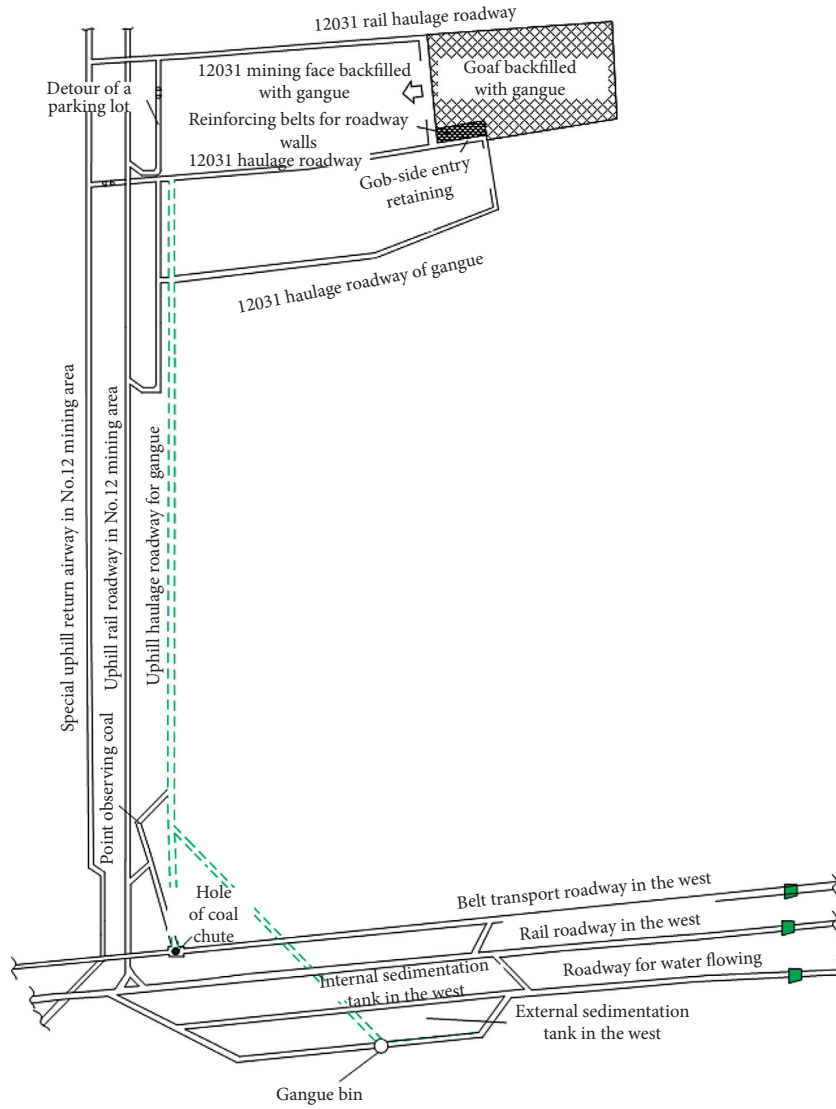
FIGURE 2: Diagram of layout of roadways in the fully mechanized coal mining face backfilled with gangue.
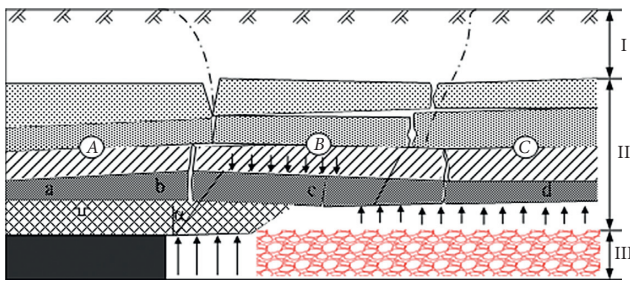
FIGURE 3: Schematic diagram of movement of overlying strata above the traditional fully mechanized mining face. A: zone affected by support of coal wall; B: bed-separation zone; C: recompacted zone; α represents the angle affected by support; I, II, and III indicate the bending and subsidence zone, the fracture zone, and the caving zone, respectively.

$$
\begin{cases}
\sigma_x = -\dfrac{2\text{EAz}}{b^2\left(1-\mu^2\right)}\left[1+\left(\dfrac{2\pi^2\mu x^2}{a^2}-1\right)\cos\dfrac{2\pi y}{a}\right], \\[4mm]
\sigma_y = -\dfrac{2\text{EAz}}{b^2\left(1-\mu^2\right)}\left[\left(\dfrac{2\pi^2 x^2}{a^2}-\mu\right)\cos\dfrac{2\pi y}{a}+\mu\right], \\[4mm]
\tau_{xy} = -\dfrac{4\text{EAz}\pi x}{(1+\mu)\text{ab}^2}\sin\dfrac{2\pi y}{a},
\end{cases}
\tag{1}
$$

where σ_x, E, A, and b represent the normal stress (MPa) acting vertically on the x-axis plane, elastic modulus (MPa) of roof rock, coefficient of the deflection surface, and length (m) of the working face, respectively; μ, a, and σ_y indicate
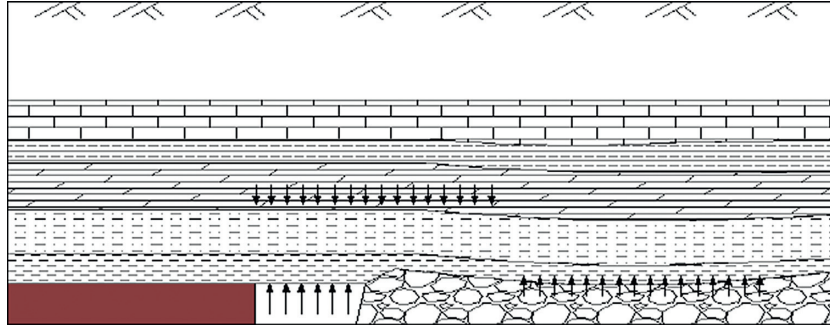
FIGURE 4: Schematic diagram of movement of overlying strata above the fully mechanized coal mining face backfilled with gangue.

(a)   (b)
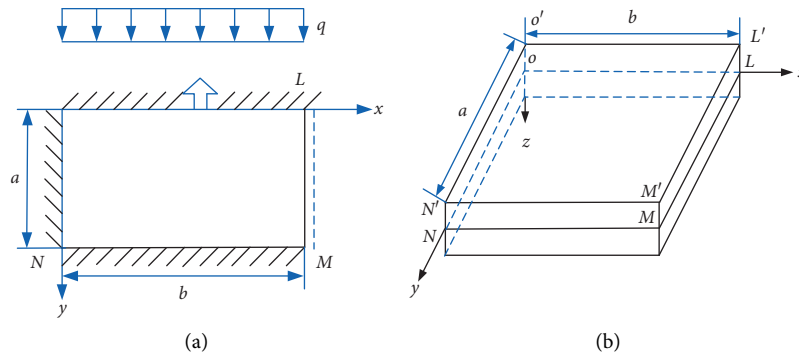
FIGURE 5: Mechanical model with fixed support on three sides and simple support on one side.

Poisson's ratio of roof rock, span (m) of the stope roof, and normal stress (MPa) acting vertically on y-axis plane, respectively; τ_{xy} denotes the shear stress (MPa) acting on the xy plane, which is positive consistent with the negative direction of the y-axis; x, y, and z are the distances (m) on the coordinate axis. By analyzing the mechanical model, it is obtained that the stress distributions at the midpoints of $O'L'$ and $N'M'$ edges and midpoint of $O'N'$ edge in Figure 5(b) are expressed in formulas (2) and (3).

$$\begin{cases} \sigma_x = \dfrac{\pi^2 E\mu Ah}{2a^2\left(1-\mu^2\right)}, \\\\ \sigma_y = \dfrac{\pi^2 EAh}{2a^2\left(1-\mu^2\right)}, \\\\ \tau_{xy} = 0, \end{cases} \tag{2}$$

$$\begin{cases} \sigma_x = \dfrac{2EAh}{b^2\left(1-\mu^2\right)}, \\\\ \sigma_y = \dfrac{2EAh\mu}{b^2\left(1-\mu^2\right)}, \\\\ \tau_{xy} = 0. \end{cases} \tag{3}$$

By comparing formulas (2) and (3), the stress at the midpoints of $O'L'$ and $N'M'$ edges is larger than that at the

midpoint of $O'N'$ edge. Due to use of gangue backfilling technology, backfilling while mining of the goaf allows the roof rock of the stope to not completely cave. Instead, with the constant advance of the working face, due to compressive deformation of the backfilling body under gravity of overlying strata, the roof is suspended and the immediate roof caves. Moreover, the main roof bends and deforms with the compressive deformation of the backfilling body. When the overhanging roof reaches its limit, it bends near the midpoints of OL and NM edges first.

4.2. Determination of the Key Strata of the Fully Mechanized Coal Mining Face Backfilled with Gangue. Academician Qian Minggao proposed the key stratum theory in the previous study [50]. When there are multilayer strata in overlying strata of the stope, the strata that control all or part of activities of rock mass are called the key strata [50]. The key strata are mainly determined based on deformation and breaking characteristics. When the key strata are broken, the subsidence and deformation of all or local strata above the key strata are coordinated and consistent with each other. The former is known as main key strata, while the latter is called inferior key strata; that is, the fracture of the key strata will lead to the overall movement of all or considerable part of overlying strata. In general, the key strata are the main bearing layers, which bear part of the weight of overlying strata in the form of slabs or simplified beam structures before breaking and form structures of voussoir beams after breaking. Its structural morphology reflects the strata

movement form. According to definition and deformation characteristics of the key strata, if n layers are deformed synchronously and coordinately, the lowest strata are the key strata. The physical and mechanical parameters of overlying strata of the 12031 working face in Jiulishan Coal Mine are listed in Table 2.

According to formula (4), the loading action of the nth stratum on the mth stratum is calculated from the lower stratum ($n > m$).

$$q_{m|n} = \frac{E_m h_m^3 \sum_{i=1}^{n} \gamma_i h_i}{\sum_{i=1}^{n} E_i h_i^3}. \tag{4}$$

If meeting $q_{m|n+1} < q_{m|n}$, then the $n+1$ stratum is regarded as a hard stratum; otherwise, load of the $n+2$th stratum on the nth stratum is continuously calculated. By substituting data in Table 2 into formula (4), load of overlying strata in each layer on A7 and A11 strata is obtained. Based on the calculation results and determination criteria, it is comprehensively considered that there are two hard strata, namely, A7 and A11, in the overlying strata above the 12031 working face of Jiulishan Coal Mine. The criteria for determining the key strata should satisfy not only the stiffness condition, but also the strength condition, which is generally expressed by the interval of roofing breaking L_k of strata as follows:

$$L_k = h_k \sqrt{\frac{2\sigma_{tk}}{q_k}}, \tag{5}$$

where h_k, σ_{tk}, and q_k indicate the thickness (m), tensile strength (MPa), and load (kN) borne by the kth hard stratum, respectively.

It is assumed that the nth and mth strata are hard ($n > m$). If $L_n > L_{m>L}$, the nth stratum is the main key stratum, while the mth and first strata are the inferior key strata. If $L_n > L_{m>L}$, then load on the nth hard stratum should be added onto the mth stratum to recalculate the interval of roofing breaking of the mth stratum. After that, by comparing with the first stratum, the stratum with the longest interval of roofing breaking is the main key stratum, followed by the inferior key stratum, while the nth stratum is not key stratum. According to the criteria for determining the key strata and the physical and mechanical parameters of overlying strata above the 12031 working face of Jiulishan Coal Mine, the key stratum in the coal seam is determined as A7, while the inferior key stratum is A11.

4.3. Analysis on Bending Deformation of the Main Roof of the Fully Mechanized Coal Mining Face Backfilled with Gangue. The analysis on the position of deformation of the main roof of the fully mechanized coal mining face backfilled with gangue based on thin-plate theory shows that the main roof firstly bends at the middle position. In accordance with the assumption of Winkler foundation [15], the main roof is assumed as an elastic beam on the foundation. Therefore, the mechanical model was established only based on the part from the main roof to the coal seam. Owing to the main key strata of the fully mechanized coal mining face backfilled

with gangue bend, rather than break [46], the uniformly distributed load q_0 of overlying strata above the main roof is only calculated from the lower part of the main key strata to the inferior key strata. Because the mechanical model is symmetrical, a half of the model was taken for mechanical analysis, and the unit length was taken in z direction. The starting point on the left end of the beam is the coal wall of the working face, and the length l of the beam is a half of the length of the backfilling zone. The bearing body in the lower part of the main roof is backfilling body and the elastic modulus is constantly changing in the process of continuous compression of the backfilling body, so the supporting force of the bearing body to the key strata is set as p (x). The mechanical model and stress model of the main roof of the fully mechanized coal mining face backfilled with gangue are shown in Figure 6.

By using the mechanical model of the main roof of the fully mechanized coal mining face backfilled with gangue in Figure 6, the main roof and the backfilling body below as the bearing body were analyzed and studied based on a beam model on Winkler elastic foundation. In accordance with the assumption of Winkler foundation [4, 31, 32], the substance at any point on the surface of the foundation is directly proportional to the pressure p on the unit area of the point, expressed as follows:

$$p = k\omega, \tag{6}$$

where ω and k separately represent the subsidence of the foundation and foundation coefficient. The bearing body in the mechanical model of the main roof belongs to the backfilling body that is the elastic foundation. Under the load q_0 of overlying strata, the displacement between the beam (main roof) and the foundation (backfilling body) is defined as x, while the pressure between them is defined as p (x). By analyzing the beam, the relationship among q_0, p (x), and deflection ω of the beam is expressed as follows:

$$q_o - p(x) = EI \frac{d^4 \omega(x)}{dx^4}, \tag{7}$$

where EI denotes the stiffness of the beam section. β is taken as the characteristic coefficient, expressed as follows:

$$\beta = \sqrt[4]{\frac{k}{4EI}}. \tag{8}$$

Formula (7) can be rewritten as follows:

$$\frac{q_o}{EI} = \frac{d^4 \omega(x)}{dx^4} + 4\beta\omega. \tag{9}$$

By solving formula (9), the general solution to formulas is attained as follows:

$$\omega(x) = e^{\beta x}(A \cos \beta x + B \sin \beta x) + e^{-\beta x} \cdot (C \cos \beta x + D \sin \beta x) + \frac{q_o}{k}. \tag{10}$$

Because the established mechanical model of the main roof is a finite-length beam, the formula for the deflection of the beam without load is obtained by solving formula (10)

TABLE 2: Physical and mechanical parameters of overlying strata.

No.	Lithology	Thickness (m)	Elastic modulus (GPa)	Compressive strength (MPa)	Tensile strength (MPa)	Volume force (kN·m^{-3})
1	Loess layer	23.56	0	—	—	18
2	Laterite layer	36.80	0	—	—	18
3	Laterite conglomerate	30.62	1.56	10.21	—	21
4	Siltstone	14.00	1.65	15.96	1.65	25
5	Sandstone	5.37	1.94	21.23	1.82	26
6	Siltstone	8.90	11.23	40.5	3.72	27
7	Sandstone	20.60	18.14	80.5	7.1	27
8	Mudstone	1.60	14.22	56.8	4.3	27
9	Sandstone	13.46	13.2	50.3	3.91	27
10	Siltstone	6.05	12.2	43.21	3.92	27
11	Sandstone	15.48	16.2	69.8	5.97	27
12	Mudstone	1.10	9.58	38.9	3.25	27
13	No. II$_1$ coal seam	5.5	1.93	13.9	0.73	15
14	Siltstone	11.71	9.26	37.5	3.16	27
15	Limestone	0.55	6.72	28.91	2.36	26
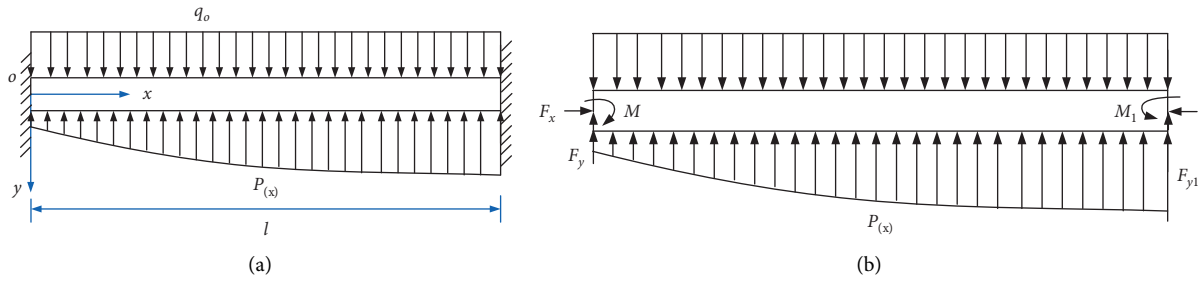
FIGURE 6: Mechanical model and stress model of the main roof. (a) Mechanical model of the main roof. (b) Stress analysis of the main roof.

with the initial parameter method in the existing studies [36, 51].

$$\omega(x) = \omega_o \cdot \varphi_1 + \theta_o \frac{\varphi_2}{\beta} - M_o \frac{\varphi_3}{EI\beta^2} - Q_O \frac{\varphi_4}{EI\beta^3}, \quad (11)$$

where M_o, θ_o, Q_o, and ω_o represent the bending moment, rotation angle, shear force, and deflection at the breaking point ($x = 0$) of the finite-length beam, respectively; Φ_1, Φ_2, Φ_3, and Φ_4 are all Krylov functions of βx.

$$\begin{cases} \varphi_1(\beta x) = ch\beta x \cos \beta x, \\\\ \varphi_2(\beta x) = \frac{1}{2}(ch\beta x \sin \beta x + sh\beta x \cos \beta x), \\\\ \varphi_3(\beta x) = \frac{1}{2}sh\beta x \sin \beta x, \\\\ \varphi_4(\beta x) = \frac{1}{4}(ch\beta x \sin \beta x + sh\beta x \cos \beta x). \end{cases} \quad (12)$$

For the uniformly distributed load q_0 borne by the beam on the foundation, formula (13) is used as the correction term of the deflection.

$$\omega(x)_{q_o} = \int_0^x q_o \theta_4 [\beta(x - \xi)]d\xi = q_o \frac{1 - \varphi_1}{k}. \quad (13)$$

After using the correction term of formula (13), when the finite-length elastic beam on the foundation bears local load, the deflection is expressed as follows:

$$\omega(x) = \omega_o \cdot \varphi_1 + \theta_o \frac{\varphi_2}{\beta} - M_o \frac{\varphi_3}{EI\beta^2} + Q_o \frac{\varphi_4}{EI\beta^3} + q_o \frac{1 - \varphi_1}{k}. \quad (14)$$

By substituting boundary conditions of the beam into formula (14), the deflection $\omega(x)$, rotation angle $\theta(x)$, bending moment $M(x)$, and shear force $Q(x)$ are expressed as follows:

$$\omega(x) = -M_o \frac{\varphi_3}{EI\beta^2} + Q_O \frac{\varphi_4}{EI\beta^3} + q_o \frac{1 - \varphi_1}{k}, \quad (15)$$

$$\theta(x) = \frac{d\omega(x)}{dx} = -M_o \frac{\varphi_2}{EI\beta} + Q_O \frac{\varphi_3}{EI\beta^2} + 4q_o \frac{\varphi_4 \beta}{k}, \quad (16)$$

$$M(x) = -EI \frac{d^2\omega(x)}{dx^2} = M_o \varphi_1 + Q_O \frac{\varphi_2}{\beta} + 4q_o \frac{EI\beta^2 \varphi_3}{k}, \quad (17)$$

$$Q(x) = -\mathrm{EI}\frac{d\omega^3(x)}{dx^3} = -4M_o\beta\varphi_4 + Q_O\varphi_1 + 4\mathrm{EI}\beta^3 q_o\frac{\varphi_2}{k}. \tag{18}$$

By substituting boundary conditions of the beam into formulas (16) and (18), binary linear equations of M_0 and Q_0 are obtained.

$$\begin{cases} -M_o\dfrac{\varphi_2}{\mathrm{EI}\beta} - Q_O\dfrac{\varphi_3}{\mathrm{EI}\beta^2} + 4q_o\dfrac{\varphi_4\beta}{k} = 0, \\[3mm] -4M_o\beta\varphi_4 - Q_O\varphi_1 + 4\mathrm{EI}\beta^3 q_o\dfrac{\varphi_2}{k} = 0. \end{cases} \tag{19}$$

Parameters M_0 and Q_0 are obtained by solving the above binary linear equations.

$$\begin{cases} M_o = \dfrac{2\mathrm{EI}\beta^2 q_0}{k} \cdot \dfrac{\mathrm{sh}(2l\beta) - \sin(2l\beta)}{\mathrm{sh}(2l\beta) + \sin(2l\beta)}, \\[3mm] Q_O = \dfrac{4\mathrm{EI}\beta^3 q_o}{k} \cdot \dfrac{\mathrm{ch}(2l\beta) - \cos(2l\beta)}{\mathrm{sh}(2l\beta) + \sin(2l\beta)}. \end{cases} \tag{20}$$

By substituting formula (20) into the formula for boundary conditions of the beam, the formula for deflection of the finite-length elastic beam on the foundation when bearing the uniformly distributed load is obtained.

$$\begin{aligned} \omega(x) = {} & \frac{2q_0\varphi_3}{k} \cdot \frac{\mathrm{sh}(2l\beta) - \sin(2l\beta)}{\mathrm{sh}(2l\beta) + \sin(2l\beta)_3} \\ & + \frac{q_0\varphi_4}{k} \cdot \frac{\mathrm{ch}(2l\beta) - \cos(2l\beta)}{\mathrm{sh}(2l\beta) + \sin(2l\beta)} + q_o\frac{1 - \varphi_1}{k}, \end{aligned} \tag{21}$$

$$\begin{aligned} M(x) = {} & \frac{2\mathrm{EI}\beta^2 q_0\varphi_1}{k} \frac{\mathrm{sh}(2l\beta) - \sin(2l\beta)}{\mathrm{sh}(2l\beta) + \sin(2l\beta)} \\ & + \frac{4\mathrm{EI}\beta^2 q_0\varphi_2}{k} \frac{\mathrm{ch}(2l\beta) - \cos(2l\beta)}{\mathrm{sh}(2l\beta) + \sin(2l\beta)} + 4q_o\frac{\mathrm{EI}\beta^2\varphi_3}{k}. \end{aligned} \tag{22}$$

According to determination based on thin-plate theory and deformation characteristics of the beam under stress, the points of the maximum deflection and bending moment of the beam appear at $x = l$, thus obtaining the maximum deflection of the beam.

$$\begin{aligned} \omega(l) = {} & \frac{2q_0\varphi_3(l\beta)}{k} \cdot \frac{sh(2l\beta) - \sin(2l\beta)}{sh(2l\beta) + \sin(2l\beta)_3} + \frac{q_0\varphi_4(l\beta)}{k} \\ & \cdot \frac{ch(2l\beta) - \cos(2l\beta)}{sh(2l\beta) + \sin(2l\beta)} + q_o\frac{1 - \varphi_1(l\beta)}{k}, \end{aligned} \tag{23}$$

$$\begin{aligned} M(l) = {} & \frac{2\mathrm{EI}\beta^2 q_0\varphi_1(l\beta)}{k} \frac{\mathrm{sh}(2l\beta) - \sin(2l\beta)}{\mathrm{sh}(2l\beta) + \sin(2l\beta)} + \frac{4\mathrm{EI}\beta^2 q_0\varphi_2(l\beta)}{k} \\ & \cdot \frac{\mathrm{ch}(2l\beta) - \cos(2l\beta)}{\mathrm{sh}(2l\beta) + \sin(2l\beta)} + 4q_o\frac{\mathrm{EI}\beta^2\varphi_3(l\beta)}{k}. \end{aligned} \tag{24}$$

In accordance with strength theory of the beam, $\sigma_{\max}$, $M_{\max}$, and W are separately shown in the following formulas:

$$\sigma_{\max} = \frac{M_{\max}}{W} = \frac{1}{10}\sigma_C, \tag{25}$$

$$M_{\max} = M(l), \tag{26}$$

$$W = \frac{1}{6}h^2, \tag{27}$$

where $M_{\max}$, W, σ_c, and h denote the maximum bending moment, bending modulus of section, bending modulus of section, and height of the beam, respectively.

By substituting formulas (24), (25), and (26) into formula (27), the relationship between the compressive strength and the maximum bending moment is shown as follows:

$$\begin{aligned} & \frac{2\mathrm{EI}\beta^2 q_0\varphi_1(l\beta)}{k} \frac{\mathrm{sh}(2l\beta) - \sin(2l\beta)}{\mathrm{sh}(2l\beta) + \sin(2l\beta)} + \frac{4\mathrm{EI}\beta^2 q_0\varphi_2(l\beta)}{k} \\ & \cdot \frac{\mathrm{ch}(2l\beta) - \cos(2l\beta)}{\mathrm{sh}(2l\beta) + \sin(2l\beta)} \\ & + 4q_o\frac{\mathrm{EI}\beta^2\varphi_3(l\beta)}{k} = \frac{\sigma_c h^2}{60}. \end{aligned} \tag{28}$$

According to the existing study [43], the maximum deflection of the main roof is shown in the following formula:

$$\omega(x)_{\max} = \frac{(\gamma h_1 + q_0) \cdot L_1^4}{384E_1 I}. \tag{29}$$

Therefore, when meeting the conditions of formula (29), the main roof is broken.

$$\omega(l) \geq \omega(x)_{\max}. \tag{30}$$

In the calculation results based on Winkler theory, the bending deformation of the main roof is calculated through the numerical calculation. Based on the actual conditions of Jiulishan Coal Mine, the results of bending deformation of the main roof are obtained through calculation according to parameters of strata above the working face and the test for determining parameters of bulking characteristics of back-filled gangue. Before the calculation, it is necessary to introduce the elastic foundation coefficient of strata [46]. According to the existing study [46], the bearing body below the main roof includes crushed rock blocks of the immediate roof and backfilling body, which belong to the elastic foundation. The C1 and C2 strata between the goaf and the immediate roof are taken as the cushion, as shown in Figure 7. The calculation results of the elastic foundation coefficient of strata in the existing research [46] are demonstrated as follows:

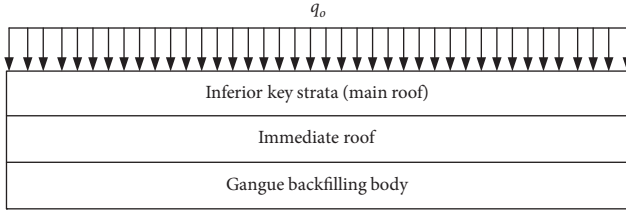$$k = \frac{1}{\sum_{i=1}^{2} h_i/E_i}. \tag{31}$$

q_o

| Inferior key strata (main roof) |
| Immediate roof |
| Gangue backfilling body |

Figure 7: Schematic diagram of strata structure.

As $q_o = \gamma H = 22\,\text{m} \times 27\,\text{kN/m}^3 = 0.594\,\text{MPa}$, $E = 16.2\,\text{GPa}$, $E_1 = 9.58\,\text{GPa}$, $E_2 = 10\,\text{GPa}$, $h = 15.48\,\text{m}$, $h_1 = 1.1\,\text{m}$, $h_2 = 3.0\,\text{m}$, and $\sigma_c = 69.8\,\text{MPa}$, the cross-sectional moments of inertia I, k, and β of the main roof are displayed as follows:

$$I = \frac{1}{12} h^3 = 309.12\,\text{m}^3,$$

$$k = \frac{1}{\sum_{i=1}^{2} h_i/E_i} = 2,410,669\,\text{KN/m}^3, \tag{32}$$

$$\beta = \sqrt[4]{\frac{k}{4EI}} = 0.105\,\text{m}^{-1}.$$

Given $h = 15.48\,\text{m}$ and $\sigma_c = 69.8\,\text{MPa}$, then $l = 22.66\,\text{m}$ can be obtained by solving formula (28).

When $l = 22.66\,\text{m}$, the maximum deflection $w(l) = 1.38\,\text{mm}$ of the main roof can be obtained by solving formula (23).

It is known that $\gamma = 27\,\text{KN/m}^3$. By substituting the measured data of the mine, namely, $L_1 = 58\,\text{m}$ into formula (29), the following result is obtained:

$$\omega(x)_{\max} = \frac{(\gamma h + q_0) \cdot L^4}{384 EI} = 5.56\,\text{mm}. \tag{33}$$

Therefore, $\omega(l) < \omega(x)_{\max}$, according to which it can be determined that the main roof does not break, but it bends and sinks with the constant compaction of the backfilling body during stopping of the working face in the test of mining Jiulishan Coal Mine with gangue backfilling.

5. Movement Laws of Overlying Strata during Gangue Backfilling Mining

5.1. Calculation Model and Parameters

5.1.1. Boundary Conditions of the Model. Based on the numerical simulation, strata movement laws were studied. Due to the limitation of the number of run units of the simulation software, the simplified method is usually adopted; that is, the strata not simulated are regarded as the uniformly distributed load that is applied on the upper boundary of the model. According to different research purposes, the boundaries of the model are correspondingly adjusted. Through the numerical simulation, this study mainly investigated changes of the main roof and key strata and surface deformation laws, and the vertical range of the model was from the floor of the coal seam to the surface [52, 53].

A strain-hardening model was used for calculation. With strike × tendency × height = 400 m × 150 m × 225 m, a plane strain model was utilized. The displacement boundary conditions of the model are shown as follows: the left and right boundaries and the lower boundary of the model are used as displacement boundaries. The displacements of the left and right boundaries in x direction and the displacement of the lower boundary in y direction are limited. The model is demonstrated in Figure 8.

5.1.2. Division of Elements of the Numerical Model and Determination of Calculation Parameters. The left, right, front, and back sides of the model are single-constraint boundaries and the horizontal constraint is applied; that is, the horizontal displacement of the boundary is zero while boundary nodes are only allowed to move along the vertical direction. The bottom of the model is a fully constrained boundary; that is, the horizontal and vertical displacements of the boundary nodes in the bottom are both zero. According to the buried depth of the model and Heim's hypothesis, the gravity stress of the original rock acts on the upper boundary. The calculation model based on FLAC^{3D} software is displayed in Figure 9.

The physical and mechanical parameters of coal seams and overlying strata above the mining face backfilled with gangue and mechanical parameters of the coal-rock contact surface are listed in Table 2. The gangue backfilling materials mostly are siltstone from the floor and mudstone from the roof, and some are sandstone from the roof. The mechanical parameters of backfilled gangue are shown in Table 3.

5.1.3. Simulation Schemes. The elastic modulus of gangue backfilling materials is one of key factors for gangue backfilling mining. For the nonlinear elastic rock, the stress-strain relationship can be expressed by a single valued function $\sigma = f(\varepsilon)$. Because $\sigma - \varepsilon$ shows a curvilinear relationship, the elastic modulus, as a variable, at any point P on the curve depends on the position of the point [4]. Because the gangue backfilling body is constantly compacted under gravity of overlying strata, the elastic modulus thereof changes continuously. When the backfilling body is completely compacted, it can be considered that the elastic modulus thereof reaches the maximum. To study movement laws of the main roof and key strata before and after complete compaction of the gangue backfilling body, the backfilling body is compacted by changing the elastic modulus of the backfilling body at different stages in the numerical simulation. It is supposed that the initial elastic modulus of the backfilling body is 1 GPa. When the elastic modulus of the backfilling body at different stages increases to 5, 10, 15, and 20 GPa with the constant compaction of the backfilling body, the movement characteristics of strata before and after complete compaction were studied by changing the elastic modulus. In addition, five numerical simulation schemes under the elastic modulus of the backfilling body of 1, 5, 10, 15, and 20 GPa were implemented. Based on the above five schemes, the bending and subsidence of the main roof of the working face, compressive
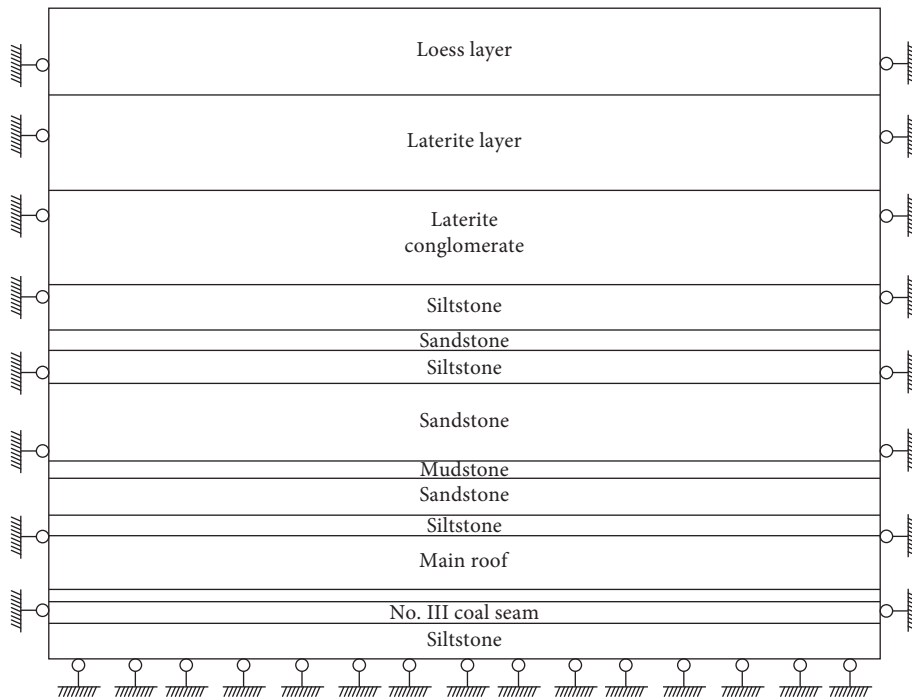
FIGURE 8: Original model.
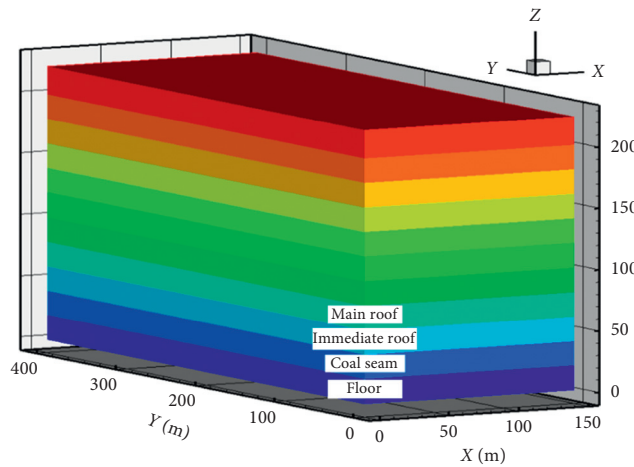
FIGURE 9: Grid model of numerical calculation based on FLAC^{3D} software.

TABLE 3: Physical and mechanical parameters of backfilled gangue.

Backfilling material	Elastic modulus (GPa)	Compressive strength (MPa)	Tensile strength (MPa)	Volume force (kN·m^{-3})
Sandstone	16.2	69.8	5.97	27
Mudstone	9.58	38.9	3.25	27
Siltstone	9.26	37.5	3.16	27

deformation of the backfilling body, surface deformation laws and floor failure were analyzed.

5.2. Movement Laws of Overlying Strata under Different Elastic Moduli of Backfilled Gangue. Through the simulation on the compressive deformation of the backfilling body, the compressive deformation laws of the backfilling body were analyzed under the elastic modulus of 1, 5, 10, 15, and 20 GPa. The simulated 12031 backfilling mining face in Jiulishan Coal Mine advances for 100 m along the strike direction in total. In this case, the deformation of the backfilling body and distributions of displacement vector of the backfilling body and vertical stress were obtained.

(1) Using gangue with the elastic modulus of 1 GPa as backfilling materials for simulation: when gangue with the elastic modulus of 1 GPa is used for backfilling, movement of overlying strata and distributions of displacement vector of surrounding rock and vertical stress when the working face advances for 100 m are obtained in Figure 10.

As displayed in Figure 10, overlying strata during gangue backfilling mining move more gently compared with those during the fully caving mining. By using this method, strata movement is well controlled and the main roof does not break, but it bends. Because the roof is effectively controlled, the abutment stress of the coal wall and roof subsidence are small. Due to influence of the advanced stress, the coal wall slightly deforms. Because of the small elastic modulus and low strength of backfilled gangue, the backfilling body exhibits great compressive deformation, but the failure depth of the floor is small. The above distribution of vertical stress suggests that the maximum abutment stress in front of the coal wall is 25 MPa.

(2) Taking gangue with the elastic modulus of 5 GPa as backfilling materials for simulation: when gangue with the elastic modulus of 5 GPa is utilized for backfilling, the movement of overlying strata and distributions of displacement vector of surrounding rock and vertical stress when the working face advances for 100 m are demonstrated in Figure 11.

As illustrated in Figure 11, overlying strata during gangue backfilling mining move more gently compared with those during the fully caving mining. Strata movement is well controlled and the main roof bends instead of breaking. Because the roof is effectively controlled, the abutment stress of the coal wall and roof subsidence are small. Because of influence of the advanced stress, the coal wall deforms slightly. Since the elastic modulus of backfilled gangue relatively rises and the strength increases accordingly, the compressive deformation of the backfilling body relatively reduces and the failure depth of the floor is still small. The above distribution of vertical stress demonstrates that the maximum abutment stress in front of the coal wall is 21 MPa.

(3) Utilizing gangue with the elastic modulus of 10 GPa as backfilling materials for simulation, when taking gangue with the elastic modulus of 10 GPa for backfilling, the movement of overlying strata and distributions of displacement vector of surrounding rock and vertical stress with the working face advancing for 100 m are illustrated in Figure 12.

As shown in Figure 12, compared with the movement of overlying strata during mining with the fully caving method, the strata movement during gangue backfilling mining is gentler. In this way, strata movement is well controlled and the main roof does not break but bends. Due to effective control on the roof, the abutment stress of the coal wall and roof subsidence are small. Affected by the advanced stress, the coal wall slightly deforms. Due to the constant increase of the elastic modulus and corresponding rise of strength of backfilled gangue, the compressive deformation of the backfilling body decreases correspondingly and the failure depth of the floor is still small. As shown in the above distribution of vertical stress, the maximum abutment stress in front of the coal wall is 20 MPa.

(4) Using gangue with the elastic modulus of 15 GPa as backfilling materials for simulation: when gangue with the elastic modulus of 15 GPa is utilized as backfilling materials, the movement of overlying strata and distributions of displacement vector of surrounding rock and vertical stress are obtained as the working face advances for 20, 40, 60, 80, and 100 m, as displayed in Figure 13.

As shown in Figure 13, overlying strata during gangue backfilling mining move more gently in comparison with that in mining with the fully caving method. Strata movement is well controlled and the main roof does not break, but it bends. Attributed to the effective control on the roof, the abutment stress of the coal wall and roof subsidence are small. Influenced by the advanced stress, the coal wall slightly deforms. When the elastic modulus of backfilled gangue rises to 15 GPa, the compressive deformation of the backfilling body is small, which changes little compared with the case under the elastic modulus of backfilled gangue of 10 GPa, and the floor is still found to have a small failure depth. The above distribution of vertical stress illustrates that the maximum abutment stress in front of the coal wall is 19 MPa.

(5) Utilizing gangue with the elastic modulus of 20 GPa as backfilling materials for simulation. When gangue with the elastic modulus of 20 GPa is used as the backfilling materials, the movement of overlying strata and distributions of displacement vector of surrounding rock and vertical stress are obtained in Figure 14 as the working face advances for 100 m.

As displayed in Figure 14, the movement of overlying strata during gangue backfilling mining is gentler in comparison with that in mining with the fully caving method. The strata movement is well controlled and the main roof bends rather than breaks. Under the effective control of the roof, the abutment stress of the coal wall and roof subsidence are small. When the elastic modulus of backfilled gangue increases to 20 GPa, the compressive deformation of the backfilling body is small, which shows a small change compared with that when the elastic modulus is 15 GPa, and the failure depth of the floor is still small. The above distribution of vertical stress shows that the maximum abutment stress in front of the coal wall is 19 MPa. Compared

(a)

(b)

FIGURE 10: Movement of overlying strata when the working face advances for 100 m under the elastic modulus of gangue of 1 GPa. (a) Displacement vector of surrounding rock. (b) Distribution of vertical stress.

(a)

(b)
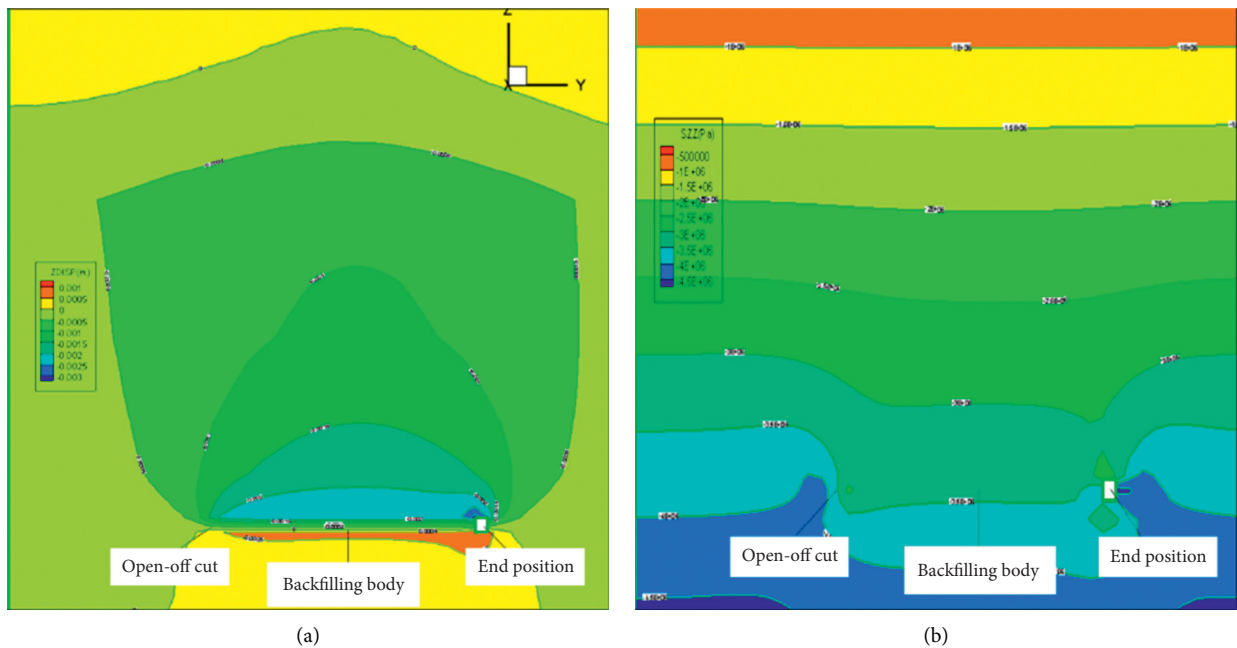
FIGURE 11: Movement of overlying strata when the working face advances for 100 m under the elastic modulus of gangue of 5 GPa. (a) Displacement vector of surrounding rock. (b) Distribution of vertical stress.

with that under the elastic modulus of 15 GPa, the maximum abutment stress changes slightly when the elastic modulus of gangue is 20 GPa.

Based on the above analysis, overlying strata during gangue backfilling mining move more gently compared with those in mining with the fully caving method. Strata movement is well controlled and the main roof does not break, but it bends. Because the roof is effectively controlled, the abutment stress of the coal wall and roof subsidence are small. With the gradual increase of the elastic modulus of backfilled gangue, the vertical stress concentration degree constantly decreases. Under the elastic modulus of backfilled gangue of 1 GPa, the gangue is of low strength, the compressive deformation of the backfilling body is large, and the

(a)   (b)
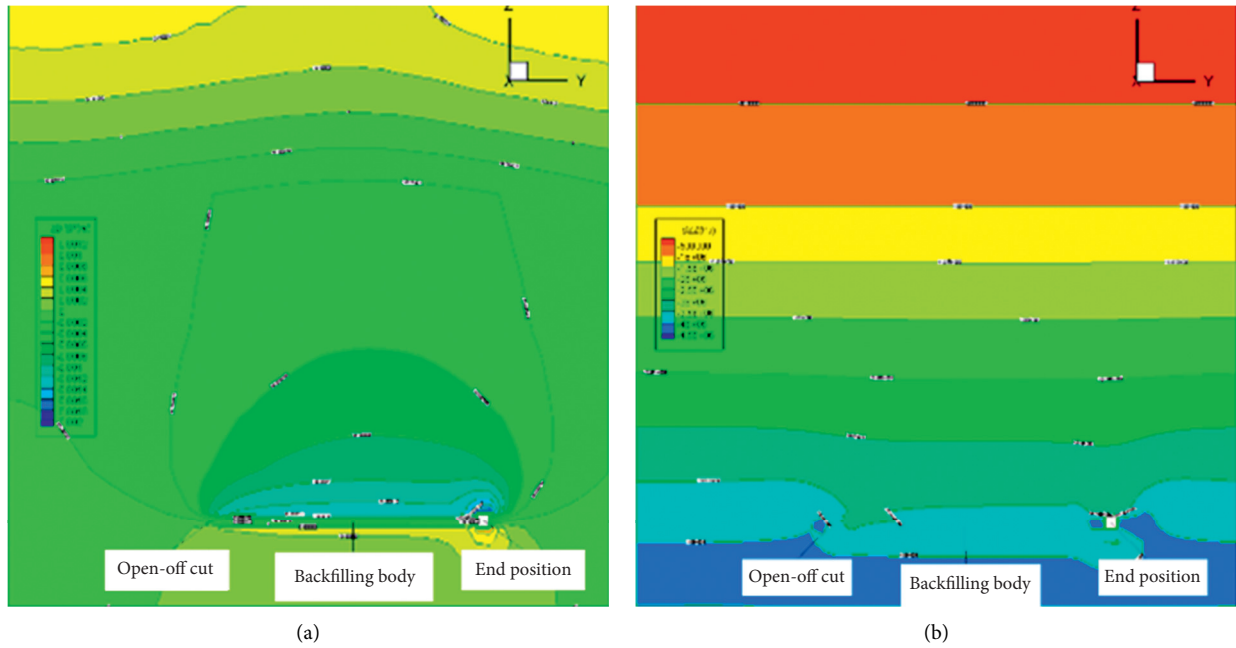
FIGURE 12: Movement of overlying strata when the working face advances for 100 m under the elastic modulus of gangue of 10 GPa. (a) Displacement vector of surrounding rock. (b) Distribution of vertical stress.

(a)   (b)

FIGURE 13: Movement of overlying strata when the working face advances for 100 m under the elastic modulus of gangue of 15 GPa. (a) Displacement vector of surrounding rock. (b) Distribution of vertical stress.

maximum abutment stress in front of the coal wall reaches 25 MPa. When the elastic modulus of backfilled gangue rises to 5 GPa, the distribution of vertical stress and movement laws of overlying strata are basically same as those under the elastic modulus of 1 GPa. However, in this case, the compressive deformation of the backfilling body is obviously

small and the vertical stress concentration degree reduces. Furthermore, the maximum abutment stress decreases obviously to 21 MPa. As the elastic modulus rises to 10, 15, and 20 GPa, movement laws of overlying strata are basically consistent and the vertical stress concentration degree constantly reduces, but its decrease amplitude is not obvious.
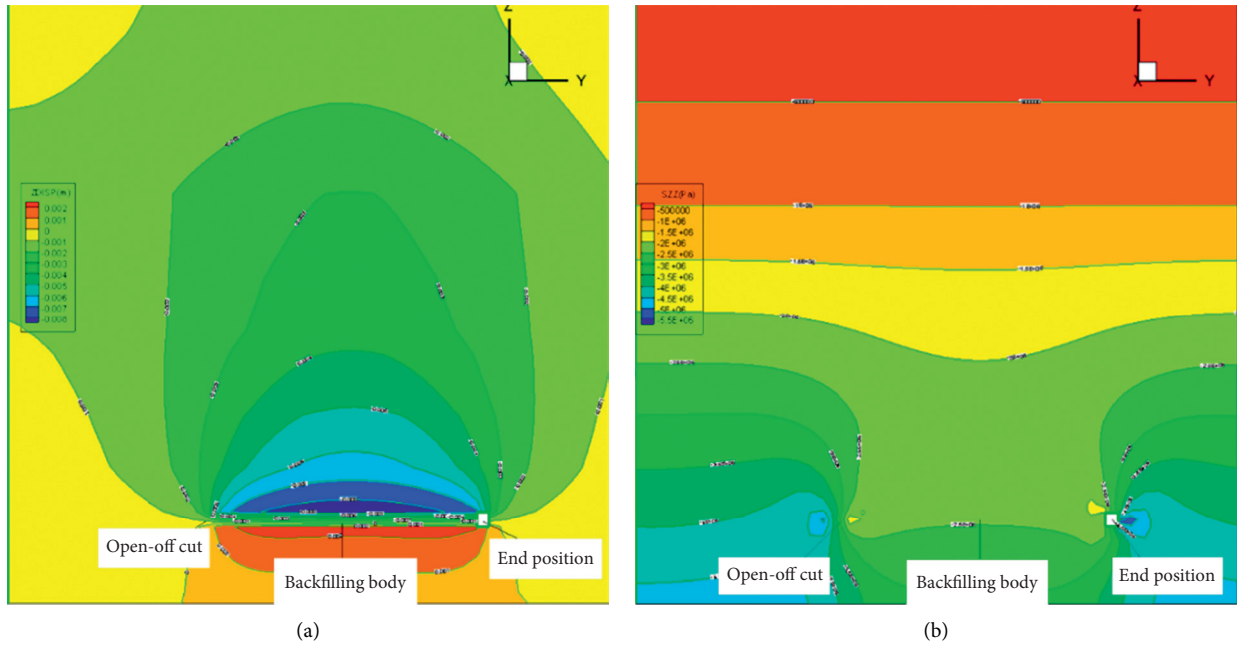
(a)

(b)

Figure 14: Movement of overlying strata when the working face advances for 100 m under the elastic modulus of gangue of 20 GPa. (a) Displacement vector of surrounding rock. (b) Distribution of vertical stress.
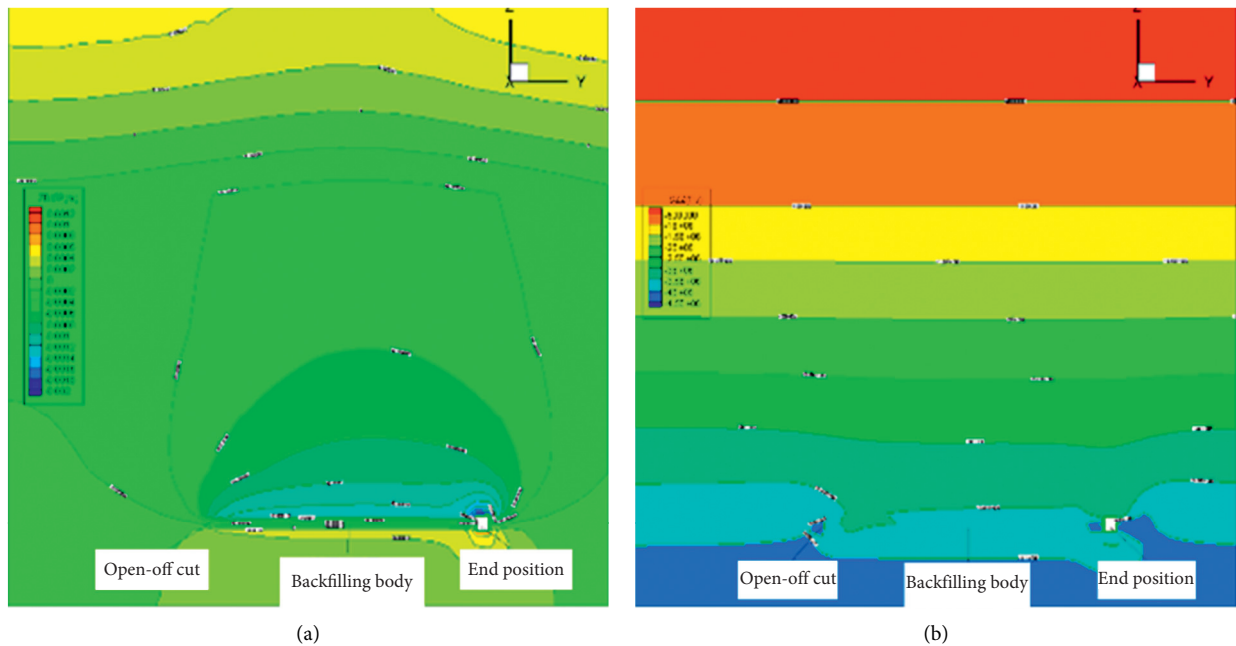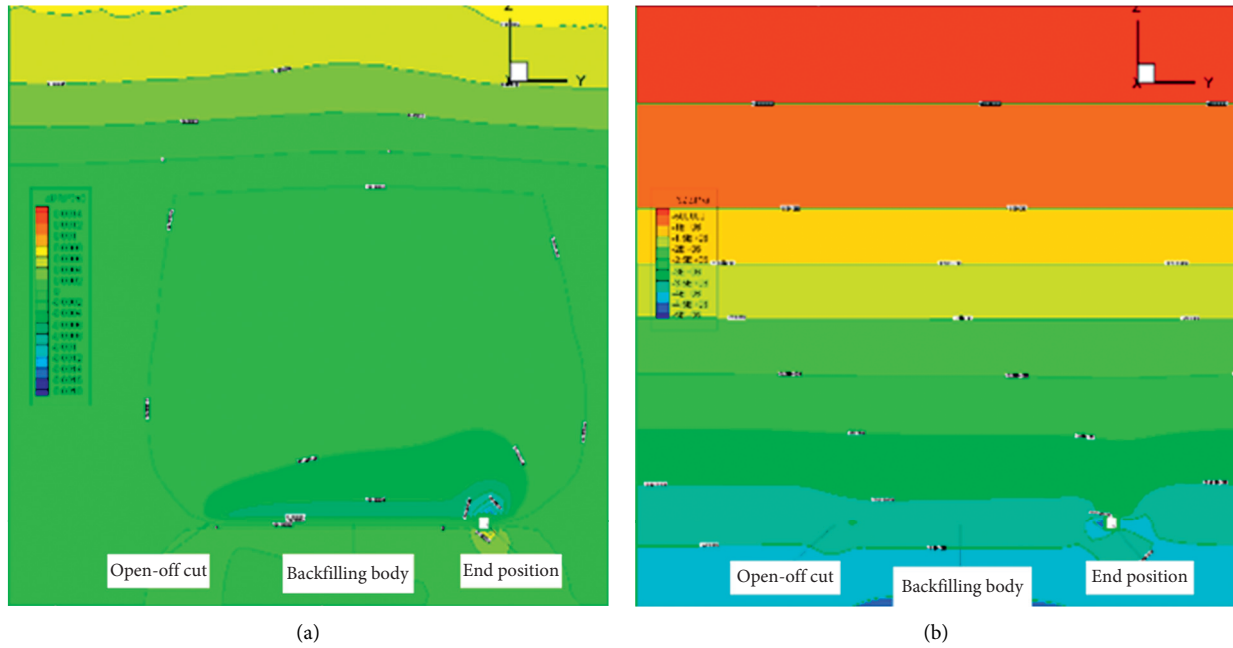
5.3. Compressive Deformation of the Backfilling Body under Different Elastic Moduli of Backfilled Gangue. When the elastic moduli of backfilled gangue are 1, 5, 10, 15, and 20 GPa, the backfilling body is compressed and deformed under load of overlying strata with the constant advance of the working face, as shown in Figure 15.

As demonstrated in Figure 15, when the elastic moduli of backfilled gangue are 1, 5, 10, 15, and 20 GPa, the maximum compressive deformations of the backfilling body are 215, 123, 66, 59, and 31 mm, respectively. It can be seen from the experiment that, with the gradual increase of the elastic modulus of backfilled gangue, the compressive deformation of the backfilling body continuously decreases, so does its decrease amplitude.

5.4. Failure Depth of the Floor under Different Elastic Moduli of Backfilled Gangue. As the elastic moduli of backfilled gangue are 1, 5, 10, 15, and 20 GPa, the failure degrees of the floor under load of overlying strata with the constant advance of the working face are illustrated in Figure 16.

As displayed in Figure 16, under the elastic moduli of backfilled gangue of 1, 5, 10, 15, and 20 GPa, the failure depths of the floor are 44, 15, 6, 5, and 5 mm, respectively. The experiment shows that the failure depth of the floor and its decrease amplitude constantly reduce as the elastic modulus of backfilled gangue gradually rises. When the elastic modulus of backfilled gangue is 10 GPa, the failure depth of the floor is very small and does not change any longer.

5.5. Bending and Subsidence of the Main Roof under Different Elastic Moduli of Backfilled Gangue. By determining the key strata, the main roof of the working face is the key stratum.

Furthermore, through analysis of the mechanical model, it is found that the main roof during gangue backfilling under this condition does not break, but it bends and sinks. When the elastic moduli of backfilled gangue are 1, 5, 10, 15, and 20 GPa, the bending and subsidence of the main roof under the load of overlying strata are obtained with the continuous advance of the working face, as displayed in Figure 17.

Figure 18 demonstrates that as the elastic moduli of backfilled gangue are 1, 5, 10, 15, and 20 GPa, the values of bending and subsidence of the main roof are 158, 45, 23, 23, and 11 mm, respectively. It can be observed from the experiment that, with gradual increase of the elastic modulus of backfilled gangue, bending and subsidence of the main roof constantly reduce, so does its decrease amplitude. When the elastic modulus of backfilled gangue is 15 GPa, the bending and subsidence of the main roof tend to stabilize, indicating that the strength of backfilled gangue determines the bending and subsidence degree of the key strata.

5.6. Surface Deformation under Different Elastic Moduli of Backfilled Gangue. Under the elastic moduli of backfilled gangue of 1, 5, 10, 15, and 20 GPa, Figure 18 shows surface subsidence, inclination deformation, curvature deformation, and horizontal deformation with the constant advance of the working face.

As illustrated in Figure 18(a), when the elastic moduli of backfilled gangue are 1, 5, 10, 15, and 20 GPa, the maximum surface subsidence is 73, 27, 11, 11, and 5 mm, respectively. The experiment demonstrates that, with the gradual rise of the elastic modulus of backfilled gangue, surface subsidence decreases and its decrease amplitude reduces constantly. Even if the elastic modulus of backfilled gangue is 1 GPa, the maximum surface subsidence is only 73 mm, which is very
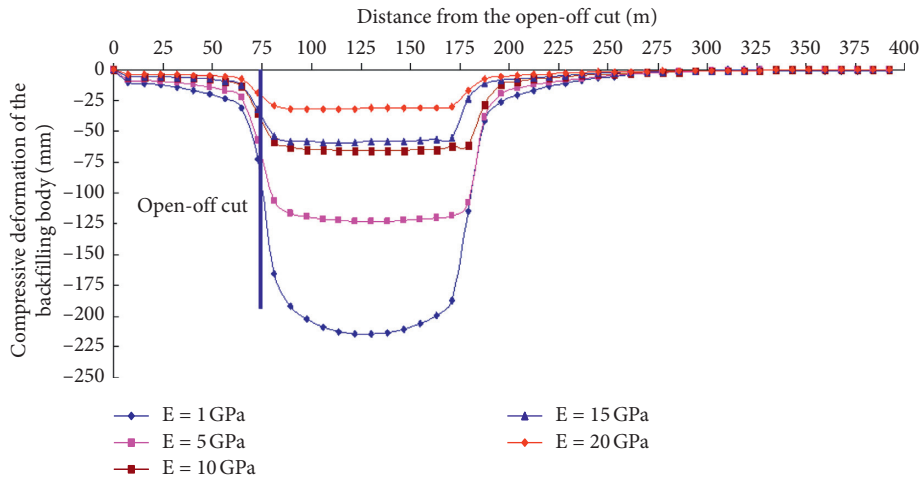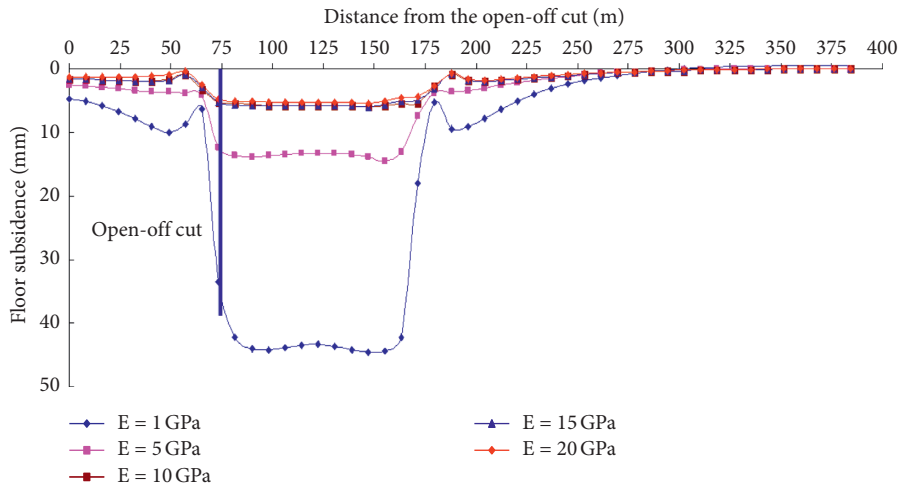
Figure 15: Compressive deformation of the backfilling body.
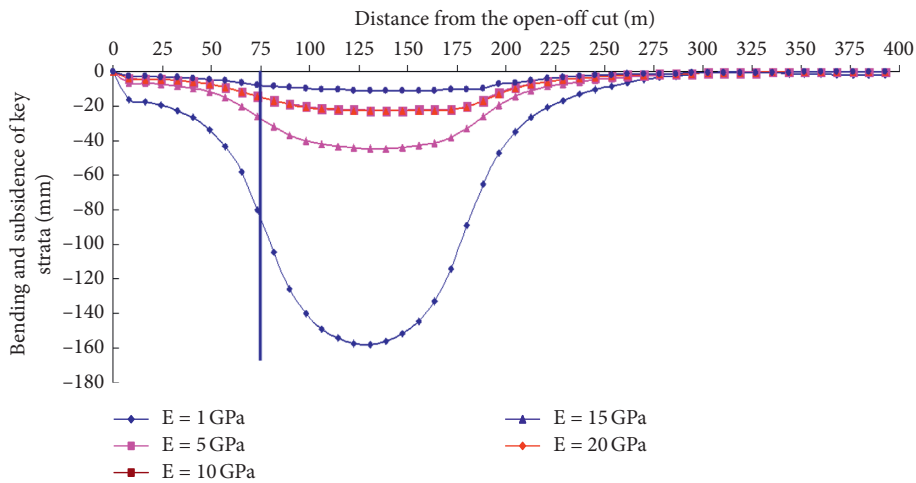
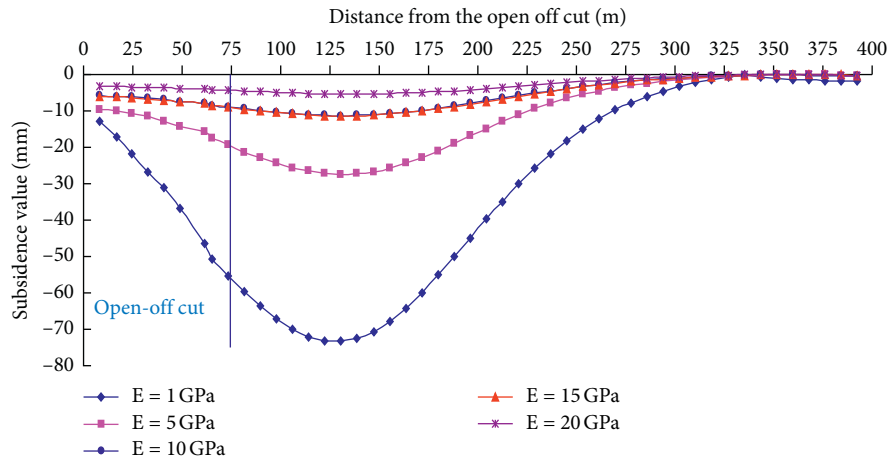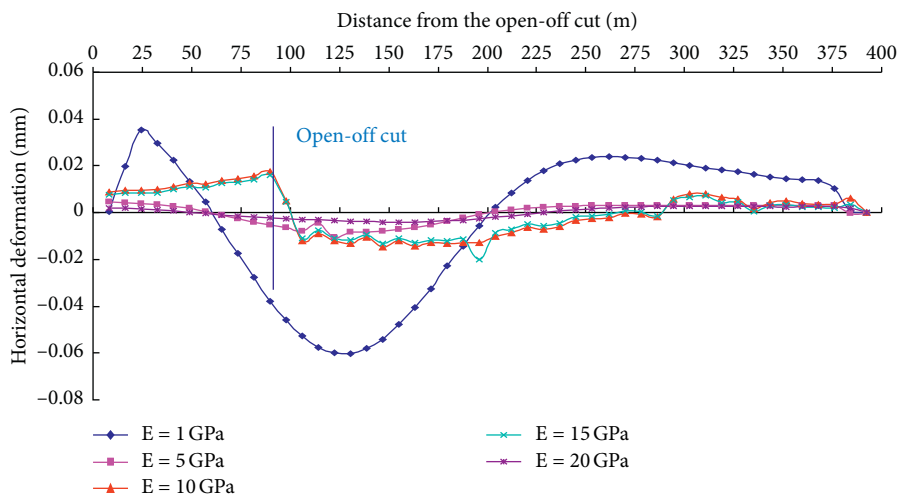Figure 16: Failure depth of the floor.

Figure 17: Bending and subsidence of the main roof.

(a)

(b)
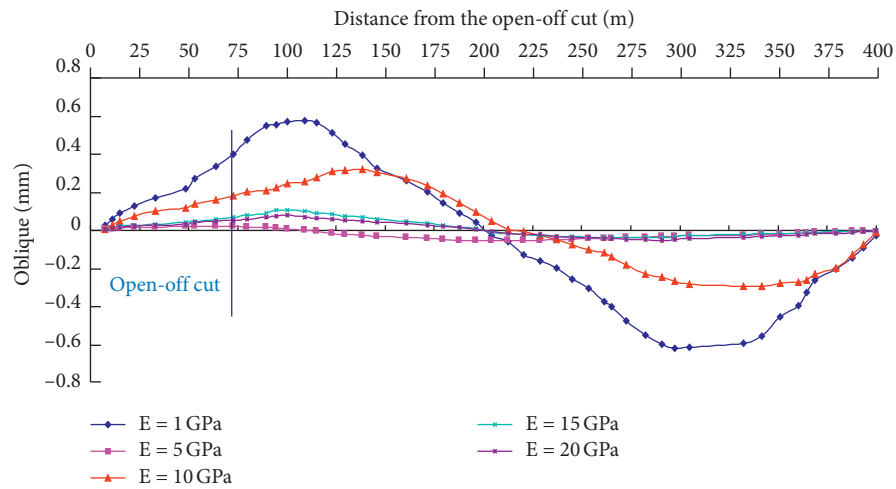
(c)

FIGURE 18: Continued.

(d)
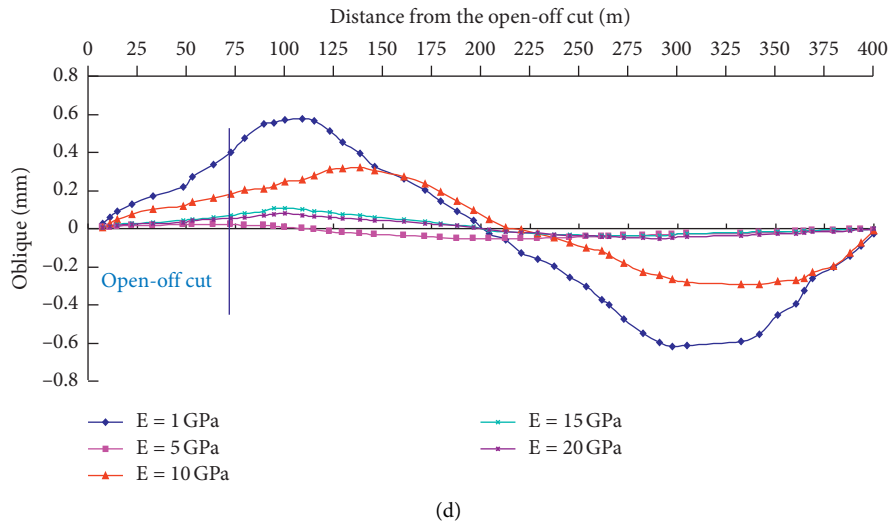
FIGURE 18: Surface deformation laws under different elastic moduli of backfilled gangue. (a) Surface subsidence. (b) Horizontal deformation. (c) Curvature deformation. (d) Inclination deformation.

small compared with that in the traditional mining, so it has a little effect on surface buildings. Under the elastic modulus of backfilled gangue of 10 GPa, surface subsidence basically tends to be stable. The horizontal, inclination, and curvature laws are basically consistent with surface subsidence laws.

6. Conclusions

Firstly, this study determined the stress distribution characteristics in the stope of the gangue backfilling face based on thin-plate theory and then conducted a theoretical analysis to determine stress distribution characteristics in overlying strata. Secondly, the key strata above the working face backfilled with gangue were determined and the deformation characteristics of the roof disturbed by mining were ascertained. Finally, this research analyzed gangue with different elastic moduli, clarified effects of mechanical parameters of gangue on surface subsidence, and determined reasonable physical and mechanical parameters of gangue. The main conclusions are made as follows:

(1) Stress distribution laws in the main roof of the fully mechanized coal mining face backfilled with gangue in a coal seam in Jiulishan Coal Mine were analyzed based on thin-plate theory. Based on this, the position of the main roof first bending and sinking under load of overlying strata was obtained. By using the determination method based on the key stratum theory, it was concluded that there were two key strata and the main roof belonged to the inferior key stratum.

(2) This study established the mechanical model of the main roof of the fully mechanized coal mining face backfilled with gangue and the calculation formula for the maximum deflection of the main roof and presented the conditions for breaking of the main roof. Based on the theoretical analysis, it was concluded that the main roof of the fully mechanized

coal mining face backfilled with gangue did not break but bent.

(3) Based on strain-hardening characteristics of the FLAC^{3D} software for numerical simulation, the strata movement under mining by backfilling with different strengths of gangue was numerically simulated. The research showed that, in the process of the elastic modulus of backfilled gangue increasing from 1 to 20 GPa, the maximum compressive deformation of the backfilling body reduced from 215 to 31 mm and the failure depth of the floor decreased from 44 to 5 mm. Moreover, the bending and subsidence of the main roof dropped from 158 to 11 mm. It was also concluded that, with the constant increase of strength of backfilled gangue, the stress concentration degree of surrounding rock continuously reduced, so did the decrease amplitude. Furthermore, the compressive deformation of the backfilling body, failure depth of the floor, and bending and subsidence of the main roof constantly reduced and tended to be stable. This revealed dynamic change laws of strata movement above the fully mechanized coal mining face backfilled with gangue.

(4) Horizontal, inclination, and curvature deformation laws were basically consistent with surface subsidence laws. When the elastic moduli of backfilled gangue were 1 and 20 GPa, the maximum surface subsidence was 73 and 5 mm, respectively. With the gradual increase of the elastic modulus of backfilled gangue, surface subsidence decreased and its decrease amplitude constantly reduced. Even if the elastic modulus of backfilled gangue was 1 GPa, the maximum surface subsidence was only 73 mm, which was very small compared with that in the traditional mining, so it had very little impact on surface buildings. As the elastic modulus of

backfilled gangue was 10 GPa, the surface subsidence basically was inclined to be stable. It was concluded that backfilling materials determined the effects of gangue backfilling technology in controlling surface subsidence and that gangue backfilling effectively controlled strata movement.

Data Availability

All the data have been included in the manuscript.

Conflicts of Interest

The authors declare that they have no conflicts of interest.

Acknowledgments

References

[1] H. U. Bingnan, "Backfill mining technology and development tendency in China coal mine," *Coal Science and Technology*, vol. 40, 2012.

[2] L. I. Jianping, K. Zheng, and D. U. Changlong, "The distribution discipline of impact crushed on coal and gangue," *Journal of china University of Mining & Technology*, vol. 38, 2013.

[3] J. Li, C. Du, and L. Xu, "Impactive crushing and separation experiment of coal and gangue," *Journal of China Coal Society*, vol. 32, 2011.

[4] X. Miao, "Principle of underground pressure control in fully-mechanized coal mining with solid filing and force analysis of mining support," *Journal of china University of Mining & Technology*, vol. 6, 2010.

[5] X. Miao and M. Qian, "Research on green mining of coal resources in China current status and future prospects," *Journal of Mining & Safety Engineering*, vol. 26, pp. 1–14, 2009.

[6] J. Zhang, J. Li, T. An et al., "Deformation characteristics of key stratum overburden by raw waste backfilling with fully-mechanized coal mining technology," *Journal of China Coal Society*, vol. 35, no. 3, pp. 357–362, 2010.

[7] K. Zheng, C. Du, and B. Qiu, "Experimental study on the fractal characteristics of crushing coal and gangue," *Journal of china University of Mining & Technology*, vol. 25, 2013.

[8] Y.-B. Jung, S. Won-Kyong, C. Dae-Sung et al., "Simple method for the identification of subsidence susceptibility above underground coal mines in Korea," *Engineering Geology*, vol. 178, 2014.

[9] L. Li, A. Tang, D. Zhao et al., "Block caving-induced strata movement and associated surface subsidence: a numerical study based on a demonstration model," *Bulletin of Engineering Geology and the Environment*, vol. 73, no. 4, pp. 1165–1182, 2014.

[10] M. Nazem and M. Karakus, "Numerical analysis of a large landslide induced by coal mining subsidence," *Engineering Geology*, vol. 217, 2017.

[11] W. Kyu-Seok, E. Erik, E. Davide et al., "Empirical investigation and characterization of surface subsidence related to block cave mining," *International Journal of Rock Mechanics and Mining Sciences*, vol. 61, 2013.

[12] Q. Zou, H. Liu, Z. Cheng, T. Zhang, and B. Lin, "Effect of slot inclination angle and borehole-slot ratio on mechanical property of pre-cracked coal: implications for ECBM recovery using hydraulic slotting," *Natural Resources Research*, vol. 29, pp. 1705–1729, 2020.

[13] Z. Quanle and L. Baiquan, "Fluid-solid coupling characteristics of gas-bearing coal subject to hydraulic slotting: an experimental investigation," *Energy & Fuels*, vol. 32, pp. 1047–1060, 2018.

[14] G. U. O. Guangli, W. FENG, Z. H. A. Jianfeng et al., "Subsidence control and farmland conservation by solid backfilling mining technology," *Transactions of Nonferrous Metals Society of China*, vol. 21, no. s1, pp. s665–s669, 2011.

[15] M. I. A. O. Xiexing, "Review of research on mechanical behavior of mining rock mass and its related engineering technology innovation progress Chinese," *Journal of Rock Mechanics and Engineering*, vol. 29, 2010.

[16] M. I. A. O. Xiexing, "Progress of fully mechanized mining with solid backfilling technology," *Journal of China Coal Society*, vol. 37, 2012.

[17] J. Lou, F. Gao, J. Yang et al., "Characteristics of evolution of mining-induced stress field in the longwall panel: insights from physical modeling," *International Journal of Coal Science & Technology*, 2021.

[18] D. Ritesh Lokhande, M. S. R. Murthy Vemavarapu, V. Vellanky et al., "Assessment of pot-hole subsidence risk for Indian coal mines," *International Journal of Mining Science and Technology*, vol. 25, 2015.

[19] Z. Quanle, L. Baiquan, C. Zheng et al., "Novel integrated techniques of drilling–slotting–separation-sealing for enhanced coal bed methane recovery in underground coal mines," *Ournal of Natural Gas Science and Engineering*, vol. 26, 2015.

[20] G. Guo, J. Zha, X. Miao et al., "Similar material and numerical simulation of strata movement laws with long wall fully mechanized gangue backfilling," *Procedia Earth and Planetary Science*, vol. 1, 2009.

[21] J. Wang, Y. A. N. G. Shengli, Y. A. N. G. Baogui et al., "Simulation experiment of overlying strata movement features of longwall with gangue backfill mining," *Journal of China Coal Society*, vol. 37, 2012.

[22] Q. Wang, G. U. O. Guangli, Z. H. A. Jianfeng et al., "Study on surface ground movement law of coal rejects backfill mining under thick and loose overburden strata," *Coal Science and Technology*, vol. 41, 2013.

[23] J. Zhang, Q. Wu, Y. Huang et al., "Strata pressure behavior by raw waste backfilling with fully-mechanized coal mining technology," *Journal of China Coal Society*, vol. 34, 2010.

[24] D. Kong, Z. B. Cheng, and S. S. Zheng, "Study on the failure mechanism and stability control measures in a large-cutting-height coal mining face with a deep-buried seam," *Bulletin of Engineering Geology and the Environment*, vol. 78, pp. 6143–6157, 2019.

[25] J. Ju and J. Xu, "Surface stepped subsidence related to top-coal caving longwall mining of extremely thick coal seam under shallow cover," *International Journal of Rock Mechanics and Mining Sciences*, vol. 78, 2015.

[26] Q. L. Zou, Y. Zhang, Q. Li, J. Fu, and Q. Hu, "Rationality evaluation of production deployment of outburst-prone coal

mines: a case study of nantong coal mine in Chongqing, China," *Safety Science*, vol. 122, 2020.

[27] I. D. Brunton, S. J. Fraser, J. H. Hodgkinson et al., "Parameters influencing full scale sublevel caving material recovery at the Ridgeway gold mine," *International Journal of Rock Mechanics and Mining Sciences*, vol. 47, 2009.

[28] Q. Hu, X. Deng, R. Feng et al., "Model for calculating the parameter of the Knothe time function based on angle of full subsidence," *International Journal of Rock Mechanics and Mining Sciences*, vol. 78, 2015.

[29] I. A. M. Suchowerska, J. P. Carter, and J. P. Hambleton, "Geomechanics of subsidence above single and multi-seam coal mining," *Journal of Rock Mechanics and Geotechnical Engineering*, vol. 8, 2016.

[30] M. Karmis, Z. Agioutantis, and A. Jarosz, "Recent developments in the application of the influence function method for ground movement predictions in the U.S," *Mining Science and Technology*, vol. 10, 1990.

[31] Q. Zhang, J. Zhang, S. Guo et al., "Design and application of solid, dense backfill advanced mining technology with two pre-driving entries," *International Journal of Mining Science and Technology*, vol. 25, 2015.

[32] T. Sasaoka, H. Takamoto, H. Shimada et al., "Surface subsidence due to underground mining operation under weak geological condition in Indonesia," *Journal of Rock Mechanics and Geotechnical Engineering*, vol. 7, 2015.

[33] V. Palchik, "Experimental investigation of apertures of mining-induced horizontal fractures," *International Journal of Rock Mechanics and Mining Sciences*, vol. 47, 2009.

[34] J.-A. Wang, H. D. Park, and Y. T. Gao, "A new technique for repairing and controlling large-scale collapse in the main transportation shaft, Chengchao iron mine, China," *International Journal of Rock Mechanics and Mining Sciences*, vol. 40, 2003.

[35] Y. Luo, "An improved influence function method for predicting subsidence caused by longwall mining operations in inclined coal seams," *International Journal of Coal Science & Technology*, vol. 2, pp. 163–169, 2015.

[36] J. Zhang, Q. Zhang, Q. Sun et al., "Surface subsidence control theory and application to backfill coal mining technology," *Environmental Earth Sciences*, vol. 74, pp. 1439–1448, 2015.

[37] J. F. Lupo, "Large-scale surface disturbances resulting from underground mass mining," *International Journal of Rock Mechanics and Mining Sciences*, vol. 16, 1998.

[38] H. E. Zhexiang, N. Wang, and C. Xie, "Analysis of surrounding rock activities partial backfill mining," *Journal of China University of Mining & Technology*, vol. 33, 2004.

[39] H. Liang: Integrated Technology of Backfill Mining and Raw Coal Separation in Underground Mine Coal Science and Technology 2013.

[40] H. U. Bingnan and G. U. O. Aiguo, "Testing study on coal waste back filling material compression simulation," *Journal of china University of Mining & Technology*, vol. 34, no. 8, pp. 1076–1080, 2009.

[41] X. Huang, L. Tao, and W. Cao, *Rock Mechanics*, Higher Education Press, Beijing, China, 2005.

[42] M. A. Zhanguo, G. U. O. Guangli, R. Chen et al., "An experimental study on the compaction of water-saturated over broken rock," *Chinese Journal of Rock Mechanics and Engineering*, vol. 24, no. 7, pp. 1139–1144, 2005.

[43] D. O. N. G. Shouyi, "Analysis and practices on integrated match of backfill mining equipment," *Coal Science and Technology*, vol. 40, 2012.

[44] H. Zhang, X. Zhang, and C. A. O. Zhong: Research on Physical and Mechanical Characteristics of Refuse Rock in Filling Coal Mining Technology 2008.

[45] P Helm, C T Davie, and S Glendinning, "Numerical modelling of shallow abandoned mine working subsidence affecting transport infrastructure," *Engineering Geology*, vol. 154, 2013.

[46] J. Liu and Z. Qingbiao, "Comprehensive mechanized filling coal mining," *Journal of China Coal Society*, vol. 35, 2010.

[47] G. Guangli, X. Zhu, Z. Jianfeng et al., "Subsidence prediction method based on equivalent mining height theory for solid backfilling mining," *Transactions of Nonferrous Metals Society of China*, vol. 24, 2014.

[48] F. Wang, B. Jiang, S. Chen et al., "Surface collapse control under thick unconsolidated layers by backfilling strip mining in coal mines," *International Journal of Rock Mechanics and Mining Sciences*, vol. 113, 2019.

[49] L. Shuncai, Z. Chen, and L. Yu, "Study on penetration features of coal rejects during constant load deformation test process," *Coal Science and Technology*, vol. 41, 2013.

[50] X. Jialin and Q. Minggao, "Application research and practice of rock formation control key layer theory," *China Mining*, vol. 13, 2001.

[51] X. Zhu, G. Guo, J. Zha et al., "Surface dynamic subsidence prediction model of solid backfill mining," *Environmental Earth Sciences*, vol. 75, 2016.

[52] W. Xie, Z. Shi, X. Chen et al., "Analysis of surrounding rock activities in partial backfill mining," *Journal of China University of Mining & Technology*, vol. 33, 2004.

[53] J. Xu, M. Qian, W. Ma et al., "Discussion on loading problem in physical and numerical simulation of strata movement," *Journal of China University of Mining & Technology*, vol. 30, 2001.

Review Article

Analysis on the Characteristics of Water Pollution Caused by Underground Mining and Research Progress of Treatment Technology

Xinfeng Wang (iD),[1,2] **Yuhao Gao,**[1] **Xiaojun Jiang** (iD),[2,3] **Qiao Zhang,**[1] **and Wengang Liu**[1]

[1]*School of Environment and Resources, Xiangtan University, Xiangtan 411105, Hunan, China*
[2]*Emergency Management Research Center, Xiangtan University, Xiangtan 411105, Hunan, China*
[3]*School of Public Administration, Xiangtan University, Xiangtan 411105, Hunan, China*

Correspondence should be addressed to Xinfeng Wang; xfw2020@xtu.edu.cn and Xiaojun Jiang; jiangxiaojun@xtu.edu.cn

Coal is the primary source of energy in China's energy structure system. With the large-scale mining of mineral resources, a large amount of mine water will be produced in the process of development, construction, and production, which will pollute and damage the ecological environment of mine water. At present, China vigorously advocates coal revolution, implements low-carbon economy, and carries out clean production of energy development and utilization. Green mining, precision mining, and other strategic ideas have been applied to mine development to guide production practice. This paper does an in-depth analysis of the physical, chemical, biological, and environmental characteristics of mine water, puts forward the basic classification of mine water, and points out the characteristics of environmental hazards of mine water. Aiming at different types of mine water, such as mine wastewater, drainage water, goaf water, mine water with suspended solids, high salinity mine water, acid mine water, and mine water with special pollution, the paper puts forward the mine water treatment and resource utilization technology with different characteristics and strong pertinence. On this basis, the comprehensive treatment and development direction of mine water in the future are prospected.

1. Introduction

China is the world's largest producer of coal and a major consumer of coal. China's coal recoverable reserves are the third largest in the world. The coal industry has become an important foundation for the rapid development of the national economy. China's coal situation: in China's natural resources, the basic characteristics are rich coal, poor oil and gas, which determine the important position of coal in primary energy. Compared with oil and natural gas, China's coal reserves are relatively abundant, accounting for 11.60% of the world's reserves. China's total coal resources are 5.6 trillion tons, of which proven reserves are 1 trillion ton, accounting for 11% of the world's total reserves. As China's basic energy and industrial raw material, coal has provided a strong guarantee for

economic and social development, national energy security, and stable supply for a long time [1–3].

In the process of coal mining, groundwater is exposed to coal seams, rock formations, and human activities, resulting in significant water quality characteristics of the coal industry. Usually containing a large amount of suspended solids, and poor sensory properties, some are highly mineralized or acidic, and even contain radioactive elements and oxides. If they are directly discharged, the formed acidic water will flow into the river or infiltrate into the underground, which will pollute the water source, causing the death of large-scale vegetation. The polluted water will spread to the farmland and easily lead to soil infertility. Declining, silting up the river, and forming serious ecological and social problems, the ecological environment is seriously deteriorated.

At present, the annual mine water discharge in China is 4.5 billion cubic meters, and the utilization rate is 43.8%, which is far lower than the standard of 80% in developed countries. Industrial production and mining will lead to a sharp decline in the groundwater level, and there will be leakage areas in the mining area and adjacent cities, which may lead to ground collapse and seawater intrusion [4].

Therefore, in order to ensure the sustainable development of coal resources, it is necessary to take relative measures for the prevention and treatment of polluted water in coal mining. In the process of coal mining, resources cannot be exploited at the expense of massive destruction and waste of water resources. After a series of treatment, the mine water can be reused for production water, urban greening, agricultural irrigation, and drinking water in the mining area, so as to further realize the resource utilization of mine water, optimize the coal production and environment, and rationalize water resources. Development has a virtuous circle.

2. Characteristics and Classification of Mine Water Pollution

2.1. Mine Water Characteristics. Mine water is the same as the general groundwater before it is polluted. The lithology and water conservancy conditions of the aquifer determine its water quality characteristics. The pH of the mine water is mostly neutral to weakly alkaline. If the mineralization is low, the toxic content is generally below the detection limit. In the process of coal mining, when the mine water flows through the coal mining face and the roadway, it is artificially affected. The rock powder, coal powder, and other organic matter are mixed into the water. If the water is polluted, then it is grayish black in color, and contains a large amount of suspended impurities and a certain amount of microorganisms [5].

Mine water in mine production is brought together in various ways, and mining and ore dressing water account for the largest proportion. The main sources of mine wastewater are as follows:

① Open-pit mine wastewater: wastewater formed by mining production process; acidic water discharged from waste rock pile after dissolution of waste rock pile after rainfall.

② Mine wastewater: mainly production-contaminated groundwater in the process.

③ Mineral processing waste water: waste water produced in the process of washing, crushing and mineral processing. A large amount of waste water usually contains ore, metal particles, or various mineral processing agents, which are seriously polluted. Wastewater accumulated in the dam.

④ Other mine wastewater: wastewater from washing vehicles, hospital wastewater, and domestic wastewater, containing solid suspended matter, oil, organic matter, and other pollutants.

2.2. Mine Water Classification. The general principles of mine sewage treatment and reuse are: clean and diversion, sewage and diversion, classification and treatment, and quality and reuse [6]. Mine drainage is divided into three main categories: dewatering water, water in the goaf, and underground sewage in the mine.

Draining water: draining water in coal mines refers to the wastewater that is generated underground due to the formation structure in the coal mining.

Water in the goaf: after long-term mining, the coal mine will easily form a goaf. The goaf needs timely measures. No water will accumulate in these goafs. If no measures are taken, the generated water will be mined. The process creates water hazards and safety issues [7].

Mine underground sewage: in coal mining operations, coal-based aquifers will be naturally drained, and these waters will merge into the bottom of the well to form mine water. Due to the different types of coal, the main pollution characteristics of mine water are also different, mainly divided into: clean mine water, suspended mine water, acidic mine water with acid pollution, high salinity mine water, and special contaminated mine water.

(1) Clean mine water: the quality of clean mine water is good, the pH is generally neutral, with low turbidity and hardening degree, and toxic and harmful ions are basically not included. This mine water can be intercepted at the water source, discharged to the bottom of the well through the pipeline, and transported to the surface by the pump. This type of water can be used as drinking water after simple disinfection, and water containing beneficial elements can be directly used as mineral water.

(2) Mine water containing suspended solids: in the mining area, mine water containing suspended solids is most common. The pH is generally neutral, the hardness and salinity are not high, the coal powder is of very small particle size, and rock dust, rock powder, etc., are present. The main component of suspended mineral water is generally black, and the content per liter is about tens to hundreds of milligrams.

(3) High salinity mine water: high salinity mine water generally refers to mine water with a salt content greater than 1000 mg/L. It is also called salt mine water. Groundwater is in contact with carbonate rock and sulfate layer, resulting in Ca^{2+} in water and an increase in Mg^{2+}, Na^+, K^+, $SO4^{2-}$, $HCO3^-$, and Cl^- plasma, so the hardness tends to be high. Such water will be discharged if it is not treated, which will cause the salt content of the river to rise, the soil to grow salinized, and the crops to reduce production.

(4) Acid mine water: acid mine water mainly refers to groundwater with a pH lower than 6. It is formed when the groundwater flows through the coal bottom layer of the coal mine, and the pyrite is oxidized to produce sulfurous acid and sulfuric acid under the action of sufficient oxygen and bacteria, resulting in

the mine water being acidic with a large amount of SO_4^{2-}, Fe^{2+}, Fe^{3+}, and Mn^{2+} plasma. When the acid mine water is discharged directly without treatment, the water quality will be deteriorated. Fe^{2+} will consume oxygen in the water, causing the death of a large number of fish, algae, and other organisms. Fe^{3+} and OH^- combine to form Fe (OH) 3 reddish brown precipitation, which leads to the red edge of the water. Acid mine water is highly corrosive, and long-term exposure of mine workers to such water can affect their health.

(5) Containing special polluted mine water: mine water containing special pollutants refers to mine water of toxic substances such as fluoride, heavy metals, and radioactive elements. The pollution of such mine water is serious and difficult to handle. Random discharge will damage the ecological environment and affect the utilization of mine water resources.

2.3. Environmental Hazards of Mine Water.

Mine water classified according to the main pollution characteristics, except for the four types of mine water other than clean mine water, has different levels of pollutants. It corrodes the surface through which the flow passes, and the larger the flow area, the larger the corrosion surface. In addition, the water temperature of groundwater will also be affected by mine water. For example, some large mining areas are affected by mine water, and the hydrological underlying surface of the basin is destroyed, resulting in water-level decline, dry ground cracks, soil erosion, etc. It will further lead to ground collapse, seawater intrusion, and other disasters. Mine water containing pollutants flows into the river. On the one hand, it is difficult to recycle, and it will destroy the ecological balance, pollute the water body, reduce the potential of the farmland near the river to be cultivated, and destroy the vegetation. On the other hand, the base flow is reduced, and the rivers are transformed into seasonal rivers, eventually forming a situation in which the time and space of the basin are unevenly distributed.

Different types of mine water have different environmental hazards.

The suspended solids particles contained in the suspended mineral water are prone to be hydrated with water molecules, which not only forms a hydrated film in the water but also hinders the aggregation of particles, and also keeps the particles in a dispersed state. The interface between the suspended particles is also affected by Brownian motion, which makes the nature of mine water more and more complex.

High-salinity mine water contains high concentrations of inorganic salts. If it is discharged into water bodies without treatment, it will easily lead to an increase in the salinity of surface water and groundwater, affecting the life of river creatures and surrounding residents, causing serious soil salinization, and reducing crop production. At the same time, for nearby factories and living areas, high-salinity mine water purification costs are high. To maintain normal industrial production and domestic water, it is necessary to develop deeper groundwater, resulting in resource abuse and economic development.

Acidic mine water is dissolved in water due to heavy metals such as Cu, Zn, Mn, As, Pb, and Cd in coal mines and surrounding rocks. It is more toxic and more harmful than monomers. Acid mine water can dissolve and erode the surrounding rock, and corrode mine working equipment and drainage pipes. If discharged directly without treatment, it will lead to an increase in the acidity of surface water. If it flows into a highly biological river, it will cause serious damage to the ecosystem, the acid-base balance will be broken, many aquatic organisms will die, nearby soil will be compacted, and production cuts in farmland crops will affect the biodiversity. It causes serious damage to the drinking water system in the living area, which worsens the disparity between supply and demand of water resources and affects human health.

Heavy metal components in heavy metal mine water are complex, because most of the nonferrous metal ore contains associated elements; so, there are cadmium, Mercury, arsenic, lead, fluorine, zinc, and other elements in the general mine wastewater. The heavy metal mine water penetrates into the groundwater through surface seepage, changing the pH of the water body, affecting the self-purification ability of the water body, and causing serious pollution damage to the surrounding rivers and farmland. In addition, heavy metals are difficult to degrade, and the toxicity is very strong. Plant growth has an impact and affects human health through the food chain. In China, the mine water discharged from most metal mines contains more lead and cadmium. The pollution by acidic mine water and excessive heavy metal mine water is shown in Figure 1.

Lead is one of the most common pollutants and has strong toxicity. Generally, the content of lead in water bodies will not exceed 0.01 mg/L. When the concentration exceeds 0.1 mg/L, it will affect the self-purification of water bodies, which will lead to algae. The death of various plants will also endanger human health through the food chain. If lead enters the human body, it will destroy the activity of protein and enzymes in the body, causing nausea and diarrhea, and lead to excessive lead ions in the blood.

Cadmium is one of the heavy metal elements that are symbiotic with zinc ore in the earth's crust and is most harmful to the human body. When cadmium ions enter the human body, cadmium can replace zinc, calcium, and other elements, which can soften the bones and affect the enzyme system in the body. In addition, the toxicity of cadmium will cause "bone pain" in Japan (long-term consumption and consumption of cadmium-containing foods). Water causes cadmium accumulation in human body and then causes kidney damage and osteoporosis.

3. Analysis on Research Progress of Mine Water Treatment Technology

3.1. Mine Wastewater Recycling.

The resource utilization of mine wastewater is put forward on the basis of solving the two serious problems that plague the coal mine

(a)   (b)

FIGURE 1: Schematic diagram of mine water pollution. (a) Acid mine wastewater. (b) Excessive heavy metal mine water.

industry, namely, severe water shortage in the coal mine area and environmental pollution by mine wastewater [8].

According to different mine water properties, the utilization direction of various mine waters is determined. Ensure that the mine water discharge obtained after the final treatment will not pollute the environment; reduce the discharge of COD, suspended solids, and other pollutants in the water; and reduce the impact on the nearby waters.

At present, domestic and foreign mine wastewater has the following uses: coal preparation, hydraulic transportation, water mining, and hydraulic filling; boiler, cooling, dust removal; the water extracted from the drainage borehole can be used for drinking purposes; mine wastewater can be used as a heat pump to regulate the indoor temperature of the building.

In China, the overall utilization rate of mine water is still low, with an average of only 22%. China's conscious comprehensive utilization of mine water is late, and the comprehensive utilization rate is only about 15%. However, with the increasing shortage of mineral water resources, many areas of the mining area have carried out various degrees of comprehensive utilization work, of which the most important is the use of industrial water, domestic water, for agricultural irrigation [9]. In addition, new utilization methods have been developed: On the one hand, use mine water and power plant waste heat to achieve office building cooling and air conditioning. Water source heat pump technology is an emerging energy-saving air-conditioning technology, which can save investment and operating costs, save energy, save water, and reduce the effect of environmental impact. On the other hand, the underground space should be treated and utilized. Mine water resources can be brought into the urban water resources management planning, and unified management can be implemented.

3.2. Mine Water Treatment Technology.
For coal mine water, the most common treatment processes in China are coagulation, precipitation, filtration, adsorption, reverse osmosis, and so on. For different kinds of mine water, the treatment technology is different, and it must be treated in a targeted

manner. Combined with the pollution characteristics of mine water, the treatment technology of mine water is shown in Table 1.

3.3. Dredging Water.
In some large coal mines, the spatial distribution of the drain water is uneven, and in areas where the drain water is abundant, in addition to being used by itself, it will cause waste of water resources; but in an area with water shortage, no water can be used. Coal mine drainage water will lead to deterioration of water quality after the runoff mining area, which makes the water quality of mine drainage water more complicated and changeable, with high hardness and high content of iron, aluminum, and manganese. Drained water must be discharged in accordance with the requirements of the effluent water quality. After treatment, it should meet the discharge (reuse) water quality standards, that is, the concentration of suspended matter in the raw water needs to be reduced to below 50 mg/L [10].

The main technological processes for the treatment of dry water are coagulation, precipitation, air floatation, filtration, and disinfection. The process uses lime milk plus soda ash to efficiently remove iron, aluminum, calcium, manganese, and other metal elements in the water, and uses the high sulfate in the raw water to remove the calcium element while removing sulfate and reducing the amount of soda ash. The drained water can be discharged into the pavement pool directly through the pipeline pump, which can be directly recycled for production and mining.

3.4. Water in the Goaf.
In the process of roadway development, excavation, and construction, the water in the goaf passes through the water flowing fracture zone and carries on the roadway under the action of hydrostatic pressure, resulting in mine water disaster accidents.

For the study of water accumulation in the goaf, engineering technology is required to discharge the water accumulation in the goaf, mainly through the following methods: field survey; working face; water hole layout;

TABLE 1: Mine water treatment technology.

Mine water type	Processing technology
Suspended mine water	Coagulation-precipitation-filtration-disinfection
Acid mine water	Neutralization method, anoxic limestone ditch, permeable reaction wall, constructed wetland, sulfate-reducing bacteria reactor, continuous alkali production system
High-salinity mine water	Chemical desalination, distillation, membrane separation
Heavy metal mine water	Precipitation method, adsorption method, membrane separation method
Fluoride-containing mine water	Electrodialysis, ion exchange, chemical precipitation

analysis calculation; numerical simulation; and comparative analysis method.

Technical route adopted:

① Collect geological and hydrological characteristics, mining conditions, and other relevant data in the study area.

② Perform statistical analysis on the collected data, mainly including the water layer, groundwater hydraulic connection, and stratum.

③ Analyze the influencing factors of water accumulation in the mined-out area, and calculate the development height of the cracked zone in the mined-out area.

④ Based on actual data, establish a hydrogeological model of the study area, and identify and verify the reliability of the model.

⑤ Use the big well method and numerical simulation method to predict the water accumulation speed of the goaf.

⑥ Prediction of the water accumulation space, water accumulation amount and water accumulation time of the goaf in different working faces.

3.5. Suspended Mine Water. Mine water with suspended solids contains more coal powder, rock powder, and clay in the water, which makes the mine water appear black, but the hardness and salinity are not high. Suspended matter mine water needs to choose different purification treatment methods according to the characteristics of the suspended matter.

The most basic treatment processes for this type of mine water are coagulation, precipitation, filtration, disinfection, and sterilization [11].

Coagulation is the most critical process for removing suspended solids from mine water. In the water treatment process, whether it is for the entire clarification process, pretreatment before biochemical treatment, or in-depth treatment after biochemical treatment, coagulation technology is a necessary procedure. Coagulation includes two processes: coagulation and flocculation. Coagulation refers to the action of colloidal particles and flocculants in water to neutralize and compress the electric double layer, to destabilize coagulation, and then aggregate into primary micro-flocculants. Large and dense settlement flocs are formed [12].

The removal effect of suspended matter is affected by factors such as the choice of coagulant, the dosage of coagulant, and the conditions of coagulation reaction. The effects of the three coagulants, PAC, $FeCL_3$, and $Al_2(SO_4)_3$, on mine water turbidity and SS removal rate were investigated, respectively. Turbidity and SS removal rate changes are shown in Figure 2. For the purification of suspended mine water, the most commonly used is aluminum salt or iron salt coagulant. At present, the most widely used and effective coagulant for removing suspended solids in mine water is PAC (Polyaluminum Chloride), and some will choose polyaluminum iron. The flocculant is polyacrylamide. PAC is an inorganic polymer type. It has strong adaptability to changes in pH and water temperature, and its turbidity removal rate is also very efficient. However, it is expensive and has certain toxicity. It is rarely used for treating mine water to convert to drinking water.

Q. Wu has studied the mine water containing suspended solids by coagulation-microfiltration membrane separation technology, and investigated the influence of the change of microfiltration membrane operating characteristics on the membrane filtration performance and the treatment effect of this process on mine water containing suspended solids, and carried out technical and economic analysis [13].

L. Zhao has determined the optimal physical and chemical treatment process by combining the site conditions and water requirements of the Gequan mine water treatment project, that is, the "high-efficiency clarification plus gravity valveless filter" combined process, wherein traditional hydraulic cycle clarification tanks and gravity valveless filter tanks have been improved to make the operation more suitable for the purification treatment of the mine wastewater.

The problems of traditional clarifiers are pointed out: the water production capacity is small, the adaptation water quantity and the water quality change are poor, the external discharge of the sludge is difficult to control, and the surface load of the water outlet is uneven, resulting in unstable water output.

Improvement of high-efficiency clarifier: ① In order to reduce the energy consumption of the pump, the nozzle diameter can be increased, thereby reducing the nozzle head loss. ② The grid-reinforced reactor was added to the first reactive type of the hydraulic circulation clarifier, which strengthened the turbulent disturbance of the water flow, shortened the reaction time, and strengthened the degree of reaction. ③ Improve the radiant water collecting trough into an unequal-distance orifice water collecting trough to
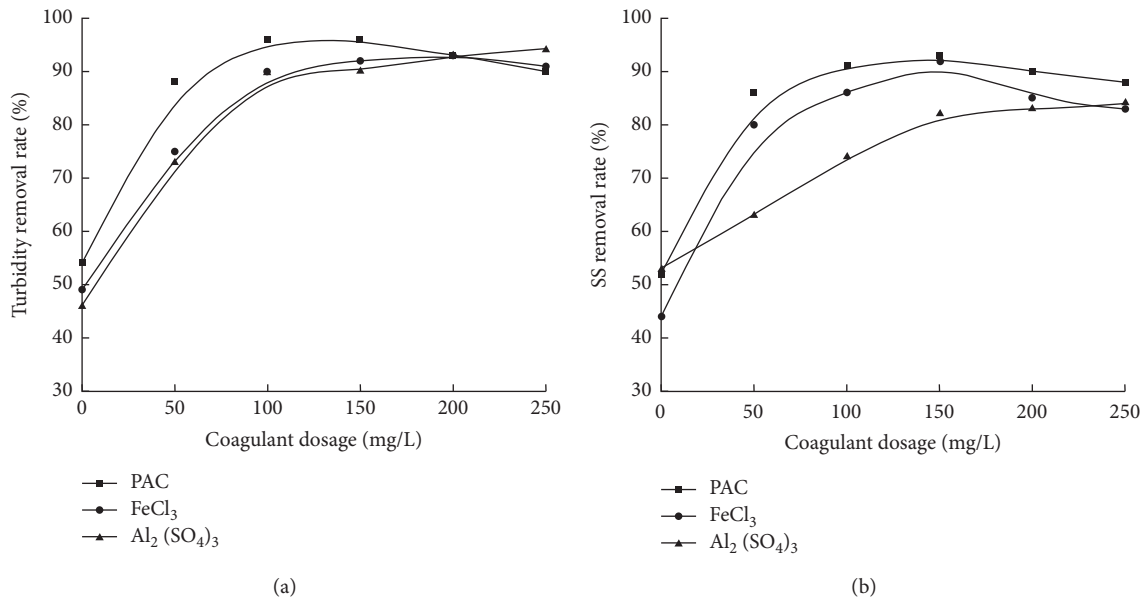
FIGURE 2: Influence of coagulant dosage on turbidity, SS removal rate. (a) Influence of coagulant dosage on turbidity removal. (b) Influence of coagulant dosage on SS.

improve the uniformity of the surface load. ④ In order to solve the problem that sludge cannot be discharged in time, which will affect the quality of the effluent, the sludge discharge system of the clarifier was renovated, and the sludge discharge time was timely, accurate, and good.

The improved clarifier is more adaptable to changes in water quantity and water quality, and the operating cost of treatment facilities is reduced to keep the effluent stable.

Problems with the traditional gravity valveless filter: the requirements for civil construction are increased; the "turning plate" in the filter plate of the water distribution system will affect the normal filtration; and the backwashing is frequent or does not automatically backwash for a long-time problem.

The improvement of the traditional gravity valveless filter: ① The transformation of the water inlet pipe can solve the problems caused by the abnormal rise of the water level, the uniformity of the water distribution in the filter chamber is improved, and the local surface filter material collapse caused by the impact of water flow is reduced. ② The steam-water separation device is installed on the U-shaped pipe, which can solve the problems of frequent backwashing. ③ Reform the setting method of the siphon auxiliary pipe to form a siphon backwash to reduce the loss of raw water.

The standard gravity valveless filter can basically meet all the requirements, but for different raw water quality and different purification processes, it is feasible to make some modifications to it.

3.6. High Salinity Mine Water. The pollutants of mine water with high salinity mainly include coal-based suspended solids, soluble total solids, sulfate, and chloride. The overall hardness is relatively high, and the content of pollutants exceeds the standard. The water quality of this mine water is very poor.

High-salinity mine water has three characteristics: The particle size of suspended particles is large in span, small in density, and unsuitable for settlement; the content of suspended matter is relatively unstable. The carbon molecules in the coal powder in mine water have organic reducibility, which causes the mine water to be contained. It will be removed along with the removal of suspended matter, so generally no biochemical treatment is required.

The direct discharge of mine water with high salinity will cause waste of water resources, soil salinization, and vegetation wilting, so desalination treatment is more necessary [14]. The purification treatment technology for the purpose of removing suspended solids and the advanced treatment technology for the purpose of desalination are used to realize the reuse of high-salinity mine water. The treatment process usually includes pretreatment and advanced desalination treatment.

Due to the high content of suspended matter, pulverized coal, and colloidal particles in mine water, it will gradually block the permeable membrane, reducing the permeation efficiency, and the service life of the membrane using co-agulation precipitation technology.

For the desalination of mine water, the current commonly used methods for desalination include chemical methods, membrane separation methods, and distillation methods.

3.6.1. Chemical Methods. The ion exchange method is the main method of chemical desalination. Anion and cation exchangers are used to remove ions in water to reduce the salt content of water. This method is more economical for water with salt content of less than 500 mg/L and can be used as a further desalination step after high-salinity mine water is treated by membrane separation. The demonstration of ion exchange principle is shown in Figure 3.
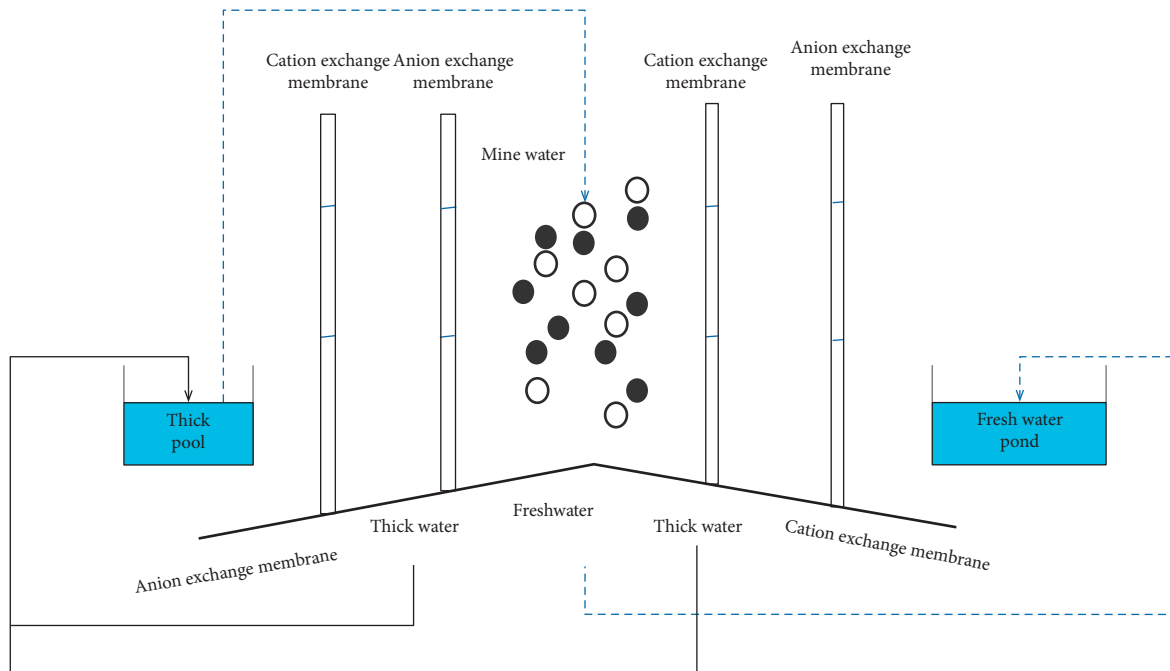
FIGURE 3: Schematic diagram of ion exchange.

3.6.2. Membrane Separation Method. Membrane separation method uses selective permeable membrane as the separation medium. When there is a certain driving force (such as pressure difference, concentration difference, potential difference) on both sides of the membrane, the solvent will be separated from the solute or particles. The most common techniques of membrane separation are reverse osmosis and electrodialysis.

The membrane separation method has the advantages of high efficiency, low energy consumption, simple device, wide application, and easy operation. Membrane water treatment has the characteristics of strong adaptability, small footprint, high efficiency, and simple and economical operation. However, the biggest disadvantage of membrane separation is membrane fouling. In order to prevent membrane fouling, the inlet water quality of these two technologies must meet strict requirements, so the inlet water must be pretreated. The general pretreatment process is coagulation, precipitation, filtration, adsorption, and disinfection.

① Reverse osmosis

Reverse osmosis RO technology was applied in foreign aerospace technology research in the 1950s and 1960s, and it was actually applied in China in the early 1980s. Reverse osmosis technology is a membrane separation technology powered by pressure difference. It can remove various impurities including ions, molecules, organic matter, colloids, bacteria, viruses, and other water. This new technology is suitable for water treatment with salt content more than 4000mg/L.

The basic process flow of reverse osmosis treatment is shown in Figure 4.

C. R. Wang has studied mine water in the Xuzhuang Coal Mine after pretreatment of de-suspension, and then through multimedia filtration and activated carbon filtration pretreatment process and reverse osmosis desalination treatment process to achieve high-salinity mine water reuse [15].

C. Tang has used magnetic separation and D-type filter technology to remove suspended solids, ultrafiltration equipment was used to further remove colloids and suspended solids, and reverse osmosis and nano-filtration equipment were used for desalination to achieve the mine water treatment effect [16].

② Electrodialysis

The process flow diagram of electrodialysis device is shown in Figure 5. The electrodialysis method ED refers to a method for separating water and impurities using electrical energy. There are two basic conditions for salt removal by electrodialysis: one is the chargeability of ions; the other is that the ion exchange membrane has selective permeability.

The electrodialysis desalination method does not require the addition of any chemical agents, the equipment is simple, and the assembly and operation are convenient. However, this technology also has some disadvantages in certain aspects, such as: high-water quality requirements; high power consumption, membrane surface is prone to fouling, and membrane life is short; the electrodialysis module is made of plastic material, which is easy to be aged, resulting in the increase of maintenance cost; the water quality and quantity of water in the electrodialysis process can affect the current and voltage during the operation. The
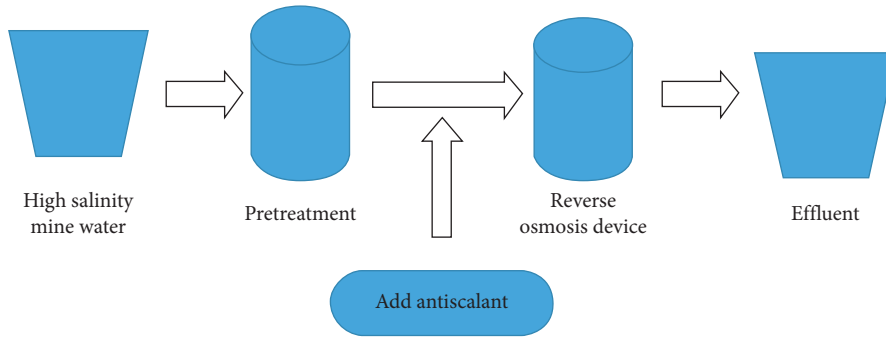
FIGURE 4: Reverse osmosis process.
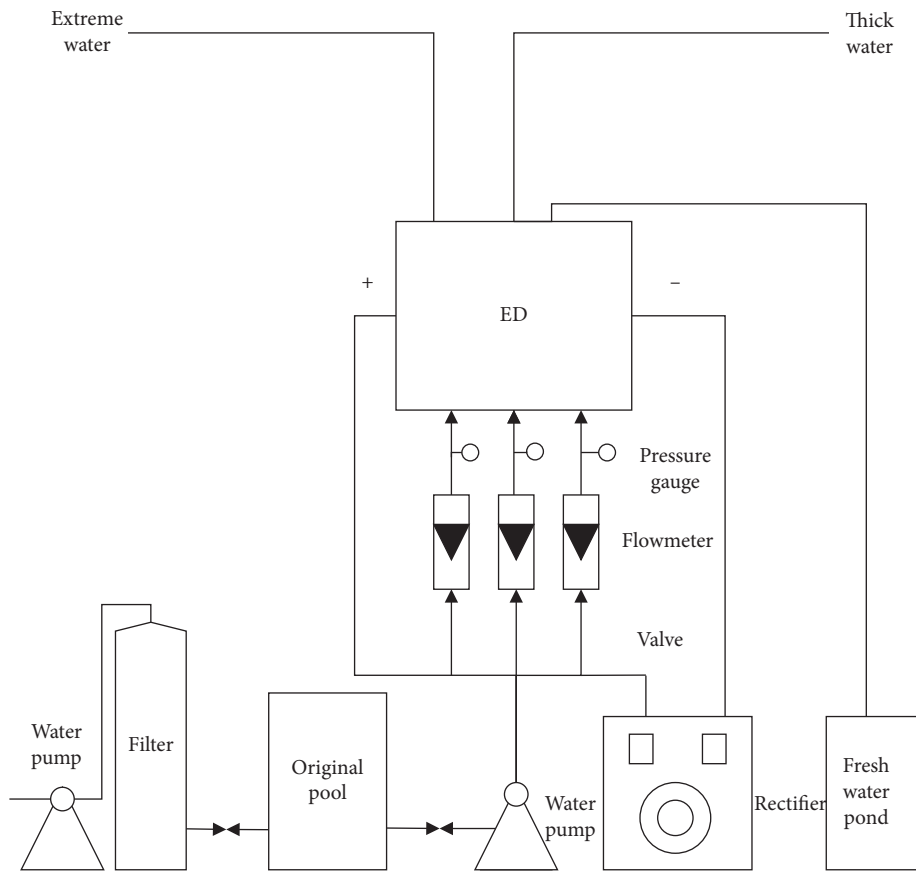
FIGURE 5: Process flow diagram of electrodialysis device.

desalination process is unstable and is prone to performance degradation.

Cui et al. jointly treated mine water through the coagulation-electrodialysis method, so that the treated mine water met the drinking water quality requirements. The best coagulant, the best voltage, and time of ion removal are determined, and the energy consumption is minimized [17].

③ Distillation

Distillation is an effective method of using thermal treatment of brine to achieve desalination [18]. The heat energy consumed by this method is very large, which is suitable for the treatment of mine water with a salt content exceeding 3000 mg/L.

Due to the high energy consumption of the distillation method, the popularization and application of this

method has also been hindered. But, it has its own unique advantages: it does not require any chemicals or ion separation membranes; the range of salt content in the treatment of mine water is very wide; the water quality of the incoming water is not high; this method produces distilled water and the rate of desalination is relatively high.

3.7. Acid Mine Water

3.7.1. Formation of Acid Mine Water. To analyze and process the acid mine water, we first need to understand the formation of coal mine acid water: in coal operations; the mining process will destroy the original reduction environment of the coal seam, and the pyrite in the coal seam and its surrounding rocks is oxidized to reduce under the action of oxygen. In the form of sulfides, groundwater is in contact with the top and bottom of the coal seam, which oxidizes the sulfides into sulfuric acid, which makes the water acidic. However, the formation of acid mine water is a complicated process, which is related to many factors, such as chemistry, physics and biology. The main reactions are as follows:

(1) First, pyrite ore reacts with mine water to generate sulfuric acid and ferrous sulfate.

$$2FeS_2 + 7O_2 + 2H_2O = 2FeSO_4 + 2H_2SO_4. \qquad (1)$$

(2) The ferrous sulfate continues to react to form ferric sulfate and other metal sulfates.

$$4FeS_2 + 15O_2 + 2H_2O = 2Fe_2(SO_4)_3 + 2H_2SO_4,$$
$$4FeSO_4 + 2H_2SO_4 + O_2 = 2Fe_2(SO_4)_3 + 2H_2O. \qquad (2)$$

The produced high-iron sulfate has the function of dissolving various sulfide minerals.

$$2Fe_2(SO_2)_3 + 2MS + 2H_2O + 3O_2$$
$$= 2MSO_4 + 4FeSO_4 + 2H_2SO_4. \qquad (3)$$
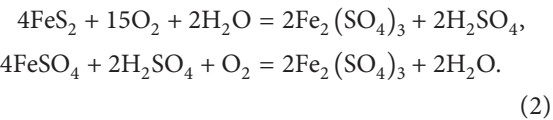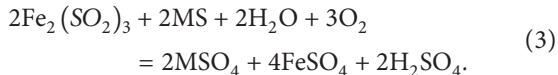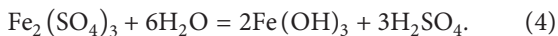
(3) Hydrolysis reaction. The high-speed sulfate produced in the second step will undergo a hydrolysis reaction when the pH value of the aqueous solution is greater than 3.5.

$$Fe_2(SO_4)_3 + 6H_2O = 2Fe(OH)_3 + 3H_2SO_4. \qquad (4)$$

(4) The role of microorganisms in the formation of acidic water in sulfide ores: Some research data indicate that microorganisms play a very important role in the oxidation process of sulfide ore deposits. Thiobacillus ferro oxidants can transform iron, zinc, copper, arsenic, and nickel Such sulfide minerals are oxidized to produce sulfuric acid and sulfate. For the typical mineral FeS_2 that produces acidic water, microorganisms play an extreme role in its oxidation process, making its natural oxidation rate slower [19].

3.7.2. Source and End Treatment of Acid Mine Water. For acid mine water, the treatment is mainly meant to control the water source, but in practical applications, the treatment effect is more affected by the outside world.

In the application of the mine environment, there are many difficulties in the control of the source, so the end treatment of acid mine water has been studied more extensively [20]. AMD source and end-processing technology is shown in Figures 6 and 7.

① Neutralization method: the neutralization method is the most widely used treatment technology for acid mine water. Neutralizing agents are added to acidic wastewater to increase the pH of the wastewater. Under alkaline conditions, metal ions generate hydroxide precipitates and are removed from the wastewater. Commonly used neutralizing agents are lime, limestone, sodium carbonate, sodium hydroxide, etc.

Ding and Ding have used the limestone-lime milk, two-stage neutralization method to treat mine acid wastewater. In Suichang Gold Mine, the amount of sediment produced by this method is only one third of that produced by lime milk neutralization method, which reduces the overall processing cost [21].

② Anoxic limestone ditch: anoxic limestone ditch is a process in which acid mine water flows through the limestone gully to dissolve limestone continuously, thereby generating alkalinity. Therefore, the method is particularly economical and has been widely used abroad [22]. ALDs are very effective for the neutralization of acidic water; when using this method, combined with other passive methods, it can greatly improve the efficiency of wastewater treatment and reduce the area of the treatment facility.

Genty et al. have used batch reaction and reaction column methods to study ALDs. The results show that the smaller the particle size, the higher the alkali production capacity, but ALDs are not suitable for the treatment of high-concentration acid mine wastewater [23].

③ Permeable reaction wall: the principle of permeable reaction wall combined with microbial remediation is used for acid mine water treatment [24]. The permeable reaction wall is obtained by digging a ditch in the direction of mine water flow and filling the ditch with active materials (such as organic solid mixture, limestone, or gravel). In the reaction wall, reducing microorganisms produce alkalinity after growing, and at the same time, the alkalinity generated by the dissolution acts on the wastewater together, removing metal ions as hydroxides, sulfates.

④ Constructed wetland: the wetland system is very distinctive and unique. It contains the soil and substrate of the wetland, unique hydrological conditions, and wetland organisms [25]. Among them, the soil-plants first intercept the suspended matter in the acid mine water by adsorption and filtration. The metal ions
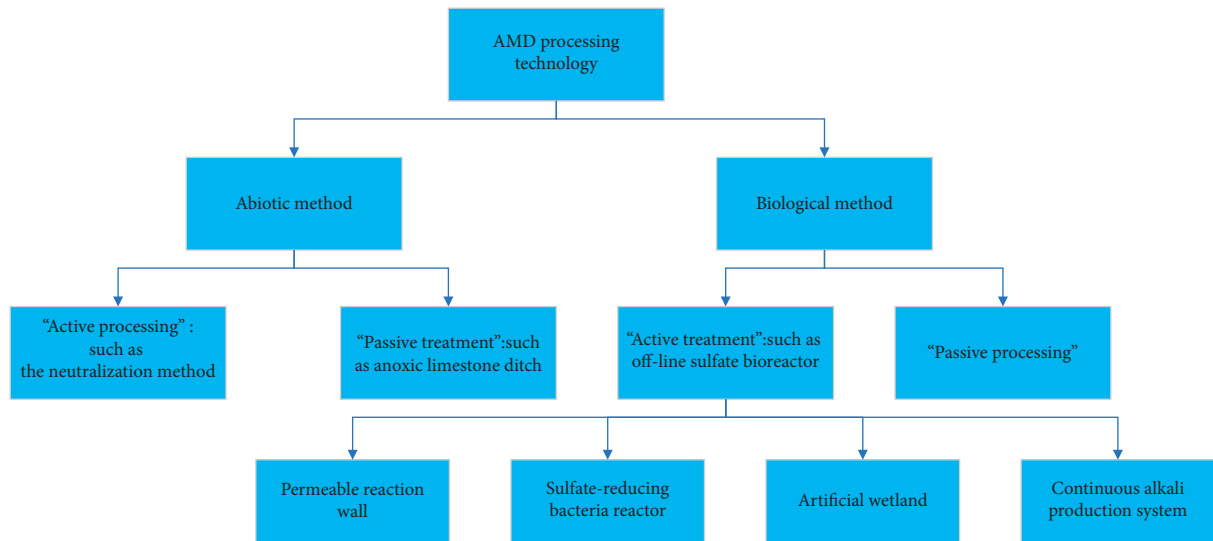
FIGURE 6: AMD processing technology.
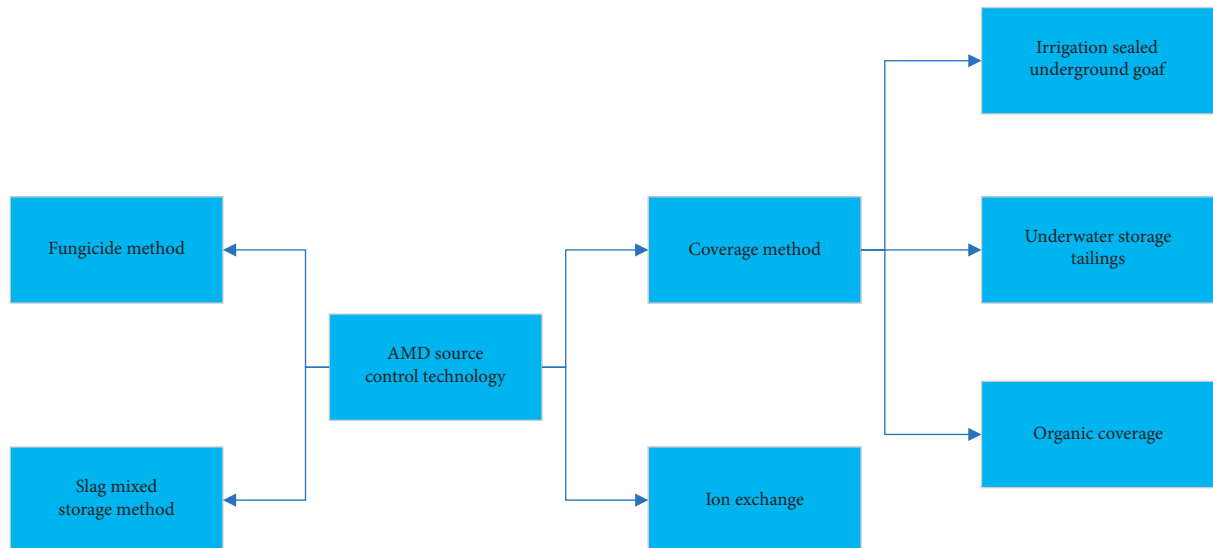
FIGURE 7: AMD source control technology.

deposited in the wetland system are removed from the water by ion exchange, oxidation, hydrolysis, and microbial action.

Constructed wetland is a new type of ecological sewage treatment technology, which has the characteristics of low investment, low energy consumption, simple operation and maintenance, and high treatment efficiency [26].

⑤ Sulfate-reducing bacteria reactor (SRB): SRB is an emerging acid mine water biological treatment technology. In this technology, in a sufficient environment, organic matter acts as an electron donor for SRB, and as an electron acceptor, oxidizes the organic matter, and obtains the energy required for life through the alienation of the organic matter, while reducing it.

Sanchez has used domestic sewage as an SRB carbon source to mix with acid mine water for treatment [27]. Liu has made a pilot-scale UASB sulfate-reducing bacteria bioreactor at the Zijinshan Copper Mine to treat mine wastewater. The project includes a two-stage sedimentation tank and a UASB reactor. The carbon source comes from activated sludge after sewage treatment [28].

⑥ Continuous alkali production system: the continuous alkali production system can continuously produce alkalinity during the flow of acid mine water. Because the process is in an anaerobic environment, it will not produce hydroxide precipitation on the limestone surface and affect the alkali production process. It combines the characteristics of anaerobic constructed wetland method, sulfate-reducing bacteria

method, and anoxic limestone ditch method, and also solves the defects of these methods when used alone.

Chen and others have used calcined carbonate rock in the continuous alkali production system, which failed to demonstrate the superiority of the shake flask experiment. The acid mine water treatment capacity was only slightly higher than that of the original rock. The complete set of treatment technology based on the continuous alkali production system can remove the sulfate and metal ions in acid mine water, step by step. It has a stable and lasting treatment effect. It is suitable for changing water quality conditions and can be constructed in the field.

3.8. Specially Contaminated Mine Water. Mine water with special pollutants refers to mine water with fluoride and heavy metal toxic substances. Such mine water is more polluted and difficult to handle. Arbitrary discharge will destroy the ecological environment and affect the utilization of mine water resources.

3.8.1. Fluoride-Containing Mine Water. China's Hebei, Henan, Shaanxi, Gansu, Qinghai, Xinjiang, and other places are high-fluorine areas. If the fluorine-containing water in the mining area is discharged without treatment, human and livestock drinking this high-fluorine water for a long time will cause chronic poisoning. Osteoporosis in mild cases, convulsions and cramps in severe cases, and even death from respiratory paralysis can also cause various skin diseases.

When groundwater flows through a mine rich in fluorine, after years of physical and chemical action, the solid state of the fluorine mountain migrates into the mine water, resulting in high fluoride in the coal mine water [29].

Because fluoride is a toxicological index, the water quality of the effluent is relatively strict. Commonly used defluorination processes include electrodialysis, ion exchange, chemical precipitation, etc.

(1) Electrodialysis method: this method relies on F- in aqueous solution under the action of an external electric field, through an ion-exchange membrane with selective permeability, so that F- that migrates together with mineral ions in aqueous solution to concentrated water was removed. The main advantage of this method is its simple operation. The disadvantages are as follows: ① while removing F-, the minerals that are beneficial to the human body in the water are removed, making the treated water often not suitable for direct drinking; ② when the fluorine content is higher than 3 mg/L, it is difficult to remove F- at one time to meet drinking water standards; ③ equipment investment is large, not suitable for large-scale water treatment projects; ④ water yield is low, generally only 50%, and water resources are wasted; ⑤ equipment management is complicated and cost is high. In view of the above reasons, the F- method of electrodialysis is rarely used in actual water treatment projects.

(2) Ion exchange method: this method relies on the ion-exchanger and F-adsorption exchange function in water to facilitate the removal of insoluble fluorides. This method, especially represented by activated alumina, is currently widely used in small domestic F-removal devices. The main advantage of this method is that the treated water meets the standard once, without changing the mineral composition of the water. The problems are as follows: ① large one-time investment and high water treatment cost; ② inorganic ion exchanger declines rapidly, and the exchange capacity is significantly reduced; ③ inorganic ion exchanger needs to be regenerated repeatedly, and the operation is troublesome.

(3) Chemical precipitation method: It is to add a certain amount of cation and F- into the aqueous solution to form an insoluble electrolyte, which produces a precipitate and is separated from water to remove F-. This method is mainly used in the treatment of some industrial wastewater with high content of F- (20–4000 mg/l). Because the solubility of CaF_2 is 16 mg/L, even if an excessive amount of Ca^{2+} is added, the residual amount of F- in its aqueous solution is difficult to be lower than 8 mg/L, so this method is not suitable for drinking water treatment with low F-.

3.8.2. Heavy Metal Pollution Mine Water. At present, the development and mining activities of mineral resources containing heavy metals have increased sharply, which has led to the production of large amounts of heavy metal wastewater in nonferrous metal mine mining and beneficiation operations, causing serious environmental pollution problems. Most nonferrous metal mines contain sulfur or symbiotic sulfides, such as pyrite, chalcopyrite, and other minerals. The sulfide in nature undergoes the comprehensive reaction of oxidation, weathering, decomposition, and water-gas-acid-mineral reaction, and can form acidic wastewater unique to mines. Most metal sulfide beds contain iron sulfide ore. The process of formation of acidic wastewater in mines is the oxidation of iron sulfide. The formation of acidic wastewater containing multiple metal ions is caused by the further reaction of sulfuric acid, ferric sulfate, etc., formed by the oxidation of iron sulfide with ores containing various metal ions.

Under the action of water and air, sulfide minerals react to form sulfuric acid, which eventually generates mine acidic heavy metal wastewater containing iron and other metal ions [30]. Because most nonferrous metals and ores contain associated elements, and the heavy metal components contained in the wastewater of nonferrous metal mines are relatively complex, elements such as mercury, arsenic, lead, cadmium, copper, zinc, and chromium are often present in general wastewater. Heavy metal ions are difficult to be degraded by microorganisms and are persistent toxic pollutants. Under the action of microorganisms, some heavy metals can even be converted into more toxic substances, such as metal-organic compounds, which not only affects the growth and production of animals and plants but also enters

the human body through bioaccumulation and bio-magnification of the food chain in the living body and may eventually damage human health.

Current status of heavy metal wastewater treatment: at present, there are a variety of treatment technologies for heavy metal wastewater, but there are three main types of methods for the treatment of heavy metal ion-containing wastewater. Heavy metal ions are precipitated and removed, mainly including neutralization precipitation method, sulfide precipitation method, ferrite precipitation method, etc.; the second type is the physical chemical method, that is, without changing the chemical conditions of heavy metal ions, by using physical separation to remove heavy metal ions in wastewater, there are mainly ion exchange method, adsorption method, and membrane separation method; the third type is to use the biological method to remove heavy metal ions in wastewater, the biological method is to use microorganisms and certain aquatic plants to absorb heavy metal ions in water. The heavy metal ions are adsorbed and fixed, and gradually accumulated to increase the amount of adsorption to remove heavy metals from wastewater. The main methods include the biological adsorption method and constructed wetland method.

The above method has a good treatment effect for heavy metal ion wastewater with conventional content, but it does not mean that all are suitable for treating low-concentration heavy metal ion wastewater. Regarding the water quality characteristics of nonferrous metal mining well water with low BOD, low pH, and the coexistence of lead, cadmium, and arsenic, the content of heavy metals required for advanced treatment in heavy metal wastewater is relatively low. Therefore, it is very important to study effective methods for treating low-concentration heavy metal wastewater.

H. Zhao and F.Q. Li have used the chitosan complex-ultrafiltration coupling process to treat heavy-metal-simulated wastewater in nonferrous metal mines. The main removal materials were lead ions and cadmium ions. The pH value, mass ratio, ionic strength, and other factors were investigated for the retention of heavy metal ions The effect of the rate and membrane flux verified the effect of recovering chitosan after acidification-decomplexation [30].

Z. Huang and J.P. Xu have domesticated the tolerance of SRB heavy metals, and optimized the process conditions of SRB system, Fe-C system, and SRB/Fe-C system for processing heavy metal ions, combined with permeable reaction bed (PRB) Structural design; the effect and influencing factors of in-situ treatment of heavy metal ions in acid mine water were studied [31].

J.X. Chen has introduced the separation mechanism and simple process technology of ion exchange resin and its research and application in the treatment of heavy metal wastewater, and introduced the research and development and research results of the use of ion exchange resin to treat heavy metal wastewater in recent years [32].

3.9. New Technology

3.9.1. The Medium Membrane Ultrafiltration Membrane Product Was Successfully Applied to the National Energy Group's Large-Scale Mine Dewatering and Reuse Project. In this project, in the face of the water treated by the coagulation plus heavy medium speed sink and V filter process, Beijing Zhonghuan Membrane Material Technology Co., Ltd. (referred to as: Central Ring Film) of the Botian Environmental Group uses thermal ultrafiltration membrane products, using the ultrafiltration plus reverse osmosis process to build a mine water reuse project with a scale of 30,000 tons per day in two phases, while achieving environmental protection standards, reducing the water consumption rate of industrial output value of enterprises, and creating an economy for enterprises benefit. The application system of mid-ring membrane thermal ultrafiltration membrane is shown in Figure 8.

According to reports, Botian Environment and user units have fully demonstrated in the early stage of the project, and have made careful considerations and project management from design, process, and parameter selection, equipment matching, installation implementation, and commissioning operation, and finally realized the ultrafiltration membrane. The operation of the device and the whole system is stable, ensuring that the overall water reuse rate index and the outflow index of the system meet the requirements, realizing the dewatering and reuse of the mine.

The project is expected to reduce nearly 8.5 million tons of annual emissions, and the treated water can be effectively used in industrial production and other purposes in general. The project will reduce the environmental cost of customers and promote the sustainable use of water resources.

Membrane products have been successfully applied in hundreds of cases in more than 20 industries around the world. With innovative technology and adherence to the quality of the ingenuity, the Central Membrane is bound to turn the project into another benchmark project in the field of deep reuse of mine water.

3.9.2. Harbin 0.5–50 m³/h Production Wastewater Treatment Project. Biochemical Oxygen Demand (BOD) is the amount of dissolved oxygen consumed by the biochemical processes performed by microorganisms in decomposing certain oxidizable substances in water, especially organic substances, under specified conditions. The larger the BOD value, the more pollutants in the water, and the more serious the pollution. BOD is an environmental monitoring method, suitable for monitoring water pollution.

The adjustment tank of Harbin 0.5–50 m³/h sewage treatment adopts the aeration method to balance water quality and water volume, avoiding the precipitation caused

FIGURE 8: Mid-ring membrane thermal ultrafiltration membrane.

by aeration and stirring. An anaerobic tank is installed after the adjustment tank, and the aerobic treatment adopts a two-stage biological contact oxidation process. Sewage treatment process is an urban sewage treatment process developed on the basis of traditional technology.

The structure includes a tank, filler, water distribution device, and aeration device. The working principle is that the filler is installed in the aeration tank and used as the carrier of the biofilm. After aeration, the wastewater to be treated flows through the filler at a certain flow rate. After the completion of the packing, contact with the biofilm and work together. Anaerobic biological treatment is a method of using facultative anaerobes and specific anaerobes to degrade macromolecular inorganic substances into low-molecular compounds, and then convert them into methane and carbon dioxide, to treat inorganic wastewater. It can be divided into acid digestion. Two stages and alkaline digestion: In the acid digestion stage, exogenous enzymes secreted by acid-producing bacteria convert macromolecular inorganic substances into complex inorganic acids and alcohols, aldehydes, ammonia, carbon dioxide, etc. In the alkaline digestion stage, the metabolites of acid digestion are further broken down into methane, carbon dioxide, and other biological gases.

The advantages of this method are as follows: ① It can reduce the floor space, the parking lot can be built above the equipment, and there is no need to build facilities. ② There is no impact on the surrounding environment, the amount of sludge generated is small, and the noise is less than the standard of the second category. ③ It is easy to operate, new technology, good effect, and long service life. ④ Equipment can be arranged according to the standard, or it can be specially arranged according to the terrain.

3.9.3. *Water Retention Coal Mining.* Water retaining coal mining is a kind of coal mining technology which can keep aquifer structure stable or water level change in a reasonable range by controlling rock movement in arid or semi-arid areas. It is a new coal mining technology to seek the optimal solution between coal mining capacity and water resources carrying capacity.

The premise of coal mining and water conservation is that there is water and coal, and they needs to be protected. If there is coal, it is possible to collect it. Water conservation

under coal mining conditions is to protect the environment and protect the ecology.

In the northern part of Shanxi, there are two ways to achieve coal mining and water conservation. One is to rationally select the mining area (mainly in the planning stage of the mining area) and the second is to adopt reasonable coal-mining methods and engineering measures (such as filling mining).

4. Conclusion and Outlook

China is a large mineral resource country. The exploitation and utilization of mineral resources is very important, and the treatment of mine water is vital to the overall environment. In general, the most widespread mineral water pollution is acid mine water, and the most serious pollution is heavy metal mine water. For different mine waters, it is necessary to adopt a relatively appropriate method. Each treatment technology has its advantages, characteristics, and deficiencies. It is necessary to select the correct process according to the specific conditions to ensure reasonable technology and economical energy conservation.

There are new technologies, such as "high-efficiency clarification plus gravity-type valveless filter," for mine water containing suspended solids. For high-salinity mine water, reverse osmosis has been applied more highly. For acid mine water, the most widely used method is the limestone trench method, and there are also many emerging treatment technologies, such as sulfate reduction bacteria reactor. The treatment method of fluoride-containing mine water widely used in China is the ion exchange method, and for heavy metal mine water, the precipitation method is widely used due to its mature technology. The treated mine water can reduce the malignant impact of the direct discharge of mine water on the whole environment, and can also reuse the wastewater to improve the water shortage in the mining area after production.

The impact of mine water on the environment has become a hot issue globally. The formation, prediction, and control of mine water pollution types and the development of new technologies are not only the challenges faced by environmental disciplines in various countries but also the important problems that must be solved for the sustainable development of national economy and society.

Data Availability

The data used to support the findings of this study are included within the article.

Conflicts of Interest

The authors declare that they have no conflicts of interest regarding the publication of this paper.

Acknowledgments

References

[1] F. Liu, W. J. Cao, J. J. Zhang et al., "Current technological innovation and development direction of the 14 th Five Year Plan period in China coal industry," *Journal of China Coal Society*, vol. 46, no. 1, pp. 1–15, 2021.

[2] J. F. Lou, H. P. Kang, F. Q. Gao et al., "Determination of large-height support resistance based on multi-factor analysis," *Journal of China Coal Society*, vol. 42, no. 11, pp. 2808–2816, 2017.

[3] J. F. Lou, F. Q. Gao, J. H. Yang et al., "Characteristics of evolution of mining-induced stress field in the longwall panel: insights from physical modeling," in *International Journal of Coal Science & Technology*, Springer, Berlin, Germany, 2021.

[4] W. Suo, *Discussion on the Status Quo and Treatment Technology of Mine Water*, China Agricultural University, Beijing, China, 2015.

[5] Y. B. Zhang, "Application of magnetic separation water treatment technology in western waterrich mines," *Journal of Mining and Safety Engineering*, vol. 30, no. 2, pp. 371–373, 2013.

[6] Z. Yuan, *Research on Water Resources Environmental Safety Assessment System in Northern Shaanxi Mining Area*, Xi'an University of Science and Technology, Xi'an, China, 2010.

[7] Z. Miao, "Hydrogeological characteristics and water damage prevention in coal mine goaf," *Chinese Science and Technology Periodical Database Engineering Technology*, vol. 12, no. 4, p. 231, 2017.

[8] J. Liu, *Study on Environmental Impact and Coal Mine Wastewater Resource Utilization in Coal Mining in Western District of Linshui County*, Chengdu University of Technology, Chengdu, China, 2007.

[9] W. F. Wan, *Research on Mine Water Resources in Binchang Mining Area and Optimized Site Selection of Water Purification Plant in Hangkou Power Station*, Chang'an University, Xi'an, China, 2006.

[10] W. Jia and D. Y. Li, "Study on the treatment technology of dewatering water in open pit coal mine," *Opencast Mining Technology*, vol. 42, no. 3, pp. 42–46, 2012.

[11] L. Zhao, *Application of "High Efficiency Clarification + Gravity Valveless Filter" in Mine Wastewater Treatment*, Tianjin University, Tianjin, China, 2012.

[12] Y. L. Jia, *Research on Key Technology Application of High Suspended Matter and High Salinity Mine Water Resources*, Hebei University of Engineering, Handan, China, 2015.

[13] Q. Wu, Z. Q. Wang, S. Y. Ye et al., "Experimental study on coagulation-microfiltration membrane separation technology in mine water treatment and reuse," *Journal of China Coal Society*, vol. 29, no. 5, pp. 581–584, 2004.

[14] D. W. Zhai and G. R. Ge, "New technology for energy saving desalination of high salinity mine water," *Coal Science and Technology*, vol. 46, no. 9, pp. 12–18, 2018.

[15] C. R. Wang, "High-mineralization mine water treatment technology and engineering practice in Xuzhuang Coal Mine," *Energy Environmental Protection*, vol. 36, no. 2, pp. 36-37, 2014.

[16] C. Tang and J. Wang, "Engineering practice of high salinity mine water treatment and utilization," *Inner Mongolia Coal Economy*, vol. 5, pp. 58-59, 2019.

[17] L. Cui and R. F. Qiu, "Study on the treatment of high salinity mine water by coagulation-electrodialysis," *Journal of Shanxi University*, vol. 33, no. 4, pp. 591–595, 2010.

[18] H. Xu and Y. Wang, "Formation and main treatment technology of acid mine water in coal mines," *Environmental Science and Management*, vol. 33, no. 9, pp. 100–102, 2008.

[19] L. B. Liu, *Study on Pollution Characteristics and Chemical Control Methods of Acid Drainage in Guizhou Coal Mining Area*, Guizhou University, Guiyang, China, 2009.

[20] Y. Chen, *Method Construction and Stability Study of Acid Alkali Wastewater Treatment by Continuous Alkali Production System*, Guizhou University, Guiyang, China, 2015.

[21] C. S. Ding, "Treatment of mine acid wastewater by limestone-lime milk second-stage neutralization method," *Energy Environmental Protection*, vol. 18, no. 2, pp. 27–29, 2004.

[22] R. R. Zhang, "Treatment of acid mine water by anoxic limestone ditch method," *Coal Mine Environmental Protection*, vol. 12, no. 1, pp. 38-39, 1998.

[23] T. Genty, B. Bussière, R. Potvin, M. Benzaazoua, and G. J. Zagury, "Dissolution of calcitic marble and dolomitic rock in high iron concentrated acid mine drainage: application to anoxic limestone drains," *Environmental Earth Sciences*, vol. 66, no. 8, pp. 2387–2401, 2012.

[24] J. P. Xu and H. J. Wan, "Study on treatment of acid mine wastewater by using activated carbon," *Water Treatment Technology*, vol. 40, no. 3, pp. 57–63, 2014.

[25] L. Dou, "Study on treatment mechanism of heavy metal constructed wetland in acid mine water," *Environmental Science and Technology*, vol. 29, no. 11, pp. 109–111, 2006.

[26] A. G. Qin, "Study on the effect of outlet location on the denitrification effect of combined subsurface flow constructed wetland," *Guangxi Light Industry*, vol. 12, no. 133, pp. 90–92, 2009.

[27] I. Sánchez-Andrea, D. Triana, and J. L. Sanz, "Bioremediation of acid mine drainage coupled with domestic wastewater treatment," *Water Science and Technology*, vol. 66, no. 11, pp. 2425–2431, 2012.

[28] X. Y. Liu, G. Zou, X. Q. Wang et al., "A novel low pH sulfidogenic bioreactor using activated sludge as carbon source to treat acid mine drainage (AMD) and recovery metal sulfides: pilot scale study," *Minerals Engineering*, vol. 48, pp. 51–55, 2013.

[29] Q. S. Zhu and G. Q. Xu, "Current status and research progress of fluorine pollution in groundwater in China," *Environmental Science and Management*, vol. 34, no. 1, pp. 42–44, 2009.

[30] H. Zhao, *Research on Advanced Treatment of Heavy Metal Wastewater in Non-ferrous Metal Mine by Complexation-Ultrafiltration Coupling Process*, Hebei University of Engineering, Handan, China, 2014.

[31] Z. Huang, *Study on In-Situ Treatment of Heavy Metal Ions in Acid Mine Water by Osmotic Reaction Bed Immobilized Sulfate-Reducing Bacteria and Fe-C*, Anhui University of Engineering, Hefei, China, 2013.

[32] J. X. Chen and H. H. Li, "Research progress in treatment of heavy metal wastewater by ion exchange resin," *Guangzhou Chemical Industry*, vol. 41, no. 9, pp. 44-45, 2013.

Research Article

Erosion Control Treatment Using Geocell and Wheat Straw for Slope Protection

Xiaoruan Song ⓘ,[1] **Miansong Huang** ⓘ,[2] **Shiqin He** ⓘ,[1] **Gaofeng Song** ⓘ,[1] **Ruozhu Shen** ⓘ,[3] **Pengzhi Huang** ⓘ,[1] **and Guanfang Zhang** ⓘ[1]

[1]*School of Civil Engineering, North China University of Technology, Beijing 100144, China*
[2]*Ningxia Capital Sponge City Construction & Development CO., Ltd., Guyuan 756000, Ningxia, China*
[3]*Beijing Capital Co. Ltd., Beijing 100044, China*

Correspondence should be addressed to Miansong Huang; hms@capitalwater.cn and Gaofeng Song; song.gaofeng@ncut.edu.cn

Slope failure triggered by soil erosion under rainfall remains one of the most difficult problems in geotechnical engineering. Slope protection with planting vegetation can be used to reinforce the soil and stabilize the slope, but the early collapse of the planting soil before the complete growth of plants becomes a major issue for this method. This paper has proposed a composite soil treatment and slope protection method using the geocell structures and the wheat straw reinforcement. The geocell structures improve the stability of the planting soil and provide a stable and fixed environment for the vegetation, while the wheat straw reinforces the soil and also increases the fertility. The authors have performed a total of 9 experiments in this work that are classified into three groups, i.e., the unsupported slopes, the geocell reinforced, and the geocell and wheat straw composite reinforced with a consideration of three different rainfall intensities. The progressive slope failure development during the rainfall was assessed, as well as the soil erosion, the slope displacement, and the water content. The results show that the slope failure increases as the rainfall continues, and the soil degradation increases with the intensity of rainfall. The soil treatment using geocell improves the slope stability, but the geocell and wheat straw composite reinforcement has the best erosion control and slope protection.

1. Introduction

Shallow slope failure refers to a superficial removal of vegetation cover and topsoil, which is a common problem typically observed in areas of hilly or mountainous terrain, engineered road, and embankments. The shallow slope failure can be addressed as the shallow landslide and shallow soil erosion. Shallow landslide occurs when the forces acting on the downslope exceed the mechanical resistance of the slope, while erosion may occur under rainfall when the rain water dislodges soil particles and carries them off a lope, forming rills and gullies that may eventually trigger landslides. Shallow slope failure is a worldwide serious geologic hazard and causes severe adverse impacts on both natural environment and human properties. Slope protection with planting vegetation is commonly used for improving the

slope stability from hydrological and mechanical aspects, such as removing water from the soil, increasing the cohesion of the soil, and anchoring the weak soil to the stable soil and the surface-mat effect. The geocell structure combining with the planting vegetation for soil reinforcement and erosion control is a new type of slope protection and ecological restoration. The cellular shade geocell structures can fix the planting soil (local soil deployed to the bare soil of the original slope for seeding) onto the slope, which offers a stable and suitable fostering environment for the plant growth. This erosion control method provides a protective layer for the slope, so that the negative impact of the rainfall does not reach the slope surface directly, while the roots of the fully grown plants on the protective layer reach down beyond the protective layer and further stabilize the slope. Other advantages such as a short construction period and

low maintenance charges can also be identified for this environmentally-friendly and ecologically-friendly method of slope protection [1–4]. The disadvantage, on the other hand, is that the soil for planting vegetation on the surface of the slope may collapse before the plants start to stabilize the slope at fully grown. The collapse of the planting soil occurs especially at the early stage of construction under a heavy rainfall. The failure of the soil reinforcement re-exposes the original slope to the rainfall, which increases the risk of landslide. Hence, the early stability of the geocell-reinforced soil with planting vegetation is the major concern for the engineers.

This paper has proposed a composite soil treatment method for slope protection using the geocell structures and the wheat straw. The geocells are buried into the planting soil, and the wheat straw is mixed with the soil for reinforcement at the shallow depth. The advantages for the composite treatment are listed as follows: (1) the straw-reinforced soil presents larger cohesion and internal angles than the original untreated soil; the shear strength is therefore enhanced with better performance against the rainfall erosion; (2) since the shallow soil at the top layer of the slope is reinforced with the wheat straw, the permeability of the soil is reduced with less pores existed, which slows down the penetration of rain water and improves the slope stability; (3) by mixing the straw with the soil, the weight of straw gradually decreases as microorganisms grow and break down the straw. The decomposition of the wheat straw increases the fertility by providing nitrogen or other nutrients in soil and fosters the growth of vegetation planting on the slope. The root system of the plants in return reinforces the geocell-reinforced soil, which further improves the slope stability.

2. Pertinent Literature Review

A number of studies on the geocell-reinforced slopes have been performed to study the design, construction, and mechanism of geocell reinforcement. Yang and Wang proposed a construction technique for reinforcement of slopes with small inclination using geocells, which was applied to the loess slope in northwest China [5]. Yan et al. performed experiments on the reinforcement of different geocells to the loess slopes and compared the reinforcement mechanism and erosion control of the geocell structures [6]. Rosen recognized the positive impacts of the geocells on stabilizing the slopes [7]. Sato and Kojma utilized the geocells and soil nailing in the embankment reinforcement to protect the slopes from the frequent heavy rainfall and earthquake [8]. Arvin et al. investigated the 3D slope stability reinforced by the geocells using strength reduction method, with a consideration of the interaction of geocells to the filling soils [9]. Wesseloo et al. performed the uniaxial compressive experiment to the geocells with different sizes and revealed the positive relationship between the strength of geocell-soil structure and the geocell size [10]. Latha et al. compared the influence of geocell tensile stiffness, size, and filling materials to the road embankment reinforcement in the laboratory and concluded that the reinforced geocells

improve the loading bearing capacity of the embankment with reduced deformation [11].

The reinforcement of soil using the wheat straw has long been recognized in China. The application of wheat straw reinforced soil is widely found in construction of soil walls, soil houses, and embankment [12]. This is because the tensile strength of the straw and its coupling with the soil improves the shear strength. Therefore, some researchers have performed studies on the properties of the wheat straw reinforced soil. Löbmann et al. believed that the herbaceous vegetation is faster than the lignose in changing and improving the soil environment [13]. Bouhicha et al. verified from laboratory tests that the wheat straw reinforcement reduces the shrinkage of the soil and that the stabilization of the soil is quicker with better strength [14]. Ashour et al. found that the straw treatment improves the strength and ductility of the reinforced soil [15]. Zhang et al. proposed a rice straw reinforcement method for erosion control and slope protection [16]. Su et al. discussed the influence of the interaction of roots with the soil and its impact to the root-soil mechanical properties [17]. Dias et al. considered the root penetrated soil as a composite material. An equivalent cohesion was proposed to the Mohr-Column equation [18]. Hao et al. performed the triaxial shear experiment on the soil at different reinforcement lengths and ratios [19]. The microstructures of the reinforced soil and the original soil under loading were scanned by CT. The results show that the wheat straw reinforcement improves the shear strength and the resistance to deformation.

Researchers have been mostly focused on the geocell-reinforced slope or the slope protection with planting vegetation independently. However, the erosion control using the composite geocell and vegetation reinforcement has not been seen in previous works. The early stability of the planting vegetation is also widely ignored. This paper attempts to study stability of the geocell and wheat straw reinforced slope under different rainfall conditions. The paper has four main goals: (1) develop a number of physical models with no reinforcement, geocell reinforcement, and the geocell and wheat straw composite reinforcement; (2) simulate the artificial rainfall at different rainfall intensities to the physical slopes; (3) obtain progressive development of slope failures at different reinforcement and rainfall intensities; and (4) assess the impacts of the reinforcement and rainfall intensity by analysing the soil erosion, slope displacement, and water content.

3. Model Development

3.1. Experimental Design. In this work, the authors have developed 9 modelling tests in 3 groups with a consideration of the geocell reinforcement to the slope soil, the wheat straw reinforcement, and the rainfall intensity. The slope ratio (rise/run) is determined as 1 : 1.5 for all the models, which is commonly seen in the studied site, Yinchuan, Ningxia province. In Group A, the slopes are unsupported and constructed using the common planting soil from Yinchuan city. The slopes in Group B are reinforced with the geocell structure with a dimension of $370 \times 370 \times 150\,\text{mm}$

(length × width × height). In Group C, however, the slope soil is reinforced with the geocell and wheat straw. Table 1 lists the total of 9 models developed in this paper.

The rainfall intensity is calculated from equation (1) that has been developed for the Yinchuan city [20, 21]:

$$q = \frac{242 \cdot (1 + 0.83 \lg P)}{t^{0.477}},\qquad(1)$$

where q is the rainstorm intensity in L/(s·ha), (L for litre, s for second, and ha for hectare); P is the time of duration for the occurrence of a rainstorm in a; and t is the duration of the rainfall in min. Based on the rainfall statistics on the studied site, the time of duration for the occurrence of a rainstorm is selected as 10 a, and the time of duration of a rainfall is 5 minutes. From equation (1), the rainfall intensity on the studied site in Yinchuan is calculated as 75 mm/h.

The rainfall intensity in the experiment is based on the calculated average value from the studied site. For comparison, another two rainfall intensities of 50 mm/h and 100 mm/h are selected to study the influence of rainfall on the stability of slopes (Table 1). Since the soil erosion of slopes in the field is a result of rainfalls for years, the duration of rainfall in the experiment is determined as 30 minutes.

3.2. Model Preparation

3.2.1. Materials and Modelling Rig.
The physical material in this study for constructing the slopes is the planting soil extracted from the studied site (Figure 1(a)). The water content and the maximum dry density is 12% and 1.7 g/cm³, respectively. The geocells are selected to reinforce and stabilize the slope soil in Groups B and C. The geocell is 370 mm in length and width and 150 mm in height, with a thickness of 1.2 mm (Figure 1(b)). The top 10 cm layer of the constructed slopes in Group C is also reinforced with the wheat straw. The wheat straw is selected from the current year and shows good resilience. The straw is 4–5 mm in diameter and cut to a length of 3–5 cm (Figure 1(c)). The wet planting soil and the wheat straw is fully mixed before construction of the model (Figure 1(d)), and the reinforcement ratio of the slope soil after the straw treatment is 0.5% in terms of weight.

The physical models are simulated by filling soil to a modelling rig with adjustable angles [22, 23]. Figure 2 shows the modelling rig used in this study for simulating the slope soil treatment using the geocells and wheat straw. The modelling rig is 3000 mm in length, 1200 in width, and 500 mm in height (Figure 2(a)). A plate is placed in the centre of the rig, so that two slope models can be developed in the rig at the same time for direct comparison, each with a width of 30 mm. Two runoff ports are forged at the front side of the modelling box to collect the rain water running down from the slope surface. Four smaller ports are also found at lower section of the front rig for collecting the penetration of water from the surface. The angle of the modelling rig can be easily adjusted by lifting the rear side of the rig, so that different slope ratios can be modelled. The slope ratio for this study is 1 : 1.5. The forged rig is shown in Figure 2(b).

3.2.2. Model Construction Procedure.
The model construction procedures consist of the setup of the drainage system, the construction of physical slopes, and the adjustment of slope angle to the designed ratio.

(1) Drainage system at the bottom: before pouring the slope soil into the modelling rig, the drain board is placed at the bottom of the box, followed by a thin layer of geotextile that is permeable. The drain board and geotextile are so placed that the penetration of water can be restored.

(2) Construction of slope: the slope is constructed on the base soil, which refers to the bare soil of the original slope before the planting of the vegetation. Therefore, the base soil is first placed evenly on the drainage system. The base soil is fully compacted so that its thickness is less than 10 cm (Figure 3(a)). The total thickness of the above slope soil is 40 cm after compaction. For the unsupported slope in Group A, the base soil and the slope soil are placed in the modelling rig layer by layer and compacted to the designed height. Extra soil is swept from the top to make sure that the slope surface is flat and has the same height with the runoff port. For the geocell-supported slope in Group B, the geocell is placed on the base soil and is fully extended and fixed using the U-shaped nails (Figure 3(b)). The geocell rooms are then filled with the slope soil (Figure 3(c)) and compacted to the same height to models in Group A. To ensure this, same amount of soil is used for all the models in three groups. The composite supported slopes in Group C, however, are extra reinforced with the wheat straw at the top 10 cm layer using the mixed soil (Figure 1(d)). The construction of the slopes at both sides of the rig is conducted at the same time.

(3) Slope ratio adjustment: the finished model is given in Figure 3(d). After the placement of all the measuring devices, the rear side of the modelling rig is lifted to the designed slope ratio of 1 : 1.5, which is shown in Figure 3(e).

3.2.3. Rainfall Simulation System.
After the construction of the slopes, the artificial rainfall simulation system is installed above the models. The system is designed based on the previous studies [24, 25] and is shown in Figure 4. The system consists of the rotermeter, sprayers, and water flow switch, which are connected by a number of PPR pipes, two connectors, and three connectors. The total 5 sprayers are uniformly distributed above the centre line of the modelling rig, so that the entire area of the two slopes can be evenly covered (Figure 4). The artificial rainfall system enables a simulation of rainfall intensity from 10 mm/h to 150 mm/h.

3.2.4. Measuring System.
This paper considers the development of slope failures during the rainfall, the amount of soil erosion, the slope displacement, and the variation of water content for the slopes. The slope failures are captured

TABLE 1: Soil reinforcement and rainfall intensity for different models.

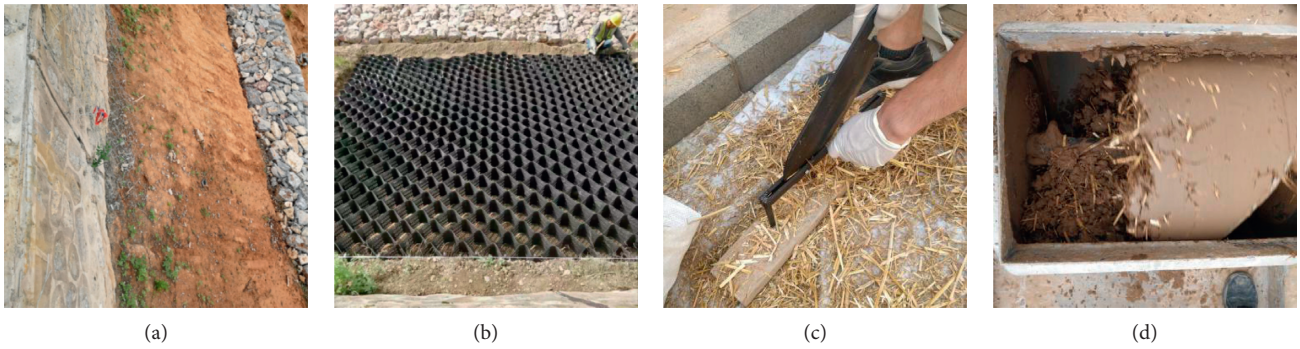| Model	Slope	Soil reinforcement	Rainfall intensity (mm/h)
A1			50
A2	Unsupported slope	Planting soil	75
A3			100
B1			50
B2	Geocell-reinforced slope	Planting soil, geocell reinforcement	75
B3			100
C1			50
C2	Composite reinforced slope	Geocell and wheat straw reinforcement	75
C3			100

(a) (b) (c) (d)

FIGURE 1: Modelling material preparation: (a) planting soil in the field; (b) geocell structures; (c) wheat straw cutting; (d) mixture of straw with the planting soil.
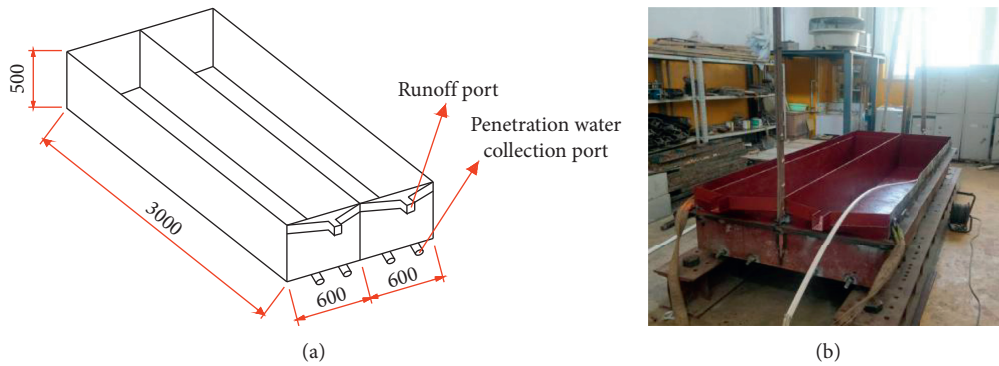

(a) (b)

FIGURE 2: Modelling rig for simulating slope soil erosion treatment: (a) schematic; (b) forged rig.

by a camera, and the rest three parameters are recorded by the measuring system.

3.3. Soil Erosion Measurement.

The finished model after construction was cured for at least 24 h before the artificial rainfall to make sure that the water content of the soil keeps the same at different depth. After the rainfall starts, the rain water was collected at the ports on the front end of the rig every 5 minutes, so that the mass ($m_{runoffi}$) and volume ($V_{runoffi}$) of the runoff (including rain water and soil) are

obtained. The mass of the soil erosion is calculated from the following Equations:

$$m_{soil_i} = \rho_{soil} V_{soil_i} = \rho_{soil} \frac{m_{runoff_i} - \rho_{water} V_{runoff_i}}{\rho_{soil} - \rho_{water}}, \quad (2)$$

$$m_{soil_{accum}} = \sum_{1}^{i} m_{soil_i}, \quad (3)$$

where $m_{runoffi}$ is the mass of the collected runoff from the port (including rain water and soil) at each collection, g;

FIGURE 3: Model construction: (a) compaction of base soil; (b) placement of geocells; (c) fill of slope soil; (d) finished model; (e) finished model at a slope ratio of 1 : 1.5.

V_{runoffi} is the volume of the collected runoff from the port (including rain water and soil) at each collection, cm [3]; m_{soili} is the mass of the soil from the i_{th} collected runoff in g; V_{soili} is the volume of the soil from the i_{th} collected runoff in cm [3]; ρ_{soil} is the density of the slope soil before rainfall selected as 2.7 g/cm^3; ρ_{water} is the density of water, 1 g/cm^3; $m_{\text{soilaccum}}$ is the accumulated mass of the soil from total 6 collected runoffs, g; and i is the number of runoff collected from the port, $i = 1, 2, \ldots, 6$.

3.4. Slope Displacement Measurement.

The displacement of the slope is measured using the measuring ruler fixed on the modelling rig. Since the rods move with the displacement of the slope, a fixed position should be selected for reference to calibrate the measurement. Therefore, a number of positioning marking rods were buried into the soil. Figure 5(a) gives a schematic of the positions of the rods. The rods on spots t_1-t_4 are placed at 1000 mm to the rear plate of the rig, while b_1-b_4 at 1000 mm to the front plate. A marking string parallel to the rig length direction is used to facilitate the displacement measurement (Figure 5(b)). The movement of the rods measured by the fixed ruler during rainfall represents the slope displacement at the top and bottom positions. For instance, the slope displacement at the top section of the slope is selected as the average value measured at spots t_1 and t_2 (Figure 5(c)). The slope displacement obtained from the poles was read at every 10 minutes during the rainfall and at every 15 minutes after the rainfall for 30 minutes.

3.5. Water Content Measurement.

The soil moisture content of the slope was tested using the water content testing device (type SDI-12) buried into the slope soil during the construction. Two of the devices were used for each slope model. Both were embedded at the central position of the slope, with one buried at 10 cm below the surface (N_1 and S_1 in Figure 5(a)) and the other at 20 cm depth (N_2 and S_2). The water content data were collected every one minute, from the beginning of the rainfall to 30–35 minutes after the experiment ceases. Therefore, the variation of the water content of the slope at the shallow and deep depth of the soil was obtained during and after the rainfall.

4. Results and Analysis

4.1. Slope Failure Development.

The progressive development of the slope failure is shown in Figure 6. Note that the unsupported slope was constructed in the right side of the

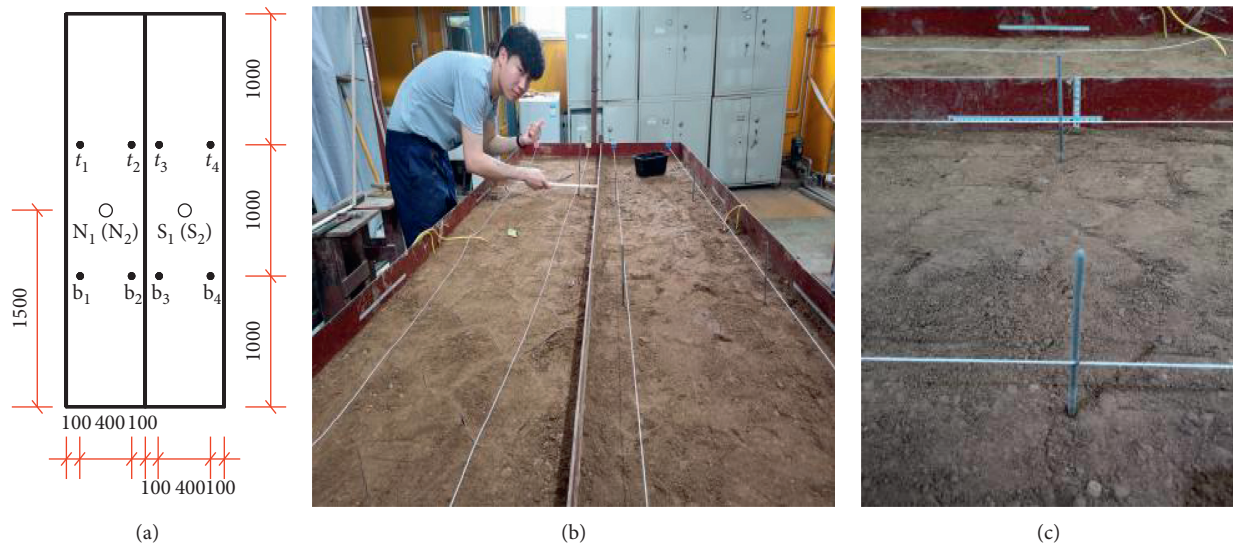FIGURE 4: Rainfall simulation sprayers installed above the model.

FIGURE 5: Placement of measurements: (a) schematic to show positions of marking rods and water content testing devices; (b) marking string to facilitate the slope displacement measurement; (c) positioning rods.

modelling rig, and the left side contains the geocell-reinforced one. The flow of rain water downward the slope surface is observed after 2 minutes of rainfall for both slopes. The runoff starts to scour away the surface soil, and the failure at the toe of unsupported slope is shown after 5 minutes of rainfall (Figure 6(a)). The soil degradation particularly at the lower side of the unsupported slope continues with the rainfall, but the reinforced slope shows good integrity (Figure 6(b)). The area of soil erosion increases on the unsupported slope as the rainfall continues for another 5–8 minutes, and the soil deterioration at toe is also observed on the reinforced slope (Figures 6(c) and 6(d)). The reappeared geocell indicates the shrink of the inner soil, which is held in position by the geocell rather than flowing with the running rain water. The rainfall further engraves the surface soil for both slopes and takes away a great amount of eroded soil (Figures 6(e) and 6(f)). A horizontal crack with a width of 0.8 cm is shown on the top of the unsupported slope

after 20 minutes of rainfall (Figure 6(e)), and grows to about 3 cm when the rainfall continues for 26 minutes (Figure 6(f)). This is mainly due to the differential displacement of the upper layer of soil between the top and bottom of the unsupported slope, while the cracks are not seen on the reinforced model.

After 30 minutes of rainfall at the intensity of 100 mm/h, the final characteristics of the three slopes are shown in Figure 7, including the unsupported slope in Figure 7(a), the geocell-reinforced slope in Figure 7(b), and the geocell and wheat straw composite reinforced slope in Figure 7(c). Apparently, the unsupported slope shows the most damage to the surface soil. The previous observed horizontal fractures with a width of 1 cm were scoured by the rainfall and are now filled with the running mud from the top. The slope with geocell reinforcement is relatively better off, but the upper part of the buried geocell is reappeared under the rainfall, especially for those installed at the top side of the

(a)   (b)   (c)

(d)   (e)   (f)
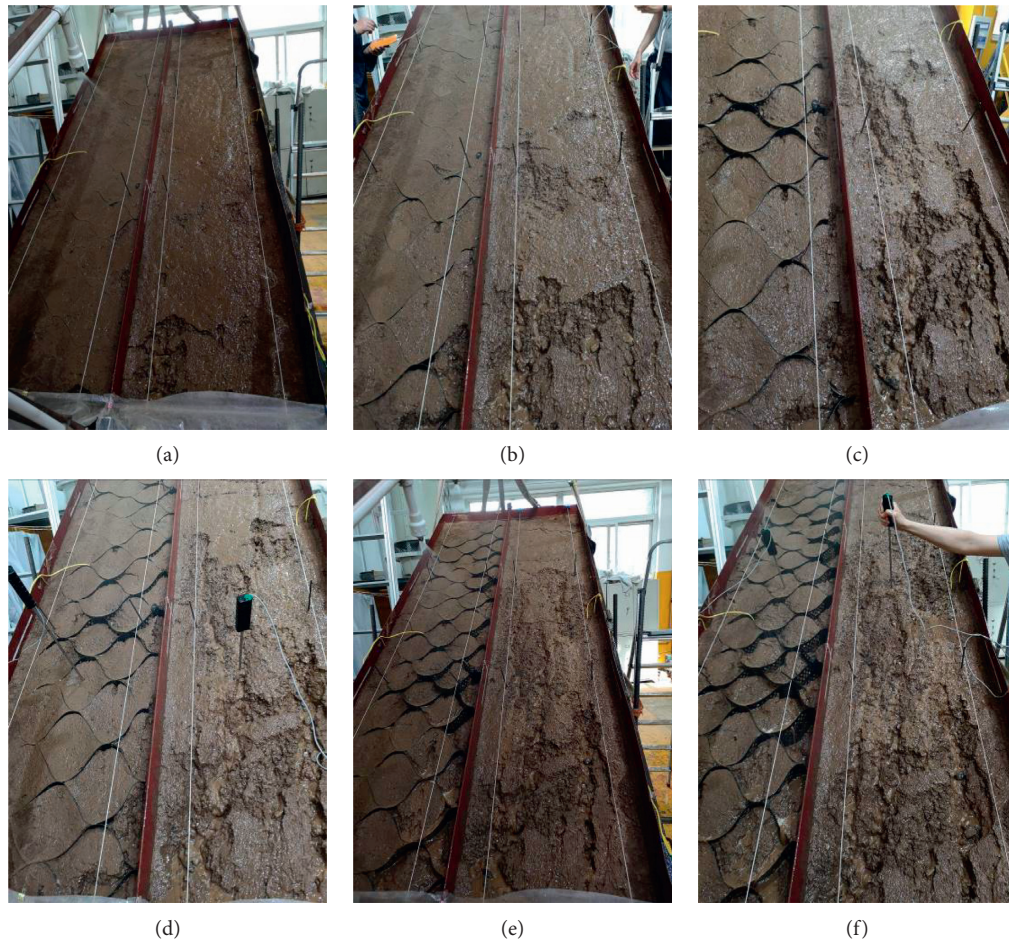
Figure 6: Development of slope erosion during rainfall. Left: geocell-supported slope; right: unsupported slope. (a) 5 min. (b) 7 min. (c) 12 min. (d) 15 min. (e) 20 min. (f) 26 min.

slope. The deep gullies indicate the loss of soil. By contrast, the composite reinforced slope shows the least damaged surface after the rainfall. This is because the wheat straw increases the internal friction angle and cohesion of the planting soil, which limits the soil erosion from the raindrops and surface runoff. The geocell also prevents the development of horizontal fractures, which slows down the erosion of the runoff.

4.2. Amount of Soil Erosion. Figure 8 gives the amount of soil erosion from the three slopes under different rainfall intensities. The lost soil was collected and recorded by a gauge every 5 minutes during the rainfall. The soil erosion increases with the rainfall and reaches the largest amount after 30 minutes at the cease of rainfall. Under the three rainfall intensities, the unsupported slope shows the largest amount of soil erosion, followed by the geocell-supported and the composited slopes in the descending order. For instance, at the rainfall intensity of 50 mm/h, the largest amount of soil erosion at the cease of rainfall is 543.1 g for the unsupported slope, which is significantly reduced to 298.5 g for the geocell-reinforced slope (a 45% reduction) and only 38.1 g for the composite reinforced one (a 93% reduction). It is

therefore not unreasonable to conclude that the loss of eroded soil under rainfall is largely controlled by the erosion control treatment, especially by the geocell and straw composite reinforcement.

A dramatic rise in the soil erosion is observed as the rainfall intensity increases. At the rainfall intensity of 75 mm/h, the lost soil from the unsupported slope increases to 9096.9 g. A 72% of reduction is found in the amount of soil erosion for the geocell treatment slope (2509.0 g), and an 84% of reduction for the composite reinforcement (1430.8 g), implying that both the erosion control treatments work well under a moderate rainfall. At the rainfall intensity of 100 mm/h, however, the amount of soil erosion for the unsupported and geocell-reinforced slopes is both raised to an extremely high level at 22452.7 g and 20928.3 g, respectively. The composite reinforced slope sees an 82% of reduction as compared to the unsupported model, indicating that the geocell and wheat straw composite treatment is more effective in protecting the slope and preventing the soil erosion especially under a heavy rainfall.

It is clear that the composite reinforced slope shows the best stability in terms of soil erosion after the rainfall. This is because the reappeared geocell after the washout of the

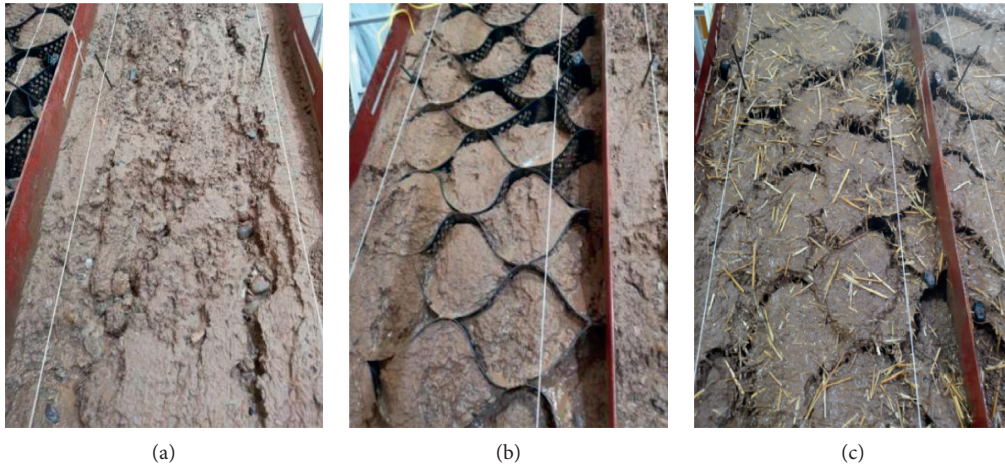(a)   (b)   (c)

FIGURE 7: Comparison of slope erosion after rainfall: (a) unsupported slope; (b) geocell-reinforced slope; (c) geocell- and wheat straw-reinforced slope.
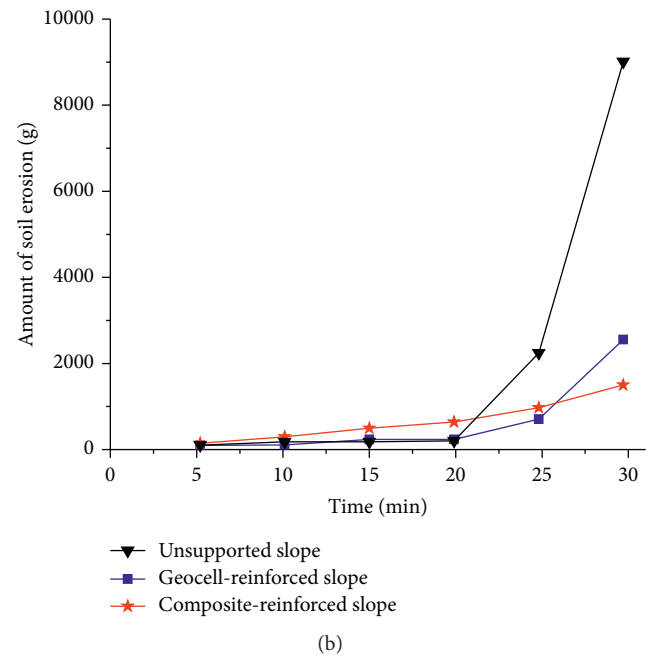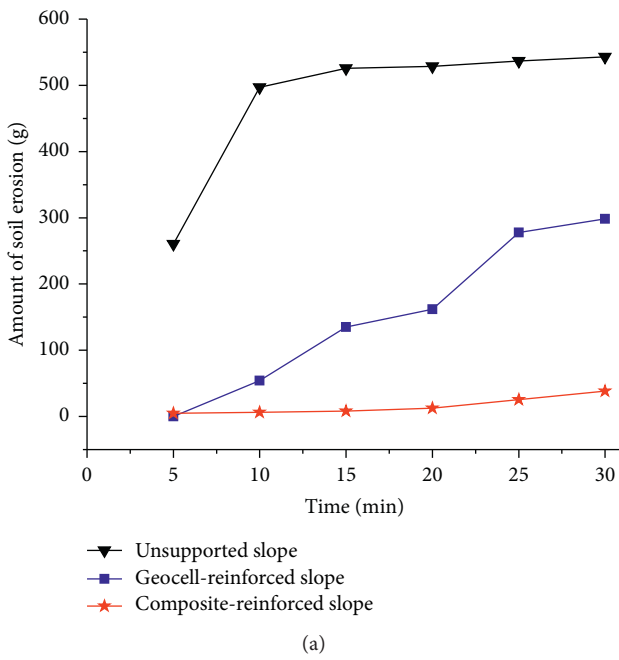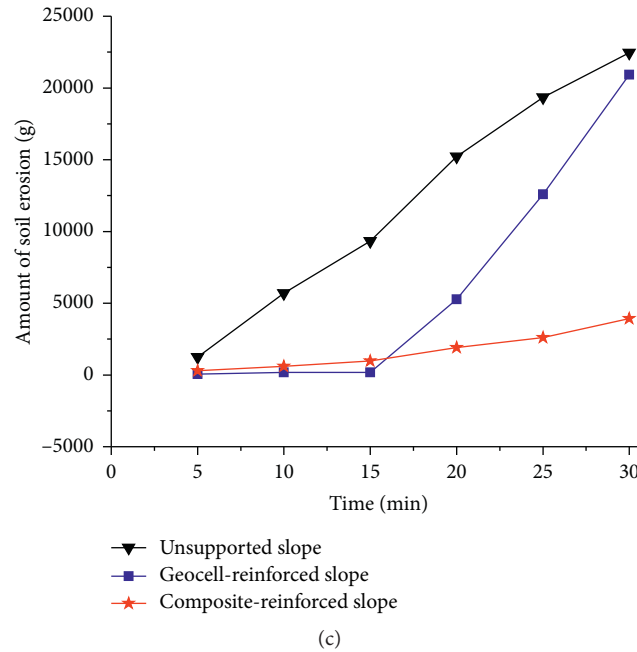

(a)

(b)

FIGURE 8: Continued.

FIGURE 8: Amount of erosion soil during rainfall: (a) rainfall intensity: 50 mm/h; (b) rainfall intensity: 75 mm/h; (c) rainfall intensity: 100 mm/h.

surface soil hinders the flow of the rainwater and reduces the negative impact of the rainfall. The geocell also protects the inner soil and prevents the forming of a large-sized gully. The wheat straw in the top layer may improve the integrity of the slope by increasing the shear strength. The penetration is also reduced due to the smaller porosity for the straw-reinforced soil. On the other hand, the scouring of the rain water down the unsupported slope results in a number of horizontal fractures and gullies with filled water. The penetration of rain water into soil also increases the pore pressure and reduces the shear strength of the soil. Therefore, the unsupported slope is more deteriorated with far more soil erosion.

4.3. Slope Displacement. The slope movement for different models at different rainfall intensities is given in Figure 9. The unsupported slope shows the largest displacement, followed by the geocell-reinforced slope and the geocell and straw composite reinforced. The slope displacement increases dramatically during the 30 minutes of rainfall. This increase slows down after the cease of rainfall. The slope stabilizes and shows unnoticeable slippage at 15 minutes after the rainfall stops. It seems that the bottom of the slope is more likely to slide, since the lower part of the slope generally displaces more as compared to the upper part. This might be due to the high water content at the bottom section of the slope: the soil is saturated first at the bottom; the range of saturated soil then develops upward with the rainfall, with reduced shear strength.

On the other hand, the slope displacement increases with the increase of rainfall intensity from 50 mm/h to 100 mm/h.

Under the rainfall intensity of 100 mm/h, the slope displacements stay at a relative high level at more than 12 mm and 7.3 mm for the unsupported and geocell-reinforced slopes, respectively, while the difference in displacement between the top and bottom is unnoticeable. The composite reinforced slopes show a larger difference between the top and bottom sides, indicating that the reinforcement has a better control to the top side.

The bottom slope is more saturated and presents larger displacement, but the difference in displacement between the top and bottom of the slope may eventually trigger the landslide. This is why horizontal cracks were observed on top position of the slope. However, the erosion of the slope may occur from the bottom to top if no reinforcement is provided. The reinforcement works well to prevent the slope movement and increase the stability. The reinforcement from the geocell and the straw protects the slope soil from erosion; the slope surface is therefore more intact with less displacement.

4.4. Water Content Analysis. The change of water content in the slope soil during rainfall is given in Figure 10 for different models. At the beginning of rainfall, the water content is about 15% for different slopes, and it stays at this level for a few minutes of rainfall before starting to increase. The water content then climbs rapidly until it maximizes at around 40%. Note that the sequence of the sudden increase of water content on the curve indicates the sequential order of water reaching the buried sensors in the soil. Generally, during the increasing stage, the sensors at 10 cm below the slope surface (see the solid dots) perceive the rainfall before those setting at 20 cm deep, i.e., the shallow soil shows larger water
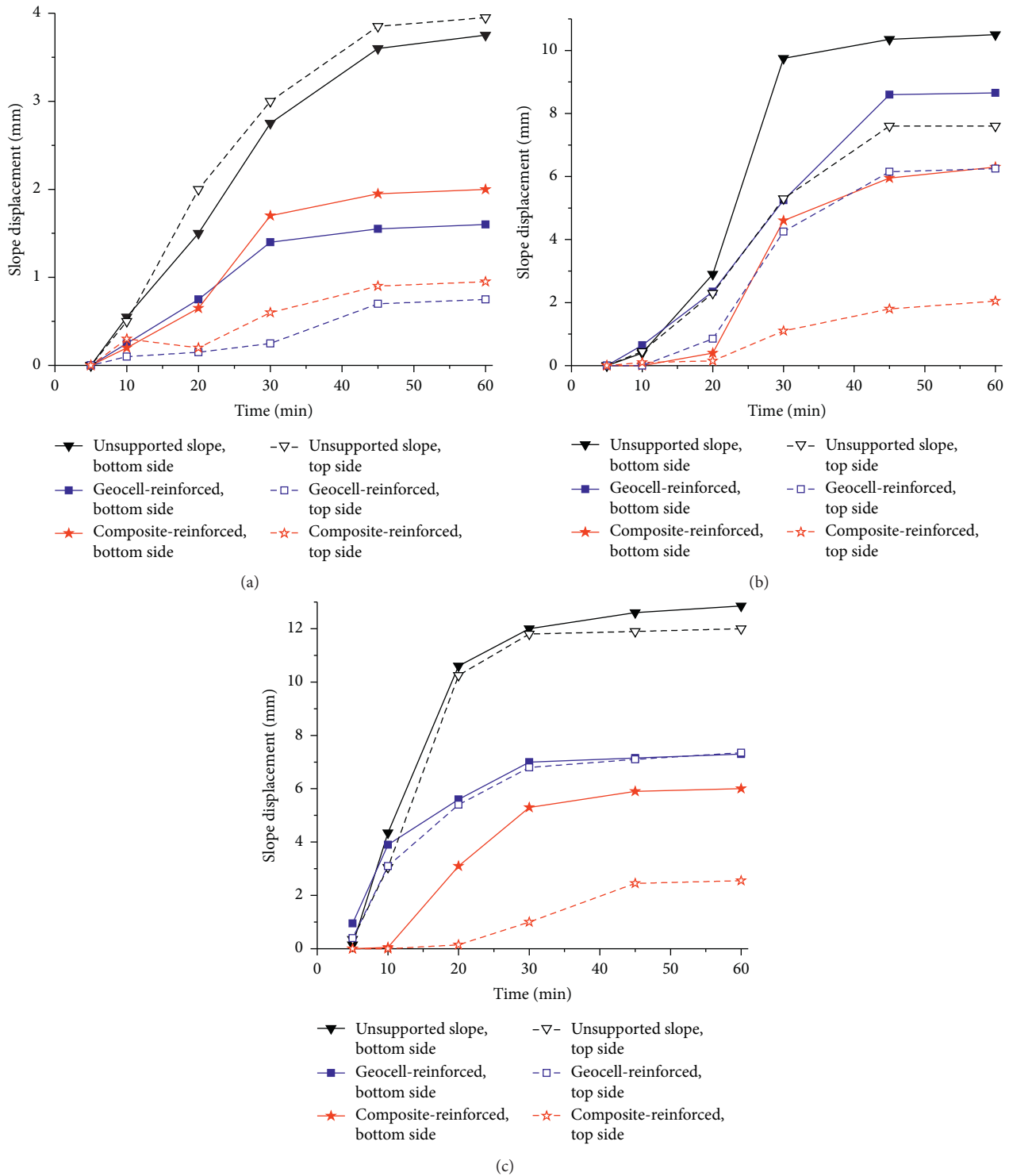
(a)

(b)

(c)

Figure 9: Slope displacement during rainfall: (a) rainfall intensity: 50 mm/h; (b) rainfall intensity: 75 mm/h; (c) rainfall intensity: 100 mm/h.

content than the deep soil. For the unsupported and geocell-reinforced slopes, the increases of water moisture start almost at the same time, and the rates of water penetration represented by the slopes of curves are also similar. By comparison, the water content for the geocell- and straw-reinforced slope starts to increase only after 13 and 25 minutes at the 10 cm at 20 cm depth, respectively, and reaches the maximum level 10–20 minutes later than the other two slopes. The rate of the increase of water content is also smaller than the other two slopes, indicating the geocell and straw reinforcement is more effective in slowing down the penetration of the rainfall.
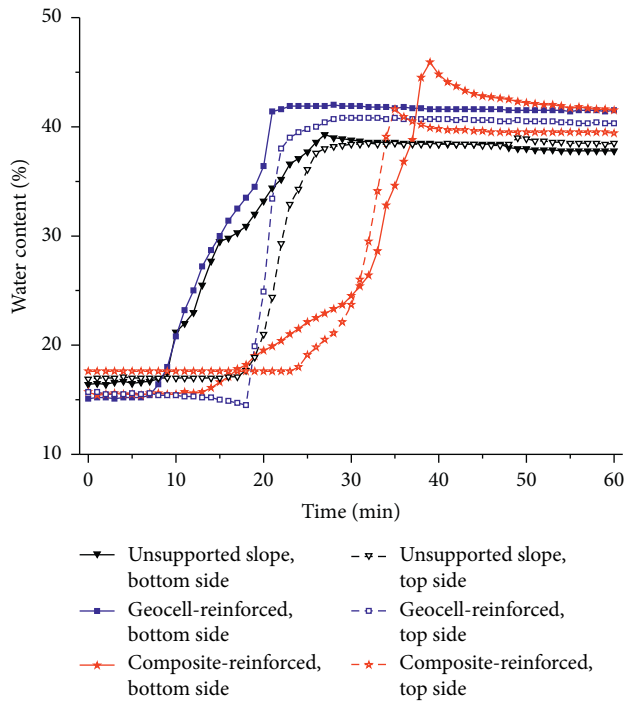
FIGURE 10: Variation of water content in the slope soil during rainfall.

5. Summary and Conclusions

Erosion control using planting vegetation for slope protection requires an adequate early stability of the planting soil. Otherwise, the collapse of the planting soil leads to the failure of the protective layer. This paper has proposed a composite soil treatment method using the geocell structures and the wheat straw reinforcement. The geocell above the slope provides a relatively stable environment for the growth of vegetation, and the wheat straw enhances the mechanical properties of the reinforced soil. The interaction of the composite reinforcement mitigates the soil erosion and improves the slope stability. A total of nine experiments were performed in the work to assess the failure process of the slope, soil erosion, slope displacement, and water content under different support strategies and different rainfall intensities. Important findings of this study are listed as follows:

(1) The erosion of the slope soil starts from the bottom of the soil and increases with the rainfall. Rills and gullies are formed as the rain water dislodges and carries soil particles off the lope. After the rainfall, a few horizontal cracks are observed on top of the slopes. This might be a result of the movement of the bottom soil pulling down the top soil. The unsupported slope shows the most damage of the soil, while the geocell and straw composite supported slope shows the best integrity.

(2) The soil erosion increases with the intensity of rainfall, but the slope reinforcement with geocell and wheat straw significantly reduces the rate and amount of the eroded soil. The unsupported slope shows that greatest amount of soil erosion under different rainfall intensities, but the geocell-reinforced slopes reduce the soil erosion to about 45–70%, and the composite reinforced reduce 80–90%.

(3) The slope displacement first increases with the rainfall and then slows down and stabilizes after the rainfall ceases. The composite reinforced slope has the least displacement, which sees a 30% and 60% reduction on average as compared to the geocell-reinforced slope and the unsupported one. The displacement of the soil at bottom of the slope is more than that for the top soil. This discrepancy leads to the massive horizontal cracks observed at the top of the slope.

(4) The water content for different slopes increases from 15% at the beginning of rainfall and maximizes at 40% after the rainfall. The shallow depth soil has larger water content than the deep soil. The composite reinforcement slope shows the least rate of increase in water content, indicating that the geocell and wheat straw improve the slope stability by slowing down the penetration of water into soil.

Data Availability

The data used to support the findings of this study are included within the article.

Conflicts of Interest

The authors declare that there are no conflicts of interest.

Acknowledgments

References

[1] X. Y. Sun, C. J. Mu, and X. H. Yang, "Application of the geocell in soil slopes at Yan-Lan line," *Subgrade Engineering*, vol. 4, pp. 55–57, 1999, in Chinese.

[2] G. W. Li, "Application of the geocell and planting vegetation on the road slope at swelling soil area," *Journal of Highway and Transportation Research and Development*, vol. 25, no. 4, pp. 46–48, 2008, in Chinese.

[3] K. Ren, X. S. Shen, H. X. Wang et al., "Application of the honeycomb shaped geocell in the hard slope at river side for ecological restoration—case study," *Soil and Water Conservation in China*, vol. 10, pp. 37–40, 2017, in Chinese.

[4] G. Y. Wang, Y. Han, and X. H. Wang, "Stability analysis of geocell flexible slope protection in rainfall," *Rock and Soil Mechanics*, vol. 33, no. 10, pp. 3020–3024, in Chinese.

[5] X. H. Yang and W. S. Wang, "Application of geocell and vegetation in road slope protection at loess area," *Highway*, vol. 8, pp. 179–182, 2004, in Chinese.

[6] C. G. Yan, X. H. Yang, Y. L. Xie et al., "Experimental research on anti-eroding effect of geocells in loess embankment," *Rock and Soil Mechanics*, vol. 26, no. 8, pp. 1342–1348, in Chinese.

[7] A. Rosen, "The use of geocells for slope protection under special conditions," in *Proceedings of the International Symposium on Design and Practice of Geosynthetic-Reinforced Soil Structures*, Bologna, Italy, October 2013.

[8] T. Sato and K. Kojma, "Development of slope protection work using geocell and soil nailing," *Japanese Railway Engineering*, vol. 2018, no. 4, pp. 1–3, 2018.

[9] M. R. Arvin, A. Zakeri, and M. Bahmani Shoorijeh, "Using finite element strength reduction method for stability analysis of geocell-reinforced slopes," *Geotechnical and Geological Engineering*, vol. 37, no. 3, pp. 1453–1467, 2019.

[10] J. Wesseloo, A. T. Visser, and E. Rust, "The stress-strain behaviour of multiple cell geocell packs," *Geotextiles and Geomembranes*, vol. 27, no. 1, pp. 31–38, 2009.

[11] G. M. Latha, K. Rajagopal, and N. R. Krishnaswamy, "Experimental and theoretical investigations on geocell-supported embankments," *International Journal of Geomechanics*, vol. 6, no. 1, pp. 30–35, 2006.

[12] Y. R. Zheng, Z. Y. Chen, G. X. Wang et al., *Management of Landslide*, China Communications Publishing, Beijing, China, 2020.

[13] M. T. Löbmann, C. Geitner, C. Wellstein, and S. Zerbe, "The influence of herbaceous vegetation on slope stability—a review," *Earth-Science Reviews*, vol. 209, Article ID 103328, 2020.

[14] M. Bouhicha, F. Aouissi, and S. Kenai, "Performance of composite soil reinforced with barley straw," *Cement and Concrete Composites*, vol. 27, no. 5, pp. 617–621, 2005.

[15] T. Ashour, A. Bahnasawey, and W. Wu, "Compressive strength of fiber reinforced earth plasters for straw bale buildings," *Australian Journal of Agricultural Engineering*, vol. 1, no. 3, pp. 86–92, 2010.

[16] H. R. Zhang, G. Y. Wang, and L. C. Sha, "Experimental study on a rice-straw mud material for slope protection and anti erosion," *Journal of Highway and Transportation Research and Development*, vol. 34, no. 1, pp. 24–31, 2017, in Chinese.

[17] M. Donat, "Bioengineering Techniques for Streambank Restoration: A Review of Central European Practices," *Watershed Restoration Project Report*, vol. 2, pp. 4–9, 1995, in Chinese.

[18] L.-J. Su, B.-L. Hu, Q.-J. Xie, F.-W. Yu, and C.-L. Zhang, "Experimental and theoretical study of mechanical properties of root-soil interface for slope protection," *Journal of Mountain Science*, vol. 17, no. 11, pp. 2784–2795, 2020.

[19] J. B. Hao, X. M. Wei, J. Yao et al., "Strength characteristics and mesostructured of wheat straw reinforced soil," *Journal of Tongji University (Natural Science)*, vol. 47, no. 6, pp. 764–768, 2019, in Chinese.

[20] Y. M. Shao and D. N. Shao, *Updated Rainstorm Intensity Formula in China*, China Architecture and Building Press, Beijing, China, 2014, in Chinese.

[21] Beijing General Municipal Engineering Design and Research Institute, *City drainage*, China Architecture and Building Press, Beijing, China, 2017, in Chinese.

[22] H. R. Zhang, G. Y. Wang, and L. C. Sha, "Experimental study on a rice-straw mud material for slope protection and anti-erosion," *Journal of Highway and Transportation Research and Development*, vol. 34, no. 1, pp. 24–31, 2017, in Chinese.

[23] H. B. Hu, L. C. Sha, and Y. J. Zhang, "Study on rain erosion test of the indoor slope protected by rice straw reinforced soil," *Highway Engineering*, vol. 43, no. 5, pp. 213–219, 2018, in Chinese.

[24] S. Y. Liu, Q. Z. Han, Z. G. Nie et al., "Study on characteristic and application of SB-YZCP artificial rainfall simulator," *Journal of Soil and Water Conservation*, vol. 4, no. 2, pp. 48–54, 1998, in Chinese.

[25] Y. Zhou, J. Wang, and S. W. Hu, "Designing and calibration of Kust 03-1 rainfall simulating system," *Journal of Kunming University of Science and Technology (Natural Science)*, vol. 2, pp. 81–85, 2008, in Chinese.

Research Article

Quantitative Evaluation of Top Coal Caving Methods at the Working Face of Extra-Thick Coal Seams Based on the Random Medium Theory

Shi Jiulin [1,2] **Zhang Quntao**, [3] **Gao Xiaojin**, [1,2] **and Xue Jisheng** [1,2]

¹*Beijing Mining Research Institute, China Coal Research Institute, Beijing 100013, China*
²*CCTEG Coal Mining Research Institute, Beijing 100013, China*
³*School of Energy and Mining Engineering, China University of Mining and Technology (Beijing), Beijing 100083, China*

Correspondence should be addressed to Shi Jiulin; sjlin1210@163.com

Adopting an effective top coal caving method is the key to enhancing coal recovery and reducing gangue content for the fully mechanized top coal caving working face with extra-thick coal seams. In this study, the movement of coal particles generated during top coal caving is considered to follow a normal distribution. Then, the caving body and coal-rock settlement along the working face during the caving process are studied based on both the random media theory and probability theory. Accordingly, the optimal caving interval and caving sequences are determined, and a novel interval symmetrical coal caving method is proposed. The proposed method is systematically verified with results from physical similarity tests, and different caving methods are assessed by field tests. The results show the following: (1) The coal-rock settlement and the caving body demonstrate clear axial symmetrical features along the working face; the size of the caving body increases as the caving height grows and its shape turns progressively from semicircular to semielliptical with a lower foot of the coal-rock settlement. (2) The caving interval is derived using the sum of the radii of the coal-rock settlement curves formed by the two largest caving bodies. (3) The symmetrical caving approach provides a symmetrical space for the subsequent movement of the broken top coal, which enables a uniform development of the caving body. (4) Compared with the traditional sequential coal caving method with the same number of supports, the interval symmetrical caving method results in a 21.7% of coal production increase, 17% caving rate promotion, and a shortened caving time by 23.4%. (5) The interval symmetrical caving method is found to improve the controllability of the caving process at the fully mechanized top coal caving working face. In general, this work presents a theoretical approach to select the optimal caving methods for the fully mechanized caving working face in extra-thick coal seams for an improved production efficiency of the work face. The results of this study can also provide theoretical significance and referencing value for quantitative analyses of the coal caving methods for work faces with similar geological conditions.

1. Introduction

After 40 years of field application and practice, the fully mechanized top coal caving mining method has become the mainstream for mining thick and extra-thick coal seams in China. However, the loss of top coal during the mining process poses a major challenge for the further development of the method [1–6]. Larger mining height can lead to higher coal losses, and the key to reducing coal losses and improving recovery lies in the selection of a more effective caving method.

To find a caving approach that enables higher coal recovery and lower gangue content, many studies have analyzed the coal breaking and moving behavior and the evolution of the caving body and coal-rock boundary during the caving process. Wu and Zhang [5] proposed the coal caving ellipsoid theory based on field measurement and similar simulation experiments. In their study, the effects of the coal caving angle, coal caving height, and the distance between the caving and the top coal breaking line on the development of the strike coal caving ellipsoid and axial deflection were studied. Using the ellipsoid

theory, Tian et al. [7] analyzed the relationship between the theoretical coal caving ellipsoid, the actual caving ellipsoid, and the loose ellipsoid. A proper caving interval that can adapt to different top coal thickness was proposed by assuming that the initial coal-rock boundary is parabolic. Liu et al. [8] numerically analyzed the relationship between the caving interval and the coal recovery in a 17 m thick coal seam of the Zhungeer Coal Mine. It was found that a lower mining to caving ratio at twice the coal cutting can provide sufficient space for loosening the top coal, which is beneficial for top coal recovery. Wang and Zhang [9–12] proposed the "BBR" caving theory containing factors including top coal, recovery rate, and gangue rate, based on the granular media flow theory. A sectioned caving method with large intervals was developed, which can expand the coal caving area, reduce top coal losses between supports, and increase the overall coal recovery. Huang et al. [13–15] studied the flow field of coal gangue based on physical similarity tests of granular media in the strike direction and argued that the coal caving process is essentially the evolution process of the coal-rock boundary and the initial top coal boundary. They proposed the concept of the caving turning point by performing excessive top coal caving to improve the overall coal recovery. Yan et al. [16] studied the relationship between the flowing behavior of the broken coal and the quadrilateral/triangular piling patterns formed by the broken gangue and the top coal behind the support. They believed that the coal loss is inversely proportional to the piling angle of the gangue and is proportional to the distance between the rear scraper conveyor and the gangue pile. The coal loss was then quantified and the cause of residual coal in the goaf during top coal caving was analyzed. Zhu and Yu [17, 18] conducted physical similarity simulation tests and found that the tail beam and caving opening of the support in the inclined direction of the working face can cause the axial deflection angle of the caving body to decrease with the increase of the caving height, and the coal gangue boundary was found to appear at the coal caving opening. The top coal recovery rate in the direction of the coal seam was quantitatively analyzed using the relationship between the gangue settlement curve and the area of the caving body. Based on laboratory and field tests on the flowing behavior of the top coal using top coal caving method, numerous scholars proposed theoretical models for the caving process according to the coal caving, ellipsoid theory, and the granular dynamics. Moreover, it was found by controlling the caving body and coal-rock boundary that the top coal recovery can be increased with reduced coal losses. Liu et al. [19, 20] determined the sequence of coal caving and the interval time difference based on the coal-rock boundary line and the theory of inclined straight lines. In addition, the multiple top coal caving windows synergetic method with the principle of opening windows at the same time and closing the window in reverse was proposed. The proposed top coal caving method can optimize the coal gangue boundary to achieve increased top coal recovery by controlling the caving time of part of the coal caving supports.

In general, existing studies mostly focus on assessing the top coal recovery along the strike direction of the work face, whereas studies on top coal recovery along the dip direction of the work face are still lacking, especially in terms of selecting the coal caving method in the fully mechanized top coal caving working face. The top coal caving method is a systematic combination of caving sequence and caving amount, and it possesses a major effect on the top coal recovery in the working face. The current selection process of top coal caving methods is mainly based on physical similarity simulation and empirical control from field tests. Therefore, this study aims to propose an effective approach to select the optimal caving method by quantitative analyses of the effect of different caving methods on the top coal recovery along the dip direction of the working face, based on the granular dynamic theory and stochastic theory.

2. Engineering Background

The 8222 work face of the Tashan Coal Mine has a buried depth of 467 m, an average thickness of 15 m, and a dip angle between 2 and 5°. The immediate roof mainly consists of mudstone and sandy mudstone, and the floor is generally of mudstone and sandy mudstone. The method of one cutting and one caving is adopted in the work face, with a mining height of 4 m, a caving height of 11 m, and a mining caving ratio of 1 : 2.75. The cutting cycle of the shearer and the caving interval of the hydraulic support are both 0.8 m. The ZF15000/27.5/42 four-column low-level coal caving support is adopted at the working face, with a center distance of 1.75 m. The overall support is divided into 3 sections (5#-50#, 51#-95#, and 96#-130#) along the direction of the working face, where single-port, sequential, and multiwheel caving is adopted in the section with three workers. According to the field measurements, the top coal recovery rate of the work face is 78.5%. To control the gangue content for improved production management, the top coal caving is stopped when the gangue appears during caving.

3. Theoretical Analysis of Top Coal Caving Law

During the top coal caving process, the broken top coal moves to the caving opening under the effect of gravity. The movement of a single broken coal is mostly random and discontinuous. However, by ignoring the effect of momentary loosening during the movement of the broken top coal, the bulk movement of the top coal can be considered continuous, and the entire moving process can be simplified to the flowing in a continuous medium [21, 22]. As the movement of the top coal is entirely continuous and locally discontinuous in the caving process, it is reasonable to study the flowing of the broken top coal using the random medium flow theory [18]. Therefore, the three following basic assumptions are made: (1) The top coal above the support and the immediate roof are considered fully broken before caving. (2) The broken top coal and the direct roof are flowing continuously during the caving process. (3) The friction coefficient remains unchanged during the caving process of the broken top coal.

3.1. Analysis Based on the Random Media Theory. Both sides of the broken top coal are subjected to almost the same external effects along the direction of the working face. When the coal caving port is opened, the top coal particles

move under the action of gravity to form a symmetrical settlement centered at the coal caving port. The space left when the top coal particles are released is supplemented by the upper coal particles. Considering the broken top coals that have not caved yet as shown in Figure 1, the volumes of blocks a, b, c, and d are all ΔV, and the friction coefficient between the coal blocks is the same. When the d block is released, it is randomly supplemented by the upper a, b, and c blocks. The probability of block movement is inversely proportional to the distance of movement. Therefore, the filling probabilities of blocks a, b, and c to the vacancies of block d are 1/4, 1/2, and 1/4, respectively. Similarly, as the layer increases, the number of participating blocks in the movement increases, and the effect of each single influencing factor is trivial on the overall movement of the block, which approximately obeys a normal distribution [21–23]. According to the central limit theorem, when the number of block layers involved in the particle movement j is large enough, the motion probability density function of the blocks can be given by

$$p(i, j) = \frac{1}{\sqrt{\pi j}} \exp\left(-\frac{i^2}{j}\right),\tag{1}$$

where (i, j) are the centroid coordinates of the block.

A previous study [18] obtained a more practical probability density function of the movement of bulk particles by introducing the granular particle flow parameters based on a series of physical similarity tests, using the Cartesian coordinate system, and it takes the following form:

$$p(x, y) = \frac{1}{\sqrt{\pi \beta y^\alpha}} \exp\left(-\frac{x^2}{\beta y^\alpha}\right),\tag{2}$$

where α, β are parameters related to the flow properties of granular particles.

Taking the center of the coal caving opening as the origin O, a two-dimensional plane coordinate system is established with the working surface direction in x and the vertical direction in y, as shown in Figure 2.

Considering the area with a width of Δl and $A(x, y)$ as the center point as the target section, when opening the coal caving port, the probability of the caving particles to travel through the neighborhood section within a unit of time is

$$P(x, y) = \int p(x, y) d\Delta\, l.\tag{3}$$

It can be observed that when $\Delta l \longrightarrow 0$, $P(x, y) = p(x, y)\Delta l$.

When the quantity of discharged coal per unit time is q, the number of particles passing the neighborhood section is

$$Q_1 = qP(x, y) = qp(x, y)\Delta l.\tag{4}$$

Supposing that the falling speed of particles in the neighboring section is $\bar{v}_y$, the number of particles passing through the neighborhood section in unit time is $Q_2 = \Delta l \bar{v}_y$. According to the mass conservation with $Q_1 = Q_2$, the following expression can be obtained:

$$\bar{v}_y = qp(x, y) = -\frac{q}{\sqrt{\pi \beta y^\alpha}} \exp\left(-\frac{x^2}{\beta y^\alpha}\right).\tag{5}$$

In the continuous flow field, the inflow and outflow of the neighborhood section are the same; that is, the flow field of the incompressible continuous granular particles must meet

$$\operatorname{div} \vec{v} = \frac{\partial v_x}{\partial x} + \frac{\partial v_y}{\partial y} = 0.\tag{6}$$

Combining equations (5) and (6), the particle moving speed can be obtained through integral calculation as

$$\begin{cases} v_y = -\dfrac{q}{\sqrt{\pi \beta y^\alpha}} \exp\left(-\dfrac{x^2}{\beta y^\alpha}\right), \\[4mm] x = \dfrac{\alpha \beta q y^{\alpha-1}}{2\sqrt{\pi}\sqrt[3]{\beta y^\alpha}} \exp-\left(\dfrac{x^2}{\beta y^\alpha}\right). \end{cases}\tag{7}$$

For any particle B (x_0, y_0) of the top coal at the y_0 layer, the tangent of its moving path is along the velocity direction with $dx/dy = v_x/v_y$. From equation (7), one can obtain

$$\frac{dy}{dx} = \frac{2y}{\alpha x}.\tag{8}$$

Integrating both sides of equation (8), the moving path of granular particles obeys

$$\frac{x^2}{y^\alpha} = \frac{x_0^2}{y_0^\alpha}.\tag{9}$$

During the downward movement of the particle, the velocity field determines the change of the displacement field. The tangential direction of the movement path of the particle at any point is collinear with the velocity direction; that is, $v_y = (dy/dx)$. Combining equations (7) and (9), we obtain

$$\frac{dy}{dx} = -\frac{q}{\sqrt{\pi \beta y^\alpha}} \exp\left(-\frac{x_0^2}{\beta y_0^\alpha}\right).\tag{10}$$

By integrating equation (10), it can be found that when the particle B (x_0, y_0) moves to the point N (x, y), the amount of top coal discharged from the caving port is

$$Q = \frac{2\sqrt{\pi \beta}}{\alpha + 2}\left(y_0^{\alpha+2/2} - y^{\alpha+2/2}\right)\exp\left(\frac{x_0^2}{\beta y_0^\alpha}\right).\tag{11}$$

Combining equations (9) and (11), the sedimentation motion trajectory equation of the top coal particles at the y_0 layer can be expressed by the following equation:

$$x^2 = \beta y^\alpha \ln\left[\frac{(\alpha + 2)Q}{2\sqrt{\pi\beta}\left(y_0^{\alpha+2/2} - y^{\alpha+2/2}\right)}\right].\tag{12}$$

Since the settlement path of the top coal is symmetrical, the lowest point of the settlement curve of the upper broken

particles must be on the y-axis when the coal caving port is opened. Supposing that the lowest point is $P(0, y_{min})$ and substituting it into equation (12), the lowest point of the sedimentation curve of broken particles in the y_0 layer is obtained as

$$y_{min} = \left[y_0^{\alpha+2/2} - \frac{(\alpha+2)}{2\sqrt{\pi\beta}} Q \right]^{\alpha+2/2}. \tag{13}$$

Supposing that the thickness of the coal seam is H, the top coal is released when the top coal particles of layer H reach the coal caving opening for the first time, that is, when the particle $(0, H)$ reaches the coal caving opening. As the coal caving continues, mixed gangue will appear. According to the principle of closing the door, when the gangue occurs during the top coal caving process and when the particle $(0, H)$ reaches the lowest coal caving opening, the caving opening is closed, and the coal caving process is terminated. The amounts of pure coal released are

$$Q_H = \frac{2\sqrt{\pi\beta}}{(\alpha+2)} H^{\alpha+2/2}. \tag{14}$$

From equations (11) and (14), the coal-rock settlement curve at a height of H is

$$x^2 = \beta y^\alpha \ln \frac{H^{\alpha+2/2}}{H^{\alpha+2/2} - y^{\alpha+2/2}}. \tag{15}$$

The amounts of coal and rock particles released from the caving port are equal to the number of particles contained in the released body during the release process. When the caving height H is obtained from equations (10) and (14), the caving particle body equation can be expressed by

$$x^2 = \frac{\alpha+2}{2} \beta y^\alpha \ln \frac{H}{y}. \tag{16}$$

3.2. Selection of the Coal Caving Method at the Working Face.
An effective coal caving method is beneficial to increasing the coal recovery rate, reducing the gangue rate, and improving the production efficiency of the working face. The key to selecting the optimal coal caving method is to determine a reasonable coal caving interval and caving sequence.

3.2.1. Patterns of the Caving Body and Evolution of the Coal-Rock Boundary.
To determine the coal-rock settlement curve and the theoretical patterns of the top coal caving body during the caving process, the parameters α, β related to the flow properties of the granular caving body should be first calculated. Taking the 8222 working face of the Tashan Coal Mine as the engineering background, from the results of the physical similarity simulation and the curve fitting of the discharged body, the coal seam mining ratio is found to be 1 : 2.75, with $a = 1.3$ and $\beta = 0.3$. From the working conditions of the 8222 working face and according to the above theoretical formulas (15) and (16), the coal-rock settlement curves and the evolution of the caving body with the increase

of the caving volume adopting the single-port caving are plotted using Matlab, as shown in Figure 3.

It can be seen from Figure 3 that the top coal particles move towards the caving opening under the action of gravity. With the increase of the discharged top coal, the slope of the settlement curve increases and rapidly approaches the centerline of the coal caving opening, with the foot of the curve decreasing along the axis. Moreover, as the coal caving height increases, the eccentricity e gradually decreases and the shape of the discharged body gradually changes from circular to elliptical, which differs from the traditional ellipsoid theory. The change of the geometry of the discharged body during the caving process is shown in Table 1.

When the coal caving height reaches 14.5 m, the endpoint of the top coal settlement curve reaches the coal caving opening, whereas the gangue reaches the critical mixing surface. As the coal caving continues, the end of the coal caving funnel damage and mixed gangue will occur. When the coal caving height is 15 m, the settlement curve of the fractured top coal develops outwards from the center of the caving opening, and the caving body exceeds the horizontal coal-rock boundary, resulting in an increased amount of mixed gangue.

3.2.2. Determination of the Coal Caving Interval.
As discussed, the shape of the caving body changes from circular to elliptical with the increase of the amount of discharged coal, although it is always symmetrical with respect to the axis. The geometry of the discharged body is mainly controlled by the coal-rock settlement curve on both sides. A more developed caving body leads to a greater amount of top coal released, and the symmetrical coal-rock settlement curve can contribute to the full development of the top coal discharge. Therefore, by setting a reasonable coal caving interval and caving sequence, the coal-rock settlement curve can be controlled to ensure the integrity of the caving body and to maximize the amount of caved coal during the interval. The end of the coal caving interval is effectively the boundary of the coal and rock settlement curve after the previous caving. Therefore, the maximum amount of caved coal is observed at the two ends of the interval, and the maximum coal caving interval is determined by the distance between the settlement curves of two completely caved bodies. For the reasonable coal caving interval L, it contains n ($n \geq 2$) supports, and the following expression can be obtained:

$$n = \frac{L}{l_f} = \left[\frac{2X}{l_f} \right], \tag{17}$$

where l_f is the width of the coal caving opening, and we use $l_f = 1.75$ m in this study.

Combining equations (15) and (17), the number of supports in the interval is

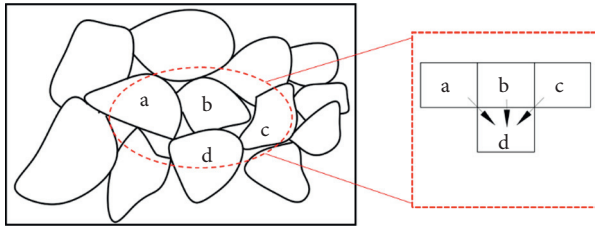$$n = \frac{2\sqrt{\beta y^\alpha \ln H^{\alpha+2/2}/H^{\alpha+2/2} - y^{\alpha+2/2}}}{l_f}. \tag{18}$$

FIGURE 1: Movement of the broken block.

3.2.3. Coal Caving Sequences within Each Interval. To ensure a symmetric space for coal caving, the first step is to open the coal caving openings 1# and n# at both ends of the caving interval until the gangue appears. The same coal-rock settlement curves are formed above the two coal caving openings, which are symmetrical at m# and tangential to the horizontal coal-rock boundary. As shown in Figure 4(a), an inverted bowl-shaped coal body (shaded area with red boundaries) occurs between the two coal caving openings, surrounded by the coal-rock boundary and the floor. Then, the next step is to turn on the coal caving opening m# until the gangue appears, which forms a pure coal body similar to that at the end, as shown in the area with magenta boundaries in Figure 4(a). Within the interval, a symmetric solid coal area (surrounded by the coal-rock subsidence curve) is formed again, as shown in the shaded area in Figure 4(b). Due to the symmetry of the entire coal caving space, a symmetrical coal caving space will be formed again when the caving openings $m-t$ and $m+t$ are opened in the interval, as shown in the area with blue boundaries in Figure 4(b). A similar procedure is applied until the entire caving process is completed in the interval. The coal caving sequence in the interval follows 1 (n)-$m+t$ $(m-t)$-..., until all coal caving openings are opened and the coal caving in the interval is completed.

Based on the above analysis, under the engineering background of the 8222 working face, the optimal caving interval $n=7$ is obtained by substituting the relevant parameters into equation (18), and the caving sequence is found to be 1–7#, 4#, 2–6#, and 3–5#.

4. Verification Using the Physical Similarity Simulation

4.1. Model Development. In this study, two-dimensional physical similarity simulation experiments were conducted based on the mining and geological conditions of the studied working face. The dimension of the test bench was $150 \times 17 \times 50$ cm with the geometric similarity ratio at $1:87$. Caving openings of the support were formed using 2×4 cm square steel to represent the 1.74 m caving opening in the mine, and a total of 29 supports were placed in the model (with an actual distance of 50.46 m). Coal caving was simulated by withdrawing the square steel to open the coal caving port of the support, and 7 square steels were placed on both sides to ensure a stable boundary condition. The supports in the experimental area are numbered 1#~15# from left to right in Figure 5. In the experiment, black stones

(5 cm in layer thickness) with a particle size between 6 and 12 mm were used to simulate the broken top coal with a height of 12 cm, which contained two layers of white stones (1 cm in layer thickness) with the same particle size as the marking layer, and the total weight was 29.58 kg. Black stones with a particle size between 15 and 25 mm were used to simulate the immediate roof with a height of 25 cm, and white stones with the same particle size were used as the marking layer, with a total weight of 61.63 kg. The initial state of the physical similarity model is shown in Figure 5.

4.2. Experiment Setup. To verify the rationality of the symmetrical sequential caving method, the tests conducted in this study compared both the top coal recovery rate and the gangue rate of the two different sequential caving approaches. The details of the coal caving sequence of the studied caving method are summarized in Table 2.

4.3. Results and Analysis. Development of the coal settlement curve reflects the changes in the top coal caving condition. The effectiveness of the selected caving method is evaluated by comparing the shape of the coal-rock settlement curve and the evolution of the remaining space of the two different interval coal caving methods. The coal-rock settlement curves of the two caving methods are shown in Figure 6.

It can be seen from Figure 6 that, following the principle of closing the door when gangue appears, the coal caving outlets 1#, 7#, and 15# were all opened at the same time. The coal-rock settlement curves of the coal caving openings 1# and 7# of Scheme 1 intersected with each other, forming a relatively symmetric area of pure coal. In Scheme 2, the coal-rock settlement curves of the coal caving openings 7# and 15# also intersected, but the coal area was inclined to the coal caving port 7#. According to the analysis in Section 4, the symmetrical coal area can contribute to the full development of the discharged body. Then, opening caving ports 4# and 11# and following the principle of closing the door when gangue appears, after closing the coal caving port, the coal-rock settlement curve of the interval is shown in Figure 7.

The coal-rock settlement curve generally descends after opening coal caving port 4. The coal-rock settlement curves between coal caving ports 1#–4# and 4#–7# form two identical coal areas depicted by the white-dotted line in Figure 7. However, the coal-rock settlement curves between coal caving ports 7#–11# and 11#–15# form two relatively symmetrical coal areas with different sizes, as shown by the red-dashed lines in Figure 7.

As the coal caving port continues to be opened, the coal-rock settlement curves continued to descend for the two schemes of sequential interval coal caving method. In Scheme 1, the coal-rock settlement curve always maintains symmetry above the support, which is beneficial to maximizing the top coal recovery and improving the management of subsequent workers. However, the size of the coal-rock settlement curve above the support becomes inconsistent in the subsequent caving process, due to the asymmetric coal-rock settlement curve formed after the first coal
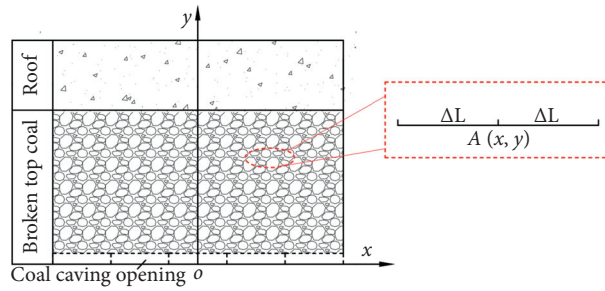
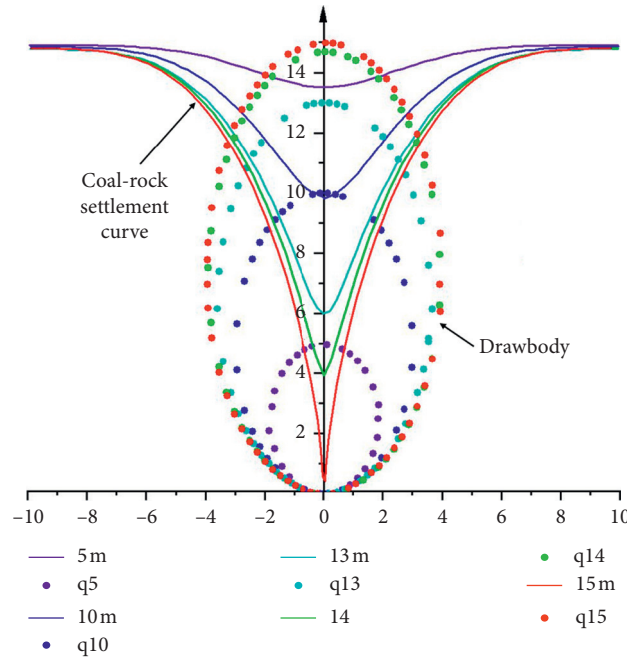FIGURE 2: Two-dimensional coordinate system along the working face.

FIGURE 3: Coal-rock settlement curves and the evolution of the caving body. The solid line indicates the evolution of the settlement path of the top coal particles, and the dotted line represents the evolution of the caving body during the coal caving process.

TABLE 1: Geometric parameters of the caving body.

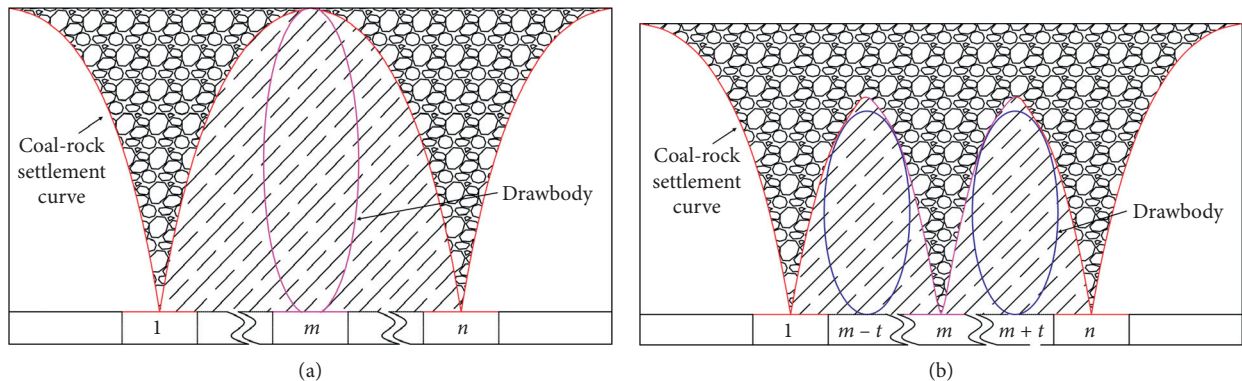| Height H	5	10	13	14	15
Width l	3.8	6	6.8	7.4	7.8
Eccentricity e	0.760	0.600	0.523	0.529	0.520

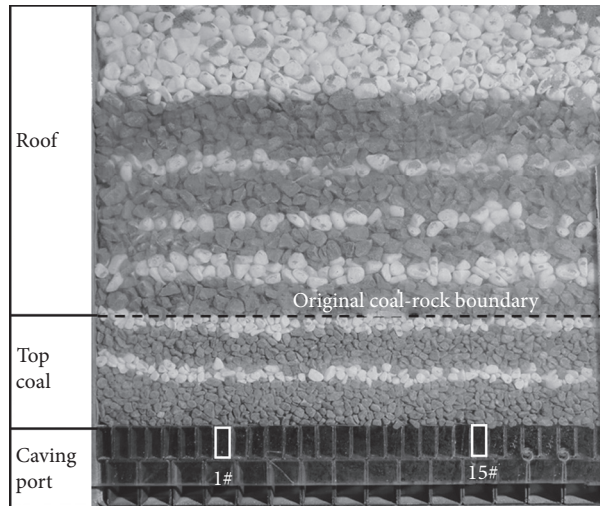FIGURE 4: Illustration of the sectional interval symmetrical coal caving method.

FIGURE 5: Initial state of physical similarity model.

TABLE 2: Caving sequences of different coal caving methods.

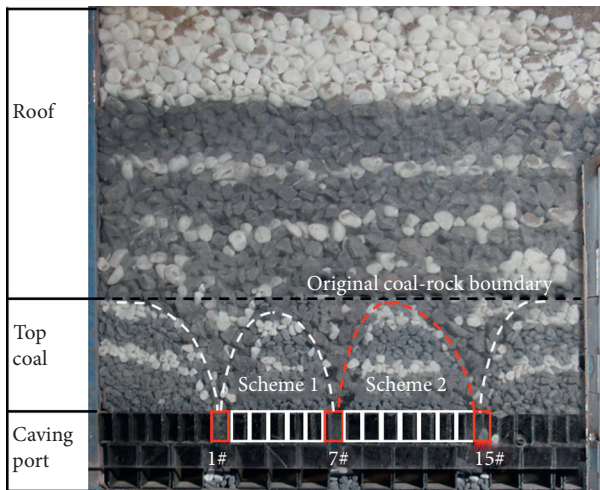| Serial number	Coal caving interval	Caving sequence of support
Scheme 1	7 supports	1–7#, 4#, 2–6#, 3–5#
Scheme 2	9 supports	7–15#, 11#, 3–7#, 2–8#, 4–6#

FIGURE 6: Coal-rock settlement curves for the two coal caving schemes (1#, 7#, and 15#).

caving in Scheme 2. The coal-rock settlement curve between the two coal caving openings turns symmetric as the coal caving interval decreases. Since the two coal areas are inconsistent in size above the support, the amount of caved coal is uneven during each caving, resulting in coal waste in the coal caving process and becomes difficult to control in practice.

5. Optimization of the Coal Caving Method at the 8222 Working Face

From the above analysis, the interval symmetrical caving method was adopted in the 8222 working face. The coal caving interval was set to be the width of 7 supports (8.75 m), and the symmetrical coal caving is adopted during each interval. The amount of caved top coal for two different caving methods is listed in Table 3. It can be shown that the largest amount of caved coal was observed at the support on both ends and in the middle, whereas the amount of caved coal gradually decreases for the remaining caving openings according to the opening sequence. Based on the field measurement, the top coal caving rate of the interval symmetrical caving is 95% with a caving time of 12,960 s; the top coal caving rate of traditional caving is 78% and the caving time is 10,502 s.

From the results of the caving volume of the interval symmetrical caving method, the amount of caved coal in the first two coal cavings accounts for 68% of the total caving volume, whereas the amount of caved coal in the last coal caving only accounts for 12%. To improve the caving efficiency and reduce the overall gangue content rate, excessive caving can be adopted during the first two cavings to shorten the coal caving time of the last caving. Compared with the traditional coal caving method, the interval symmetrical coal caving method increased the amount of caved coal by 21.7%, and the coal recovery rate increased by 17%. With the same coal caving interval, the caving time is shortened by 23.4% for the interval symmetrical caving, compared with the sequential caving. In general, the interval symmetrical coal caving always maintains the symmetry of the coal-rock settlement curve, enables a full development of the top coal caving bodies, effectively reduces coal losses during coal caving, and greatly improves the recovery rate of top coal. Moreover, the method is also convenient for on-site manual operation, which enhances the controllability of the coal caving process.
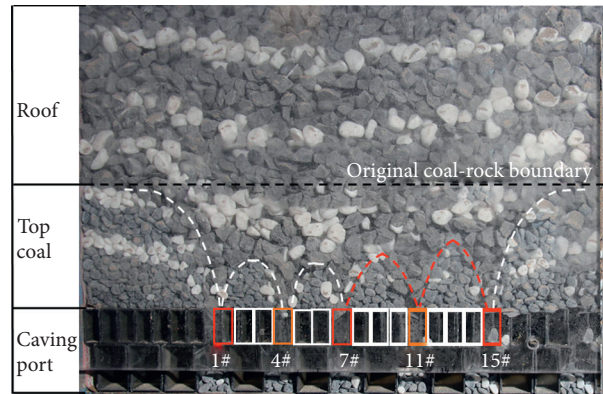
FIGURE 7: Coal-rock settlement curves for the two coal caving schemes (4# and 11#).

TABLE 3: Performance of different coal caving methods.

	Interval symmetrical caving	Single-port multiround sequential caving
Top coal discharge/kg	67.41	50.35
Recovery rate/%	95%	78%
Caving time/s	105024 s	129600 s

6. Conclusions

The following conclusions can be drawn from this study:

(1) The broken top coal discharges as the caving port opens in the fully mechanized caving mining. Although the movement of single particles in the caving process is random and disordered, the movement of a large number of particles generally obeys the normal distribution. By combining the statistical probability theory and random medium flow theory, the top coal caving body and coal-rock settlement curve equations are established along the direction of the fully mechanized caving working face. According to the derived equations, the settlement curves of the caving body and coal rock are axial symmetrical, and the foot of the coal-rock settlement curve decreases during the caving process; as the amount of coal caving increases, the shape of the caving body gradually changes from circular to elliptic.

(2) According to the coal settlement curve and the caving body equation described in this study, the interval symmetrical coal caving is found to be the optimal mining method. The coal caving interval L is defined as the sum of the radii of the coal and rock settlement curves formed by the two largest caving bodies. In practice, L is normally multiple times of the support number. The symmetrical coal-rock settlement curve also leads to a symmetrical subsequent caving space, which is conducive to a fully developed caving body. The caving sequence is symmetrical on both sides during each interval, which results in a consistent shape for the top coal caving body, and is beneficial to manual control

during the coal caving process for improved top coal recovery.

(3) Compared with the single-port multiround sequential caving method, the proposed interval symmetrical caving can increase the amount of caved coal and the top coal caving rate by 21.7% and 17%, respectively, reducing effectively the coal losses at the working face. In addition, the coal caving time is shortened by 23.4% with the same interval supports. According to the characteristics of interval symmetrical coal caving, the coal caving time may be shortened in the later stage of coal caving to improve the production efficiency of the working face.

Data Availability

The data used to support the findings of this study are available from the corresponding author upon request.

Conflicts of Interest

The authors declare that there are no conflicts of interest.

Acknowledgments

References

[1] S. Yan, Y. U. Lei, and Q. Liu, *Full-mechanized Top Coal Caving: Forming Mechanism and Application of "Combined Short Hanging Beam-Hinged Beam Structure"*, China Coal Industry Publishing House, Beijing, China, 2017.

[2] J. Wang, *The Theory and Technique on the Thick Coal Seam Mining*, Metallurgical Industry Press, Beijing, China, 2009.

[3] J. Wang and Q. Fu, "Low top-coal caving off the loose medium flow theory and application," *Journal of China Coal Society*, vol. 27, no. 4, pp. 337–341, 2002.

[4] J. Wang, Z. Li, Y. Chen, and H.-F. Zheng, "The experimental study of loose medium flow field on the longwall top-coal caving," *Journal of China Coal Society*, vol. 29, no. 3, pp. 260–263, 2004.

[5] J. Wu and Y. Zhang, "Study on the basic theory of longwall top-coal caving system," *Journal of China University of Mining and Technology*, vol. 27, no. 4, pp. 332–335, 1998.

[6] J. Zhang, *Simulation Study on the Three-Dimensional Caving Mechanism of Loose Top-Coal in Longwall Top-Cpal Caving Mining Panel*, China University of Mining & Technology, Beijing, China, 2017.

[7] D. Tian, S. H. I. Hao-yu, E.-J. Fu et al., "Study on relationship between coal caving step distance and top coal caving step distance and top coal caving recovery rate based on ellipsoid theory," *Coal Science and Technology*, vol. 43, no. 5, pp. 51–53, 2015.

[8] Q. Liu, M. Tu, and B. Fu, "Study on mining and caving ratio of fully mechanized top coal caving mining face affected to top coal recovery rate," *Coal Science and Technology*, vol. 41, no. 3, pp. 55–58, 2013.

[9] J. Wang, W. Chen, and J. Zhang, "Optimization study on drawing technique of longwall top-coal caving in extra-thick coal seam based on BBR system," *Coal Engineering*, vol. 48, no. 2, pp. 1–4, 2016.

[10] J. Wang, S. Yang, G. Huang et al., "Research on top coal tracker of fully mechanized top coal caving mining and measurement of top coal recovery rate," *Coal Science and Technology*, vol. 41, no. 1, pp. 36–39, 2013.

[11] J. Wang, J. Zhang, and C. Yi, "Research on technology of improving top-coal recovery in longwall top-coal caving mining based on BBR system," *Journal of Mining Science and Technology*, vol. 1, no. 1, pp. 38–48, 2016.

[12] J. Wang, W. Wei, and J. Zhang, "Theoretical description of drawing body shape in an inclined seam with longwall top coal caving mining," *International Journal of Coal Science & Technology*, vol. 7, no. 1, pp. 182–195, 2020.

[13] B.-X. Huang, C.-Y. Liu, and Q.-Y. Cheng, "Relation between top-coal drawing ratio and refuse content for fully mechanized top coal carving," *Journal of China Coal Society*, vol. 32, no. 8, pp. 789–793, 2007.

[14] B.-X. Huang, C.-Y. Liu, H. Niu et al., "Research on coal-gangue flow field character resulted from great cutting height fully mechanized top coal caving," *Journal of Mining & Safety Engineering*, vol. 25, no. 4, pp. 415–419, 2008.

[15] N. Zhang and C. Liu, "Arch structure effect of the coal gangue flow of the fully mechanized caving in special thick coal seam and its impact on the loss of top coal," *International Journal of Mining Science and Technology*, vol. 26, no. 3, pp. 593–599, 2016.

[16] S. Yan, H. Zhang, Q. Liu et al., "The theoretical study on loss rate of top coal and quantitative characteristics of piled waste," *Journal of China Coal Society*, vol. 34, no. 11, pp. 1441–1445, 2009.

[17] D. Zhu, Z. Chen, Y. Chang et al., "Study on top coal caving law of fully-mechanized top coal caving mining based on random medium theory," *Coal Science and Technology*, vol. 46, no. 1, pp. 167–174, 2018.

[18] B. Yu, D. Zhu, and Z. Chen, "Top-coal drawing law of LTCC mining based on stochastic medium theory," *Journal of China Coal Society*, vol. 42, no. 6, pp. 1366–1371, 2017.

[19] C. Liu, H. Li, Y. Zhou et al., "Method of synergetic multi-windows caving in longwall top coal caving working face," *Journal of China Coal Society*, vol. 44, no. 9, pp. 2632–2640, 2019.

[20] C. Liu, *Research on the Method of Synergetic Multi-Windows Top Coal Caving and the Mechanism of Coal-Gangue Identification in Longwall Top Coal Caving Working Face*, Henan University of Engineering, Zhengzhou, China, 2018.

[21] Y.-C. Zhang and F. Gao, *Congtinuum Mechanics Fundamentals and Application*, China University of science and Technology Press, Shanghai, China, 2019.

[22] Y. Ren, *Random Medium Drawing Theory and its Application*, Metallurgical Industry Press, Beijing, China, 1994.

[23] J. Cheng, S. Xie, and C. Pan, *Probability Theory and Mathematical Statistics*, Higher Education Press, Beijing, China, 2008.